ISBN: 978-605-68918-1-6

OEMT2018

FULL TEXT BOOK

3rd International Conference on Organic Electronic Material Technologies

Sep 20-22, 2018, İğneada - Kırklareli / TURKEY

ISBN: 978-605-68918-1-6

Book of Full Text of the 3rd International Conference on Organic Electronic Material Technologies (OEMT2018)

Editors

Dr. Burhan COŞKUN

Prof. Dr. Fahrettin YAKUPHANOĞLU

Published, 2018

oemt2018.klu.edu.tr

oemt2018@klu.edu.tr

FOREWORD

It is a pleasure for us to offer you this Book of Full Text of the 3rd International Conference on Organic Electronic Material Technologies (OEMT2018). Our goal was to create a platform that introduces the newest results on internationally recognized experts to local students and colleagues and simultaneously displays relevant Turkish achievements to the world. The positive feedback of the community encouraged us to proceed and transform a single event into a conference series. Now, OEMT2018 is honored by the presence of over 120 colleagues from various countries. We stayed true to the original OEMT2018 concept and accepted contributions from all fields of materials science and technology to promote multidisciplinary discussions. The focal points of the conference emerged spontaneously from the submitted abstracts: energy applications, advanced materials, electronic and optoelectronic devices, organic electronic materials, chemistry, physics, environmental science, medical science, applied and engineering science, computer simulation of organic structures, biomedical applications and advanced characterization techniques of nanostructured materials. Further fields of interest include e.g. new advanced and functional materials, advanced-functional composites, biomaterials, dielectric materials, optical materials, magnetic materials, organic semiconductors, inorganic semiconductors, electronic materials, graphene, and more.

Therefore, we hope that getting first-hand access to so many new results, establishing new connections and enjoying the İğneada, Kırklareli / TURKEY ambience will make you feel that your resources were spent well in OEMT2018.

Our warmest thanks go to all invited speakers, authors, and contributors of OEMT2018 for accepting our invitation, visiting Kırklareli and using OEMT2018 as a medium for communicating your research results.

We hope that you will enjoy the conference and look forward to meeting you again in one of the forthcoming **OEMT2019** event.

Best regards,
Chairmen's of Conference

Asst. Prof. Burhan COŞKUN

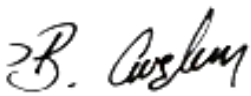

Prof. Dr. Fahrettin YAKUPHANOĞLU

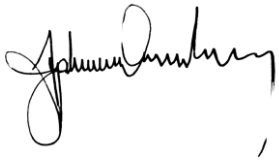

HONORARY PRESIDENT

Prof. Dr. Bülent ŞENGÖRÜR (Rector of Kırklareli University)

CONFERENCE PRESIDENT

Asst. Prof. Burhan COŞKUN (Kırklareli University)

Prof. Dr. Fahrettin YAKUPHANOĞLU (Fırat University)

ORGANIZING COMMITTEE

Fahrettin YAKUPHANOĞLU (Fırat University)

Burhan COŞKUN (Kırklareli University)

Berna AKGENÇ (Kırklareli University)

Cem S. ÇETİNARSLAN (Trakya University)

Cemile ÖZCAN (Kırklareli University)

Dilek BAKIRCIOĞLU (Trakya University)

Erol TÜRKEŞ (Kırklareli University)

Evren ÇAĞLARER (Kırklareli University)

Fatma KURŞUN (Kırklareli University)

H. Hale KARAYER (Kırklareli University)

Hatice ŞANLIDERE ALOĞLU (Kırklareli University)

Meryem ÇAMUR (Kırklareli University)

Murat ATEŞ (Namık Kemal University)

Mustafa ARSLAN (Kırklareli University)

Mümin Mehmet KOÇ (Kırklareli University)

Nihat AKKURT (Kırklareli University)

Nurdan KURNAZ YETİM (Kırklareli University)

Osman ÜNER (Kırklareli University)

Özlem AYTEKİN (Kırklareli University)

Tanju GÜREL (Namık Kemal University)

Serpil AKÖZCAN (Kırklareli University)

Yusuf DİLGİN (Çanakkale Onsekiz Mart University)

SCIENTIFIC COMMITTEE

Abdel Salam Hamdy MAKHLOUF, University of Texas / UNITED STATES

Abdelkarim MEKKI, King Fahd University of Petroleum Minerals / SAUDI ARABIA

Abdullah G. AL-SEHEMI, King Khalid University / SAUDI ARABIA

Abdülmecit TÜRÜT, Medeniyet University / TURKEY

Adem TATAROĞLU, Gazi University / TURKEY

Adrian M.T. SILVA, University of Porto / PORTUGAL

Afaf M. BABEER, Jazan University / SAUDI ARABIA

Ahmet EKİCİBİL, Çukurova University / TURKEY

Ahmed A. ALGHAMDI, King Abdulaziz University / SAUDI ARABIA

Ahmad UMAR, Najran University / SAUDI ARABIA

Ali GÜRSEL, International University of Sarajevo / BOSNIA

Ali Osman AYAŞ, Adıyaman University / TURKEY

Asmaa HENDI, King Abdulaziz University / SAUDI ARABIA

Atif MUHAMMED, King Saud University / SAUDI ARABIA

Attieh ALGHAMDI, King Abdulaziz University / SAUDI ARABIA

A. T. M. FARAG, Al-Azhar University / EGYPT

Bayram ÇETİN, Kırklareli University/ TURKEY

Berna BÜLBÜL, Balıkesir University / TURKEY

Birgül YAZICI, Çukurova University / TURKEY

Byeong-Kwon JU, Korea University / KOREA

Canan Aksu CANBAY, Fırat University / TURKEY

Christian WENGER, Innov. for High Performance Microelectronics / GERMANY

Chung GWIY-SANG, Ulsan University / KOREA

Darina ARSOVA, Institute of Solid State Physics / BULGARIA

Denis NIKA, Moldova University / MOLDOVA

Dilek KAZICI, Namık Kemal University/ TURKEY

Dionysios DIONYSIOU, University of Cincinnati / USA

Doğan KAYA, Çukurova University / TURKEY

D. S. PATIL, North Maharashtra University / INDIA

D. D. ZAITSEV, Moscow State University / RUSSIA

Ebru ŞENADIM TÜZEMEN, University of Cumhuriyet / TURKEY

Elias STATHATOS, Tecnological-Educational Institute of Patras / GREECE

Elizabeth BLACKBURN, University of Birmingham / UNITED KINGDOM

Emel PELİT, Kırklareli University/ TURKEY

Emin ÜNAL, Iskenderun Technical University / TURKEY

Emmanuel KOUDOUMAS, Technological Educational Institute of Crete / GREECE

Emmanuel KYMAKIS, Technological Educational Institute of Crete / GREECE

Erdinç KESKİN, Kırklareli University/ TURKEY

Esra ALVEROGLU, Istanbul Technical University / TURKEY

Evangelos VITORATOS, University of Patras / GREECE

Evren ÇAĞLARER, Kırklareli University/ TURKEY

E. Hassan ALY, Ain Shams University / EGYPT

Farid EL-TANTAWY, Suez Canal University / EGYPT

Faruk KARADAĞ, Çukurova University / TURKEY

Fatih SEMERCİ, Kırklareli University/ TURKEY

Feng Hua ZHANG, Nanyang Technological University / SINGAPORE

Filiz ŞENKAL, Istanbul Technical University / TURKEY

Fumihiko HIROSE, Yamagata University / JAPAN

F. AL-HAZMI, King Abdulaziz University / SAUDI ARABIA

F. M. AMANULLAH, King Saud University / SAUDI ARABIA

Gamze BARIM, Adıyaman University / TURKEY

Giorgio SBERVEGLIERI, University of Brescia / ITALY

Gökhan SAVAROĞLU, Osmangazi University / TURKEY

Gülfeza KARDAŞ, Cukurova University / TURKEY

Grzegorz KARCZEWSKI, Polish Academicy of Sciences / POLAND

Hakan USTA, Abdullah Gül University / TURKEY

Hülya Metin GÜBÜR, Mersin University / TURKEY

Hwan Kyu KIM, Korea University / KOREA

H. GHANEM, Fayoum University / EGYPT

Ibrahim. S. YAHIA, Khalid University / SAUDI ARABIA

İbrahim Yasin ERDOĞAN, Bingol University / TURKEY

Jingkun XU, Technology Normal University / CHINA

Jongeun RYU, Portugal University of California / USA

José M. KENNY, University of Perugia / ITALY

Juan Carlos Martinez-ANTON, Complutense University of Madrid / SPAIN

Kadir ERTÜRK, Namık Kemal University / TURKEY

Katerina POMONI, University of Patras / GREECE

Khasan S. KARIMOV, GIK Institute / PAKISTAN

Lee XINLIANG, Technische Universitat Dresden / GERMANY

Luis BANARES, Universidad Complutense de Madrid / SPAIN

Luisa TORSI, Universita Bari Aldo Moro / ITALY

Marco Antonio SCHIAVON, Universidade Federal de São João Del Rei / BRAZIL

Mark LAVER, University of Birmingham / UNITED KINGDOM

Metin ÖZDEMİR, University of Çukurova / TURKEY

Mikhail I. VASILEVSKIY, University of Minho / PORTUGAL

Mohamed BOUOUDINA, University of Bahrain / KINGDOM OF BAHRAIN

Mohammed Saleh AL-SALIHI, King Saud University / SAUDI ARABIA

Muhammad Hassan SAYYAD, Ghulam Ishaq Khan Institute / PAKISTAN

Muharrem KARAASLAN, Iskenderun Technical University / TURKEY

Mujdat ÇAĞLAR, Eskişehir Anadolu University / TURKEY

Murat ÖZER, Yıldız Technical University / TURKEY

Murat SOYLU, Bingöl University / TURKEY

Mustafa AKYOL, Adana Science and Technology University / TURKEY

Mustafa ERKOVAN, Sakarya University / TURKEY

Mustafa GÜNEŞ, Adana Science and Technology University / TURKEY

Nadia ABDEL-AAL, Suez Canal University / EGYPT

Nihal KUŞ, Anadolu University / TURKEY

Niyazi ÖZDEMİR, Fırat University / TURKEY

Nouredine SENGOUGA, Université de Biskra / ALGERIA

Omar A. ALHARTOMY, Tabuk University / SAUDI ARABIA

Osman DAYAN, Çanakkale Onsekiz Mart University / TURKEY

Oğuzhan AKGÖL, İskenderun Technical University / TURKEY

Ömer Suat TAŞKIN, İstanbul University / TURKEY

Önder METİN, Atatürk University / TURKEY

Panagiotis LIANOS, University of Patras / GREECE

Polycarpos FALARAS, Scientific Research Center / GREECE

Ram K. GUPTA, Pittsburg State University / UNITED STATES

Ramazan SOLMAZ, Bingöl University / TURKEY

Ramin YOUSEFI, Islamic Azad University / IRAN

Raşit TURAN, Middle East Technical University / TURKEY

Recep ZAN, Ömer Halisdemir University / TURKEY

Reem AL-WAFI, King Abdulaziz University / SAUDI ARABIA

Reem M. AL-TUWIRQI, King Abdulaziz University / SAUDI ARABIA

R. H. Al ORAINY, King Abdulaziz University / SAUDI ARABIA

R. O. OCAYA, University of the Free State / SOUTH AFRICA

Saad Hamad BINOMRAN, King Saud Univeristy / SAUDI ARABIA

Safar saaed Saad AL-GHAMDI, King Saud University / SAUDI ARABIA

Saliha ILICAN, Eskişehir Anadolu University / TURKEY

Salem EL-FAIFY, Khalid University / SAUDI ARABIA

Sarani ZAKARIA, Universiti Kebangsaan Malaysia / MALAYSIA

Savaş SÖNMEZOĞLU, Kahramanoğlu Mehmet Bey University / TURKEY

Seda BEYAZ, Balıkesir University / TURKEY

Sencer Süreyya KARABEYOĞLU, Kırklareli University/ TURKEY

Serap ŞENTÜRK DALGIÇ, Trakya University / TURKEY

Serdar SARIÇİFTÇİ, Johannes Kepler Linz University / TURKEY

Seyfettin ÇAKMAK, Süleyman Demirel University / TURKEY

Sezai ALAGÖZ, Cumhuriyet University / TURKEY

Sinem ŞİMŞEK, Kırklareli University/ TURKEY

Subhash CHAND, National Institute of Technology / INDIA

Şükrü KARATAŞ, Kahramanmaraş Sütçü İmam University / TURKEY

S. MANSOURI, University of Gabès / TUNUSIA

S. WAGEH, Menoufia University / EGYPT

Tamer ABDALLAH, Ain Shams University / EGYPT

Türker TÜZEMEN, Cumhuriyet University / TURKEY

Yasemin ÇAĞLAR, Eskişehir Anadolu University / TURKEY

Yassine SLIMANI, University of Dammam / SAUDI ARABIA

Yelda YALÇIN GÜRKAN, Namık Kemal University / TURKEY

Young HEE, Sungkyunkwan University / SOUTH KOREA

Yusuf Al-TURKI, King Abdulaziz University / SAUDI ARABIA

Zafer ŞERBETÇİ, Bingöl University / TURKEY

Zeyad A. ALAHMED, King Saud University / SAUDI ARABIA

Z. LIU, Peking University / CHINA

V. DOROZHKIN, Kudrinskaja Moscow / RUSSIA

Walid Tawfiq YOUNES, King Saud University / SAUDI ARABIA

Vasilios KARANIKOLAS, Patras University / GREECE

Witold Daniel DOBROWOLSKI, Polish Academicy of Sciences / POLAND

Wojtek WLODARSKI, RMIT University / AUSTRALIA

Wolfgang ENSINGER, Technische Universität Darmstadt / GERMANY

W. Aslam FAROOQ, King Saud University / SAUDI ARABIA

3rd International Conference on Organic Electronic Material Technologies (OEMT2018)
Sep 20-22, 2018, Kırklareli / TURKEY

GREEN BIO-CHEMISTRY APPROACH FOR FABRICATION OF GO: Cu/p-Si DEVICE APPLICATION

T. Çakıcı[1], M. Özdal[2], and Mutlu Kundakcı[3]

[1]*Department of Electrical and Energy, Ispir Hamza Polat Vocational School of Higher Education, Ataturk University, Erzurum, Turkey*
[2]*Department of Biology, Atatürk University, Erzurum, Turkey*
[3]*Department of Physics, Atatürk University, Erzurum, Turkey*

E-mail: tuba.cakici@atauni.edu.tr

Abstract

Microbial production of nanoparticles is a green chemistry approach that interconnects nanotechnology and microbial biotechnology. Some bacteria are unique to tolerate high chemical concentration. Graphene oxide nanoparticles (GO:Cu-NPs) have been synthesized by using special bacteria under aerobic conditions. The synthesized GO:Cu-NPs solution dropped on glass and p-Si substrates and then they annealed. Optical properties of the GO:Cu thin film have been investigated by UV-Vis. Spectrophotometer method. Fabricated GO:Cu/p-Si structure characterized X-ray diffraction (XRD) and Field-emission scanning electron microscopy (FE-SEM) with energy dispersive X-ray spectroscopy (EDS) techniques. Some electrical parameters of GO:Cu/p-Si structure are investigated with Current-Voltage (I-V) measurements at room temperature.

Keywords: GO:Cu, green chemistry, thin film, nanoparticles

1. INTRODUCTION

Plants, bacteria, fungi and algae are used for green synthesis of metallic nanoparticles. Microbial synthesis of nanoparticles is a green chemistry approach that interconnects nanotechnology and microbial biotechnology. It is advantageous over chemical and physical methods as it is safe, simple, eco-friendly, cheap, reproducible, and often results in more stable materials [1-2].

Copper nanoparticles have various properties such as optical, catalytic, anti-bacterial, anti-fungal and anti-cancerous ones [3-4]. GONPs have been proposed to be incorporated into heavy metal detecting sensors [5], electrodes [6], and biomedical applications [7]. The excellent tensile and compressive strengths, high hardness and good electrical conductivity has been obtained simultaneously in the RGO-Cu composites [8]

It is well known that nanoparticles melt at lower temperature than corresponding bulk material [9]. However, significant reduction in melting temperature is observed on sub-10 nm nanoparticles only. This property allows a lower thermal energy budget during annealing of nanoparticle-based films. It is worth noting that annealing is a critical process in the fabrication of high quality films even when vacuum deposition techniques are used [10].

It is very difficult to fabricate directly high-quality GO:Cu thin films by using chemical and physical methods based on the homogeneous nucleation and growth mechanism. We fabricated GO:Cu nanoparticles via microbial biosynthesized method and also we sintered these particles as a thin film. In this study, we report firstly ecofriendly approach microbial biosynthesized GO:Cu nanoparticles used as metal semiconductor interlayer thin films. Thus, we fabricated GO:Cu/p-Si heterojunction.

2. MATERIAL AND METHODS

Au/ GO:Cu /p-Si/Al and device structures used in this study were fabricated on p-type Si wafer with (100) surface orientation and glass. The p-Si wafer Si was sliced to 15mm×10mm pieces. Then they were cleaned chemically. Finally, the substrates were rinsed thoroughly in de-ionized water with resistivity of 18 MΩ cm. After this process, we prepared one of these substrates for the fabrication of the Au/GO:Cu/p-Si/Al diode. We formed an ohmic contact thermally evaporating Al onto the backside of this substrate in a vacuum system with a pressure of 1×10^{-5} Tor. To obtain low resistivity back ohmic contact, p-Si/Al structure was annealed at about 550 ^{o}C for 3 min in flowing dry nitrogen ambient.

P. aeruginosa strain OG1 [11] was cultured in the Tryptic Soya Broth for 24 h at 150 rpm and 30°C. The cell suspension (100 µl, OD600 1) was inoculated into the Luria Bertani Broth medium (20 mL) containing 1 mM $CuSO_4$, 1 mM Graphene oxide and 0.5 mM $CuSO_4$ + 0.5 mM Graphene oxide. All the nanoparticles biosynthesis was conducted at 30 °C for a period of 96 h on rotating shaker (150 rpm) at dark conditions. Control experiments without $CuSO_4$ and Graphene oxide were performed simultaneously.

GO:Cu nanoparticles particles were removed from the cellular material by a procedure modified from [12]. This solution of GO:Cu nanoparticles were dropped on p-Si and glass substrates (50cc solution) and they were dried on hot plate at 300^{o}C for 60 min. Thus, GO:Cu thin films were obtained. At the end, another Au metal was again directly evaporated on the GO:Cu thin films surfaces as rectifying contact with shadow mask cylindrical geometry of 1.00 mm diameter in vacuum pump (1.5 10^{-5} Torr). Au/ GO:Cu /p-Si/Al device were fabricated.

After completing the fabrication of the samples, we performed the characterization of the thin film samples. We determined the optical properties, crystal structures, surface morphology, and qualitative analysis of GO:Cu thin films by using UV-VIS spectrometer (Perkin-Elmer Lambda 2S UV-Visible spectrometer), X-rays diffractometer (XRD Bruker D2, Kα, λ=1.54 A, Scanning angle 70^{o}), Scanning electron (FE-SEM) (Sigma 300 Model Zeiss Gemini) and electron diffusion X ray (EDX associated with FE-SEM), respectively. Electrical properties of the Au Au/ GO:Cu /p-Si/Al device were obtained by Keithley 2400 Picoammeter/Voltage Source meter.

3. RESULTS AND DISCUSSION

The band gap energy of GO:Cu thin film have been determined as 2.25 eV by the extrapolation of the linear region on the energy axis (hυ) as shown in Fig. 1. The Eg value is calculated using αhυ=A (hυ-Eg)^{n} plot by extrapolation of the linear region of the curve.

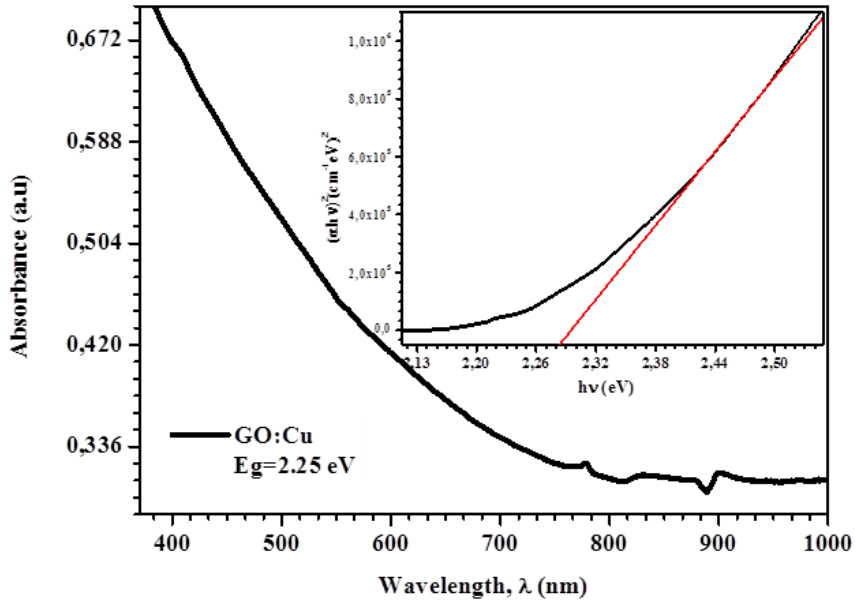

Figure 1. $(ah\upsilon)^2$ versus hυ and variation of optical absorbance versus the wave-length of incident photons of the as-deposited GO:Cu thin film at room temperature.

Table 1 shows the structural parameters of GO:Cu thin film on p-Si substrate. According to XRD pattern of GO:Cu peak at about 28.27° belongs to (002) plane of graphide, and it has 0.38 nm interlayer distance. The strong peak at about 9.36° shows (002) plane of graphene oxide with 0.94 nm interlayer distance. The increase at the interlayer distance of the GO can be attributed to presence of the oxygen-containing functional groups and some other structural defects [13-14].

The peak of 31.31 2θ angle corresponds to CuO cubic phases (JCPDS no. 05-0661) [15-17]. The strongest peaks and 2θ angles corresponds to and p-Si (100) crystallization.

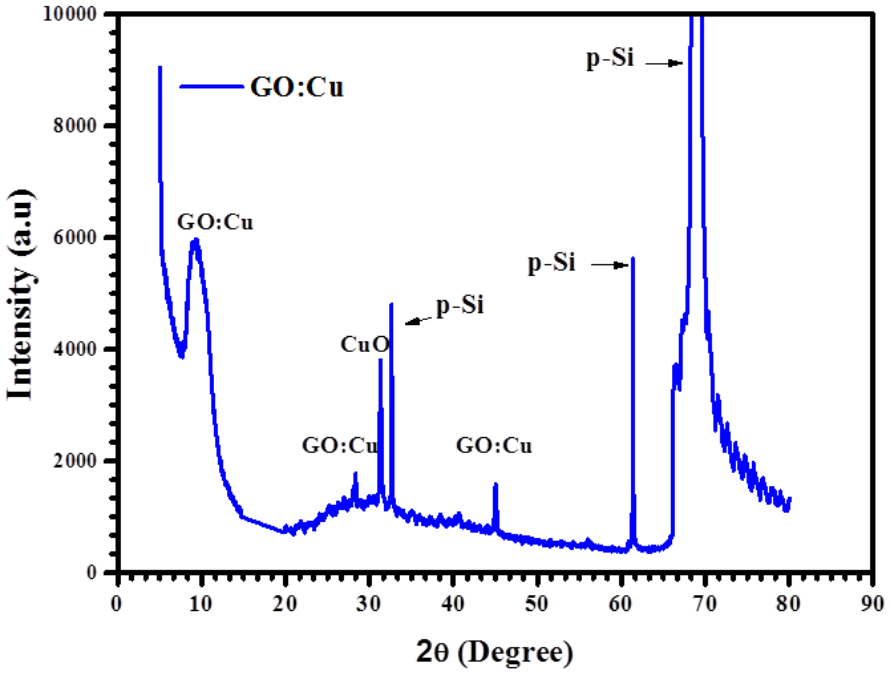

Figure 2. XRD patens of the CuSe thin film grown on p-Si substrate

Table 1. The kinetic parameters of the glow peak about 501 K measured by 2 $K.s^{-1}$ of GAG:Ce phosphor attained by PS methods.

(hkl)	FWHM	FWHM (rad)	Intensity (a.u.)	2θ° (Observed)	d-values (nm)	Crystal size (D) nm	Crystal
(002)	3.58	0.062	4745.10	9.36	0,94	2,23	GO
(101)	0,38	0.006	383,16	28.27	0,35	21,60	Graphite
(110)	0.20	0.004	2467.33	31.31	0.29	41.51	CuO
(200)	0.255	0.004	790.87	45.02	0.20	33.73	GO

Fig 3 (a) shows the FE-SEM image of prepared GO:Cu/p-Si structure, it can be observed that the GO:Cu thin films are uniform and cover the substrate well. The surface morphology and film composition of the prepared sample was obtained from the FE-SEM and EDX analysis techniques. Fig. 3 (a) displays FE-SEM images of GO:Cu thin film grown on p-Si substrate. The image clearly indicates graphene oxide layers [18]. As seen from Fig. 3 (a) GO:Cu FE-SEM image exhibits sheeted structure with nanometer scale and distribution of the crystallites are very uniform and homogeneous.

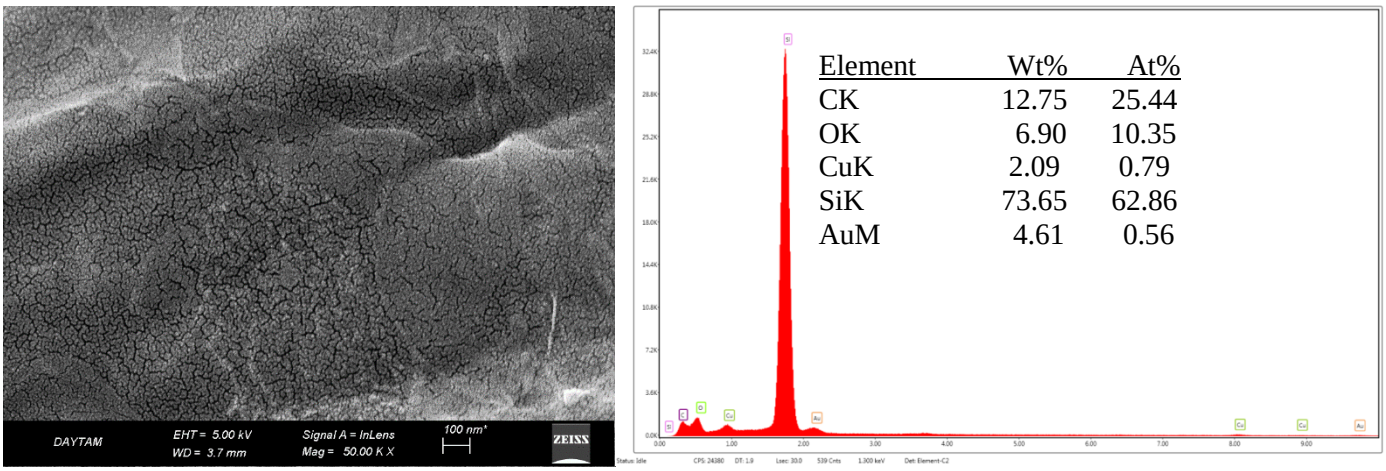

(a) **(b)**

Figure 3. FE-SEM image and EDX spectrum of GO:Cu/p-Si structure a) FE-SEM image with magnification scale (100nm) b) EDX spectrum.

Fig. 4 presents I-V characteristics graph of Au/GO:Cu/p-Si/Al devices for dark room conditions. The devices exhibit good rectifying properties. According to the thermionic emission theory, the current, I, is expressed as follows:

$$I = \underbrace{AA^{*}T^{2}exp\left(\frac{q\Phi_{B}}{nkT}\right)}_{I_0}\left[exp\left(\frac{qV}{nkT}\right) - 1\right] \quad (1)$$

where I_0 is saturation current which is obtained by the intercept of the linear region at the I-V graph. Au/GO:Cu/p-Si/Al devices have $5.20\times E^{-10}$ A saturation current values at room temperature. Ideality factor and barrier height values of Au/GO:Cu/p-Si/Al l structure are 1.72 and 0.81 eV, respectively. Higher ideality factor values in study can be attributed to barrier inhomogeneity and non-uniform distribution of the carriers in the interface [19].

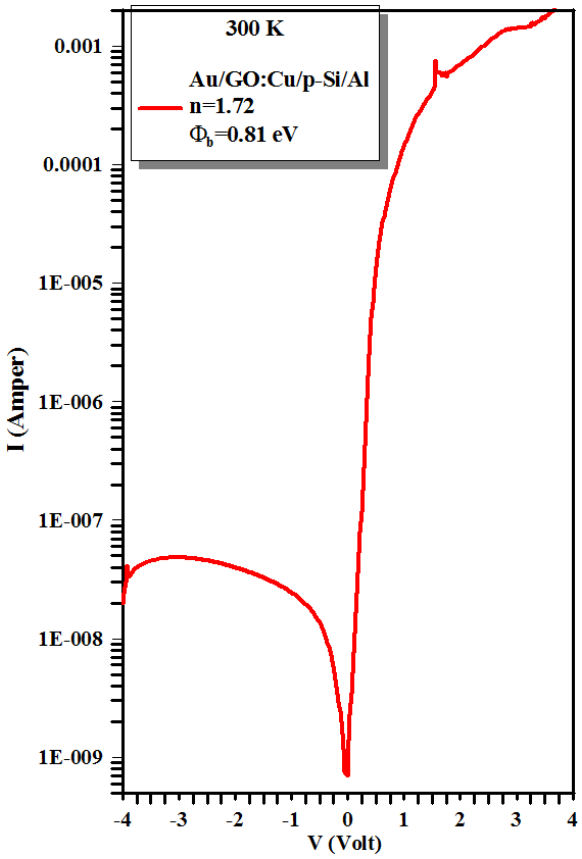

Figure 4.. I-V characteristic of Au/GO:Cu/p-Si/Al structure

4. CONCLUSION

We synthesized GO:Cu nanoparticles via microbial green method and used these as a interfacial thin film on Au/GO:Cu/p-Si/Al device structure. GO:Cu thin film obtained on p-Si and glass substrates. Thin film properties were investigated UV-Vis. Spectrophotometer method, XRD, FE-SEM with EDS and these results showed that GO:Cu thin film were obtained successfully. XRD graph indicates that GO:Cu thin film have polycrystalline structure. FE-SEM image revealed that the GO:Cu thin film has nano sheet structure and the structures composed to expected elements checked with EDS. The GO:Cu thin film inserted between the Au metal and p-type Si, and Au/GO:Cu /p-Si/Al device was obtained. The device tested by I-V measurements under dark. The obtained device has 1.72 ideality factor and 0.81 eV barrier height according to thermionic emission theory. Device has good and stabile rectifying properties. It can be considered as photodiode in industrial applications

REFERENCE

[1] Shah, M., Fawcett, D., Sharma, S., Tripathy, S. K., & Poinern, G. E. J.. Green synthesis of metallic nanoparticles via biological entities. Materials, 8(11), 7278-7308, 2015.

[2] Hulkoti, N. I., Taranath, T. C., Biosynthesis of nanoparticles using microbes—a review. Colloids and Surfaces B: Biointerfaces, 121, 474-483. 2014.

[3] Khanna, P. K., Gaikwad, S., Adhyapak, P. V., Singh, N., & Marimuthu, R., Synthesis and characterization of copper nanoparticles. Materials Letters, 61(25), 4711-4714. 2007.

[4] Rasool, U., Hemalatha, S., Marine endophytic actinomycetes assisted synthesis of copper nanoparticles (CuNPs): Characterization and antibacterial efficacy against human pathogens. Materials Letters, 194, 176-180, 2017.

[5] Li J.-L., Hou X.-L., Bao H.-C., Sun L., Tang B., Wang J.-F., Wang X.-G., and Gu M. Graphene oxide nanoparticles for enhanced photothermal cancer cell therapy under the irradiation of a femtosecond laser beam. J. Biomed. Mater. Res. 2013b.

[6] Chen D., Feng H.B., and Li J.H.. Graphene oxide: Preparation, functionalization, and electrochemical applications. Chem. Rev. 112, 6027, 2012a.

[7] Li M., Gou H., Al-Ogaidi I., Wu N. Nanostructured sensors for detection of heavy metals: A review. ACS Sustain. Chem. Eng. 1, 713, 2013a.

[8] Wang, L., Yang, Z., Cui, Y., Wei, B., Xu, S., Sheng, J., Fei, W. Graphene-copper composite with micro-layered grains and ultrahigh strength. Scientific reports, 7, 41896, 2017.

[9] Hankare, P.P., Khomane, A.S., Chate, P.A., Rathod, K.C., Garadkar, K.M., Journal of Alloys and Compounds 469, 478, 2009.

[10] Malik, M. A., O'Brien, P., & Revaprasadu, N. A novel route for the preparation of CuSe and $CuInSe_2$ nanoparticles. Advanced Materials, 11(17), 1441-1444, 1999.

[11] Ozdal, M., Ozdal, O.G., Algur, O.F., *Pol J Microbiol*, *65*(1), 63-68, 2016a.

[12] Oremland RS, Herbel MJ, Switzer-Blum J, Langley S, Beveridge TJ, Ajayan PM, Sutto T, Ellis AV, Curran S Structural and spectral features of selenium nanospheres produced by Se-respiring bacteria. Applied and Environmental Microbiology, 70(1), 52-60, 2004.

[13] Wang, X., Zhi, L., Müllen, K., Nano Lett. 8 323–327, 2008.

[14] Karteri, İ., Güneş, M., J. Mater. Sci. Mater. Electron. 27, 11502–11508, 2016.

[15] Balamurugan, J., Thanh, T. D., Heo, S. B., Kim, N. H., & Lee, J. H., Novel route to synthesis of N-doped graphene/Cu–Ni oxide composite for high electrochemical performance. *Carbon*, *94*, 962-970, 2015.

[16] Wang, Y., Wen, Z., Zhang, H., Cao, G., Sun, Q., & Cao, J. CuO Nanorods-Decorated Reduced Graphene Oxide Nanocatalysts for Catalytic Oxidation of CO. *Catalysts*, *6*(12), 214, 2016.

[17] Wang, Y., Wen, Z., Zhang, H., Cao, G., Sun, Q., & Cao, J. CuO Nanorods-Decorated Reduced Graphene Oxide Nanocatalysts for Catalytic Oxidation of CO. *Catalysts*, *6*(12), 214, 2016.

[18] Karteri, İ., Güneş, M., J. Mater. Sci. Mater. Electron. 27, 11502–11508, 2016.

[19] Çakıcı, T., Güzeldir, B., Sağlam, M., Temperature dependent of electrical characteristics of Au/n-GaAs/In Schottky diode with In_2S_3 interfacial layer obtained by using spray pyrolysis method, Journal of Alloys and Compounds 646, 954-965, 2015.

BIOSYNTHESIS OF GO: SE NANOPARTICLES USING AS THIN FILMS AND GO: Se /p-Si DEVICE APPLICATION

T. Çakıcı[1], M. Özdal[2],and Mutlu Kundakcı [3]

[1]*Department of Electrical and Energy, Ispir Hamza Polat Vocational School of Higher Education, Ataturk University, Erzurum, Turkey*
[2]*Department of Biology, Atatürk University, Erzurum, Turkey*
[3]*Department of Physics, Atatürk University, Erzurum, Turkey*

E-mail: tuba.cakici@atauni.edu.tr

Abstract

In recent years, researchers are concentrating on use of microorganisms as “nanofactories” for production of metal nanoparticles. In this research simple, ecofriendly, low cost and a new approach are used for deposition GO:Se thin film. Graphene oxide nanoparticles (GO:Se-NPs) have been synthesized by using *special bacteria* in Luria-Bertani medium under aerobic conditions. Biosynthesized GO:Se-NPs solution dropped on glass and p-Si substrates and then they annealed for the formation thin film structure. Band gap of GO:Se thin film investigated by using UV-Vis. Spectrophotometer method. Obtained GO:Se/p-Si structure characterized X-ray diffraction (XRD) and Field-emission scanning electron microscopy (FE-SEM) with energy dispersive X-ray spectroscopy (EDS) Some electrical parameters of GO:Se/p-Si structure are investigated with Current-Voltage (I-V) measurements at room temperature.

Keywords: GO: Se, thin film, nanoparticles, biosynthesis

1. INTRODUCTION

In recent years, nanoparticles can be produced using different approaches including chemical, physical, and biological. Chemicals used for nanoparticles synthesis are toxic and lead to non-environmentally friendly by products [1]. Biological approaches are easy, eco-friendly and low cost. Thus, there is an increasing demand for "green nanotechnology" [2]. Bacteria, fungi, algae and plants can provide a number of metal or metal containing nanoparticles.

Graphene is very popular material and studied by researchers to find its new technological application areas because it has very good electrical, optical and mechanical properties [3]. Especially, the oxide form of the graphene which is called graphene oxide (GO) has controllable band gap, high transmittance and governable conductivity close to insulators [4,5]. Due to these properties of the GO, it has been employed as interfacial layer in the metal-semiconductor heterojunctions in recently. Kocyigit et al. [6] researched GO-SiO_2 composites were inserted between Al metal and p-type Si semiconductor by spin coating technique, and they obtained Al/GO-SiO_2/p-type Si device. They revealed photodiode characteristic from IV measurement under dark, room and illumination conditions. Kaya et al. [7] investigated Au/GO-dopedPrBaCoO nanoceramic/n-Si capacitor in detail by impedance spectroscopy method in the wide frequency range of 1 kHz to 1 MHz at room temperature. Mekki et al. [8] studied the GO and coumarin as composite in the interface of Au metal and p-Si for photodiode applications..

As can be seen from above the investigations that the researchers studied separately the GO and SiO_2 as interfacial layer between the metal and semiconductor but in this study, it is firstly fabricated GO:Se structure as an interlayer. Also, GO:Se nanoparticles are firstly synthesized by eco-friendly biological method with bacteria. Furthermore they are sintered and inserted between the Au metal and p type semiconductor as interfacial layer and then, characterized the device via I-V measurements.

2. MATERIAL AND METHODS

Au/GO:Se/p-Si/Al device structure used in this study were fabricated on phosphor doped (n-type) Si wafer with (100) surface orientation and glass. Before the fabrication of the Au/GO:Se/p-Si/Al structure, the p-Si wafer Si was sliced to 15mm×10mm pieces. Then they were degreased for 10 min, acetone and methanol in an ultrasonic cleaner, consecutively and then etched in a sequence of H_2O:H_2O_2:HNO_3 (6:1:1) at 60ºC, 20% HF, a solution of H_2O:H_2O_2: HCl (6:1:1) at 60ºC, 20% HF. After that the wafer was rinsed thoroughly in de-ionized water with resistivity of 18 MΩ cm. After the surface cleaning of wafer, the Al was thermally evaporated onto the whole backside of the p-Si wafer at a pressure of 1×10^{-5} Torr in vacuum

pump system. To obtain low resistivity back ohmic contact, p-Si/Au structure was annealed at about 550 ^{o}C for 3 min in flowing dry nitrogen ambient.

To obtain GO:Se nano particles in a solution, was synthesized the selected special bacteria [2-9] was cultured in the Tryptic Soya Broth at 150 rpm and 30 °C. The bacteria were cultured for 24 h and used as inoculum. The cell suspension (100 µl, OD_{600} 1) was inoculated into the Luria Bertani Broth medium (20 mL) containing 1 mM SeO_3^{2-}, 1 mM graphene oxide and 0.5 mM SeO_3^{2-} + 0.5 mM graphene oxide. All the nanoparticles biosynthesis was conducted at 30 °C for a period of 96 h on rotating shaker (150 rpm) at dark conditions. Control experiments without SeO_3^{2-} and Graphene oxide were performed simultaneously.

Then recovery of Se NPs from the culture, nanoparticles particles were removed from the cellular material by a procedure modified from Oremland et al. [1]. Briefly, cell suspensions containing Se (0) were sonicated in an ultrasonic bath (Elma/S30) at 100 W for 2 min and centrifuged at 10,0009g for 10 min. Pellets were resuspended, sonicated, and centrifuged (10,0009g) sequentially in SDS 0.1 %/ 1 M NaOH and finally the cleaned Se (0) was suspended in distilled water. Se (0) nanoparticles were analyzed by scanning electron microscopy (SEM). The other Np GO and GO:Se were removed from the cellular material.

The final solution was filtered, washed with DI water and the GO:Se NP are obtained in a solution. This solution of GO:Se NP was coated on the front surface of the n-Si and glass substrates by dropping 50cc solution and they were dryied on hot plate at 65^{o}C for 60 min. At the end, another Au metal contact was again evaporated on the GO:Se thin film surface as rectifying contact. Thus, the Au/GO:Se/p- Si device was obtained.

After completing the fabrication of the samples, we performed the characterization of the thin film samples. We determined the optical properties, crystal structure, surface morphology, qualitative analysis and electronic properties of these device by using UV-VIS spectrometer (Perkin-Elmer Lambda 2S UV-Visible spectrometer), X-rays difractometer (XRD Bruker D2, K_{α}, λ=1.54 A, Scanning angle 70^{o}), scanning electron (FE-SEM) (Sigma 300 Model Zeiss Gemini) and electron diffusion X ray (EDX associated with FE-SEM) and, Keithley 2400 Picoammeter/Voltage Source meter, respectively.

3. RESULTS AND DISCUSSION

Fig. 1 shows the optical absorption spectra for GO:Se thin film. To calculate the optical band gap energy values we used the transmittance spectra of these samples. The optical band gap energy (Eg) values are determined from the equation:

$$ah\upsilon = A\,(h\upsilon - E_g)^{n} \quad (1)$$

where A is a constant related to the effective masses of charge carriers, h is the Planck constant, Eg is the band gap energy, hυ is the energy of the photon, and n is the exponent that depends on the nature of the optical transition (n = 0.5 and 2 for direct and indirect transition, respectively) [10]. To find the band gap energy, Eg, of GO:Se thin film samples, we applied the extrapolation method and the intercept of the extrapolation to zero absorption with photon energy axis gave the values of the direct energy gap Eg. As seen from Fig.1, the intercepts corresponding to the band gap energy of GO:Se thin film sample is 1.70 eV.

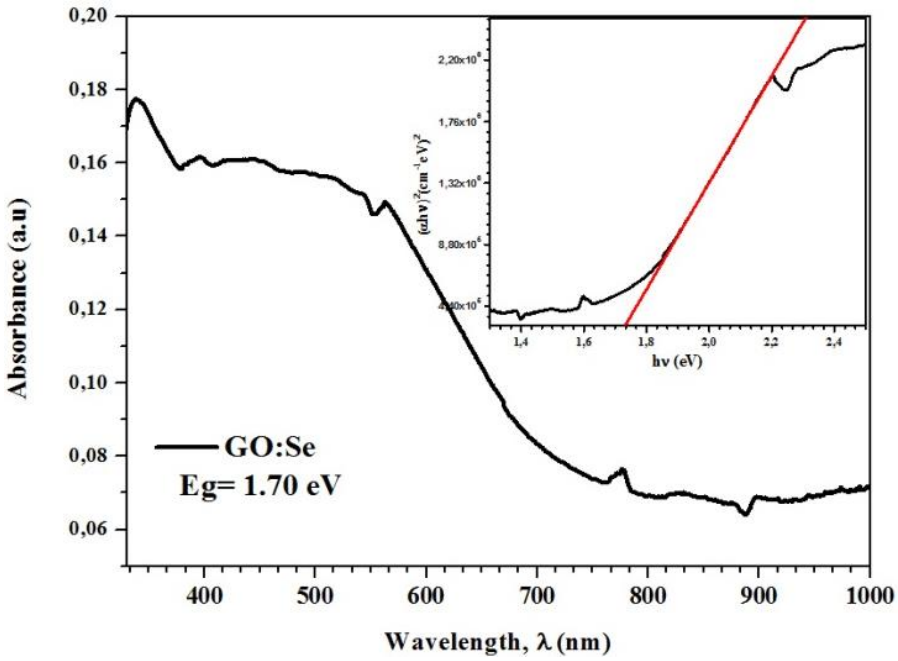

Figure 1. (ahυ) 2 versus hυ and variation of optical absorbance versus the wave-length of incident photons of the as-deposited GO:Se thin film at room temperature.

Fig. 2 shows the XRD patterns of the GO:Se/p-Si structure. The (h,k,l) diffraction planes of the mentioned XRD peaks of pure GO:Se thin film has also been labeled in Fig. 2. GO:Se thin films are found to have polycrystalline nature. Crystallite size can be evaluated by using Debye-Scherrer's formula.

$$D = \frac{0{,}9\lambda}{\beta \cos\theta} \quad (2)$$

where λ is the wavelength of the X-ray (λ=1.5405 Å) and β is the full width at half maximum (FWHM) of the considered peak and θ the corresponding Bragg's angle.

Table 2 shows the structural parameters of GO:Se thin film on the p-Si substrate The strongest peak and 2θ angles corresponds to and p-Si (100) cubic crystallization. According to XRD pattern of GO:Se, the weak peak at about 23.11° belongs to (002) plane of graphene oxide, and it has 0.38 nm interlayer distance. The strong peak at about 9.14° shows (002) plane of graphene oxide with 0.97 nm interlayer distance. The increase at the interlayer distance of the GO can be attributed to presence of the oxygen-containing functional groups and some other structural defects [11-12].

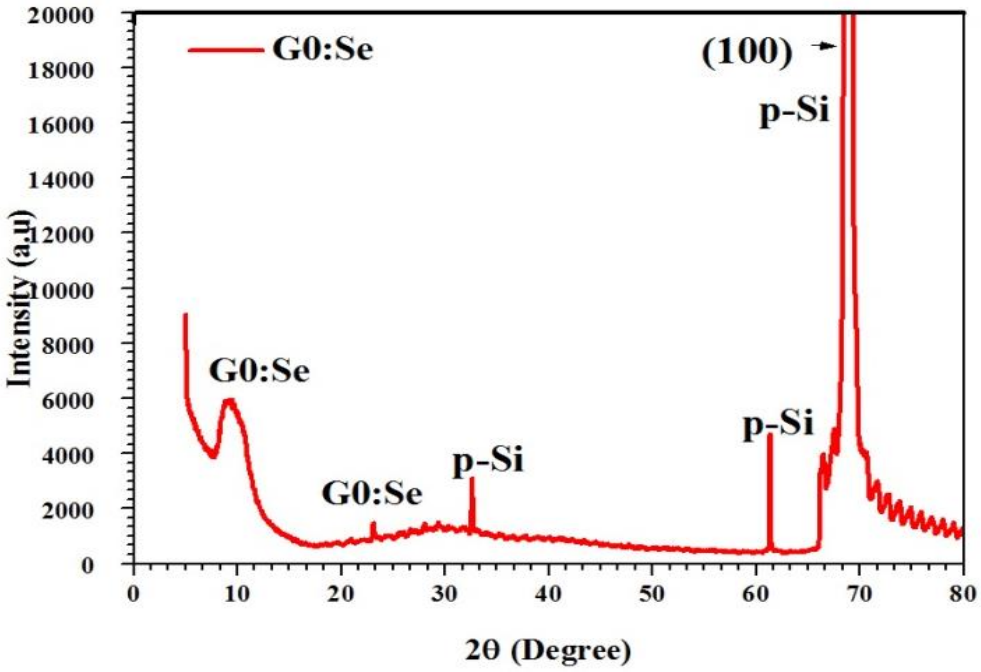

Figure 2. XRD pattern of the GO:Se /p-Si structure

Table 2. Crystal structural parameters of GO:Se/p-Si structure

(hkl)	FWHM	FWHM (rad)	Intensity (a.u.)	2θ° (Observed)	d-values (nm)	Crystal size (D) nm
(002)	3.58	0.062	4745.10	9.36	0,94	2,23
(002)	0.165	0.003	559.12	23.11	0,38	49,15

The surface morphology and film composition of the prepared sample was obtained from the FE-SEM and EDX analysis techniques. Fig. 3 (a) displays FE-SEM images of GO:Se thin film grown on p-Si substrate. The image clearly indicates graphene oxide layers [13]. As seen from Fig. 3 (a) GO:Se FE-SEM image exhibits sheeted structure with nanometer scale and distribution of the crystallites are very uniform and homogeneous.

The typical EDX spectrum shown in Fig. 3 (b) indicates the composition information on ingredients in the GO:Se/p-Si structure. As seen from Fig. 3 (b), the elements taking place in the composition of GO:Se/p-Si structure and their percentages obtained from EDX measurements are given in the list. As seen from this list, the elemental composition of the structure is consisted of O, Se, C and Si elements. Elements like O, Se, C and Si are the elements to take place in the composition of the GO:Se/p-Si structure.

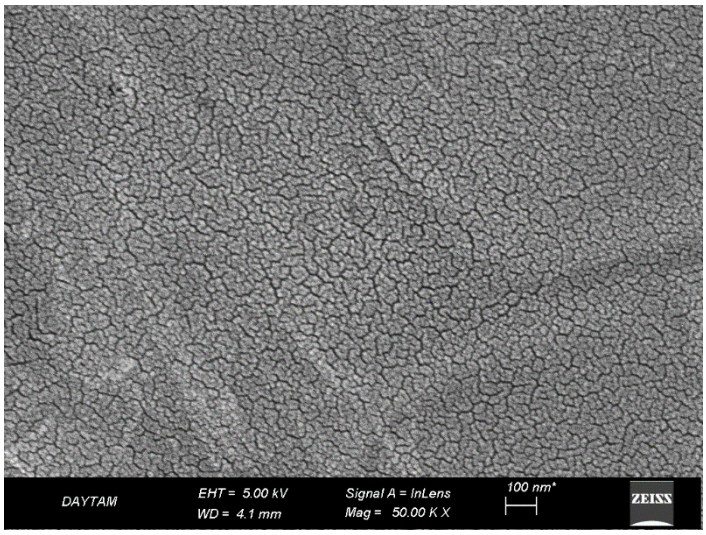

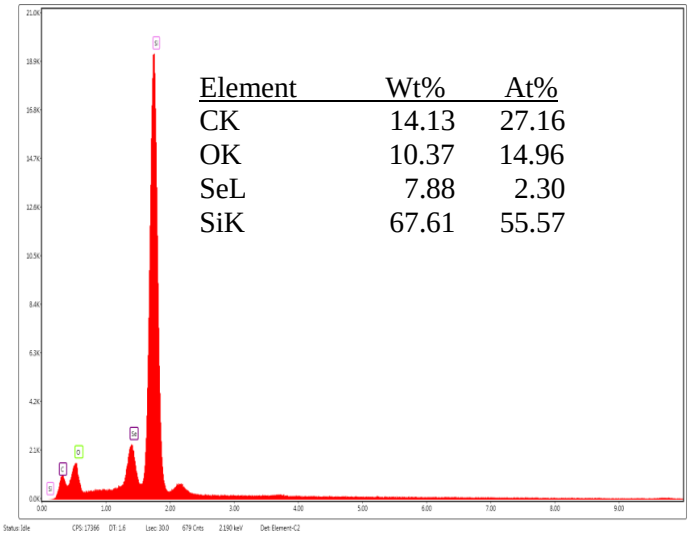

(a) **(b)**

Figure 3. FE-SEM images and EDX spectrum of GO:Se /p-Si heterostructure with magnification scale (100nm)

The GO:Se thin film was inserted in a metal-semiconductor as interfacial layer. The obtained Au/GO:Se/p-Si/Al device was tested under dark, room conditions with I-V measurements. Fig. 4 presents I-V characteristics graph of Au/GO:Se/p-Si/Al device for dark room conditions. The device exhibits good rectifying properties.

In order to investigate diode properties of the device, thermionic emission theory was used. Some important device parameters, such as ideality factor and barrier height were calculated from I-V

characteristics graph of the device. According to the thermionic emission theory, the current, I, is expressed as follows:

$$I = \underbrace{AA^{*}T^{2}exp\left(\frac{q\Phi_{B}}{nkT}\right)}_{I_0}\left[exp\left(\frac{qV}{nkT}\right) - 1\right] \quad (3)$$

Where, I_0 is saturation current which is obtained by the intercept of the linear region at the I-V graph. I_0 is given as the above equation (Equ.3). Also, where; q, V, k are charge of electron, the applied bias voltage and Boltzmann's constant, respectively. T, A* and A represent the temperature, Richardson constant (A^*=32Acm^{-2} K^{-2} for p-type Si), diode area (=7.85×10^{-3} cm^2), respectively. Device has 2.23×10^{-7} A saturation current values at room. For V≥3kT/ q, the ideality factor and barrier height have been rearranged (Equ.3) and they were calculated.

Ideality factor and barrier height values were calculated from I-V characteristics for 1.25 and 0.66 eV, respectively. Higher ideality factor values in study can be attributed to barrier inhomogeneity and non-uniform distribution of the carriers in the interface [14].

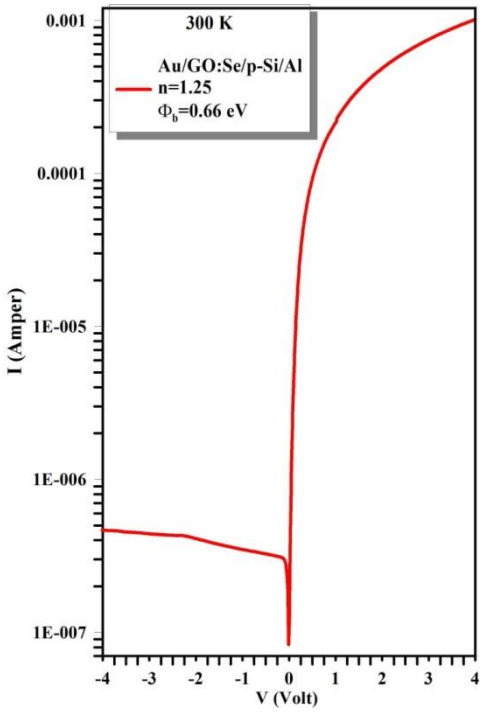

Figure 4. I-V characteristics graph of Au/GO:Se/p-Si/Al

4. CONCLUSION

We synthesized GO:Se nanoparticles via microbial green method and used these as a interfacial thin film on Au/GO:Se/p-Si/Al device structure. GO:Se thin film obtained on p-Si and glass substrates. Thin film properties were investigated UV-Vis. Spectrophotometer method, XRD, FE-SEM with EDS and these results showed that GO:Se thin film were obtained successfully. XRD graph indicates that GO:Se thin film have polycrystalline structure. FE-SEM image revealed that the GO:Se thin film has nano sheet structure and the structures composed to expected elements checked with EDS. The GO:Se thin film inserted between the Ag metal and p-type Si, and Au/GO:Se/p-Si/Al device was obtained. The device tested by I-V measurements under dark. The obtained device has 1.25 ideality factor and 0.66 eV barrier height according to thermionic emission theory. Device has good and stabile rectifying properties. It can be considered as photodiode in industrial applications

REFERENCES

[1] Oremland RS, Herbel MJ, Switzer-Blum J, Langley S, Beveridge TJ, Ajayan PM, Sutto T, Ellis AV, Curran S Structural and spectral features of selenium nanospheres produced by Se-respiring bacteria. Applied and Environmental Microbiology, 70(1), 52-60, 2004.

[2] Ozdal, M. Ozdal, O.G., Algur, O.F., *Pol J Microbiol*, *65*(1) (2016a) 63-68.

[3] Bakir, M., Meyer, J.L., Hussainova, I., Sutrisno, A., J. Economy, I. Jasiuk, Macromol. Chem. Phys. (2017) 1700338.

[4] Mekki, A., Dere, A., Mensah-Darkwa, K., Al Ghamdi, A., Gupta R.K., Harrabi, K., Farooq, W.A., Tantawy, F.E., Yakuphanoglu, F., Synth. Met. 217, 43-56., 2016

[5] Kang, S.H. . Fang, T.H.,. Hong, Z.H., J. Phys. Chem. Solid., 74, 1783-1793, 2013.

[6] Kocyigit, A., Karteri, İ., Orak, I., Uruş, S., Çaylar, M., Physica E: Low-dimensional Systems and Nanostructures, 103, 452–458, 2018.

[7] Kaya, A., Alialy, S., Demirezen, S., Balbaşı, M., Yerişkin S.A., Aytimur, A., Ceramics International 42, 3322–3329, 2016.

[8] Mekki, A., Ocaya, R.O., Dere, A., Al-Ghamdi, A.A., Harrabi, K., Yakuphanoglu, F., Synth. Met. 213, 47–56, 2016.

[9] Ozdal, M. Gurkok, S., Ozdal, O. G., 3 Biotech, 7(2), 117, 2017a.

[10] Çakıcı, T., Sağlam, M., Güzeldir, B., Materials Science and Engineering B, 193, 61–69, 2015.

[11] Robinson, J.T., Zalalutdinov, M., Baldwin, J.W., Snow, E.S., Wei, Z., Sheehan, P., Houston, B.H., Nano Lett. 8, 3441–3445, 2008.

[12] Wang, X., Zhi, L., Müllen, K., Nano Lett. 8, 323–327, 2008.

[13] Karteri, İ., Güneş, M., J. Mater. Sci. Mater. Electron., 27, 11502–11508, 2016.

[14] Çakıcı, T., Güzeldir, B. , Sağlam, M., Journal of Alloys and Compounds 646, 954-965**,** 2015.

STUDIES ON THE OPTICAL, STRUCTURAL AND ELECTRICAL PROPERTIES OF CADMIUM DOPED ZINC FERRITE AND MAGNESIUM FERRITE

S. Sarıtaş[1], M. Kundakcı[2] and M. Yıldırım[2]

[1]*Department of Electrical and Energy, Ispir Hamza Polat Vocational School of Higher Education, Ataturk University, 25250, Erzurum, Turkey*

[2]*Department of Physics, Faculty of Science, Ataturk University, 25240, Erzurum, Turkey*

E-mail: sevda.saritas@atauni.edu.tr

Abstract

A photoelectrochemical (PEC) system is a potentially effective method of producing hydrogen from sunlight and water. While a great deal of progress has been made in our understanding of PEC systems, practical, inexpensive, efficient, and stable devices have not yet been realized. The search for efficient photocatalysts for water splitting under visible light irradiation has been approached from several directions: to find new single phase materials, to tailor the band gap by modifying cations or anions of UV or visible photocatalysts with substitutional doping and to improve PEC properties of photocatalysts by loading or doping with a metal or noble metal.

Many studies have sought to improve the PEC properties of iron oxide by doping with various metals. Most dopants have been shown to increase carrier concentrations, but some have decreased the photocurrent by introducing electron or hole traps. Extensive research has been conducted on the introduction of certain defects or dopants into iron oxide which could enhance PEC performance. Cadmium doped zinc ferrite and magnesium ferrite films were synthesized on glass substrates by Chemical Spray Pyrolysis (CSP) method.

The technique of CSP without the requirement of vacuum is a method that can be preferred in the industry, in order to allow the production of large size films in both cheap. However, there are some disadvantages of films made with this technique, such as their thickness being not uniform and the size of the film-forming atoms being limited and the film in chemical solution to be grown must be homogeneous. Many parameters such as substrate, substrate temperature, the salts, solvent type, molarity and deposition time have carefully been chosen to obtain the best growth condition in this technique.

The effects of doped cadmium metal on the thin films were analyzed through Scanning Electron Microscopy (SEM), Atomic Force Microscopy (AFM), X-ray Diffraction (XRD) and UV-Vis double beam spectrophotometer technique. The change in the surface morphology of the thin films has been observed with the SEM and AFM measurements.

Keywords: Photoelectrochemical; zinc ferrite; magnesium ferrite

1. INTRODUCTION

Photoelectrochemical (PEC) mechanism was investigated as one of the most promising technology for solar energy conversion as the repeatedly increasing energy demand. The photoactive semiconductor electrodes of photoelectrochemical cells can generate photo-excited carriers under light irradiation and transfer minority carriers to water to perform one half of the water splitting reaction.

However, the efficiency of iron oxide photoanodes is limited by low absorption coefficient [5,6], low carrier conduction, short hole diffusion lengths (2-20 nm) and the slow kinetics of the oxygen evolution reaction .

Nowadays, because of fossil energy crisis and global warming, the clean energy of hydrogen has more attention and considered to as one of potential solutions to solve above urgent issues. Photoelectrochemical (PEC) water splitting is a promise method to convert solar energy into hydrogen gas.

In order to solve the flaws and improve the PEC performance of a-Fe2O3 photoelectrode, various improvement processes such as morphology control, reduction of the charge transfer resistance or impurity element doping of a-Fe2O3 have been reported to improve its PEC conversion efficiency [7-14].

2. MATERIAL AND METHODS

In SP (Fig. 1) technique many parameters such as, the salts (Table 1), molarity, deposition time and substrate temperature have carefully been choosen to obtain the best growth condition in this tecnique. The salts in the Table 1 are dissolved in 100 ml of deionized water and the solution is prepared. The solution was sprayed with argon gas onto a substrate heated to 320-340 °C at a distance of 25-30 cm. All films grown times were 28-30 min.

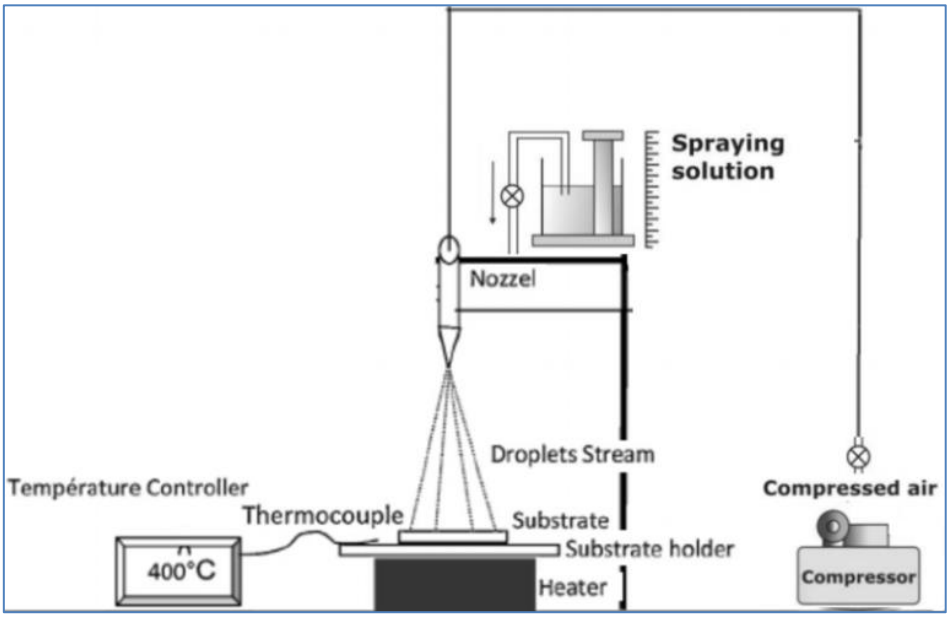

Figure. 1. Schematic diagram of Spray pyrolysis system

Table 1. Experimental details of the $Mg_xFe_{3-x}O_4$, Cd: $Mg_xFe_{3-x}O_4$, $Zn_xFe_{3-x}O_4$, Cd: $Zn_xFe_{3-x}O_4$ thin films.

Film	**Used Chemical Salt**	**Solution Molar Ratio**
$Mg_xFe_{3-x}O_4$	$FeCl_3.6H_2O$+$FeCl_2.4H_2O$+NaOH+$Mg(NO_3)_2\cdot6H_2O$	1:2:0.25:0.1
Cd:$Mg_xFe_{3-x}O_4$	$FeCl_3.6H_2O$+$FeCl_2.4H_2O$+NaOH+$Mg(NO_3)_2\cdot6H_2O$ $Cd(NO_3)_2\cdot6H_2O$	1:2:0.25:0.1:0.1
$Zn_xFe_{3-x}O_4$	$FeCl_3.6H_2O$+$FeCl_2.4H_2O$+NaOH+$Zn(NO_3)_2\cdot6H_2O$	1:2:0.25:0.1
Cd:$Zn_xFe_{3-x}O_4$	$FeCl_3.6H_2O$+$FeCl_2.4H_2O$+NaOH+$Zn(NO_3)_2\cdot6H_2O$ $Cd(NO_3)_2\cdot6H_2O$	1:2:0.25:0.1:0.1

3. RESULTS AND DISCUSSION

The morphologic and structure (particle size, pore size, etc.) properties of $Zn_xFe_{3-x}O_4$, Cd: $Zn_xFe_{3-x}O_4$, $Mg_xFe_{3-x}O_4$, Cd: $Mg_xFe_{3-x}O_4$ thin films have been generally and carefully investigated. XRD and AFM (Fig. 6,8) (for topographic properties) techniques have been used for structural analysis also SEM (Fig. 7,9) techniques have been used. According to XRD (Fig. 4,5) measurements, the crystal structure of the materials have changed. Optic properties of films have been give by absorption measurements. According to absorption measurements (Fig.2-3 and Table 2) band gab energy og films changed with doped metals.

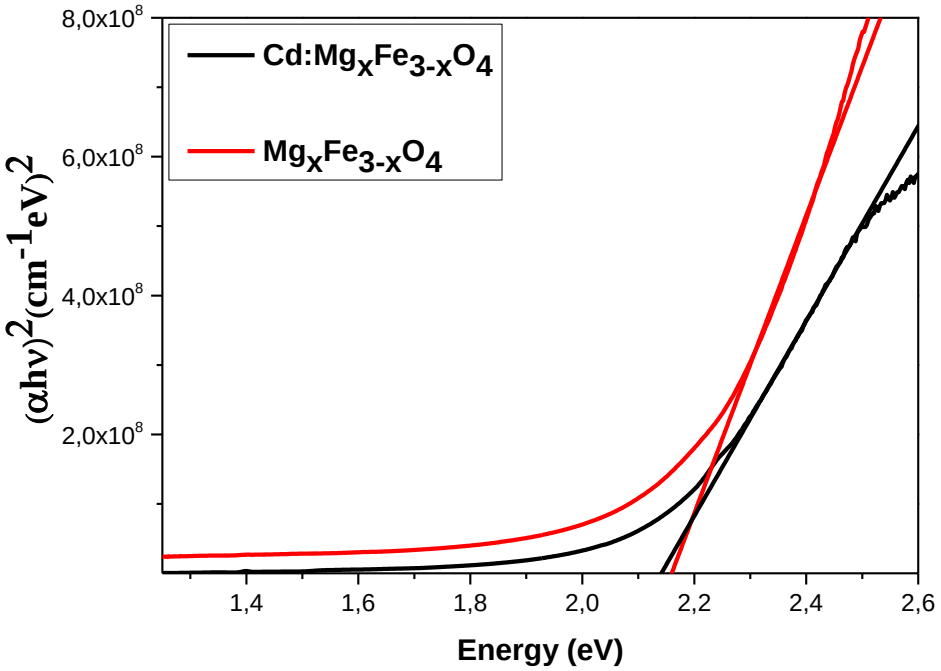

Figure 2. Plots of $(ah\upsilon)^2$ versus hυ hy and variation of Cd: $Mg_xFe_{3-x}O_4$ compare with $Mg_xFe_{3-x}O_4$ thin films on the glass substrate.

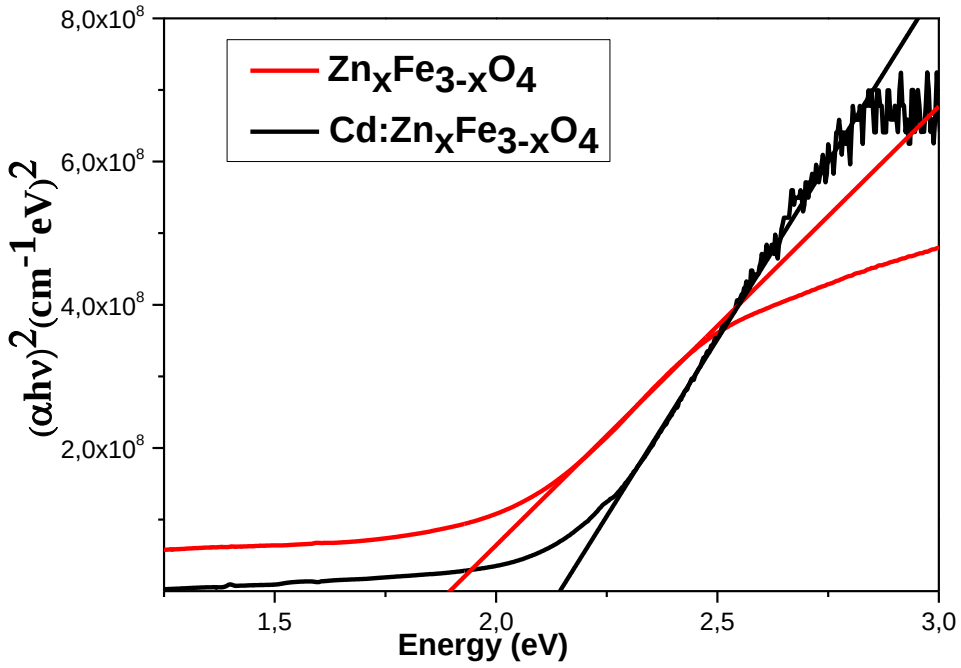

Figure 3. Plots of $(ah\upsilon)^2$ versus hυ hy and variation of Cd:$Zn_xFe_{3-x}O_4$ compare with $Zn_xFe_{3-x}O_4$ thin films on the glass substrate

Table 2 Band gab values of Cd: $Mg_xFe_{3-x}O_4$ Cd: $Zn_xFe_{3-x}O_4$, $Zn_xFe_{3-x}O_4$, $Mg_xFe_{3-x}O_4$ thin films.

Eg(eV)	Crystal
2.14	**Cd:$Mg_xFe_{3-x}O_4$**
2.10	Cd:$Zn_xFe_{3-x}O_4$
1.90	$Zn_xFe_{3-x}O_4$
2.17	$Mg_xFe_{3-x}O_4$

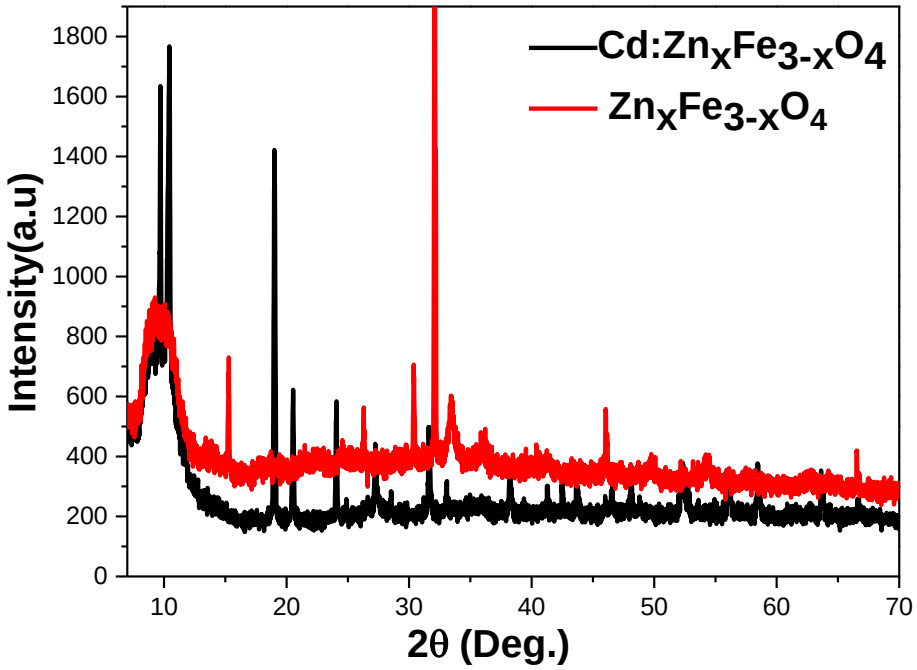

Figure 4. XRD patterns of Cd: $Zn_xFe_{3-x}O_4$ thin film

Table 3. Crystal structural parameters of Cd: $Zn_xFe_{3-x}O_4$ and Cd: $Mg_xFe_{3-x}O_4$ thin films

FWHM	FWHM (rad)	Intensity (a.u.)	2θ° (Observed)	Crystal size (D) nm	Crystal
0.329	0.0057	2059	31.95	25.1	$Zn_xFe_{3-x}O_4$
0.216	0.0037	643	32.82	38.3	$Mg_xFe_{3-x}O_4$
0.157	0.0027	1226	19.01	54.6	Cd:$Zn_xFe_{3-x}O_4$
0.619	0.010	327	16.09	13	Cd:$Mg_xFe_{3-x}O_4$

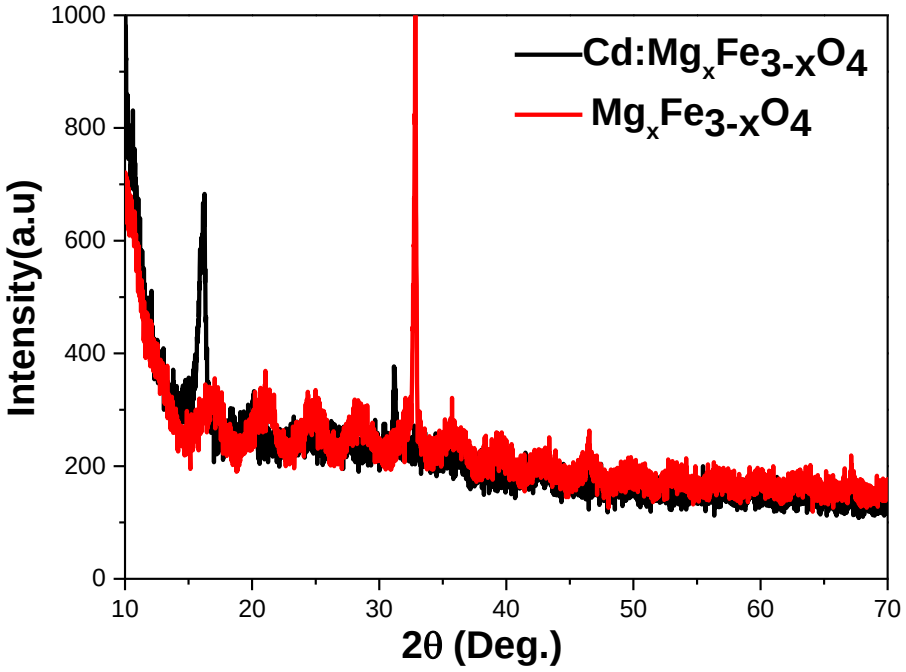

Figure 5. XRD patterns of Cd: $Mg_xFe_{3-x}O_4$ thin films

SEM and AFM (for topographic properties) techniques have been used for structural and morphologic analysis of thin films. The Cd: $Mg_xFe_{3-x}O_4$ films line roughness value is about 14.2 nm. The Cd: $Zn_xFe_{3-x}O_4$ films line roughness value is about 41 nm.

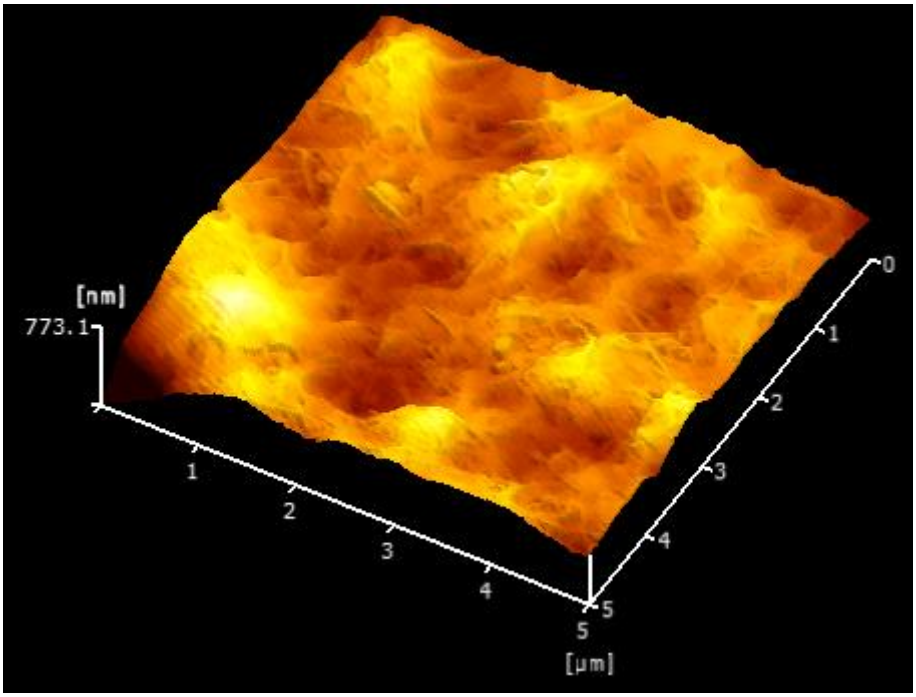

Figure.6. Three-dimensional AFM images of the Cd: $Mg_xFe_{3-x}O_4$ thin films

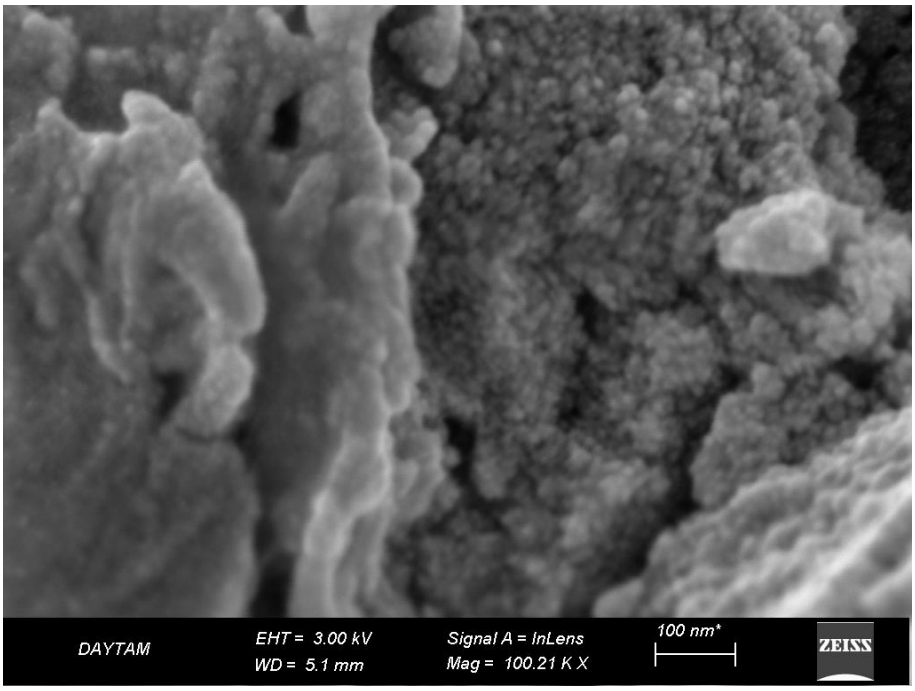

Figure.7. FE-SEM images of Cd: $Mg_xFe_{3-x}O_4$ thin films

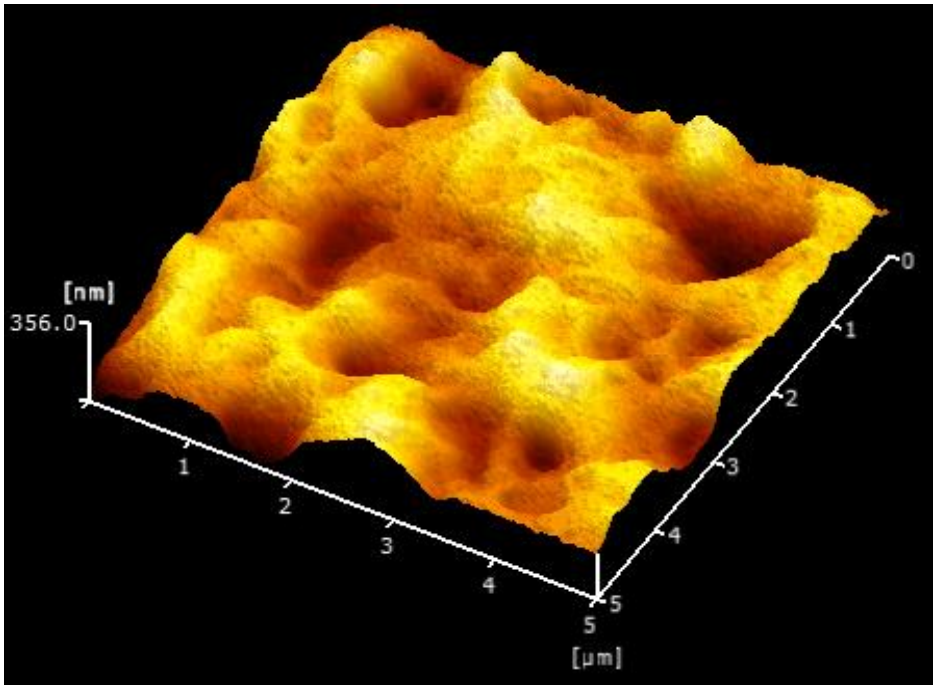

Figure.8. Three-dimensional AFM images of the Cd: $Zn_xFe_{3-x}O_4$ thin films

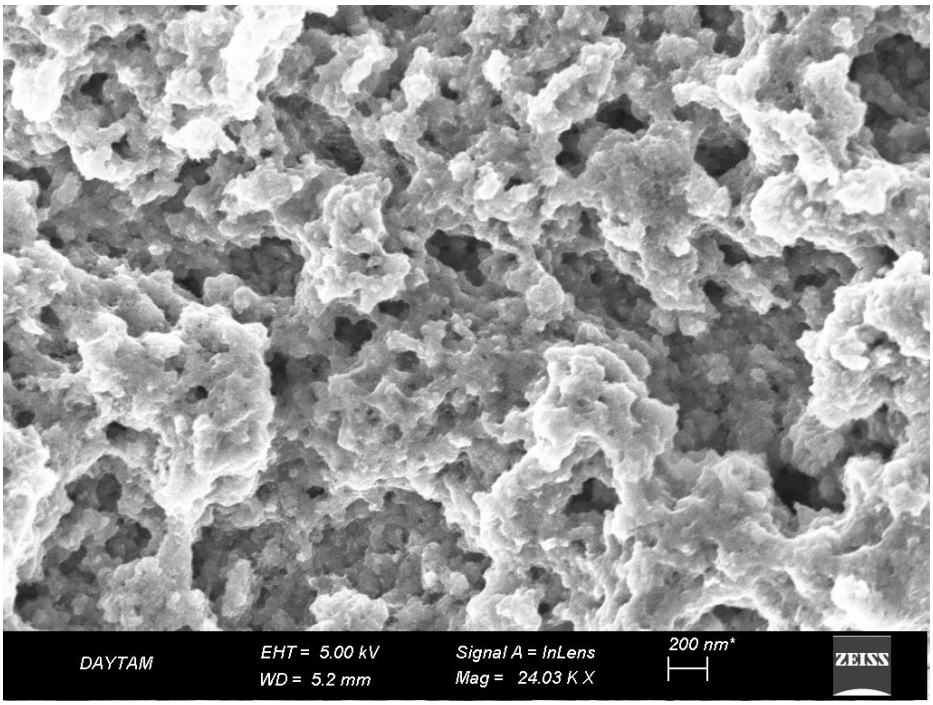

Figure.9. FE-SEM images of Cd: $Zn_xFe_{3-x}O_4$ thin films

4. CONCLUSION

According to XRD measurements, the crystal structure of Cd: $Mg_xFe_{3-x}O_4$ materials have changed. XRD patterns of thin film can be seen cubic structure to be converted hexagonal structure (Cadmium Magnesium Mg3Cd). And Cd: $Zn_xFe_{3-x}O_4$ thin film has a cubic structure (Cadmium Zinc Iron Oxide $Cd_{0.5}Fe_2O_4Zn_{0.5}$). Crystal structural parameters of Cd: $Zn_xFe_{3-x}O_4$ and Cd: $Mg_xFe_{3-x}O_4$ thin films have been give in Table 3. Optic properties of films have been give by absorption measurements. According to absorption measurements (Fig.2-3 and Table 2) band gab energy of films changed with doped metals.

REFERENCES

[1] Itoh K., Bockris JM., Stacked thin-film photoelectrode using iron oxide. J Appl Phys 1984;56:874-6.

[2] Itoh K., Bockris JM.. Thin film photoelectrochemistry: iron oxide. J Electrochem Soc 1984;131:1266-71.

[3] Morin FJ., Electrical properties of a-Fe2O3 and a-Fe2O3 containing titanium. Phys Rev 1951;83:1005.

[4] Kennedy JH., Frese KW.. Photooxidation of water at a-Fe2O3 (III) oxide electrodes. Chem Inf 1978;9:709-14.

[5] Dare-Edwards MP., Goodenough JB., Hamnett A., Trevellick PR.. Electrochemistry and photoelectrochemistry of iron (III) oxide. J Chem Soc Faraday Trans 1 Phys Chem Condens Phases 1983;79:2027-41.

[6] Lindgren T., Wang H., Beermann N.,. Vayssieres L, Hagfeldt A., Lindquist SE. Aqueous photoelectrochemistry of hematite nanorod array. Sol Energy Mater Sol Cells 2002;71:231-43.

[7] Wang G., Ling Y., Wheeler D.A., George K.E.N., Horsley K., Heske C.,. Zhang J.Z, Li Y., Nano Lett. 11 (2011) 3503–3509.

[8] Cesar I., Kay A., Martinez J.A.G., Gratzel M., J. Am. Chem. Soc. 128 (2006) 4582– 4583.

[9] Kumar P., Sharma P., Shrivastav R., Dass S., Satsangi V.R., Int. J. Hydrogen Energy 36 (2011) 2777–2784.

[10] Rioult M., Magnan H., Stanescu D., Barbier A., J. Phys. Chem. C 118 (2014) 3007–3014.

[11] Y.-S. Hu, A. Kleiman-Shwarsctein, A.J. Forman, D. Hazen, J.-N. Park, E.W. McFarland, Chem. Mater. 20 (2008) 3803–3805.

[12] Bohn C.D., Agrawal A.K.,. Walter E.C, Vaudin M.D., Herzing A.A., Haney P.M., Talin A.A., Szalai V.A., J. Phys. Chem. C 116 (2012) 15290–15296.

[13] Yang T.-Y., Kang H.-Y., Sim U., Lee Y.-J.,. Lee J.-H, Koo B., Nam K.T.,. Joo Y.-C, Phys. Chem. Chem. Phys. 15 (2013) 2117–2124.

[14] Wang L., Lee C.-Y., Schmuki P., Electrochem. Commun. 30 (2013) 21–25.7.

GALLIUM DOPED SPINEL ZINC FERRITE AND MAGNESIUM FERRITE THIN FILMS GROWN BY SPRAY PYROLYSIS

S. Sarıtaş[1], M. Kundakcı[2] and M. Yıldırım[2]

[1]*Department of Electrical and Energy, Ispir Hamza Polat Vocational School of Higher Education, Ataturk University, 25250, Erzurum, Turkey*

[2]*Department of Physics, Faculty of Science, Ataturk University, 25240, Erzurum, Turkey*

E-mail: sevda.saritas@atauni.edu.tr

Abstract

Magnetic nano spinel ferrites have grabbed attention due to their fascinating size dependent optical, electronic, magnetic, thermal, mechanical and chemical properties. The properties of such nano-structured materials are deeply influenced by their chemical composition and microstructure, which are sensitive to the manufacturing process. Spinel ferrites have the general formula AFe_2O_4 (where A^{2+} = Co, Ni, Zn, Mg, etc.) and the unit cell contains 32 oxygen atoms in cubic close packing with 8 tetrahedral (T_d) and 16 octahedral (O_h) occupied sites. By changing the type of divalent cation, it is possible to obtain a wide range of different physical and magnetic properties.

Spintronic semiconductors have been extensively researched in view of their potential to become the breakthrough technology in modern electronic and computing devices. Spintronics technology can potentially lead to novel and far superior semiconductor devices that are capable of multiple functions, such as logic, information storage (memory), optoelectronics, and quantum computation, with much improved power consumption profile, stability, scalability, and speed. Gallium doped spinel zinc ferrite and magnesium ferrite thin films were synthesized on glass substrates by Spray Pyrolysis (SP) method. The effects of doped gallium metal on the thin films were analyzed through Scanning Electron Microscopy (SEM), Atomic Force Microscopy (AFM), X-ray Diffraction (XRD) and UV-Vis double beam spectrophotometer and for electrical properties of films were ussed Van der Pauw technique. The change in the surface morphology of the thin films has been observed with the SEM and AFM measurements.

Keywords: Gallium; Zinc ferrite; Spray Pyrolysis

1. INTRODUCTION

Magnetoresistance (MR) is the change of the electrical resistance (R) of a material when an external magnetic field (H) is applied. Magnetic recording uses a write and read head to record and retrieve information from a magnetic media The data (bits) are stored as a regular succession of (equal size) difierently magnetized regions in the magnetic storage media. The write head consists of a series of coils winded around high permeability magnetic poles. When an electrical current flows through the coils the write head provides an in-plane magnetic field near the write gap (penetrating into the magnetized region), enabling the switching of the magnetic state of a bit.

Besides being used in read heads, the highly sensitive magnetoresistive detectors can be used whenever a magnetic field can be generated to monitor some other physical quantity. For example, successful applications include electrical current, position and speed sensing and control [1,3,4]. A bridge confuguration, with four magnetoresistive elements, is usually used in sensor applications [2]. This enables thermal variations in resistance to be minimized and zero output in the absence of an external magnetic field. Two of the elements are usually shielded, while the other two are incorporated in flux guides to enhance sensitivity. Also, the easy axis of the pinned and free layer are set perpendicular to each other. The resistance will then change linearly with the applied external magnetic field. Also iron oxide being used in photoelectrochemical applications.

Photoelectrochemical (PEC) water splitting is a promising method of transforming solar energy into chemical energy stored in the form of hydrogen in an environmentally benign manner. Considerable progress is currently being made in the development of suitable semiconductor materials as photoanodes for this solar driven fuel generation [5-16]. Among different metal oxide materials, a-Fe_2O_3 has attracted particular interest due to its relatively small bandgap (2.1 eV), its chemical stability in aqueous alkaline solution, low toxicity, abundance in the earth's crust and scalability as thin film at low cost.

2. MATERIAL AND METHODS

In SP (Fig. 1) technique many parameters such as, the salts (Table 1), molarity, deposition time and substrate temperature have carefully been choosen to obtain the best growth condition in this tecnique. The salts in the Table 1 are dissolved in 100 ml of deionized water and the solution is prepared. The solution was sprayed with argon gas onto a substrate heated to 320-340 °C at a distance of 25-30 cm. All films grown times were 28-30 min.

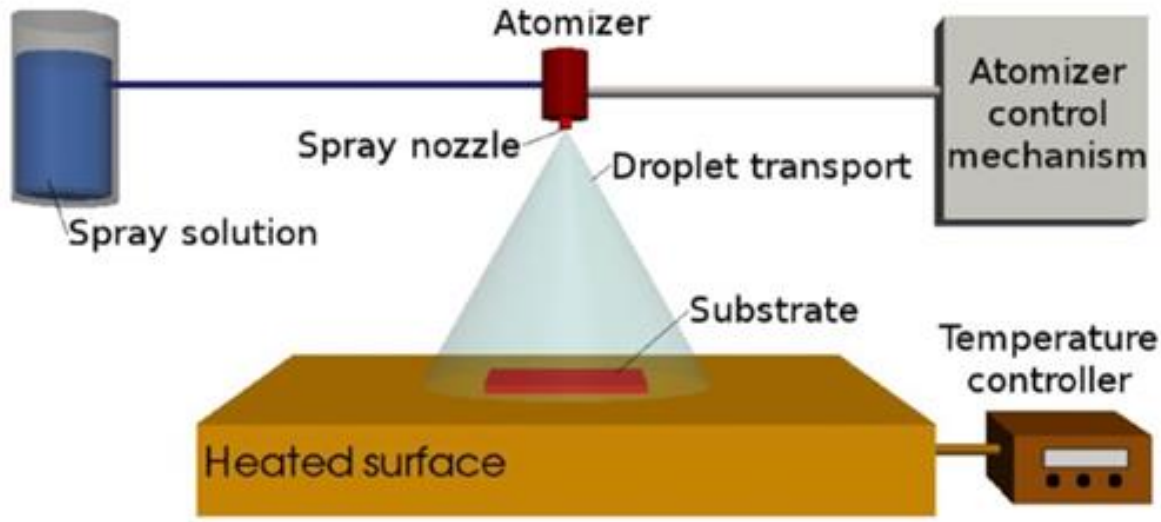

Figure. 1. Schematic diagram of Spray pyrolysis system

Table 1. Experimental details of the $Mg_xFe_{3-x}O_4$, Ga:$Mg_xFe_{3-x}O_4$, $Zn_xFe_{3-x}O_4$, Ga:$Zn_xFe_{3-x}O_4$ thin films.

Film	**Used Chemical Salt**	**Solution Molar Ratio**
$Mg_xFe_{3-x}O_4$	$FeCl_3.6H_2O$+$FeCl_2.4H_2O$+NaOH+$Mg(NO_3)_2\cdot6H_2O$	1:2:0.25:0.1
Ga:$Mg_xFe_{3-x}O_4$	$FeCl_3.6H_2O$+$FeCl_2.4H_2O$+NaOH+$Mg(NO_3)_2\cdot6H_2O$ $Ga(NO_3)_2\cdot6H_2O$	1:2:0.25:0.1:0.1
$Zn_xFe_{3-x}O_4$	$FeCl_3.6H_2O$+$FeCl_2.4H_2O$+NaOH+$Zn(NO_3)_2\cdot6H_2O$	1:2:0.25:0.1
Ga:$Zn_xFe_{3-x}O_4$	$FeCl_3.6H_2O$+$FeCl_2.4H_2O$+NaOH+$Zn(NO_3)_2\cdot6H_2O$ $Ga(NO_3)_2\cdot6H_2O$	1:2:0.25:0.1:0.1

3. RESULTS AND DISCUSSION

The morphologic and structure (particle size, pore size, etc.) properties of $Zn_xFe_{3-x}O_4$, Cd: $Zn_xFe_{3-x}O_4$, $Mg_xFe_{3-x}O_4$, Cd: $Mg_xFe_{3-x}O_4$thin films have been generally and carefully investigated. XRD and AFM

(Fig.6a-6b and Fig. 7a-7b) (for topographic properties) techniques have been used for structural analysis. According to XRD (Fig. 4,5) measurements, the crystal structure of the materials have changed. The morphologic properties of films have been generally and carefully investigated by SEM (Fig.6a-6b and Fig. 7a-7b) techniques.

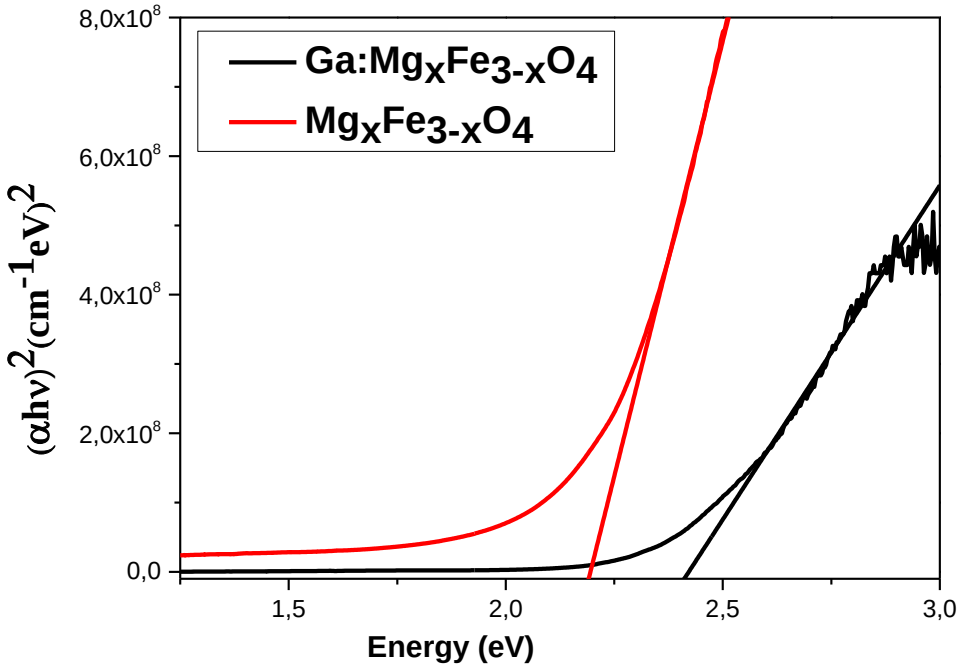

Figure 2. Plots of (ahυ)2 versus hυ hy and variation of Ga: $Mg_xFe_{3-x}O_4$compare with $Mg_xFe_{3-x}O_4$thin films on the glass substrate.

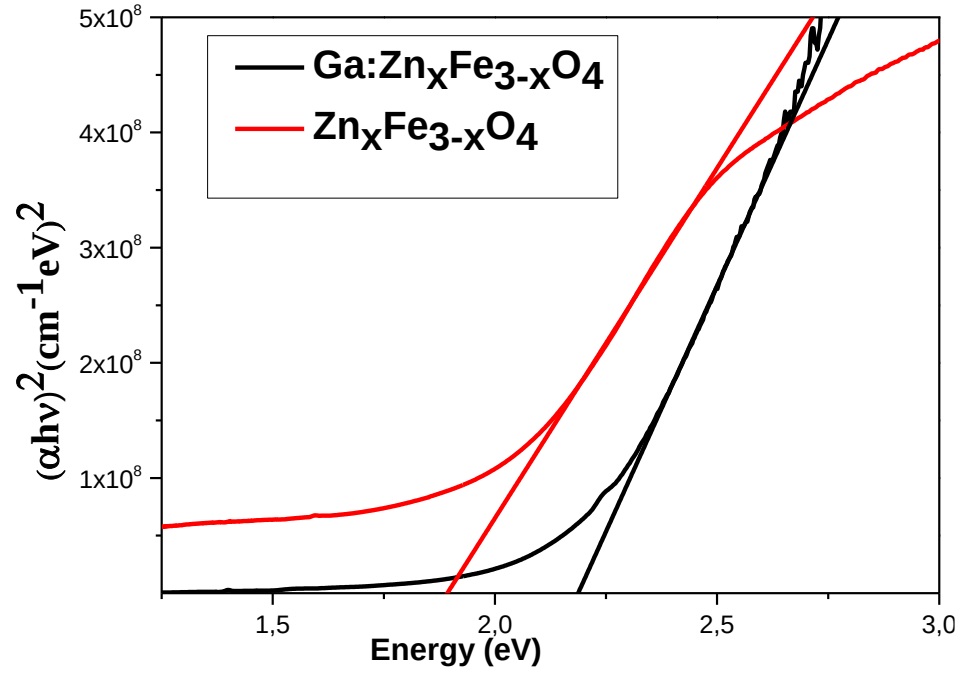

Figure 3. Plots of (ahυ)2 versus hυ hy and variation of Ga: $Zn_xFe_{3-x}O_4$ compare with $Zn_xFe_{3-x}O_4$ thin films on the glass substrate

Table 2 Band gab values of Ga: $Mg_xFe_{3-x}O_4$, Ga: $Zn_xFe_{3-x}O_4$, $Zn_xFe_{3-x}O_4$, $Mg_xFe_{3-x}O_4$thin films

Eg(eV)	Crystal
2.40	**Ga:$Mg_xFe_{3-x}O_4$**
2.18	Ga:$Zn_xFe_{3-x}O_4$
1.90	$Zn_xFe_{3-x}O_4$
2.17	$Mg_xFe_{3-x}O_4$

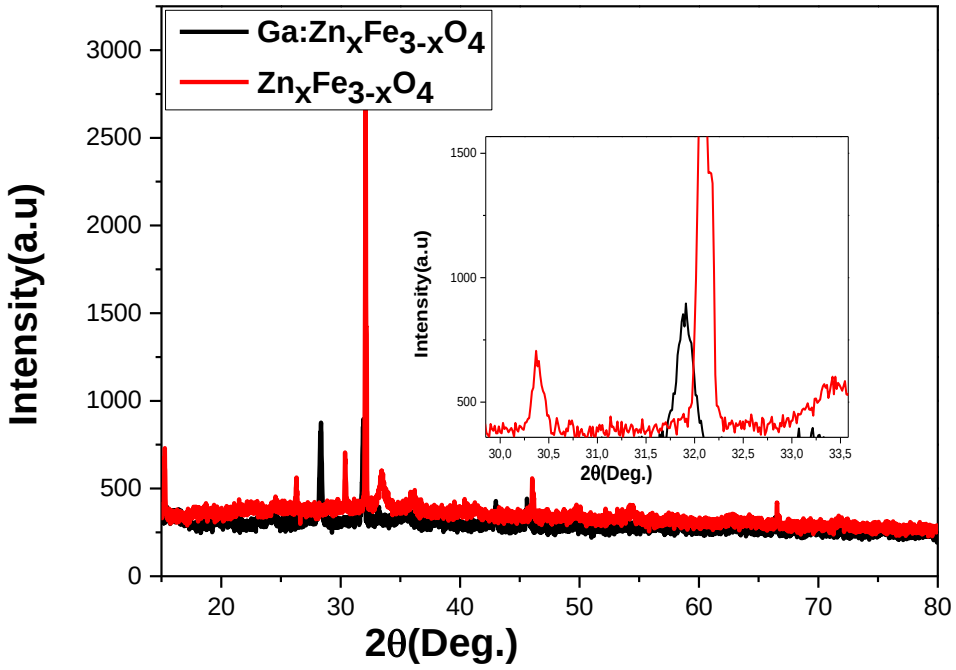

Figure 4. XRD patterns of Ga: $Zn_xFe_{3-x}O_4$ thin film

Table 4. Crystal structural parameters of Ga: $Zn_xFe_{3-x}O_4$ and Ga: $Mg_xFe_{3-x}O_4$thin films

FWHM	FWHM (rad)	Intensity (a.u.)	2θ° (Observed)	Crystal size (D) nm	Crystal
0.329	0.0057	2059	31.95	25.1	$Zn_xFe_{3-x}O_4$
0.216	0.0037	643	32.82	38.3	$Mg_xFe_{3-x}O_4$
0.215	0.0037	529	28.33	38.1	Ga:$Zn_xFe_{3-x}O_4$
0.410	0.007	185	32.48	20.2	Ga:$Mg_xFe_{3-x}O_4$

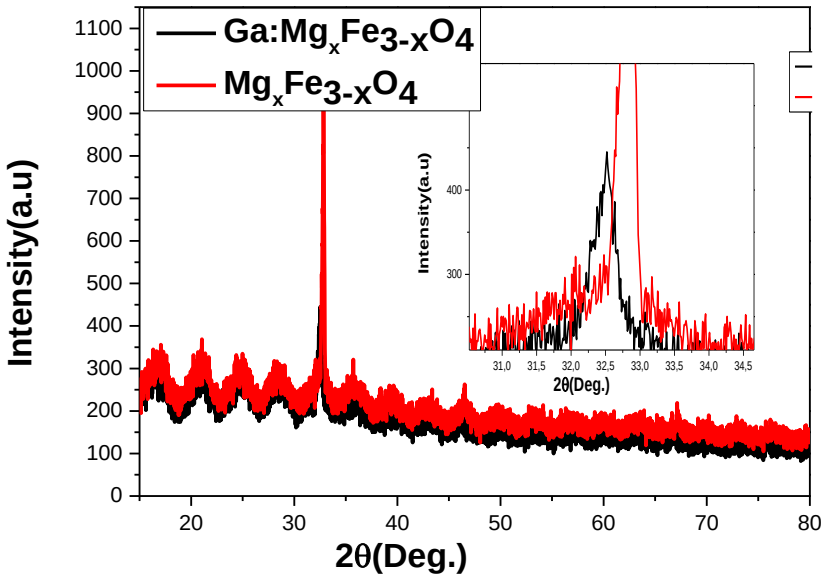

Figure. 5 XRD patterns of Ga: $Mg_xFe_{3-x}O_4$thin film

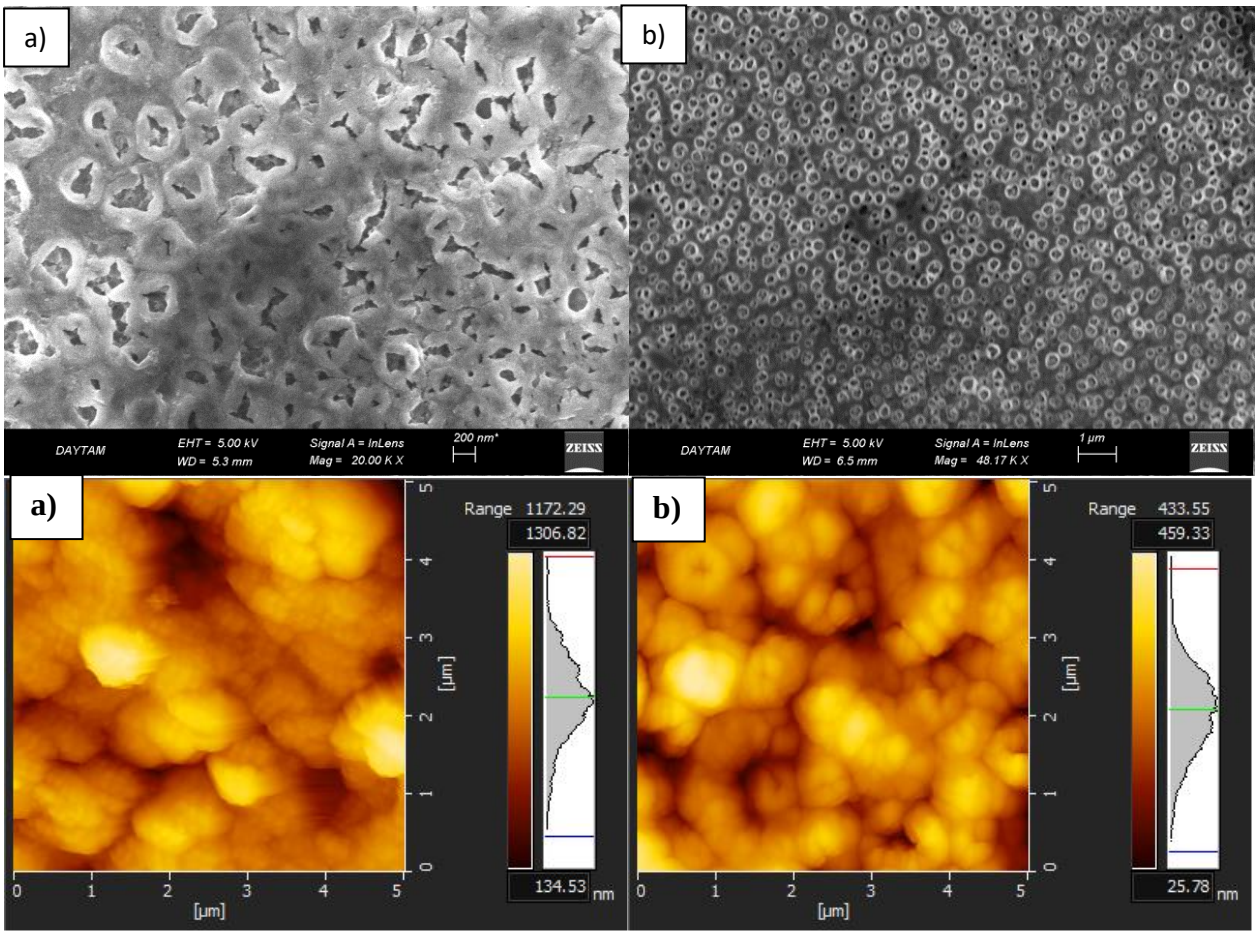

Figure.6. Two-dimensional AFM images of the a) Ga: $Mg_xFe_{3-x}O_4$ b) $Mg_xFe_{3-x}O_4$ [17] thin film. FE-SEM images of a) Ga: $Mg_xFe_{3-x}O_4$ b) $Mg_xFe_{3-x}O_4$ thin film.

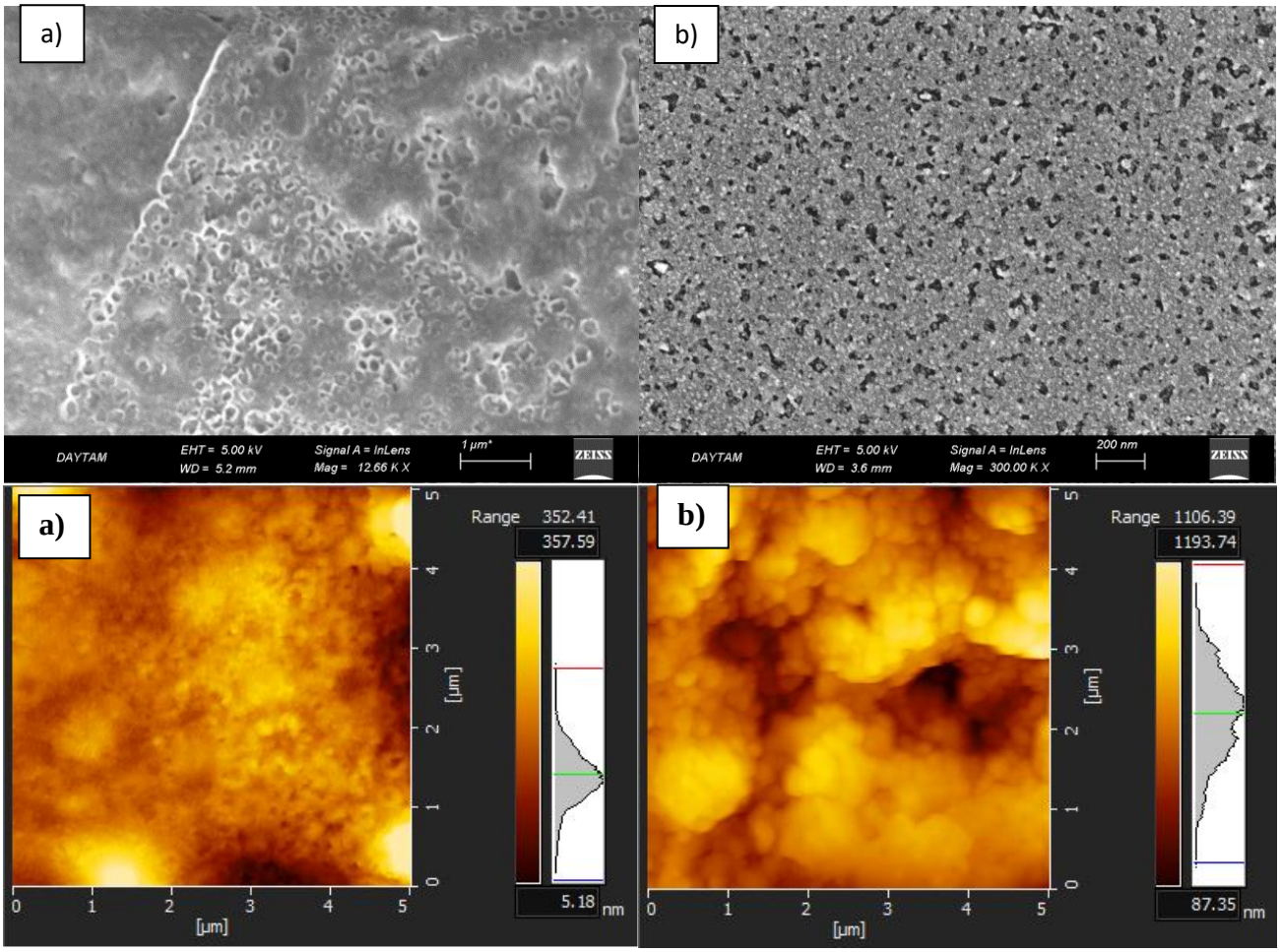

Figure.8. Two-dimensional AFM images of the a) Ga: $Zn_xFe_{3-x}O_4$ b) $Zn_xFe_{3-x}O_4$ [18] thin film. FE-SEM images of a) Ga: $Zn_xFe_{3-x}O_4$ b) $Zn_xFe_{3-x}O_4$ thin film.

4. CONCLUSION

According to XRD measurements, Ga: $Zn_xFe_{3-x}O_4$ thin film has a cubic structure (Reference code:01-074-2229) ($FeGa_2O_4$ Iron Gallium Oxide). of Ga: $Mg_xFe_{3-x}O_4$ thin film has a hexagonal Structure (Reference code:01-085-0599). Crystal structural parameters of Ga: $Zn_xFe_{3-x}O_4$ and Ga: $Mg_xFe_{3-x}O_4$ thin films have been give in Table 3. Optic properties of films have been give by absorption measurements. According to absorption measurements (Fig.2-3 and Table 2) band gab energy of films changed with doped metals. The Ga: $Zn_xFe_{3-x}O_4$ films line roughness value is about 27 nm and The Ga: $Mg_xFe_{3-x}O_4$ films line roughness value is about 124 nm.

REFERENCES

[1] Freitas P. P., Silva F., Oliveira N. J., Melo L. V., Costa L., and Almeida N., Spin valve sensors, Sensors and Actuators A - Physical, vol. 81, pp. 2-8, April 2000.

[2] Prinz G. A., Magnetoelectronics applications, J. Magn. Magn. Mater., vol. 200, pp.57-68, October 1999.

[3] Baselt D. R., Lee G. U., Natesan M., Metzger S. W., Sheehan P. E., and Colton R. J., A biosensor based on magnetoresistance technology_, Biosens. Bioelectron., vol. 13, no. 7, pp. 731_739, October 1998.

[4] Liu Y., Zhang Z., Freitas P. P., and Martins J. L., Current-induced magnetization switching in magnetic tunnel junctions, Appl. Phys. Lett., vol. 82, pp. 2871-2873, April 2003.

[5] Sun J.W., Zhong D.K., Gamelin D.R., Energy Environ. Sci. 3 (2010) 1252-1261.

[6] Krol R. van de, Liang Y.Q., Schoonman J., J. Mater. Chem. 18 (2008) 2311-2320.

[7] Maeda K., Domen K., J. Phys. Chem. Lett. 1 (2010) 2655-2661.

[8] Han S., Hu L., Liang Z., Wageh S., -Ghamdi A.A. AL, Chen Y., Fang X., Adv. Funct. Mater. 24 (2014) 5719-5727.

[9] Wheeler D.A., Wang G.M., Ling Y.C., Li Y., Zhang J.Z., Energy Environ. Sci. 5 (2012) 6682-6702.

[10] M. Roland, Adv. Funct. Mater. 24 (2014) 2421-2440.

[11] Fujishima A., Honda K., Nature 238 (1972) 37-38.

[12] Wang H.Q., Jia L.C., Bogdanoff P., Fiechter S., M€ohwald H., Shchukin D., Energy Environ. Sci. 6 (2013) 799-804.

[13] Abdi F.F.,. Han L.H,. Smets A.H.M,. Zeman M, Dam B., Krol R. van de, Nat. Comm. 4 (2013) 2195.

[14] Hern_andez-Alonso M.D., Fresno F., Su_arez S.,. Coronado J.M, Energy Environ. Sci. 2 (2009) 1231-1257.

[15] Liu X., Wang F.Y., Wang Q., Phys. Chem. Chem. Phys. 14 (2012) 7894-7911.

[16] Khoshakhlagh A., Nazari A., Khalaj G., J. Mater. Sci. Technol. 28 (2012) 73-82.

[17] Saritaş, S., Sakar, B. C., Kundakci, M., & Yildirim, M. (2018). The effect of Mg dopants on magnetic and structural properties of iron oxide and zinc ferrite thin films. *Results in Physics*, *9*, 416-423.

[18] Saritaş, S., Turgut, E., Kundakci, M., Gürbulak, B., & Yildirim, M. (2017). Compared with a-Fe2O3 and ZnXFe3-XO4 thin films grown by Chemical Spray Pyrolysis. *Int J Sens Netw Data Commun*, *6*(152), 2.

THE INFLUENCE OF *ORIGANUM VULGARE* L. ON HEMOLYSIS AND OXIDATIVE DAMAGE IN HUMAN ERYTHROCYTES EXPOSED TO HIGH GLUCOSE CONCENTRATION

Seda BALKAN

Department of Molecular Biology and Genetic, Sciences and Art Faculty, Kırklareli University, Kırklareli, Turkey

E-mail: balkan.seda@hotmail.com

Abstract

Hyperglycemia was found to increase the production of reactive oxygen species (ROS), leading to oxidative damage and hemolysis. Erythrocytes are the primary targets free radicals owing to their high membrane concentration of polyunsaturated fatty acids which are potent promoters of ROS. *Origanum vulgare* L. has been used in traditional native herbal medicine of Turkey. The purpose of this study was evaluate the effects of *O. vulgare* on oxidative damage and hemolysis in an experiment model of hyperglycemia in human erythrocytes *in vitro*. Human erythrocytes were treated with 20 mM and 40 mM glucose in the absence or presence of five different doses of *O. vulgare* aqueous extracts in the culture medium of 24h. After incubation malondialdehyde (MDA) and hemolysis (%) levels were analyzed. When the % hemolysis values of erythrocytes which were treated with only glucose and erythrocytes which were treated with the aqueous extracts of *O. vulgare*, the % hemolysis values of erythrocytes treated with the aqueous extracts of were determined to be lower. The lowest % hemolysis values were determined to be from 200 µg/ml concentration *O. vulgare* aqueous extracts (for 20 mM glucose, 2.67%±1.38; for 40 mM glucose, 4.43%±2.86). When the MDA levels were investigated, the MDA levels of erythrocytes which were treated with glucose as well as plant extracts have been determined to be lower. The MDA levels for 20 and 40 mM glucose were 296.5±0.058 (nmol/gHb) ve 349.2±0.051 (nmol/gHb) respectively while the MDA levels for 20 mM glucose and 200 µg/ml plant extract treated erythrocytes was 229.6±0.021 (nmol/gHb), and the 40 mM glucose and 200 µg/ml plant extract treated erythrocytes MDA value was 271.4±0.07 (nmol/gHb). These results imply that *O. vulgare* may have protect human erythrocytes exposed to high glucose concentration against oxidative damage.

Key words: *Origanum vulgare*, erythrocytes, glucose, *in vitro*

1. INTRODUCTION

In recent years, the interest in medicinal plants with antioxidant properties used for treatment of human diseases, including Diabetes mellitus (DM), has increased [1].

Origanum vulgare is widely used in traditional medicine for treatment of a variety of disease [2]. Studies investigating of the chemical content of *O. vulgare* were reported that the plant has phenolic acid and flavanol [3]. These compounds are compounds with low toxicity antioxidant properties [4].

DM is defined as a group of metabolic disorders characterized by the impaired insulin production or inability to properly use the insulin produced in human body [5]. Chronic hyperglycemia was found to increase the production of reactive oxygen species (ROS), leading to oxidative stress, a conditional that could be associated with cell dysfunction [6]. Oxidative stress is described as imbalance between formation of ROS and antioxidant defense mechanisms [7].

Human erythrocytes are continuously exposed to glucose in plasma during their circulatory life span of 120 days [8]. Erythrocytes, potentially powerful promoters of oxidative processes, are extremely susceptible to oxidative damage as a result of the high polyunsaturated fatty acid (PUFA) content of their membranes and high cellular oxygen and hemoglobin concentrations [9].

Oxidants, in fact, produce alterations in the erythrocyte membrane as manifested by a decreased cytoskeletal protein content and production of high molecular weight proteins which can lead to abnormalties in erythrocytes shape [4]. Oxidants also cause lipid peroxidation (LPO) by affecting the erythrocyte membrane. Reactive aldehydes such as malondialdehyde (MDA) occur after series of chain reaction. The measure of MDA levels is a basic parameter to prove the existence of LPO [10].

The aim of the present study is to evaluate the effects of *O. vulgare* on oxidative damage and hemolysis in human erythrocytes exposed to high glucose concentration.

2. MATERIAL AND METHODS

Plant materials and extract preparation

Confirmation of the taxonomic identification of *O. vulgare* was done by Dr. Hüseyin ERSOY of Trakya University (Edirne, Turkey). From different parts of Yıldız Mountains (Kırklareli, Turkey), the plant from various locations was collected in the months of May and June 2016. Aqueous extracts were prepared in accordance with the method introduced by Khadri et al., [11]. The obtained aqueous extracts were lyophilized and, then stored at 4^{o}C until use.

Preparation of human erythrocytes

Whole blood samples were collected from 10 healthy volunteers aged 20-40 years who were not smoking, were not obese, and did not use any medicines or alcohol. The anticoagulant used was Ethylenediamine tetra acetic acid (EDTA) and blood samples were centrifuged for 10 min at 2500 rpm and 4°C. After that, buffy coat layers and the plasma were discarded. The erythrocytes layers were washed three times with 0.9% NaCl and centrifuged at the same values as specified above. After each centrifugation, the supernatants were discarded. The erythrocytes layers were re-suspended (1:10) in phosphate-buffered saline (PBS, pH:7.4, 0.01 M) [12].

In vitro treatment of erythrocytes with glucose and *O. vulgare*

Three milliliters of diluted and washed erythrocytes was incubated with an equal amount of PBS, 20 and 40 mM glucose levels. *O. vulgare* at concentrations of 200, 100, 50, 25 and 12.5 µg/ml were added. The reaction mixtures, using a shaking water bath at 37°C, were incubated for 24h. In some tests, the erythrocytes suspension was preincubated with *O.vulgare* concentrations for 30 min before the addition of glucose to the suspension. All incubations included 10 µl penicillin-streptomycin solution/ml cell suspensions, to avert microbial growth. The penicillin-streptomycin solution contained 500 mg streptomycin in 10 ml PBS and 300 mg penicillin G [13]. Each treatment included three replicates.

Experimental design

For the in vitro treatment of erythrocytes, the erythrocytes suspensions were randomly divided into 12 groups consisting of ten erythrocyte samples;

1. Group: Treatment at 20 mM glucose
2. Group: Treatment at 20 mM glucose and 200 µg/ml *O. vulgare*
3. Group: Treatment at 20 mM glucose and 100 µg/ml *O. vulgare*
4. Group: Treatment at 20 mM glucose and 50 µg/ml *O. vulgare*
5. Group: Treatment at 20 mM glucose and 25 µg/ml *O. vulgare*
6. Group: Treatment at 20 mM glucose and 12.5 µg/ml *O. vulgare*
7. Group: Treatment at 40 mM glucose
8. Group: Treatment at 40 mM glucose and 200 µg/ml *O. vulgare*
9. Group: Treatment at 40 mM glucose and 100 µg/ml *O. vulgare*
10. Group: Treatment at 40 mM glucose and 50 µg/ml *O. vulgare*
11. Group: Treatment at 40 mM glucose and 25 µg/ml *O. vulgare*
12. Group: Treatment at 40 mM glucose and 12.5 µg/ml *O. vulgare*

Estimation of hemolysis

The hemoglobin content of the samples centrifuged at 2500 rpm for 10 minutes was recorded at 540 nm after incubation (A). A value of 100% lysis was assigned to the supernatant of the sample with control hemolysate, obtained by freezing and thawing the cell suspensions (A1) [14]. The percentage of hemolysis (H %) in each assay tube was calculated by the equation: Percent hemolysis (H %) for each sample was computed by the equation:

H% = A/A1*100

Preparation of erythrocyte ghosts and measurement of erythrocyte malondialdehyde (MDA)

Erythrocyte ghosts were prepared from washed erythrocytes as stated by Dodge et al. [15].

MDA is a secondary product of LPO. Sodium dodecyl sulphate (SDS) (8.1%) was added to the erythrocyte ghosts, mixed well as well as being incubated at room temperature. The samples to which thiobarbituric acid (0.6%) and acetic acid (20%) were added were incubated in a water bath at 100°C. Butanol-pyridine (15:1) mixture was used to treat the cooled samples. After centrifugation, the absorbance of the colored layer was recorded at 532 nm. MDA levels were represented as nmol/g Hb [16].

3. RESULTS

Effects of *O. vulgare* on hemolysis

In Table 1, the effects of *O. vulgare* on percent hemolysis in erythrocytes treated with glucose are shown. A decline in the levels of percent hemolysis with plant extract concentrations (200, 100, 50, 25 and 12.5 µg/ml) were observed compared to erythrocytes with glucose (20 and 40 mM). The levels of percent hemolysis in all plant extract concentrations compared to each other were determined the lowest percent hemolysis in 200 µg/ml concentration of *O. vulgare.*

Table 1. Effects of *O. vulgare* (200, 100, 50, 25 and 12.5 µg/ml) on percent hemolysis in erythrocytes treated with 20 mM and 40 mM glucose

Groups	Hemolysis%
1. Group: 20 mM glucose	10.47±2.42
2. Group: 20 mM glucose and 200 µg/ml *O. vulgare*	2.67±1.38
3. Group: 20 mM glucose and 100 µg/ml *O. vulgare*	3.06±1.25
4. Group: 20 mM glucose and 50 µg/ml *O. vulgare*	5.27±0.01
5. Group: 20 mM glucose and 25 µg/ml *O. vulgare*	7.11±5.20

6. Group: 20 mM glucose and 12,5 µg/ml *O. vulgare*	6.50±3.90
7. Group: 40 mM glucose	11.96±2.71
8. Group: 40 mM glucose and 200 µg/ml *O. vulgare*	4.43±2.86
9. Group: 40 mM glucose and 100 µg/ml *O. vulgare*	4.53±1.39
10. Group: 40 mM glucose and 50 µg/ml *O. vulgare*	4.82±1.89
11. Group: 40 mM glucose and 25 µg/ml *O. vulgare*	5.97±2.86
12. Group: 40 mM glucose and 12,5 µg/ml *O. vulgare*	6.62±2.86

Effect on *O. vulgare* on malondialdehyde (MDA) content

MDA content of erythrocytes in all groups are offered in Table 2. As shown in Table 2, The MDA values for 20 and 40 mM glucose were 296.5±0.058 (nmol/gHb) ve 349.2±0.051 (nmol/gHb) respectively while the MDA values for 20 mM glucose and 200 µg/ml plant extract treated erythrocytes was 229.6±0.021 (nmol/gHb), and the 40 mM glucose and 200 µg/ml plant extract treated erythrocytes MDA value was 271.4±0.07 (nmol/gHb).

Table 2. Effects of *O. vulgare* on MDA content in erythrocytes treated with 20 mM and 40 mM glucose

Groups	**MDA (nmol/g.Hb)**
1. Group: 20 mM glucose	296.5±38.99
2. Group: 20 mM glucose and 200 µg/ml *O. vulgare*	229.6±25.83
3. Group: 20 mM glucose and 100 µg/ml *O. vulgare*	241.5±20.08
4. Group: 20 mM glucose and 50 µg/ml *O. vulgare*	247.5±14.56
5. Group: 20 mM glucose and 25 µg/ml *O. vulgare*	249.9±16.78
6. Group: 20 mM glucose and 12.5 µg/ml *O. vulgare*	254.7±22.68
7. Group: 40 mM glucose	349.2±24.97
8. Group: 40 mM glucose and 200 µg/ml *O. vulgare*	271±68.92
9. Group: 40 mM glucose and 100µg/ml *O. vulgare*	277.4±22.45
10. Group: 40 mM glucose and 50 µg/ml *O. vulgare*	297.7±32.87
11. Group: 40 mM glucose and 25 µg/ml *O. vulgare*	326.4±12.56
12. Group: 40 mM glucose and 12.5 µg/ml *O. vulgare*	338.4±26.0

4. DISCUSSION

O. vulgare widely used in Turkey is a medicinal plant. This plant is known to have pain relief, cough suppressants, soothing and muscle relaxant properties [2]. In our study, we investigated the effects of *O. vulgare* on oxidative damage on high glucose-treated erythrocytes. De Bona et al. [5] investigated the effect of *Syzygium cumini* on erythrocytes with hyperglycemia. They indicated that *S. cumini* extract significantly reduced the MDA levels and could be a good antioxidant. This result is similar to our findings. In another study performed with *Bauhinia forficita*, it was observed that the plant extracts treated against glucose decreased MDA values [17]. In a study evaluating hemolysis percentes, 10 different plant extracts were applied against glucose in erythrocytes and the lowesthemolysis % values were obtained in the extracts of the *Galium verum* and *Scutelleria tournefortii.* It has been reported that these two plant extracts can be used as a natural antioxidant in the pharmacology industry [9].

According to our results, *O. vulgare* decreased the MDA value and the percentage of hemolysis in erythrocytes treated with glucose. Therefore, *O. vulgare* may decrease oxidative damage in erythrocytes. It can be said that O. vulgare may also be a good antioxidant substance because the compounds that can reduce oxidative damage can be considered as good antioxidants.

REFERENCES

[1] Oliveira, V.B., Yamada, L.T., Fagg C.W. and Brandao, M.G.L., Native foods from Brazilian biodiversity as a source of bioactive compounds, Food Research International, 48, 170-179, 2012.

[2] http://www.ebitki.com/index.php?hq=Origanum%20vulgare&gr=Latince

[3] Balkan, B., Balkan, S., Aydoğdu, H. et al., Evaluation of Antioxidant Activities and Antifungal Activity of Different Plants Species Against Pink Mold Rot-Causing Trichothecium roseum. Arab. J. Sci. Eng. 42, 2279-2289, 2017.

[4] Suwalsky, M., Orellana, P., Avello, M. and Vellena, F., Protective effect of *Ugni molinae* Turcz against oxidative damage of human erythrocytes, Food and Chemical Toxicology, 45, 130-135, 2007.

[5] De Bona, K.S., Belle, L.P., Bittencourt, P.E.R., Bonfanti, G., Cargnelluti, L.O., Pimentel, V.C., Ruviaro, A.R., Schetinger, M.R.C., Emanuelli, T. and Moretto, M.B., Erythrocytic enzymes and antioxidant status in people with type 2 diabetes: Benificial effect of *Syzygium cumini* leaf extract in vitro. Diabetes Research and Clinical Practice, 94, 84-90, 2011.

[6] Kassab A. and A. Piwowar, Cell oxidant stress delivery and cell dysfunction onset in type 2 diabetes, Biochimie, 94, 1837-1848, 2012.

[7] Memişoğulları, R., Diyabette serbest radikallerin rolü ve antioksidanların etkisi, Düzce Tıp Fakültesi Dergisi, 3, 30-39, 2005.

[8] Viskupicova, J., Blaskovic, D., Galiniak, S., Soszyński, M., Bartosz, G., Horakova, A., Sadowska-Bartos, I.L., Effect of high glucose concentrationson human erythrocytes in vitro. Redox Biology, 5, 381–387, 2015.

[9] Khalili, M., Ebrahimzadeh, M. A., and Safdari, Y., Antihaemolytic activity of thirty herbal extracts in mouse red blood cells, Arh. Hig. Rada. Toksikol., 65, 399-406, 2014.

[10] Balkan, S., Aktaç, T., Study on the liver functions in rats exposed to benomyl, Journal of Biological Science, 5(5), 666-669, 2005.

[11] Khadri, A., Neffati, M., Smiti, S., Fale, P., Lino, A.R.L., Serralheiro, M.L.M. and Araujo, M.E.M., Antioxidant, antiacetylcholin esterase and antimicrobial activities of Cymbopogon schoenanthus L. Spreng (lemon grass) from Tunisia. LWT-Food Sci. Technol., 43, 331-336. 2010.

[12] Marar, T., Amelioration of glucose induced hemolysis of human erythrocytes by vitamin E. Chemico-Biological Interactions, 193, 149-153, 2011.

[13] Jain, K.J., Palmer, M. and Chen, Y., Effect of vitamin E and *N*-aseytlcysteine on phosphatidylserine extrernalization and induntion of coagulation by high-glucose-treated human erythrocytes. Metabolism, 48(8), 957-959, 1999.

[14] Verma, R.J., Shukla, R.S., Mehta, D.N., Ameliration of cytotoxic effects of aflatoxin by vitamin A: an *in vitro* study on erythrocytes. Toxicology in Vitro, 15: 39-41, 2001.

[15] Dodge, J.T., Mitchell, C., and Hanahan, D.J., The preparation and characterisation of hemoglobin-free ghosts of human erythrocytes. Arch. Biochem. Biophys. 100, 119-130, 1963.

[16] Ohkawa, H., Nobukoi, O., Kunio, Y., Assay for lipid peroxides in animal tissues by thiobarbituric acid reaction, Analytical Biochemistry, 95(2), 351-358, 1979.

[17] Salgueiro, A.C., Leal, C.Q., Bianchini, M.C., Prado, I.O., Mendez, A.S., Puntel, R.L., Folmer, V., Soares, F.A., Avila, D.S., Puntel, G.O., The influence of Bauhinia forficata Link subsp. pruinosa tea on lipid peroxidation and non-protein SH groups in human erythrocytes exposed to high glucose concentrations. Journal Ethnopharmacolology, 148(1), 81-7, 2013.

CHATTER VIBRATION AND STABILITY ANALYSIS FOR ORTHOGONAL CUTTING IN TURNING

Erol Türkeş[1], Mümin Şahin[2] and Selçuk Selvi[3]

[1]*Department of Mechanical Engineering, Kirklareli University, Kirklareli, Turkey*
[2]*Department of Mechanical Engineering, Trakya University, Edirne, Turkey*
[3]*Department of Mechanical Engineering, Trakya University, Edirne, Turkey*

E-mail: selcukselvi@trakya.edu.tr

Abstract

In machining, tool vibrations are one of the most important factors affecting production efficiency negatively. One of the main factor limiting the cutting operation in high-speed turning is chatter vibrations. There is a relationship between the required cutting power and shear forces for chip removal. The shear forces can either be calculated theoretically or measured with a dynamometer. Excessive pressure and friction during operation cause forces on the cutting edge in various directions. Variable chip thickness generated during cutting more triggers system instability. If the amplitude of the vibration does not decrease when compared to the amplitude generated in the previous pass, or if the amplitude of the vibration is constantly growing, this vibration is called chatter vibration. Chatter vibrations may generate high dynamic loads and these loads can cause damage on spindle, workpiece and machine. Researchers continue to work on predictable solutions for years but cutting system has to be modeled in great detail to predict in advance. In this study, chatter vibration prediction in turning was adapted for orthogonal cutting. Single degree of freedom (SDOF) model was performed and chatter frequencies obtained from forms of modal analysis and cutting tests.

Keywords: Chatter, Turning, Orthogonal Cutting, Stability Analysis

1. INTRODUCTION

Machining is one of the important production method in the field of manufacturing. The tolerance range of the parts produced by the machining decreases gradually with the progressive production quality. The surface quality of the parts obtained by machining is directly or indirectly affected by the processing parameters. Machine tool vibrations consist of a self-excited mechanism during the cutting process. Chatter vibration is a self-excited vibration that occurs between the cutting tool and workpiece in high rates of metal removal rates. Large tool nose radius makes the tool more prone to vibration [1]. Before starting machininig, selecting of the cutting parameters have great importance to achieve expected results. It is important to predict cutting forces, cutting speed, depth of cut and feed rate to avoid chatter vibrations [2]. For analysing of chatter vibration, firstly the cutting system has to be modelled. The forces that acting on the cutting edges have to be identified. Stability Lobe Diagrams can be generated as a result of analyzes. Stable and unstable regions can be plotted according to cutting parameters. Two models exist Nyquist criterion and Time Domain Simulation techniques. Analytical and numerical analysis of the cutting process can be made using these techniques. In last years, Tlusty and Merchant [3,4] have introduced various approaches to cutting mechanics and cutting models. Another work was carried out with Turkes et al. [5] about the stability analysis of orthogonal cutting in turning. They compared two different prediction methods and they found predicted chatter frequency greater than the natural frequency.

In this study, SDOF turning process was investigated in terms of cutting stability and chatter vibrations. Cutting tests were carried out with different lengths of tool holders. Results were evaluated after modal analysis and cutting tests. Stability diagrams were plotted with the help of computer software after obtaining cutting system modals.

2. MATERIAL AND METHODS

Chatter prediction and stability analysis are adapted for SDOF turning process. Cutting system was modelled with mass, spring and damper can be seen in Figure 1.

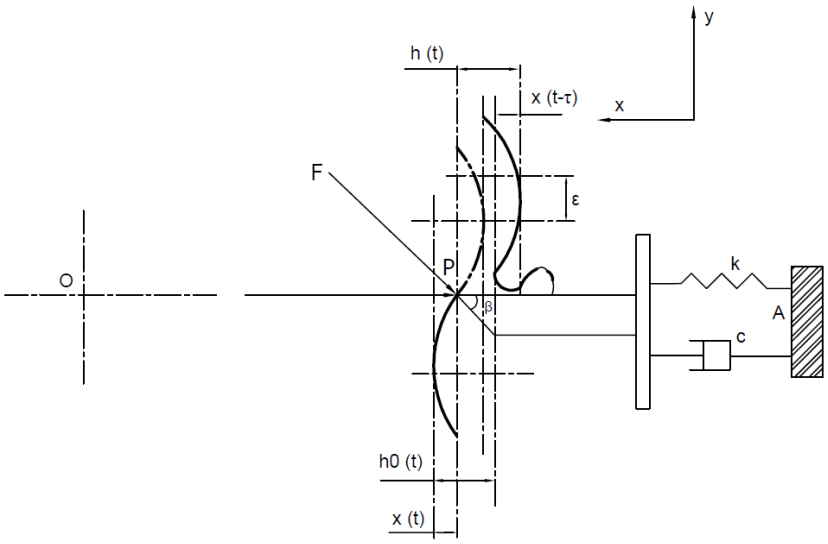

Figure 1. SDOF orthogonal cutting system

The equation of motion in feed direction (x) is,

$$m_x.\ddot{x}(t) + c_x.\dot{x}(t) + k_x.x(t) = F_x(t) \quad (1)$$

Fx(t), $F_x(t) = -F(t).\cos\beta$ is in terms of cutting force and the value of this force;

$$F_x(t) = w.C.h(t) \quad (2)$$

and (w), chip width (mm); C, specific cutting energy of the material (N/m^2) and h(t), immediate chip thickness. Instant chip thickness;

$$h(t) = h_0 - x(t) + x(t-\tau) \quad (3)$$

From the equation, $\left[x(t) - x(t-\tau)\right]$ is the dynamic chip width.

2.1. Oriented Transfer Function

Oriented transfer function of the system was obtained from equations (1) - (3);

$$m_x.\ddot{x}(t) + c_x.\dot{x}(t) + k_x.x(t) = F_x(t) = w.C.h(t) \quad (4)$$

the equation of movement is written in Laplace domain, and the force in the direction of feeding to be written,

$$m_x.s^2.x(s) + c_x.s.x(s) + k_x.x(s) = F_x(s) \quad (5)$$

transfer function of the open loop between x(s) and $F_x(s)$, can be written as follows,

$$G(s)=\frac{x(s)}{F(s)}=\frac{1}{m.s^2+c.s+k} \quad (6)$$

closed loop transfer function between dynamic and reference chip loads is obtained by taking Laplace transformation of the equation (3) and replacing it in h(s) by x(s)=G(s).Fx(s)

$$\frac{h(s)}{h_0(s)}=\frac{1}{1+C.w.G(s).(1-e^{-\tau s})} \quad (7)$$

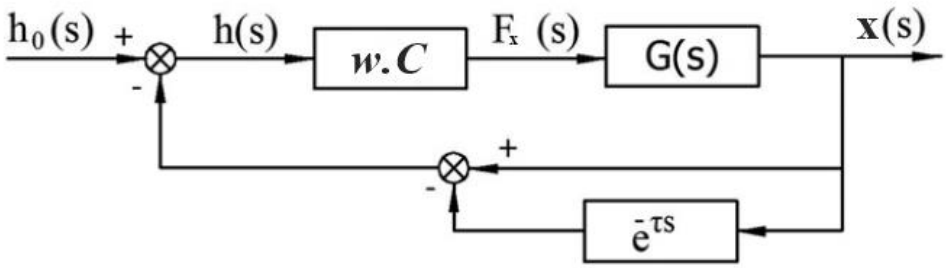

Figure 2. Block diagram of chip depth of a SDOF turning system [5]

Closed loop transfer function between x(s) and (s) is written as the equation (4)

$$m_x.\ddot{x}(t)+c_x.\dot{x}(t)+k_x.x(t)=w.C.\left[h_0-x(t)+x(t-\tau)\right] \quad (8)$$

if Laplace transformation is applied on both sides.

$$\frac{x(s)}{h_0(s)}=\frac{C.w.G(s)}{1+C.w.G(s).(1-e^{-\tau s})} \quad (9)$$

Denominators of the equations (7) and (8) are the characteristic equation of the system.

2.1.1. According to Oriented Transfer Function

First the denominator of the equation (7), is equaled to zero,

$$1+C.w_{\lim}.G(s).(1-e^{-\tau s})=0 \quad (10)$$

the roots of equation will give the chatter frequency of the system in the form of $s=\sigma+j\omega$. If the real part of the roots is zero $(s=j\omega)$, system will stay stable. Since work piece will has a constant vibration at a (ω) chatter frequency, if $s=j\omega$ is placed in characteristic equation for critic stability analysis, equation (11), can be written as,

$$1+C.w_{\lim}.G(j\omega).(1-e^{-\tau j\omega})=0 \quad (11)$$

characteristic equation can be written if it is placed in the equation (12) in the form of real and imaginary parts $G(j\omega) = \mathrm{Re} + j\,\mathrm{Im}$,

$$\left\{1 + C.w_{\lim}\left[\mathrm{Re}(1-\cos\omega\tau) - \mathrm{Im}\sin\omega\tau\right]\right\} + j\left\{C.w_{\lim}\left[\mathrm{Re}\sin\omega\tau + \mathrm{Im}(1-\cos\omega\tau)\right]\right\} = 0$$

real and imaginary parts of the equation must be zero. If the imaginary part is equaled to zero first, $\mathrm{Re}\sin\omega\tau + \mathrm{Im}(1-\cos\omega\tau) = 0$, the ratio of real and imaginary parts gives the phase angle of the root (ψ) on Nyquist diagram,

$$\tan\psi = \frac{\mathrm{Im}(\omega)}{\mathrm{Re}(\omega)} = \frac{\sin\omega\tau}{\cos\omega\tau - 1} \qquad (12)$$

ψ is the phase delay of the frequency transfer function of the system. Then,

$$\omega\tau = 3\pi + 2\psi \qquad (13)$$

the phase effect is written as follows,

$$n + \frac{\varepsilon}{2\pi} = \frac{f}{\Omega} = f.\tau \qquad (14)$$

Where, f is frequency of the cutting tool (Hz); Ω is the spindle speed (1/s); ε/2π the fractional number of waves formed on he surface. Phase delay is $\varepsilon = 3\pi + 2\psi$. Max. spindle speed in the stable part is found,

$$\tau = \frac{2n\pi + \varepsilon}{2\pi f} \quad \rightarrow \quad N = \frac{60}{\tau} \qquad \text{n=0,1,2,3,...} \qquad (15)$$

If the real part of the equation is equaled to zero, then stable depth of cut is found,

$$w_{\lim} = \frac{-1}{C.\mathrm{Re}\left[(1-\cos\omega\tau) - (\mathrm{Im}/\mathrm{Re})\sin\omega\tau\right]} \rightarrow \quad \frac{\mathrm{Im}(\omega)}{\mathrm{Re}(\omega)} = \frac{\sin\omega\tau}{\cos\omega\tau - 1},$$

$$w_{\lim} = \frac{-1}{2.C.\mathrm{Re}(\omega)} \qquad (16)$$

3. THE EXPERIMENTAL PROCEDURE

In the cutting experiments, cylindrical AISI-1050 steel with diameter of 60mm was used as an experimental material. Two different lengths of tool holder were used in the tests. Impact hammer and accelerometer were used for modal analysis anlysis. Tool direction in y axis was neglected becasue of the lower frequency in this direciton. Therefore, the movement in this direction was not affected by the natural frequency and

has no effect on the system stability. The method of oriented transfer function was used to determine the chatter frequency of the system. Cutting tests have to be applied before the computational method. When the graphs were plotted, stable and unstable regions of the system can be seen from the charts. With this information, stable regions are selected safely for the machining.

For the tool holder of (b x h x l) = (20 x 20 x 80) mm modal test results and predicted chatter limits are given below:

Table 1. Modal analysis of L=80 mm length of tool

Modal Analysis Data (L=80)	
k (N/m)	$2{,}12x10^7$
ω_n (Hz)	1178
ξ (%)	2,38

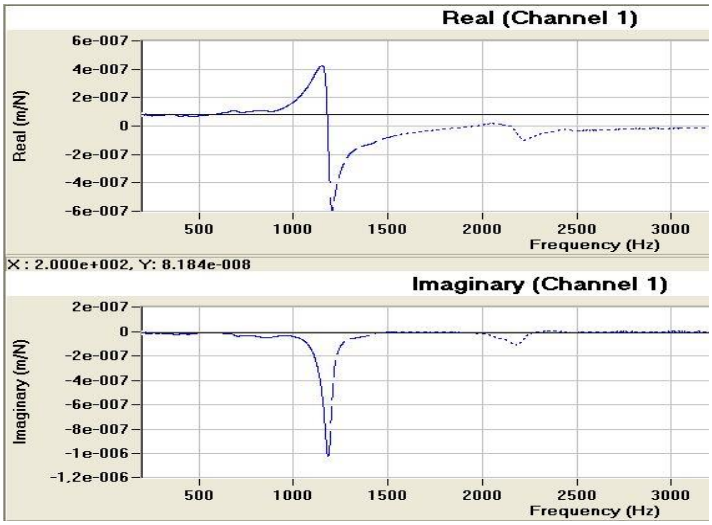

Figure 3. Modal analysis graphic of the system with L=80mm tool holder

Real and imaginary parts of the function are shown below according to oriented transfer function of the system.

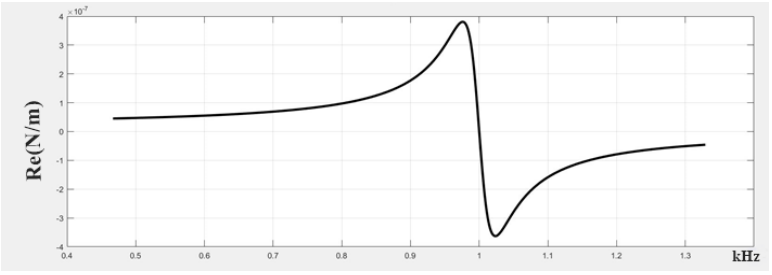

Figure 4. Real part of transfer function with L=80mm tool holder

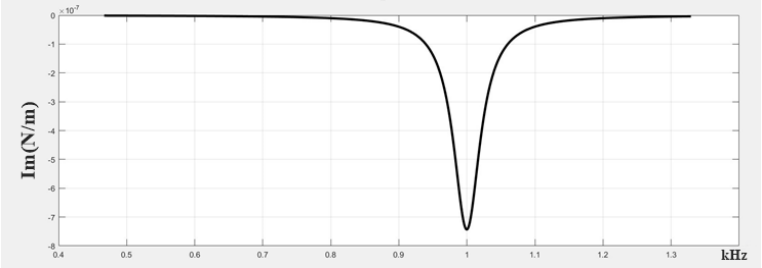

Figure 5. Imaginary part of transfer function with L=80mm tool holder

According to oriented transfer function stability lobes diagram of the cutting system was plotted as given in Figure 6.

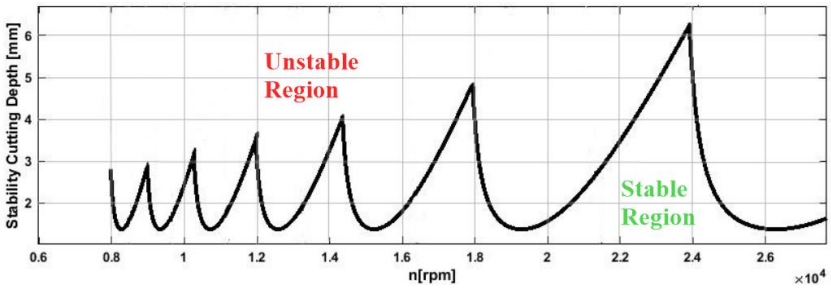

Figure 6. Stability lobe diagram of the system with L=80mm tool holder

For the tool holder of (b x h x l) = (20 x 20 x 100) mm modal test results and predicted chatter limits are given below:

Table 2. Modal analysis of L=100 mm length of tool

Modal Analysis Data (L=100)	
k (N/m)	$1{,}41 \times 10^7$
ω_n (Hz)	982
ξ (%)	3,33

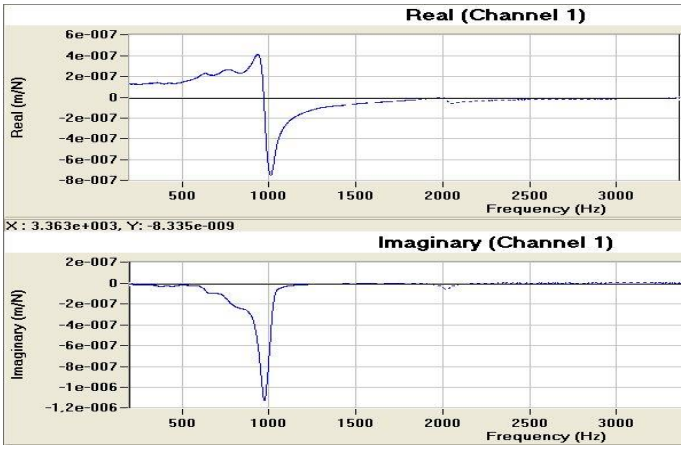

Figure 7. Modal analysis graphic of the system with L=100mm tool holder

For the second cutting conditions, real and imaginary parts of the function are shown below according to oriented transfer function of the system.

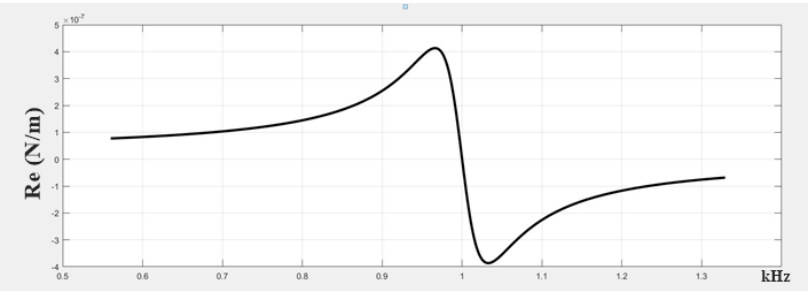

Figure 8. Real part of transfer function with L=100mm tool holder

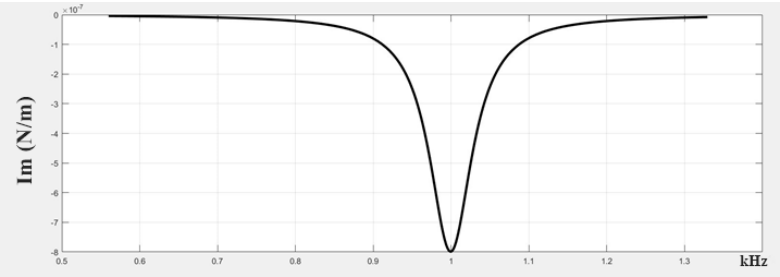

Figure 9. Imaginary part of transfer function with L=100mm tool holder

According to oriented transfer function stability lobes diagram of the cutting system was plotted as given in Figure 10.

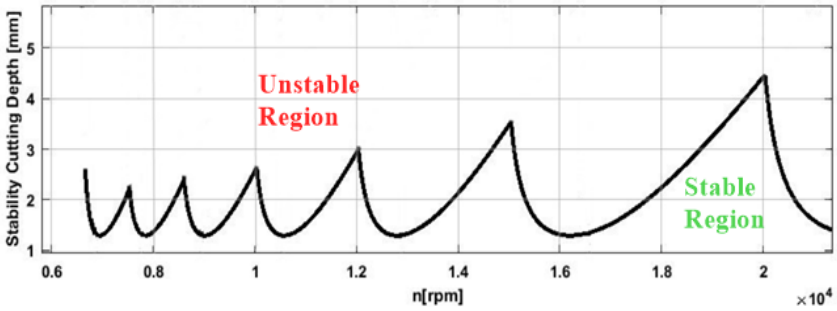

Figure 10. Stability lobe diagram of the system with L=100mm tool holder

4. RESULTS AND DISCUSSION

In this study, chatter stability prediction has been investigated for SDOF turning system in orthogonal cutting. The investigation of stability was predicted in oriented transfer function form. Cutting test results and predicted results were compared after analysis. Although it is an important factor, damping in the cutting was not included into calculations. Beside this, other factors such as rigidity of the holder and wear of the tool were not considered within the system. After prediction of oriented transfer function results,

predicted stability and system stability were very close to each other. According to cutting test results chatter frequency of L=80mm tool holder is 1218 Hz and L=100mm tool holder is 1006 Hz; when compared to the calculated results minor deviations were observed. Also, modal analysis natural frequency results were found numerically less than predicted and calculated chatter frequencies. If more detailed models are created, the results can be expected to be closer.

REFERENCES

[1] Altintas Y. Manufacturing automation; metal cutting mechanics, machine tool vibrations and CNC design. first ed. New York: Cambridge University Press; 2000.

[2] I.S. Jawahir and C.A. van Luttervalt. Recent developments in chip control research and applications. CIRP Annals, 42/2:49–54, 1993.

[3] Tlusty J. Machine dynamics. In: King RI, editor. Handbook of high speed machining technology. New York: Chapman & Hall; 1985.

[4] Merchant ME. Basic mechanics of the metal-cutting process. J App Mech II Trans ASME 1944;66 A-168.

[5] Turkes E., Orak S., Neseli S., Yaldiz S. "Linear analysis of chatter vibration and stability analysis for orthogonal cutting in turning", International Journal of Refractory Metals and Hard Materials 29 (2011) 163-169

EFFECTS OF SOURCE-DRAIN METAL ON ELECTRICAL CHARACTERISTICS OF BOTTOM – GATE POLY (3 – HEXYLTHIOPHENE) (P3HT) BASED OFET

D. Taşkın Gazioğlu[1], F. Dumludağ[2*], M. H. Yu. Seyidov[1,3]

[1]*Department of Physics, Gebze Technical University, 41400 Gebze, Kocaeli, Turkey*

[2]*Department of Physics, Marmara University, 34722 Kadıköy, Istanbul, Turkey*

[3]*Institute of Physics Azerbaijan National Academy of Sciences, AZ - 1143 Bakû, Azerbaijan*

[*]E-mail: fatihdumludag@marmara.edu.tr

Abstract

During the last several decades, solution-processible OFETs have received considerable attention due to their potential applications in low cost, flexible, low temperature and large area devices; such as active matrix organic displays, chemical sensors, logic circuits and flexible integrated circuits.In this study, we fabricated bottom-gate top-contact poly (3–hexylthiophene) (P3HT) based organic field-effect transistors (OFET) on gold (Au)-coated glass substrates which functioned as the gate electrode. Silver and gold (Ag-Au) were selected as source-drain electrodes and were deposited using thermal evaporation system in high vacuum ambient ($<10^{-6}$ mbar). Thermoplastic Polyurethane (TPU) as gate dielectric was deposited onto the Au, gate electrodes by using electro-spinning method. The samples which were fabricated in top contact bottom gate structure were examined using semiconductor characterization system (Keithley 4200 SCS) in air ambient and results were discussed.

Keywords: OFET, P3HT, polymer, TPU

1. INTRODUCTION

Over the past decade organic field effect transistors (OFET) has attracted a great of attention and have been utilized for integrated circuits, displays, sensors and electronic barcodes because OFETs have many advantages such as low cost, low temperature process, easy processability, chemical stability, cost-effective production and using flexible substrate. OFET essentially operates as an electronic switch by changing the channel conductance from insulated to conductive. Soluble and processable poly-3-alkylthiophene's have many potential applications such as light emitting diodes, nonlinear optical devices, rechargeable battery electrodes, and field-effect transistors [1]. The semiconducting properties of Poly (3 – hexylthiophene) (P3HT) conjugated organic polymer compatible with ease of synthesis and processing, excellent mechanical (flexibility) and electrical properties, large area coverage possibility, non - toxicity, lightweight, good thermal/chemical stability, possibility of low temperature processing of semiconductor layer on different flexible plastic substrates, and its relatively high field effect mobility make this organic material promising candidates for application in a variety of low cost electronic and optoelectronic devices [2]. Solution processability of P3HT have another the key advantage of potentially simple, large area coverage, structural flexibility and low-temperature thin-film processing, using techniques spin coating, ink jet printing or stamping, screen printing and spray-coating. P3HT–based field-effect transistors are usually fabricated by spin coating, drop casting and inkjet printing techniques [3]. The spin-coating method is one of the most commonly used thin-film deposition technique which is easy, fast and controllable method for the formation uniformity of thin film onto the substrates. The coated film thickness depends on the solution concentration, viscosity as well as rotation speed and coating time [4]. Generally this technique is preferred for the fabrication of P3HT based Organic field-effect transistors (OFETs).

One disadvantage of organic semiconductors in comparison with inorganic semiconductors is a higher defect density. Traps in organic semiconductors mostly affect electronic transport; therefore carrier density in organic materials drastically decreases as a result of a trapping effect. Consequently, the charge carrier drift mobility in organic semiconductors is lower than those in inorganic semiconductors. In organic semiconductors, typically very high voltages are required for the charge carrier high field - effect mobility values; mainly high electric field drastically reduces the number of trapped charges.

Organic field effect transistors do not work without an appropriate dielectric. Usually insulating polymers are opted as gate dielectrics. Polymer gate dielectrics could be useful in OFETs due to their facile solution processability and compatibility with various (including flexible) substrates. They can also provide

smooth surfaces on transparent glass or plastic substrates. Several polymer gate dielectrics have been used in high-performance OFETs, including poly(4-vinylphenol) (PVP), poly(vinylalcohol) (PVA), poly(methylmethacrylate) (PMMA), polystyrene (PS), and polyimide (PI) [5]. Non-interacting nature of organic-organic interface also provides an advantage for the applications of polymers as dielectrics indicating that high quality interfaces can be obtained using polymers [6, 7].

The selection of an appropriate insulator is not easy task, and usually depends on the intended applications. Thermoplastic polyurethane (TPU) is thermoplastic elastomer that is compatible with organic solvent and suitable for rapid prototyping [8]. Due to their wide range of mechanical properties, high abrasion resistance, high tensile strength, elasticity as well as low crystallinity, flexibility and processibility, TPU have been used for various application such as insulators, biomedical devices, degradable implants and tissue engineering scaffolds [9].

Another important element for the OFETs to obtain high performance is drain and source contacts. Energy level mismatch of work function of drain – source metal electrode and HOMO level of active layer, occurrence of traps between contacts and active layer, and interface structure between active layer and drain – source electrodes are some of the important elements affecting flow of charge through the device and essential parameters such as field – effect mobility (μ), threshold voltage (V_{th}) [10]. Because the contacts can significantly affect the flow of charge through the device and essential parameters, as mentioned above, it has great importance to investigate the effect of junctions on characteristics of the OFETs under investigation.

According to our best of knowledge OFETs with TPU as gate insulator has not been reported. Therefore, effects of source – drain electrodes on performance of OFETs with TPU as insulator, P3HT as active layer, and *Au* as gate electrode have not been investigated, before. In this paper, we present bottom - gate top - contact P3HT – based organic thin film transistors on *Au* coated glass substrate which functioned as the gate electrode. Thermoplastic polyurethane (TPU) was employed as dielectric layer. Fabricated OFET devices were reproducible and had excellent environmental stability. Electronic properties of P3HT - based OFETs have been carried out by $I - V$ measurements by using semiconductor characterization system (Keithley 4200 SCS) in air ambient.

The effects of kind of source / drain metals (*Au* and *Ag*) of OFETs with TPU gate insulator on the electrical performance of fabricated devices, with structure of Au/Ag source-drain /P3HT/TPU/Au gate, such as field – effect mobility (μ), threshold voltage (V_{th}), and V_{on} were reported.

2. EXPERIMENTAL PROCEDURE AND DEVICE FABRICATION

We fabricated bottom – gate top – contact P3HT based OFETs on *Au*-coated glass substrates which functioned as the gate electrode (Figure. 1). Thermoplastic Polyurethane (TPU) was used as gate dielectric. Prior to deposition process of *Au* gate electrode, the glass substrates were cleaned by glassware washer. Washer agents were de-ionized water, acetone, isopropyl alcohol and glassware detergent. Glass substrates were cleaned in an ultrasonic cleaner bath (f ~ 47 kHz) by using above - mentioned washer agents for ~ 10 min for each. Finally, the glass substrates were rinsed with distilled water and purged with dry nitrogen. Gold (*Au*) thin film gate electrodes were deposited in high vacuum ambient ($<10^{-6}$ mbar) by using a physical vapor deposition system. Rate of the deposition was kept constant around 10 Å/s. The thickness of the *Au* film was measured as 150 nm. Thin film of the dielectric layer was prepared by dissolving TPU in dimehylformamide (DMF). The solution was deposited onto the *Au* coated glass substrate by using electro - spinning process. After drying the TPU film at 130 ^{o}C for 10 min in air atmosphere, solution of regioregular P3HT (active layer, purchased from Aldrich) in chloroform with a concentration of 10 mg/ml was spun onto the TPU film rotating at 2000 rpm for 35 s in ambient condition. The deposited films were then dried in the nitrogen atmosphere at 120 ^{o}C for 15 min to allow complete evaporation of solvent and surface moisture. The spin coating was done using Speciality Coatings Systems Inc., Spin Coater Model P6700 Series. Thickness of the TPU was measured as 2000 nm by using Veeco Dektak 8 surface profilometer.

Finally, 100 nm *Ag*/*Au* source and drain electrodes were deposited by using thermal evaporation system onto the P3HT layer in high vacuum condition ($<10^{-6}$ mbar). Deposition of *Au*/*Ag* top contacts was performed through a mechanical shadow mask. Channel length (L) and width (W) of the fabricated OFETs were 80 µm and 4 mm respectively. The electrical characteristics of all the devices were determined by using Keithley 4200 - SCS Semiconductor Characterization System, under ambient conditions.

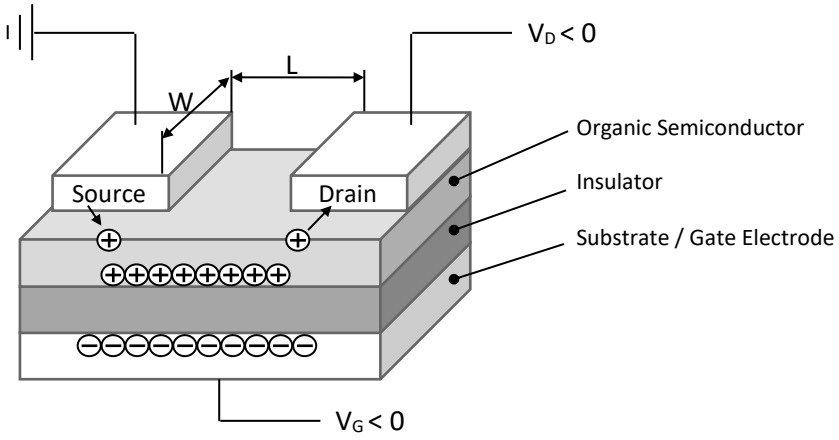

Figure 1. Schematic structure of the fabricated bottom – gate top – contact OFETs.

3. RESULTS AND DISCUSSIONS

In order to characterize fabricated bottom – gate top – contact P3HT based OFET, output and transfer characteristics were obtained by applying sweep voltages from 0 to –50 volts to the source – drain electrodes and from 0 to –140 volts to the gate electrode. Drain – source current (I_{DS}) values were recorded as a function of drain – source voltage (V_{DS}) at different gate voltages (V_{GS}). Gold (*Au*) is selected as gate metal and Thermoplastic Polyurethane (TPU) as gate insulator. Thickness of the TPU was measured as 2000 nm by using Veeco Dektak 8 surface profilometer. I_{DS} versus V_{DS} plot of the OFET is called the output characteristic of OFET. Essential OFET parameters, such as mobility (μ) and threshold voltage (V_{th}) can be determined by the output and transfer characteristics. Output characteristic of fabricated P3HT – based organic field – effect transistor with gold (*Au*) source – drain electrode is presented in Figure 2. As seen from the figure that output characteristic of the OFET showed typical I_{DS} – V_{DS} behavior, indicating well modulated drain – source current (I_{DS}) by the applied gate voltage (V_{GS}). The output characteristic of the organic field-effect transistor can be studied in two regimes, linear regime and saturated regime. For p – channel OFETS, a negative voltage must be applied to the gate metal in order to OFET to be in accumulation mode. Output characteristic obtained from fabricated P3HT based organic field – effect transistors showed that an increase in applied negative gate voltage (V_{GS}) caused to increase in drain-source current (I_{DS}) indicating p – channel behavior of the OFETs. The maximum drain – source currents (I_{DS}) were measured as 0.53 μA and 0.77 μA at V_{GS}= –140 V for the OFET with gold and silver source – drain electrodes, respectively.

An *off* state of OFET occurs when no voltage is applied between the gate and source electrodes (V_{GS}=0). Ideally, the drain – source current must be equal to zero (I_{DS}=0) at V_{GS}=0. However a non - vanishing current (I_{off}) is measured for both fabricated P3HT – based OFETs with gold and silver drain - source electrodes. Mobility (μ) is defined as the carrier velocity per unit electric field and threshold voltage is defined as the gate voltage (V_{GS}) needed to establish a conducting channel between the source and drain contact.

For linear region of the output characteristic ($V_{DS} << |V_{GS} - V_{th}|$), the relationship between the I_{DS} and V_{DS} is given by [11-14],

$$I_{DS} = \frac{W}{L}\mu_{lin}C_i(V_{GS} - V_{th})V_{DS}, \qquad (1)$$

where C_i is the capacitance of the TPU insulating layer per unit area, μ_{lin} is the field - effect mobility of carriers in the channel in linear regime, V_{th} is the threshold voltage, and W and L are the channel width and length, respectively. C_i can be calculated using $\varepsilon_0\varepsilon/d$ where ε is the dielectric constant of the TPU gate insulator, ε_o is the permittivity of free space, and d is the thickness of the gate insulator. It must be mentioned that under these conditions OFETs operate as accumulation mode enhancement transistors, which turns the transistor *on*.

The field effect mobility for the linear region can be rewritten as:

$$\mu_{lin} = \frac{L}{WC_i}\left(\frac{\partial I_{DS}}{\partial V_{GS}}\right)\cdot\frac{1}{V_{DS}}, \qquad (2)$$

where $(\partial I_{DS}/\partial V_{GS})$ is the transconductance.

The expression for I_{DS} in the saturation regime is given by the equation (3) [15-17] at $V_{DS} > V_{GS} - V_{th}$:

$$I_{DS} = \frac{W}{2L}\mu_{sat}C_i(V_{GS} - V_{th})^2 \quad \text{for } V_{DS} > V_{GS} - V_{th}, \qquad (3)$$

where μ_{sat} is the field - effect mobility of carriers in the channel in saturation regime.

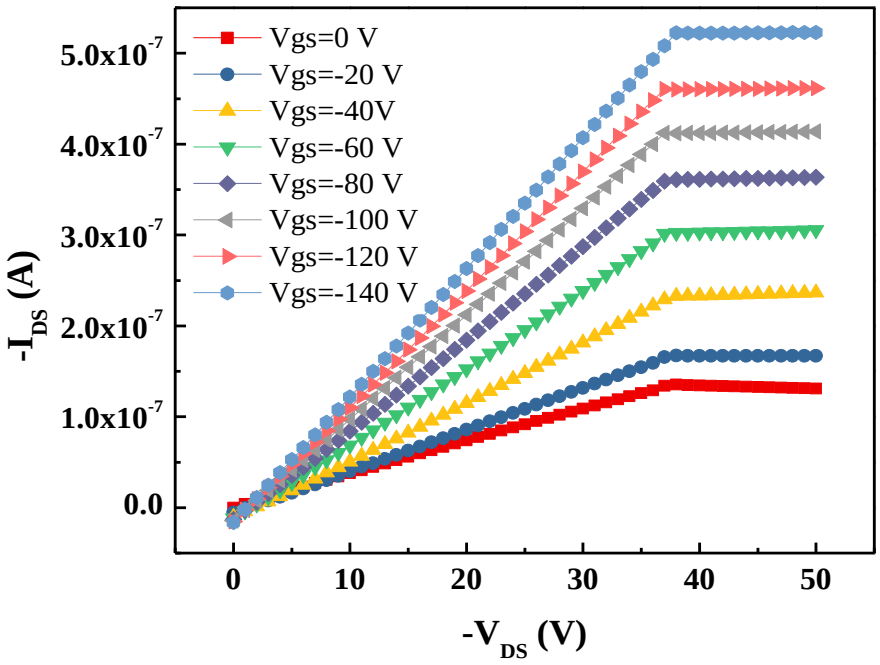

Figure 2. Output characteristics of the OFET with *Au* drain – source electrode.

In order to compare effects of the type of source – drain metal electrodes on the performance of the OFETs, (I_{DS} - V_{DS}) characteristics of two OFET devices with source – drain electrodes fabricated from gold (*Au*) and from silver (*Ag*), were presented in Fig. 3.

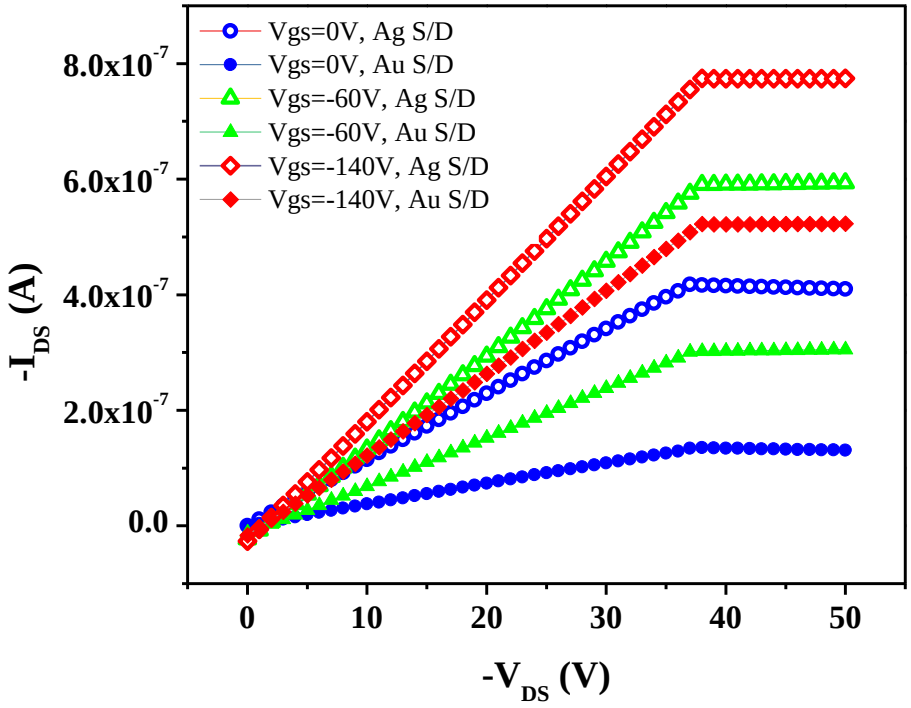

Fig 3. Comparison of output characteristics of OFETs with *Au* and *Ag* drain – source electrodes for gate voltages of V_{GS}=0, -60, and -140 V.

As is well known, the source and drain electrodes, specific requirements have to be met. They have to be energetically well - matched with the organic semiconductor layer so that ohmic contact can be formed to allow efficient charge injection. For p – type organic semiconductor material, the work function of source/drain electrodes can be match or close to highest occupied molecular orbital (HOMO) of p – type organic semiconductor material for an efficient holes injection from or onto HOMO levels due to a low injection barrier. The work function of *Au* is 5.31 – 5.47 eV [18] while that of *Ag* is 4.52 – 4.74 eV [18]. Thus, it is expected that, *Au* forms good ohmic contact with p – type P3HT semiconducting polymer with qualitatively lower contact resistance. Very likely, *Ag* formed a potential barrier (Schottky barrier) at the *Ag* – P3HT semiconductor interfaces with relatively high contact resistance. However, measured drain current in saturation regime of the OFET with *Au* drain - source metal was measured as 0.135, 0.303, and 0.522 μA for V_{DS} = 0, –60, and –140 volts respectively. The values for the OFET with *Ag* drain - source metal was measured as 0.416, 0.591, and 0.774 μA for V_{DS} = 0, –60, and –140 volts respectively. The values revealed that maximum current values in saturation regime were measured from the OFETs with *Ag*

drain – source electrodes, contrary to expected behavior as mentioned above, due to close matching of work function of *Au* and HOMO level of P3HT (~5.2 eV) [19, 20]. This behavior can be explained as follows:

The metal–polymer interface (and morphology of a polymer film near the interface) plays a critical role in governing the carrier injection/collection efficiency [21]. It was reported by Bhargava and coworkers that the current – voltage ($I - V$) characteristics of *Au*(top)/ P3HT/*Au*(bottom) devices in sandwich form showed nearly a non-ohmic hole injection from top *Au* electrode into the P3HT and, against to the behavior, ohmic hole injection from bottom *Au* electrode into the P3HT. The difference in hole injection behavior for the top *Au* electrode configuration has been concluded as the formation of distorted π-conjugation due to the diffusion of *Au* metal into the polymer matrix, during vacuum deposition of the metal. It was considered as formation of the distortion results a mismatch between the Fermi level of the *Au* metal and highest occupied molecular orbital (HOMO) energy level of the polymer (a junction with large barrier for carrier injection) that hinders the charge injection process from *Au* into polymer. [22]. Similar results were also reported earlier [23]. Interface in top electrode arrangement (*Au*/P3HT) is not similar to that of the bottom electrode arrangement, (P3HT/*Au*). The studies for change in work function for pre- and post-deposited *Au* (P3HT/*Au* and *Au*/P3HT) revealed that uncontrolled contamination of the *Au* electrode could decrease the work function of *Au* as low as 4.7 eV [24, 25] and 4.8 eV [26]. Similar changes as an increase in work function may occur for top contact and bottom contact silver metal onto P3HT. Another explanation is reported by Liyana and coworkers [20]. In this study, an OFET with P3HT – as an active layer and aluminum source – drain device was fabricated. It was reported that P3HT / aluminum contacts showed ohmic behavior although misalignment of energy levels between work function of aluminum (~4.08 eV) [20] and HOMO level of P3HT (~5.2 eV). This behavior was attributed to the improved charge injection due to air exposure. It can be concluded that similar improved charge injection behavior might be occurred between *Ag* drain – source electrode and P3HT interface of our fabricated OFET device.

Figure 4 shows the drain – source current versus gate voltage ($I_{DS} - V_{GS}$) and square root of the drain – source current, ($\sqrt{|I_{DS}|} - V_{GS}$) characteristics for P3HT based OFETs transistor with a *Au* drain – source metal. The curves were obtained at V_{DS}= –40 V. As shown by equation (3), a plot of $\sqrt{|I_{DS}|}$ vs. V_{GS} gives a straight line with the slope proportional to μ_{sat}. By plotting I_{DS} versus V_{GS} on a linear scale, V_{th} and μ_{lin} are determined by calculating the x – axis intercept and slope of I_{DS} vs. V_{GS} line, respectively. Mobility (μ), threshold voltages (V_{th}), and V_{on} potential of the OFETs studied are given in table 1. As can be seen from the table 1, OFET with *Ag* drain – source showed greater field – effect mobility than that of *Au* ($\mu_{Ag} > \mu_{Au}$).

Magnitude of the threshold voltage (V_{th}) of OFET with *Au* drain – source is found less than that of OFET with *Ag* drain – source metal ($|V_{th\ (Au)}| < |V_{th\ (Ag)}|$). The mobility values found in this study are better than some of the values for P3HT based OFETs reported earlier [27-31]. Figure 5 is presented to compare transfer characteristics of the OFETs with *Au* and *Ag* drain – source electrodes at $V_{DS} = -40$ V.

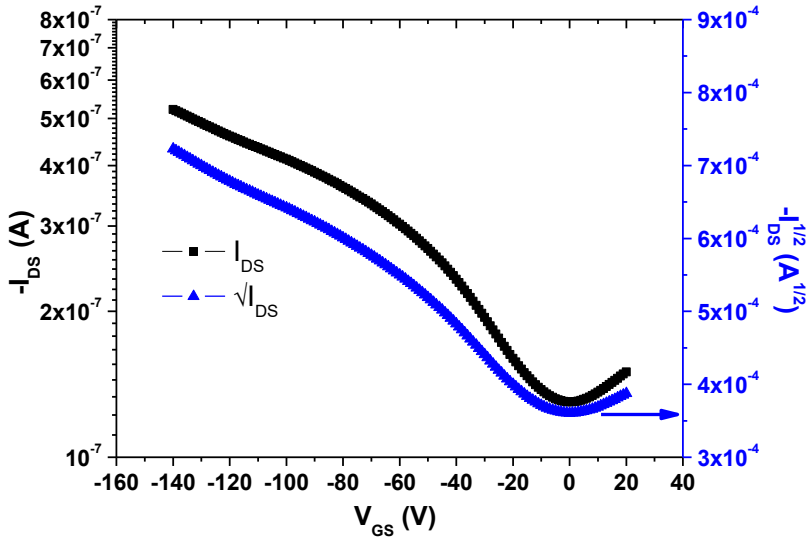

Figure 4. Transfer characteristics of OFET with *Au* drain – source electrode at $V_{DS} = -40$ V.

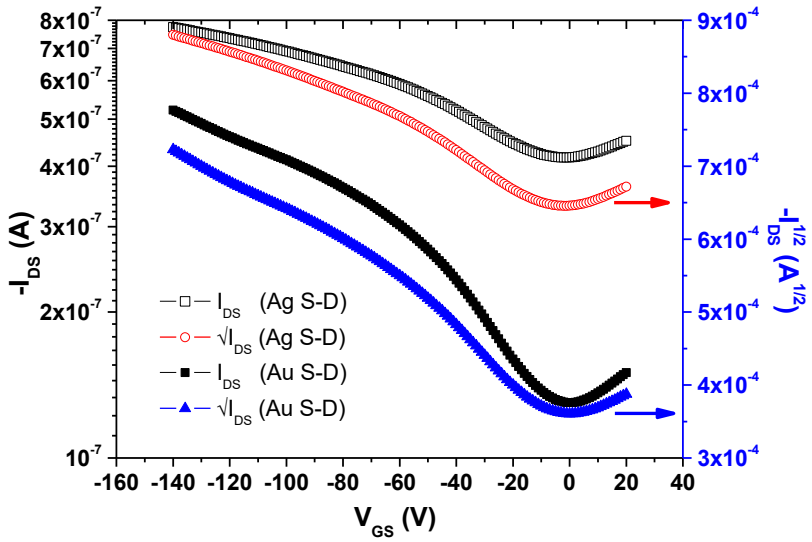

Figure 5. Comparison of transfer characteristics of OFETs with *Au* and *Ag* drain – source electrodes at $V_{DS} = -40$ V.

Table 1. Performance parameters (μ_{sat}, μ_{lin}, V_{th}, and V_{on}) of the fabricated OFETs.

Drain – Source Metal	μ_{sat} (cm²/Vs)	μ_{lin} (cm²/Vs)	V_{th} (V)	V_{on} (V)
Ag	2.17×10^{-2}	2.31×10^{-1}	-6.5	-20
Au	7.88×10^{-3}	4.06×10^{-2}	-3.0	-17

4. CONCLUSIONS

In this study, we fabricated P3HT based OFETs on gold coated glass substrate using TPU as gate dielectric and *Au* as a gate electrode. P3HT – based OFET devices with two different set of *Au*/*Ag* metallic source - drain electrodes were manufactured. Output and transfer electrical characteristics of all fabricated P3HT – OFETs are tested. It was expected that OFETs with *Au* drain – source electrodes govern the charge - injection better than that of OFETs with *Ag* drain – source electrodes due to work function of *Au* is more close to highest molecular orbital (HOMO) level of P3HT than work function of *Ag*. It was shown that silver (*Ag*) as a source – drain metallic electrode material is more preferable for governing the charge - injection and extraction process. This behavior can be explained as decreasing of work function of the *Au* during deposited on P3HT, as reported previously. Similar changes as an increase in work function may occur for top contact silver metal onto P3HT. Fabricated devices with TPU - gate insulator and *Ag* source – drain metallic electrodes show a significant improvement in field - effect mobility compared to manufactured P3HT – OFETs with *Au* drain – source metallic electrodes ($\mu_{Ag} > \mu_{Au}$). Magnitude of the threshold voltage (V_{th}) of OFET with *Au* drain – source is found less than that of OFET with *Ag* drain – source metal ($|V_{th\ (Au)}| < |V_{th\ (Ag)}|$). The values found in this study are better than some of the values for P3HT based OFETs reported earlier.

ACKNOWLEDGEMENTS

We are thankful to the Research Foundation of Marmara University (BAPKO), Commission of Scientific Research Projects. [Grant Numbers FEN-A-130711-0258 and FEN-BGS-290506-0114].

REFERENCES

[1] Z. Bao, A. Dodabalapur, and A. J. Lovinger, Applied Physics Letters 69, 4108 (1996)

[2] Yu Fu, Ching Lin, Feng-Yu Tsai, Organic Electronics 10 (2009) 883–888

[3] S. Tiwari, R. Prakash, S. K. Balasubramanian, 2013 Annual IEEE India Conference, Kamran Ali, Ullrich Pietsch and Souren Grigorian, Journal of Applied Crystallography, 46, (2013), 908-911

[4] N.G. Semaltianos, Microelectronics Journal 38 (2007) 754–761

[5] G.P. Mikhailov, T.I. Borisova, D.A. Dmitrochenko, J. Tech. Phys. (USSR) 26 (1956) 1924 2 (1961) 387

[6] L. Shang, M. Liu, D. Tu, Ge Liu, X. Liu, and Z. Ji, Low-Voltage Organic Field-Effect Transistor with PMMA/ZrO2 Bilayer Dielectric, IEEE Transactions on Electron Devices, 56, (2009), 370-376

[7] A.-L. Deman, J. Tardy, PMMA–Ta2O5 bilayer gate dielectric for low operating voltage organic FETs, Organic Electronics 6 (2005) 78–84

[8] K. Ali, U. Pietsch and S. Grigorian, Journal of Applied Crystallography, 46, (2013), 908-911

[9] H. Mi, X. Jing, B. S.Hagerty, G. Chan, An huang, Lih-S. Tuing, Materials&Design 127 (2017) 106-114.

[10] M. Aljada, K. Mutkins, G. Vamvounis, P. Burn, and P.Meredith, High quality shadow masks for top contact organic field effect transistors using deep reactive ion etching, J. Micromech. Microeng. 20 (2010) 075037

[11] Sze SM. Physics of Semiconductor Devices. Wiley, New York, 1981

[12] Th. Birendra Singh and Niyazi Serdar Sariciftci, Progress In Plastic Electronics Devices, Annu. Rev. Mater. Res. 2006. 36:199–230

[13] Yong Xu, Chuan Liu, Dongyoon Khim, Yong-Young Noh, Development of high-performance printed organic field-effect transistors and integrated circuits, Phys.Chem. Chem. Phys., (2015), 17, 26553

[14] H. C. Avila, P. Serrano, A. R.J. Barreto, Z. Ahmed, C. de P. Gouvêa, C. Vilani, R. B. Capaz, Cleber F.N. Marchiori, M. Cremona, High hole-mobility of rrP3HT in organic field - effect transistors using low - polarity polyurethane gate dielectric, Organic Electronics, 58, (2018), 33 - 37

[15] T. W. Lee, J. H. Shin, I. N. Kang and S. Y. Lee, Photocurable Organic Gate Insulator for the Fabrication of High-Field Effect Mobility Organic Transistors by Low Temperature and Solution Processing, Advanced Materials, 2007, 19, 2702–2706

[16] A. Khaliq, F. Liang Xue, K. Varahramyan, Numerical simulation of spin coated P3HT organic thin film transistors with field dependent mobility and distributed contact resistance, Microelectronic Engineering, 86, (2009), 2312–2315

[17] Wu Ren-lei, Cheng Xiao-man, Zheng Hong, and Yin Shou-gen, Performance of pentacene-based organic field effect transistors using different polymer gate dielectrics, Optoelectronics Letters, Vol.5, 2009

[18] https://public.wsu.edu/~pchemlab/documents/Work-functionvalues.pdf, last accessed date: 01.11.2018

[19] A. K. Thakur, A. K. Mukherjee, D. M. G. Preethichandra, W. Takashima, and K. Kaneto, Charge injection mechanism across the Au-poly(3-hexylthiophene-2,5-diyl) interface, Journal of Applied Physics, 101, 104508, 2007

[20] V.P. Liyana, Stephania Ann Mathew, K. Shiju, and P. Predeep, Effect of source – drain electrodes on the performance parameters of P3HT based OFET, AIP Conference Proceedings, 1620, (2014), 596

[21] D.B.A. Rep, A.F. Morpurgo, T.M. Klapwijk, Doping-dependent charge injection into regioregular poly(3-hexylthiopehene), Organic Electronics, 4 (2003) 201–207

[22] K. Bhargava, V. Singh, Investigation of Gold and Poly(3-Alkylthiophene) interface in top and bottom contact structures, Synthetic Metals, 211 (2016) 49–57

[23] D.B.A. Rep, A.F. Morpurgo, T.M. Klapwijk, Doping-dependent charge injection into regioregular poly(3-hexylthiopehene), Organic Electronics, 4 (2003) 201–207

[24] A. Wan, J. Hwang, F. Amy, and A. Kahn, Impact of electrode contamination on the a-NPD/Au hole injection barrier, Organic Electronics, 6, (2005), 47-54

[25] A. K. Thakur, A. K. Mukherjee, D. M. G. Preethichandra, W. Takashima, and K. Kaneto, Charge injection mechanism across the Au-poly(3-hexylthiophene-2,5-diyl) interface, Journal of Applied Physics, 101, 104508, 2007

[26] J. Hwang, A. Wan, A. Kahn, Energetics of metal–organic interfaces: New experiments and assessment of the field, Materials Science and Engineering R 64 (2009) 1–31

[27] Feng-Yu Yang, Meei-Yu Hsu, Gue-Wuu Hwang, Kuo-Jui Chang, High-performance poly(3-hexylthiophene) top-gate transistors incorporating TiO2 nanocomposite dielectrics, Organic Electronics 11 (2010) 81–88

[28] U. Bielecka, P. Lutsyk, K. Janus, J. Sworakowski, W. Bartkowiak, Effect of solution aging on morphology and electrical characteristics of regioregular P3HT FETs fabricated by spin coating and spray coating, Organic Electronics 12 (2011) 1768–1776

[29] S.W. Lin, Y.M. Sun, A.M. Song, Enhanced stability of poly (3-hexylthiophene) transistors with optimally cured poly (methyl methacrylate) dielectric layers, Synthetic Metals 160 (2010) 2430–2434

[30] S. Tiwari, A. Kumar Singh, L. Joshi, P. Chakrabarti, W. Takashima, Keiichi Kaneto, Rajiv Prakash, Poly-3-hexylthiophene based organic field-effect transistor: Detection of low concentration of ammonia, Sensors and Actuators B 171– 172 (2012) 962– 968

[31] M. Estrada, I. Mejia, A. Cerdeira, B. Iniguez, MIS polymeric structures and OTFTs using PMMA on P3HT layers, Solid-State Electronics 52 (2008) 53–59

STRUCTURE ANALYSIS AND SOLID STATE LUMINESCENCE PROPERTIES OF THE NEW TB (III) COMPOUND WITH 1-D HEXAGONAL CHANNEL

Y. Acar[1], M. B. Coban[1,2] and H. Kara[1,3]

[1]*Department of Physics, Faculty of Art and Science, Balikesir University, Balikesir. Turkey*

[2]*Center of Science and Technology Application and Research,Balikesir University, Balikesir, Turkey*

[3]*Department of Physics, Faculty of Science, Mugla Sitki Kocman University, Mugla. Turkey*

E-mail: yahsi@balikesir.edu.tr

Abstract

In this study, three-dimensional Tb (III) Metal-Organic Framework (MOF) was synthesized under solvothermal condition. The compound can be formulated as [Tb (III).1/2(btb).(H_2O)](H_2O) (**1**) (btb= 1,3,5-Tris(4-carboxyphenyl) benzene). Single crystal diffraction techniques were used find out crystal structures and features of the Tb (III) compound. Single crystal analysis reveals that compound **1** crystallizes in trigonal R32 space group with the unit cell parameter of a=b=28.6303(7), and c=12.0960(4) and α=β= 90° and γ=120°. The asymmetric unit consists of a Tb (III) ion, half btb^{2-} anion, one coordinated water molecule and one lattice water molecule. Each Tb (III) atom adopts a distorted monocapped square-antiprismatic geometry, which the nine-coordinated environment around Tb (III) center is completed by eight oxygen atoms from phenyl group of the btb ligand and one oxygen atoms from the coordinated water molecule. All bond lengths and angles are comparable to similar structures. Furthermore, Tb (III) ion emits intense green luminescence in the visible region.

Keywords: Tb-MOF, Crystal structure, Luminescence properties

1. INTRODUCTION

Recently, the design and synthesis of metal-organic frameworks (MOFs) with large pores have attached a great deal of attention due to their interesting topologies and also their potential applications as functional materials [1–3]. Although there are many studies on MOFs, the number of lanthanide metal based MOFs are very limited compared to transition metal based MOFs [4,5]. The selection of lanthanides which have high coordination numbers than transition metals makes these materials popular due to their interesting geometries and multidimensional (2D or 3D) structures and also interesting magnetic and photoluminescence behavior [6,7]. However Organic Light Emitting Diodes (OLEDs) have been widely investigated for many potential applications such as display technologies and electronic devices recently. Unique luminescent properties, long lifetimes and large Stokes shifts make lanthanide-based metal-organic frameworks (Ln-MOFs) perfect materials for OLED technologies [8].

In this study, Tb^{III}-MOFs (**1**) has been synthesized using the solvothermal method and characterized by single crystal X-ray diffraction analysis, UV-Visible spectroscopy. Furthermore, solid-state photoluminescence properties in the visible region of this lanthanide-based compound have also been investigated at room temperature.

2. MATERIAL AND METHODS

2.1. General Methods and Measurements

All the reagents and solvents were commercially available. Powder X-ray diffraction was measured with a Bruker-AXS D8 diffractometer ($\lambda_{Cu\text{-}K\alpha}$ = 1.5418 Å). The UV-Visible spectra in solid state were recorded on Ocean Optics Maya 2000Pro. The solid-state photoluminescence spectra in the visible region were recorded using an ANDOR SR500i-BL at room temperature. Single crystal X-ray measurement was done with an Xcalibur diffractometer ($\lambda_{Mo\text{-}K\alpha}$ = 0.71073 Å) at room temperature. The crystal structure was solved by direct methods and refined on F^2 with SHELXTL [9] using Olex2 [10]. The crystallographic data and the details of structure solution and refinements for compound **1** are listed briefly in Table 1. ‡ CCDC 1875196 contains the crystallographic data for the structural analyses of Tb^{III}-MOFs (**1**). These data can be obtained free of charge via www.ccdc.cam.ac.uk.

2.2. Synthesis of Tb-MOF (1)

The solvothermal reaction of $TbCl_3.6(H_2O)$ (0.1 mmol) and H_3btb [1,3,5-Tris(4-carboxyphenyl) benzene] (0.1mmol) and mixed solvent dimethylformamide (10 ml) and water (5 ml) were sealed in a 45 ml Teflon-lined stainless steel autoclave. The autoclave was heated at 130 °C for 5 days under pressure and then cooled to the room temperature. The single crystals of Tb^{III}-MOF (**1**) were obtained and washed with DMF. The schematic diagram of **1** has been given in Scheme 1.

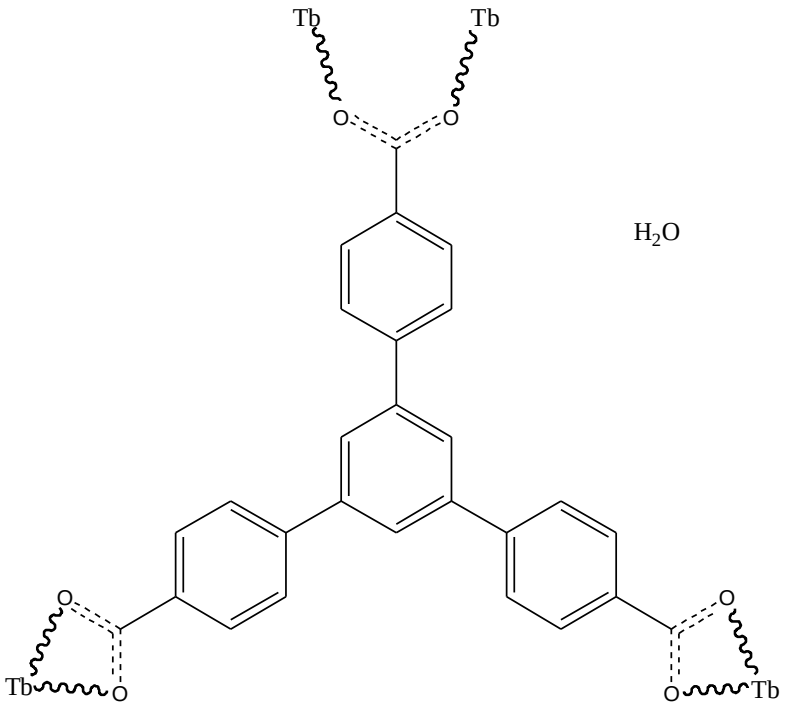

Scheme 1: Schematic diagram of compound **1**.

3. RESULTS AND DISCUSSION

3.1. Crystal Structure Determination

The crystal structure of **1** is shown in Figure 1 and some bond lengths and angles for compound **1** are listed in Table 2. The X-ray structure analysis of Tb^{III}-MOF, **1,** shows that each Tb (III) ion is nine-coordinated by eight oxygen atoms from H_3btb ligand and one oxygen atom from coordinated water molecule. The environment around this metal center is described as distorted monocapped square-antiprismatic geometry (Figure 1b). In compound **1**, Tb(III) atoms have been connected by μ-$oxo_{carboxylate}$ bridges from btb ligands to form 2D layers and these layers are further interlinked via by μ-$oxo_{carboxylate}$ bridges resulting in 3D architecture (Figure 2 and 3). As seen in Figure 2b, the chain structure of Tb (III)

compound led to 1D hexagonal channels along the *c*-axis as a result of bridged with tripodal carboxylate ligand (H_3btb). The distance between Tb (III) atoms in hexagonal pores is 16.789 Å while the shortest non-bonding Tb…Tb distance is 4.064 Å. The wide pore structure could also make this Tb-MOF a good candidate for gas absorption.

Table 1. Crystal data and structure refinement

Empirical formula	$C_{27}H_{21}O_9Tb$
Formula weight ($g.mol^{-1}$)	648.36
Temperature (K)	150
Crystal system, Space group	Trigonal, R32
Unit cell dimensions	a= 28.6303(7) Å α=90° b= 28.6303(7) Å β=90° c= 12.0960(4) Å γ= 120°
Volume ($Å^3$)	8586.7(5)
Z	9
ρ_{calc} ($g.cm^{-3}$)	1.128
μ (mm^{-1})	1.89
Reflections collected	6077
Independent reflections	3610 [R_{int} = 0.024]
Goodness-of-fit on F^2	1.120
R indices [I>2σ (I)]	R_1 = 0.027, wR_2 = 0.065

Table 2. Selected bond lengths [Å] and angles [°].

Bond lengths (Å)			
Tb1—O1	2.412 (6)	Tb1—O4^{iv}	2.358 (4)
Tb1—O2^{i}	2.335 (4)	Tb1—O4^{ii}	2.715 (4)
Tb1—O3^{ii}	2.442 (4)	Tb1—C16^{ii}	2.901 (6)
Bond Angles (°)			
O1—Tb1—O3^{ii}	142.81 (10)	O3^{iii}—Tb1—O3^{ii}	74.4 (2)
O1—Tb1—O4^{iii}	129.66 (8)	O3^{ii}—Tb1—O4^{iii}	67.58 (12)
O2—Tb1—O1	79.01 (11)	O3^{ii}—Tb1—O4^{ii}	50.55 (12)
O2—Tb1—O2^{i}	158.0 (2)	O4^{iv}—Tb1—O1	72.08 (9)

O2—Tb1—O3^{ii}	122.00 (14)	O4^{iv}—Tb1—O3^{iii}	77.29 (13)
O2^{i}—Tb1—O3^{ii}	76.93 (14)	O4^{iv}—Tb1—O3^{ii}	135.25 (13)
O2—Tb1—O4^{ii}	72.11 (14)	O4^{v}—Tb1—O4^{ii}	67.67 (14)
O2—Tb1—O4^{iv}	83.32 (14)	O4^{iv}—Tb1—O4^{v}	144.15 (18)
O2—Tb1—O4^{iii}	123.40 (14)	O4^{iv}—Tb1—O4^{ii}	140.60 (6)
O2^{i}—Tb1—O4^{iv}	89.94 (15)	O4^{ii}—Tb1—O4^{iii}	100.69 (16)
O2^{i}—Tb1—O4^{iii}	72.11 (14)	Tb1^{viii}—O4—Tb1^{vii}	106.23 (14)

Symmetry codes: (i) *x*−*y*+1, −*y*+2, −*z*+1; (ii) −*y*+1, *x*−*y*+1, *z*; (iii) −*x*+1, −*x*+*y*+1, −*z*+1; (iv) −*x*+*y*+2/3, −*x*+4/3, *z*+1/3; (v) *y*+1/3, *x*+2/3, −*z*+2/3; (vi) −*x*+4/3, −*x*+*y*+2/3, −*z*+2/3; (vii) −*x*+*y*, −*x*+1, *z*; (viii) −*y*+4/3, *x*−*y*+2/3, *z*−1/3.

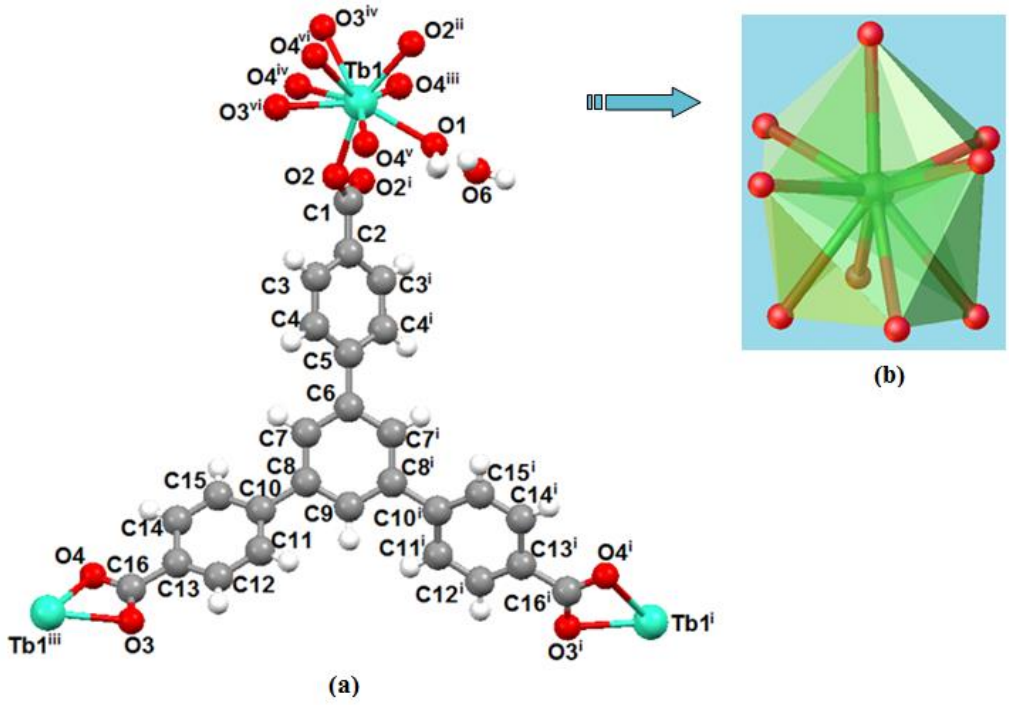

Figure 1. (a) A view of the molecular structure of **1**. **(b)** Coordination environment of Tb (III) ion.

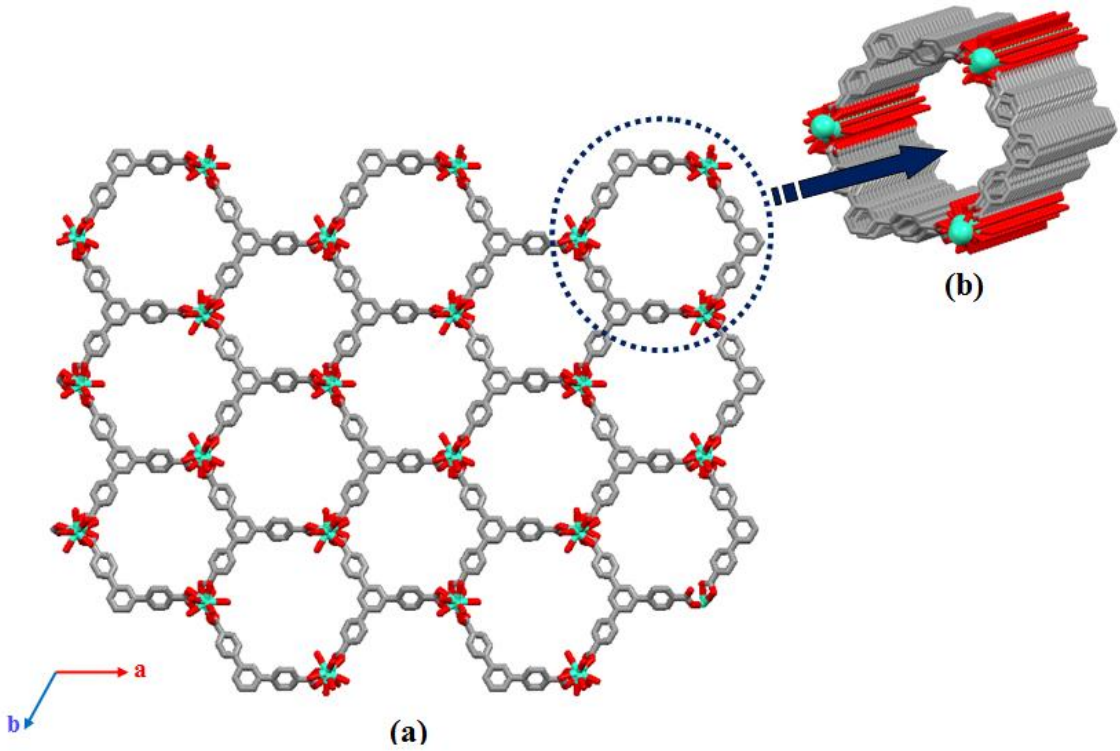

Figure 2. (a) 2D layer structure and **(b)** 1D hexagonal channel of compound **1**.

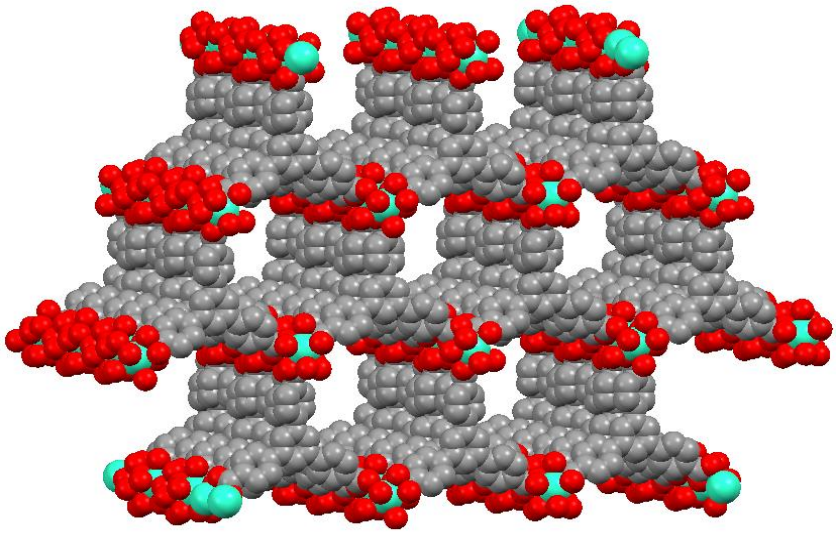

Figure 3. A view of spacefill illustration of a 3D network of **1**.

3.2. UV-Vis Absorption Spectroscopy

The UV-Vis absorption spectra of the ligand (H_3btb) and compound **1** were determined in the solid state (Fig. 4). The absorption spectra of the H_3btb ligand display two maximum absorptions at 342 and 438

nm which may be assigned to the singlet-singlet π–π* and n–π* transitions, respectively [11]. As seen in Fig. 4, the Tb^{III} compound display one strong absorption band at 426 nm and also indicates one shoulder at 294 nm, which may be assigned to n–π* and π–π*, respectively.

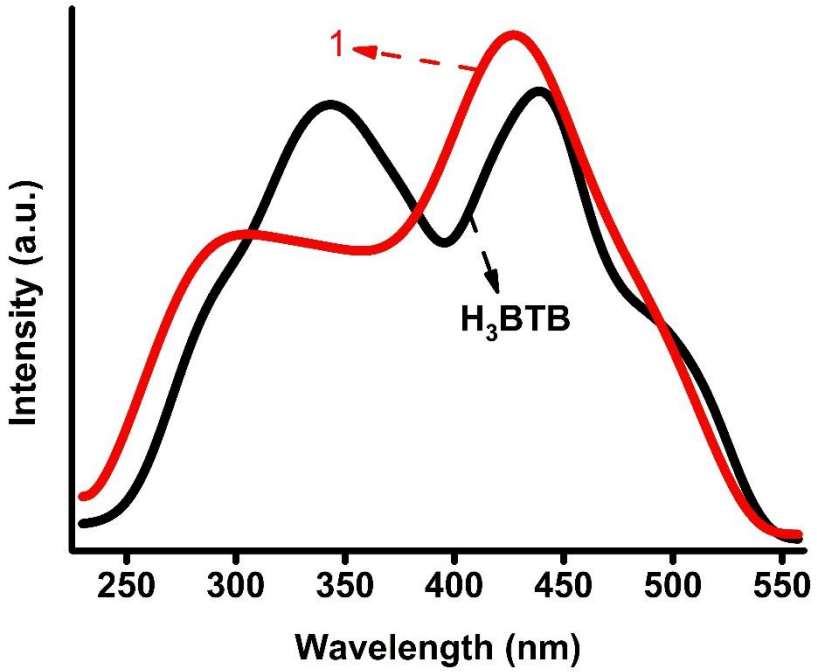

Figure 4. The UV-Vis. absorption spectrums of the ligand (H_3btb) and compound **1**.

3.3. Solid State Luminescence Properties

The luminescent properties of compound **1** and the ligand (H_3btb) were explored at room temperature in the solid state (λ_{ex} = 349 nm). As shown Fig.5a, the ligand (H_3btb) shows blue emission at 450 nm and a shoulder attached to a wide band at 565 nm, which may be assigned to the n→π* or π→π* intra-ligand electron transitions [12]. As seen Fig.5b, Tb (III) ion emits intense green luminescence in the visible region and four characteristic peaks appear at 488, 543, 582 and 621 nm correspond to $^5D_4 \rightarrow {}^7F_j$ (j = 6-3) transition respectively. The $^5D_4 \rightarrow {}^7F_6$ and $^5D_4 \rightarrow {}^7F_5$ emissions result from an electric dipole transition and a magnetic dipole transition, respectively. The most intense emission is centered at 546 nm, which corresponds to the hypersensitive transition, exhibiting a strong green luminescent emission for the solid pattern. Besides, the absence of the emission bands of the ligand in the emission spectra of compound **1** indicates the efficient transfer of the excitation energy from the ligand to metal ion [13].

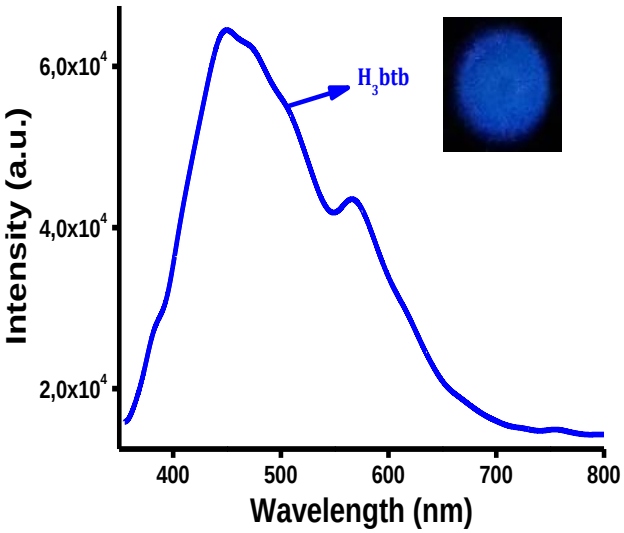

(a)

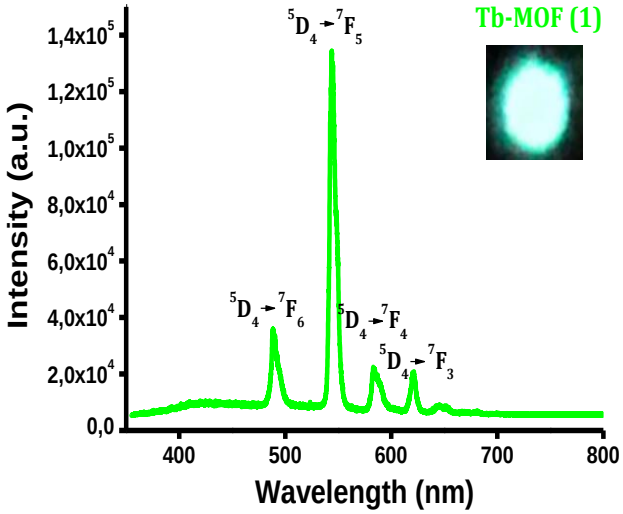

(b)

Figure 5. (a) The solid-state emission spectrum of the ligand (H_3BTB) (inset photo is a photoluminescent image). (b) The solid-state emission spectrum of compound **1** (inset photo is a photoluminescent image).

Meanwhile, the absorption coefficients of trivalent lanthanide ions are too low, so they don't become excited directly. The use of suitable organic ligands to coordinate these lanthanide ions can lead to overcoming this problem. To sensitize lanthanide luminescence in MOFs generally antenna effect of the ligands is utilized which effectively transfer the energy acquired to the Ln ions in the complex (Figure 6).

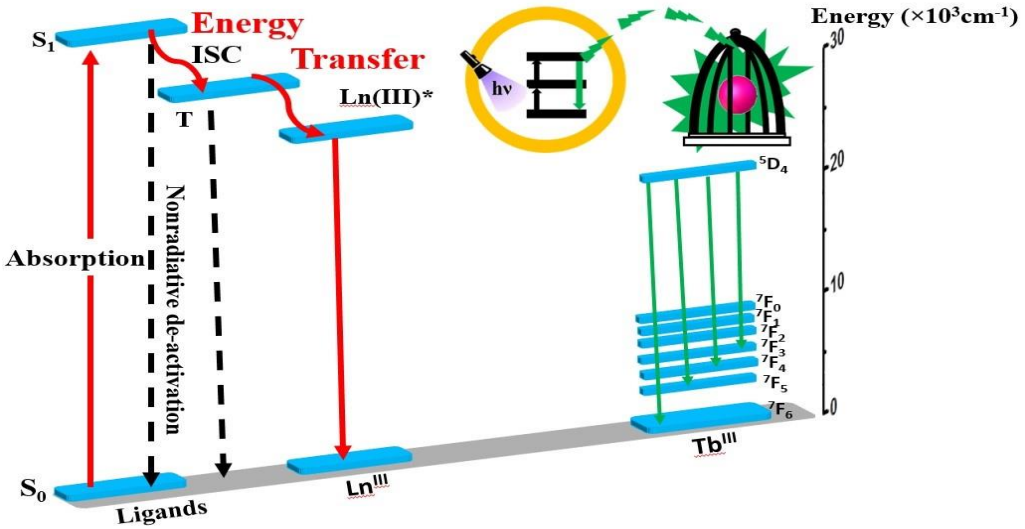

Figure 6. The schematic diagram for the energy transfer mechanism (left side) and energy level diagrams (right side) of compound **1**.

The antenna effect can be determined by overlapping regions between the absorption spectra of free ligands and the excitation spectra of the compound [14]. The overlapping of the excitation spectrum of Tb^{III}-MOF and the absorption spectra of H_3btb ligand are shown in Fig. 7. The overlap between excitation and absorption spectra points that the central Tb^{3+} ions in compound **1** can be sensitized by H_3btb ligand via the antenna effect. Additionally, with a prominent π–conjugate system composed of the benzene rings and three carboxylate groups, H_3btb ligand behaves as an efficient antenna linker for achieving effective and powerful lanthanide ion' luminescence. And such an O-donor ligand can enhance the fluorescence emissions of complexes, which are present of interest for the development of fluorescent materials.

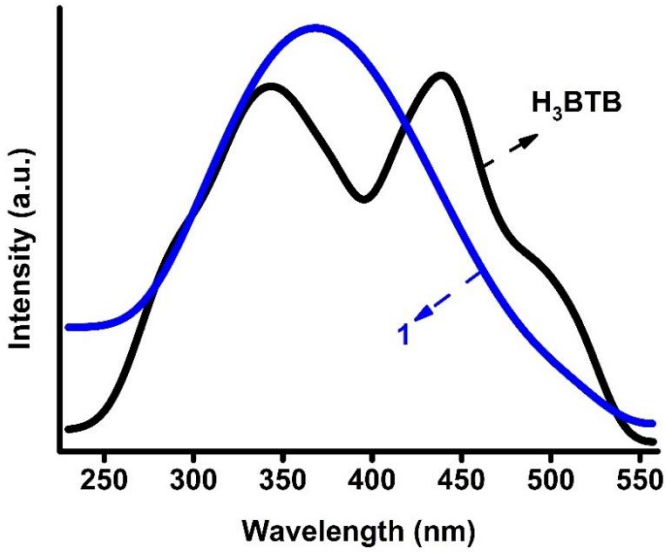

Figure 7. The overlap of the UV-absorption spectrum of the ligand (H_3btb) and the excitation spectrum of compound **1.**

4. CONCLUSION

In this study, lanthanide-based organic framework Tb^{III}-MOF (**1**) has been synthesized by the solvothermal method using H3btb as O-donor ligand and characterized by single crystal X-ray diffraction method. The X-ray results show that Tb (III) atom is eight-coordinated and the environment around the metal center is described as a distorted monocapped square-antiprismatic geometry. The Tb (III) organic framework exhibits good photoluminescence emission which in the visible region Tb (III) ion emits intense green luminescence in the solid state. Thus, this compound can be used as phosphor material in new functional materials and OLEDs with fascinating properties.

ACKNOWLEDGMENTS

This work was supported by the Scientific Research Projects Coordination Unit of Balikesir University under the project number BAP 2017/183. The authors are grateful to Dokuz Eylul University for the use of X-Ray diffractometer (Research grant No. 2010.KB.FEN.13) and Balikesir University, Science and Technology Application and Research Center (BUBTAM), for the use of the photoluminescence spectrometer.

REFERENCES

[1] Zhao, B., Chen, X., Cheng, P., Liao, D., Yan, S., Jiang, Coordination Polymers Containing 1D Channels as Selective Luminescent Probes, Journal of the American Chemical Society, 126, 15394–15395, 2004.

[2] Zhu, H., Fan, J., Okamura, T., Zhang, Z., Liu, G., Yu, K., Metal − Organic Architectures of Silver (I), Cadmium (II), and Copper (II) with a Flexible Tricarboxylate Ligand, Inorganic Chemistry, 45, 3941–3948, 2006.

[3] Bao, S. S., Li-Fang, M., Wang, Y., Fang, L., Zhu, C. J., Li, Y. Z., Zheng, L. M., Anion-directed self-assembly of lanthanide - Notp compounds and their fluorescence, magnetic, and catalytic properties, Chemistry – A European Journal, 13, 2333–2343, 2007.

[4] Rodrigues, C. V., Luz, L. L., Dutra, J. D. L., Junior, S. A., Malta, O. L., Gatto, C. C., Streit, H. C., Freire, R. O., Wickleder, C., Rodrigues, M. O., Unusual photoluminescence properties of the 3D mixed-lanthanide-organic frameworks induced by dimeric structures: A theoretical and experimental approach, Physical Chemistry Chemical Physics, 16, 14858–14866, 2014.

[5] Lu, Z., Wen, L., Yao, J., Zhu, H., Meng, Q., Two types of novel layer framework structures

assembled from 5-sulfosalicylic acid and lanthanide ions, Crystal Engineering Communication, 8, 847–853, 2006.

[6] Zhang, J., Ji, H., Wei, Y., Wang, Y., Wu, N., Low-temperature synthesis of superparamagnetic nanocomposite particles composed of platinum and maghemite, Journal of Physical Chemistry C, 112, 10688–10691, 2008.

[7] Cañadillas-Delgado, L., Fabelo, O., Pasán, J., Delgado, F. S., Lloret, F., Julve, M., Ruiz-Pérez, C., Intramolecular ferro- and antiferromagnetic interactions in oxo-carboxylate bridged digadolinium(III) complexes, Dalton Transactions, 39, 7286–7293, 2010.

[8] Hashimoto, M., Igawa, S., Yashima, M., Kawata, I., Hoshino, M., Osawa, M., Highly Efficient Green Organic Light-Emitting Diodes Containing Luminescent Three-Coordinate Copper(I) Complexes, Journal of the American Chemical Society, 133, 10348–10351, 2011.

[9] Sheldrick, G. M., Crystal structure refinement with SHELXL, Acta Crystallographica Section C: Structural Chemistry, 71, 3–8, 2015.

[10] Dolomanov, O. V., Bourhis, L. J., Gildea, R. J., Howard, J. A. K., Puschmann, H. *J.*, OLEX2 : a complete structure solution, refinement and analysis program, Journal of Applied Crystallography, 42, 339–341, 2009.

[11] Gungor, E., Coban, M. B., Kara, H., Acar, Y., Antiferromagnetic Coupling in a New Mn(III) Schiff Base Complex with Open-Cubane Core: Structure, Spectroscopic and Luminescence Properties, Journal of Cluster Science, 29, 533–540, 2018.

[12] Coban, M. B., Magnetic and photophysical properties of new TbIII –based two-dimensional hydrogen-bonded polymer, Journal of Molecular Structure, 1177, 331–337, 2019.

[13] Jiao, C., Zhang, J., Zhao, Y., Sun, Z., Zhu, Y., Dai, L., Shi, S., Zhou, W., Lanthanide(III) oxalatophosphonates: syntheses, crystal structures and luminescence properties, Dalton Transactions, 43, 1542–1549, 2014.

[14] Coban, M. B., Amjad, A., Aygun, M., Kara, H., Sensitization of Ho^{III} and Sm^{III} luminescence by efficient energy transfer from antenna ligands: Magnetic, visible and NIR photoluminescence properties of Gd^{III}, Ho^{III} and Sm^{III} coordination polymers, Inorganica Chimica Acta, 455, 25–33, 2017.

EFFECTS OF DIFFERENT AGGRESSIVE CONDITIONS ON CEMENT MORTARS CONTAINING RICE HUSK ASH

C. Demirel [1], B. Öztoprak[2], and O. Şimşek[3]

[1]*Department of Construction, Kırklareli University, Kırklareli, Turkey*
[2]*Department of Construction, Bolu İzzet BaysalUniversity, Bolu, Turkey*
[3]*Department of Civil Engineering, Gazi University, Ankara, Turkey*

E-mail: candemirel@klu.edu.tr

Abstract

The rice husk is an organic waste and is the result of the removal of the grains of the paddy grains during the grinding process of paddy. The rice husk ash is obtained by incinerating the rice husk.

In this study, 40x40x160 mm prisms were produced for the bending and compressive strengths by replacing the cement 10%, 20% and 30% of the weight of the rice husk ash. Produced mortar samples were stored at 20 ± 3 ºC temperature for 7, 28 and 90 days under three different conditions as drinking, waste and sea water. Concretes produced by rice husk ash replacement are less permeable and more resistant to aggressive waters. An economy will also be achieved at the same time by replacing the rice husk ash with cement.

Keywords: Rice Husk Ash, Cement Mortars, Bending and Compressive Strengths

1. INTRODUCTION

There are many types of materials used as mineral admixtures in concrete production. Mineral admixtures are grouped into three groups according to the sources they are obtained. These include natural admixtures such as volcanic ash, truss and stone dust; artificial materials such as fly ash and silica fume which are obtained as side products of an industry with no direct relation to concrete production; and heat-processed materials such as burnt clay, burnt shale and rice husk ash. Almost all of the materials, apart from stone dust, used as mineral admixtures in concrete are materials of pozzolanic nature [1].

Amorphous silica is obtained by burning the rice husk at temperatures lower than 700 ^{o}C. The ash resulting from the burning of rice husk is a highly reactive pozzolanic material. Rice husk ash contains high amounts of SiO2 and its reactivity with lime depends mainly on two factors. These are amorphous silica content and specific surface. The amorphous phase in rice husk ash is first obtained when Si-O generated from sintering and decomposing of opaline and hydro silica during the melting process is mixed at temperatures below 600 ^{o}C. It is stated that if ash is elicited amok, it will have weak pozzolanic properties. However, rice husk ash with high reactivity can be obtained by burning the rice husk in a controlled manner. Therefore, the reactivity of the rice husk ash, a pozzolanic material, depends on the crystal / amorphous ratio it contains. Thus, for the characterization of rice husk ash, it is very important to determine the ratio of amorphous silica in contains. This ash can be used as a good pozzolan in cementitious materials by grinding until it reaches a very fine grain size. Pozzolanic indexes of this type vary depending on the degree of grinding and combustion temperatures. Reactive rice husk ash can be used in the production of high quality concrete, but also reduces the porosity of concrete and Ca (OH) 2 ratio [2, 3, 4, 5, 6].

Sensale (2006), in his study, prepared the concrete samples he produced with rice husk ash substituted cement with 0.32-0.40 and 0.50 water / cement ratios and obtained the rice husk ash which he substituted by 10% to 20% in cement from the two different regions. According to the results of the study, he stated that only 90 day reinforced concrete gives higher compressive strength values than control concrete [7].

Expansion test with 5% sulphate solution has been conducted and it has been stated that as a result of 360-day measurements, 40% of rice husk ash-substituted cements expand much less than normal cement. In pH measurements with sodium sulphate solution, it has been stated that pH values decrease as the admixture ratio increases according to 90 and 180 day measurements [4].

In this literature study, the effects of the rice husk ash, which is one of the mineral admixtures and which has the feature of pozzolanic material, on the physical and mechanical properties of the concrete under aggressive conditions have been investigated.

2. MATERIAL AND METHODS

In this study, CEM I 42.5cement obtained from Limak Cement Plant in Ankara was used.

Rice husk was obtained from Edirne province and generated by burning in clay pots at 700 ^{o}C. The husks were burned in the oven at 700 ^{o}C for approximately 3 hours.

In the preparation of mortar samples, Rilem Standard Sand, produced by Trakya Limak Factory, and as mixing water, Ankara city water supply were used.

Physical and chemical properties of cement and rice husk ash are shown in Table 1.

Table 1. Physical and chemical properties of cement and rice husk ash

Chemical composition	**Cement (%)**	**Rice husk Ash (%)**
SiO_2	20.35	91.15
Al_2O_3	5.98	3.84
Fe_2O_3	3.06	1.87
CaO	63.35	0.81
MgO	1.89	0.59
SO_3	2.71	-
Na_2O	0.58	0.17
K_2O	0.88	0.21

In the study, cement mortar mixtures; standard sand, cement and water ratios were prepared to be 3: 1: 0.5, respectively. They were manufactured in 40 x 40 x 160 mm size in compliance with TS-EN 196-1 [8] to determine the mechanical properties of mortars. The produced mortar samples were removed from the mold after 24 hours at 20 ° C and they were matured for 7, 28, 90 days in the municipal water, sea water and waste water curing pools.

Table 2. Particle size distribution of standard sand

Square eye aperture (mm)	Cumulative retained (%)
2.00	0
1.60	7±5
1.00	33±5
0.50	67±5
0.16	87±5
0.08	99±1

Pressure and flexural strength tests were performed according to TS EN 196-1. The compressive strength device is set at the appropriate capacity and at the N / s loading speed (2400 ± 200) for the test. Systems that can adjust the loading speed and record results are used in the device. The half prisms obtained after the bending test were placed between the plates of the device by centring in a way not to exceed ± 5 mm. Loading with device and at (2400±200) N/s speed continued until the prism broke [8].

2. RESULTS AND DISCUSSION

The compressive strength of the samples containing 10% rice husk ash in the network water cure was 10.38%, 9.08% and 7.03% more than the control concrete 7th, 28th, 90th days respectively. Despite the increase in the strength of the concrete containing 10% rice husk ash, a systematic reduction in the compressive strength of the concrete is observed as the amount of ash in the concrete increases.

Table 3. Compressive Strength Values

Samples	**Network Water**			**Sea Water**			**Waste Water**		
	7thday	**28thday**	**90thday**	**7thday**	**28thday**	**90thday**	**7thday**	**28thday**	**90thday**
%0	30.52	38.63	49.92	25.44	26.49	20.57	26.58	28.64	21.54
%10	33.69	42.14	53.43	28.76	35.08	49.66	31.39	38.67	48.42
%20	24.12	36.03	39.14	18.14	30.49	31.39	20.32	35.58	33.44
%30	15.74	20.76	23.18	12.39	26.33	25.21	13.20	28.13	19.63

Samples containing 10% and 20% rice husk ash in sea water and wastewater cures have given a higher compressive strength value than the reference sample. High values as in seawater cure of, respectively, 32.42%, 15.10%, and in waste water cure of, respectively, 34.91%, 24.23% have been obtained.

The fact that the strengths of the samples containing rice husk ash result in high values in aggressive waters compared to the reference sample show that the use of rice husk ash reduces permeability.

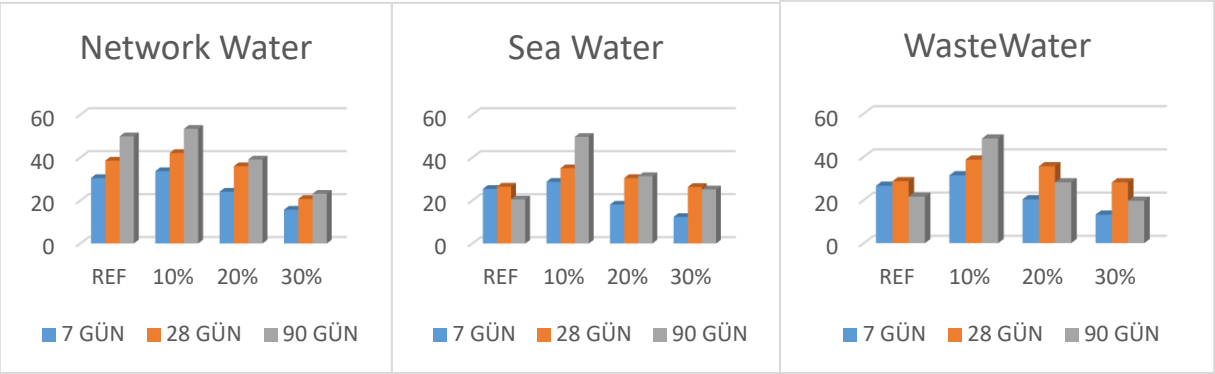

Figure 1. Compressive strength graphs of rice husk ash samples.

The fact that the strengths of the samples containing rice husk ash result in high values in aggressive waters compared to the reference sample show that the use of rice husk ash reduces permeability.

4. CONCLUSION

The results obtained in this study have showed that the rice husk, a waste product, could be burned in a controlled manner and used as a pozzolan. The conducted pozzolanic activity experiments showed that the rice husk ash had pozzolanic activity as a result of the reaction with lime and cement. The pozzolanic activity of rice husk ash is within the limits specified in the standards.

Water requirements of concrete samples prepared by adding rice husk ash at the rates 10%, 20, 30% of the cement weight into the concrete have increased. For this reason, a certain amount of reduction has been observed in the strength of the concrete samples with high content of rice husk ash. Plasticizer can be used to eliminate this situation.

It has been observed that the use of rice husk ash in aggressive waters increases the compressive strength. Samples containing 10% and 20% rice husk ash in seawater and wastewater cures have been observed to give higher compressive strength values compared to the reference sample.

Rice husk ash has been shown to have a greater impact on the strength of the concrete at later ages rather than its strength at early age.

The concrete produced by substituting the rice husk ash to the cement is less permeable and thus more resistant to aggressive waters. Economicality is achieved by adding rice husk ash in cement.

REFERENCES

[1] Erdoğan, T. Y., 2007, "Beton", MetuPress, 2. Baskı, Ankara.

[2] G. Görhanand O. Şimşek, Effect of Rice HuskAsh on PhysicalandMechanicalProperties of Concrete, Electronic Journal of ConstructionTechnologiesVol: 7, No: 1, 107-117, 2011.

[3] Chandrasekhar, S., Satyanarayana K. G., Pramada, P. N., Raghavan, P., Gupta, T. N., , "Processing, propertiesandapplications of reactivesilicafromricehusk- An overview", *Journal of MaterialsScience*, **38** (15), 3159-3168, 2003.

[4] Chindaprasirt, P., Kanchanda, P., "Sulfateresistance of blended cements containing fly ash and rice huskash", Construction and BuildingMaterials, 21 (6), 1356-1361, 2007.

[5] Paya, J., Monzo, J., Borrachero, M. V., Mellado, A., Ordonez, L. M., "Determination of amorphoussilica in ricehuskashby a rapidanalyticalmethod", CementandConcreteResearch, 31 (2), 227-231, 2001.

[6] Saraswathy, V., Song, H. W., "Corrosionperformance of ricehuskashblendedconcrete", Construction andBuildingMaterials, 21 (8), 1779-1784, 2007.

[7] Sensale, G. R., "Strengthdevelopment of concretewithrice-huskash", Cement&ConcreteComposites, 28 (2), 158-160, 2006.

[8] TS EN 196–1, Çimento Deney Metotları- Bölüm 1: Dayanım, TSE, 2002.

[9] TS 639/T1, Uçucu Küller-Çimentoda Kullanılan, Türk Standartları Enstitüsü, Ankara, 1998.

EVALUATION OF MECHANICAL CHARACTERISTICS OF THE INTERLOCKING CONCRETE PAVES PRODUCED FLY ASH

C. Demirel [1], B. Öztoprak[2], and O. Şimşek[3]

[1]*Department of Construction, Kırklareli University, Kırklareli, Turkey*
[2]*Department of Construction, Bolu İzzet BaysalUniversity, Bolu, Turkey*
[3]*Department of Civil Engineering, Gazi University, Ankara, Turkey*

E-mail: candemirel@klu.edu.tr

Abstract

Fly ashes are used as pozzolanic admixtures or filler materials in concrete production. Increasing the use of fly ash is important both in terms of economy and environmental pollution. The interlocking concrete paves are commonly used in urban streets and pavements, in factory surroundings and etc. Interlocking concrete paves shall be above the minimum strength specified in TS 2824 EN 1338 standard.

In this study, fly ash has been used as a substitute to cement in 0, 10, 20, 30, 40 and 50% ratios. The splitting tensile strength and water absorption characteristics of the pave have been determined. The usage of the FA in the production concrete pave is a more high quality production, more economical and a more environmentally friendly approach.

Keywords: Concrete Paves, Fly Ash, Splitting tensile strength test

1. INTRODUCTION

Concrete lock parquet stones are constructional components produced via parquet machine by mixing concrete, aggregate, water and other additives when required at certain amounts [1].

Parquet road construction is a type of superstructure used since the Romans. Stone block pavement application was the only solution with the application of pavement coating, durability, clean and as a surface appropriate for wheel-rolling was the only solution before the use of hydrocarbon bonding agents (asphalt, tar etc.). It still possible to encounter this type of paved roads, which are called as "Albanian Pavement" in our country [2].

As a result of the increase in demand of aesthetics over time, parquet stones with smooth sized natural stone materials that require a certain workmanship have been used. However, the long production period of the production of the parquet stones provided from natural sources and the increasing demand have caused the costs to increase. Due to the fact that it is formed of rigid parts which are clamped together, prefabricated concrete pavements approaching to the rigid coating category, on the other hand, thanks to the interlace to the lower layer present elastic behaviour in conveying the load to this layer and can show the quality of flexible coating. Therefore, it is possible to place locked concrete parquet coatings among rigid and flexible coatings due to the approach sometimes to asphalt and sometimes to the concrete coating [1].

Joints must be checked in concrete roads and joints fillings should be changed every 4-5 years. As for asphalt roads, it is necessary to repair the defects caused by cracking, cavitation or decompositions in shorter periods. However, it has been determined that the locked concrete paving coating does not require maintenance for 25 years after construction [3].

When the physical, chemical and mineralogical properties of the UK are examined, it is considered possible that these can be used easily in the construction sector and thus while the economy is ensured in the production of materials and energy, it is also possible to protect the ecological balance by preventing the pollution of the environment [4].

Low calciferous UKs, observed according to the results of different research; reduce the water need in a constant N / E ratio; that is to say, increase processability. UKs with high levels of lime reduce processability [5, 6, 7, 8].

2. MATERIAL AND METHODS

In the production of the concrete lock stone, the P 42.5 cement provided from Limak Çimento, Ankara, and the 0-4 class of broken stone from Ankara Limak Beton administration were used.

In this study Çayırhan fly ash was used. It is also included in limy ash class since its SiO2 , AL2O3, Fe2O3 levels are over % 70, and besides including class F (low calciferous), its analytical CaO amount is over % 10 [9].

Ankara network water was used as mixing water.

Table 1. Chemical characteristics of CEM I 42.5 R and UK

Chemical composition	Cement (%)	Fly ash (%)
SiO_2	14.73	50.88
Al_2O_3	4.80	13.34
Fe_2O_3	3.61	10.09
CaO	64.29	13.09
MgO	0.85	5.50
SO_3	2.40	3.32
Na_2O	0.30	2.59
K_2O	0.79	2.72

In the visual inspection of the locked paving stone there should be no cracks, gaps on the surface, cavitations and roughness. Prepared mortar is manufactured by applying 10sec vibration in the locked parquet stone machine. Samples from the mould were irrigated via sprinkler method 2 times a day for 1 week (morning and evening) and once a day on other days.

Figure 1. Concrete locked paving stone

Table 2. Material amount put into the concrete mixture (for 1m3)

Materials	Ref.	%10 UK	%20 UK	%30 UK	%40 UK	%50 UK
Aggregate 0-4 mm. (kg.)	1573	1573	1573	1573	1573	1573
Cement (kg.)	340	306	272	238	204	170
UK (kg.)	0	34	68	102	136	170
Water (Lt.)	180	180	180	180	180	180

Figure 2. Concrete locked parquet stone production

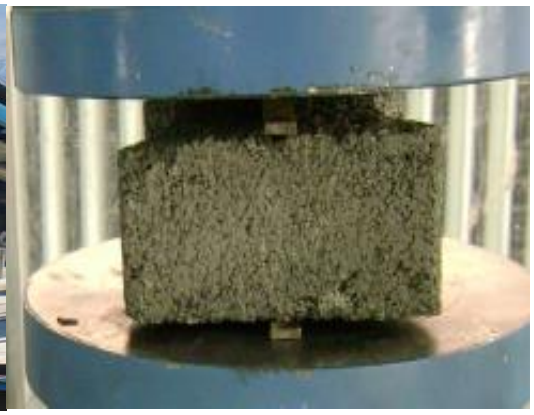

Figure 3. Splitting tensile test

Splitting tensile test was conducted according to TS 2824 EN 1338. Concrete lock was steeped in water at (20 ± 5) ° C for (24 ± 3) hours before testing. When taken out of water, the sample was dried a cloth and tested [10].

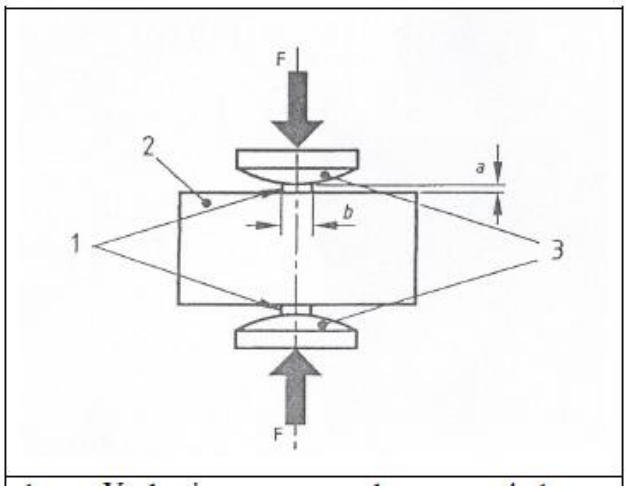

Figure 4. Splitting tensile strength test principle [9].

The fracture plane area of the concrete keypads tested is calculated using the equation given below:

$S=l\times t$'

Here;

S: Refraction area, mm^2

l: Length of the fracture cross-section as the average of the two measurements made at the top and bottom of the concrete lock stone

t: the thickness of the concrete lock stone on fracture plane area as the average of three measurements, one in the middle and the other two from the sides, (mm).

According to TS 2824 EN 1338, the mean values of the splitting tensile strengths are demanded not to be less than 3.6 MPa or each result should not be less than 2.8 MPa. The splitting tensile strength (T) of the specimen which undergo a test is calculated by the equation below:

$T = 0637\times k\times P/S$

Here;

T: Strength, MPa

P: Breaking load, N

k: It is the adjustment coefficient for the thickness of the parquet stone which is calculated by the following equation or taken from Table 3.

Table 3."k" adjustment coefficient.

(mm)	40	50	60	70	80	90	100	110	120	130	140
k	0,71	0,79	0,84	0,94	1,00	1,06	1,11	1,15	1,19	1,23	1,25

Before water absorption is determined, dust, loose parts, etc. on Test samples are cleaned with a brush and the samples are ensured to be at (20 ± 5) ° C. Water absorption test was conducted according to TS 2824 EN1338 [10]. After the samples were stored in water at 20 ± 2 C for 72 hours, their saturated surface dry-weights were recorded (M1). In order to determine the dry weight values (M2) of the samples, the dry weights of the samples, which were kept at 105 72C for 72 hours in ventilated ovens, were recorded. Water absorption of each sample (ta) is calculated in percent by mass using the equation given below [10].

$t_a = (M_1-M_2)/M_2$ %

Here;
M1 first mass of the test sample, g.
M2 last mass of test sample, g.

According to TS 2824 EN 1338 (9), the water absorption rate should not be more than 5% on average and should not be more than 7% at a single sample.

Abrasion strength, according to ASTM C 944 (21); has been executed by abrasing the upper side of the parquet stone with abrasive wheel under standard conditions.

3. RESULTS AND DISCUSSION

The water absorption rate values of the prepared samples are given in Table 4.

Table 4. Water absorption rate test results

Samples	N	Water absorption rate
Ref	9	5.91
%10	9	6.03
%20	9	6.21
%30	9	6.62
%40	9	7.48
%50	9	7.73

Generally speaking, the rate of water absorption increases as the UK substitution rate increases. 50% UK substituted mixture exhibits the highest water absorption rate. It is 31% higher than the arbitration sample. 10% UK substituted mixture is 2% more than the reference mixture.

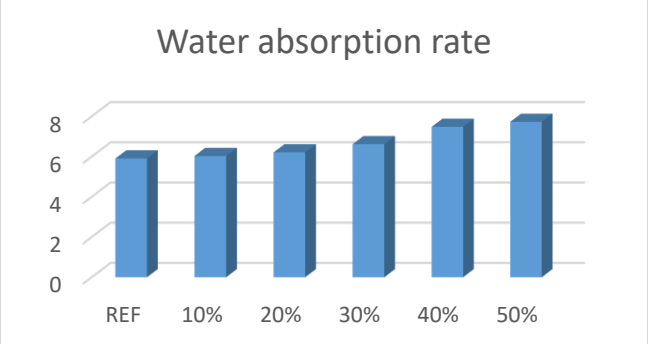

Water absorption values; values above the recommended limit value in TS 2824 EN1338 / AC in all samples.

The results of the abrasion test results of the prepared samples are given in Table 5.

Table 5. Abrasion test results

Samples	Water absorption rate
Ref	0.145
%10	0.193
%20	0.256
%30	0.324
%40	0.429
%50	0.567

As the substitution rate increases, the abrasion resistance decreases proportionally. K 50% UK substituted samples have exhibited the lowest abrasion resistance. Abrasion resistance decreases as UK substitution rate increases.

The splitting tensile strengths in the prepared samples are given in Table 6. When Table 6 is examined, increase in the strength of the concrete lock stone is observed as the age increases.

In the 7-day test results, 10% substitution mixture exhibited higher resistance than the arbitration sample. It was seen that there was a %5.19 increase compared to the arbitration sample. The lowest value is seen in 40% and 50% fly ash substituted mixtures.

When the 28-day test results were examined, 10% substitution mixture showed higher strength than the arbitration sample. An increase of %5.34 in proportion to the arbitration sample has been observed.

When 90-day test results were examined, %10 substitution mixture and %20 substitution mixture increased %14 and %1.3 relatively compared to the arbitration sample. The lowest values are seen in mixtures with 40% and 50% fly ash substitutes. Relatively %20 and %23 lower strength has been observed compared to the arbitration sample. 30% fly ash substitution mixture has exhibited 3% less strength than the arbitration sample.

Table 6. Splitting tensile test results

Samples	N	7 Days (Average Mpa)	28 Days (Average Mpa)	90 Days (Average Mpa)
Ref	9	2.19	2.62	3.27
%10	9	2.31	2.76	3.72
%20	9	2.11	2.48	3.31
%30	9	2.05	2.32	3.16
%40	9	1.98	2.19	2.60
%50	9	1.76	2.08	2.52

The increase in the UK substitution rate caused an increase in the water demand of fresh concrete. Since the S/ Ç ratio is kept stable, the high UK samples are not well tightened. Therefore, strength in 40% and 50% fly ash substituted mixtures can be considered to be low.

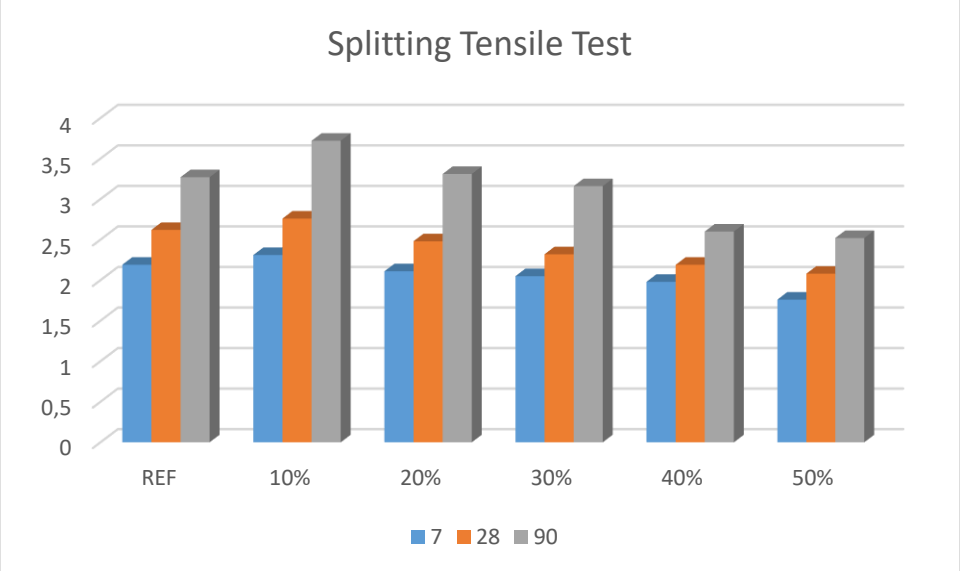

Figure 5. Splitting tensile test graphics of the samples

4. CONCLUSION

A key factor in the production of locked parquet stones is the cost. The most important factor increasing the cost is the amount of cement. Therefore, the amount of aggregate can be increased to reduce the amount of cement or the amount of cement can be reduced by using waste materials such as fly ash and slag in KBPB composition. Thus, the cost will reduce with use of these wastes. In addition, these waste materials will be reintroduced to the economy and environmental pollution will be prevented.

It is thought that in samples with high UK substitution rate, the compression time applied during production can bear better results if kept longer.

The increase in the UK substitution rate caused an increase in the water demand of fresh concrete. Since the S/ Ç ratio is kept stable, the samples with high UK rates are not well tightened. Therefore, strength in 40% and 50% fly ash substituted mixtures can be considered to be low.

UK use reduced the abrasion resistance.

REFERENCES

[1]Semiz, M, "Beton Kilit Taslarının Fiziksel Özellikleri ve Alternatif Üretimin Arastırılması", Yüksek Lisans tezi, Gazi Üniversitesi Fen Bilimleri Enstitüsü, Ankara, 1-20 (2006).

[2]Tunç, A, "Yol Malzemeleri ve Uygulamaları", Atlas yayın dağıtım, İstanbul, 466-467 (2001)

[3]Öztaş, G., Ağar, E, Kilitli Beton Parke Kaplamalar, şantiye insaat Makine ve Mimarlık Dergisi, (18): 98-102 (2005)

[4]Aruntaş, H.Y. Uçucu Küllerin inşaat Sektöründe Kullanım Potansiyeli, Gazi Üni. Müh. Mim. Fakültesi Dergisi, 21 (1): 193-203 (2006).

[5]Simsek O., Aruntaş H.Y., Fırat S., " Çayırhan ve Soma-B Termik santrali uçucu küllerinin beton basınç dayanımına etkisi", Türkiye inşaat Mühendisliği16.Teknik Kongre ve Sergisi, 199-205 (2001).

[6]Erdoğan T.Y, "BETON" ODTÜ, Ankara,183-189 (2003)

[7]Türker, P, Erdoğan, B, Kantaş, F, Yeğinobalı, A, Türkiye'deki Uçucu Küllerin Sınıflandırılması ve Özellikleri, Türkiye Çimento Müstahsilleri Birligi Ankara 20-34 (2003).

[8]D. Gökhan, O. Şimşek Türk Bilim Araştırma Vakfı Bilim Dergisi 1(1) (2008) 1-6.

[9] ASTM C 618, Standart specificationforCoalFlyAshandRaworCalcined Natural PozzalanforUse as a Mineral Admixture in Concrate, AnnualBook ofASTM Standarts, 4-16 (1998)

[10]TS 2824 EN1338/AC: Zemindöşemesiiçinbetonkaplamablokları – GerekliŞartlarveDeneyMetotları, TSE, Ankara-Türkiye, (2009).

[11]ASTM C 944, "Standart Test MethodForAbrasionResistance ofConcrateorMortarSurfacesbyTheRotating-CutterMethod", *AmericanSociestyForTestingandMaterials*, USA, 1- 4.

THE EFFECT OF DIFFERENT MINERAL WATER USED AS CURE AND MIX WATER ON THE BENDING AND COMPRESSIVE STRENGTH OF CEMENT MORTAR

C. Demirel [1], İ. Kılıç[2]

[1]*Department of Construction, Kırklareli University, Kırklareli, Turkey*
[2]*Department of Civil Engineering, Kırklareli University, Kırklareli, Turkey*

E-mail: candemirel@klu.edu.tr

As it is known, concrete mix and contact water shall not show acid reaction, it shall be equal to and above PH 7. In this study, the effect of using mineral waters of different structures in Kırklareli Province and surrounding area as mix water and cure water on the bending compressive strength of cement mortar was researched. Kırklareli municipal drinking water, Kırklareli spring water, Kırklareli Şeytan Deresi water, natural mineral water and prepared water were used. A total of 20 specimens were prepared for each mixture from 40 × 40 × 160 mm mortar samples replaced mix waters for 7 and 28 days: half of the samples were stored in cistern water and the other half were kept in their mix water. The pH values of the mix and contact waters used in the samples were measured and bending-compressive experiments were performed on samples 7 and 28 days.

In this experimental study, it is aimed to increase the compressive strength of mortars by using mineral waters as cure water and mix water to the concrete.

Keywords: Cement Mortar, Concrete Mix And Contact Water, pH.

1. INTRODUCTION

Mineral water is formed by the penetration of snow and rain water into the depths of the earth and incorporating some minerals in rocks in the depths during infiltration. The mineral enriched water then emerges from the cracks that it finds and forms the mineral water resources.

Na +, K + and OH- ions in pore water keep the pH value of the concrete in the range of 12.5-13.5. The corollary that can be drawn here is that the concrete will lose its chemical stability when faced with an acidic environment. Theoretically, waters with low pH leads to dissolution of cement hydrate components. When considered from this point of view, many industrial wastes and natural water can be considered aggressive for concrete. However, the severity of the chemical attack is the function of the pH value of the liquid and the permeability of the concrete. In the event that the pH value of the liquid is above 6.5 and the permeability of the concrete is too small, the chemical attack develops very slowly and the result can remain at ignorable levels. If the pH is under 5.5, the attack will be severe, and if it is below 4.5, the attack will be extremely severe. However, the transport speed of liquid in concrete is also an important factor [1].

pH is a measure parameter that expresses the degree of acidity of the product. pH expression stands for "power of hydrogen." pH is the activity of hydrogen ions. It is a logarithmic expression of H + or OH- concentrations in aqueous solutions [2]. The pH concentration in water is measured from 1 to 14 in numbers. At pH 7, hydrogen and hydroxyl ion levels are equal. Water is neuter at pH 7. If the hydrogen ions increase, the pH value of water decreases and the water becomes acidic. On the contrary, when the hydrogen ions are increased, the pH value rises and the water becomes alkaline. Therefore, if the pH in water is below 7, it is acidic water, and if the pH is over 7 it is basic water [2].

In their study, Çelik et al. (2005) investigated the effect of different types of mineral waters on concrete compressive strength as concrete curing water. 10x10x10 cm. 18 cubic samples of BS20 concrete grade were prepared. As a result of the experiment, they have stated that the concrete samples kept in the natural mineral water of Beypazarı exhibited high values in terms of 7 and 28 day compressive strengths compared to the samples kept in other curing waters [3].

P. Kumar Mehta and Paulo J. M. Monteiro, point that the pH function will be effective in permeability of concrete and chemical attack rate in aggressive conditions. They have elucidated that because the chemical attacks have too little effect when the pH value of the chemical attacks is over 6 and in low aggressive environments, the permeability of concrete will not pose serious damages [4].

2. MATERIAL AND METHODS

Portland cement (PC 42.5) to be used in the study has been produced by Limaş Cement Factory in Kırklareli. Physical and chemical properties of Portland cements have been determined in the laboratories of Kırklareli Limak Cement Factory.

Table 1. Chemical properties of cement and rice husk ash

Chemical composition	Cement (%)	Rice husk Ash (%)
SiO_2	20.35	91.15
Al_2O_3	5.98	3.84
Fe_2O_3	3.06	1.87
CaO	63.35	0.81
MgO	1.89	0.59
SO_3	2.71	-
Na_2O	0.58	0.17
K_2O	0.88	0.21

Cement mortar mixtures; standard sand, cement and water ratios have been prepared to be 3: 1: 0.5, respectively. Mortar samples shall be obtained by using mortar moulds of 40 * 40 * 160 mm size according to TS-EN 196-1 [2].

Table 2. Mixture Ratio

Mixture water	Cement	Sand	Water
Network Water	450	1350	225
Bottled Water	450	1350	225
Stream Water	450	1350	225
Spring Water	450	1350	225
Mineral Water	450	1350	225

The produced mortar samples will be removed from the mould and put into curing water after being kept at 20^{o}C room temperature for 24 hours.

3. RESULTS AND DISCUSSION

In the measurements of mixture and curing waters, the values have been found as 8.01 for Kırklareli network water, 7.52 for bottled water, 6.80 for mineral water, 8.18 for Seytan Deresi stream water and 7.38 for Kırklareli Spring water.

As is seen in Table 3, the bottled water and the Şeytan Deresi stream water used as mixture water give values close to the reference sample. Looking at the 28-day strength of the bottled water, it is seen that it has the same 46.1 MPa as the reference sample and the Seytan Deresi stream water has 45.8 MPa. The lowest 28-day strength is observed in samples in which mineral water with the lowest pH value is used as 35.3 Mpa.

When the 28-day bending strengths are considered, the lowest strength is found as 8.927 MPa in the samples in which the Seytan Deresi stream water is used as the mixing water. Values close to each other have been obtained for bending strengths in all samples.

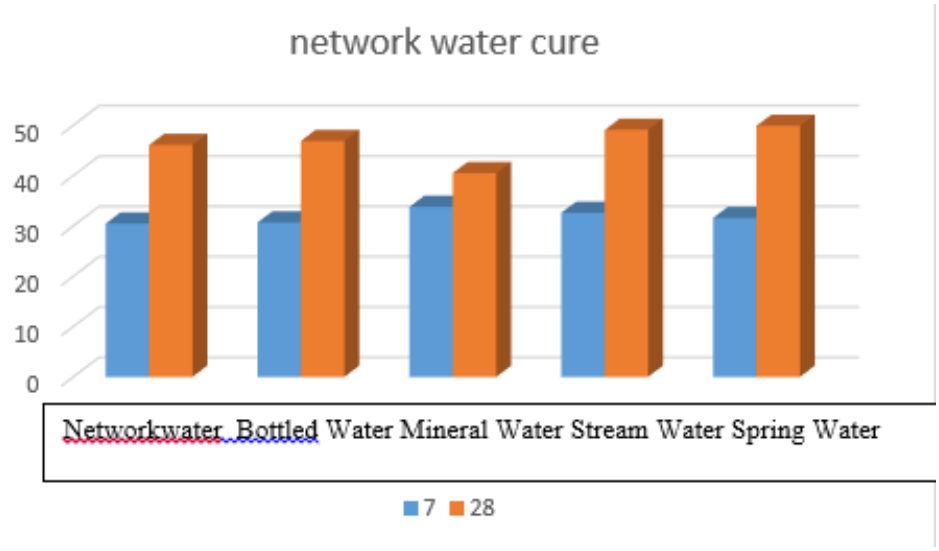

Figure 1. 7 and 28-day compressive strength of samples in water cure (Mpa).

Table 3. 7-and 28-day compression-bending strength of samples in water cure (Mpa).

		Compression Strengths				
	PH	**8,01**	**7,52**	**6,80**	**8.18**	**7.38**
	Day	**Kırklareli network water**	**Bottled water**	**Mineral water**	**Şeytan stream water**	**Kırklareli spring water**
Water Cure (Mpa)	**7**	30.5	38.1	36.2	34.7	31.6
	28	46.1	46.1	35.3	45.8	38.2
		Bending Strengths				
	7	7.453	7.516	7.336	8.242	8.292
	28	9.660	9.520	9.403	8.927	9.417

When the samples that are cured in the mixing water are examined, it is seen that the water with the highest resistance in the 28-day durations is given by the Seytan stream water. It is thought to be resulted from high pH value.

Table 4. 7 and 28-day compression-bending strengths of the samples cured in mixing water (Mpa).

		Compression Strengths				
	PH	**8,01**	**7,52**	**6,80**	**8.18**	**7.38**
	Day	**Kırklareli network water**	**Bottled water**	**Mineral water**	**Şeytan stream water**	**Kırklareli spring water**
Cure in mixing water	**7**	30.5	30.7	33.8	32.6	31.6
	28	46.1	45.9	40.5	49.1	49.9
		Bending Strengths				
	7	7.453	7.485	7.584	7.211	8.492
	28	9.660	9.587	8.320	9.940	9.985

As is seen in Table 4, the bottled water used as mixing water and curing water has given values close to the reference sample. When the 28-day strength of the bottled water is examined, it is observed to be 45.9 MPa. Lowest 28-day strength is observed in the samples in which mineral water with the lowest pH value is used as 40.5 MPa.

When 28-day bending strengths are considered, the lowest strength is observed as 8.320 Mpa in the samples in which Seytan stream water is used as mixing water. Values close to each other have been obtained for bending strengths in all samples.

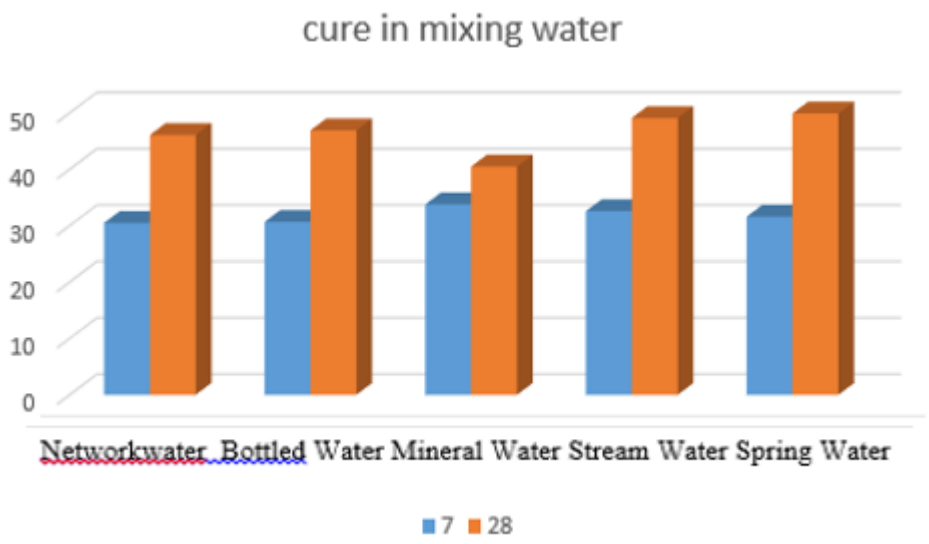

Figure 2. 7 and 28-day compressive strength of samples cured in mixing water (Mpa).

4. CONCLUSION

Values close to each other has been obtained in all samples for the bending strength of the samples used as mixture and curing waters.

The lowest 28-day strength has been observed in the samples in which mineral water with the lowest pH value is used.

The obtained experiment results will provide insight for discovery of alternative water resources when the concrete plants around Kırklareli fail to obtain mixing and curing waters.

REFERENCES

[1] Baradan, B., Yazıcı, H., Ün, H., "Beton ve Betonarme Yapılarda Kalıcılık (Durabilite)", Türkiye Hazır Beton Birliği, İstanbul, Türkiye, 2010.

[2] Kimya Teknolojisi, Asitler ve Bazlar, M.E.B. Ankara, 2011.

[3] Çelik M. H., Orhan M., Özel M. (2005), 'Kür Suyu Olarak Kullanılan Değişik Mineralli Suların Betonun Basınç Dayanımı Etkisi Üzerine Bir Araştırma', Politeknik Dergisi, Cilt: 8 Sayı: 2 s. 203-207.

[4] P. Kumar Mehta and Paulo J. M. Monteiro "Concrete, Microstructure, Properties andMaterials" Department of Civil and Environmental Engineering University of California at Berkeley, Third Edition, A.B.D. 2005.

[5] TS EN 196–1, Çimento Deney Metotları- Bölüm 1: Dayanım, TSE, 2002.

DETERMINATION WITH QUECHERS EXTRACTION METHOD OF IMAZAMOX IN ROOT AND LEAF OF THE SUNFLOWER PLANT BY GC-MS

Cihan TORLAK[1], Barış Can KÖRÜKÇÜ[1] Fatma KURŞUN[1] Cemile ÖZCAN[1*]

[1]*Kirklareli University, Science and Art Faculty, Chemistry Department, Kirklareli, Turkey*

E-mail: cemilebal.ozcan@klu.edu.tr

Abstract

Sunflower (Helianthus annuus L.) is the most important oil plant grown in our country. In our country, %60 of sunflower production is done in Thrace region and pesticides are used extensively in this agriculture, especially imidazolinone (IMI) herbicides. Because, these herbicides (Imazapyr, Imazapic, Imazethapyr, Imazamox and Imazaquin) are known to inhibit the biosynthesis of aromatic and branched-chain amino acids [1]. It is used systems such as GC-MS, LC-MS, LC, GC, LC-MS-MS and GC-MS-MS for determination of pesticides.

The aim of this study was to evaluate the application of quick, easy, cheap, effective, rugged and safe method (QuEChERS) for simultaneous determination of Imazamox residue in sunflower plant parts (root, body and leaf). The samples prepared with QuEChERS extraction method were analyzed by gas chromatography-mass spectrometry for Imazamox. The concentration of Imazamox in sunflower plant parts was determined to be among 11.4-27.7 µg kg^{-1}, 2.1- 55.9 µg kg^{-1} and 4.53-68.8 µg kg^{-1} for root, body and leaf, respectively.

Keywords: Sunflower plant parts, Imazamox, QuEChERS.

1. INTRODUCTION

The most important problem of today's world is the significant increase in the human population. As a result, it has become inevitable in the increase of food product needs and a significant part of these needs constitute the vegetable oils such as sunflower, canola, palm, soybean and peanut oil. Besides, the most preferred oil plant in the world and in our country is sunflower plant. Sunflower is an important oil plant, which can be grown in almost every region of our country, has a high quality oil ratio, has a higher cultivation area and is at the top of oil production. In addition, sunflower oil has an important place in consumption of humans due to its rich nutrient content, lower levels of saturated fat in seed, high degree of linoelic acid, not cause cardiovascular disorders, and lowering cholesterol [1, 2].

In recent years, due to the low and limited cultivation area in the sunflower production, vegetable oil is insufficient to meet the need. The main reason for the decrease in sunflower production is foreign weeds [3]. In order to control the weeds, pesticides have become indispensable substances for further production on existing agricultural areas [4]. The sunflower plant in the Clearfield in development have a good level of tolerance against injury from imazamox (shown in Figure 1) and are one of the most important goals in sunflower breeding programs to ensure effective and sustainable weed resistance [5]. Imazamox is a herbicide from imidazolinone group which was first developed by Brady et al. [6]. This herbicide which can easily be absorbed by the leaves and roots is its inhibition of the acetolactate synthase enzyme [7, 8]. The maximum residual limit (MRL) value for Imazamox was 0.05 mg / kg in the European Union standard (FAO) and Turkish Food Codex and 0.095 mg / kg by the World Health Organization (WHO) [9, 10].

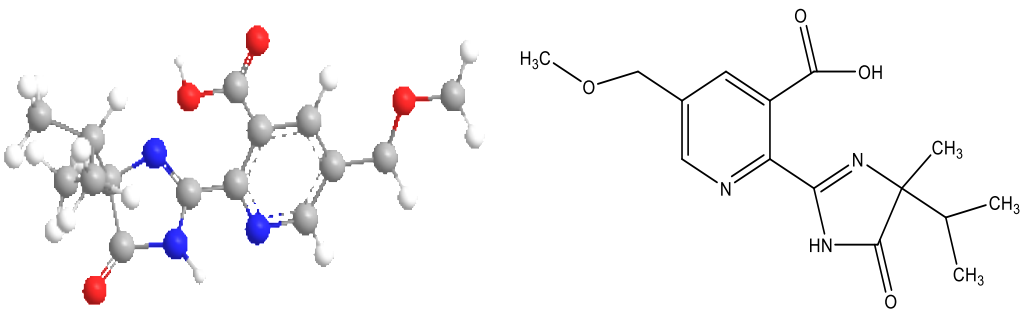

Figure 1: The molecular structure and 3D representation of Imazamox.

For the quantitative analysis of low concentration pesticides in plant samples such as sunflower, wheat and soybean, are used for high sensitivity analytical techniques such as GC-MS, HPLC-MS, HPLC, GC [11-13]. In addition, useful methods for the preparation of samples in a short time for pesticides in plants have been developed and continued to be developed. The most commonly used method is QuEChERS (fast, easy, inexpensive, effective, rugged and safe) extraction method developed by Anastassiades et al in 2000s [14, 15]. QuEChERS method implementation is simple and reliable, but it can be easily modified according to the purpose of analysis, a method that becomes indispensable for rapid pesticide analysis [16, 17].

With this method for simultaneous analysis of pesticide residues may be provided as determination accurate data in a short time. Because of the big importance of sunflower as an oilseed crop that is mainly used for human consumption, In terms of human health of Imazamox herbicide is also required that determination and monitoring. With this aim was to evaluate the application of quick, easy, cheap, effective, rugged and safe method for simultaneous determination of Imazamox and pesticide residues in sunflower plant parts (root, body and leaf). The concentration of Imazamox was determined by GC-MS.

2. MATERIAL AND METHODS

Material

The quantitative analysis of Imazamox herbicide was performed by GC-MS, using an Agilent 7890A model GC and 5975C MSD system at Kirklareli University- Advanced Technologies Application and Center Research (ITUAM) laboratory. HP-5 MS IU capillary column (30 m x 250 μm x 0.25 μm) and was used with pure helium (99.999%) as the carrier gas. In addition, TAB 40-WEL with a light nitrogen stream was used during sample preparation.

This study was carried out on the sunflower crops of 2015, which were determined in the regions of Kırklareli city center and Kavaklı town, where sunflowers were made with two different pHs. Three different times (1st week, 6th weeks and harvest) sunflower crops collected from root, body and leaf were analyzed by analyzing the samples.

Soil pH of working land; the soil of Kırklareli region agricultural land has neutral pH (7.28) and the soil farmland to Kavaklı region is acidic pH (4.95).

Properties of Imazamox herbicide; the Imazamox herbicide, which is used in the study, has a water-soluble formulation and contains 40 g L^{-1} of the Imazamox active substance. In the 4-10 actual leaf period of the sunflower plant, 125 mL da^{-1} (the application dose to the plant is used on the label of the commercial product to 125 mL da^{-1} as proposed by the company for field conditions) is known to be used against weeds (*Amaranthus retroflexus, Xanthium strumarium, Echinochloa crus galli, Solanum nigrum, Orabanche* spp and *Amaranthus albus*). Sunflower plant seed used in farmland is tolerant of Imidazolinone (IMI) group "SANAY MR SUNFLOWER SEED" is a strong, safe and highly efficient sunflower variety. In the study, sampling times are shown in Table 1.

Table 1. Sampling time of sunflower parts (root, body and leaf).

Sampling time	Sample code
1st week	I
6th week	II
Harvest	III

Method

The root, body, leaf samples were collected the adult components (root, body, leaf) from the sunflower field were first passed through tap water and then washed with 5% wash acid solution and then dried to 40 °C. Dry samples were homogenized and grinded with the mixer.

QuEChERS Method Extraction of Plant Components; After the samples of the sunflower components were homogenized, samples of approximate 0.5 g were taken into a 50 mL falcon centrifuge tube and 2 mL of ultrapure water and 5 mL of dichloromethane were added. After vortexing for at least 1 minute, it was centrifuged at 5 °C and 5 minutes at 7000 rpm. The organic phase was separated off and the AOAC 2007.01 extraction kit was added and vortexed again under the same conditions. The filtrate was decanted by passing QuEChERS (PSA) through silica gel and taken to the falcon centrifuge tube. The mixture was evaporated to dryness using nitrogen in the evaporation system (evaporation of the solvent by evaporation of the solvent, the nitrogen temperature of the evaporator, the temperature did not exceed 35 °C). The evaporated sample was taken to vials by passing through 1.5 mL hexane and 0.45 µm filter and analyzed in GC-MS. The same sample was injected into the device 5 times and calculations were made.

Preparation of imazamox standards; A standard stock of 5000 mg kg^{-1} was prepared in the imazamox standard acetonitrile (CAS Number 114311-32-9). 5 mg kg^{-1} of intermediate solution was prepared. Dilutions were made from the intermediate stock to draw the calibration graph and the standard solutions of 0.1–1000 µg kg^{-1} (0.1, 0.5, 1, 5, 10, 25, 50, 100, 250, 500 and 1000 µg kg^{-1}) were prepared in hexane. The optimization studies performed by Ozcan et al. are given in the literatüre [18].

3. RESULTS AND DISCUSSION

Imazamox residues were determined as a result of the analyzes performed in sunflower plants grown in different pH environments in Kırklareli center (KM) and Kavaklı (KB) (Table 2). The identification of the metabolites of Imazamox was conducted by gas chromatography/mass spectrometer confirmatory analysis in accurate mode (SIM) owing to the complexity of plant extracts.

Table 2. Average amounts of Imazamox residues in sunflower plant components (n=6).

KM (pH: 7.28)			KB (pH: 4.95)		
Plant parts	Sample code	Imazamox (µg kg^{-1})	Plant Parts	Sample code	Imazamox (µg kg^{-1})
Root		11.4 ± 0.1	Root		14.9 ± 4.6
Body	I	12.1 ± 0.4	Body	I	13.6 ± 1.1
Leaf		11.8 ± 0.6	Leaf		11.9 ± 0.5
Root		13.2 ± 0.9	Root		19.1 ± 0.6
Body	II	16.7 ± 1.7	Body	II	12.8 ± 2.6
Leaf		17.4 ± 0.4	Leaf		18.2 ± 0.7
Root		27.7 ± 0.2	Root		16.3 ± 1.1
Body	III	55.9 ± 9.1	Body	III	16.7 ± 1.1
Leaf		68.8 ± 1.2	Leaf		4.53 ± 0.71

Imazamox which is a systematic herbicide moves through the plant tissue and is advancing with enzyme synthesis, in animals and plants. Pesticide application is recommended for specific dose adjustments, otherwise the plant may be resistant to herbicide [13,19–21]. The herbicide is applied when

the actual leaves of the sunflower plant reach the number 4-10. Imazamox which is applied by spraying to the leaves of plants are adsorbed by the leaves of the plant.

Imazamox reaches the soil where the plant grows by planting in other plant parts (root, body and leaf) by systematic progression in plant tissues. The pH of the soil, in which the plant grows is of great importance in realization of this process. Because, Imazamox is less adsorbed by soil and plant at low pH, and at the higher pH is showed exactly the opposite effect in this case. Imazamox enables the control of plants over a wide range, but its effectiveness depends on the plant's growth stage and the amount used. It can be used at any time during the growth period of the plant. In order to obtain the best yield, herbicide should be used at the beginning of the plant's active growth period [22].

According to our knowledge, the previously by QuEChERS extraction method has not been reported the presence of Imazamox in rice. When the first, second and third stages in the leaves of the product grown in the neutral area are examined, an increase (about 6 times as much) is observed (shown in Fig. 2). In the acidic region until harvest time was determined a decrease in imazamox concentration (shown in Fig. 3).

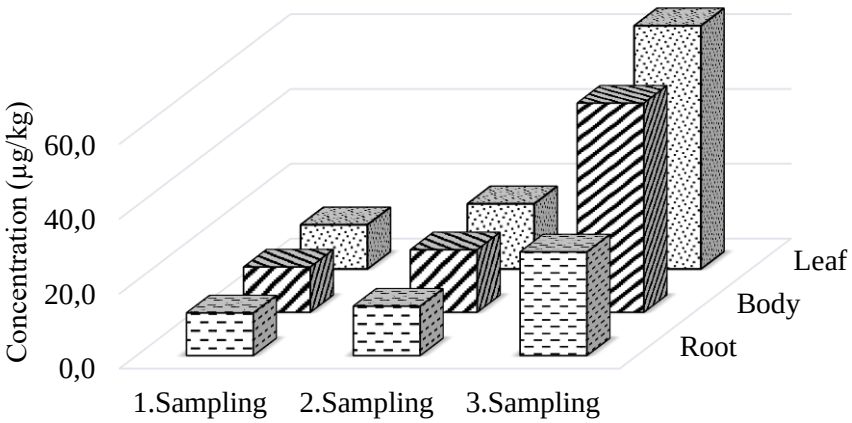

Figure 2. The relationship between the distribution of Imazamox residue levels in KM plant sampling (pH 7.28).

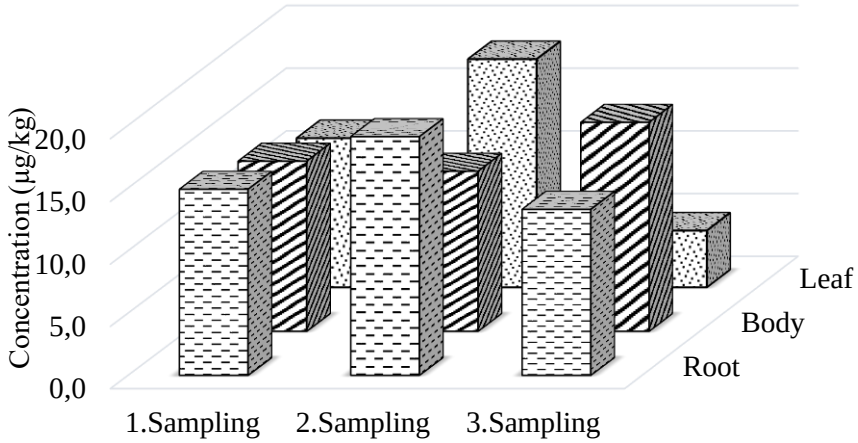

Figure 3. The relationship between the distribution of Imazamox residue levels in KB plant sampling (pH 4.95).

The reason for, this is due to the fact that the of imazamox in the area is more sorbed in soil (due to property acidic) and does not pass into the plant [23], On the other hand, it was determined that there was transport through the root, stem and leaf in the neutral zone, and it was determined that more accumulation in sunflower leaves.

4. CONCLUSION

As a result of the analyzes performed on the components of the sunflower plant (root, stem, leaf) collected from two different pH media in the Kırklareli center and Kavaklı district, Imazamox residue amounts remained below the limit values. According to our knowledge, the presence of Imazamox in rice has not been previously reported by QuEChERS extraction method. Imazamox residual values during harvest only were found to exceed the limit value. The absence of residues in sunflower plant parts, or being below the MRL value, indicates that Imazamox herbicide is used safely and consciously in sunflower cultivation.

ACKNOWLEDGMENTS

This study was supported by Scientific Project Unit of Kırklareli University under project number: KLUBAP 121.

REFERENCES

[1] Dor, E., Galili, S., Smirnov, E., Hacham, Y., Amir, R., Hershenhorn, J., The Effects of Herbicides Targeting Aromatic and Branched Chain Amino Acid Biosynthesis Support the Presence of Functional Pathways in Broomrape, Front Plant Science, 8, 1-15, 2017.

[2] Aysu, A., Türkiye'de ayçiçeği tarımı. Gümrük ve Ticaret Bakanlığı, kooperatifçilik genel müdürlüğü raporu, Edirne, 2017.

[3] Süzer, S., Büyük, H., Residual Effects Of Spraying Imidazolinone-Family Herbicides on Clearfield®* Sunflower Production From The Point of View of Crop Rotation, Helia, 33-52, 25-36, 2010.

[4] Yücel, U., 'Pestisitler ile alakalı değerlendirme' Ankara Nükleer Araştırma ve Eğitim Merkezi, Nükleer Kimya Bölümü, Ankara, 2000.

[5] Colquhoun, J., Mallory-Smith, C., Ball, D., Weed management in Clearfield wheat with imazamox. Oregon State University Extension Publication (EM8833), Corvallis, 2003.

[6] Brady, T.M., Cross, B., Doehner, R.F., Finn, J., Ladner, D.L., The discovery of imazamox, a new broad-spectrum imidazolinone herbicide. In: Baker DR, American Chemical Society (eds) Synthesis and chemistry of agrochemicals V. ACS Symposium Series, New Jersey, pp 30–37, 1998.

[7] Tan, S,, Evans, R.R., Dahmer, M.L., Singh, B.K., Shaner, D.L., Imidazolinone-tolerant crops: history, current status and future. Pest Manag Sci 61:246–257, 2005.

[8] Li, D., Barclay, I., Jose, K., Stefanova, K., Appels, R., A mutation at the Ala122 position of acetohydroxyacid synthase (AHAS) located on chromosome 6D of wheat: improved resistance to imidazolinone and a faster assay for marker assisted selection. Mol Breeding, 22, 217–225,2008.

[9] EFSA 2013, Reasoned opinion on the review of the existing maximum residue levels (MRLs) for imazamox according to Article 12 of Regulation (EC) No 396/2005, 2013, 11(6):3282.

[10] FAO (Food and Agriculture Organisation of the United Nations), 2009. Submission and evaluation of pesticide residues data for the estimation of Maximum Residue Levels in food and feed. Pesticide Residues. 2nd Ed. FAO Plant Production and Protection Paper 197, 264 pp.

[11] Vural, N., "Toksikoloji", Ankara Üniversitesi Eczacılık Fakültesi Yayınları, No: 73, Ankara, 342 - 363, 2005.

[12] Rajendran, R.B., Venugopalan, V.K., Ramesh, R., Pesticide residues in air from coastal environment, South India. Chemosphere, 39, S 1699-1706, 1999.

[13] Bukun, B., Nissen, S.J., Shaner, D.L., Vassios, J.D., Imazamox absorption, translocation, and metabolism in red lentil and dry bean. Weed Science 60:350–354, 2012.

[14] Anastassiades, M.,. Lehotay, S.J, Stajnbaher, D., Schenck, F. J., Fast and Easy Multiresidue Method Employing Extraction for the Determination of Pesticide Residues in Produce, Journal of AOAC International, 86(2), 412, 2003.

[15] Anastassiades, M., E. Scherbaum, B. Tas, D. Stajnbaher, H. Ohkawa, H. Miyagawa, Lee, P.W., Crop Protection, Public Health, Environmental Safety, Wiley-VCH, Weinheim, Germany, 439, 2007.

[16] Lehotay, S.J., De Kok, A., Hiemstra, M., and Van Bodegraven, P.,Validation of a Fast and Easy Method for the Determination of Residues from 229 Pesticides in Fruits and Vegetables Using Gas and Liquid Chromatography and Mass Spectrometric Detection, J.AOAC Int. Vol. 88(2), S 595-614, 2005.

[17] Türköz, G. ve Hışıl, Y., Pestisit Kalıntılarının Analizlerinde Son Gelişmeler, Dünya Gıda, 5, S 76-79, 2008.

[18] Ozcan, C., Kanburoglu Cebi, U., Gurbuz, M.A., Ozer S., Residue Analysis and Determination of IMI Herbicides in Sunflower and Soil by GC–MS, Chromatographia, 80(6), 941–950, 2017.

[19] Tan S., Evans R.R., Dahmer M.L., Singh B.K., Shaner D.L., Imidazolinone-Tolerant Crops: History, Current Status and Future, Pest Management Science, 61, 246–257, 2005.

[20] Pfenning, M., Palfay, G., Guillet, T. The CLEARFIELD® Technology – A New Broad-Spectrum Post-Emergence Weed Control System for European Sunflower Growers, Journal of Plant Diseases and Protection, Special Issue XXI, 000–000, ISSN 1861-4051, 2008.

[21] Rojano-Delgado, A.M., Priego-Capote, F., de Castro, M.D.L., De Prado, R., Mechanism of imazamox resistance of the Clearfield® wheat cultivar for better weed control, Agronomy for Sustainable Development, 35, 639–648, 2015.

[22] Hamel K. (2012)., Environmental Impact Statement for Penoxsulam, Imazamox, Bispyribac-sodium, Flumioxazin, & Carfentrazone-ethyl(27-40). Water Quality Program Washington State Department of Ecology Olympia, Washington.

[23] Aichele, T.M., Donald, P., Adsorption, desorption, and degradation of imidazolinones in soil. Weed Technology, 19, 154–159, 2005..

CONTROLLING SERVO MOTORS WITH SPEECH RECOGNITION BY USING 802.15.4 WIRELESS PROTOCOL ZIGBEE

M. Duman

Department of Electrical and Electronics Eng., Faculty of Technology, Düzce University, Düzce, Turkey

E-mail: mehmetduman@duzce.edu.tr

Abstract

In this work, 802.15.4 wireless communication protocol which has a specific name ZigBee is studied. It is very popular wireless technology at last years in electronic society because of relating to the Industry 4.0. ZigBee can connect things, such as, fridge, oven and dishwasher. Even markets, and fridge that is at home can be connected each other. It is known as internet of things (IoT).

With the help of the XCTU Program, the computer and two servo motors are wirelessly connected via XBee modules. Transmitter XBee module is connected to the computer through USB port with XBee USB Explorer and receiver XBee module is connected to the circuit of control of servo motors which are far away from computer about 15 meters. At this stage; Arduino Duemilanove is also used in control circuits. The codes which understand the commands are embedded in the XCTU Program and the user can control the servo motors with appropriate commands. If the user say “right” the motor of left runs and the motor of right stops, as a result; the toy car that has got two motors in wheels turns to the right and vice versa.

MatLab speech recognition is used in this work; consequently, the oral order commands are understood by the computer. They are processed in the XCTU Program after MatLab Program. Finally, the commands are sent to the motors through XBee modules. The 15 meter distance between receiver and transmitter can be increased by using intermediate XBee modules. In adition, increasing the power of the transmitter XBee module allows to increase the communication distance.

Keywords: servo motors, speech recognition, wireless protocol ZigBee

1. INTRODUCTION

The electronics industry is creating new inventions from day to day to make life easier. One of the new technologies developed is ZigBee technology. With ZigBee, which has 802.15.4 internet protocol, the equipment can communicate with each other. ZigBee, which only turns on the power when needed and is in standby mode for other times, consumes very little energy [1-4].

ZigBee devices can be used to communicate with each other such as refrigerators, ovens, dishwashers in the home, as well as the shelves in the shopping mall. Cooking in the oven may be the news that the dishwasher will work. The end of the cheese in the refrigerator may send a message to the shop to buy cheese. Decreasing of the products on the markets shelves can order new products from the supplier [4-9].

In this study, wireless communication is established between computer and motors of the wheels of the toy car. Commands sent from the computer via ZigBee have been received by the receiver ZigBee through internet protocol 802.15.4. According to the user commands, the toy car turns to the right or left. MatLab voice recognition with linear predictive coding theory is used for commands sent from the computer. The user gave orders using the external microphone [1, 10].

2. MATERIAL AND METHODS

The XCTU Program has to be used to upload the program codes to the XBee. There are two XBee modules which are transmitter and receiver given in Fig. 1. (a). Each of them connects to the computer separately and codes are uploaded through XBee terminal station that is given in Fig. 1. (b) one by one. The transmitter XBee connects to the computer USB input by terminal station and receiver XBee connects to the Arduino Duemilanove control card given in Fig. 1. (c) by XBee Pro Shield given in Fig. 1. (d) [1].

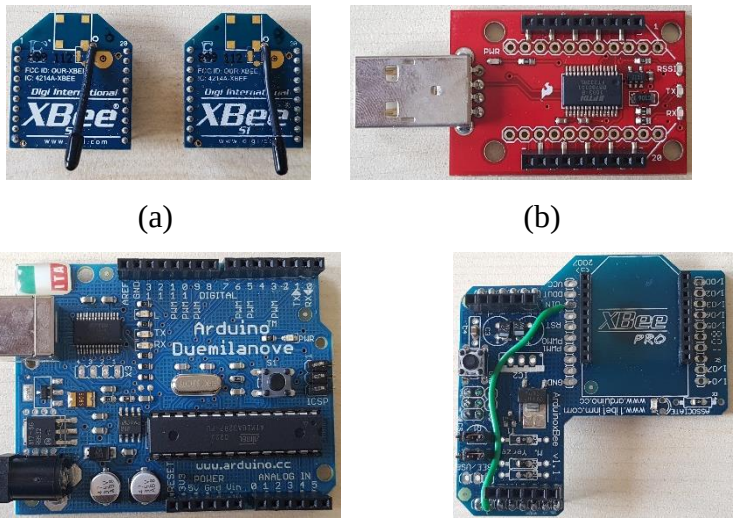

Figure 1. (a) Transmitter and receiver XBee modules (b) XBee terminal station (c) Arduino Duemilanove control card (d) XBee Pro Shield.

The servo motors are located to the Arduino Duemilanove control card output pins. By means of receiver XBee module and XBee Pro Shield the Arduino Duemilanove control card can understand the commands which are given by the user. The user gives the commands by talking to the computer external microphone. The commands compared to the previously taken samples are processed by the MatLab Program and transferred to the transmitter XBee module. At this time; wireless protocol ZigBee communication which is 802.15.4 protocol is activated. According to the power of ZigBee modules, the command transfer distance can increase.

The commands and direction of rotation of the motors are very important in this experiment. If the motors on the right side of the toy car run, the right wheel will rotate. As a result; the toy car turns to the left and vice versa. If all motors work, the toy car will go forward. The user can say “right”, “left”, “forward” and “stop”.

The sample installation image is shown in Figure 2. In the full study, there are 2 motors, wheels and toy car. There are also computer and external microphone. The Arduino card can get energy from 9 Volt battery or computer USB port. Arduino and XBee Pro Shield are integrated together. Receiver XBee module may get the commands from 15 meters and transmits them to the servo motor by means of its connected circuits [1, 10].

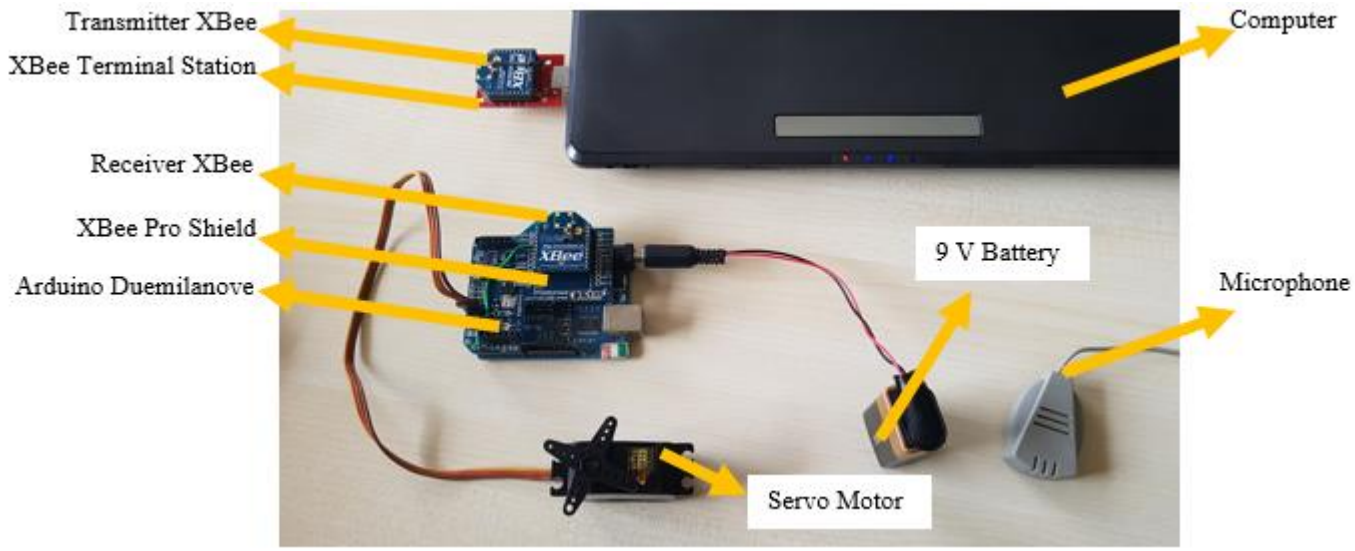

Figure 2. The sample installation image of ZigBee Communication

3. RESULTS AND DISCUSSION

At the end of the experiments and works, it can be said that the ZigBee communication is realized with level 1 XBee modules approximately 15 meters range. The motors turn to the right directions according to the appropriate commands. If the experiments are carried out with the same person, the result is 100% success and with different people, the result is 80% success. It is quite well results for the project.

The transmitter XBee module is also named XBee coordinator and receiver XBee module is also named end device. If the router XBee module is used, the range can be increased. Power of ZigBee modules is effective on increasing distances too. By using router XBees, lots of devices such as motors, lambs, ect. can be controlled.

4. CONCLUSION

ZigBee technology can be used in new generation vehicles and automotive industry. Through this study, we have shown an example of how to use it in automotive industry thanks to XBee which is one of the ZigBee products. It is a new and evolving project in wireless communication. Using a combination of dozens of modules, a wide range of wireless communications can be generated.

REFERENCES

[1] Duman M., Çelik B., IEEE 802.15.4 Standardına Uygun ZigBee ile Kablosuz Haberleşme Uygulaması ve Servo Motor Kontrolü, Graduation Project, Electronics Engineering, Gebze Istitute of Technology, 2011.

[2] Schneider Electric Industries, ZigBee, Setting Standards for Energy-Efficient, 2005.

[3] Bayılmış C., Ertürk İ. Çeken C., Kablosuz Bilgisayar Ağlarının Karşılaştırmalı İncelemesi, Journal of Polytechnic, 7, 3, pp. 201-210, 2004.

[4] Köybaşı Z., Kaya İ., Security and power consumption comparisons of wireless sensor networks, 21st Signal Processing and Communications Applications Conference (SIU), Haspolat, Turkey, 2011.

[5] Karasulu B., Toker L., Korukoğlu S., ZigBee - IEEE 802.15.4 Standartı Temelli Kablosuz Algılayıcı Ağları, XIV. Türkiye'de İnternet Konferansı Bildirileri, Bilgi University, İstanbul, 2009.

[6] http://www.zigbee.org, ZigBee Alliance website, 26 September 2018.

[7] Aktaş F., Çeken C., Erdemli Y. E., Nesnelerin İnterneti Teknolojisinin Biyomedikal Alanındaki Uygulamaları, Düzce University Journal of Science and Technology, 4, pp. 37-54, 2016.

[8] Somani N. A., Patel Y., ZigBee: A Low Power Wireless Technology for Industrial Applications, International Journal of Control Theory and Computer Modelling (IJCTCM), 2, 3, 2012.

[9] Wheeler A., Commercial Applications of Wireless Sensor Networks Using ZigBee, IEEE Communications Magazine, 45, 4, 2007.

[10] Duman M., Linear Predictive Coding in MatLab to Communicate with ZigBee, 3rd International Conference on Organic Electronic Material Technologies, Kırklareli, Turkey, 2018.

LINEAR PREDICTIVE CODING IN MATLAB TO COMMUNICATE WITH ZIGBEE

M. Duman

Department of Electrical and Electronics Eng., Faculty of Technology, Düzce University, Düzce, Turkey

E-mail: mehmetduman@duzce.edu.tr

Abstract

One of the popular wireless communicating technology which is ZigBee is studied in this work. It has 802.15.4 wireless communication protocol in the literature. XBee brand transmitter and receiver modules are used to fulfill the requirements of ZigBee. The transmitter XBee is connected to the computer and the receiver XBee is connected to the motors located on Arduino 15 meters away. This system already communicates wirelessly, as a second wireless communication tool, MatLab voice recognition algorithm is introduced into the system. The linear predictive coding (LPC) algorithm, which is the base of this study, is one of the most important methods for voice recognition. By means of this algorithm, the commands will be transmitted to the transmitter XBee by sound, not by pressing the keys of the PC. The LPC takes into account the sound properties as well as the human larynx and mouth structure. LPC is based on the output of a linear and time-varying system, which is stimulated by periodic impulses or random noise. This system can be expressed as a linear filter transfer function. The inverse Z transform is applied to this transfer function. The LPC works with the principle that the next sample can be approximated from a previous sample.

The voices of the same person were recorded and embedded in the MatLab Program. The test was 100% successful with the same user. However, voice recordings were taken from different people so that the system could be controlled by other users. When sampling voice records of different persons, several samples were taken to increase the accuracy rate. The success rate was around 80% when different matrices composed of different people's voices were used. MatLab codes were developed to provide the best performance. The external microphone, was used when the voice command for servo motor control was given and the commands were embedded firstly in the program. At the end, the user can control the servo motors with appropriate commands wirelessly. The first wireless communication is ZigBee communication, here XBee, and the second wireless communication is voice commands through MatLab Program.

Keywords: communication, linear predictive coding, ZigBee

1. INTRODUCTION

ZigBee is a new technology for communication especially in industry. It consumes very little energy and can turn on to standby mode easily. The coordinator, end and router devices are used in this technology to connect different types of electronical equipments. By means of router ZigBee devices the communication range may increase to kilometers [1-6].

In this work, wireless communication is established between PC and servo motors to run the toy car. Commands are sent by the coordinator device ZigBee and they are received by the end device ZigBee via internet communication protocol 802.15.4. According to the user voice commands, the toy car turns to the right or left [6-7]. Speech recognition with linear predictive coding theory in MatLab Program is used to send commands. The user gave orders using the external microphone [6].

The characteristic of the LPC is that it can predict other spoken forms of command. It works with the principle that the following sample can be approximated from a previous one. Consequently; it gets the "predictive" name. It is linear and time-varying (LTV) system so that it is named "linear" [8].

2. MATERIAL AND METHODS

The XCTU Program and MatLab Program should be used to realize the project. By XCTU Program, the coordinator and end device assignments are done. If there is a router device, it can be also assigned with XCTU Program. By MatLab Program, the samples are taken from various people, the code about speech recognition is written, the commands are taken from one person and the digital commands are sent to the coordinator ZigBee device, here XBee device which is given in Fig. 1. (a). Coordinator XBee device is connected to the XBee terminal station and it has USB output shown in Fig. 1. (b). It connects to the PC thanks to its USB port.

The other communications are done with ZigBee wireless protocol. In this study, the important part is LPC and decreasing the error and misunderstanding from the PC using MatLab Code.

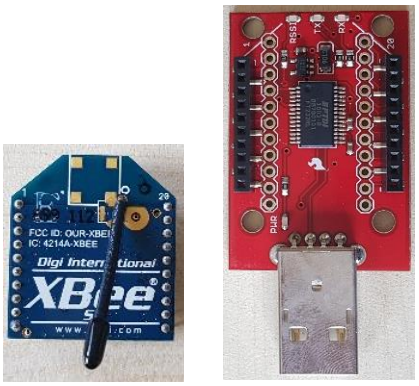

(a) (b)

Figure 1. (a) Transmitter and receiver XBee modules (b) XBee terminal station

2. 1. Creating Speech Recognition Code

There are several LPC codes in the literature. The code which has 11025 Hz sample frequency is used and there are 16 (n) samples in LPC function in this work. Baud rate is 9600 and COM5 PC port is used. 10 samples will be taken from the each user to create library. All the users should say “right”, “left”, “forward” and “stop” 10 times. There is only 1 second for each word. While the users are speaking to the microphone, they can read the commands on the screen so that they can understand what they will do.

Their sounds are recorded and played. If the users samples are suitable for library, the program which includes least squares method and autocorrelation method is done. After all users give their voices to the library, the workspaces file is created. The MatLab codes can be got from [6].

2. 2. Running Speech Recognition Code

The new person whose voice record is not in the system library says one of the commands to the microphone. After this operation, the MatLab program runs and compiles the codes. The computer tries to predict the users speech and generate new similar samples. The computer screen shows what the given command is, and graphs about the similarity of commands. Consequently; the computer sends the commands through USB port to the coordinator device and the device is ready to send 15 meters away to the end device which is integrated to the XBee Pro Shield and Arduino Duemilanove, therefore; servo motors and toy car can move.

The XBee Pro Shield, Arduino and servo motor are given in Fig. 2. With XBees, computer, battery and microphone.

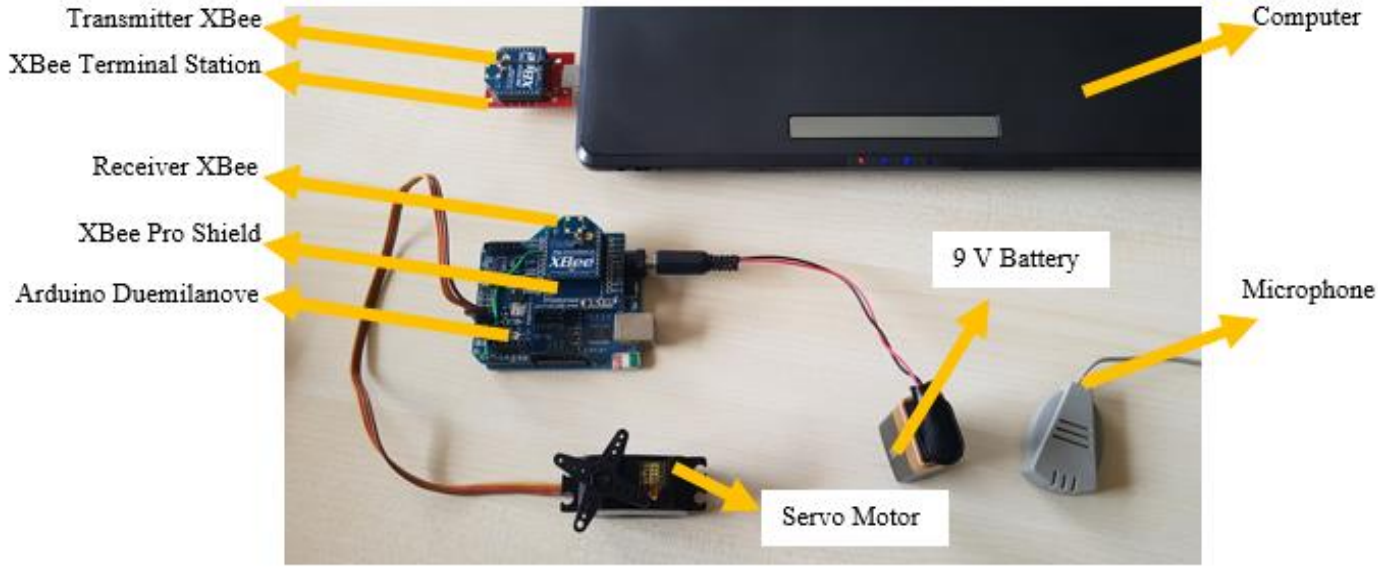

Figure 2. ZigBee (XBee) Communication

3. RESULTS AND DISCUSSION

The communication process was made with WiFi, bluetooth and GSM technologies. However, these technologies were not adequate for Industry 4.0. Thanks to ZigBee (XBee), a new technology has been developed which can work with little energy and connect many electronic equipment.

In this study, project of sending computer-based commands to the circuit connected to the toy car 15 meters ahead with ZigBee method is supplemented with LPC. LPC is developed and errors which are in the program codes are minimized. 80% success is achieved in experiments with different people.

4. CONCLUSION

As a result of this study, we have supported the data exchange via wireless communication with voice commands and created a completely wireless system. It is also a sample study which is created for the voice control of passenger cars.

REFERENCES

[1] Schneider Electric Industries, ZigBee, Setting Standards for Energy-Efficient, 2005.

[2] Karasulu B., Toker L., Korukoğlu S., ZigBee - IEEE 802.15.4 Standartı Temelli Kablosuz Algılayıcı Ağları, XIV. Türkiye'de İnternet Konferansı Bildirileri, Bilgi University, İstanbul, 2009.

[3] Bayılmış C., Ertürk İ. Çeken C., Kablosuz Bilgisayar Ağlarının Karşılaştırmalı İncelemesi, Journal of Polytechnic, 7, 3, pp. 201-210, 2004.

[4] http://www.zigbee.org, ZigBee Alliance website, 26 September 2018.

[5] Wheeler A., Commercial Applications of Wireless Sensor Networks Using ZigBee, IEEE Communications Magazine, 45, 4, 2007.

[6] Duman M., Çelik B., IEEE 802.15.4 Standardına Uygun ZigBee ile Kablosuz Haberleşme Uygulaması ve Servo Motor Kontrolü, Graduation Project, Electronics Engineering, Gebze Istitute of Technology, 2011.

[7] Duman M., Controlling Servo Motors with Speech Recognition by Using 802.15.4 Wireless Protocol ZigBee, 3rd International Conference on Organic Electronic Material Technologies, Kırklareli, Turkey, 2018.

[8] Erfani S., Ahmadi M., Bayan N., Signal analysis in linear time-varying systems, International Symposium on Signals, Circuits and Systems ISSCS2013, Romania, 2013.

THE CONNECTION TYPES TO MINIMIZE LOSS OF GAIN BETWEEN LOW NOISE AMPLIFIER AND ANTENNA

M. Duman[1] and A. O. Salman[2]

[1]*Department of Electrical and Electronics, Faculty of Technology, Düzce Uni., Düzce, Turkey*

[2]*Department of Electronics and Communication, Faculty of Engineering, Kocaeli Uni., Kocaeli, Turkey*

E-mail: mehmetduman@duzce.edu.tr

Abstract

In this work, the low noise amplifier (LNA) is designed at the Rogers 4350 copper plate for Passive Millimeterwave Imaging System (PMMWIS). Some designs are done at 35 GHz frequency window which is specific frequency window for PMMWIS to detect targets for different air conditions, such as; fog, rain, dusty air [1]. The antenna which will be connected to the LNA should be designed at the copper plate. It is the most convenient connection to get minimum loss because of being at the same plate. However, other types of connections for LNA and antenna have also been studied.

One of the connector type is 2.92 mm connector. The LNA can be connected to the micro strip antipodal Vivaldi antenna [2] or Vivaldi fed antenna [3] with 2.92 mm connector. The LNA output has female pins and the antenna input has male pins. So that, they can be connected each other. Both the LNA and the antenna are on the same type of plate, but they are designed separately to be able to measure one by one. As a result; there are some attenuation at the connection point. Another investigated type is a wave guide to micro strip converter. The LNA can be connected with horn antenna but the horn antenna has WR28 standart to work at Ka band (35 GHz frequency band). Consequently; if the antenna connects to the LNA, it has to be converted to the wave guide. The system can work in this situation but the attenuation may be more than the others.

In the passive imaging, the attenuation of the connections can be neglected if the gain is enough to be able to get the images and see the figure on computer screen. In this study, the comparison of attenuation between low noise amplifier and antenna is analyzed for each case. Finally, the connection types of the LNA and the antenna are chosen.

Keywords: antenna, loss of gain, low noise amplifier

1. INTRODUCTION

The passive millimeter imaging systems are new technologies about scanning images or recognizing things which can be dangerous materials inside of clothes [1, 4-6]. There are also several areas of use, such as measuring the sky temperature [7]. Some systems are done with wave guides and some of them are integrated into copper plates [1, 5, 8]. There are various techniques when making connections between different type of circuits. Each type of connection has its own advantages and disadvantages. The wave guide antenna can be connected to the low noise amplifier (LNA) which is on micro strip copper plate or Vivaldi antenna [2-3] can be integrated to the wave guide LNA [8-9]. In this study, suitable connection types are described.

2. MATERIAL AND METHODS

Within the scope of this study, 3 connection types were examined. The first of these types is that different circuits made on the same copper plate are combined with micro strip lines on the copper plate without using any connecting equipment. This is the least lossy method, but it does not allow separate examination of the circuits. If an active circuit is created, the measurement of this circuit cannot be carried out like conventional circuit measurements. The input-output ports of the network analyzer must be connected to the circuit individually to be measured. Otherwise measurement is not possible.

In this study, the second type of connection examined is to assemble the circuits in the same kind of plates and connect them with the connectors. 2.92 mm connector is selected as connector type since the operating frequency is 35 GHz. The antenna has male 2.92 mm connector and the LNA has female. There may be some loss in this connection, but it is possible to measure circuits separately. Repair work can be done easily in any defective condition. In Fig. 1. (a), the antenna and the LNA are given with 2.92 mm connector.

Another form of connection is to connect the waveguide structure to the normal copper plate circuit structure. It is the case where the antenna has the highest directionality and gain. To connect to the micro strip circuit from the waveguide, a micro strip circuit converter is required. The loss of the converter is very high in the entire circuit. In this case, the optimum condition is selected within the triad of directionality, gain and loss. In Fig. 1. (b), the wave guide (WG) antenna is connected to the LNA with WG to 2.92 mm converter.

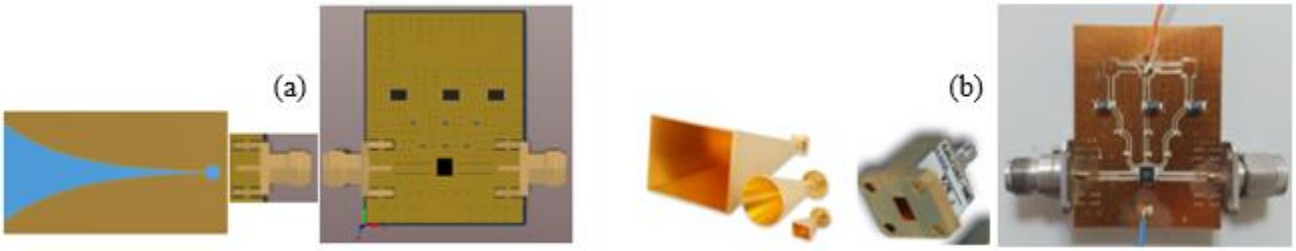

Figure 1. (a) Vivaldi antenna and circuit on copper plate are connected with 2.92 mm connector (b) Horn antenna and LNA circuit are connected with WG to 2.92 mm converter [10]

3. RESULTS AND DISCUSSION

The third method which has wave guide to micro strip circuit connector is chosen in our passive millimeter wave imaging system because of the orientation of the imaging system is very important and the extent of exposure can be compensated. Although there is loss of gain, the system works correctly.

If there is a situation where the directionality and gain is better and the individual tests can be made more easily, then the system can be changed.

4. CONCLUSION

As a result of the study, passive millimeter wave imaging system was produced and the connection points were determined. A passive system operating at a frequency of 35 GHz, containing waveguide structures and micro strip circuits, consisting of active circuits, capable of displaying the image at approximately 65 meters away even in a variety of weather conditions without emitting any wave signal is generated.

Various additions can be made to the system to increase the distance of imaging or to find dangerous hidden objects under clothes.

ACKNOWLEDGMENTS

This research has been supported by Kocaeli University no: 2013/18 (MİLGÖR BAP) and the authors thank to the Kocaeli University.

M.D. thanks The Scientific and Technological Research Council of Turkey (TÜBİTAK) and Düzce University for their support.

REFERENCES

[1] Yujiri L., Shoucri M. and Moffa P., Passive millimeter-wave imaging, Microwave Magazine IEEE, 4, 3, pp. 39-50, 2003.

[2] Duman M. and Salman A. O., Antipodal Vivaldi Antenna for Passive Imaging Technology in Ka Frequency Band, Sakarya University Journal of Science, 22, 4, 2018.

[3] Duman M. and Salman A. O., 35 GHz Vivaldi Fed Antenna Design for Passive Millimeter Wave Imaging System in Ka Band, Journal of Electrical Engineering, 6, 6, 2017.

[4] Daniels D. J., EM Detection of Concealed Targets, Wiley Series in Microwave and Optical Engineering, 2010.

[5] Skou N., Le Vine D., Microwave Radiometer Systems, Design and Analysis, Second Edition, Artech House, 2006.

[6] Ulaby F. T., Moore R. K., Fung A. K., Microwave Remote Sensing, Active and Passive, Volume 1, Microwave Remote Sensing Fundamentals and Radiometry, Artech House Inc., 1981.

[7] Duman M. and Salman A. O., Obtaining the sky - temperature depending on voltage value by the passive millimeter wave imaging system, Acta Physica Polonica A, Polish Academy of Sciences, Institute of Physics, in review, 2018.

[8] Pozar D. M., Microwave Engineer, 2nd Edition, John Wiley & Sons Inc., 1998.

[9] Balanis C. A., Antenna Theory Analysis and Design, 3rd Edition Nobel Publications, Wiley, 2013.

[10] Quinstar Technology, QWA-28S29ME0 datasheet and QWH-APRS00 datasheet.

THE ELECTRICAL AND OPTICAL CHARACTERIZATION OF ELECTRODEPOSITED Ni /n-GaAs SCHOTTKY BARRIER DIODES

T. Batmaz, B. Kirezli, M. Haciismailoglu, M.Alper, M. Ahmetoglu

Department of Physics, Uludağ University, 16059, Görükle, Bursa, Turkey

E-mail: tugcebatmaz@hotmail.com

Abstract

In this paper we report the electrical and optical characteristics of the Schottky diodes formed by electrodeposition of Nickel on n- GaAs from 0.125 M $NiSO_4$ + 0.25 M H_3BO_3 + 0.25 M Na_2SO4 (pH=4.4) solution. The electrodeposition was performed at room temperature and at -1.5 vs. SCE. We measured current-voltage (I-V) between 200 K and 360 K with 20 K temperature. Based on these results, the ideal factor n, barrier heights Φ_b were calculated from the I-V curve. These values at room temperature are 1.04 and1.11 eV respectively. Light current characteristics were investigated. Spectral photoresponse measurements of the structure are carried out at room temperature.

1. Introduction

Semiconductors form the majority of electronic devices that make up today's technology. Metal (M) and semiconductor (S) combinations are important optoelectronic and electronic devices applications for science world during recent years [1,3]. In especially Schottky Barrier contacts manufactured by combination of earth elements (Fe, Ni, Co) with semiconductors are for the device optical detectors, solar cells [1] and chemical sensors [2,3]. Gallium arsenide (GaAs) is one of the most popular semiconductor materials. The most important feature of GaAs is saturated electron velocity and high electron mobility. The other advantages of GaAs; Low-temperature coefficient, good low light performance, high efficiency, flexible and lightweight.

The electrodeposition method offers unmatched opportunities due to high efficiency and low cost. At the same time electrodeposition depends on the interaction of the metal and the semiconductor surface. The electronic features of the substrate defines the mechanism and kinetics of the metal deposition electrode when the electrodeposition process occurs on semiconductor substrates [4]. The electrodeposition on N-type semiconductor surfaces includes electrons in the conduction band and therefore is generally selected [5].

In this work, we attempted to investigate the effects of the interface states, I-V characteristics, ideality and barrier height with optical characterization on the mechanism of Ni/n-GaAs Schottky diodes at a wide temperature range of 200-360 K.

2. Experimental Procedure

The substrates used in this work are n-type GaAs single crystals with a (100) orientation, 400 µm thickness and 508 mm diameter. To make ohmic contact Indium were thermally evaporated on the unpolished side of the wafer in a thermal evaporation system (Vaksis PVD Hand2S-TM). Before the evaporation chamber vacuumed under $1x10^{-5}$ Torr pressure. For electrodeposition, the wafer was masked with a tape except a circular area with the diameter of 2.5 mm. After that, the masked wafer was chemically cleaned using "Piranha followed by Hydrochloric" cleaning procedure as below. Firstly, the n-GaAs wafer was dipped in $5H_2SO_4 + H_2O_2 + H_2O$ (1:8:500) solution for 30 seconds to remove surface damage layer and undesirable impurities, transferred to the DI water beaker for 5 mins, dipped in H_2O+HCl (1:1) solution for 2 mins and again rinsed with DI water for 5 mins. Finally, the wafer was dried and inserted into the deposition solution immediately. The solution contains from 0.125 M $NiSO_4$ + 0.25 M H_3BO_3 + 0.25 M Na_2SO_4 (pH=4.4). In a three-electrode system, the n-type GaAs was used as working electrode, a Pt sheet and a saturated calomel

electrode (SCE) were served as counter and reference electrode respectively. The Ni layer was deposited -1.5 vs. SCE.

The current-voltage *(I–V)* measurements were performed by the use of KEITHLEY 6487 picoampere/voltage source using a temperature controlled Janis CCS-150 cryostat, which enables us to make measurements in the temperature range of 77K-380K.

Photoresponse spectra of the Ni/n-GaAs structure were measured in the range of 860-1160 nm with a setup of Oriel Apex2 100 W quartz tungsten halogen lamb, Cornerstone 260 monochromator and SR830 DSP Lock-In-Amplifier at two several temperatures.

The light-current-voltage measurements were performed by using of He-Ne Laser with 633 nm. The Intensity of a incident light were measured using THORLABS P100D – Compact Power and Energy Meter Console with S401 Thermal power sensor head. The results of measurements were fed via an IEEE-488 interface into a computer for storage and processing.

3. Result and Discussion

3.1 *Electrical Properties*

The electrical characterizations of the device were achieved through I-V measurements at a several temperatures. The formation of a Schottky barrier between a Ni layer and n-doped GaAs at several temperatures is shown in Fig 1.

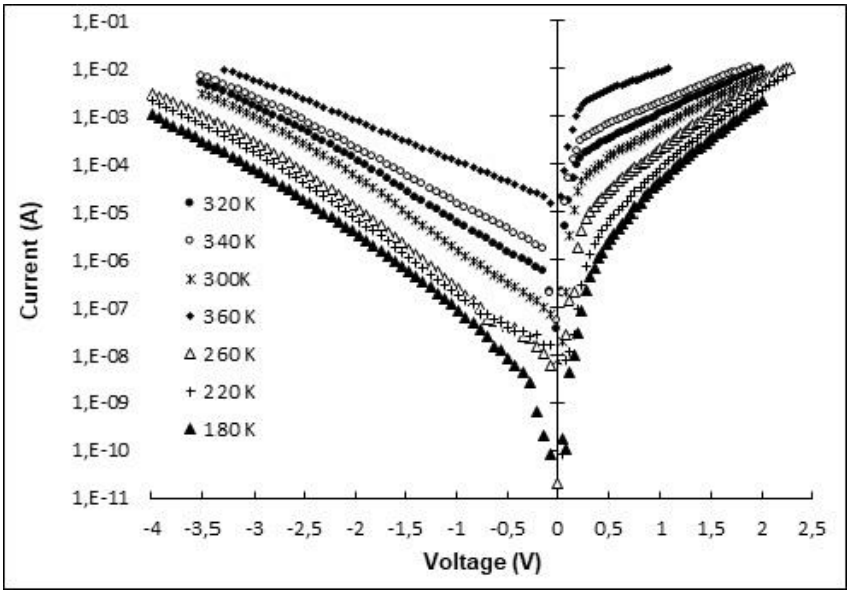

Fig 1. The experimental forward and reverse bias current versus voltage characteristics in a semilog scale of Ni/n-GaAs Schottky barrier diodes at several temperatures.

The current through a Schottky barrier diode at a forward bias V, based on the thermionic emission theory, is given by the relation

$$I = I_0 \exp\left(\frac{qV}{nkT}\right)\left[1 - exp\left(-\frac{qV}{kT}\right)\right] \quad (1)$$

Where I_0 is the saturation current derived from the straight line intercept of ln I at $V = 0$ and is given by

$$I_0 = AA^*T^2 exp\left(-\frac{q\emptyset_b}{kT}\right) \quad (2)$$

Where q is the electron charge, V is the forward bias voltage, k is the Boltzmann constant, T is the absolute temperature , A is the effective diode area , A^* is teh effective Richardson constant and equals 8.39x10^5 A.m^{-2}K^{-2} for n-type GaAs [6,7]. ϕ_b is the zero bias apparent barrier height (BH) and n ideality factor. The ideality factor is calculated from the slope of the linear region of the forward bias ln I-V plot and can be written from Eq.1 as:

$$n = \frac{q}{kT}\left(\frac{dV}{dIn(I)}\right) \quad (3)$$

The zero-bias barrier height $\emptyset_b$ is determined from extrapolated I_0 , and is given by:

$$\emptyset_b = \frac{kT}{q} In\left(\frac{AA^*T^2}{I_0}\right) \quad (4)$$

The experimental values of $\emptyset_b$ and n were determined from intercepts and slopes of the forward bias ln I versus V plot of each temperature, respectively, and shown in Table 1.As shown in Table 1, the experimental values of $\emptyset_b$ and n for the Ni/n-GaAs Schottky barrier diode ranged 1,11 eV and 1,04 (at 300 K).

Table 1.

T (K)	I_0 (A)	n	$\emptyset_b$ (eV)
360	9,60x10^{-8}	0,21	1,26
340	5,19x10^{-8}	0,36	1,22
320	3,42x10^{-8}	0,8	1,15
300	8,06x10^{-9}	1,04	1,11
260	3,00x10^{-9}	1,27	0,98
220	6,00x10^{-11}	1,76	0,89
180	8,10x10^{-11}	2,01	0,72

As shown in Fig 2, the values of $\emptyset_b$ and n determined from forward bias I-V characteristics are strong functions of temperature.

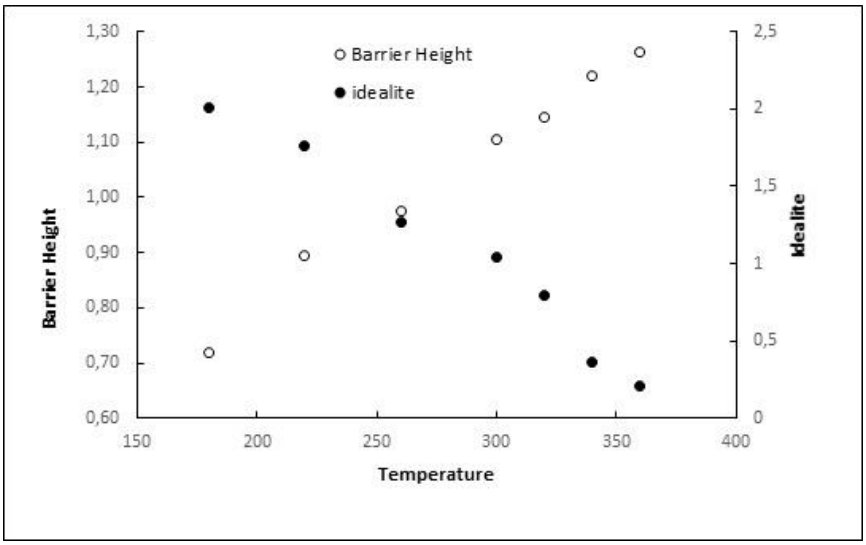

Fig 2. Temperature dependence of the ideality factor and barrier height for Ni/n-GaAs Schottky barrier diode in the range 180-360 K.

The ideality factor n was found to increase, while the $\emptyset_b$ decreased with decreasing temperature. As explained in Refs. [8,9], once current transport across the metal-semiconductor flowing through the patches of lower Schottky barrier height and a larger ideality factor. As a result, barrier height will increase with the temperature and bias voltage.

The Richardson constant can be determined from the intersection with the y-axis in the ln (J_0/T^2)-1000/T graph. By using this relation, A^* is found as 8.39×10^5 A·m^{-2}K^{-2} [8] for the diode in Fig 3.

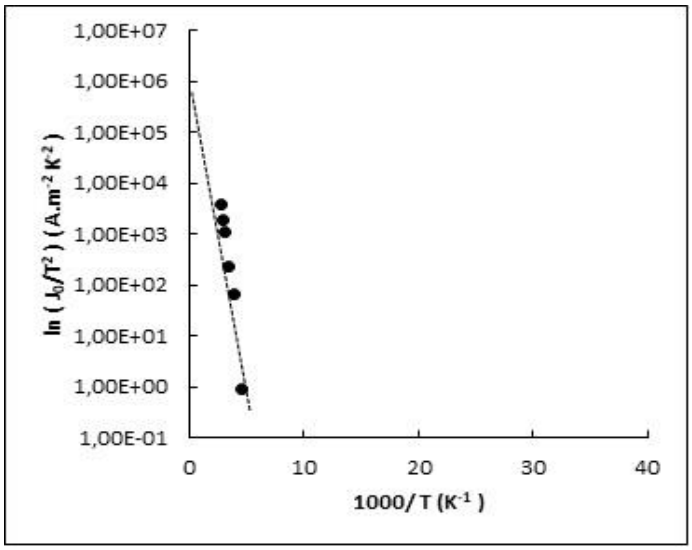

Fig 3. Ln (J_0/T^2)-1000/T graph of the Ag/n-GaAs Schottky diode

At high currents, there is forever a deviation which has been clearly shown to depend on parameters such as the interfacial layer thickness, the interface states density, and series resistance, as one would be expected [10].

Norde proposed a method to determine value of the series resistance and BH by considering equation (1) and the situation where the voltage across the diode is higher than 3kT / q. Norde's function F(V) is defined as [12].

$$F(V) = \frac{V}{\gamma} - \frac{k_\beta T}{q}\ln(\frac{I}{AA^*T^2}) \quad \textbf{(5)}$$

to avoid the serial resistance problem. The minimum of F (V) gives the barrier height:

$$\phi_b = F(V_0) + \frac{V_0}{\gamma} - \frac{k_\beta T}{q} \quad \textbf{(6)}$$

where $F(V_0)$ is the minimum value of $F(V)$ at the voltage of V_0. F (V) vs V plot for the Ag/n-GaAs Schottky diode is given in Fig 4. The obtained values are V_0=0.3 V, F (V_0)=0.68 V and ϕ_b=0.805 eV.

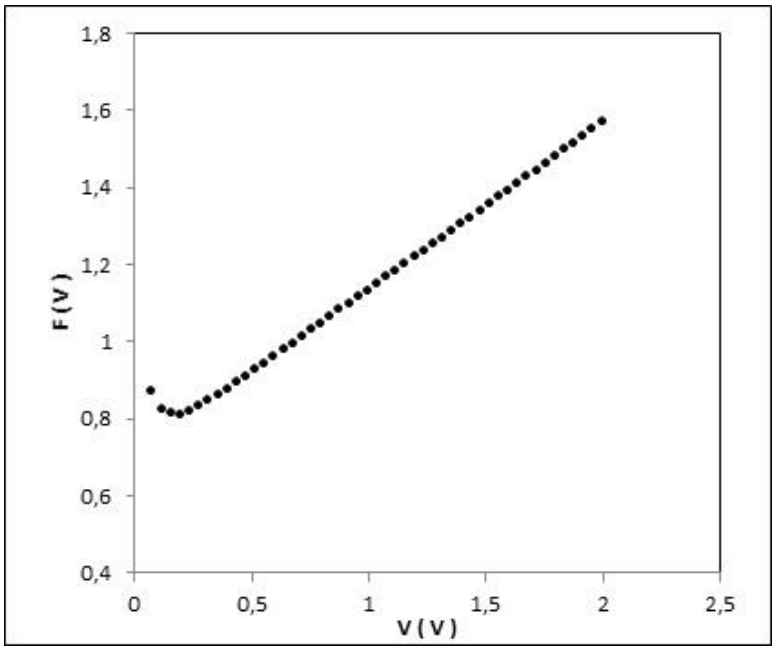

Fig 4. F(V)-V plot of the Ag/n-GaAs Schottky diode

The interface state energy distribution curve of the Ni/n-GaAs Schottky barrier diode is given in Fig 4. One of the critical parameters affecting the device performance is the density of the interface states. For a metal-semiconductor diode having interface states in equilibrium with the semiconductor, the ideality factor, n becomes higher than unity as proposed by Card and Rhoderick [13] is given by

$$N_{ss}(V) = \frac{1}{q}\left[\frac{\varepsilon_i}{\delta}\left[\, n(V) - 1 \,\right] - \frac{\varepsilon_s}{W_D}\right] \qquad \textbf{(7)}$$

where q is the electron charge, n (V) is the ideality factor, W_D is the depletion region width, δ is the thickness of the interfacial layer, N_{ss} is the density of interface states, ε_i and ε_s are the dielectric coefficients of the interfacial layer and the semiconductor, respectively. The interfacial insulator layer thickness ($W_D = 2{,}24 \times 10^{-4}$ Cm) was obtained from high-frequency (1 MHz) C-V characteristic using the equation for insulator layer capacitance $\left(C = C_{0x} = \frac{\varepsilon' A}{\delta} \right)$, and ε_0 is the permittivity of free space. Furthermore, in n-type semiconductors, the energy of the interface states with respect to the top of the conduction band at the surface of the semiconductor is given by [11-14]

$$E_c = E_{ss} = q\,(\phi_e - V) \qquad \textbf{(8)}$$

Where V is the applied voltage drop across the depletion layer, ϕ_e is the effective barrier height, E_c is the minimum of the conduction band, E_{ss} is the interface states and n the ideality factor. Consequently, the connection between effective barrier height, voltage and ideality factor in given by

$$\phi_e = \phi_{b0} + (1 - 1/n\,(V)) \qquad \textbf{(9)}$$

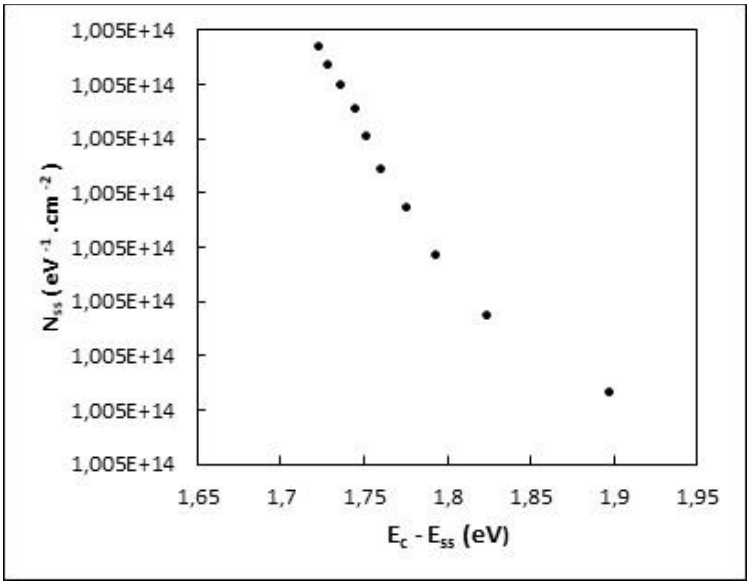

Fig 5. Density of interface states N_{ss} as a function of $E_{ss} - E_c$ obtained from the I-V measurements at room temperature.

3.2 *Optical Properties*

The spectral distribution of sensitivity for a Ni/n-GaAs Schottky diode at two several temperatures is shown in Fig 6. From the shift of the long-wavelength edge of the photoresponse, we estimated the temperature coefficient of the gap width of GaAs layer. The temperature coefficient of the energy gap of the GaAs layer was found to be $\Delta E_g/\Delta T$ = 4,34x10^{-4} eV/K. This value very close to the temperature coefficient obtained from the temperature dependence of the energy gap of GaAs [15]:

$$E_g = 1{,}519 - (5{,}405 \times 10^{-4})\frac{T^2}{T + 204}\ (eV) \qquad \textbf{(10)}$$

The value obtained at two several temperatures is $\Delta E_g/\Delta T$ = 4,24x10^{-4} eV/K.

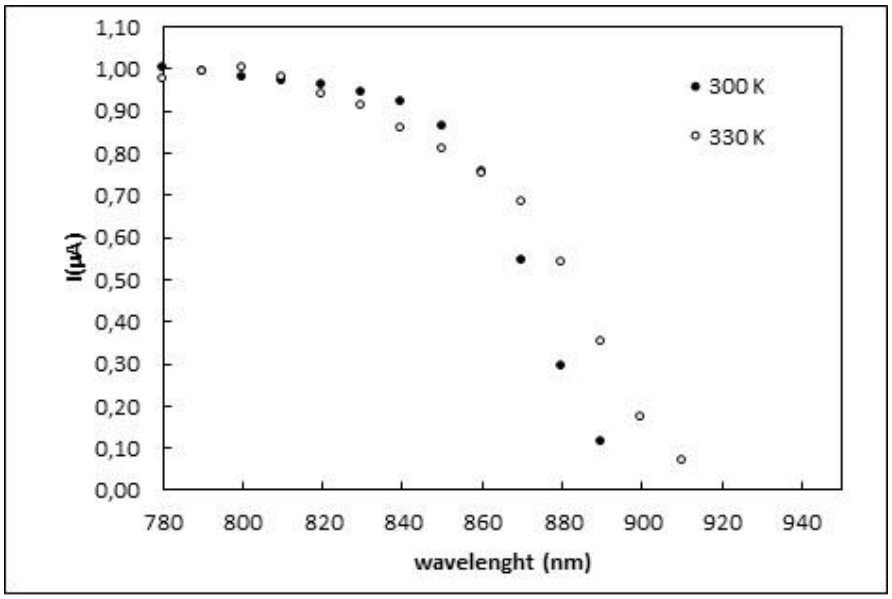

Fig 6. The spectral distribution of sensitivity of the Ni / n-GaAs Schottky diode at two different temperatures.

The energy gap of the GaAs layers determined from the wavelength corresponding to a twofold decrease in sensitivity is 1.425 ± 0.02 eV at T = 300 K. This value is very close to the energy gap values of the GaAs at a room temperature. The short wavelength cut-off of the photosensitivity is due to strong absorption of the short-wavelength radiation in the Ni metal layer.

Also, the type of band gap of GaAs can be determined from the experimental results of Fig 6 near the cutoff. The amount of the photocurrent produced during absorption of a photon depends on the excess energy generated from the difference of the photon energy *hv* and the bandgap energy E_g. Near the bandgap edge of the semiconductor, the proportionality of the photocurrent in relation to the excess energy determines the type of the bandgap as shown in the following equations:

Direct Bandgap:

$$I \ \alpha \ (hv - E_g)^{1/2} \quad \textbf{(11)}$$

$$I^2 \ \alpha \ (hv - E_g) \quad \textbf{(12)}$$

Plotting the values of the photocurrent near the cutoff of 870 nm as a function of the photon energy in relation to equation it is possible to determine the type of GaAs bandgap. The intercept of the line at x-axis gives the bandgap of GaAs and found to be about 1.4 eV for T=300 K. Also 1.38 eV for T=330 K.

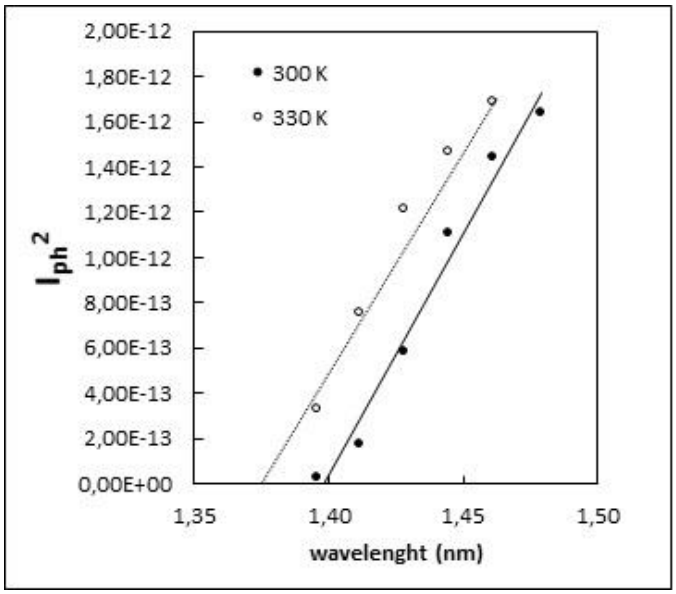

Fig 7. The room temperature plot of the square of photocurrent versus photon energy near the band edge

Fig 8 shows the light current-voltage characteristics of the investigated photodiodes under different illumination intensities by photons with a wavelength of 633nm. Illuminating the Schottky diode with optical radiation, shifts the *I–V* curve by the amount of photocurrent. Thus:

$$I = I_0\left(\frac{eV}{nkT}\right) - I_P \qquad \textbf{(13)}$$

where I_P is the photocurrent.

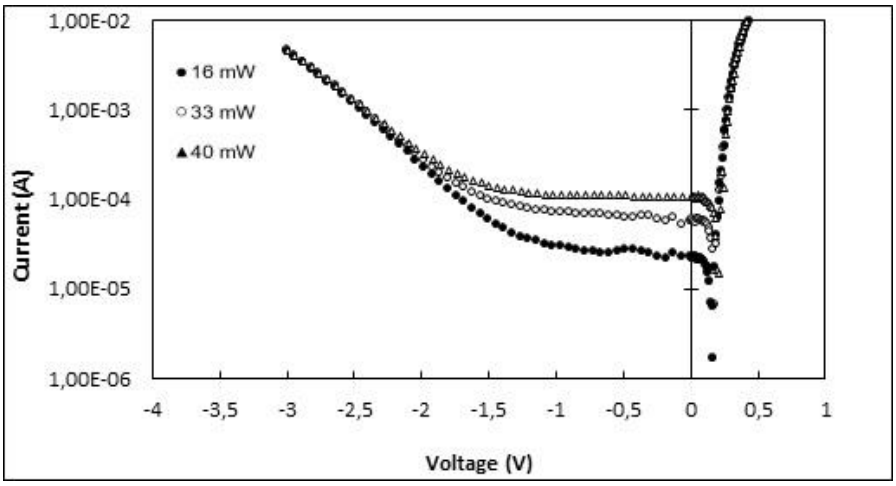

Fig 8. Room temperature current-voltage characteristics under various illumination intensities by 633 nm wavelength photons (He-Ne Laser).

Photodiodes or solar cells operate without an externally applied voltage, and the collection of carriers results from the internal field at the junction. This is referred as the fourth quadrant in As seen in Fig 8, the light on reverse *I–V* characteristic under various illumination intensities is translated upward moved in the I direction along the current axis, giving an open circuit voltage (*Voc*) along with a short-circuit current (Isc). The maximum open circuit voltage V_{oc} value for the diode under 20 mW/cm^2 illumination were found to be 0.24 V.

4. Conclusion

Ni/n-GaAs Schottky diode structures were fabricated using the electrodeposition method. Before making contacts, the wafer was chemically cleaned using RCA cleaning procedure. Electrical and optical properties were achieved at various temperatures. Barrier height of the structure was obtained from *I-V* measurements. The barrier height was obtained as 1.11 eV and the ideality factor as 1.04 respectively. Light volt-current characteristics under various illumination light intensities were investigated. Spectral photoresponse measurements of the structure are carried out at two several temperatures. The energy gap values of the GaAs semiconductor layer were obtained from both spectral distributions of sensitivity and the dependence of the root of photocurrent on photon energy. It is shown that the fabricated structure by surface polymerization technique exhibits rectification behavior that makes it a good candidate for electronic device applications.

Acknowledgment

This work was supported by Uludag University; Scientific Research Project Unit grant No. OUAP(F)-2016/11. The authors would like to thank for this support.

References

[1] S. M. Sze, Physics of Semiconductor Devices, second ed., Wiley, New York, 1981.

[2] H. Nienhaus, H. S. Bergh, A. Majumdar, W. H. Weinberg, E. W. McFarland, Phys. Rev. Lett. **82**, 446 (1999).

[3] W. Göpel, K. D. Schierbaum, in Sensors, edited by W. Göpel, J. Hesse and J. N. Zemel, Weinheim VCH, **2**, 429 (1991)

[4] M. Ahmetoglu, K. Ertürk, Temperature dependence of electrical characteristics of Cu/n-Si shottky barrier diodes formed by electrodeposition**,** Journal Of Optoelectronics and Advanced Materials Vol.10, No.2, February 2008, p. 298-301

[5] M. S. Tyagi, Introduction to Semiconductor Materials and Devices, New York, 1991.

[6] O. Güllü, M. Biber, S. Duman, A. Türüt, Appl. Surf. Sci. 253 (2007) 7246.

[7] M. K. Hudait, S. B. Kruppanidhi, Solid- State Electron., **44**, 1089 (200)

[8] T. Göksu, N. Yıldırım, H. Korkut, A. F. Özdemir, A. Türüt, A. Kökçe. Microelectronic Engineering **87**, 1781 (2010).

[9] R. F. Schmitsdorf, T. U. Kampen, W. Mönch, Surf. Sci. **324**, 249 (1995)

[10] R. T. Tung, Phys. Rev. B **45**, 13509 (1992)

[11] A.Gümüş, A. Türüt, N. Yalçın, J. Appl. Phys. 91, 245 (2002).

[12] H. Norde, *J. Appl. Phys.* 50, 5052 (1979).

[13] E. H. Rhoderick, Metal-Semiconductor Contacts, Oxford University Press, 1978, p. 121.

[14] A. Turut, M. Saglam, H. Efeoglu, N. Yalcın, M. Yıldırım, B. Abay, Physica B 205, 41 (1995)

[15] M Levinshtein, Michail Shur and S. Rumyantsev, Handbook Series on Semiconductor Parameters, Vol.1. World Scientific, 1996, p. 3.

PHOTOELECTRICAL PROPERTIES OF Ag/n-GaAs SCHOTTKY DIODES

T.Batmaz, B. Kirezli, M. C. Haciismailoglu, M. Ahmetoglu

Department of Physics, Uludağ University, 16059, Görükle, Bursa, Turkey

E-mail: tugcebatmaz@hotmail.com

Abstract

In this research, electrical and optical properties of metal-semiconductor Schottky diode were investigated. Schottky diode was fabricated by physical vacuum deposition of silver onto GaAs substrate. Ideality factor and barrier height were calculated from current-voltage (*I-V*) measurements at room temperature and found as 1.8 and 0.72 eV, respectively. It was observed that the diode showed non-ideal behavior because of serial resistance and presence of an interfacial layer. Ideality factor, barrier height and serial resistance values were also determined using Cheung's and Norde's methods and found to be in a good agreement with the values obtained from the *I-V* measurements. Light volt-current characteristics were investigated. Spectral photoresponse measurements of the structure are carried out at room temperature. Those were shown that the fabricated structure exhibited rectification behavior that makes it a good candidate for optoelectronic device applications.

1. Introduction

Semiconductors, which have great importance in today's technology, are widely used in space and military applications. Transistors, rectifying diodes and solar cells are some examples of the semiconductor devices [1].

Because of increase in global warming and environmental pollution, clean energy sources attract great attention in last researches. Solar cells are one of the most important devices, which use the solar energy in a highly effective way. Thin films are largely used in micro and optoelectronic industry and forefront of the research and development topics in recent years.

Thin films, deposited on a substrate, have much more optic and electronic properties than the substrate, which could not be used as it is. Because of these properties, thin films are used as advanced technology materials in the micro and optoelectronics.

Schottky diodes are fabricated by depositing a metal thin film on a semiconductor substrate. An interfacial layer can be formed between the metal film and the semiconductor naturally or this layer can be intentionally formed. The interfacial layer changes the electrical properties of the metal-semiconductor contact. Because of this effect, researches are focused on metal-insulator-semiconductor (MIS) structures [2]. Especially, insulator-semiconductor interface structure and current mechanism at the interface are extensively studied. Because of its high speed and low power consumption [3], GaAs has an important place for devices like diodes, transistors, solar cells, etc. [4].

In this research, photoelectrical characteristics of Ag/n-GaAs Schottky diode are investigated and barrier height, saturation current and Richardson constant of the diode are determined. The energy gap values of the GaAs semiconductor layer were obtained from both spectral distributions of sensitivity and the dependence of the root of photocurrent on photon energy.

2. Device fabrication and measurements

n-type GaAs wafer used for the fabrication of the Ag/n-GaAs structure has (100) orientation, 400 μm thickness and 508 mm diameter. Before making contacts, the wafer was chemically cleaned using RCA cleaning procedure (i.e. 10 min boiling in $H_2SO_4 + H_2O_2$ followed by a 10 min $HCl + H_2O_2 + 6H_2O$ at 60°C). It was immersed in diluted 20% HF for 60 s. The wafer was rinsed in deionized water of resistivity 18 MΩ cm with ultrasonic cleaning in each step. After that, the sample was dried in the high-purity nitrogen stream and inserted into the deposition chamber. Au (88%) and Ge (12%) were used for ohmic contact

[5,6]. The ohmic contact with a thickness of ≈1875 Å was made by evaporating 99.995% purity Au metal and germanium on the back of the surface wafer in a thermal evaporator unit at 10^{-6} Torr. Then it was annealed at 450°C for 5 min in flowing N_2 in a quartz tube furnace.

300 nm thick silver has been deposited with a thermal evaporation system in order to form the ohmic contact to the non-polished side of n-type GaAs wafer. Commercially sold 99.95% pure silver pieces were used. The wafer was placed in evaporation chamber approximately 16 cm above from evaporation source then the system was vacuumed to pressure the $1x10^{-5}$ Torr before start the evaporation of silver. The substrate was rotated at a speed of 9 rpm during the deposition and the deposition rate kept around 4 Å/s and the deposition took around 12 mins. The top ohmic contact on the Ag layer was formed by silver contact paste.

The current-voltage (I–V) measurements were performed by the use of KEITHLEY 6487 picoampere/voltage source using a temperature controlled Janis CCS-150 cryostat, which enables us to make measurements in the temperature range of 77K-380K. Photoresponse spectra of the Ag/n-GaAs structure were measured in the range of 860-1200 nm with a setup of Oriel Apex2 100 W quartz tungsten halogen lamb, Cornerstone 260 monochromator and SR830 DSP Lock-In-Amplifier at room temperature. The light-current-voltage measurements were performed by using of High Power Laser Diode with 905 nm. The results of measurements were fed via an IEEE-488 interface into a computer for storage and processing.

3. Results and Discussion

According to thermionic emission theory [7], the total current of a Schottky diode is given by

$$I = I_0 \exp\frac{qV}{nk_BT}\left[1-\exp\left(-\frac{qV}{k_BT}\right)\right] \quad (1)$$

where, q is the electron charge, V is the voltage, n is the ideality factor, k_B is the Boltzmann's constant, T is the temperature and

$$I_0 = AA^*T^2\exp\left(-\frac{q\phi_b}{k_BT}\right) \quad (2)$$

is called saturation current. The parameters A, A^* and ϕ_b are diode area, Richardson constant and barrier height, respectively. Using Eq.6 and Eq.7, the ideality factor and barrier height can be derived as

$$n = \frac{q}{k_B T} \frac{dV}{d\ln(I)} \tag{3}$$

And

$$\phi_b = \frac{k_B T}{q} \ln\left(\frac{I_0}{A A^* T^2}\right) \tag{4}$$

The measured I-V values for the Schottky diode in the temperature range of 100-360 K are plotted in Fig 1.

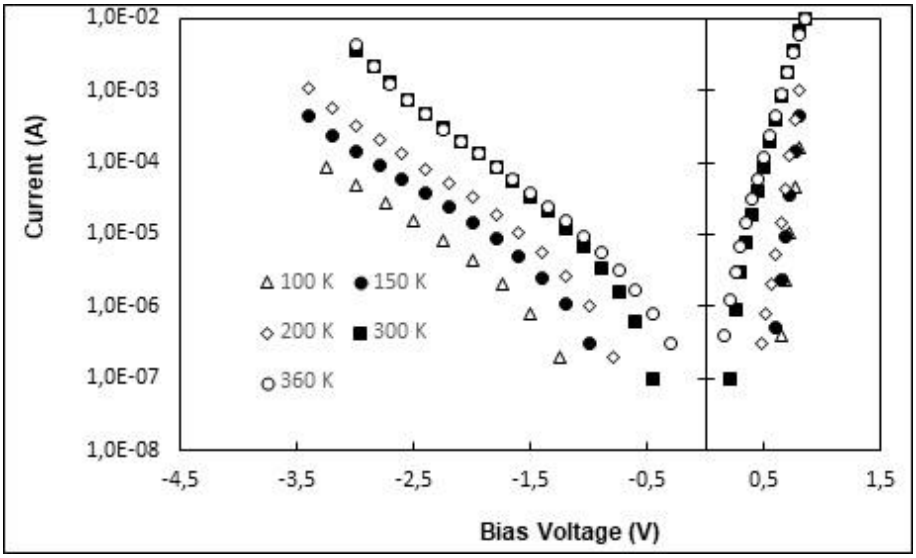

Fig 1. I-V curves of the Ag/n-GaAs Schottky diode in the temperature range of 100-360K

The ideality factor and the barrier height are obtained as 1.8 and 0.72 eV, respectively, for 300 K. The experimental I-V values are compared with the theoretical values, which are calculated from Eq.6 and it is found that these values are in good agreement with the theory up to specific forward bias.

The temperature dependence of the barrier height and the ideality factor of the Ag/n-GaAs Schottky diode is given in Fig 5. These parameters are strongly dependent to the temperature. The ideality factor is decreased from 2.36 to 1.4 and the barrier height is increased from 0.272 eV to 0.855 eV for the temperature range of 75-360 K. These calculated values are consistent with the literature [8,9]. High values of the ideality factor can be related with a natural oxide layer, inhomogeneous film thickness and serial resistance.

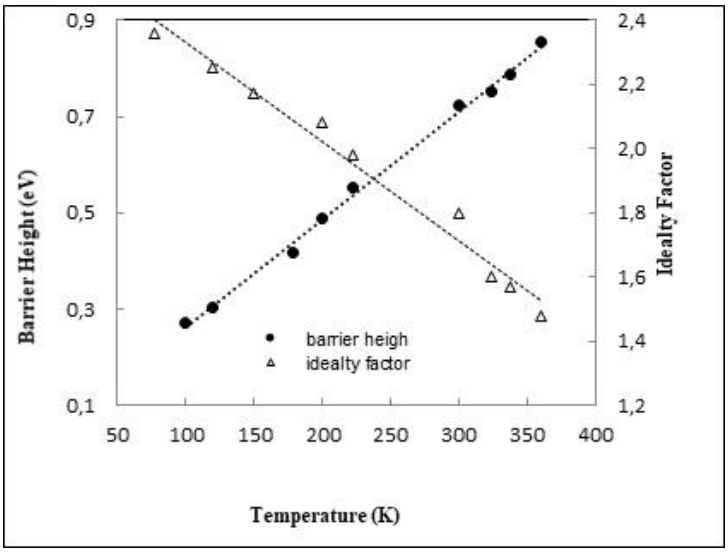

Fig 2. Temperature dependence of the barrier height and the ideality factor of the Ag/n-GaAs Schottky diode

The Richardson constant can be determined from the intersection with the *y*-axis in the $\ln(J_0/T^2)$-1000/*T* graph. By using this relation, A^* is found as 1.09×10^5 A·m^{-2}K^{-2} for the diode in Fig.3.

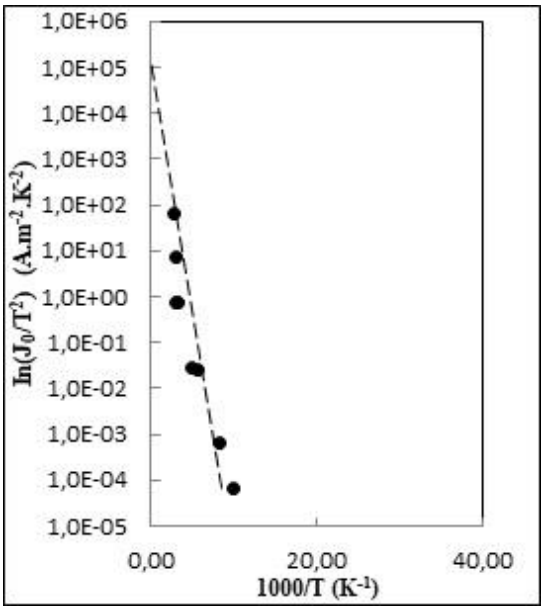

Fig 3. ln (J_0/T^2)-1000/T graph of the Ag/n-GaAs Schottky diode

The serial resistance is an important parameter for the electrical characteristics of the Schottky diodes. High serial resistance is not desired because of the negative effects on the device performance. There are several

methods in the literature to calculate the serial resistance. Another method to calculate the serial resistance is suggested by Norde [10]. According to Norde, a function $F(V)$ can be written as

$$F(V) = \frac{V}{2} - \frac{k_B T}{q} \ln\left(\frac{I}{AA^* T^2}\right) \tag{5}$$

to avoid the serial resistance problem. The minimum of $F(V)$ gives the barrier height:

$$\phi_b = F(V_0) + \frac{V_0}{2} - \frac{k_B T}{q} \tag{6}$$

where $F(V_0)$ is the minimum value of $F(V)$ at the voltage of V_0. $F(V)$ vs V plot for the Ag/n-GaAs Schottky diode is given in Fig 4. The obtained values are V_0=0.25 V, $F(V_0)$=0.78 V and ϕ_b=0.88 eV.

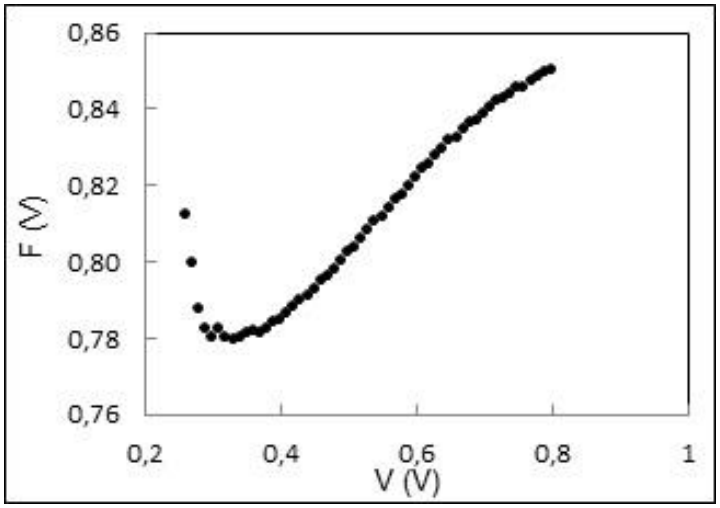

Fig 4. F (V)-V plot of the Ag/n-GaAs Schottky diode

One of the important parameters affecting the device performance is the density of the interface states which is given by [11]

$$N_{ss}(V) = \frac{1}{q}\left[\frac{\varepsilon_i}{\delta}[n(V) - 1] - \frac{\varepsilon_s}{w_D}\right] \tag{7}$$

where q is the electron charge, $n(V)$ is the ideality factor, W_D is the depletion region width, δ is the thickness of the interfacial layer, ε_i and ε_s are the dielectric coefficients of the interfacial layer and the semiconductor, respectively. For an n-type semiconductor, the energy of the

$$E_c - E_{ss} = q(f_e - V) \tag{8}$$

where E_c is the minimum of the conduction band, E_{ss} is the interface states and ϕ_e is the effective barrier height. Depending on the voltage V and the ideality factor n, the effective barrier height can be written as

$$f_e = f_{b0} + \left(1 - \frac{1}{n}\right)V \tag{9}$$

The energy distribution of N_{ss} as a function of E_c-E_{ss} for the Ag/n-GaAs Schottky diode is shown Fig 5. As seen in Fig 8, there is a decrease in the density of interface states from the bottom of the conduction band towards the midgap of GaAs. According to this result, it is confirmed that the density of interface states changes with the applied voltage and each value of the voltage corresponds to a different position in the band gap of GaAs.

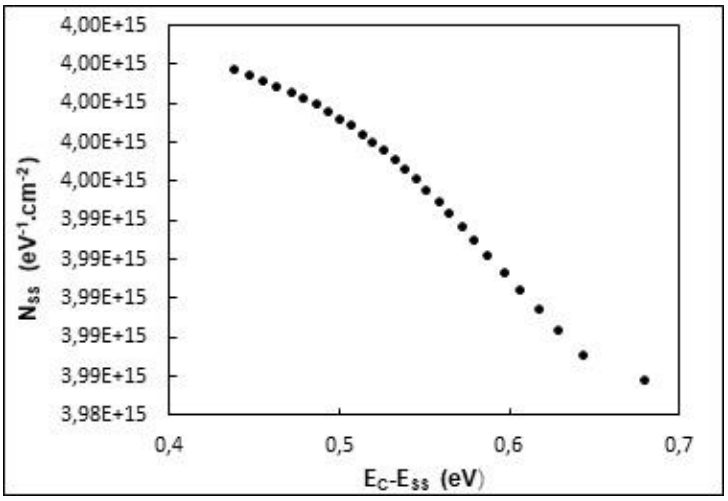

Fig 5. The distribution of the interface state density of Ag/n-GaAs Schottky diode

3.2 Optical Properties

The spectral distribution of sensitivity for an Ag/n-GaAs Schottky diode at room temperature is shown in Fig 6. The energy gap of the narrow-gap GaAs layers determined from the wavelength corresponding to a twofold decrease in sensitivity is 1.42 ± 0.02 eV at T = 300 K. This value very close to the energy gap values of the GaAs obtained from the temperature dependence of the energy gap of GaAs at room temperature [13]:

$$E_g = 1{,}519 - (5{,}405 \times 10^{-4})\frac{T^2}{T + 204}\ (eV) \qquad (10)$$

The short wavelength cut-off of the photosensitivity is due to strong absorption of the short-wavelength radiation in the Ag metal layer.

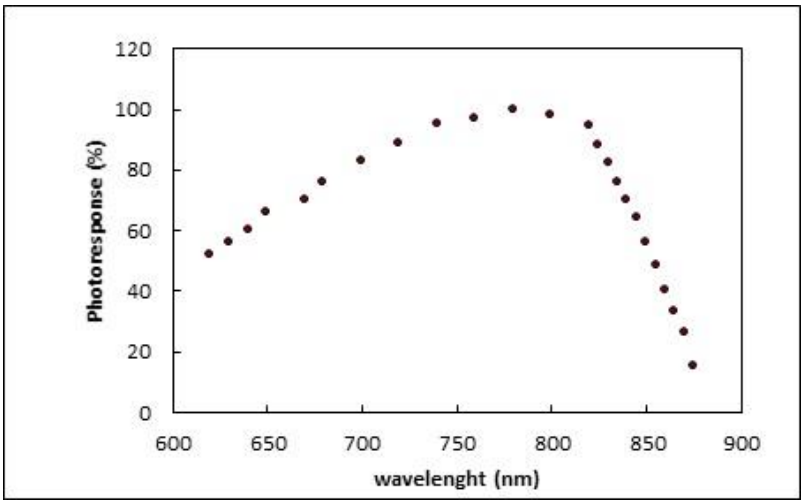

Fig 6. The spectral distribution of sensitivity for an Ag/n-GaAs Schottky diode at room temperature.

The value of band gap of GaAs can be determined from the experimental results of Fig 7 near the cutoff. The amount of the photocurrent produced during absorption of a photon depends on the excess energy produced from the difference of the photon energy hγ and the bandgap energy. Near the bandgap edge of the semiconductor, the proportionality of the photocurrent in relation to the excess energy determines the type of the bandgap as shown in the following equations for direct bandgap semiconductor

$$I \ \alpha \ (hv - E_g)^2 \qquad (11)$$

$$I^2 \ \alpha \ (hv - E_g) \qquad (12)$$

Plotting the values of the photocurrent near the cutoff of 870 nm as a function of the photon energy about the equation it is possible to determine the type of GaAs bandgap. The intercept of the line at x-axis gives the bandgap of GaAs and found to be about 1.42 eV.

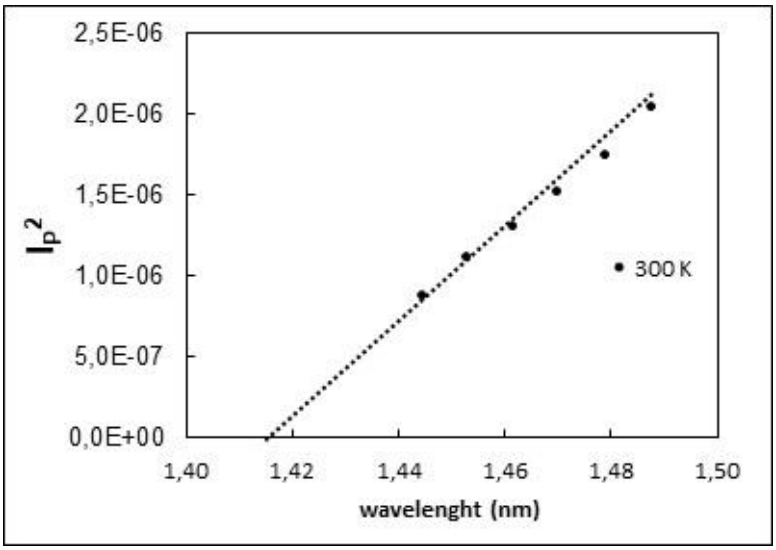

Fig 7 The plot of the root of photocurrent versus photon energy near the band edge

The typical Light I–V characteristics of the Ag/n-GaAs Schottky diodes were measured using a KEITHLEY 6487 picoampere/voltage source in the dark and with NIR illumination at 905 nm, as shown in Fig 8. The photocurrent to the dark current ratio at 0.24 V reverse bias is approximately 25. The photoresponse at zero bias voltage indicated that the Ag-GaAs Schottky junction diodes could act as a low-consumption device that is capable of detecting NIR irradiation without external power supply.

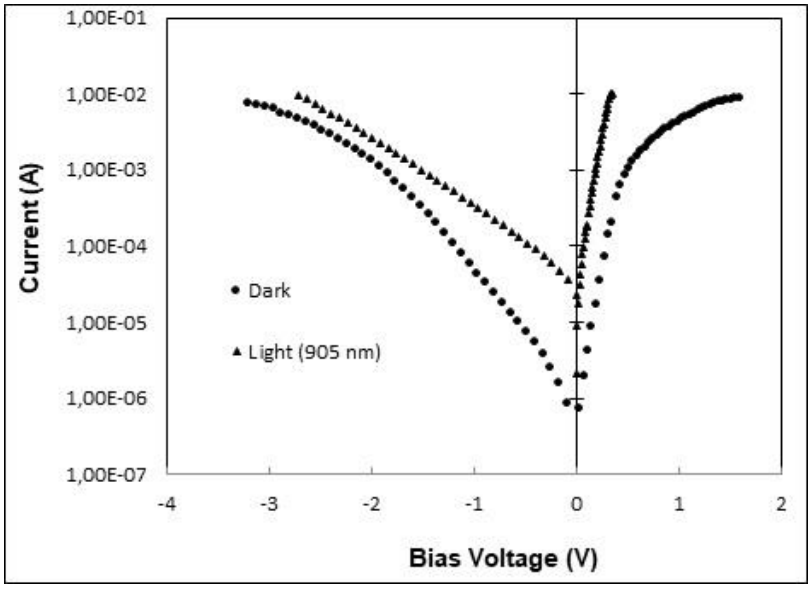

Fig 8. Typical dark and light I–V characteristics of the Ag/n-GaAs Schottky diode

4. Conclusion

The Ag/n-GaAs Schottky diode was fabricated using thermal vacuum evaporation. Electrical and optical properties of the diode were investigated. From *I-V* and *C-V* measurements, the ideality factor and the barrier height of the diode were found to be 1.8 and 0.72 eV, respectively. The ideality factor, the barrier height and the serial resistance of the diode were alternatively obtained using Cheung's and Norde's methods and compared with the other values determined from *I-V* and *C-V* measurements. It was found that there was an agreement with these values. Also, the density of the interface states was calculated from forward bias *I-V* measurements. It was seen that the density of interface states was decreased from 4.001×10^{15} $eV^{-1}cm^{-2}$ to 3.988×10^{15} $eV^{-1}cm^{-2}$ from the conduction band minimum towards the midgap of GaAs. The band gap of GaAs was found as 1.42±0.01 eV from the photoresponse spectra of the Ag/n-GaAs Schottky diode and it was consistent with the value, which was determined from the photocurrent vs. the photon energy plot. It was concluded from zero bias photoresponse that the Ag/n-GaAs Schottky diode could detect NIR irradiation without any external power supply.

Acknowledgment

This work was supported by Uludag University; Scientific Research Project Unit grant No. OUAP (F)-2016/11. The authors would like to thank for this support.

REFERENCES

[1] Sze, S. M., "Metal-Semiconductor Contacts, Physics of Semiconductors Devices 2nd ed Wiley, New York, 225 (1981)

[2] Kar, S., Panchal, K. M. Brattacharya, S., and Varma S., "On The Mechanism of Carrier Transport In Metal-Thin-Oxide-Semiconductor Diodes On Polycrystalline Silicon," IEEE Trans. On Electron. Devices, 29: 1839-1845 (1982)

[3] Wang, O.C. at all, Solid state Electronics 48, 1683-1686 (2004)

[4] Ambica, M. at all, Solid-State Electronics 49, 413-419 (2005)

[5] K.Ng. Kwok, Complete Guide to Semiconductor Devices, McGraw-Hill, New York (1995)

[6] A. Kırsoy, M. Ahmetoglu (Afrailov), A. Asimov, B. Kucur, Acta Phys. Pol. A 128, B-170 (2015)

[7] E. H. Rhoderick, R.H. Williams, Metal-Semiconductor Contacts, Clarendon Press, Oxford 1988

[8] S. Karatas, S. Altındal, A. Turut, M. Cakar, "Electrical transport characteristics of Sn/p-Si Schottky contacts revealed from I–V–T and C–V–T measurements", Physica B 392 43–50 (2007)

[9] A. Asimov, M. Ahmetoğlu, B. Kucur, I. Gucuyener, "Electrical characteristics of Al/n-type GaAs Schottky barrier diodes at room temperature," Optoelectronics and Advanced Materials-Rapid Communications, 8, 3-4, 306-310 (1914)

[10] H. Norde, J. Appl. Phys. 50, 5052 (1979)

[11] H. C. Card, E.H. Rhoderick, J. Phys. D Appl. Phys. 4, 1589 (1971)

[12] M. K. Hudait, S.B. Kruppanidhi, Solid State Electron. 44, 1089 (2000)

[13] M. Levinshtein, Michail Shur and S. Rumyantsev, Handbook Series on Semiconductor Parameters, Vol.1. World Scientific, 1996

SYNTHESES, STRUCTURE, NEAR-INFRARED AND VISIBLE LUMINESCENCE OF Nd (III) - COORDINATION POLYMER

H. Kara[1,2], M. B. Coban[1,3], and Y. Acar[1]

[1]*Department of Physics, Faculty of Art and Science, Balikesir University, Balikesir, Turkey*

[2]*Department of Physics, Faculty of Science, Mugla Sitki Kocman University, Mugla, Turkey*

[3]*Center of Science and Technology Application and Research, Balikesir University, Balikesir, Turkey*

E-mail: hkara@balikesir.edu.tr

Abstract

In this work, three dimensional (3D) Nd (III) coordination polymer, $\{[Nd(ssa)(H_2O)_2].(H_2O)\}_n$ (ssa= 5-sulfosalicylic acid has been synthesized with hydrothermally and characterized by single crystal X-ray diffraction, UV-Vis absorption spectra, UV-Vis and NIR photoluminescence. The structural analyses show that the compound crystallizes in the monoclinic $P2_1/n$ space group. The asymmetrical unit of this compound contains one ssa ligand, one Nd (III) ion, two coordinated water molecules, and one solvent water molecule. Moreover, the solid-state photoluminescent properties indicate that the compound gives a very strong and typical emission peak of Nd (III) ion in the UV-Vis and NIR region. As a result, this material can potentially be candidates for laser systems.

Keywords: Nd (III) coordination polymer, Crystal structure, Solid-state photoluminescence properties

1. INTRODUCTION

Nowadays, the design and construction of Lanthanide coordination polymers (LnCPs) have become a very attractive research area. These materials are potentially applicable to optical displays, sensor and bio-imaging since their excellent spectroscopic features such as long life, large Stokes shift, high photoluminescent yield, as well as characteristic narrow lines such as emission peaks ranging from UV-Vis to NIR region [1]. Meanwhile, they often exhibit unusual coordination modes and strongly optical properties arising from 4f electrons. For instance, the NIR luminescence of Nd-containing polymers has been recognized as the most popular infrared luminescence materials for application in laser systems [2]. In the built of coordination polymers, the selection of a suitable ligand containing certain properties, such as flexibility and multiple binding modes, is very important.

For the following reasons, 5-sulfosalicylic acid (ssa) ligand was selected in this study; (a) this ligand has three coordination groups: –COOH, –SO_3H, and –OH in which the oxygen atoms can be as coordinated by Nd(III) ions behaved as hard acids, (b) this ligand has a high configuration effect, since the π-system and donor oxygen atoms play a role in hydrogen bonding, and the aromatic ring can act as a sensitizer for Nd(III) ions luminescence by transferring energy from a ligand-centered excited state (antenna effect) [3]. (c) this ligand has an asymmetric geometry, which can lead to compounds with common crystal structures, and only such compounds can act as an applicant for second order NLO materials [4].

Lately, our research group and others have focused to rationally design new lanthanide coordination polymers because of their intriguing variety of architectures, topologies and potential applications [1,3,5,6]. In view of the recent important progress on the NIR luminescence of the Nd(III) coordination polymers, in this work, 3D Nd(III) coordination polymer, $\{[Nd(ssa)(H_2O)_2].(H_2O)\}_n$ has been synthesized and characterized by single crystal X-ray diffraction, UV-Vis absorption spectra, UV-Vis and NIR photoluminescence.

2. MATERIAL AND METHODS

2.1. Materials and measurements

All chemicals were obtained from commercial sources and used without further purification. The UV spectrum was measured with Ocean Optics Maya 2000Pro Spectrophotometer. Luminescence measurements were performed using ANDOR SR500i-BL Spectrophotometer. The Nd:YLF laser (λ=349 nm) was used and 1.3 mJ and 5 ns pulse width energy per pulse were applied to the laser source. Single

crystal X-ray diffraction data were collected by an Xcalibur, Eos diffractometer with graphite monochromated Mo-Kα radiation (λ = 0.71073 Å) at 293 K. The crystal structure was solved by direct methods and the full matrix in F^2 was refined using the least squares. Non-hydrogen atoms were anisotropically refined and hydrogen atom positions were fixed using idealized geometry. ‡ CCDC 1874957 contains the crystallographic data for the structural analyses of Nd (III) coordination polymer. These data can be obtained free of charge via www.ccdc.cam.ac.uk.

2.2. Synthesis of Nd (III) coordination polymer

A mixture of $NdCl_3.6(H_2O)$ (0.179 g, 0.5 mmol) and 5-sulfosalicylic acid (0.127 g, 0.5 mmol) in water (15 ml) were sealed in a 23 ml Teflon-lined stainless steel autoclave. The autoclave was heated at 120 °C for 5 days under autogenous pressure and then cooled to room temperature at a rate of 5 °C/h under ambient conditions. The purple crystals were obtained and washed with cold water.

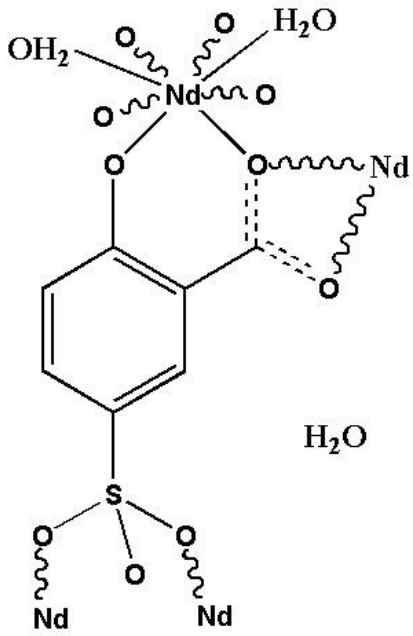

Scheme 1: Schematic representation of Nd (III) coordination polymer.

3. RESULTS AND DISCUSSION

3.1. Single crystal structure of Nd (III) coordination polymer

The structural analyses show that the compound crystallizes in the monoclinic $P2_1/n$ space group. The asymmetrical unit of this coordination polymer contains one ssa ligand, one Nd (III) ion, two coordinated water molecules, and one solvent water molecule. The Nd(III) ion have eight coordination, in

which two oxygen atoms from the sulfonate group, one oxygen atom from the benzene-hydroxyl oxygen group, three oxygen atoms from the carboxylates groups, and two oxygen atom from coordinated water molecules (Figure 1). The Nd-O distances range from 2.349(5) to 2.573(5) Å, and O-Nd-O bond angles range from 71.82(16) to 143.11(15)°, which are comparable with similar structures [5,7].

The ssa ligand acts as a bidentate bridging mode of the sulfonate, bidentate chelating bridging mode of the carboxylate and monodentate mode of the hydroxyl group to bridge linking four Nd (III) (Scheme 1) ions ultimately causing the 2D layer structure (Figure 2a). In addition, 2D layers are connected by O-H…O hydrogen bonding network which results to 3D structures (Figure 2b).

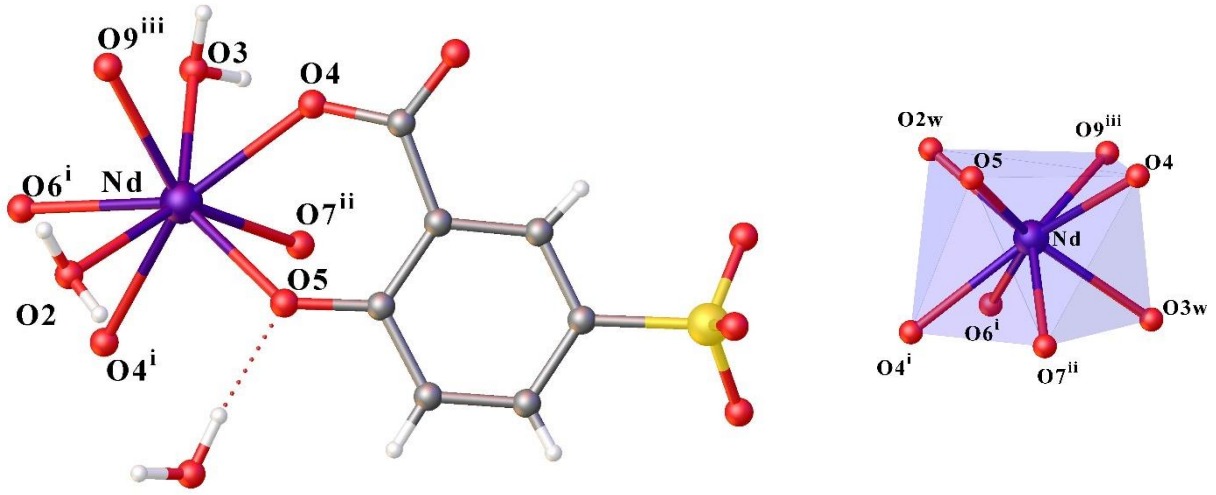

Figure 1. (a) View of the asymmetric unit of the Nd (III) coordination polymer (b) The coordination of the Nd^{III} ion.

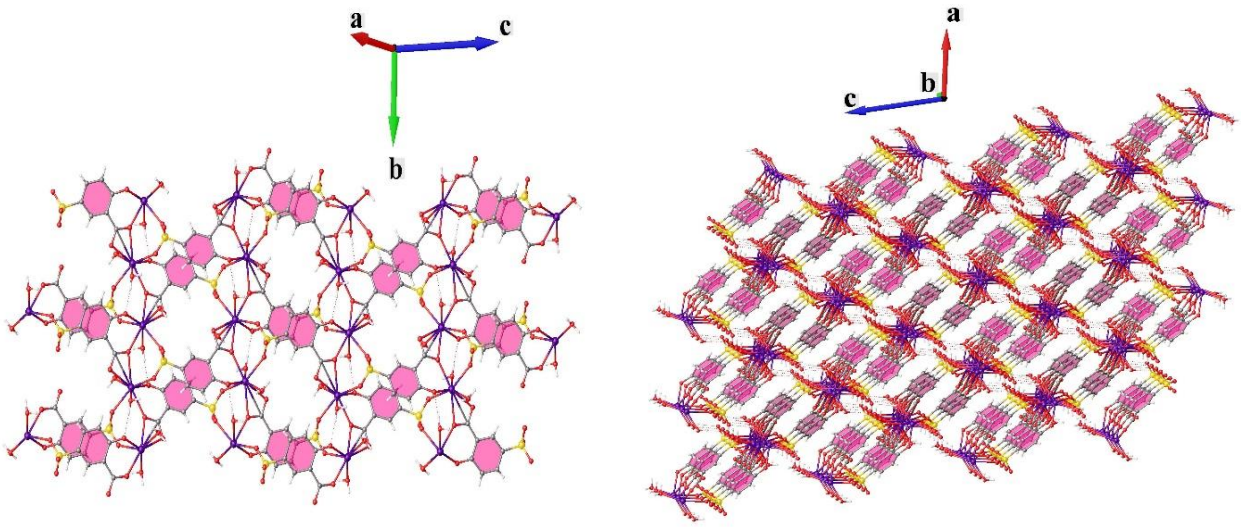

(a) **(b)**

Figure 2. (a) 2D structures for Nd (III) coordination polymer (b) Hydrogen bonded 3D structures for Nd(III) coordination polymer.

Table 1: Crystal data and structure refinement for Nd (III) coordination polymer.

Chemical Formula	$C_7H_9NdO_9S$
Formula weight (g mol^{-1})	413.44
Crystal system	Monoclinic
Space group	$P2_1/n$
Unit cell dimensions	a=8.8733(4), b=8.9365(5), c=14.3844(6) Å β=100.784(4)°
V / $Å^3$	1120.49(9)
Z	4
ρ_{calc} / g cm^{-3}	2.451
μ/mm^{-1}	4.859
Temperature (K)	292
Collected, Independent reflections	3738, 2260, [R_{int}=0.033]
Goodness–of–fit on F^2	1.013
R indices [$I>2\sigma(I)$]	R_1 = 0.0393, wR_2 = 0.0874

Table 2: Selected bond distance (Å) and bond angles (°) for Nd (III) coordination polymer.

Nd1 – O_{CO}	2.349(5)	Nd1 – O_{SO3}	2.409(5) – 2.435(4)
Nd1 – O_{CO2}	2.427(5) – 2.573(5)	Nd1 – O_w	2.448(4) – 2.463(4)
O_{CO} – Nd1 – O_{CO2}	71.82(2) – 139.52(2)	O_{CO2} – Nd1 – O_{SO3}	73.41(2) – 130.34(2)
O_{CO} – Nd1 – O_{SO3}	79.16(2) – 118.15(2)	O_{CO2} – Nd1 – O_w	73.88(2) – 117.88(2)
O_{CO} – Nd1 – O_w	78.36(2) – 138.54(2)	O_{SO3} – Nd1 – O_{SO3}	143.11(2)
O_{CO2} – Nd1 – O_{CO2}	148.01(2)	O_{SO3} – Nd1 – O_w	70.80(2) – 141.82(2)
		O_w – Nd1 – O_w	141.61(2)

3.2. Photophysical properties of Nd (III) coordination polymer

For the sake of more broadly exploring the photophysical properties, the solid-state UV (Fig. 3) and the solid-state photoluminescent (Fig.4 and 5) spectrums of the free ligand (ssa) and Nd (III) coordination polymer were carried out by using the powder sample under room temperature.

As seen the UV spectrum in Fig. 3, the free ligand (ssa) showed two maximum absorptions at 306 and 400 nm, which may be assigned to π-π* transition. Whereas, the Nd (III) complex exhibited two absorptions at 298 and 439 nm, which are shifted according to the free ligand (ssa).

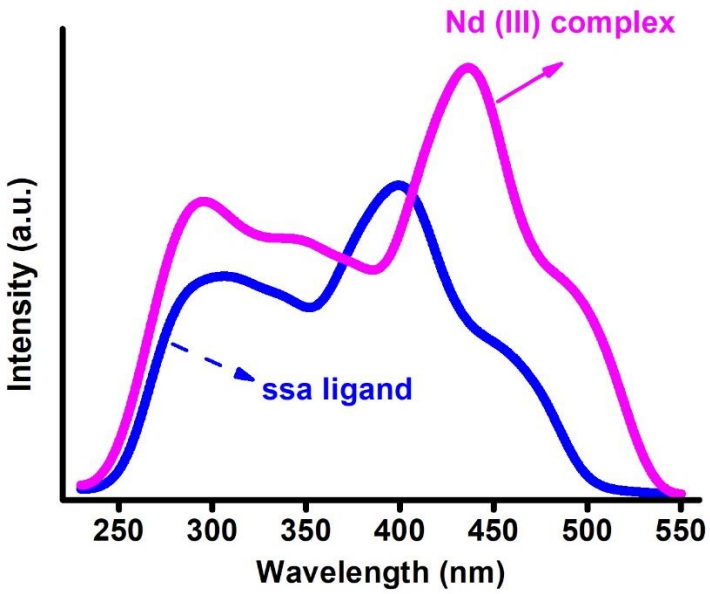

Figure 3. The UV absorption spectrum of the free ligand (ssa) and Nd (III) coordination polymer.

As shown the photoluminescent spectrum in Fig. 4, the free ligand (ssa) displayed a maximum emission at 465 nm (λ_{ex} = 349 nm). The emission of the ligand can be attributed to the n $\rightarrow\pi^*$ and charge transfer transitions of the carbonyl groups [8], which is similar to our previous report [9,10]. In the emission spectra of the Nd (III) coordination polymer, a broad emission band is observed at 418 nm (λ_{ex}=349 nm) in the UV-Vis-region (Fig. 5a). This broad band is probably originated from π-electron transitions within coordinated ligand (ssa) connected to the polymeric structure. In addition, Nd (III) coordination polymer showed the sharp and narrow photoluminescence characteristic emissions in the NIR region with a maximum at 866, 1047 and 1318 nm upon excitation at 349 nm as shown in Fig. 5b. These emission peaks are assigned to the transitions of $^4F_{3/2} \rightarrow {}^4I_j$ (j = 9/2, 11/2 and 13/2) of Nd(III) ion [7]. The second peak (λ_{max} = 1047 nm) is potentially applicable to laser emission and in vivo detection [11].

The mechanism of energy transfer from ligand to the metal ion has been extensively studied to evaluate the luminescence of Ln complex [12]. The luminescence studies mentioned above have shown that the ssa ligand can strongly sensitize the luminescence of Nd (III) ions by UV radiation. Therefore, the ssa ligand has the appropriate energy level to act as an effective sensitizer to the Nd^{III}. The results were also illustrated in Figure 6.

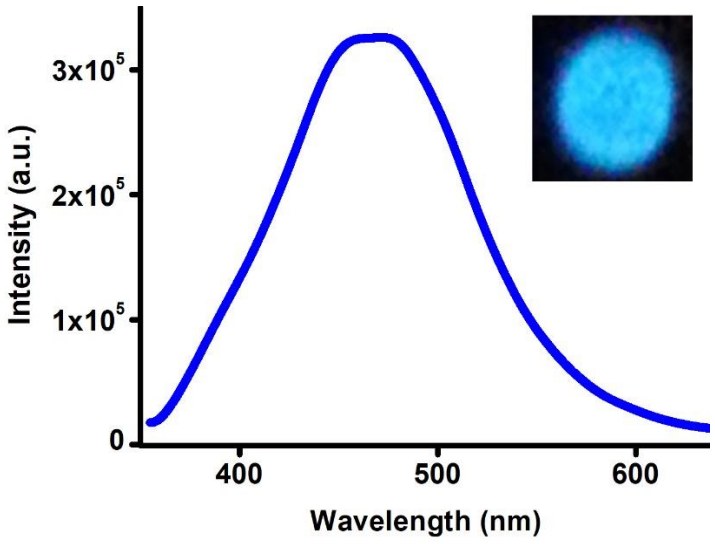

Figure 4. The solid-state photoluminescent spectrum of the free ligand (ssa) (inset photo is a photoluminescent image).

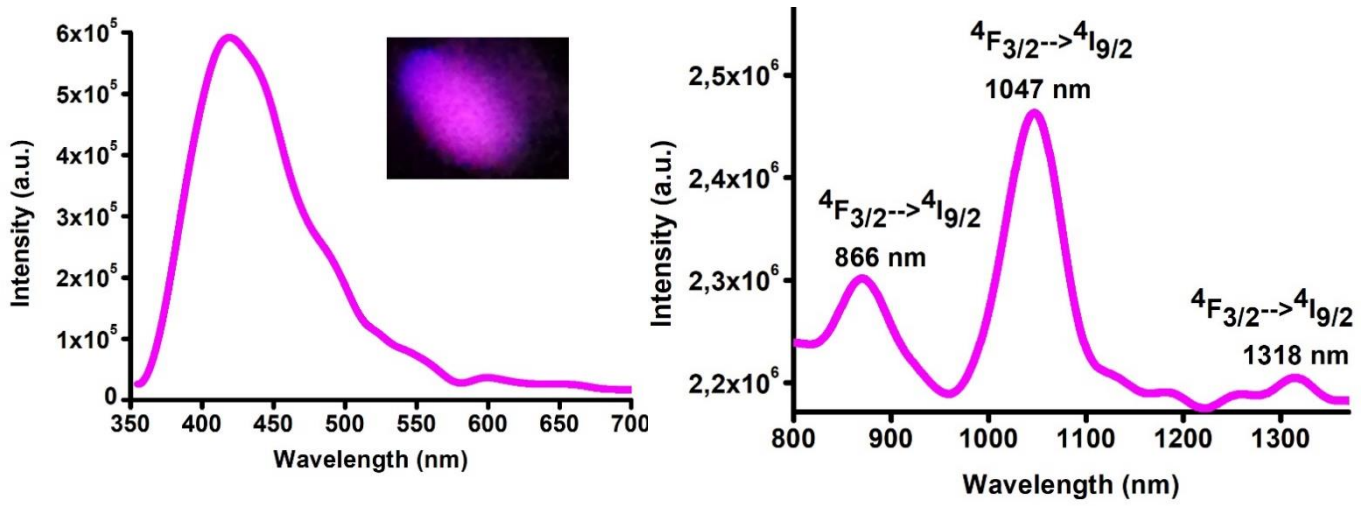

(a) **(b)**

Figure 5. The solid-state photoluminescent spectrums of the Nd (III) coordination polymer (a) in the Vis-region (inset: Upper-right photo is a photoluminescent image). (b) in the NIR region.

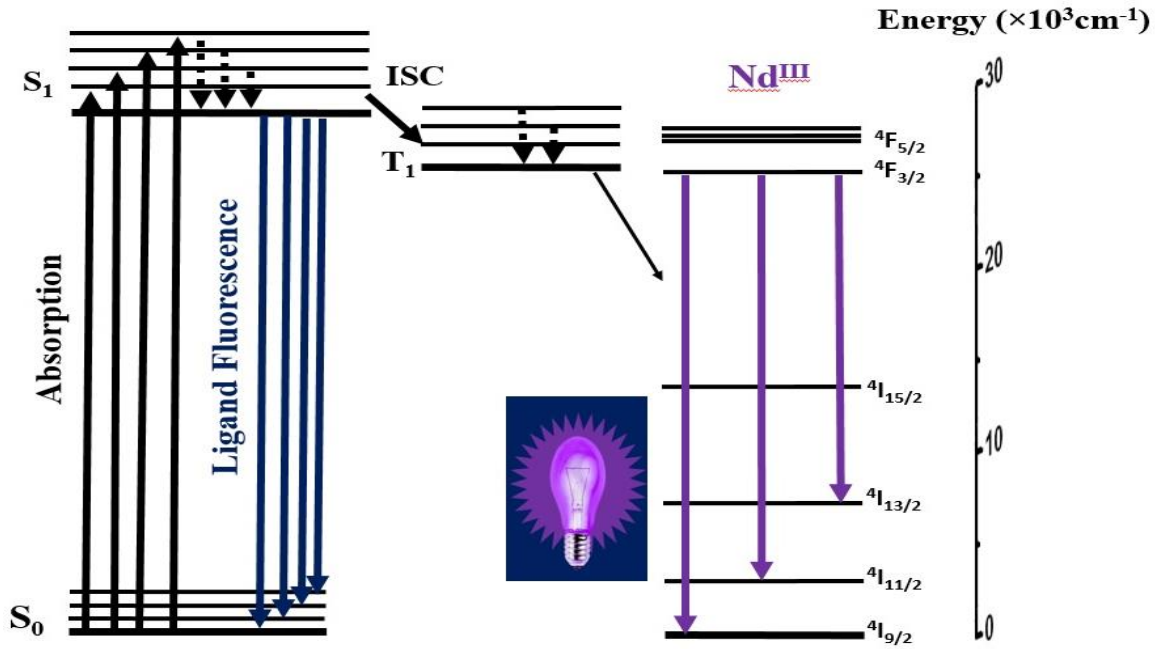

Figure 6. Schematic diagram for the sensitization mechanism of the Nd (III) ion by ssa ligand

4. CONCLUSION

In summary, we have successfully synthesized Nd (III) coordination polymer from the reaction mixture of $NdCl_3$6 (H_2O) and 5-sulfosalicylic acid via hydrothermal conditions and structurally characterized. The X-ray results showed that 5-sulfosalicylic acid ligand coordinated to the Nd (III) center, giving an eight coordination. In addition, the Nd (III) coordination polymer exhibits good photoluminescence emission in the solid state in the NIR region. As a result, this material can potentially be candidates for laser systems.

ACKNOWLEDGMENTS

This work was supported by the Scientific Project Unit of Balikesir University under project number BAP-2017/200. The authors acknowledge to Dokuz Eylul University for the use of X-Ray diffractometer (Research grant No. 2010.KB.FEN.13) and Balikesir University, Science and Technology Application and Research Center (BUBTAM), for the use of the photoluminescence spectrometer.

REFERENCES

[1] Erkarslan, U., Donmez, A., Kara, H., Aygun, M., Coban, M. B., Synthesis, Structure and Photoluminescence Performance of a New Er3+-Cluster-Based 2D Coordination Polymer, Journal of Cluster Science, 29, 1177–1183, 2018.

[2] Rogalski, A., Chrzanowski, K., Infrared devices and techniques, Opto-Electronics Reviev, 10, 111–136, 2002.

[3] Coban, M. B., Amjad, A., Aygun, M., Kara, H., Sensitization of HoIII and SmIII luminescence by efficient energy transfer from antenna ligands: Magnetic, visible and NIR photoluminescence properties of GdIII, HoIII and SmIII coordination polymers, Inorganica Chimia Acta, 455, 25–33, 2017.

[4] Chakrabarty, R., Dutta, A., Roy, S., Das, G., Ledoux-Rak, I., Mondal, P., Prasad, S. K., Rao, D. S. S., Bhattacharjee, C. R., Multifunctional Lanthanide Complexes: Mesomorphism, Photoluminescence and Second Order NLO Property, ChemistrySelect, 3, 8245–8251, 2018.

[5] Li, X., Lu, Y., Bing, Y., Zha, M. Q., Synthesis, photoluminescent, and magnetic properties of two lanthanide sulfosalicylate complexes, Synthesis and Reactivity in Inorganic Metal-Organic and Nano-Metal Chemistry, 42, 698–704, 2012.

[6] Zhang, H. Bin, Tian, C. Bin, Wu, S. T., Lin, J. Di, Li, Z. H., Du, S. W., Synthesis, structures and physical properties of new 3D lanthanide coordination polymers constructed from 1,2,4,5-benzenetetracarboxylic acid, Journal of Molecular Structure, 985, 355–360, 2011.

[7] Wang, Y. P., Li, X. Y., Li, H. H. H., Zhang, H. Z., Sun, H. Y., Guo, Q., Li, H. H. H., Niu, Z., A novel 3D Nd(III) metal-organic frameworks based on furan-2,5-dicarboxylic acid exhibits new topology and rare near-infrared luminescence property, Inorganic Chemistry Communications, 70, 27–30, 2016.

[8] Ay, B., Yildiz, E., Kani, İ., Semiconducting lanthanide polymers of pyridine-2,6-dicarboxylate: Hydrothermal synthesis, structural characterization, electrical conductivity and luminescence properties, Polyhedron, 142, 1–8, 2018.

[9] Coban, M. B., Kocak, C., Kara, H., Aygun, M., Amjad, A., Magnetic properties and sensitized visible and NIR luminescence of Dy^{III} and Eu^{III} coordination polymers by energy transfer antenna ligands, Molecular Crystals and Liquid Crystals, 648, 202–215, 2017.

[10] Oylumluoglu, G., Coban, M. B., Kocak, C., Aygun, M., Kara, H., 2-and 1-D coordination polymers of Dy(III) and Ho(III) with near infrared and visible luminescence by efficient charge-transfer antenna ligand, Journal of Molecular Structure, 1146, 356–364, 2017.

[11] Bünzli, J. C. G., Eliseeva, S. V., Lanthanide NIR luminescence for telecommunications, bioanalyses and solar energy conversion, Journal of Rare Earths, 28, 824–842, 2010.

[12] Song, X. Q., Zhang, M., Wang, C. yun, Shamshooma, A. A. A., Meng, H. H., Xi, W., Mixed lanthanide coordination polymers for temperature sensing and enhanced Nd^{III} NIR luminescence, Journal of Luminescence, 201, 410–418, 2018.

CRYSTAL STRUCTURE AND RED-PHOTOLUMINESCENCE BEHAVIOUR OF Eu (III) BASED METAL-ORGANIK FRAMEWORK

M.B. Coban[1,2], H. Kara[2,3], and Y. Acar[2]

[1]*Center of Science and Technology Application and Research,Balikesir University, Balikesir, Turkey*

[2]*Department of Physics, Faculty of Science and Art, Balikesir University, Balikesir, Turkey*

[3] *Department of Physics, Faculty of Science, Mugla Sitki Kocman University, Mugla, Turkey*

E-mail: burakcoban@balikesir.edu.tr

Abstract

The metal-organic frameworks (MOFs), have attracted interest in their excellent surface structures and potential applications in different fields such as gas adsorption, molecular recognition, separation, dye enrichment, catalysis, chemical detection and so on. In particular, great research has been carried out on the optical properties of lanthanide metal-organic frames (Ln-MOFs) due to their large Stokes shifts, high color purity and the long lifetime resulting mainly from f-f transitions. In addition, the Ln^{III} compounds show outstanding luminescent properties emitted in the Vis and NIR region of the spectrum, indicating that this compound has potential application for OLEDs. In this work, a new 2D Eu(III)-MOFs, $\{[Eu(btb)(H_2O)_2].(DMF)\}_n$ (**1**) [H_3btb= 1,3,5-Tris(4-carboxyphenyl)benzene] has been synthesized by solvothermal methods and characterized using single crystal and powder crystal X-ray diffraction, solid-state UV-Vis and photoluminescence spectroscopy.

Keywords: Eu-MOF, Crystal structure, Solid-State luminescence

1. INTRODUCTION

Nowadays, the preparation and structural elucidation of MOFs have taken attention since these materials can potentially be used in gas storage, separation, catalysis, optical, ion-exchange and molecular recognition [1]. Lanthanide-based metal-organic frames (Ln-MOFs) have increased interest among the various MOFs that combine the advantages of MOFs and the internal electronic properties of lanthanides such as a wide emission range, large Stokes shift and high quantum yields when sensitized by efficient "antenna effects" of ligand [2].

Furthermore, lanthanide ions are an important part of the supramolecular structure leading to a number of topological structures and their optical and electronic properties, thanks to the electronic level of 4^{fn}, the large coordination environment, and the variable coordination nodes. In this sense, Eu^{III}-MOFs has unique photoluminescent properties, such as long luminescence lifetime and sharp emission bands. Eu^{III}-MOFs have been used in luminescence materials, such as luminescent probes for structural analysis of biological systems. In addition, under UV light, Eu^{III} compounds can emit strong red emission from Eu^{III} ion, which can be more easily detected with the naked eye [3].

In this study, we chose H_3btb = 1,3,5-Tris(4-carboxyphenyl)benzene ligand for coordination to the Eu^{III} ion, because it has good chemical versatility and multi-binding capabilities which produce multidimensional networks, including 2D or 3D structures [4,5].

We describe here the synthesis, crystal structure, solid-state UV-Vis and photoluminescence spectroscopic properties of 2D Eu(III)-MOFs, $\{[Eu(btb)(H_2O)_2].(DMF)\}_n$ (**1**) [H3btb= 1,3,5-Tris(4-carboxyphenyl)benzene].

2. MATERIAL AND METHODS

2.1. General Methods and Measurements

All chemicals were purchased from Sigma&Aldrich. Powder X-ray diffraction measurements were carried out with a Bruker D8 diffractometer ($\lambda_{Cu\text{-}K\alpha}$ = 1.5418 Å). FT-IR spectroscopy measurements were performed using a Perkin-Elmer Spectrophotometer. UV absorption spectrums were measured with Ocean Optics Maya 2000Pro. The luminescence properties were recorded using powder samples with ANDOR SR500i-BL Spectrophotometer. Single crystal X-ray diffraction data were collected with an Xcalibur diffractometer ($\lambda_{Mo\text{-}K\alpha}$ = 0.71073 Å) at 293 K. The crystal structure was solved and refined using the OLEX2 program. The hydrogen atom positions were fixed using idealized geometry. Non-hydrogen atoms were

refined anisotropically. The electron density of the DMF molecule was removed by the MASK routine in OLEX2. ‡ CCDC 1875059 contains the crystallographic data for the structural analyses of compound **1**. These data can be obtained free of charge via www.ccdc.cam.ac.uk.

2.2. Synthesis

The solvothermal reaction of $EuCl_3.6(H2O)$ (0.0366 g, 0.1 mmol) and H_3btb (0.0438 g, 0.1mmol) in DMF, (10 ml) and H_2O (5 ml) were mixed and put in a 45 ml autoclave. The autoclave was heated under pressure at 120 °C for 5 days and then cooled to the room temperature. The colorless crystals were found for x-ray measurement.

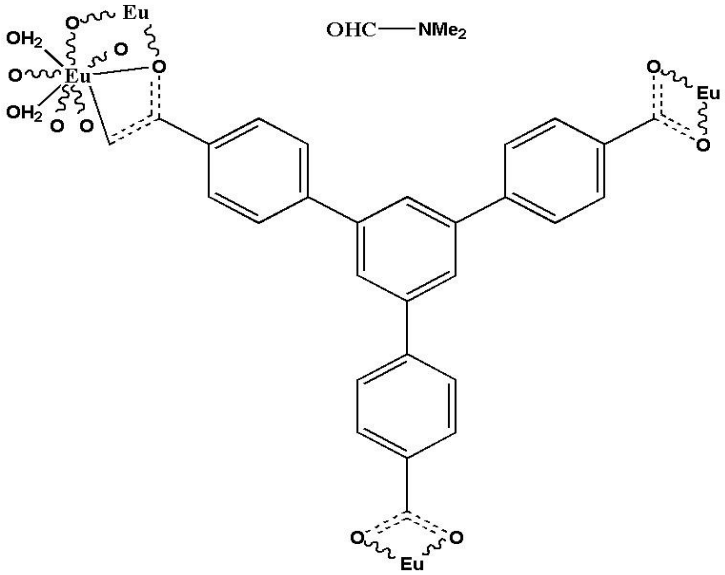

Scheme 1: Schematic illustration of the polymeric compound **1**.

3. RESULTS AND DISCUSSION

3.1. Crystal Structure

Compound **1** crystallizes in triclinic space group, P -1 and its asymmetric unit consists of one Eu^{III} ion, one H_3btb ligand, two coordinated water molecules and one lattice DMF molecule (Fig.1a). The H_3btb ligand adopts $\eta^1:\eta^2:\eta^1:\eta^1:\eta^1:\eta^1:\mu_4$ mode linking four Eu^{III} ions in **1** (Scheme 1). Eu^{III} atom is surrounded by four H_3btb ligands. Eu^{III} atom has nine coordination which is completed by seven oxygen atoms from H_3btb

ligands and two oxygen atoms from coordinated water molecules (Fig. 1b). Bond lengths and angles of the compound **1** can be compared to similar structures [6,7].

In addition, the Eu^{III} atoms are bridged with btb ligand in dimeric form, resulting in the 2D layer structure, which is consist of hexagonal channel connection modes (Fig. 2a). Besides, this structure is further linked by a btb^{3-} ligand which results in 3D structures exhibiting 1D open channels (Fig. 2b).

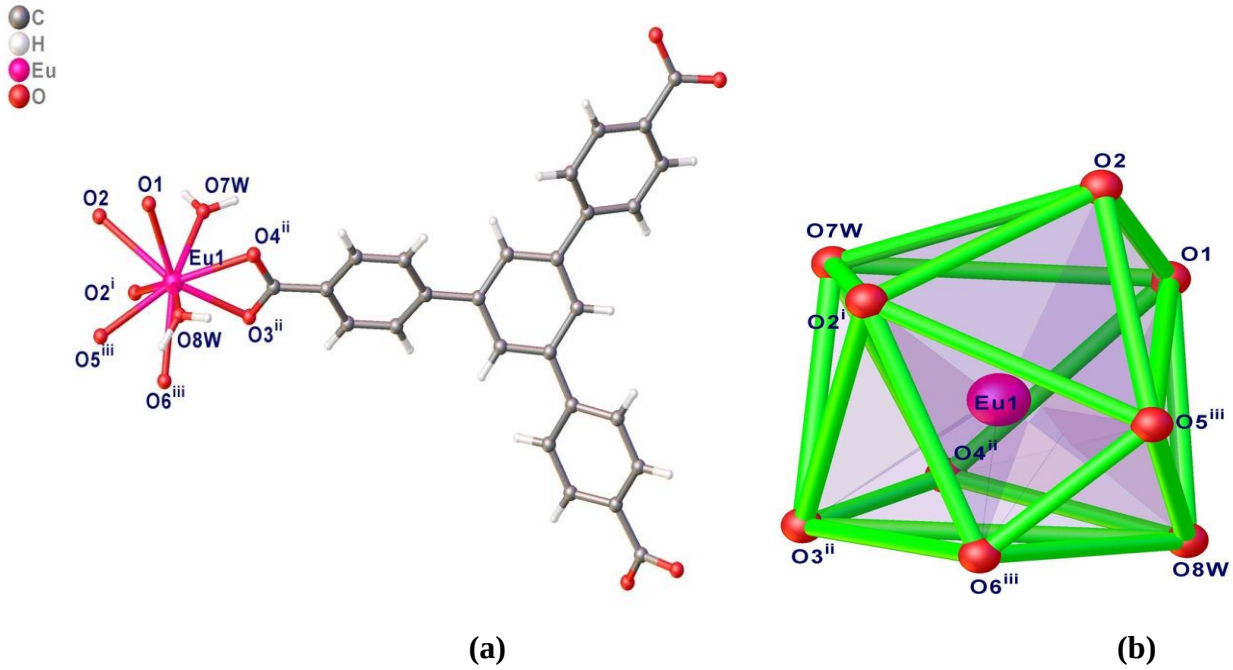

(a) **(b)**

Figure 1. (a) View of the molecular structure of compound **1**. Lattice DMF molecule are omitted for clarity. (i= 1-x,-1-y,-z; ii= x,-1+y,-1+z; iii= -1+x, y,-1+z;) (b) Coordination of Eu(III) atom.

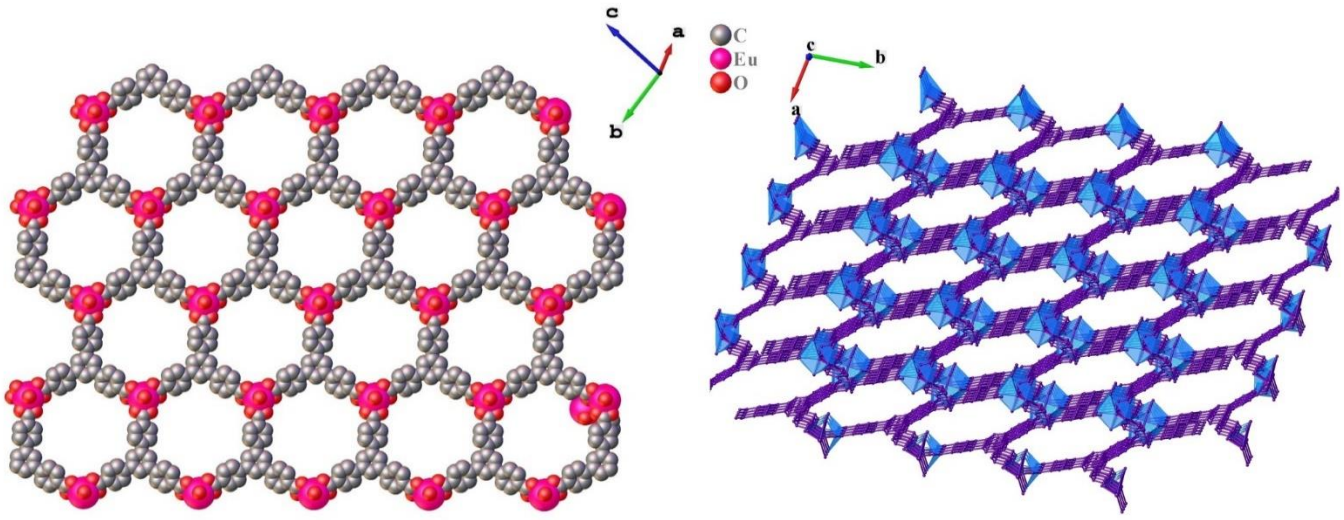

(a) **(b)**

Figure 2. (a) The illustration of the layer structure, which combined with two 1D hexagonal channel connection modes forming from stacking of 2D bilayer structure. **(b)** 3D stacking structure of **1** (color online).

Table 1: Single crystal data and structure refinement information

Chemical Formula	$C_{30}H_{26}EuNO_9$
Formula weight (g mol^{-1})	696.48
Crystal system	Triclinic
Space group	P -1
Unit cell dimensions	a=8.9942(4), b=13.3132(7), c=15.2289(7)Å α=104.451(4)° β=95.009(4)° γ=99.902(4)°
V / Å^3	1723.25(15)
Z	2
ρ_{calc} / g cm^{-3}	1.342
μ/mm^{-1}	1.865
Temperature (K)	150
Collected, Independent reflections	9684,6056, [R_{int}=0.043]
Goodness–of–fit on F^2	0.974
R indices [$I>2\sigma(I)$]	R_1 = 0.0457, wR_2 = 0.0911

Table 2: Selected bond distance (Å) and bond angles (°)

Eu1 – O_{CO2}	2.400(4) – 2.645(3)	Eu1 – O_w	2.401(3) – 2.426(4)
Eu1 – $Eu1^i$	4.2566(6)		
O_{CO2} – Eu1 – O_{CO2}	50.95(11) – 150.34(12)	O_{CO2} – Eu1 – O_w	72.38(13) – 146.27(14)
O_w – Eu1 – O_w	141.31(16)		

Table 3: Hydrogen bond geometry (Å, °)

D – H···A	**D – H**	**H···A**	**D···A**	**D – H···A**
O7 – H7A$_W$···O9^{iv}	0.95	1.81	2.749(8)	168
O7 – H7B$_W$···O5^{v}	0.96	1.76	2.659(6)	155
O8 – H8B$_W$···O9^{iii}	0.96	1.91	2.873(8)	174
CgI···CgJ	**CgI···CgJ**	**CgI_Perp**	**CgJ_Perp**	
Cg1···Cg2^{v}	4.457(3)	2.8126(19)	3.326(2)	
Cg2···Cg3^{vi}	3.897(3)	-3.763(2)	-2.989(2)	
Cg2···Cg4^{v}	4.500(3)	2.075(2)	4.237(2)	

Symmetry codes: i= 1-x,1-y,-z; ii +x,-1+y,-1+z; iii= -1+x,+y,-1+z; iv: x,y,-1+z; v: 2-x,1-y,1-z; vi: 1-x,1-y,1-z

CgI is the plane number I, CgI···CgJ is the distance between ring centroids, CgI Perp is the perpendicular distance of CgI on ring J, CgJ_Perp is the perpendicular distance of CgJ on ring I and Cg1: O5 – C20 – O6 – Eu1; Cg2: C2 – C3 – C4 – C5 – C6 – C7; Cg3: C8 – C9 – C10 – C11 – C12 – C13; Cg4: C14 – C15 – C16 – C17 – C18 – C19.

3.2. Powder X-ray diffraction pattern

To verify the phase purity of the crystal product, powder X-ray diffraction was measured of compound **1**, the results shown in Fig. 3. We considered that X-ray powder patterns were consistent with the presence of the phase defined in the single crystal experiment.

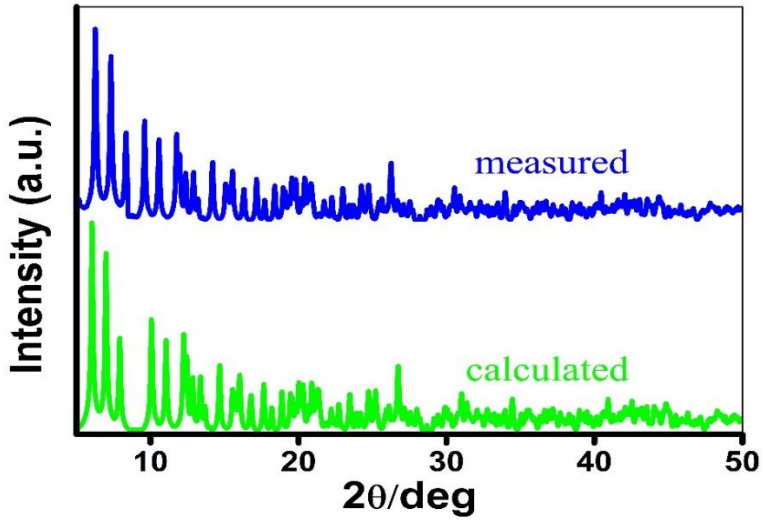

Figure 3. Powder X-ray diffraction graph for compound **1**.

3.3. Spectroscopic Analysis

The solid-state UV-Vis spectra of compound **1** and free ligand (H_3btb) were analyzed in Fig. 4. The H_3btb ligand gives two broad peaks at 342 and 438 nm. Whereas, compound **1** shows two prominent absorption peaks at 384 and 499 nm. These absorption bands can be assigned to the π–π* or n-π* transitions of the btb ligand [8].

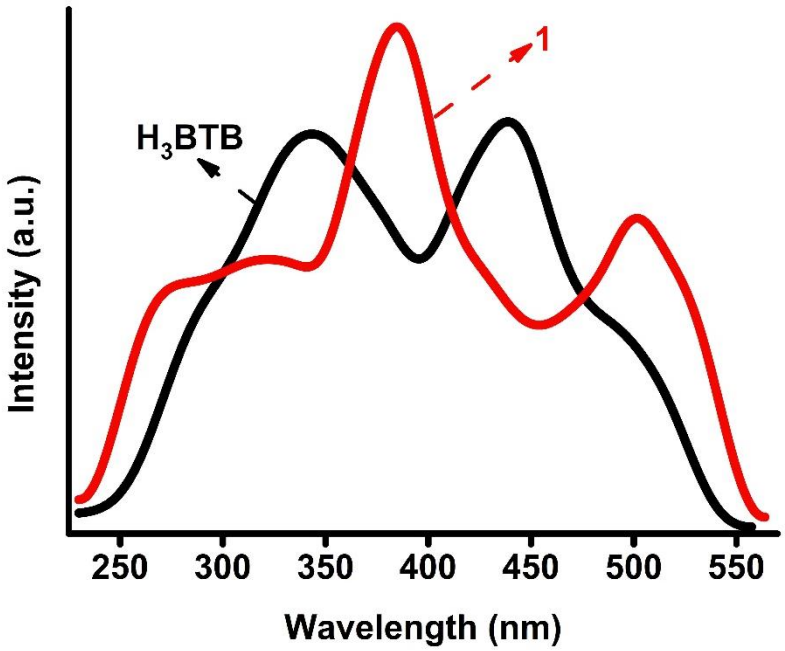

Figure 4. The solid-state absorption spectrum of compound **1** (red) and the ligand H_3btb (black).

The luminescence properties of compound **1** and the ligand (H_3btb) were investigated upon excitation at 349 nm (Fig. 5). As shown Fig. 5a, the H_3btb ligand shows a blue emission at 450 nm and a shoulder attached to a wide band at 565 nm, which may be assigned to the n→π* or π→π* electron transitions of the ligand [9]. As seen Fig. 5b, the compound **1** exhibits strong red luminescence under excitation at 349 nm. The emission spectrum consists of five characteristic peaks appearing at 580, 590, 615, 649 and 702 nm correspond to $^5D_0 \rightarrow {}^7F_j$ (j = 0-4) transitions respectively. Sharp and strong band emission at 615 nm causes a bright red emission. The $^5D_0 \rightarrow {}^7F_1$ magnetic dipole transition is insensitive and almost unchanged with the coordination of metal ion, while the $^5D_0 \rightarrow {}^7F_2$ electrical dipole transition is an extremely sensitive that its density is very sensitive and suitable to be affected from the host environment [10]. The $^5D_0 \rightarrow {}^7F_2$ emission is obviously higher intensity than that of the $^5D_0 \rightarrow {}^7F_1$ emission when Eu(III) ions occupy non-inversion symmetry confirmed by a single crystal structure work [11].

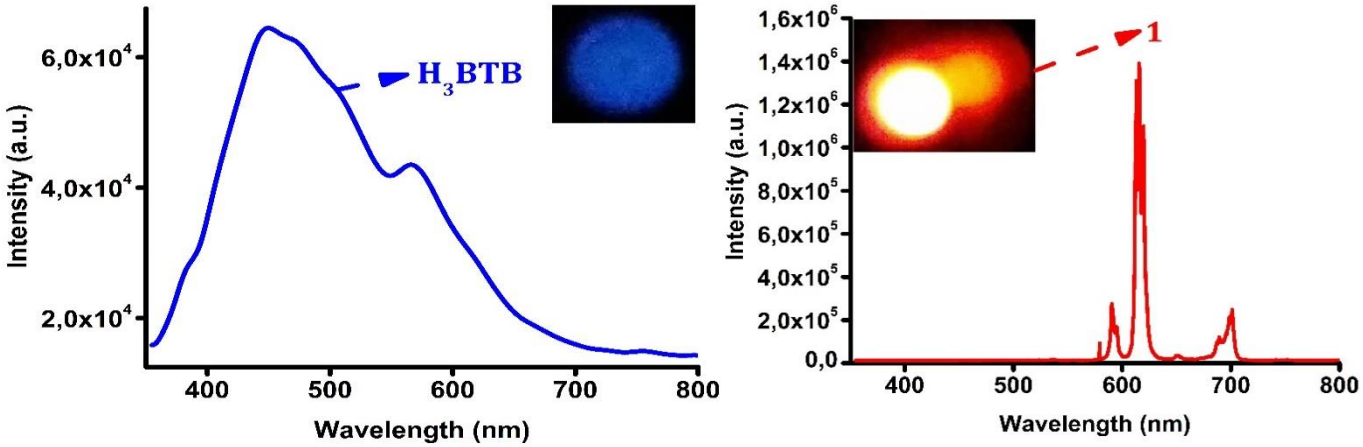

(a) **(b)**

Figure 5. (a) The luminescence spectrum of the ligand H_3BTB (inset photo is a photoluminescent image). **(b)** The luminescence spectrum of the compound **1** (inset photo is a photoluminescent image).

4. CONCLUSION

In this work, we presented detailed structural and optical characterization of H_3btb based Eu-MOF. In this compound, the Eu^{III} atoms are bridged with btb ligand in dimeric form, resulting in 2D layer structure which is further linked by btb ligand result 3D structure exhibiting 1D open channels. The solid-state photoluminescence measurements display remarkable red emission for compound **1**, suggesting it may have potential applications as LED and new photoactive materials.

ACKNOWLEDGMENTS

This work was supported by the Scientific Project Unit of Balikesir University under project number BAP-2017/200. The authors acknowledge to Dokuz Eylul University for the use of X-Ray diffractometer (Research grant No. 2010.KB.FEN.13) and Balikesir University, Science and Technology Application and Research Center (BUBTAM), for the use of the photoluminescence spectrometer.

REFERENCES

[1] Zhang, H. Bin, Tian, C. Bin, Wu, S. T., Lin, J. Di, Li, Z. H., Du, S. W., Synthesis, structures and physical properties of new 3D lanthanide coordination polymers constructed from 1,2,4,5-benzenetetracarboxylic acid, Journal of Molecular Structure, 985, 355–360, 2011.

[2] Zhu, Y., Wang, L., Chen, X., Wang, P., Fan, Y., Zhang, P., 3D lanthanide metal-organic frameworks constructed from 2,6-naphthalenedicarboxylate ligand: synthesis, structure, luminescence and dye adsorption, Journal of Solid State Chemistry, 251, 248–254, 2017.

[3] Li, J.-M., Li, R., Li, X., Construction of metal–organic frameworks (MOFs) and highly luminescent Eu(III)-MOF for the detection of inorganic ions and antibiotics in aqueous medium, Crystal Engineering Communication, 20, 4962–4972, 2018.

[4] Lahoud, M. G., Frem, R. C. G., Marques, L. F., Arroyos, G., Brandão, P., Ferreira, R. A. S., Carlos, L. D., A novel near monochromatic red emissive europium(III) metal-organic framework based on 1,2,4,5-benzenetetracarboxylate: From synthesis to photoluminescence studies, Journal of Solid State Chemistry 253, 176–183, 2017.

[5] Zhao, M., Yao, Z. Q., Xu, Y. L., Chang, Z., Bu, X. H., Guest dependent structure and acetone sensing properties of a 2D Eu3+coordination polymer, Royal Society of Chemistry Advences, 7, 2258–2263, 2017.

[6] Li, X., Xie, Z., Lin, J., Cao, R., Lanthanide-organic frameworks constructed from multi-functional ligands: Syntheses, structures, near-infrared and visible photoluminescence properties, Journal of Solid State Chemistry 182, 2290–2297, 2009.

[7] Casanovas, B., Font-bardía, M., Speed, S., El, S., Vicente, R., Field-Induced SMM and Visible / NIR-Luminescence Behaviour of Dinuclear Ln III Complexes with 2-Fluorobenzoate, European Journal of Inorganic Chemistry, 1928–1937, 2018.

[8] Donmez, A., Coban, M.B., Kocak, C., Oylumluoglu, G., Baisch, U., Kara, H., Synthesis, characterization and photoluminescence studies of new Cu(II) complex, Molecular Crystals and Liquid Crystals, 652, 213–222, 2017.

[9] Oylumluoglu, G., Coban, M. B., Kocak, C., Aygun, M., Kara, H., 2-and 1-D coordination polymers of Dy(III) and Ho(III) with near infrared and visible luminescence by efficient charge-transfer antenna ligand, Journal of Molecular Structure, 1146, 356–364, 2017.

[10] Zhang, K., Wang, Z., You, X., Yu, Z., A new family of two-dimensional lanthanide(III) coordination polymers: synthesis, structures and properties of $[Ln(SIP)(H_2O)_4]_n$ (Ln=Eu, Gd, Ce, and NaH_2SIP=5-sulfoisophthalic acid monosodium salt), Inorganic Chemistry Communications, 5, 230–234, 2002.

[11] Ma, P., Wan, R., Si, Y., Hu, F., Wang, Y., Niu, J., Wang, J., Double-malate bridging tri-lanthanoid cluster encapsulated arsenotungstates: syntheses, structures, luminescence and magnetic properties, Dalton Transactions, 44, 11514–11523, 2015.

ON THE PRINCIPAL NORMAL AND TRINORMAL SPHERICAL INDICATRICES OF A SPACELIKE W-CURVE WITH TIMELIKE PRINCIPAL NORMAL VECTOR IN MINKOWSKI SPACETIME

Yasin Ünlütürk[1*], Talat Körpınar[2]

[1]*Department of Mathematics, Faculty of Art and Science,*
Kırklareli University, 39100, Kırklareli, TURKEY
[2]*Department of Mathematics, Faculty of Art and Science,*
Muş Alparslan University, 49250 Muş, TURKEY

*E-mail: yasinunluturk@klu.edu.tr

Abstract

In this study, we investigate the principal normal, trinormal spherical indicatrices of a spacelike W-curve in Minkowski space time. All spherical images studied in this work are spacelike curves. The Frenet-Serret invariants of the mentioned indicatrix curves are obtained in terms of the invariants of spacelike W-curve. Also some characterizations for these spherical indicatrices being ccr-curves and general helices are studied in Minkowski spacetime.

Keywords: Classical differential geometry, spherical Indicatrices, W-curves, spacelike W-curves, general helix, ccr-curves.

MSC (2000): 53C50, 53C40.

1. INTRODUCTION

A tetrad of mutually orthogonal unit vectors (called tangent, normal, binormal and trinormal) was defined and constructed at each point of a differentiable curve. The rates of change of these vectors along the curve define the curvatures of the curve in the space E_1^4. Spherical indicatrix (image) is a well-known concept in classical differential geometry of curves [6].

Einstein's theory opened a door to new geometries such as Minkowski space-time, which is simultaneously the geometry of special relativity and the geometry induced on each fixed tangent space of an arbitrary Lorentzian manifold At the beginning of the twentieth century.

In recent years, the theory of degenerate submanifolds are treated by the researchers and some of classical differential geometry topics are extented to Lorentz manifolds. Some of authors aimed to determine Frenet-Serret invariants in higher dimensions. There exists a vast literature on this subject, for instance [13], [14], [15], [16], [17]. In the light of the existing literature, in [14], the author extended spherical indicatrices of curves to four dimensional Lorentzian space and studied such curves in the case of base curve is a space-like curve according to signature $(+,+,+,-)$.

In this work, we study spherical indicatrices of a spacelike W-curve lying on the pseudohyperbolic space H_0^3 in Minkowski space-time. We investigate relations among Frenet-Serret invariants of spherical indicatrices and base curve. Additionally, some characterizations of spherical indicatrices being general helices are presented.

2. MATERIAL AND METHODS

Minkowski space-time E_1^4 is Euclidean space E^4 provided with the standard flat metric given by

$$g = -dx_1^2 + dx_2^2 + dx_3^2 + dx_4^2,$$

where (x_1, x_2, x_3, x_4) is a rectangular coordinate system in E_1^4 [8]. Since g is an indefinite metric, recall that a vector $v \in \mathrm{E}_1^4$ can have one of the three causal characters; it can be spacelike if $g(v,v) > 0$ or $v = 0$, timelike if $g(v,v) < 0$ and null (lightlike) if $g(v,v) = 0$ and $v \neq 0$. Similary, an arbitrary curve $\alpha = \alpha(s)$ in E_1^4 can be locally spacelike, timelike or null (lightlike), if all of its velocity vectors $\alpha'(s)$ are respectively spacelike, timelike or null. Also, recall the norm of a vector v is given by

$$\|v\| = \sqrt{|g(v,v)|}.$$

Therefore, v is a unit vector if $g(v,v) = \pm 1$. Next, vectors v, w in E_1^4 are said to be orthogonal if

$g(v,w)=0$. The velocity of the curve $\alpha(s)$ is given by $\|\alpha'(s)\|$ [5]. Let a and b be two spacelike vectors in E_1^4, then there is a unique real number $0\le\delta\le\pi$, called the angle between a and b, such that $g(a,b)=\|a\|.\|b\|\cos\delta$ [10].

The pseudohyperbolic space with center $m=(m_1,m_2,m_3,m_4)\in E_1^4$ and radius $r\in R^+$ in the space-time E_1^4 is the hyperquadric

$$H_0^3(r)=\{a=(a_1,a_2,a_3,a_4)\in E_1^4 \mid g(a-m,a-m)=-r^2\}.$$

with dimension 3 and index 0 [8].

Let $\vartheta=\vartheta(s)$ be a curve in E_1^4. If the tangent vector field of this curve forms a constant angle with a constant vector field U, then this curve is called a general helix. Recall that, if a regular curve in E_1^4 has constant Frenet-Serret curvatures ratios, (i.e., $\frac{\tau}{\kappa}$ and $\frac{\sigma}{\tau}$ are constants), then it is called a *ccr-curve* [7], [9]. Also if these curvatures are non-zero constants, curve is said to be W-curve (or helix) [11].

Denote by $\{T(s),N(s),B_1(s),B_2(s)\}$ the moving Frenet-Serret frame along the curve $\alpha(s)$ in the space E_1^4. Then T,N,B_1,B_2 are, respectively, the tangent, the principal normal, the binormal (the first binormal) and the trinormal (the second binormal) vector fields. A spacelike or timelike curve $\alpha(s)$ is said to be parametrized by arclength function s, if $g(\alpha'(s),\alpha'(s))=\pm1$.

Let $\alpha(s)$ be a spacelike curve with timelike principal normal vector in the space-time E_1^4, parametrized by arclength function s. Then, the following Frenet-Serret equations are given in [13]:

$$\begin{bmatrix} T' \\ N' \\ B_1' \\ B_2' \end{bmatrix} = \begin{bmatrix} 0 & \kappa & 0 & 0 \\ \kappa & 0 & \tau & 0 \\ 0 & \tau & 0 & \sigma \\ 0 & 0 & -\sigma & 0 \end{bmatrix} \begin{bmatrix} T \\ N \\ B_1 \\ B_2 \end{bmatrix},$$

where T,N,B_1 and B_2 are mutually orthogonal vectors satisfying equations

$$g(T,T)=g(B_1,B_1)=g(B_2,B_2)=1, g(N,N)=-1,$$

and where, κ,τ and σ are first, second and third curvature of the curve α, respectively.

In the same space, in [1], the authors express a characterization of spacelike curves lying on H_0^3 by the following theorem:

Theorem 1. Let $\alpha(s)$ be a unit speed spacelike curve in E_1^4, with spacelike N,B_1 and curvatures

$\kappa \neq 0, \tau \neq 0, \sigma \neq 0$ for each $s \in I \subset R$. Then, α lies on pseudohyperbolic space if and only if

$$\frac{\sigma}{\tau}\frac{d\rho}{ds} = \frac{d}{ds}\left[\frac{1}{\sigma}\left(\rho\tau + \frac{d}{ds}\left(\frac{1}{\tau}\frac{d\rho}{ds}\right)\right)\right],$$
$$\left\{\frac{1}{\sigma}\left[\rho\tau + \frac{d}{ds}\left(\frac{1}{\tau}\frac{d\rho}{ds}\right)\right]\right\}^2 > \rho^2 + \left(\frac{1}{\tau}\frac{d\rho}{ds}\right)^2, \quad (1)$$

where $\rho = \frac{1}{\kappa}$.

In the same space, in [15] authors defined a vector product and gave a method to determine the Frenet-Serret invariants for an arbitrary curve by following definition and theorem:

Definition 1. Let $a = (a_1, a_2, a_3, a_4)$, $b = (b_1, b_2, b_3, b_4)$ and $c = (c_1, c_2, c_3, c_4)$ be vectors in E_1^4. The vector product in Minkowski space-time E_1^4 is defined by the determinant

$$a \wedge b \wedge c = -\begin{vmatrix} -e_1 & e_2 & e_3 & e_4 \\ a_1 & a_2 & a_3 & a_4 \\ b_1 & b_2 & b_3 & b_4 \\ c_1 & c_2 & c_3 & c_4 \end{vmatrix},$$

where e_1, e_2, e_3 and e_4 are mutually orthogonal vectors (coordinate direction vectors) satisfying equation $e_1 \wedge e_2 \wedge e_3 = e_4$, $e_2 \wedge e_3 \wedge e_4 = e_1$, $e_3 \wedge e_4 \wedge e_1 = e_2$, $e_4 \wedge e_1 \wedge e_2 = -e_3$.

Theorem 2. Let $\alpha = \alpha(t)$ be an arbitrary spacelike curve in Minkowski space-time E_1^4. The Frenet-Serret apparatus of α can be written as follows;

$$T = \frac{\alpha'}{\|\alpha'\|}, \; N = \frac{\|\alpha'\|^2 \alpha'' - g(\alpha', \alpha'')\alpha'}{\left\|\|\alpha'\|^2 \alpha'' - g(\alpha', \alpha'')\alpha'\right\|}, \; B_1 = \mu N \wedge T \wedge B_2, \; B_2 = \mu \frac{T \wedge N \wedge \alpha'''}{\|T \wedge N \wedge \alpha'''\|}, \quad (2)$$

$$\kappa = \frac{\left\|\|\alpha'\|^2 \alpha'' - g(\alpha', \alpha'')\alpha'\right\|}{\|\alpha'\|^4}, \; \tau = \frac{\|T \wedge N \wedge \alpha'''\|\|\alpha'\|}{\left\|\|\alpha'\|^2 \alpha'' - g(\alpha', \alpha'')\alpha'\right\|}, \sigma = \frac{g(\alpha^{(IV)}, B_2)}{\|T \wedge N \wedge \alpha'''\|\|\alpha'\|}, \quad (2)$$

where μ is taken -1 or $+1$ to make $+1$ the determinant of $[T, N, B_1, B_2]$ matrix [15].

Here, we shall use timelike curve's Frenet-Serret invariants. Therefore, our calculations do not exist null vectors.

3. RESULTS AND DISCUSSION

3.1. The principal normal spherical indicatrix of a spacelike W-curve lying on $\mathbf{H}_0^3$

By the spirit of the paper [15], first we adapt the principal normal spherical indicatrix definition to spacelike W-curves of Minkowski space-time. Moreover, we give the definition of trinormal spherical indicatrix for spacelike W-curves at the beginning of the section 3.1.

Definition 2. Let $\beta = \beta(s)$ be an unit speed spacelike W-curve in Minkowski space-time. If we translate the principal normal vector to the center O of the pseudohyperbolic space H_0^3, we obtain a curve $\delta = \delta(s_\delta)$. This curve is called the principal normal spherical indicatrix or image of the curve β in E_1^4.

Theorem 3. Let $\beta = \beta(s)$ be an unit speed spacelike W-curve and $\delta = \delta(s_\delta)$ be its principal normal spherical indicatrix. Then;

i) $\delta = \delta(s_\delta)$ is a space-like curve.

ii) The Frenet-Serret apparatus of δ, $\{T_\delta, N_\delta, B_{1\delta}, B_{2\delta}, \kappa_\delta, \tau_\delta, \sigma_\delta\}$ can be formed by the apparatus of β, $\{T, N, B_1, B_2, \kappa, \tau, \sigma\}$.

iii) The spherical image curve $\delta = \delta(s_\delta)$ lies in Euclidean 3-space.

Proof. Let $\beta = \beta(s)$ be an unit speed spacelike W-curve and $\delta = \delta(s_\delta)$ be its principal normal spherical indicatrix. It can be written as

$$\delta = N(s). \tag{3}$$

Differentiating (4) with respect to s, we find

$$\delta' = \dot{\delta}\frac{ds_\delta}{ds} = \kappa N.$$

Here we shall denote differentiation according to s by a dash, and differentiation according to s_δ by a dot. Thus we obtain the unit tangent vector of the principal normal spherical indicatrix curve δ as

$$T_\delta = N \tag{4}$$

and

$$\left\|\delta'\right\| = \frac{ds_\delta}{ds} = \kappa.$$

The causal character of the the principal normal spherical indicatrix curve $\delta(s_\delta)$ is determined by the following inner product:

$$g(\delta', \delta') = \kappa^2 > 0. \tag{5}$$

By (6), we will take the spherical indicatrix curve as spacelike one.

Considering the previous method and using the property of the curve to be W-curve, we form the following differentiations with respect to s:

$$\begin{cases} \delta'' = \kappa^2 T + \kappa\tau B_1, \\ \delta''' = \kappa(\kappa^2+\tau^2)N + \kappa\tau\sigma B_2, \\ \delta^{(IV)} = \kappa^2(\kappa^2+\tau^2)T + \kappa\tau(\kappa^2+\tau^2-\sigma^2)B_1. \end{cases}$$

By equation (2) we arrive

$$\left\|\delta'\right\|^2 \delta'' - g(\delta', \delta'')\delta' = \kappa^4 T + \kappa^3\tau B_1.$$

Then we can get the principal normal vector as

$$N_\delta = \frac{\kappa}{\sqrt{\kappa^2+\tau^2}} T + \frac{\tau}{\sqrt{\kappa^2+\tau^2}} B_1 \tag{6}$$

and the first curvature as

$$\kappa_\delta = \frac{\sqrt{\kappa^2+\tau^2}}{\kappa}. \tag{7}$$

Now let us calculate the vector $T_\delta \wedge N_\delta \wedge \delta'''$, that is,

$$T_\delta \wedge N_\delta \wedge \delta''' = -\begin{vmatrix} -T & N & B_1 & B_2 \\ 0 & 1 & 0 & 0 \\ \dfrac{\kappa}{\sqrt{\kappa^2+\tau^2}} & 0 & \dfrac{\tau}{\sqrt{\kappa^2+\tau^2}} & 0 \\ 0 & \kappa(\kappa^2+\tau^2) & 0 & \kappa\tau\sigma \end{vmatrix}.$$

This product yields

$$T_\delta \wedge N_\delta \wedge \delta''' = \frac{\kappa\tau^2\sigma}{\sqrt{\kappa^2+\tau^2}} T + \frac{\kappa^2\tau\sigma}{\sqrt{\kappa^2+\tau^2}} B_1. \tag{8}$$

Hence, we obtain the trinormal (second binormal) vector field of the curve $\delta(s_\delta)$ as follows:

$$B_{2\delta} = \frac{\mu\tau}{\sqrt{\kappa^2+\tau^2}} T + \frac{\mu\kappa}{\sqrt{\kappa^2+\tau^2}} B_1. \tag{9}$$

Taking the norm of both sides of (9), we find the second curvature

$$\tau_\delta = \frac{\tau\sigma}{\kappa\sqrt{\kappa^2+\tau^2}}. \tag{10}$$

Finding the binormal vector field, we express

$$N_\delta \wedge T_\delta \wedge B_{2\delta} = -\begin{vmatrix} -T & N & B_1 & B_2 \\ \frac{\kappa}{\sqrt{\kappa^2+\tau^2}} & 0 & \frac{\tau}{\sqrt{\kappa^2+\tau^2}} & 0 \\ 0 & 1 & 0 & 0 \\ \frac{\mu\tau}{\sqrt{\kappa^2+\tau^2}} & 0 & \frac{\mu\kappa}{\sqrt{\kappa^2+\tau^2}} & 0 \end{vmatrix}.$$

(11)

Calculating (12), we have

$$N_\delta \wedge T_\delta \wedge B_{2\delta} = \mu\frac{\kappa^2-\tau^2}{\kappa^2+\tau^2}B_2.$$

So we obtain the binormal vector as

$$B_{1\delta} = \frac{\kappa^2-\tau^2}{\kappa^2+\tau^2}B_2.$$

(12)

Finally, using (3) and the obtained equations, we arrive the third curvature as

$$\sigma_\delta = 0.$$

(13)

Corollary 4. $\{T_\delta, N_\delta, B_{1\delta}, B_{2\delta}\}$ is an orthonormal frame of Minkowski space-time.

Proof. It can be straightforwardly seen by using the equations (5), (7), (10) and (13).

Considering above theorem, we also give:

Corollary 5. Let $\beta = \beta(s)$ be a unit speed spacelike W-curve and $\delta(s_\delta)$ be its principal normal spherical indicatrix. Then, δ is also a helix.

Proof. Let $\beta = \beta(s)$ be a unit speed spacelike W-curve. Then we know that the curvature functions are constants. Therefore, we straightforwardly see that the curvature functions of principal normal spherical indicatrix $\delta(s_\delta)$ are constants by means of the equations (8), (11) and (14). Hence the curve $\delta(s_\delta)$ becomes W-curve which is the special case of helix.

Theorem 6. Let $\beta = \beta(s)$ be a unit speed spacelike W-curve and $\delta(s_\delta)$ be its principal normal spherical indicatrix. Then, δ is a general helix and also its fixed direction U is composed as

$$U = (-c_1\kappa s + c_2)T + c_1 N + (\frac{c_1\kappa^2}{\tau}s + c_3)B_1 + (c_4\cos(\sigma s) + c_5\sin(\sigma s) + \frac{c_1\tau}{\kappa})B_2,$$

where c_1 is a non-zero constant and c_2, c_3, c_4, c_5 are constants.

Proof. Let $\beta = \beta(s)$ be a unit speed spacelike W-curve and $\delta = \delta(s_\delta)$ be its space-like principal normal spherical image. If $\delta = \delta(s_\delta)$ is a general helix, then, for a constant space-like vector U, we may express

$$g(T_\delta, U) = \cos\theta,$$

(14)

where θ is a constant angle. The equation (15) is also congruent to

$$g(N, U) = \cos\theta.$$

One can form constant vector U according to $\{T, N, B_1, B_2\}$ as the following

$$U = \varepsilon_1 T + \varepsilon_2 N + \varepsilon_3 B_1 + \varepsilon_4 B_2.$$

(15)

Differentiating (18) with respect to s, we have the following system of ordinary differential equations

$$\begin{cases} \varepsilon_1' + \varepsilon_2 \kappa = 0 \\ \varepsilon_1 \kappa + \varepsilon_3 \tau = 0 \\ \varepsilon_2 \tau - \varepsilon_4 \sigma = 0 \\ \varepsilon_4' + \varepsilon_3 \sigma = 0 \end{cases}.$$

(16)

We know that $\varepsilon_2 = c_1 \neq 0$ is a constant. Also since the curve $\beta = \beta(s)$ is a W-curve, its curvature funcions are constants. Then the solution of the system (17) can be obtained as:

$$\begin{aligned} \varepsilon_1 &= -c_1 \kappa s + c_2, \\ \varepsilon_2 &= c_1, \\ \varepsilon_3 &= \frac{c_1 \kappa^2}{\tau} s + c_3, \\ \varepsilon_4 &= c_4 \cos(\sigma s) + c_5 \sin(\sigma s) + \frac{c_1 \tau}{\kappa}, \end{aligned}$$

where c_1 is a non-zero constant and c_2, c_3, c_4, c_5 are constants.

3.2. The trinormal spherical indicatrix of a spacelike W-curve lying on $\mathbf{H}_0^3$

By the spirit of the paper [15], first we adapt the principal normal spherical indicatrix definition to spacelike W-curves of Minkowski space-time. Moreover, we give the definition of trinormal spherical indicatrix for spacelike W-curves at the beginning of the section 3.2.

Definition 3. Let $\beta = \beta(s)$ be a unit speed spacelike W-curve in Minkowski space-time. If we translate

the trinormal vector to the center O of the pseudohyperbolic space H_0^3, we obtain a curve $\varphi = \varphi(s_\varphi)$. This curve $\varphi = \varphi(s_\varphi)$ is called the trinormal spherical indicatrix or image of the curve β in E_1^4.

Theorem 7. Let $\beta = \beta(s)$ be a unit speed spacelike W-curve and $\varphi = \varphi(s_\varphi)$ be its trinormal spherical indicatrix. Then;

i) $\varphi = \varphi(s_\varphi)$ is a space-like curve.

ii) The Frenet-Serret apparatus of φ, $\{T_\varphi, N_\varphi, B_{1\varphi}, B_{2\varphi}, \kappa_\varphi, \tau_\varphi, \sigma_\varphi\}$ can be formed by the apparatus of β, $\{T, N, B_1, B_2, \kappa, \tau, \sigma\}$.

Proof. Let $\beta = \beta(s)$ be a unit speed spacelike W-curve and $\varphi = \varphi(s_\varphi)$ be its trinormal spherical indicatrix. It can be written as

$$\varphi = B_2. \tag{17}$$

Differentiating (18) with respect to s, we find

$$\varphi' = \dot{\varphi}\frac{ds_\varphi}{ds} = -\sigma B_1.$$

Here we shall denote differentiation according to s by a dash, and differentiation according to s_φ by a dot. Thus we obtain the unit tangent vector of the trinormal spherical indicatrix curve φ as

$$T_\varphi = -B_1 \tag{18}$$

and

$$\|\varphi'\| = \frac{ds_\varphi}{ds} = \sigma.$$

The causal character of the the trinormal spherical indicatrix curve $\varphi(s_\varphi)$ is determined by the following inner product:

$$g(\varphi', \varphi') = \sigma^2 > 0. \tag{19}$$

By (20), we will take the spherical indicatrix curve as spacelike one.

Considering the previous method and using the property of the curve to be W-curve, we form the following differentiations with respect to s:

$$\begin{cases} \varphi'' = -\tau\sigma N - \sigma^2 B_2, \\ \varphi''' = -\kappa\tau\sigma T - \sigma(\tau^2 - \sigma^2) B_1, \\ \varphi^{(IV)} = \tau\sigma(\sigma^2 - \tau^2 - \kappa^2) N - \sigma^2(\tau^2 - \sigma^2) B_2. \end{cases}$$

By equation (2) we arrive

$$\left\|\varphi'\right\|^2 \varphi'' - g(\varphi', \varphi'')\varphi' = -\tau\sigma^3 N - \sigma^4 B_2.$$

Then we can get the principal normal vector as

$$N_\varphi = -\frac{\tau}{\sqrt{\left|\sigma^2 - \tau^2\right|}} N - \frac{\sigma}{\sqrt{\left|\sigma^2 - \tau^2\right|}} B_2$$

(20)

and the first curvature as

$$\kappa_\varphi = \frac{\sqrt{\left|\sigma^2 - \tau^2\right|}}{\sigma}.$$

(21)

Now let us calculate the vector $T_\varphi \wedge N_\varphi \wedge \varphi'''$, that is,

$$T_\varphi \wedge N_\varphi \wedge \varphi''' = -\begin{vmatrix} -T & N & B_1 & B_2 \\ 0 & 0 & -1 & 0 \\ 0 & -\frac{\tau}{\sqrt{\left|\sigma^2 - \tau^2\right|}} & 0 & -\frac{\sigma}{\sqrt{\left|\sigma^2 - \tau^2\right|}} \\ -\kappa\tau\sigma & 0 & -\sigma(\tau^2 - \sigma^2) & 0 \end{vmatrix}.$$

This product yields

$$T_\varphi \wedge N_\varphi \wedge \varphi''' = -\frac{\kappa\tau\sigma^2}{\sqrt{\left|\sigma^2 - \tau^2\right|}} N + \frac{\kappa\tau^2\sigma}{\sqrt{\left|\sigma^2 - \tau^2\right|}} B_2.$$

(22)

Hence, we obtain the trinormal (second binormal) vector field of the curve $\varphi(s_\varphi)$ as follows:

$$B_{2\varphi} = \mu\{-\frac{\sigma}{\sqrt{\left|\sigma^2 - \tau^2\right|}} N + \frac{\tau}{\sqrt{\left|\sigma^2 - \tau^2\right|}} B_2\}.$$

(23)

Taking the norm of both sides of (23), we find the second curvature

$$\tau_\varphi = \frac{\kappa\tau}{\sigma\sqrt{|\sigma^2-\tau^2|}}.$$

(24)

Finding the binormal vector field, we express

$$N_\varphi \wedge T_\varphi \wedge B_{2\varphi} = -\begin{vmatrix} -T & N & B_1 & B_2 \\ 0 & -\frac{\tau}{\sqrt{|\sigma^2-\tau^2|}} & 0 & -\frac{\sigma}{\sqrt{|\sigma^2-\tau^2|}} \\ 0 & 0 & -1 & 0 \\ 0 & -\frac{\mu\sigma}{\sqrt{|\sigma^2-\tau^2|}} & 0 & \frac{\mu\tau}{\sqrt{|\sigma^2-\tau^2|}} \end{vmatrix}.$$

(25)

Calculating (26), we have

$$N_\varphi \wedge T_\varphi \wedge B_{2\varphi} = \mu\frac{\tau^2+\sigma^2}{\sigma^2-\tau^2}T.$$

So we obtain the binormal vector as

$$B_{1\varphi} = \frac{\tau^2+\sigma^2}{\sigma^2-\tau^2}T.$$

(26)

Finally, using (3) and the obtained equations, we arrive the third curvature as

$$\sigma_\varphi = \frac{\sigma^2-\tau^2}{\kappa\tau}.$$

(27)

Corollary 8. $\{T_\varphi, N_\varphi, B_{1\varphi}, B_{2\varphi}\}$ is an orthonormal frame of Minkowski space-time.

Proof. It can be straightforwardly seen by using the equations (19), (21), (24) and (27).

Considering above theorem, we also give:

Corollary 9. Let $\beta = \beta(s)$ be a unit speed spacelike W-curve and $\varphi(s_\varphi)$ be its trinormal spherical indicatrix. Then, φ is also a helix.

Proof. Let $\beta = \beta(s)$ be a unit speed spacelike W-curve. Then we know that the curvature functions are constants. Therefore, we straightforwardly see that the curvature functions of principal normal spherical indicatrix $\varphi(s_\varphi)$ are constants by means of the equations (22), (25) and (28). Hence the curve $\varphi(s_\varphi)$

becomes W-curve which is the special case of helix.

Theorem 10. Let $\beta = \beta(s)$ be a unit speed spacelike W-curve and $\varphi(s_\varphi)$ be its trinormal spherical indicatrix. Then, φ is a general helix and also its fixed direction U is composed as

$$U = (-c_3 e^{\kappa s} - c_4 e^{\kappa s} + c_5)T + (c_3 e^{\kappa s} + c_4 e^{-\kappa s})N + c_1 B_1 + (-c_1 \sigma s + c_2)B_2,$$

where c_1 is a non-zero constant and c_2, c_3, c_4, c_5 are constants.

Proof. Let $\beta = \beta(s)$ be a unit speed spacelike W-curve and $\varphi = \varphi(s_\varphi)$ be its space-like trinormal spherical image. If $\varphi = \varphi(s_\varphi)$ is a general helix, then, for a constant space-like vector U, we may express

$$g(T_\varphi, U) = \cos\theta,$$

(28)

where θ is a constant angle. The equation (4.12) is also congruent to

$$g(-B_1, U) = \cos\theta.$$

One can form constant vector U according to $\{T, N, B_1, B_2\}$ as the following

$$U = \varepsilon_1 T + \varepsilon_2 N + \varepsilon_3 B_1 + \varepsilon_4 B_2.$$

(29)

Differentiating (30) with respect to s, we have the following system of ordinary differential equations

$$\begin{cases} \varepsilon_1' + \varepsilon_2 \kappa = 0 \\ \varepsilon_1 \kappa + \varepsilon_2' + \varepsilon_3 \tau = 0 \\ \varepsilon_2 \tau - \varepsilon_4 \sigma = 0 \\ \varepsilon_4' + \varepsilon_3 \sigma = 0 \end{cases}.$$

(30)

We know that $\varepsilon_3 = c_1 \neq 0$ is a constant. Also since the curve $\beta = \beta(s)$ is a W-curve, its curvature functions are constants. Then the solution of the system (31) can be found as:

$$\begin{aligned} \varepsilon_1 &= -c_3 e^{\kappa s} - c_4 e^{\kappa s} + c_5, \\ \varepsilon_2 &= c_3 e^{\kappa s} + c_4 e^{-\kappa s}, \\ \varepsilon_3 &= c_1, \\ \varepsilon_4 &= -c_1 \sigma s + c_2, \end{aligned}$$

where c_1 is a non-zero constant and c_2, c_3, c_4, c_5 are constants.

5 CONCLUSION

In this work, we extend spherical indicatrix concept to the spacelike W-curves of Minkowski space-time. We investigate principal normal and trinormal spherical indicatrices of a spacelike W-curve and observe that both of these spherical curves are space-like curves. Thereafter, we determine relations among Frenet-Serret invariants of spherical indicatrices and base curve. Finally, we give some characterizations of the spherical indicatrices to be helices. As a further research, one can study the spherical indicatrices of spacelike curves without putting any condition for the base curve.

REFERENCES

[1] Ç. Camcı, K., İlarslan, and E. Sucurovic, On pseudohyperbolical curves in Minkowski space-time, *Turk J. Math.*, 2003, **27**, 315-328.

[2] K. İlarslan, Ö. Boyacıoğlu, Position vectors of a spacelike W-curve in Minkowski 3-space E_1^3, *Bull. Korean Math. Soc.*, 2007,**44**(3), 429–438.

[3] K. İlarslan, and E. Sucurovic, Some characterizations of null, pseudo null and partially null rectifying curves in Minkowski space-time. Taiwan. J. Math., 2008, 12(5), 1035–1044.

[4] E. İyigün, The tangent spherical image and ccr-curve of a time-like curve in L^3, J Inequal Appl (2013) 2013: 55.

[5] R. Lopez, Differential geometry of curves and surfaces in Lorentz-Minkowski space, Int. Elec. Journ. Geom. 3(2) (2010) 67-101.

[6] R.S. Milman, and G.D. Parker, *Elements of Differential Geometry*, Prentice-Hall Inc., Englewood Cliffs, New Jersey, 1977.

[7] J. Monterde, Curves with constant curvature ratios, *Bol. Soc. Mat. Mexicana*, 2007, **3**, 177-186.

[8] B. O 'Neill, Semi-Riemannian geometry with applications to relativity, Academic press Inc, London, 1983.

[9] G. Öztürk, K. Arslan, and H.H. Hacısalihoglu, A Characterization of ccr-curves in R^m, *Proc. Estonian Acad. Sci.*, 2008, **57**, 217-224.

[10] J.G. Ratcliffe, Foundations of Hyperbolic Manifolds, Springer Science+Business Media, LLC, New York, USA, pp. 68-72, 2006.

[11] M. Petrovic-Torgasev, E. Sucurovic, W-curves in Minkowski space-time, Novi Sad J. Math. 32(2), 55-65, 2002.

[12] M. Petrovic–Torgasev, K. İlarslan and E. Nesovic, On partially null and pseudo null curves in the

semi-euclidean space , J. Geom., 84, 106-116, 2005.

[13] J. Walrave, Curves and Surfaces in Minkowski Space, Dissertation, K. U. Leuven, Fac. of Science, Leuven, 1995.

[14] S.Yılmaz, Spherical Indicators of Curves and Characterizations of Some Special Curves in four dimensional Lorentzian Space $\mathbf{L}^4$, Dissertation, Dokuz Eylül University, 2001.

[15] S.Yılmaz and M. Turgut, On the Differential Geometry of the Curves in Minkowski Space-time I, *Int. J. Contemp. Math. Sci.*, 2008, **3**, 1343-1349.

[16] S.Yılmaz, E. Özyılmaz, and M. Turgut, On the Differential Geometry of the Curves in Minkowski Space-time II, *Int. J. Comput. Math. Sci.*, 2009, **3**, 53-55.

[17] S.Yılmaz, E. Özyılmaz, Y. Yaylı, M. Turgut, Tangent and trinormal spherical images of a time-like curve on the pseudohyperbolic space , Proc. Est. Acad. Sci. 59(3), 216-224, 2010.

ON INEXTENSIBLE FLOWS OF M_2 BISHOP SPHERICAL IMAGES ACCORDING TO BISHOP FRAME IN E^3

Talat Körpınar[1], Yasin Ünlütürk[2*]

[1]*Department of Mathematics, Faculty of Art and Science,*
Muş Alparslan University, 49250 Muş, TURKEY
[2]*Department of Mathematics, Faculty of Art and Science,*
Kırklareli University, 39100, Kırklareli, TURKEY

E-mail: yasinunluturk@klu.edu.tr

Abstract

In this paper, we study $\mathbf{M}_2$ Bishop spherical images in Euclidean space E^3. Using the Bishop frame of the given curve, we present partial differential equations. We give some characterizations for curvatures of a curve in Euclidean space E^3.

Keywords: Bishop frame, Bishop spherical images, Curvatures, Flows.

MSC (2000): 53A04, 53A10.

1. INTRODUCTION

Physically, the inextensible curve flows give rise to motions in which no strain energy is induced. The swinging motion of a cord of fixed length, for example, or of a piece of paper carried by the wind, can be described by inextensible curve and surface flows. Such motions arise quite naturally in a wide range of the physical applications, [6,16].

In this paper, we study $\mathbf{M}_2$ Bishop spherical images in Euclidean space E^3. Using the Bishop frame of the given curve, we present partial differential equations. We give some characterizations for curvatures of a curve in Euclidean space E^3.

2. MATERIAL AND METHODS

Assume that $\{\mathbf{T},\mathbf{N},\mathbf{B}\}$ be the Frenet frame field along α. Then, the Frenet frame satisfies the following Frenet--Serret equations:

$$\begin{aligned}\nabla_{\mathbf{T}}\mathbf{T} &= \kappa\mathbf{N},\\ \nabla_{\mathbf{T}}\mathbf{N} &= -\kappa\mathbf{T}+\tau\mathbf{B},\\ \nabla_{\mathbf{T}}\mathbf{B} &= -\tau\mathbf{N},\end{aligned} \tag{2.1}$$

where κ is the curvature of α and τ its torsion and

$$g(\mathbf{T},\mathbf{T}) = 1, g(\mathbf{N},\mathbf{N})=1, g(\mathbf{B},\mathbf{B})=1, g(\mathbf{T},\mathbf{N}) = g(\mathbf{T},\mathbf{B})=g(\mathbf{N},\mathbf{B})=0.$$

The Bishop frame or parallel transport frame is an alternative approach to defining a moving frame that is well defined even when the curve has vanishing second derivative, [1]. The Bishop frame is expressed as

$$\begin{aligned}\nabla_{\mathbf{T}}\mathbf{T} &= k_1\mathbf{M}_1+k_2\mathbf{M}_2,\\ \nabla_{\mathbf{T}}\mathbf{M}_1 &= -k_1\mathbf{T},\\ \nabla_{\mathbf{T}}\mathbf{M}_2 &= -k_2\mathbf{T},\end{aligned} \tag{2.2}$$

where

$$g(\mathbf{T},\mathbf{T}) = 1, g(\mathbf{M}_1,\mathbf{M}_1)=1, g(\mathbf{M}_2,\mathbf{M}_2)=1, g(\mathbf{T},\mathbf{M}_1) = g(\mathbf{T},\mathbf{M}_2)=g(\mathbf{M}_1,\mathbf{M}_2)=0.$$

Here, we shall call the set $\{\mathbf{T},\mathbf{M}_1,\mathbf{M}_2\}$ as Bishop trihedra, k_1 and k_2 as Bishop curvatures and $\mathsf{U}(s)=\arctan\frac{k_2}{k_1}$, $\tau(s)=\mathsf{U}'(s)$ and $\kappa(s)=\sqrt{k_1^2+k_2^2}$.

Bishop curvatures are defined by

$$k_1 = \kappa(s)\cos u(s), k_2 = \kappa(s)\sin u(s).$$

Definition 2.1. Let α be a regular curve in E^3. If we translate of the third vector field of Bishop frame to the center O of the unit sphere S^2, we obtain a spherical image μ. This curve is called $\mathbf{M}_2$ Bishop spherical image or indicatrix of the curve α [17].

3. RESULTS AND DISCUSSION

3.1. Inextensible Flows of $\mathbf{M}_2$ Bishop Spherical Image according to Bishop Frame

Let $\alpha(u,t)$ is a one parameter family of smooth curves in E^3. The arclength of α is given by

$$s(u) = \int_0^u \left|\frac{\partial\alpha}{\partial u}\right| du \tag{3.1}$$

where

$$\left|\frac{\partial\alpha}{\partial u}\right| = \left|\left\langle \frac{\partial\alpha}{\partial u}, \frac{\partial\alpha}{\partial u}\right\rangle\right|^{\frac{1}{2}}. \tag{3.2}$$

The operator $\frac{\partial}{\partial s}$ is given in terms of u by

$$\frac{\partial}{\partial s} = \frac{1}{v}\frac{\partial}{\partial u},$$

where $v = \left|\frac{\partial\alpha}{\partial u}\right|$ and the arclength parameter is $ds = vdu$.

Any flow of α can be represented as $\{\mathbf{T}, \mathbf{M}_1, \mathbf{M}_2\}$

$$\frac{\partial\alpha}{\partial t} = \mathsf{Y}_1\mathbf{T} + \mathsf{Y}_2\mathbf{M}_1 + \mathsf{Y}_3\mathbf{M}_2, \tag{3.3}$$

where $\mathsf{Y}_1, \mathsf{Y}_2, \mathsf{Y}_3 \in C^\infty(\mathsf{E}^3)$.

Definition 3.1. *The flow* $\frac{\partial\alpha}{\partial t}$ *in* E^3 *are said to be inextensible if*

$$\frac{\partial}{\partial t}\left|\frac{\partial\alpha}{\partial u}\right| = 0. \tag{3.4}$$

Theorem 3.2. *Let* $\frac{\partial\alpha}{\partial t} = \mathsf{Y}_1\mathbf{T} + \mathsf{Y}_2\mathbf{M}_1 + \mathsf{Y}_3\mathbf{M}_2$ *be a smooth flow of the curve* α. *The flow is inextensible if and only if*

$$\frac{\partial\mathsf{Y}_1}{\partial s} = \mathsf{Y}_2 k_1 + \mathsf{Y}_3 k_2.$$

Lemma 3.3.

$$\begin{aligned}
\frac{\partial \mathbf{T}}{\partial t} &= (\mathsf{Y}_1 k_1 + \frac{\partial \mathsf{Y}_2}{\partial s})\mathbf{M}_1 + (\mathsf{Y}_1 k_2 + \frac{\partial \mathsf{Y}_3}{\partial s})\mathbf{M}_2, \\
\frac{\partial \mathbf{M}_1}{\partial t} &= -(\mathsf{Y}_1 k_1 + \frac{\partial \mathsf{Y}_2}{\partial s})\mathbf{T} + \mathsf{k}\mathbf{M}_2, \\
\frac{\partial \mathbf{M}_2}{\partial t} &= -(\mathsf{Y}_1 k_2 + \frac{\partial \mathsf{Y}_3}{\partial s})\mathbf{T} - \mathsf{k}\mathbf{M}_1,
\end{aligned}$$

where $\mathsf{k} = \left\langle \frac{\partial \mathbf{M}_1}{\partial t}, \mathbf{M}_2 \right\rangle$.

Theorem 3.4.

$$\frac{\partial \mathbf{T}^{\mu}}{\partial t} = (\mathsf{Y}_1 k_1 + \frac{\partial \mathsf{Y}_2}{\partial s})\mathbf{M}_1 + (\mathsf{Y}_1 k_2 + \frac{\partial \mathsf{Y}_3}{\partial s})\mathbf{M}_2,$$

$$\begin{aligned}
\frac{\partial \mathbf{N}^{\mu}}{\partial t} &= [(\frac{k_1}{k_2 \kappa^{\mu}})(\mathsf{Y}_1 k_1 + \frac{\partial \mathsf{Y}_2}{\partial s}) + (\frac{1}{\kappa^{\mu}})(\mathsf{Y}_1 k_2 + \frac{\partial \mathsf{Y}_3}{\partial s})]\mathbf{T} \\
&+ [(\frac{1}{\kappa^{\mu}})\mathsf{k} - \frac{\partial}{\partial t}(\frac{k_1}{k_2 \kappa^{\mu}})]\mathbf{M}_1 - [(\frac{k_1}{k_2 \kappa^{\mu}})\mathsf{k} + \frac{\partial}{\partial t}(\frac{1}{\kappa^{\mu}})]\mathbf{M}_2,
\end{aligned}$$

$$\begin{aligned}
\frac{\partial \mathbf{B}^{\mu}}{\partial t} &= [(\frac{k_1}{k_2 \kappa^{\mu}})(\mathsf{Y}_1 k_2 + \frac{\partial \mathsf{Y}_3}{\partial s}) - (\frac{1}{\kappa^{\mu}})(\mathsf{Y}_1 k_1 + \frac{\partial \mathsf{Y}_2}{\partial s})]\mathbf{T} \\
&+ [\frac{\partial}{\partial t}(\frac{1}{\kappa^{\mu}}) + (\frac{k_1}{k_2 \kappa^{\mu}})\mathsf{k}]\mathbf{M}_1 + [(\frac{1}{\kappa^{\mu}})\mathsf{k} - \frac{\partial}{\partial t}(\frac{k_1}{k_2 \kappa^{\mu}})]\mathbf{M}_2,
\end{aligned}$$

where $\mathsf{Y}_1, \mathsf{Y}_2, \mathsf{Y}_3$ *are smooth functions of time and arc length and*

$$\mathsf{k} = \left\langle \frac{\partial \mathbf{M}_1}{\partial t}, \mathbf{M}_2 \right\rangle.$$

Proof. Using definition of μ, we have

$$\frac{\partial \mathbf{T}^{\mu}}{\partial t} = (\mathsf{Y}_1 k_1 + \frac{\partial \mathsf{Y}_2}{\partial s})\mathbf{M}_1 + (\mathsf{Y}_1 k_2 + \frac{\partial \mathsf{Y}_3}{\partial s})\mathbf{M}_2.$$

Using the (2.3) equations, we have

$$\mathbf{N}^{\mu} = -\frac{k_1}{k_2 \kappa^{\mu}}\mathbf{M}_1 - \frac{1}{\kappa^{\mu}}\mathbf{M}_2.$$

Then,

$$\frac{\partial \mathbf{N}^{\mu}}{\partial t} = [(\frac{k_1}{k_2\kappa^{\mu}})(\mathsf{Y}_1 k_1 + \frac{\partial \mathsf{Y}_2}{\partial s}) + (\frac{1}{\kappa^{\mu}})(\mathsf{Y}_1 k_2 + \frac{\partial \mathsf{Y}_3}{\partial s})]\mathbf{T}$$
$$+[(\frac{1}{\kappa^{\mu}})\mathsf{k} - \frac{\partial}{\partial t}(\frac{k_1}{k_2\kappa^{\mu}})]\mathbf{M}_1 - [(\frac{k_1}{k_2\kappa^{\mu}})\mathsf{k} + \frac{\partial}{\partial t}(\frac{1}{\kappa^{\mu}})]\mathbf{M}_2$$

On the other hand,

$$\mathbf{B}^{\mu} = \frac{1}{\kappa^{\mu}}\mathbf{M}_1 - \frac{k_1}{k_2\kappa^{\mu}}\mathbf{M}_2.$$

This implies

$$\frac{\partial \mathbf{B}^{\mu}}{\partial t} = [(\frac{k_1}{k_2\kappa^{\mu}})(\mathsf{Y}_1 k_2 + \frac{\partial \mathsf{Y}_3}{\partial s}) - (\frac{1}{\kappa^{\mu}})(\mathsf{Y}_1 k_1 + \frac{\partial \mathsf{Y}_2}{\partial s})]\mathbf{T}$$
$$+[\frac{\partial}{\partial t}(\frac{1}{\kappa^{\mu}}) + (\frac{k_1}{k_2\kappa^{\mu}})\mathsf{k}]\mathbf{M}_1 + [(\frac{1}{\kappa^{\mu}})\mathsf{k} - \frac{\partial}{\partial t}(\frac{k_1}{k_2\kappa^{\mu}})]\mathbf{M}_2.$$

Then, we obtain the theorem. So, theorem is proved.

Theorem 3.5. *Let* $\frac{\partial \alpha}{\partial t}$ *be inextensible according to Bishop frame. If* μ *is* $\mathbf{M}_2$ *Bishop spherical image of* α, *then,*

$$\frac{\partial}{\partial s}(\mathsf{Y}_1 k_1 + \frac{\partial \mathsf{Y}_2}{\partial s}) = [\frac{\partial}{\partial t}(\kappa^{\mu} k_2)\frac{k_1}{k_2\kappa^{\mu}} - (\kappa^{\mu} k_2)[(\frac{1}{\kappa^{\mu}})\mathsf{k} - \frac{\partial}{\partial t}(\frac{k_1}{k_2\kappa^{\mu}})]],$$

where $\mathsf{Y}_1, \mathsf{Y}_2, \mathsf{Y}_3$ *are smooth functions of time and arc length and*

$$\mathsf{k} = \left\langle \frac{\partial \mathbf{M}_1}{\partial t}, \mathbf{M}_2 \right\rangle.$$

Proof. From Bishop frame, we obtain

$$\frac{\partial}{\partial s}\frac{\partial \mathbf{T}^{\mu}}{\partial t} = \frac{\partial}{\partial s}(\mathsf{Y}_1 k_1 + \frac{\partial \mathsf{Y}_2}{\partial s})\mathbf{M}_1 + \frac{\partial}{\partial s}(\mathsf{Y}_1 k_2 + \frac{\partial \mathsf{Y}_3}{\partial s})\mathbf{M}_2$$
$$-[k_1(\mathsf{Y}_1 k_1 + \frac{\partial \mathsf{Y}_2}{\partial s}) - k_2(\mathsf{Y}_1 k_2 + \frac{\partial \mathsf{Y}_3}{\partial s})]\mathbf{T}.$$

Also, we have the following

$$\frac{\partial}{\partial t}\frac{\partial}{\partial s}\mathbf{T}^{\mu} = -(\kappa^{\mu} k_2)[(\frac{k_1}{k_2\kappa^{\mu}})(\mathsf{Y}_1 k_1 + \frac{\partial \mathsf{Y}_2}{\partial s}) + (\frac{1}{\kappa^{\mu}})(\mathsf{Y}_1 k_2 + \frac{\partial \mathsf{Y}_3}{\partial s})]\mathbf{T}$$
$$+[\frac{\partial}{\partial t}(\kappa^{\mu} k_2)\frac{k_1}{k_2\kappa^{\mu}} - (\kappa^{\mu} k_2)[(\frac{1}{\kappa^{\mu}})\mathsf{k} - \frac{\partial}{\partial t}(\frac{k_1}{k_2\kappa^{\mu}})]]\mathbf{M}_1$$
$$+[\frac{\partial}{\partial t}(\kappa^{\mu} k_2)\frac{1}{\kappa^{\mu}} + (\kappa^{\mu} k_2)[(\frac{k_1}{k_2\kappa^{\mu}})\mathsf{k} + \frac{\partial}{\partial t}(\frac{1}{\kappa^{\mu}})]]\mathbf{M}_2.$$

Thus, we obtain the theorem.

In the light of Theorem 3.5, we express the following corollary without proof:

Corollary 3.6.

$$\frac{\partial}{\partial s}(\mathsf{Y}_1 k_2 + \frac{\partial \mathsf{Y}_3}{\partial s}) = [\frac{\partial}{\partial t}(\kappa^{\mu} k_2)\frac{1}{\kappa^{\mu}} + (\kappa^{\mu} k_2)[(\frac{k_1}{k_2 \kappa^{\mu}})\mathsf{k} + \frac{\partial}{\partial t}(\frac{1}{\kappa^{\mu}})]],$$

where $\mathsf{Y}_1, \mathsf{Y}_2, \mathsf{Y}_3$ *are smooth functions of time and arclength and*

$$\mathsf{k} = \left\langle \frac{\partial \mathbf{M}_1}{\partial t}, \mathbf{M}_2 \right\rangle.$$

Theorem 3.7. *Let* $\frac{\partial \alpha}{\partial t}$ *be inextensible according to Bishop frame. If* μ *is* $\mathbf{M}_2$ *Bishop spherical image of* α*, then,*

$$\begin{aligned}
&[\frac{\partial}{\partial s}[(\frac{k_1}{k_2 \kappa^{\mu}})(\mathsf{Y}_1 k_1 + \frac{\partial \mathsf{Y}_2}{\partial s}) + (\frac{1}{\kappa^{\mu}})(\mathsf{Y}_1 k_2 + \frac{\partial \mathsf{Y}_3}{\partial s})] \\
&- k_1[(\frac{1}{\kappa^{\mu}})\mathsf{k} - \frac{\partial}{\partial t}(\frac{k_1}{k_2 \kappa^{\mu}})] + k_2[(\frac{k_1}{k_2 \kappa^{\mu}})\mathsf{k} + \frac{\partial}{\partial t}(\frac{1}{\kappa^{\mu}})]] \\
= \; &[\frac{\partial}{\partial t}(\kappa^{\phi} k_2) - (\tau^{\phi} k_2)[(\frac{k_1}{k_2 \kappa^{\mu}})(\mathsf{Y}_1 k_2 + \frac{\partial \mathsf{Y}_3}{\partial s}) - (\frac{1}{\kappa^{\mu}})(\mathsf{Y}_1 k_1 + \frac{\partial \mathsf{Y}_2}{\partial s})]],
\end{aligned}$$

where $\mathsf{Y}_1, \mathsf{Y}_2, \mathsf{Y}_3$ *are smooth functions of time and arc length and*

$$\mathsf{k} = \left\langle \frac{\partial \mathbf{M}_1}{\partial t}, \mathbf{M}_2 \right\rangle.$$

Proof. We can write

$$\begin{aligned}
\frac{\partial}{\partial s}\frac{\partial \mathbf{N}^{\mu}}{\partial t} \; = \; &[\frac{\partial}{\partial s}[(\frac{k_1}{k_2 \kappa^{\mu}})(\mathsf{Y}_1 k_1 + \frac{\partial \mathsf{Y}_2}{\partial s}) + (\frac{1}{\kappa^{\mu}})(\mathsf{Y}_1 k_2 + \frac{\partial \mathsf{Y}_3}{\partial s})] \\
&- k_1[(\frac{1}{\kappa^{\mu}})\mathsf{k} - \frac{\partial}{\partial t}(\frac{k_1}{k_2 \kappa^{\mu}})] + k_2[(\frac{k_1}{k_2 \kappa^{\mu}})\mathsf{k} + \frac{\partial}{\partial t}(\frac{1}{\kappa^{\mu}})]]\mathbf{T} \\
&+ [k_1[(\frac{k_1}{k_2 \kappa^{\mu}})(\mathsf{Y}_1 k_1 + \frac{\partial \mathsf{Y}_2}{\partial s}) + (\frac{1}{\kappa^{\mu}})(\mathsf{Y}_1 k_2 + \frac{\partial \mathsf{Y}_3}{\partial s})] \\
&+ \frac{\partial}{\partial s}[(\frac{1}{\kappa^{\mu}})\mathsf{k} - \frac{\partial}{\partial t}(\frac{k_1}{k_2 \kappa^{\mu}})]]\mathbf{M}_1 + [k_2[(\frac{k_1}{k_2 \kappa^{\mu}})(\mathsf{Y}_1 k_1 + \frac{\partial \mathsf{Y}_2}{\partial s}) \\
&+ (\frac{1}{\kappa^{\mu}})(\mathsf{Y}_1 k_2 + \frac{\partial \mathsf{Y}_3}{\partial s})] - \frac{\partial}{\partial s}[(\frac{k_1}{k_2 \kappa^{\mu}})\mathsf{k} + \frac{\partial}{\partial t}(\frac{1}{\kappa^{\mu}})]]\mathbf{M}_2.
\end{aligned}$$

By a direct computation, we have

$$\frac{\partial}{\partial t}\frac{\partial}{\partial s}\mathbf{N}^{\mu} = [\frac{\partial}{\partial t}(\kappa^{\phi}k_2)-(\tau^{\phi}k_2)[(\frac{k_1}{k_2\kappa^{\mu}})(\mathrm{Y}_1k_2+\frac{\partial \mathrm{Y}_3}{\partial s})-(\frac{1}{\kappa^{\mu}})(\mathrm{Y}_1k_1+\frac{\partial \mathrm{Y}_2}{\partial s})]]\mathbf{T}$$
$$+[(\kappa^{\phi}k_2)(\mathrm{Y}_1k_1+\frac{\partial \mathrm{Y}_2}{\partial s})-\frac{\partial}{\partial t}(\tau^{\phi}k_2)\frac{1}{\kappa^{\mu}}-(\tau^{\phi}k_2)[\frac{\partial}{\partial t}(\frac{1}{\kappa^{\mu}})+(\frac{k_1}{k_2\kappa^{\mu}})\mathrm{k}]]\mathbf{M}_1$$
$$+[\frac{\partial}{\partial t}(\tau^{\phi}k_2)\frac{k_1}{k_2\kappa^{\mu}}+(\kappa^{\phi}k_2)(\mathrm{Y}_1k_2+\frac{\partial \mathrm{Y}_3}{\partial s})-(\tau^{\phi}k_2)[(\frac{1}{\kappa^{\mu}})\mathrm{k}-\frac{\partial}{\partial t}(\frac{k_1}{k_2\kappa^{\mu}})]]\mathbf{M}_2.$$

Combining above equations, we have theorem. Hence the proof is completed.

In the light of Theorem 3.7, we express the following corollary without proof:

Corollary 3.8.

$$[k_1[(\frac{k_1}{k_2\kappa^{\mu}})(\mathrm{Y}_1k_1+\frac{\partial \mathrm{Y}_2}{\partial s})+(\frac{1}{\kappa^{\mu}})(\mathrm{Y}_1k_2+\frac{\partial \mathrm{Y}_3}{\partial s})]+\frac{\partial}{\partial s}[(\frac{1}{\kappa^{\mu}})\mathrm{k}-\frac{\partial}{\partial t}(\frac{k_1}{k_2\kappa^{\mu}})]]$$
$$= [(\kappa^{\phi}k_2)(\mathrm{Y}_1k_1+\frac{\partial \mathrm{Y}_2}{\partial s})-\frac{\partial}{\partial t}(\tau^{\phi}k_2)\frac{1}{\kappa^{\mu}}-(\tau^{\phi}k_2)[\frac{\partial}{\partial t}(\frac{1}{\kappa^{\mu}})+(\frac{k_1}{k_2\kappa^{\mu}})\mathrm{k}]],$$

where $\mathrm{Y}_1, \mathrm{Y}_2, \mathrm{Y}_3$ *are smooth functions of time and arclength and*

$$\mathrm{k}=\left\langle \frac{\partial \mathbf{M}_1}{\partial t}, \mathbf{M}_2 \right\rangle.$$

Corollary 3.9.

$$[k_2[(\frac{k_1}{k_2\kappa^{\mu}})(\mathrm{Y}_1k_1+\frac{\partial \mathrm{Y}_2}{\partial s})+(\frac{1}{\kappa^{\mu}})(\mathrm{Y}_1k_2+\frac{\partial \mathrm{Y}_3}{\partial s})]-\frac{\partial}{\partial s}[(\frac{k_1}{k_2\kappa^{\mu}})\mathrm{k}+\frac{\partial}{\partial t}(\frac{1}{\kappa^{\mu}})]]$$
$$= [\frac{\partial}{\partial t}(\tau^{\phi}k_2)\frac{k_1}{k_2\kappa^{\mu}}+(\kappa^{\phi}k_2)(\mathrm{Y}_1k_2+\frac{\partial \mathrm{Y}_3}{\partial s})-(\tau^{\phi}k_2)[(\frac{1}{\kappa^{\mu}})\mathrm{k}-\frac{\partial}{\partial t}(\frac{k_1}{k_2\kappa^{\mu}})]],$$

where $\mathrm{Y}_1, \mathrm{Y}_2, \mathrm{Y}_3$ *are smooth functions of time and arclength and*

$$\mathrm{k}=\left\langle \frac{\partial \mathbf{M}_1}{\partial t}, \mathbf{M}_2 \right\rangle.$$

Theorem 3.10. *Let* $\frac{\partial \alpha}{\partial t}$ *be inextensible according to Bishop frame. If* μ *is* $\mathbf{M}_2$ *Bishop spherical image of* α*, then,*

$$[\frac{\partial}{\partial s}[(\frac{k_1}{k_2\kappa^{\mu}})(\mathrm{Y}_1k_2+\frac{\partial \mathrm{Y}_3}{\partial s})-(\frac{1}{\kappa^{\mu}})(\mathrm{Y}_1k_1+\frac{\partial \mathrm{Y}_2}{\partial s})]$$
$$-k_1[\frac{\partial}{\partial t}(\frac{1}{\kappa^{\mu}})+(\frac{k_1}{k_2\kappa^{\mu}})\mathrm{k}]-k_2[(\frac{1}{\kappa^{\mu}})\mathrm{k}-\frac{\partial}{\partial t}(\frac{k_1}{k_2\kappa^{\mu}})]]$$
$$= (\tau^{\mu}k_2)[(\frac{k_1}{k_2\kappa^{\mu}})(\mathrm{Y}_1k_2+\frac{\partial \mathrm{Y}_3}{\partial s})-(\frac{1}{\kappa^{\mu}})(\mathrm{Y}_1k_1+\frac{\partial \mathrm{Y}_2}{\partial s})],$$

where $\mathrm{Y}_1, \mathrm{Y}_2, \mathrm{Y}_3$ *are smooth functions of time and arclength and*

$$\mathsf{k} = \left\langle \frac{\partial \mathbf{M}_1}{\partial t}, \mathbf{M}_2 \right\rangle.$$

Proof. Using Theorem 3.4, we have

$$\begin{aligned}
\frac{\partial}{\partial s}\frac{\partial \mathbf{B}^{\mu}}{\partial t} &= [\frac{\partial}{\partial s}[(\frac{k_1}{k_2\kappa^{\mu}})(\mathsf{Y}_1 k_2 + \frac{\partial \mathsf{Y}_3}{\partial s}) - (\frac{1}{\kappa^{\mu}})(\mathsf{Y}_1 k_1 + \frac{\partial \mathsf{Y}_2}{\partial s})] \\
&\quad - k_1[\frac{\partial}{\partial t}(\frac{1}{\kappa^{\mu}}) + (\frac{k_1}{k_2\kappa^{\mu}})\mathsf{k}] - k_2[(\frac{1}{\kappa^{\mu}})\mathsf{k} - \frac{\partial}{\partial t}(\frac{k_1}{k_2\kappa^{\mu}})]]\mathbf{T} \\
&\quad + [\frac{\partial}{\partial s}[\frac{\partial}{\partial t}(\frac{1}{\kappa^{\mu}}) + (\frac{k_1}{k_2\kappa^{\mu}})\mathsf{k}] + k_1[(\frac{k_1}{k_2\kappa^{\mu}})(\mathsf{Y}_1 k_2 + \frac{\partial \mathsf{Y}_3}{\partial s}) \\
&\quad - (\frac{1}{\kappa^{\mu}})(\mathsf{Y}_1 k_1 + \frac{\partial \mathsf{Y}_2}{\partial s})]]\mathbf{M}_1 + [\frac{\partial}{\partial s}[(\frac{1}{\kappa^{\mu}})\mathsf{k} - \frac{\partial}{\partial t}(\frac{k_1}{k_2\kappa^{\mu}})] \\
&\quad + k_2[(\frac{k_1}{k_2\kappa^{\mu}})(\mathsf{Y}_1 k_2 + \frac{\partial \mathsf{Y}_3}{\partial s}) - (\frac{1}{\kappa^{\mu}})(\mathsf{Y}_1 k_1 + \frac{\partial \mathsf{Y}_2}{\partial s})]\mathbf{M}_2,
\end{aligned}$$

or, equivalently

$$\begin{aligned}
\frac{\partial}{\partial t}\frac{\partial}{\partial s}\mathbf{B}^{\mu} &= (\tau^{\mu} k_2)[(\frac{k_1}{k_2\kappa^{\mu}})(\mathsf{Y}_1 k_2 + \frac{\partial \mathsf{Y}_3}{\partial s}) - (\frac{1}{\kappa^{\mu}})(\mathsf{Y}_1 k_1 + \frac{\partial \mathsf{Y}_2}{\partial s})]\mathbf{T} \\
&\quad + [\frac{\partial}{\partial t}(\tau^{\mu} k_2)\frac{1}{\kappa^{\mu}} + (\tau^{\mu} k_2)[\frac{\partial}{\partial t}(\frac{1}{\kappa^{\mu}}) + (\frac{k_1}{k_2\kappa^{\mu}})\mathsf{k}]]\mathbf{M}_1 \\
&\quad + [(\tau^{\mu} k_2)[(\frac{1}{\kappa^{\mu}})\mathsf{k} - \frac{\partial}{\partial t}(\frac{k_1}{k_2\kappa^{\mu}})] - \frac{\partial}{\partial t}(\tau^{\mu} k_2)\frac{k_1}{k_2\kappa^{\mu}}]\mathbf{M}_2.
\end{aligned}$$

Thus, we obtain the theorem.

In the light of Theorem 3.10, we express the following corollary without proof:

Corollary 3.11.

$$\begin{aligned}
&\frac{\partial}{\partial s}[\frac{\partial}{\partial t}(\frac{1}{\kappa^{\mu}}) + (\frac{k_1}{k_2\kappa^{\mu}})\mathsf{k}] + k_1[(\frac{k_1}{k_2\kappa^{\mu}})(\mathsf{Y}_1 k_2 + \frac{\partial \mathsf{Y}_3}{\partial s}) - (\frac{1}{\kappa^{\mu}})(\mathsf{Y}_1 k_1 + \frac{\partial \mathsf{Y}_2}{\partial s})]] \\
&= [\frac{\partial}{\partial t}(\tau^{\mu} k_2)\frac{1}{\kappa^{\mu}} + (\tau^{\mu} k_2)[\frac{\partial}{\partial t}(\frac{1}{\kappa^{\mu}}) + (\frac{k_1}{k_2\kappa^{\mu}})\mathsf{k}]],
\end{aligned}$$

where $\mathsf{Y}_1, \mathsf{Y}_2, \mathsf{Y}_3$ *are smooth functions of time and arclength and*

$$\mathsf{k} = \left\langle \frac{\partial \mathbf{M}_1}{\partial t}, \mathbf{M}_2 \right\rangle.$$

Corollary 3.12.

$$\begin{aligned}
&(\tau^{\mu} k_2)[(\frac{1}{\kappa^{\mu}})\mathsf{k} - \frac{\partial}{\partial t}(\frac{k_1}{k_2\kappa^{\mu}})] - \frac{\partial}{\partial t}(\tau^{\mu} k_2)\frac{k_1}{k_2\kappa^{\mu}}] \\
&= [\frac{\partial}{\partial s}[(\frac{1}{\kappa^{\mu}})\mathsf{k} - \frac{\partial}{\partial t}(\frac{k_1}{k_2\kappa^{\mu}})] + k_2[(\frac{k_1}{k_2\kappa^{\mu}})(\mathsf{Y}_1 k_2 + \frac{\partial \mathsf{Y}_3}{\partial s}) - (\frac{1}{\kappa^{\mu}})(\mathsf{Y}_1 k_1 + \frac{\partial \mathsf{Y}_2}{\partial s})],
\end{aligned}$$

where Y_1, Y_2, Y_3 *are smooth functions of time and arclength and*

$$k = \left\langle \frac{\partial \mathbf{M}_1}{\partial t}, \mathbf{M}_2 \right\rangle.$$

For constant coefficient Y_1, Y_2, Y_3, we have

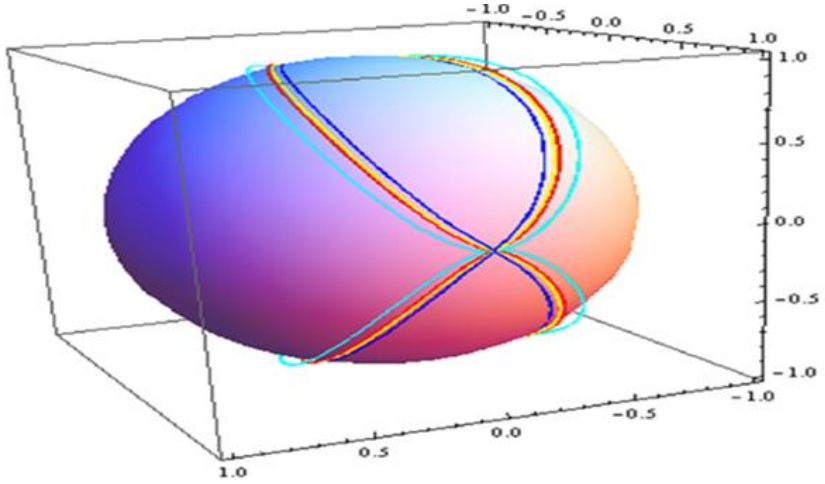

Figure 1: $\mathbf{M}_2$ *Bishop spherical image is illustrated colour Red, Blue, Purple, Orange, Magenta, Cyan, Green at the time* $t = 1$, $t = 1.2$, $t = 1.4$, $t = 1.6$, $t = 1.8$, $t = 2$, $t = 2.2$, *respectively.*

REFERENCES

[1] L. R. Bishop: There is More Than One Way to Frame a Curve, Amer. Math. Monthly 82 (3) (1975) 246-251.

[2] M. do Carmo: Differential Geometry of Curves and Surfaces, Prentice-Hall, Englewood Cliffs, 1976.

[3] I. Dimitric: Submanifolds of E^m with harmonic mean curvature vector, Bull. Inst. Math. Acad. Sinica 20 (1992), 53--65.

[4] J. Eells and L. Lemaire: A report on harmonic maps, Bull. London Math. Soc. 10 (1978), 1--68.

[5] J. Eells and J. H. Sampson: Harmonic mappings of Riemannian manifolds, Amer. J. Math. 86 (1964), 109--160.

[6] M. Gage, R.S. Hamilton: The heat equation shrinking convex plane curves, J. Differential Geom. 23 (1986), 69--96.

[7] T. Körpınar, V. Asil, S. Baş: On Characterization Inextensible flows of Curves According to Bishop frame in E^3, Revista Notas de Matematica, 7 (2011), 37-45.

[8] T. Körpınar and E. Turhan: Integral Equations of Biharmonic Constant Π_1 − Slope Curves according to New Type-2 Bishop Frame in Sol Space SOL^3, Bol. Soc. Paran. Mat., 31 2 (2013), 205--212.

[9] D. Y. Kwon, F.C. Park: Evolution of inelastic plane curves, Appl. Math. Lett. 12 (1999), 115-119.

[10] DY. Kwon, FC. Park, DP Chi: Inextensible flows of curves and developable surfaces, Appl. Math. Lett. 18 (2005), 1156-1162.

[11] T. Lamm: Biharmonic map heat flow into manifolds of nonpositive curvature, Calc. Var. 22 (2005), 421-445.

[12] D. J. Struik: Lectures on Classical Differential Geometry, Dover, New-York, 1988.

[13] E. Turhan and T. Körpınar: On Characterization Of Timelike Horizontal Biharmonic Curves In The Lorentzian Heisenberg Group $Heis^3$, Zeitschrift für Naturforschung A- A Journal of Physical Sciences 65a (2010), 641-648.

[14] E. Turhan and T. Körpınar: Parametric equations of general helices in the sol space, Bol. Soc. Paran. Mat., 31 (1) (2013), 99--104.

[15] D.J. Unger: Developable surfaces in elastoplastic fracture mechanics, Int. J. Fract. 50 (1991) 33--38.

[16] S. Yılmaz, E. Özyılmaz and M. Turgut: New spherical indicatrices and their characterizations, An. S t. Univ. Ovidius Constanta, 18(2) 2010, 337-354.

[17] S. Yılmaz and M. Turgut: A new version of Bishop frame and an application to spherical images, J. Math. Anal. Appl., 371 (2010), 764-776.

UNCONSCIOUS ANTIBIOTIC USE AND BACTERIAL ANTIBIOTIC RESISTANCE PROBLEM

B. Çetin[1], M.Konak-Usal[1]

[1]*Department of Food Engineering, Faculty of Engineering, Kirklareli, Turkey*

E-mail: bayram.cetin@klu.edu.tr

Abstract

Antibiotics widely used in the field of human and veterinary medicine can reach the receiving environment in different ways. It is known that antibiotic residues are toxic at high concentrations. Antibiotics in low concentrations cause bacteria to develop resistance to antibiotics. As a result, bacterial strains resistant to antibiotics are developing, which poses a significant risk to human health and the ecosystem.

Mortality due to infections in which a resistant bacterium is the cause is twice as much as infections in which a susceptible bacterium is the causative agent. In addition, antibiotic resistance leads to the use of more toxic, broader spectrum or more expensive antibiotics in patients. The use of bacteria in animal husbandry as well as human use should also be considered in the development of antibiotic resistance. Because of this, the identification of low amounts of antibiotics in animal-derived foods is very important. Knowing the antibiotic resistance mechanisms in bacteria and the antibiotics that best determine these resistance mechanisms make it easier to determine antibiotic resistance.

Attention should be paid to the identification of the correct natural bacteria and to the extent that they are as low as possible in order to detect known natural resistance or susceptibility in bacteria. Determination of antimicrobial resistance / susceptibility of bacteria was carried out by Bauer et al. (1966) has been widely used for antibiotic disc diffusion. Especially in dairy enterprises, while milk is being collected as raw material, enterprises try to determine the presence of antibiotics qualitatively by using antibiotic detection kits. The amount of antibiotic residues can be quantitatively determined by reliable methods such as LS-MS / MS, especially in meat and milk. Attention should be paid to the identification of the correct natural bacteria and to the extent that they are as low as possible in order to detect known natural resistance or susceptibility in bacteria. This is possible with molecular methods.

Key words: antibiotics, antibiotic resistance

1. INTRODUCTION

Antibiotics are the most active chemotherapeutics among drugs; they exert their therapeutic effect by antagonizing the growth of bacteria. Since 1910 many antibiotics have been developed with different mechanisms of action including:

- inhibition of bacteria‘s cell wall synthesis; this class of antibiotics includes vancomycin and β-lactam antibiotics such as penicillins, cephalosporins and carbapenems,
- inhibition of protein synthesis including tetracyclines, aminoglycosides, macrolides and chloramphenicol
- DNA synthesis inhibitors such as fluoroquinolones and sulfonamides that inhibit folic acid synthesis [1].

Antibiotics are used in the treatment of a variety of diseases in medicine to combat bacterial infections. They are also used for the healing at animal and plant diseases and used as protective at animal food [2].

1.1. Common Antibiotics

Table 1. Some common antibiotics [3]

Aminoglycosides	**Carbapenems**	**Broad spectrum Penicillins**	**Broad-spectrum cephalosporins**	**Fluoroquinolones**	**Linezolid**
• Kanamycin • Neomycin • Apramycin • Amikacin • Arbekacin • Bekanamycin • Dibekacin • Tobramycin • Streptomycin • Spektinomycin • Higromycin B • Paromomycin • Gentamicin • Netilmicin • Sisomicin • İzepamicin • Verdamicin • Astromicin	• İmipenem • Meropenem • Ertapenem • Doripenem	• Natural penicillins • Aminopenisilins • Carboxypheni cillins • Ureidopenicillins • Penicillinase-resistant penicillins			

Aminoglycosides are used in veterinary medicines for the treatment or protection of bacterial infections, especially in mammals and animal farms, such as breast inflammation. They are sometimes used as food supplements at high rates or in drinking water to prevent diseases. Carbapenems are the group with the broadest spectrum of effect in beta-lactams. The carbapenem group antibiotics used today are imipenem, meropenem, ertapenem and doripenem. Carbapenems are among the first treatment options for infections caused by multidrug resistant Gram-negative bacteria because of their wide range of antibacterial spectra, rapid passage through bacterial membranes, resistance to AmpC and ESBL enzymes [3].

Penicillins are derivatives of a 6-aminopenisilanic acid (6-APA) containing a double-ring resulting from the incorporation of β-lactam and thiazolidine rings. Penicillins, besides their potent bactericidal effects, are relatively low-toxic and frequently used natural or semi-synthetic antibiotics. Penicillins are the most rapidly developing antibiotic group, due to the introduction of new derivatives in the first place and at short intervals.

Penicillins are examined in five groups;

• Natural penicillins; Penicillin species are the most effective in gram positive microorganisms.

• Aminopenisilins; This group includes ampicillin, amoxicillin and bakampicillin.

• Carboxypenicillins; The carbenicillin and ticarcillin in this group are penicillin species which are effective on many aerop gram negative rods including *P. aeruginosa*, but which are ineffective in *Klebsiella* species.

• Ureidopenicillins; In this group are azlosilin, mezlosilin and piperacillin. They can only be used parenterally.

Penicillinase-resistant penicillins; It is an β-lactam antibiotic developed for staphylococci producing penicillinase-degrading penicillin. These are oxacillin, cloxacillin, dicloxacillin and flucloxacillin, so called methicillin, nafcillin and isoxazolyl penicillins [4].

Cephalosporins, like all other β-lactam antibiotics, act by disrupting bacterial cell wall construction. The goal of all beta-lactam antibiotics is to inhibit penicillin-binding proteins (PBPs) involved in the transpeptidation phase of cell wall synthesis. As the transpeptidation step does not occur, the bacterium wall cannot be fully synthesized and the bacteria undergoes lysis due to internal pressure. Cephalosporins are bactericidal agents [5].

Fluoroquinolones have a bactericidal effect in the bacterium by inhibiting the DNA gyrase enzyme, which allows the bacterial DNA to fit into the cell. Bacteria that encounter quinolone lose their ability to cleave,

extend to the length and eventually die. Chromosomal mutations are the most common role in resistance against quinolones [6].

Linezolid, the first of the oxazolidinone class antibiotics, is an agent of bacterial protein synthesis inhibitor. Resistant to other antibiotics, many gram-positive active in the microorganism [20].

1.2.Antibacterial Resistance

Bacteria have a remarkable genetic plasticity that allows them to respond to a wide array of environmental threats, including the presence of antibiotic molecules that may jeopardize their existence. As mentioned, bacteria sharing the same ecological niche with antimicrobial-producing organisms have evolved ancient mechanisms to withstand the effect of the harmful antibiotic molecule and, consequently, their intrinsic resistance permits them to thrive in its presence. From an evolutionary perspective, bacteria use two major genetic strategies to adapt to the antibiotic "attack", mutations in gene(s) often associated with the mechanism of action of the compound, and acquisition of foreign DNA coding for resistance determinants through horizontal gene transfer [19].

The duration of treatment of patients infected with an antibiotic-resistant bacterium is longer than those of those infected with a susceptible bacterium. The mortality rate due to infections caused by a resistant bacterium is two times higher than that of a susceptible bacterium. In addition, antibiotic resistance leads to the use of antibiotics that are more toxic, wider spectrum, or more expensive in patients. In the development of antibiotic resistance of bacteria, human use as well as animal use are considered. Therefore, the determination of low amount of antibiotics in foods of animal origin is very important [7].

Antibiotic resistance can be defined in three parts as intrinsic (natural), environmental and conditional resistance and acquired resistance (extrinsic).

Intrinsic (Natural): These bacteria do not contain either the target of the drug or the drug does not act due to its specific cell properties. For example, gram negative bacteria are naturally resistant to vancomycin because the drug cannot pass through the outer membrane.

Resistance to Environment and Conditions: Indicates the difference between in vitro and in vivo activity of the antibiotic. Antibiotics, which are effective in microorganisms in laboratories, may not show effect on human body due to various environmental conditions. Some of these conditions; oxygen pressure and pH changes in the tissue or the drug can not reach the infection site conditions such as. For example, first-generation cefolosporins cannot be used to treat meningitis because they cannot cross the blood-brain

barrier and therefore cannot be used to treat meningitis. Aminoglycosides likewise lose their effectiveness in vivo at low pH or anaerobic conditions.

Acquired Resistance: It represents the resistance gained later. The antibiotic is effective on the microorganism when the antibiotic is given to this type of resistance, but resistance to antibiotic substance develops in the bacterial population during contact time or during repeated treatments. This resistance is caused by mutations in the DNA or by a new DNA from the bacteria. Mutations usually occur in chromosomal DNA. It is known that there may be mutations in genes found on plasmids or transposons [8].

In recent years, it has been reported that some transposon or plasmids contain genetic structures that allow the acquisition of new genes called integrons. These elements have been found to play the role of a bacterium in a very short period of time when multiple antibiotics become multiple resistant [7].

Resistance mechanisms due to transposon:

- Forming enzymes that break down antibiotics.
- Resistance mechanism causing cell wall permeability to deteriorate.
- Resistance mechanism that causes the drug to be pumped out of the cell.
- Mechanism to reduce the removal of the drug from the external environment.
- Mechanism to reduce the binding of the drug to its target within the cell.

A bacterium can gain resistance to antibiotics with different mechanisms of action using several of these mechanisms simultaneously [8].

1.2.1. Frequent Resistance Microorganisms

Expanded-spectrum beta-lactamase-forming microorganisms (ESBL) is the most clinically important group in among the beta-lactamases. ESBLs are formed by the introduction of different amino acids instead of one of the amino acids in the molecular structure of the parent enzyme. This change in the structure of the enzyme leads to a new modeling in the active site where the enzyme-substrate relationship is achieved, allowing broad-spectrum cephalosporins and aztreonamine to enter the spectrum of action of these enzymes. Microbiologically, oxyimino is defined as enzymes that can hydrolyze cephalosporins and can be inhibited by clavulanic acid. ESBLs can be found in many gram negative bacteria such as *K. pneumoniae*, *Escherichia coli*, *Enterobacter* spp., *Salmonella* spp., *Proteus* spp., *Citrobacter* spp. One of the problems caused by ESBL expressing bacteria is the resistance problem. Gram-negative bacteria found

to synthesize one of these enzymes should be considered resistant to all broad-spectrum cephalosporins and aztreonama. Resistance to quinolone, tetracycline, chloramphenicol and trimethoprim / sulfomethoxazole can be found simultaneously in ESBL-borne bacteria. *Acinetobacter* infections have started to cause infections in the hospital environment, especially in intensive care units. *Acinetobacter* species can be easily colonized in patients due to their high resistance to antibiotics and long-term survival in hospital environment. In particular, hospital-acquired pneumonia can be seen as a causative agent in urinary tract infections, bacteremia, meningitis and wound infections. *Pseudomonas aeruginosa;* due to its outer membrane in the structure of its lipopolysaccharide (LPS) structure, it is resistant to many antibiotics. They tend to form biofilm in air and waterproof properties, which prevent entry into the cells, on their surfaces, against antibiotic concentrations in therapeutic doses. In addition, as they live in the environment in which they live naturally related to bacilli, actinomyces, molds and yeasts, it is natural that they are resistant to the naturally occurring antibacterials in their environment. They also contain antibiotic resistant plasmids. Only a few antibiotics are effective against *Pseudomonas,* which are flouroquinolones, gentamicin and imipenem [9].

Methicillin is known as a semisynthetic penicillin which is the first to be used in penicillin group antibiotics resistant to hydrolysis of staphylococcal beta-lactamase enzyme. With the introduction of methicillin, great success has been gained in the treatment of staphylococcal infections. However, it was reported that the first methylin resistant *Staphylococcus aureus* (MRSA) isolates were isolated in England in 1961. The most important factor that protects the severity of MRSA infections and complicates the treatment is the increased resistance to methicillin as well as the multiple antibiotic resistance that develops in the strains. In the period from the first reporting of MRSA to the present day, isolates have become widespread all over the world, and the resistance against penicillin has developed in the form of multiple resistances. MRSA strains that are resistant to 3 or more antibiotics are called multi-resistant strains and tend to be more virulent in nature than other methicillin-sensitive *S. aureus* (MRSA) strains. MRSA is generally a multidrug-resistant pathogen and has been resistant to all current beta-lactam group antibiotics including penicillins, cephalosporins, carbapenems and their derivatives. In addition to these, it has been determined that it also resists resistance to linkozamides, macrolides and aminoglycosides [10].

Another common resistance group is *Enterococci. Enterococci* have high resistance to penicillin and aminoglycosides and the development of vancomycin resistance in enterococci is a problem in the treatment of infections caused by these microorganisms [11].

1.3.Antibiogram

The antibiogram is the process of deciding which antibiotic will be used as a result of examining the sample from the infection of bacteria in the human body. Antibiotic test is used to determine which antibiotics are resistant to bacteria and treatment is started after appropriate antibiotics are determined. In determining antibiotic resistance / susceptibility of bacteria, Bauer et al. (1966) recommended by the antibiotic disc diffusion method is widely used [12]. In order to determine the natural resistance or sensitivity known in bacteria, attention should be given to the identification of the identification as much as possible to the serotypes. This is possible by molecular methods such as PCR. A correct identification helps to know antibiotics that a bacterium is naturally resistant and cannot be resistant at all. *Klebsiella* strains, for example, due to chromosomal beta-lactamases; *Enterobacter*, *Serratia* and *Citrobacter freundii* strains include aminopenicillins, combinations of aminopenicillins with beta-lactamase inhibitors, 1st generation cephalosporins and cefoxitin; *Serratia* and *Proteus vulgaris* 1st generation cephalosporins and cefuroxime; *Stenotrophomonas maltophilia* to carbapenems; *Bacillus* strains are naturally resistant to cephalotine and cefotaxis. Antibiotic susceptibility tests should be regulated to determine resistance mechanisms and the results should be evaluated together with the resistance mechanisms. The correct interpretation of antibiotic susceptibility tests is possible by knowing the biochemical structures, mechanisms of action, resistance mechanisms of antibiotics [13].

1.4. Unconcusious Antbiotic Use

Due to misuse of antibiotics over the last decade, deaths due to hospital infections have been observed especially in intensive care patients and infants [14]. Unconscious and unnecessary use of antibiotics continues to pose a risk because the legal practices related to the use of antibiotics in our country are not yet sufficient. In animals with unconscious antimicrobial drugs, there is a risk of not only the resistance of pathogens in animals, but also the risk of being transferred from animals to humans [15]. In addition, the use of antibiotics as inappropriate growth in animal nutrition is a selective agent in the emergence of resistant *Enterococcus* species [16].

The most reliable information on the production and use of antibiotics belongs to the US and EU Member States. 70% (15-25 thousand tons) of antibiotics produced in the United States are used for non-therapeutic purposes in animal husbandry. In the US, the use of antibiotics in the field of animal husbandry is 8 times the consumption in medicine. There are no healthy data on the use of veterinary drugs in our country. Due to the fact that the animals are given more than the prescribed doses and especially the animals administered

to the slaughter without adhering to the statutory waiting period of the drug, as a result of which the antibiotics are not completely metabolized or excreted completely from the body, the animals tissues and organs and the animal foods obtained from them can have antibiotic residues [17]

A few examples of the negative effects of antibiotic residues on humans are given; Antibiotics in which enrofloxacin is a member of the quinolone group increase antibiotic resistance in food pathogens; the effects of penicillins such as redness, urticaria and advanced anaphylactic shock, chloramphenicol leading to irreversible blood anomalies and especially teratogenic effects of nitrofuran, nephrotoxicity of aminoglycosides and formation of thyroid hyperplasia of sulfamethasine can be considered [18].

2. CONCLUSION

Antibiotics should not be used without the advice of a doctor. Besides the safety of raw materials, the presence of antibiotic residues in foods such as meat and milk should be investigated for public health. Microbial flora should be determined by performing field studies in our country in regional scale and antibiotic resistance of isolated bacteria should be investigated. In addition, an antibiogram test should be performed to isolates and appropriate antibiotics should be used in disease cases. Thus, both unnecessary and unconscious antibiotic use and prevention of microbial resistance will be prevented.

REFERENCES

[1] Jumaa, S., Karaman, R., Antibiotics, Nova Science Publishers, ISBN: 978-1-63463-828-9, 2015.

[2] Ammor, M. S., Florez, A. B., Mayo, B., 2007. Antibiotic resistance in non-enterococcal lactic acid bacteria and bifidobacteria, Food Microbiology, 24, 559-570, 2007.

[3] Bulut A., *Enterobacteriaceae* üyelerinde karbapenem direnci ve dirençten sorumlu enzimlerin varlığının araştırılması, Yüksek Lisans Tezi, Afyonkarahisar, Tez No: 2014-018, 2014.

[4] Üstün Z., Penisilinaza dirençli penisilinlerin iyonlaşma sabitlerinin ters faz sıvı kromatografi yöntemiyle tayini, Yüksek Lisans Tezi, Isparta, 2014

[5] İpekçi S., Bazı sefalosporin grubu antibiyotiklerin elektrokimyasal karakterizasyonu ve voltametrik tayinleri, Yüksek Lisans Tezi, Isparta, 2014

[6] Deniz İ., Tigesiklinin tek başına ve florokinolonlarla kombinasyonunun ın vıtro etkinliği, 2008

[7] Beyazıt H., Solunumsal yoğun bakım ünitesinde izole edilen mikroorganizmalar ve antibiyotik direnç durumları, 2009

[8] Gülhan M., Hastanemiz enfeksiyon hastalıkları ve klinik mikrobiyoloji laboratuvarına gelen örneklerden izole edilen non-fermentatif bakterilerin antibiyotik duyarlılıklarının belirlenmesi, 2013

[9] Şahin C., Sığırların klinik mastitislerinden *Pseudomonas aeruginosa*'nın izolasyonu ve antibiyotiklere duyarlılıkları, 2015

[10] Ektik N., Balıkesir ilinde süt ve süt ürünlerindeki metisilin dirençli staphylococcus aureus'un prevalansı ve antibiyotik dirençliliği, Yükseklisans tezi, 2015.

[11] Erçal B., Vankomisine dirençli Enterokokların moleküler epidemiyolojisi. 2011

[12] A.W. Bauer, W.M.M. Kirby, J.C. Sherris and M. Turk. Antibiotic susceptibility testing by a standardized single disk method. American Journal of Clinical Pathology, 45, 493-496 (1996).

[13] Kaygusuz A., Hastanede sık rastlanılan antibiyogram örnekleri, 2000

[14] Mathur, S., Sıngh, R., 2005. Antibiotic resistance in food lactic acid bacteria-a review. International Journal of Food Microbiology, 105, 281-295.

[15] Gülay Z., Antibiyotik Duyarlılık Testlerinin Yorumu, Toraks Dergisi, 1,75-85, 2003.

[16] Cocconcellı, P., S.; Cattıvellı, D.; Gazzola, S.; 2003. Gene transfer of vankomisin and tetracycline resistances among *Enterococcs faecalis* during cheese and sausage fermentations. International Journal of Food Microbiology, 88, 315-323, 2003.

[17] Taşçı, F., Canbey, S.H., Gıda amaçlı yetiştirilen hayvanlarda antibiyotik kullanımının halk sağlığı üzerine etkileri, Göller Bölgesi Aylık Hakemli Ekonomi ve Kültür Dergisi Ayrıntı, 31-36, 2016.

[18] Yıbar, A., Soyutemiz, E., Gıda değeri olan hayvanlarda antibiyotik kullanımı ve muhtemel kalıntı riski, Atatürk Üniversitesi Vet. Bil. Derg. 8, 97-104, 2013.

[19] Munita, J.M., Arias, C.A., Mechanisms of Antibiotic Resistance, Microbiol Spectr., 4,10.,2016.

[20] Acar, M., Somer, A., Salman, N., Yeni antibiyotikler, Çocuk Dergisi, 15, 99-103, 2015.

MOLECULAR METHODS USED IN MICROORGANISM DEFINITION

M. Konak-Usal[1], B. Çetin[1]

[1]*Department of Food Engineering, Faculty of Engineering, Kırklareli University, Turkey*

E-mail: mervekonak@klu.edu.tr

Abstract

Molecular identification methods are one of the most important innovations in the field of microbiology of developing technology. The addition of a new molecule to molecular identification techniques day by day is of great benefit to scientific studies carried out for different purposes. Molecular methods in the field of food; It can be used in the detection of target microorganism in food, in the determination of microorganism numbers, sensitivity and shortness of isolation and identification of microorganisms, characterization of suspicious isolate in food microbiology due to pathogenicity.

The available conventional methods used for detection of microbes in foods are time consuming and unable to analyze new organisms, thus many food analyses need rapid detection approaches. Rapid detection approaches can be classified into nucleic-acid sequence based techniques (like polymerase chain reaction (PCR), multiplex-PCR, real-time PCR, loop mediated isothermal amplification, nucleic-acid sequence based amplification and DNA microarrays), biosensor based technology (like optical biosensors, electrochemical biosensors, mass based biosensors and biochemical sensors) and immunological based methods (like lateral flow immunoassay and ELISA (enzyme-linked immunosorbent assay)).

The most common uses of nucleic acid-based techniques are; colony (DNA) hybridization technique, PCR (Polymerase chain reaction) technique, ribotyping technique and 16S rRNA techniques. The most important advantages of nucleic acid-based methods, when compared to conventional methods, the accuracy is high because it is possible to get results in a short time, the need for living cells is not needed (Especially in order to show the source of contamination in hygiene controls), the damaged cells can be detected and they are very specific techniques.

Keywords: Molecular methods, Microorganisms, PCR

1. INTRODUCTION

Foodborne pathogenic microorganisms cause disease, death and serious economic losses, and can cause serious public health problems that can reach epidemics by contaminating foods at any stage of the process, from the production of foodstuffs to production. As a result of the release of contaminated foodstuffs, pathogenic microorganisms and toxins show signs of intoxication such as nausea, vomiting and diarrhea after 6-7 hours by acting on intestines. Foodborne infections are mostly animal origin (Meat and meat products, milk and milk products, etc.) and vegetable food origin. Infants, children, elderly, immunosuppressive people are more vulnerable to these diseases [1]. It has been predicted that foodborne infections have increased especially in recent years and this is due to factors such as globalization of food industry, international mobility, change in people's life and eating habits, environmental pollution and climate change, and changes in microorganism populations [2]. Some foodborne pathogen microorganisms and their infections are seemed at Table 1.

For this reason, microbiological quality control programs are becoming more and more important in all food chains from production to consumption in order to prevent foodborne infections. Considering the speed of mobility in the export and import of foods in the developing world conjuncture, it is of great importance that the analytical methods to be used in these control programs are fast and reliable, as well as the amount of contamination of the pathogen microorganism. The most important points in limiting food-borne microbial diseases are the identification of the agent at the species level in the shortest possible time from the relevant foodstuff and the accurate determination of the low amounts of microbial populations. It is extremely important to identify these pathogenic microorganisms with accurate, current, and reproducible techniques, which can often have a minimal infective dose of 10 bacteria [3].

Molecular identification methods are one of the most important innovations in developing microbiology. Adding a new one to the molecular identification techniques every day is of great benefit to the scientific studies carried out for different purposes. Although the most important factors affecting the widespread use of these methods are cost and experienced personnel, these methods, which have its own advantages and disadvantages, are widely used all over the world. In this context, scientific researches have gained momentum in our country in recent years. Molecular identification methods most commonly used in studies in Turkey are PFGE (Pulsed Field Gel Electrophoresis), PCR (Polymerase Chain Reaction) and the 16S rDNA sequence analysis and a new molecular technique is added to them every day [1].

Table 1. Some foodborne pathogen microorganisms and their infections [4]

Name of microorganism	Infections
• *Salmonella typhi, Salmonella paratyphi*	• Typhoid, paratyphoid
• *Shigella dysenteriae*	• Shigellozis (Bacillary dysentery)
• *Vibrio cholera*	• Cholera
• Hepatit A virus	• Infectious hepatitis (Hepatit A)
• *Brucella melitensis*	• Brucellosis (Maltese fever)
• Polio virus	• Poliomyelitis (Polio)
• *Escherichia coli*	• Diarrhea
• *Listeria monocytogenes*	• Listeriosis
• *Coxiella burnetii*	• Q-fever
• *Clostridium botulinum*	• Botulism

1.1.PCR(Polymerase Chain Reaction)

PCR, a molecular biology technique developed relatively recently that is useful for the microbiological diagnosis of infections, is based on the amplification and subsequent detection of bacterial deoxyribonucleic acid (DNA) in a biological sample. DNA is a polymer of nucleotides (Polynucleotide), each of which consists of a phosphate group associated with a sugar (Deoxyribose) that is linked to a nitrogenous base in a double helix structure. Four bases are found in DNA: adenine, thymine, cytosine, and guanine. A strand of DNA is formed by the ordered repetition of these nucleotides. The nitrogenous bases form complementary pairs: adenine associates with thymine and guanine with cytosine. The second DNA strand is therefore complementary to the first, and the paired nitrogenous bases are linked through hydrogen bonds to form base pairs. The order of succession of these four nucleotides throughout the genome is specific to each individual and forms the genetic code that is the basis of protein synthesis. At each cell division, the double-stranded DNA molecule is replicated into two doublestranded daughter DNA molecules. During replication, the double helix is first denatured by breaking the hydrogen bonds between the DNA strands. A replication fork then forms, resulting in two distinct single-stranded DNA molecules. Each of these strands is copied by the action of DNA polymerases, which associate the complementary nucleotide to each base to form two new double-stranded DNA molecules identical to the original molecule [5-8].

Many of the DNA-based techniques currently used (Gene cloning, DNA sequencing, and studies with genetically modified microorganisms) are based on PCR. The substances required for gene replication by PCR are target DNA, deoxyribonucleotides (dATP, dCTP, dGTP, dTTP and dUTP), DNA polymerase enzyme (Taq polymerase), gene specific or general primers and the appropriate PCR buffer necessary for the reaction to take place (Table 2).

Table 2. Main components used in PCR [9]

Main components used in PCR
Target DNA or RNA (templeyt)
taq DNA polymeras enzyme
Primers,
Deoxyribonucleotides,
Buffer water,
pH,
Mg+2 ions

Principle of technique; these substances are placed in the same ambient together with the target DNA and homogeneously mixed and placed in the PCR instrument to replicate the target DNA. The PCR reaction takes place in three steps. These are respectively; target DNA double chain opening (Denaturation; 30 to 90 seconds at 94 ˚C), binding of the primer (Annealing; After this temperature cycle is repeated 30-35 times, the reaction is completed by waiting for 5 minutes in the final stage for complete polymerization. PCR products are incubated at 4-25 ˚C until the next use. The chains formed after each cycle serve as the target chain of the new cycle [6-7]. Applications of PCR are seemed at table 3.

Table 3. Applications of PCR [8]

1. Identif|cation and analysis ofmutations in eukaryotic DNA ➢ DNAdeletions andinsertions can be detected by a change inthe size of the PCRproduct. ➢ Failure to produce any PCR fragment indicates thatthe primer is foundin an area of deletion. ➢ Mutations can be identif|ed by hybridizing PCR-generated DNAfragments to radioactivelylabelled RNAprobes and digesting the DNA--RNAcomplexeswith RNase A.Digestionwill occur if the complex contains anymismatches. ➢ Localization ofmutations has also been achieved by examining PCRproducts using denaturing gradient gel electrophoresis (DGGE).This separates about 50% of DNA strandso1000 bp inlength that have single base changes.
2. Detection of amplif|ed oncogenes-differential PCR ➢ The oncogene of interest and a single-copy reference gene are co-amplif|edinthe same PCR tube.Gene amplif|cationis determined by comparing the intensityof the oncogene PCRproductwiththatof the amplif|ed reference single-copy gene.
3. Detection of pathogenic organisms in clinical samples
4. Identification of biological and forensic samples
5. Gene polymorphisms
6. Gene expression ➢ Growth factors duringwound healing. ➢ Gene expression during embryogenesis. ➢ Quantitation of gene expressionin various organs, e.g. dystrophin.

1.1.1. Real Time PCR(RT-PCR)

In recent years, combining devices used to provide temperature cycles in PCR reactions with precision measuring instruments has led to the development of a new method called Real-time PCR. Analysis of products in real-time PCR is performed during the reaction. Therefore, there is no need for processing applications such as agarose gel electrophoresis, DNA bands being displayed under ultraviolet light. Qualitative and quantitative analysis of Real-time PCR products utilize non-specific fluorescent dyes or sequence-specific probes. Real-time PCR is a system that operates according to the fluorescence light given by the product in each PCR cycle and controls the product gradually until the end of the reaction [10].

The possibility of Real-Time PCR monitoring has revolutionized the quantification process of DNA and RNA fragments. Real-Time PCR allows the precise quantification of these nucleic acids with greater reproducibility. This technique provides a sensitive method for the accurate quantification of individual species, which could be very relevant to the diagnosis of pathogens and genetic diseases. Advantages of

Real-Time PCR include the ease of quantification, greater sensitivity, reproducibility and precision, rapid analysis, better control of quality in the process and a lower risk of contamination [11].

1.2.PFGE

Pulsed Field Gel Electrophoresis (PFGE) is a method of cutting, moving and separating large fragments of chromosomal DNA. The fragments are able to move in an electric field because of the negatively charged phosphate backbone. It will migrate toward the anode (Positively charged) at a rate proportional to the net charge on the molecule, which is an inverse measure of the size of DNA. Small pieces of DNA will move through a gel matrix in a straight path. PFGE fractionates large DNA molecules in the size range from 10 kb to 10 Mb. PFGE has shown excellent ability to separate small, natural linear chromosomal DNAs ranging in size from 50-kb parasite microchromosomes to multimillion-bp yeast chromosomes. However, intact human chromosomes range in size from 50 million to 250 million bp (Mb), too large for direct PFGE separations the gel is a matrix that consists of agarose molecules. If the concentration of the gel is decreased, larger DNA molecules are able to pass through it, although the resolution of the resultant bands will be poor and the gel will be difficult to manipulate [12-14-15].

PFGE is considered to be a method of high discrimination. The PFGE restriction format is stable over time, repeatable and standard criteria for interpretation are available. Therefore, this method has been reported to be a useful tool in the identification and classification of species. However, this method makes it necessary to spend a lot of time / work force. It also requires a species-specific approach (Different restriction enzymes and electrophoresis conditions), and is therefore often used for the separation of bacterial strains, in the elaboration of in-species differentiation or relationships [13].

1.3.16S rDNA

16S rDNA gene is universally conserved and has a high degree of diversity across bacterial species. One method that has been used for target-specific metagenomics is the direct-sequencing approach, in which the entire microflora is sequenced without prior cultivation [16]. The use of 16S rRNA gene sequencing for bacterial identification depends on a significant inter-species difference and a small intra-species difference in 16S rRNA gene sequences. Therefore, one of the major limitations is that when two different bacterial species share almost the same 16S rRNA gene sequence; this technique alone would not be useful for distinguishing them confidently [17].

Use of broad-range 16S rRNA gene PCR as a tool for identification of bacteria is possible because the 16S rRNA gene is present in all bacteria. The 16S rRNA gene consists of highly conserved nucleotide sequences, interspersed with variable regions that are genus- or species-specific. PCR primers targeting the conserved regions of rRNA amplify variable sequences of the rRNA gene. Bacteria can be identified by nucleotide sequence analysis of the PCR product followed by comparison of this sequence with known sequences stored in a database [18].

2. CONCLUSION

Molecular identification methods are one of the most important innovations in developing microbiology. Adding a new one to the molecular identification techniques every day is of great benefit to the scientific studies carried out for different purposes. Although the most important factors affecting the widespread use of these methods are cost and experienced personnel, these methods, which have its own advantages and disadvantages, are widely used all over the world. The most important advantages of nucleic acid-based methods, when compared to conventional methods, the accuracy is high because it is possible to get results in a short time, the need for living cells is not needed (Especially in order to show the source of contamination in hygiene controls) the damaged cells can be detected and they are very specific techniques. In this context, scientific researches have gained momentum in our country in recent years.

REFERENCES

[1] Çetinkaya, E. Ayhan, K., Mikrobiyolojide kullanılan bazı moleküler teknikler, Karaelmas Fen ve Mühendislik Dergisi, 2, 53-62, 2012.

[2] Hameed, S., Xie, L., Ying, Y., Conventional and emerging detection techniques for pathogenic bacteria in food science: a review, Trends in Food Science and Technology, 2244, 30768-8, 2018.

[3] Aydın, A., Sudağıdan, M., Gıda mikrobiyolojisinde moleküler biyolojik tekniklerin kullanımı ve tiplendirme yontemleri, Türkiye Klinikleri J Food Hyg Technol., 2, 1-9, 2016.

[4] Özkaya, F.D., Cömert, M., Gıda zehirlenmelerinde etken faktörler**,** Türk Hijyen ve Deneysel Biyoloji Dergisi, 65, 149-158, 2008.

[5] Cornut, P. L., Boisset, S., Romanet, J. P., Maurin, M., Carricajo, A., Benito, Y., Vandenesch, F., Chiquet, C., Principles and applications of molecular biology techniques for the microbiological diagnosis of acute post-operative endophthalmitis, Survey of Ophthalmology, 59, 286-303, 2014.

[6] Çakır, İ., Çakmakçı, M.L., Gıdalarda patojen mikroorganizma aranmasında kullanılan moleküler genetik yöntemler, Orlab On-Line Mikrobiyoloji Dergisi, 12, 1-7, 2005.

[7] Dennis Lo,Y.M., Chiu, R.W.K., Chan, K.C.A., Applications of PCR, 2nd Edition, 1-2, 2006.

[8] Bermingham, N., Luettich, K., Polymerase chain reaction and its applications, Current Diagnostic Pathology, 9, 159-164, 2003.

[9] Kahya, S., Büyükcangaz, E., Carlı, K. T., Polimeraz Zincir Reaksiyonu (PCR) Optimizasyonu, Uludag Univ. J. Fac. Vet. Med. 32, 31-38, 2013.

[10] Yerlikaya, O., Laktik asit bakterilerinin tanılanmasında kullanılan başlıca fenotipik ve moleküler yöntemler, Gıda ve Yem Bilimi Teknolojisi Dergisi, 14, 8-22, 2014.

[11] Alves Valones, M.A., Guimarães, R.L., Cavalcanti Brandão, L.A., Eleutério de Souza, P.R., Tavares Carvalho, A.A., Crovela, S., Principles and applications of polymerase chain reaction in medical diagnostic fields: a review, Brazilian Journal of Microbiology, 40,1-11, 2009.

[12] Townsend KM. & Dawkins HJ Journal of Chromatography, 618, 223-49, 1993.

[13] Kıran, F., Osmanaoğlu, Ö., Laktik asit bakterilerinin (LAB) identifikasyonunda/ tiplendirmesinde kullanılan moleküler yöntemler, Erciyes Üniversitesi Fen Bilimleri Enstitüsü Dergisi, 27, 62-74, 2011.

[14] Nassonova, E.S., Pulsed field gel electrophoresis: theory, instruments and application, Cell and Tissue Biology, 2, 557–565, 2008.

[15] Nsofor, C.A., Pulsed-Field Gel Electrophoresis (PFGE): Principles and Applications in Molecular Epidemiology: A Review, Int. J. Curr. Res. Med. Sci., 2, 38-51, 2016.

[16] Hansen, T., Skånseng, B., Hoorfar, J., Löfström, C., Evaluation of direct 16S rDNA sequencing as a metagenomics-based approach to screening bacteria in bottled water, Biosecurity and Bioterrorism: Biodefense Strategy, Practice, and Science, 11, 156-165, 2013.

[17] Woo, P.C.Y.,Teng, J.L.L., Wu, J.K.L., Leung, F.P.S., Tse, H., Fung, A.M.Y., Lau, S.K.P., YueN, K., Guidelines for interpretation of 16S rRNA gene sequence-based results for identification of medically important aerobic Gram-positive bacteria, Journal of Medical Microbiology, 58, 1030–1036, 2009.

[18] Jenkins, C, Ling, C.L., Ciesielczuk, H.L., Lockwood, J., Hopkins, S., McHugh, D.T., Gillespie, S.H., Kibbler, C.C., Detection and identification of bacteria in clinical samples by 16S rRNA gene sequencing: comparison of two different approaches in clinical practice, Journal of Medical Microbiology, 61, 483–488, 2012.

BALANCING THE LIMB MASSES OF THE MECHANISMS

E. Türkeş[1], M. M. A. Usal[1]

[1]*Department of Mechanical Engineering, Faculty of Engineering, Kırklareli University, Kırklareli, Turkey*

E-mail: m.usal@klu.edu.tr

Abstract

In this study, the problem of the equilibrium of the inertial forces acting on the moving limbs of the mechanism due to the motion of the mechanisms and the balance of the limb masses on the basis of the mechanism is investigated in order to reduce the imbalance of the moments in the mechanism. The solution of this problem is addressed by balancing the general inertial force vector and the general moment of inertia created by the limb masses. With the assumption that the lengths of the limbs are known in order to achieve the balancing conditions, the necessity of determining the limb masses in the form of the position of the resultant center of gravity of all moving limbs in the mechanism and the centrifugal moment of inertia of all moving limbs remains fixed.

Keywords: Mechanisms, Balancing, Limb masses

1. INTRODUCTION

Mass imbalances in the mechanisms that form machines cause excessive jolts, noisy operation and amplitude rising vibrations in machines operating at high speeds. These negative effects cause fatigue, wear, breakage in machine elements and cause high and unbalanced power consumption of the machine. It requires respectively static and dynamic balancing operations for the elimination of imbalances in the mechanism. Starting from kinematic synthesis and kinematic analysis, which is the first design stage of the mechanisms for the elimination of mass imbalances, is very useful in solving this problem. Because this problem is not taken into consideration in the first design phase of the mechanisms, the measures to be taken for mass balancing at the final design stages of the machine require the addition of additional masses on the machine. As a result, the designed machine will be too bulky and heavy. The efficiency of the machine will decrease and more power will be needed [1, 2].

The inertial forces that occur in the movement of the limbs create additional dynamic loads in kinematic pairs. Such loads are delivered from the limbs to the fixed limb (chassis) and from there to the foundation. Additional dynamic forces increase friction forces in kinematic pairs. These forces cause the vibrations of both the limbs and the base and create additional stresses in the limbs. In order to prevent such dynamic forces in machine design, the problem of finding the rational values of the masses of the limbs is faced. This solution is called the balancing of the mass of the mechanism. Sometimes it is called the balancing of the inertial forces of the limbs in the mechanisms. This problem is divided into two parts: the balancing of dynamic loads on the foundation and the balancing of dynamic loads in kinematic pairs. It is known that; it is possible to replace the system of forces affecting the solid object with a force and a moment reduced to an arbitrary point of the same object. It is also possible to change the inertia forces of the limbs with a force and a moment [3-5].

An arbitrary point (O) is determined as the beginning of the coordinate and the reduction point. At this point, any point on the shaft of the input member is selected and the coordinate system is passed through this point.

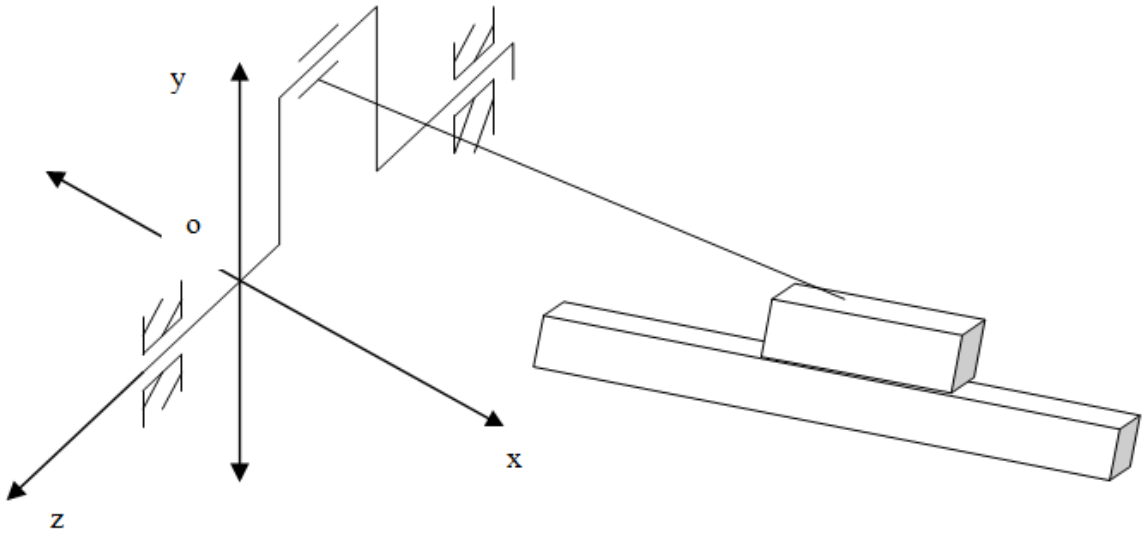

Fig. 1. Balancing of dynamic loads on chassis and foundation (Artobolevsky, 1988)

Projection of the general vectors of all inertial forces on the coordinate axes;

$$F_{ax} = -\sum m_i \ddot{x}_i \qquad F_{ay} = -\sum m_i \ddot{y}_i \qquad F_{az} = -\sum m_i \ddot{z}_i \tag{1}$$

In this formula,

m_i : mass of i numbered limb

$\ddot{x}_i$, $\ddot{y}_i$, $\ddot{z}_i$: projections of the acceleration of i numbered limb on the x, y, z axes

Projection of the general moments of all inertial forces on the x, y, z axes according to point (O);

$$M_{ax} = \sum(y_i F_{az_i} - z_i F_{ay_i}) = -\sum m_i (y_i \ddot{z}_i - z_i \ddot{y}_i)$$

$$M_{ay} = \sum(z_i F_{ax_i} - x_i F_{az_i}) = -\sum m_i (z_i \ddot{x}_i - x_i \ddot{z}_i)$$

$$M_{az} = \sum(x_i F_{ay_i} - y_i F_{ax_i}) = -\sum m_i (x_i \ddot{y}_i - y_i \ddot{x}_i) \tag{2}$$

These equations apply to spatial mechanisms. Since the motion in planar mechanisms is on a plane, $F_{az} = 0$ and the equations for planar mechanisms can be written as follows:

$$F_{ax} = -\sum m_i \ddot{x}_i$$

$$F_{ay} = -\sum m_i \ddot{y}_i$$

$$F_{az} = 0 \tag{3}$$

$$M_{ax} = -\sum(z_i\, F_{ay_i}) = \sum m_i\,(z_i\, \ddot{y}_i)$$

$$M_{ay} = \sum(z_i\, F_{ax_i}) = -\sum m_i\,(z_i\, \ddot{x}_i\,)$$

$$M_{az} = \sum(x_i\, F_{ay_i} - y_i\, F_{ax_i}) = -\sum m_i\,(x_i\, \ddot{y}_i\, - y_i\, \ddot{x}_i) \qquad (4)$$

x_i, y_i ; The x_i and y_i coordinates are the function of the angle of rotation(φ). Since the angle of rotation is the function of the time, the second derivative of the x_i and y_i coordinates can be written as follows:

$$\ddot{x}_i = \frac{d^2x_i}{d\varphi^2}\,\omega^2 + \frac{dx_i}{d\varphi}\,\varepsilon \qquad\qquad \ddot{y}_i = \frac{d^2y_i}{d\varphi^2}\,\omega^2 + \frac{dy_i}{d\varphi}\,\varepsilon \qquad (5)$$

In this formula, ω and ε are respectively angular velocity and angular acceleration of point i of the inlet limb. If their (5) equations are written in the (3) and (4) equations;

$$F_{ax} = -(\omega^2)\,\sum m_i\,\frac{d^2x_i}{d\varphi^2} - \varepsilon\,\sum m_i\,\frac{dx_i}{d\varphi}$$

$$F_{ay} = -(\omega^2)\,\sum m_i\,\frac{d^2y_i}{d\varphi^2} - \varepsilon\,\sum m_i\,\frac{dy_i}{d\varphi} \qquad (6)$$

$$M_{ax} = (\omega^2)\sum m_i\,z_i\,\frac{d^2y_i}{d\varphi^2} + \varepsilon\,\sum m_i\,z_i\,\frac{dy_i}{d\varphi}$$

$$M_{ay} = -(\omega^2)\sum m_i\,z_i\,\frac{d^2x_i}{d\varphi^2} - \varepsilon\,\sum m_i\,z_i\,\frac{dx_i}{d\varphi}$$

$$M_{az} = (\omega^2)\left(\sum m_i\,y_i\,\frac{d^2x_i}{d\varphi^2} - \sum m_i\,x_i\,\frac{d^2y_i}{d\varphi^2}\right) + \varepsilon\,\left(\sum m_i\,y_i\,\frac{dx_i}{d\varphi} - \sum m_i\,x_i\,\frac{dy_i}{d\varphi}\right) \qquad (7)$$

They can be expressed as. In order to fully compensate the inertial forces of the planar mechanisms, $F_{ax} = 0$, $F_{ay} = 0$, $M_{ax} = 0$, $M_{ay} = 0$, $M_{az} = 0$. The effect of moment M_{az} on the foundation is on the z-axis perpendicular to the working plane of the mechanism. It is necessary to investigate the effect of this moment with the moments of the driving forces and the moments of the resistive forces. First, if the first four conditions are examined; ($F_{ax} = 0$; $F_{ay} = 0$; $M_{ax} = 0$; $M_{ay} = 0$)

$$F_{ax} = -(\omega^2)\,\sum m_i\,\frac{d^2x_i}{d\varphi^2} - \varepsilon\,\sum m_i\,\frac{dx_i}{d\varphi} = 0$$

$$F_{ay} = -(\omega^2)\,\sum m_i\,\frac{d^2y_i}{d\varphi^2} - \varepsilon\,\sum m_i\,\frac{dy_i}{d\varphi} = 0 \qquad (8)$$

$$M_{ax} = (\omega^2) \sum m_i \, z_i \, \frac{d^2 y_i}{d\varphi^2} + \varepsilon \sum m_i \, z_i \, \frac{dy_i}{d\varphi} = 0$$

$$M_{ay} = -(\omega^2) \sum m_i \, z_i \, \frac{d^2 x_i}{d\varphi^2} - \varepsilon \sum m_i \, z_i \, \frac{dx_i}{d\varphi} = 0 \qquad (9)$$

In order for the angular velocities and angular accelerations of the input limb to provide the correlations (8) and (9) in the desired values, both terms in the equations must be equal to zero.

$$\sum m_i \, \frac{dx_i}{d\varphi} = 0 \qquad (10)$$

$$\sum m_i \, \frac{dy_i}{d\varphi} = 0 \qquad (11)$$

$$\sum m_i \, z_i \, \frac{dx_i}{d\varphi} = 0 \qquad (12)$$

$$\sum m_i \, z_i \, \frac{dy_i}{d\varphi} = 0 \qquad (13)$$

$$\sum m_i \, \frac{d^2 x_i}{d\varphi^2} = 0 \qquad (14)$$

$$\sum m_i \, \frac{d^2 y_i}{d\varphi^2} = 0 \qquad (15)$$

$$\sum m_i \, z_i \, \frac{d^2 x_i}{d\varphi^2} = 0 \qquad (16)$$

$$\sum m_i \, z_i \, \frac{d^2 y_i}{d\varphi^2} = 0 \qquad (17)$$

As can be seen from the equations (10) to (17) above, the masses and dimensions of the limbs of the mechanism for complete balancing of any mechanism should be taken to provide these equations. When the differential is received of the expressions between the above (10) and (13) equations is obtained according to A, the equations between (14) and (17) are obtained. In this case, when the equations between (10) and (13) are provided, others will be provided and only the examination of these equations will be sufficient.

Statements $\sum m_i \, x_i$ and $\sum m_i \, y_i$ are called the Static Moment of the limb masses according to x_i and y_i coordinates. Static Moment is also expressed with the coordinates of the total mass and the general center of gravity. In other saying;

$$\sum m_i \, x_i = m \, x_s \quad , \quad \sum m_i \, y_i = m \, y_s \qquad (18)$$

Here, m is the total mass of the mechanism members, x_s and y_s are the coordinates of the overall center of gravity of the mechanism. When these expressions are differentiated according to (φ),

$$\sum m_i \frac{dx_i}{d\varphi} = m \frac{dx_s}{d\varphi} \quad \text{and} \quad \sum m_i \frac{dy_i}{d\varphi} = m \frac{dy_s}{d\varphi} \tag{19}$$

These expressions (10) and (11) are written in place of the equations,

$$m \frac{dx_s}{d\varphi} = 0 \quad \text{and} \quad m \frac{dy_s}{d\varphi} = 0 \tag{20}$$

Equations are obtained.

Given the terms $\sum m_i z_i x_i$ and $\sum m_i z_i y_i$, these expressions are the centrifugal moment of inertia of the limb masses relative to the xz and yz planes. These expressions are represented by j_{xz} and j_{yz}. When these expressions are differentiated according to (φ),

$$\sum m_i z_i \frac{dx_i}{d\varphi} = \frac{dj_{xz}}{d\varphi} \quad \text{and} \quad \sum m_i z_i \frac{dy_i}{d\varphi} = \frac{dj_{yz}}{d\varphi} \tag{21}$$

These expressions (12) and (13) are written in place of the equations,

$$\frac{dj_{xz}}{d\varphi} = 0 \quad \text{and} \quad \frac{dj_{yz}}{d\varphi} = 0 \tag{22}$$

Equations are obtained.

It can be seen from this that when the equations (20) and (22) are provided, the inertial forces of the planar mechanisms are balanced. For provide these equations,

$$x_s = \text{constant}, \; j_{xz} = \text{constant}, \; y_s = \text{constant} \quad \text{and} \quad j_{yz} = \text{constant} \tag{23}$$

2. LOCATING THE OVERALL CENTER OF GRAVITY OF THE MECHANISM

The overall center of gravity must be fixed to compensate for the general inertia force vector. Based on the rules of physics, the vector r_s, which determines the position of the center of gravity, can be written as follows;

$$r_s = \frac{m_1 r_1 + m_2 r_2 + m_3 r_3 + \cdots + m_n r_n}{m_1 + m_2 + m_3 + \cdots + m_n} = \frac{\sum m_i r_i}{\sum m_i} \tag{24}$$

Here; m_1, m_2, m_3, ……; are the masses of the limbs. r_1, r_2, r_3, ……; are vectors indicating the position of the center of gravity of the limbs. $m_1\ r_1$, $m_2\ r_2$, … …; are the static moments of the limb masses. Using the above formula it is possible to find the center of gravity of the desired kinematic chain.

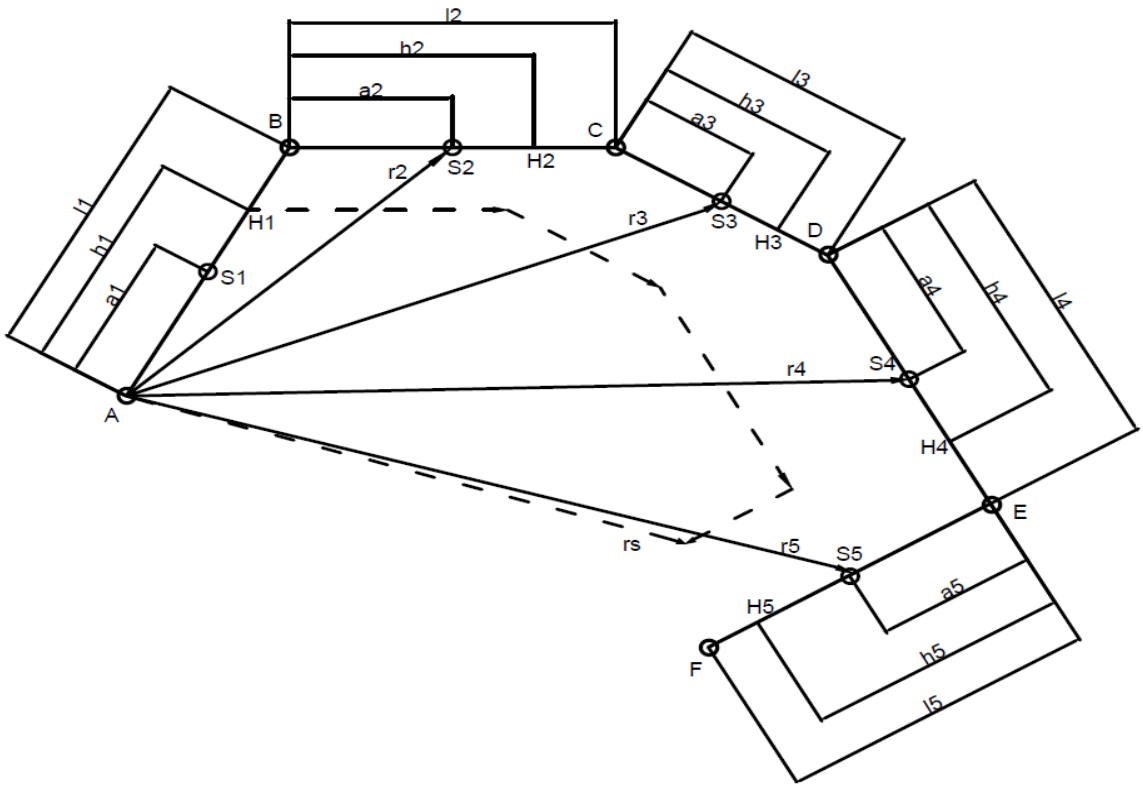

Fig. 2. Locating the overall center of gravity of the mechanism (Artobolevsky, 1988)

l_1, l_2, l_3, ……, l_n are the length of the limbs, s, s_2, s_3, ……, s_n are the center of gravity, a_1, a_2, a_3, ……, a_n are the distances of the center of gravity from the left hinge, r_1, r_2, r_3, ……, r_n are vectors indicating the position of the center of gravity relative to point A. According to Figure 2, the following statements can be written;

$$r_1 = a_1 \ \ ; \ \ r_2 = l_1 + a_2 \ \ ; \ \ r_3 = l_1 + l_2 + a_3 \ \ ; \ \ r_n = l_1 + l_2 + l_3 + \cdots + l_{n-1} + a_n$$

These expressions (24) is written in place of the equation,

$$r_s = \frac{m_1\, a_1 + m_2\, (l_1 + a_2) + \cdots + m_n\, (l_1 + l_2 + l_3 + \cdots + l_{n-1} + a_n)}{m_1 + m_2 + \cdots + m_n} \qquad (25)$$

With the help of this equation;

$$r_s = \frac{m_1\, a_1 + (m_2+m_3+\cdots+m_n)\, l_1}{m} + \frac{m_2\, a_2+(m_3+m_4+\cdots+m_n)\, l_2}{m} + \cdots + \frac{m_{n-1}\, a_{n-1}+m_n\, l_{n-1}}{m} + \frac{m_n\, a_n}{m} \quad (26)$$

Here it is expressed as $m = m_1 + m_2 + m_3 + \cdots + m_n$

Considering the equation (26); it is seen that the masses of the limbs preceding each limb are collected at the starting point of the limb. It is seen that the masses of the limbs after the limb are collected at the end point of the limb. It is seen that the mass of the limb is represented at point A, the center of gravity of the limb. This is shown schematically in Figure 3.

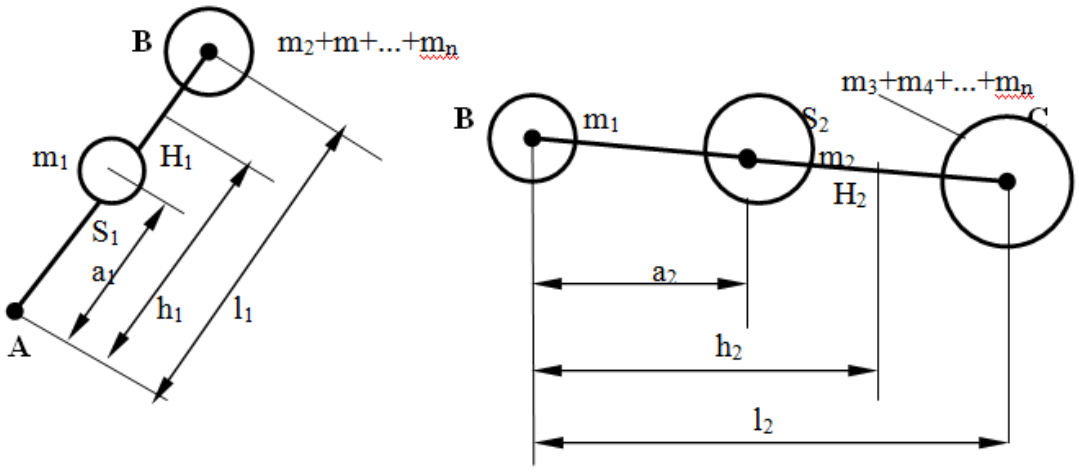

Fig.3. Collection of limb masses

As shown in Figure 3, when a mass reduction is made, according to this new situation; the centers of gravity of the limbs will also change. That is, as shown in Figure 3, $(H_1,\ H_2,\ \ldots, H_n)$ consists of virtual centers of gravity bearing the name of the fictitious center of gravity. The terms $(h_1, h_2, \ldots, h_n)$ represent the distance from the starting point of the limb to the focal center of the same limb.

$$h_1 = \frac{m_1\, a_1 + (m_2+m_3+\cdots+m_n)\, l_1}{m}$$

$$h_2 = \frac{m_2\, a_2+(m_3+m_4+\cdots+m_n)\, l_2}{m}$$

…

…

…

$$h_{n-1} = \frac{m_{n-1}\, a_{n-1} + m_n\, l_{n-1}}{m}$$

$$h_n = \frac{m_n\, a_n}{m} \qquad (27)$$

They can be expressed as. Here, the static moment of mass m_1 is zero.

$$r_s = h_1 + h_2 + h_3 + \cdots + h_n \qquad (28)$$

The vectors $h_1, h_2, h_3, \ldots, h_n$ are always parallel to the limbs for each position of the mechanism. Since the masses of the limbs and the lengths a and l are always constant, the modules of the vectors $h_1, h_2, h_3, \ldots, h_n$ will always be constant. Thus, the presence of the center of gravity of the kinematic chain of mechanisms can be accomplished by collecting fixed vectors parallel to the limbs.

3. BALANCING THE INERTIA FORCES OF THE MECHANISMS LIMBS

As previously described, the overall center of gravity of the mechanism must remain constant to compensate only for the overall vector of the inertial force of the planar mechanisms. So; x_s = constant, y_s = constant or r_s = constant. For example; For a planar four-arm mechanism, $r_s = h_1 + h_2 + h_3$ must be constant. For this,

$$\frac{h_1}{l_1} = \frac{h_2}{l_2} = \frac{h_3}{l_3} \qquad (29)$$

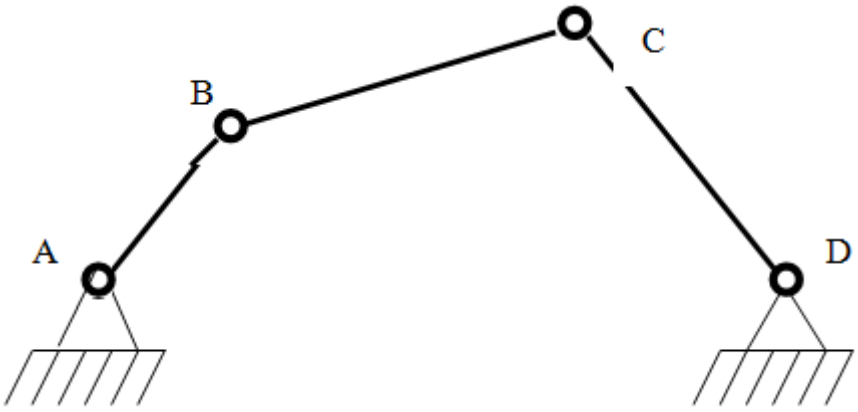

Fig. 4. Balancing the inertial forces of the limbs of the mechanisms (Artobolevsky, 1988)

For a simple planar four-lever mechanism shown in Figure 4;

$$h_1 = \frac{m_1\, a_1 + (m_2 + m_3)\, l_1}{m} \qquad (30)$$

$$h_2 = \frac{m_2\, a_2 + m_3\, l_2}{m} \tag{31}$$

$$h_3 = \frac{m_3\, a_3}{m} \tag{32}$$

If the equations between (30) and (32) are applied to equation (29);

$$m_1\, a_1 = -\frac{l_1}{l_2}\,[m_2(l_2 - a_2)] \tag{33}$$

$$m_2\, a_2 = -\frac{l_2}{l_3}\,[m_3(l_3 - a_3)] \tag{34}$$

4. CONCLUSION

If the length of the limbs (l_i) and the limb masses (m_i) in the (33) and (34) equations are known for an existing mechanism and the location of the center of gravity of the mechanism is known to be $r_1 = a_1$, then other unknowns can be easily solved.

Or in the above equations, if it is assumed that other values are not known except for the length of the limbs, six unknowns occur. If four of these six unknown values are selected arbitrarily, the values for the remaining two can be found.

The masses of the mechanism limbs for balancing the general inertial force vector of the planar mechanisms should be chosen as the overall centers of gravity of all limbs remain constant.

The masses of limbs of the mechanism for balancing the general moment of inertia must be chosen in such a way that the centrifugal moment of inertia of all limbs is constant relative to the *xz* and *yz* planes.

REFERENCES

[1] Kazıhan, K., Okutan, N., Aslan Z., Makine ve Mekanizmalar Teorisi, 1996, 212 s., İstanbul.

[2] Shigley, J.E., Uicker, J.J., Theory of machines and mechanisms, 1995, 719 p., Singapore.

[3] Artobolovsky, I.I., Makine mekanizmalarının teorisi, 1988, 420 s., Moskova.

[4] Dukumacı, E., Ergüven, H.N., TMMOB Makine Mühendisliği el kitabı üretim ve tasarım 'Mekanik titreşimler ve gürültü kontrolü', 1994, 517 s., Ankara.

[5] Türkeş E., Köse, R., Mekanizmaların uzuv kütlelerinin temel üzerinde dengelenmesi, 10. Ulusal Makine Teorisi Sempozyumu, Selçuk Üniversitesi, Konya, Eylül 2001. Bildiri Kitabı, 838-846 s.

NANOTECHNOLOGY APPLICATIONS IN FOOD PACKAGING

B.E. Kocamaz Özcan, H. Şanlıdere Aloğlu and H. Uran

Department of Food Engineering, Kırklareli University, Faculty of Engineering, Kırklareli, Turkey

E-mail: basakebrukocamaz@klu.edu.tr

Abstract

Nowadays, awareness of consumers about food safety and quality has led to an increase in consumer demand for food that has remained fresh for a long time and is not quickly disturbed. As a result, the importance given to food packages consisting of containers, cases or wrappers made from special materials such as metal, glass, paper, plastic which protects food from external influences and facilitates consumption has increased. In the packaging industry, environmental pollution caused by their wastes has become an important problem today, although petroleum-based plastics, which are used frequently from past to present, have features such as low weight, flexibility, durability and possible recycling. Recent studies on these and similar reasons have focused on packaging produced with nanotechnology. Nanotechnology involves the reduction of materials to dimensions of 100 nm or less, their characterization and analysis. In the food industry, nanotechnology applications are often used for purposes such as improving the barrier properties of packaging materials and making active and intelligent packaging materials more functional. Monitoring of the product during transport and distribution, thanks to packaging with nanoscale material, is among the active and intelligent packaging applications of nanotechnology. Among these applications, active packagings containing nanocomposite films obtained by the addition of nanoparticles are widely used in the food industry. The recyclability and biodegradability properties of nanocomposite packages are expected to contribute greatly to the reduction of environmental packaging waste quantities. The packaging obtained through nanotechnology takes the place of traditional packaging thanks to the important advantages it provides and is the subject of many new researches. In this study, information about using of nanotechnology applications in the production of food packaging is given.

Keywords: Nanotechnology, intelligent packaging, nanocomposite, food packaging

1. INTRODUCTION

Food packaging is container, sheath or wrap made of special material such as metal, glass, paper, plastic that protects food from external effects and facilitates marketing and consumption. The necessary conditions for food safety and quality are required during the packaging and storage stages as well as during the production phase. The packaging of the final product in accordance with the storage and transport conditions maintains the quality characteristics and thus increases the shelf life of the product [1].

In line with the demands of the consumers and the trends of the food industry, the functions of food packaging are evolving day by day. In packaging production, it is aimed to keep food fresh for longer while consumers want to see the freshness of food without opening the package [2]. Although petroleum based plastics, which are frequently used in the packaging industry from the past to the present, have features such as low weight, flexibility, durability and possible recycling, environmental pollution caused by their waste has become an important problem today. In line with these and similar reasons, recent studies have focused on nanotechnology-produced packages.

Nanotechnology is an area of science and technology that aims to provide advanced or completely new physical, chemical and biological properties at the atom and molecule level by means of processing, measurement, design, modeling and regulation carried out on materials with dimensions smaller than 100 nano-meter [3]. Nanotechnology has a wide range of applications in the food industry, such as improving food safety, reducing agricultural inputs, nutrition and especially packaging [4]. The application areas of nanotechnology in the food and food packaging industry are shown in Figure 1.

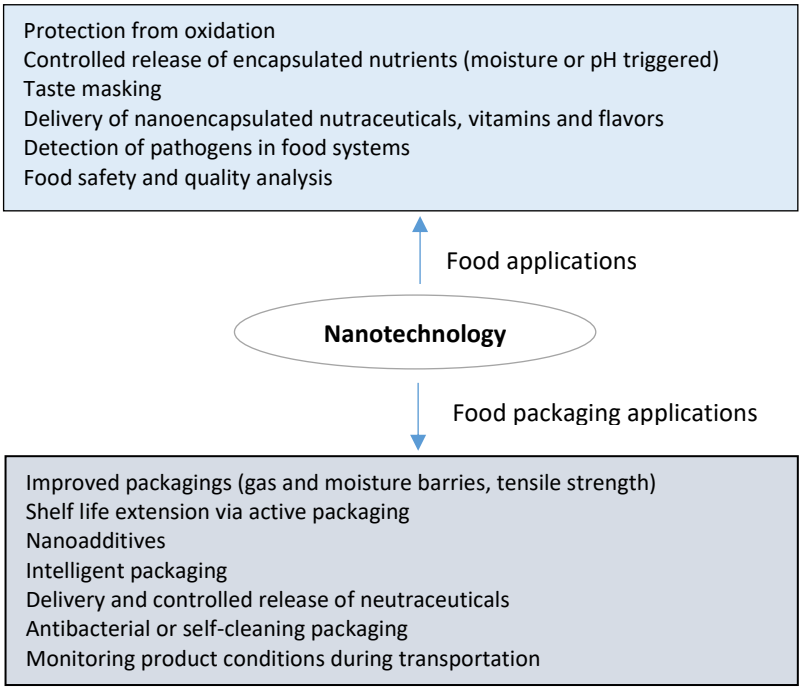

Figure 1. The potential applications of nanotechnology in the food and food packaging industries [5].

The structure of the packaging material can be changed at the molecular level by using nanotechnology. With this new technology, the molecules can be re-engineered to combine many functions and achieve different gas and liquid permeability. Light resistance, strong mechanical performance and high barrier properties against gases are provided by adding nanoparticles. It is possible to maintain the freshness of the food and to see whether the frozen products have been dissolved before. Oxygen absorber, antimicrobial and gas permeable packaging materials can be obtained by means of nanostructured materials. Nanocomposite materials can be used to expel the dirty air inside the package. When the polymers structured with nanoparticles are combined with radiation curing, very strong and durable materials can be obtained [6].

2. USAGE AREAS OF NANOTECHNOLOGY IN FOOD PACKAGING

Food packaging materials using nanotechnology are now the main field of nanotechnological applications in the food sector. Nanotechnology in the packaging of food, the production of the nanocomposite packaging materials, including active features of active packaging material and the development of smart packaging using nanoparticles are used in three different categories.

2.1 Production of Nanocomposite Packaging Materials

The nanoparticles, defined as powders of 100 nm or less in size, form the basis of nanospheres and therefore nanotechnology. Nanocomposite materials are formed by dispersing the nanometer-sized particles in a matrix. Powders in nanoscale may be used as supporters in materials such as ceramic, metal or polymer to form advanced nanocomposites.

The use of nanocomposite materials in the packaging of foods started in the 1990s [7]. Improved packaging material consists of a polymer matrix embedded in the matrix and filler. These fillers can be a metal-metal oxide, nano-tubes, nano-fibers or nano-clays. Many polymers, such as montmorillonite clay (MMT) containing polyethylene, nylon, polyvinyl chloride and starch, which are preferred as nanoparticles, are among the first polymer nanostructured materials that have been introduced as improved materials in food packaging [7, 8]. The use of nano-particulate materials in food packaging gives the packaging material flexibility, durability, heat / moisture stability, high barrier properties to gases, light resistance and strong mechanical performance. It can be ensured that the nano particle and packaging material are light, tearproof, high thermal resistance and improve mechanical properties at the same time. By adding a variety of

nanoparticles to food packaging, modifying the permeability property of the material, it is also frequently used to create an anaerobic environment by providing oxygen absorption to the food contacting surface of the package and thus to provide antimicrobial and antifungal surface formation [9].

Non-biodegradable petrochemical-based plastic packaging materials cause environmental waste problems. For this reason, research on the development of biodegradable packaging materials using renewable natural biopolymers such as polysaccharides and proteins has intensified [10]. By adding nano materials to biodegradable materials, new materials with different properties are developed and the negative properties of the materials are improved. Bionanocomposites are nano-structured materials that improve the mechanical, thermal and gas barrier properties of the material being integrated. The use of bionanocomposites in food packaging increases the shelf life of the food and reduces the use of plastics as a packaging material and thus creates a more environmentally friendly solution. The biodegradability of a packaging material can be improved by the addition of inorganic particles such as clay into the biopolymer matrix and can be controlled by the surfactants used in the modification of layered silicates [5]. The formation of bionanocomposites is shown in Figure 2.

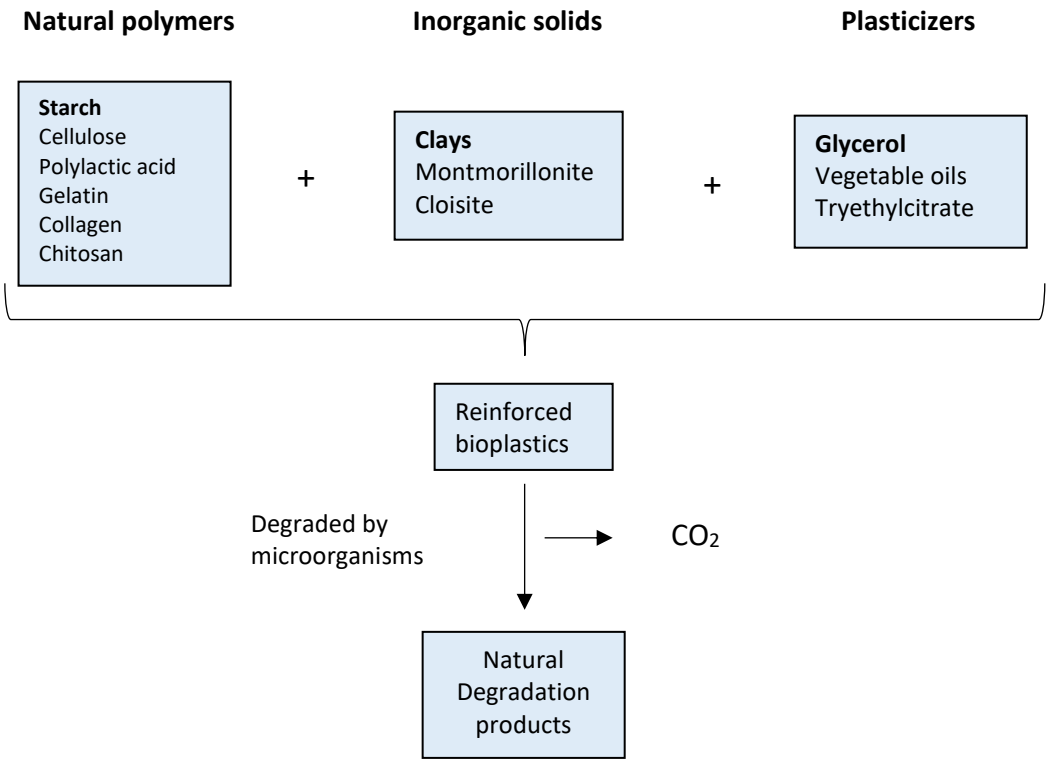

Figure 2. Representation of the formation of bionanocomposites [5].

An American firm used nanocomposite materials contained montmorillonite to extend food shelf life and improve the gas permeability properties of bottles. Thus, the shelf life of the products such as beer is extended to 30 weeks in plastic bottles with nanocomposites while it is 11 weeks [11]. In another study, antimicrobial peptides such as nisin were used as nano-sized coating material and antimicrobial materials were obtained [12]. In a study by Lepot et al. [13], two-way stretched polypropylene-based nanocomposite films were produced using different shapes and concentrations of ZnO nanoparticles. In the study, it was emphasized that the mechanical and oxygen barrier properties of two-way stretched polypropylene films can be significantly increased depending on the nanoparticle shape and concentration. Li et al. [14] produced 40 μm thick nanocomposite film based on polyethylene using Ag, TiO_2 and kaolin nanoparticles. Compared to control films of the same thickness, the use of nanoparticles has been found to reduce water vapor and oxygen permeability of the films by 28.07% and 2.1%, respectively.

2.2 Improve of Active Packaging Material

Active packaging systems are designed to deliberately incorporate components that would release or absorbsubstances into or from the packaged food or the environment surrounding the food. Thanks to this packaging system, various functions can be achieved. Some of those; antimicrobial and antioxidant activity, removing unwanted odor and flavorings from the package and controlling the oxygen, moisture and ethylene concentrations in the package [15].

The application of oxygen scavengers is one of the main active packaging technologies that aims to remove any residual oxygen present in the food package or improve barrier properties by acting as an active barrier. Delaying maturation, which is an important criterion in fruits and vegetables, can be provided with ethylene absorber. Ethanol emitter systems, one of the most commonly used methods in active packaging, are preferred to slow the growth of mold in baked foods. Thanks to the water vapor release pouches, the fruits and vegetables that are ready to be cooked can be keep fresh. Sulfur dioxide emitter packages are especially used to prevent mold growth of grapes. [16].

Antimicrobial packaging has an important role in active packaging systems and its functions can be improved by the addition of nanoparticles [17]. Nanostructured antimicrobials have a larger surface area than ordinary antimicrobials and they can be integrated packaging materials by coating or insert into [18]. Antimicrobial food packaging materials prolong lag phase and reduce microbial growth rate [19]. Antimicrobials such as organic acids, bacteriocins, enzymes, spices and polysaccharides, as well as nanoparticles such as metal structures Ag, ZnO, MgO and TiO_2 are also used as antimicrobials [20].

Several studies have demonstrated that silver (Ag^{+}) nanoparticles exhibit antimicrobial activity against Gram-positive and Gram-negative bacteria and that the packaging material obtained from these particles prolongs the shelf life of food [21, 22]. In another study to determine the effects of silver nanoparticles on the shelf life of foods, carrots and pears coated with alginate films containing silver nanoparticles were found to be less water loss after 10 days of storage compared to uncoated and only those coated with alginate. In addition, samples coated with alginate films containing silver nanoparticles have been found to be more acceptable to consumers in terms of color, texture and flavor [23].

2.3 Development of Intelligent Packaging and Production of Nanosensors

Intelligent packaging technology is a system for monitoring the quality of the packaged food during transportation and storage. With this system, mechanical, chemical, enzymatic or microbial changes in food can be observed [24]. It is designed to convey information about the state of food to the consumer. Intelligent packagings are evaluated in three groups: sensors, indicators and RFID tags [25].

Radio Frequency Identification (RFID) system is a system that makes identification with radio waves and enables remote monitoring of the product. Provides traceability of the product during transportation and storage by using these tags in food packaging [25]. The indicators developed based on the principle of detection of various metabolite residues during storage can be integrated into the package as well as the packaging material. Sensors used in food packaging inform about the temperature changes in the packaging, whether there is any contamination or microbial deterioration in the products, the freshness and maturity of the products and the oxidation. Gas sensors, biosensors and fluorescent based gas sensors are some of these sensors [24].

By integrating the nanosensors into the packaging material, smart nano packages are developed and it is possible to follow the different characteristics of the foods. For this purpose, semiconductor systems containing nano-sized metal oxide are generally used. The current nanosensor types and their potential applications in the food sector are summarized in Figure 3 [5].

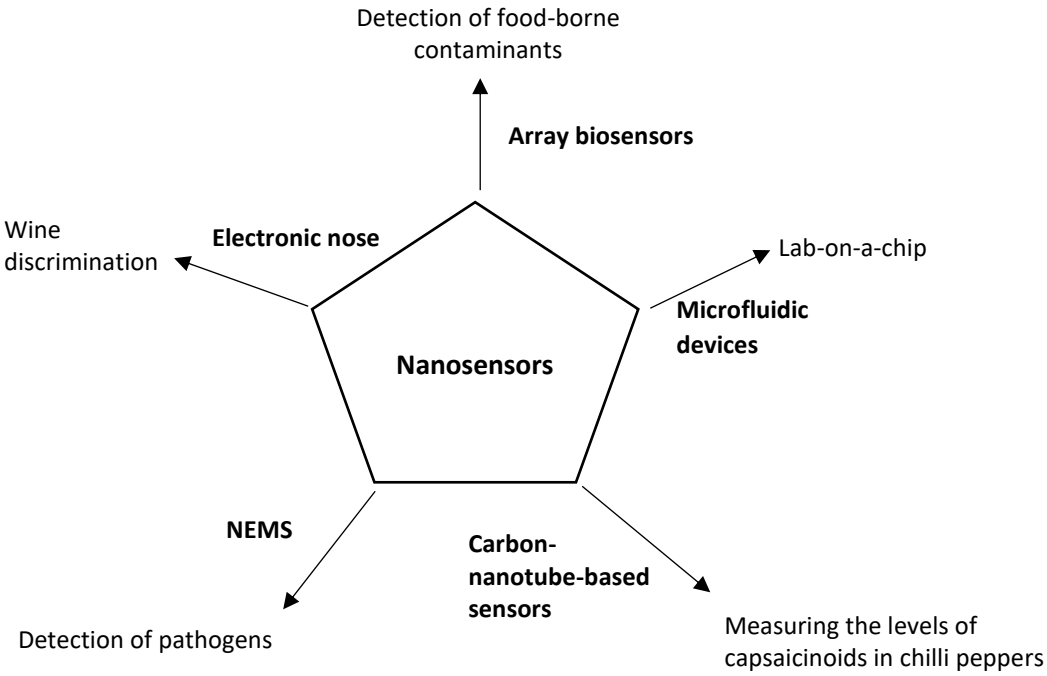

Figure 3. Types of nanosensors and examples of their application in the food sector [5].

Biosensors using modified carbon nanotubes in the United States are used to monitor microorganisms, toxic substances and spoilage in foods and beverages. Biosensors developed by the company named Opal using 50 nm black carbon nanoparticles allow the color to change as a result of food spoilage. Nanosensors are available that can detect bacteria and other contaminants such as Salmonella on the food surface [26].

Nanocantilevers are another innovative class of biosensors. Their detection principle is based on their ability to determine biological-binding interactions, such as between antigen and antibody, enzyme and substrate or cofactor and receptor, through physical or electromechanical signaling. These consist of small parts of silicon-based materials. These materials are capable of recognizing proteins, pathogenic bacteria and viruses. The principle in the detection of pathogens is that the Nanocantilever may vibrate at various frequencies in relation to the biomass of the organism [5]. Nanokantilever's surface can be coated with special chemicals. Gfeller et al. [27] were able to determine *Escherichia coli*, which is an indicator of fecal pollution of water and food products, with the help of a cantilever coated with agarose.

3. CONCLUSION

With increasing consumer awareness, people want to consume more nutritious and fresh food for themselves. In addition, the environmental pollution caused by plastic packages, which have been used frequently from the past to the present, has become an important problem today. Preferred food packages have an important place in the protection of human health and the environment. Therefore, nanotechnology is becoming increasingly important for the food packaging industry. Hopeful results have been obtained from nanotechnological studies in food packaging. The incorporation of nanomaterials into the food packaging improves the barrier properties of packaging materials, thereby helping to reduce the use of valuable raw materials and waste generation. As a result, the packages obtained with nanotechnology replace traditional packagings due to the important advantages and are subject to many new researches.

REFERENCES

[1] Şahin, O.I., Bayizit, A.A., Nanokompozit filmlerin gıda sanayi uygulamaları, Türkiye 10. Gıda Kongresi, 21-23 Mayıs, Erzurum, 2008.

[2] Sürengil, G., Kılınç, B., Gıda ambalaj sektöründe nanoteknolojik uygulamalar ve su ürünleri açısından önemi, Journal of Fisheries Sciences 5(4): 317-325, 2011.

[3] Tarhan, Ö., Gökmen V., Harsal Ş., Nanoteknolojinin gıda bilim ve teknolojisi alanındaki uygulamaları, Gıda, 35(2): 219-225, 2010.

[4] Schnettler, B, Crisostomo G, Mora M, Lobos G, Miranda H, Grunert KG, Acceptance of nanotechnology applications and satisfaction with food-related life in southern Chile, Food Sci Technol, 34(1): 157-163, 2013.

[5] Sözer, N., Kokini, J. L., Nanotechnology and Its Applications in the Food Sector, Trends in Biotechnology, 27(2): 82-89, 2009.

[6] Çeliker, G., Nanotechnology in Packaging Industry and Its Applications, Yaşar Paint and Chemical Group, 8 s, 2006.

[7] Brody, AL, Bugusu, B, Han JH, Sand, CK, Mchugh T.H, Innovative Food Packaging Solutions, J Food Sci, Vol. 73 (8): 107-116, 2008.

[8] Var, I., Sağlam, S., Gıda endüstrisinde nanoteknoloji uygulamaları, Gıda 40 (2): 101-108, 2015.

[9] Mahalik, N. P, Nambiar A N., Trends in food packaging and manufacturing systems and technology, Trends in Food Science & Technology, 21 (3): 117-128, 2010.

[10] Rhim, J. W., Ng P. K. W., Natural biopolymer-based nanocomposite films for packaging applications, Critical Reviews in Food Science and Nutrition, 47(4): 411-433, 2007.

[11] Jones, A, Nye, J, Greenberg, A., Nanotechnology in agriculture and food technology, 2011. http://ice. chem. wisc. edu/NanoDecisions/PDF/ Agriculture.pdf (Acceessed: 18.10.2018).

[12] Azeredo, H M C., Nanocomposites for food packaging applications, Food Res Int, 42 (9:)1240-1253, 2009.

[13] Lepot, N., Van Bael, MK., Van Den Rul, H., D'haen. J, Peeters. R, Franco. D, Mullens J., Influence of incorporation of zno nanoparticles and biaxial orientation on mechanical and oxygen barrier properties of polypropylene films for food packaging applications, J Appl Poly Sci, 120(3), 1616-1623, 2011.

[14] Li, H., Li, F., Wang, L., Sheng, J., Xin, Z., Zhao, L., Xiao, H., Zheng, Y., Hu, Q., Effect of nano-packing on preservation quality of Chinese Jujube (*Ziziphus jujuba Mill.* var. *inermis* (Bunge) Rehd), Food Chem, 114 (2), 547-552, 2009.

[15] Çelik, İ., Tümer, G., Gıda ambalajlamada son gelişmeler, Akademik Gıda 14(2) 180-188, 2016.

[16] Danielli, D., Gontard, D., Spyropoulos, D., Beuken, E.Z., Tobback, P., Active and intelligent food packaging: legal aspects and safety concerns, Trends in Food Science & Technology 19: 103-112 p, 2008.

[17] Mangalassary, S., Antimicrobial food packaging to enhance food safety: current developments and future challenges, J Food Process Technol, 3:5, 2012.

[18] Azeredo, HMC., Antimicrobial nanostructures in food packaging, Trends Food Sci Tech, 30 (2013): 56-69, 2013.

[19] Othman, SH., Salam, NRA., Zainal, N., Basha, RK., Talib, RA., Antimicrobial activity of tio_2 nanoparticle-coated film for potential food packaging applications, Int J Photoenergy, p.1-6, 2014.

[20] Polat S., Fenercioğlu, Gıda Ambalajlamasında Nanoteknoloji Uygulamaları: inorganik Nanopartiküllerin Kullanımı. GIDA (2014) 39 (3):187-194, 2014.

[21] Lok, C.-N., Ho, C.-M., Chen, R., He, Q.-Y., Yu, W.-Y., Sun, H., Proteomic analysis of the mode of antibacterial action of silver nanoparticles, Journal of Proteome Research, 5, 916e924, 2006.

[22] Lewington, S., Antimicrobial nanostructures in food packaging, Food New Zealand, 13, 40, 2013.

[23] Fayaz, AM., Balaji, K., Girilal, M., Kalaichelvan, PT., Venkatesan, R., Mycobased synthesis of silver nanoparticles and their incorporation into sodium alginate films for vegetable and fruit preservation, J Agric Food Chem, 57 (14), 6246-6252, 2009.

[24] Gök, V., Batu, A., Telli, R., Akıllı paketleme teknolojisi. Türkiye 9. Gıda Kongresi, 24-26 Mayıs, Bolu, 2006.

[25] Kokangül, G., Fenercioğlu, H., Gıda endüstrisinde akıllı ambalaj kullanımı, Gıda Teknolojileri Elektronik Dergisi, 7 (2): 31-43, 2012.

[26] Qureshi, MA., Karthikeyan, S., Karthikeyan, P., Khan, PA., Uprit, S., Mishra, UK., Application of nanotechnology in food and dairy processing: An overview. Pak J Food Sci, 22(1): 23-31, 2012.

[27] Gfeller, KY., Nugaeva, N., Hegner, M., Micromechanical oscillators as rapid biosensor for the detection of active growth of *Escherichia coli*, Biosens Bioelectron. 21: 528–533, 2005.

3rd International Conference on Organic Electronic Material Technologies (OEMT2018)
Sep 20-22, 2018, Kırklareli / TURKEY

FORMULATION OF LINEAR CONSTITUTIVE EQUATIONS OF THERMO-VISCOELASTIC MEDIUM

M. M. A. Usal[1], M. R. Usal[2], and M. Usal[3]

[1]*Department of Mechanical Engineering, Kırklareli University, Kırklareli, Turkey*
[2]*Department of Mechanical Engineering, Süleyman Demirel University, Isparta, Turkey*
[3]*Department of Mechanical and Manufacturing Engineering, Isparta Applied Sciences University, Isparta, Turkey*

E-mail: melekusal@sdu.edu.tr

Abstract

In this study, the mathematical formulation of linear linear constitutive equations of a heat-conducting viscoelastic medium is discussed. Viscoelastic materials are known to be elastic and exhibit a flow behavior depending on time. Two important constitutive models for viscoelastic materials are known as Kelvin-Voigt Body and Maxwell Body. In this study, a Kelvin-Voigt body has been chosen as the viscoelastic medium model. In order to account for heat transfer, a material temperature gradient vector, which is defined as identified as $\mathbf{G} \equiv \theta_{,K}\, \mathbf{I}_K$, is included between independent constitutive variables. In order to obtain the linear constitutive equations, a viscoelastic medium is considered at the $T_0 > 0$ temperature and in the natural state without stress. It is assumed that the strain tensor and the rates of deformation tensor, which they have occured when the viscoelastic medium changes shape, satisfy the $\|\mathbf{E}\| << 1$ and $\|\dot{\mathbf{E}}\| << 1$ conditions and the temperature changes are very small. The small temperature change refers to $\theta = T_0 + T$, $T_0 > 0$, $|T| << T_0$. As a result, the mathematical formulation of Cauchy stress tensör (as elastic part ${}_{\mathbf{E}}\mathbf{t}$ and dissipative part ${}_{\mathbf{D}}\mathbf{t}$) and heat flow vector, which are constitutive equations of a thermo-viscoelastic medium, has been obtained.

Keywords: Linear constitutive equations, Thermo-viscoelastic medium, Stress tensör, Heat flow vector

1. INTRODUCTION

Continuum mechanics is a branch of science that deals with determining the mechanical behavior of solids (rubber, metal, ceramic, wood and living tissue, etc.) and fluids (water, oil, air, etc.) [1]. Almost all engineering materials have a certain degree of elasticity [2]. Elastic materials are simple materials which the most commonly used in the industry. In some of these materials, the temperature is not constant and such materials are in the class of thermoelastic materials. Behavior of a thermoelastic material under thermomechanical loading is the stress tansör and the heat flux vector [3]. Viscoelastic materials are both elastic and show a fluid behavior depending on time. Viscoelastic materials are also called time-dependent materials because time plays a very important role in determining the behavior of the medium [4]. Two major models for viscoelastic materials are known as Kelvin-Voigt body and Maxwell body. In this study, the model of viscoelastic medium has been chosen as the Kelvin-Voigt body. The viscoelastic property means taking into account water retention, transmission and resistance to movement of water, within a biological structural element [5]. In addition, temperature changes in a biological structural element remain very small. For this reason, the linear constituent equations presented in this study can be adapted for biological structural elements.

2. MATERIAL AND METHODS

2. 1 Equilibrium Equations

Local equilibrium equations (conservation of mass, conservation of linear momentum, conservation of angular momentum, conservation of energy) and entropy inequality are summarized as follows [4,6].

Conservation of Mass

$$\dot{\rho}+\rho \mathrm{v}_{k,k}=0 \tag{1}$$

$$\rho(\mathbf{x},t)=\frac{\rho_0(\mathbf{X})}{J(\mathbf{x},t)} \quad \text{(Conservation of Mass in material representation)} \tag{2}$$

Conservation of Linear Momentum

$$\rho \dot{\mathrm{v}}_p=\rho \mathrm{f}_p+t_{rp,r} \tag{3}$$

Conservation of Moment of Momentum

$$\varepsilon_{krp}\, t_{rp}=0, \quad t_{rp}=t_{pr} \tag{4}$$

Conservation of Energy

$$\rho\,\dot{\varepsilon} = t_{kl}\;\mathrm{v}_{l,k} - q_{k,k} + \rho\,h \tag{5}$$

Clausius-Duhem Inequality

$$\rho\dot{\eta} - \rho\frac{\mathrm{h}}{\theta} + \frac{1}{\theta}\nabla\cdot\mathbf{q} - \frac{1}{\theta^2}\mathbf{q}\cdot\nabla\,\theta \equiv \rho\gamma \geq 0 \tag{6}$$

Here, $\mathbf{v}$ stands for the velocity field in a continuous medium, ρ_0 for mass density before deformation, ρ for mass density after deformation, $J \equiv \det[x_{k,K}] = \frac{\rho_0}{\rho(\mathbf{x},t)}$ for jacobian, $\dot{\mathbf{v}}$ for acceleration, t_{lk} for stress tensor, f_k for the mechanical volumetric force per unit of mass, ε for internal energy density per unit of mass, q_k for heat flux vector, h for heat source per unit of mass, η for entropy density per unit of mass, $\theta(\mathbf{X},t)$ for the absolute temperature of a material point $\mathbf{X}$ at any time (t), $\rho\gamma$ entropy production per unit mass and ε_{ijk} for permutation tensor.

2.2 Thermodynamic Conditions and Constitutive Model

ρh is taken from the local energy equation (5), and if it is written in entropy inequality (6) the following expression is obtained.

$$\rho\gamma \equiv -\frac{\rho}{\theta}(\dot{\varepsilon} - \theta\dot{\eta}) + \frac{1}{\theta}t_{kl}v_{l,k} + \frac{1}{\theta^2}q_k\theta_{,k} \geq 0 \tag{7}$$

Since the material derivative of the entropy density in this expression cannot be controlled inside a thermodynamic process, a defined Legendre transformation like the one provided below can be used to transform the derivative of these values into the controllable value θ.

$$\psi \equiv \varepsilon - \theta\eta \tag{8}$$

The entropy inequality in terms of new terms is written in the material form as follows.

$$-(\dot{\Sigma} + \rho_0\,\dot{\theta}\,\eta) + \frac{1}{2}\,T_{KL}\,\dot{C}_{KL} + \frac{1}{\theta}\,\theta_{,K}Q_K \geq 0 \tag{9}$$

The terms in this inequality are defined as follows [7]:

$$\Sigma \equiv \rho_0\;\psi \tag{10}$$

$$\dot{C}_{KL} = 2\mathrm{d}_{kl} x_{k,K} x_{l,L} \Rightarrow d_{kl} = \frac{1}{2}\dot{C}_{KL} X_{K,k} X_{L,l} \tag{11}$$

$$T_{KL} \equiv J X_{K,k} X_{L,l} t_{kl} \Rightarrow t_{kl} = J^{-1} x_{k,K} x_{l,L} T_{KL} \tag{12}$$

$$G_K \equiv \theta_{,K} = x_{k,K}\theta_{,k} \Rightarrow g_k \equiv \theta_{,k} = X_{K,k}\theta_{,K} \tag{13}$$

$$Q_K \equiv J X_{K,k} q_k \Rightarrow q_k = J^{-1} x_{k,K} Q_K \tag{14}$$

To be able to use the inequality (9), it is necessary to know how the thermodynamic potential Σ depends on which independent variables. According to the selected material, the AAD's arguments and the variables to which they depend have been found using constitutive axioms. Using the results of causality, determinism, objectivity, smooth neighborhood, memory and admissibility axioms [4, 6], the arguments on which Σ depends in a thermo-viscoelastic medium exposed to mechanical loading and temperature change can be expressed as follows:

$$\Sigma(X_K, t) = \Sigma\,[C_{KL}(X_K, t), \dot{C}_{KL}(\mathbf{X}, t), G_K(X_K, t), \theta(X_K, t), X_K] \tag{15}$$

Assuming that the materials are homogenous, $\mathbf{X}$ is eliminated from among the arguments given in the expression (15) on which Σ depends. And the following expression is obtained by taking the material derivative of the expression (15).

$$\dot{\Sigma} = \frac{\partial \Sigma}{\partial C_{KL}}\dot{C}_{KL} + \frac{\partial \Sigma}{\partial \dot{C}_{KL}}\ddot{C}_{KL} + \frac{\partial \Sigma}{\partial \theta_{,K}}\dot{G} + \frac{\partial \Sigma}{\partial \theta}\dot{\theta} \tag{16}$$

If this expression is written instead of the equation (9), the following inequality is obtained.

$$\frac{1}{2}(T_{KL} - 2\frac{\partial \Sigma}{\partial C_{KL}})\dot{C}_{KL} - \frac{\partial \Sigma}{\partial \dot{C}_{KL}}\ddot{C}_{KL} - \rho_0(\eta + \frac{1}{\rho_0}\frac{\partial \Sigma}{\partial \theta})\dot{\theta} - \frac{\partial \Sigma}{\partial G_K}\dot{G}_K + \frac{1}{\theta}G_K Q_K \geq 0 \tag{17}$$

For inequality (17) to be true for any arbitrary independent thermodynamic process, coefficients of the terms $\ddot{C}_{KL}, \dot{\theta}$ and $\dot{G}_K$ which are not in the arguments of the stress potential, should be equal to zero. (Because $\dot{C}_{KL}$ and G_K are in the arguments of Σ, coefficients of $\dot{C}_{KL}$ and G_K in this inequality cannot be equal to zero). A describing as follows can be made for the coefficient of $\dot{C}_{KL}$.

$$ {}_{D}T_{KL} \equiv T_{KL} - 2\frac{\partial \Sigma}{\partial C_{KL}} \Rightarrow T_{KL} = 2\frac{\partial \Sigma}{\partial C_{KL}} + {}_{D}T_{KL} \tag{18} $$

By equalizing to zero the coefficients of $\ddot{C}_{KL}$, $\dot{\theta}$ and $\dot{G}_K$ in inequality (17), the following expressions are obtained.

$$ \frac{\partial \Sigma}{\partial \dot{C}_{KL}} = 0 \tag{19} $$

$$ \eta = -\frac{1}{\rho_0}\frac{\partial \Sigma}{\partial \theta} \tag{20} $$

$$ \frac{\partial \Sigma}{\partial G_K} = 0 \tag{21} $$

It is understood from the expressions (19) and (21) that the stress potential does not depend on $\dot{C}_{KL}$ and G_K. Therefore, arguments on which the stress potential Σ depends are expressed as follows.

$$ \Sigma = \Sigma(C_{KL}, \theta) \tag{22} $$

In this case, (17) the inequality is reduced to the following form.

$$ \frac{1}{2}\,{}_{D}T_{KL}\dot{C}_{KL} + \frac{1}{\theta}G_K Q_K \geq 0 \tag{23} $$

(23) expression gives the Clausius-Duhem inequality for the heat flux vector and the dissipative stress tensor. The following expressions indicate the arguments on which the heat flux vector and dissipative stress depend.

$$ {}_{D}T_{KL} = {}_{D}T_{KL}(C_{KL}, \dot{C}_{KL}, G_K, \theta) \tag{24} $$

$$ Q_K = Q_K(C_{Kl}, \dot{C}_{KL}, G_K, \theta) \tag{25} $$

Considering the fact that tensor ${}_{D}T_{KL}$ and Q_K vector in the inequality (23) is a continuous function in terms of $\dot{C}_{KL}$ and G_K, when $\dot{C}_{KL} = 0$ and $G_K = 0$, ${}_{D}T_{KL}$ and Q_K must also be equal to zero. Accordingly,

maintaining the order of independent constitutive variables in the expressions (24) and (25) the following expressions should be written.

$${}_{D}T_{KL}\,(C_{KL},0,0,\theta)=0 \tag{26}$$

$$Q_K\,(C_{KL},0,\,0,\,\theta,X_K)=0 \tag{27}$$

Because a viscoelastic material is being considered in this study, the symmetric stress tensor T_{KL} occurring in the material are comprised of two different stress tensors. Both of them symmetric, such stress tensors are called elastic stress and dissipative stress. Accordingly, stress tensor T_{KL} can be defined as follows in terms of material and spatial coordinates.

$$T_{KL} \equiv {}_{E}T_{KL} + {}_{D}T_{KL}, \qquad t_{kl}={}_{E}t_{kl} + {}_{D}t_{kl} \tag{28}$$

${}_{D}T_{KL}$ in the expression $(28)_1$ has been defined with the expression (24). According to (18) and (28), the elastic stress tensor ${}_{E}T_{KL}$ can be written as follows.

$${}_{E}T_{KL} \equiv 2\,\frac{\partial\,\Sigma}{\partial\,C_{KL}} \tag{29}$$

This expression is a constitutive equation for the elastic stress and arguments determining Σ in the elastic stress have been previously stated with the equation (22).

From the constitutive equations given by expressions (24), (25) and (29), it is understood that the constitutive equations of elastic stress, dissipative stress and heat flux vector will be fully determined by means of scalar-valued $\Sigma=\Sigma(C_{KL},\theta)$ function, the symmetric matrix-valued ${}_{D}T_{KL}={}_{D}T_{KL}\,(C_{KL},\dot{C}_{KL},G_K,\theta)$ function having six independent components, and vector-valued $Q_K=Q_K\,(C_{Kl},\dot{C}_{KL},G_K,\theta)$ function having three independent components. Additional constraints on these functions, which are called constitutive functionals, are originated from the material symmetry of the medium. According to the material symmetry axiom, constitutive functionals under the conversion in the form of created using the orthogonal matrix $\underline{\underline{S}}$ should remain form-invariant.

$$X_K^{'}=S_{KL}X_L\ ,\ X_L=S_{LK}^{T}X_K^{'}\ ,\ \underline{\underline{S}}^{-1}=\underline{\underline{S}}^{T} \tag{30}$$

This points to the mathematical validity of the transformations [4,6].

$$\Sigma\,(\underline{\underline{S}}\,\underline{\underline{C}}\,\underline{\underline{S}}^{T},\ \theta)=\Sigma\,(\underline{\underline{C}},\theta) \tag{31}$$

$$\underline{Q}(\underline{\underline{S}}\,\underline{\underline{C}}\,\underline{\underline{S}}^{T},\underline{\underline{S}}\,\dot{\underline{\underline{C}}}\,\underline{\underline{S}}^{T},\underline{\underline{S}}\,\underline{G},\theta)=\underline{\underline{S}}\,\underline{Q}(\underline{\underline{C}},\dot{\underline{\underline{C}}},\underline{G},\theta) \tag{32}$$

$$_{D}\underline{\underline{T}}(\underline{\underline{S}}\,\underline{\underline{C}}\,\underline{\underline{S}}^{T},\underline{\underline{S}}\,\dot{\underline{\underline{C}}}\,\underline{\underline{S}}^{T},\underline{\underline{S}}\,\underline{G},\theta)=\underline{\underline{S}}\ {}_{D}\underline{\underline{T}}(\underline{\underline{C}},\dot{\underline{\underline{C}}},\underline{G},\theta)\underline{\underline{S}}^{T} \tag{33}$$

On the other hand, the incompressibility of the medium is broadly accepted in practice in terms of formulation. The following condition must be fulfilled when the medium is assumed to be incompressible.

$$J=\det\mathbf{C}=III=1 \tag{34}$$

In this case, constitutive equation for elastic stress is obtained as follows in material and spatial coordinates.

$$_{E}T_{KL}=-p\,C_{KL}^{-1}+2\,\frac{\partial\,\Sigma}{\partial\,C_{KL}} \tag{35}$$

$$_{E}t_{kl}=-p\,\delta_{kl}+2\,x_{k,K}\,x_{l,L}\,\frac{\partial\,\Sigma}{\partial\,C_{KL}} \tag{36}$$

In these expressions, p is the Lagrange coefficient and is determined by the field equations and boundary conditions. Thus, according to (12)-(14), elastic stress tensor, dissipative stress tensor and heat flux vector can be written as follows by taking J = 1.

$$_{E}t_{kl}=x_{k,K}x_{l,L}\ {}_{E}T_{KL} \tag{37}$$

$$_{D}t_{kl}=x_{k,K}x_{l,L}\ {}_{D}T_{KL} \tag{38}$$

$$q_{k}=x_{k,K}\,Q_{K} \tag{39}$$

In this study, since the matrix material has been considered as an anisotropic medium, stress potential, dissipative stress and heat flux vector functionals are expanded in the power series in terms of the components of arguments on which they depend, and the type and number of terms taken in the series expansion are determined by the linearity of the medium. In uniform $T_0>0$ temperature and in a stress free natural state, a viscoelastic medium is considered, and it is assumed that the strain tensor and the rates of deformation tensor, which composed when the medium is deformed, provide the $\|\mathbf{E}\|<<1$, $\|\dot{\mathbf{E}}\|<<1$

constraints.It is also assumed that the temperature changes are very small, in other words, T/T_0 is $T/T_0 << 1$ when θ is written as $\theta = T_0 + T$.

3. RESULTS AND DISCUSSION

3.1 Linear Theory

Since the relation $C_{KL} = \delta_{KL} + 2E_{KL}$ exists between the Green deformation tensor and strain tensor, and E_{KL} can be expressed as $E_{KL} \cong \tilde{E}_{KL} \equiv \frac{1}{2}(U_{K,L} + U_{L,K})$ in the linear theory, the arguments of the stress potential given by the expression (22) can be written down as follows:

$$\Sigma = \Sigma(\tilde{E}_{KL}, \theta) \tag{40}$$

Assuming that this function is analytic in terms of the $\tilde{\mathbf{E}}$ value, if this function is expanded in Taylor series around $\tilde{\mathbf{E}} = \mathbf{0}$ the expression shall be obtained for the stress potential:

$$\Sigma(\tilde{E}_{KL}, \theta) = \Sigma_0(\theta, \mathbf{X}) + \Sigma_{KL}(\theta, \mathbf{X})\tilde{E}_{KL} + \frac{1}{2}\Sigma_{KLMN}(\theta, \mathbf{X})\tilde{E}_{KL}\tilde{E}_{MN} + \ldots \tag{41}$$

Coefficients in this equation have been defined as follows:

$$\Sigma_0 = \Sigma(\underline{0}, \underline{0}), \quad \Sigma_{KL} \equiv \left.\frac{\partial \Sigma}{\partial \tilde{E}_{KL}}\right|_0, \Sigma_{KLMN} \equiv \left.\frac{\partial^2 \Sigma}{\partial \tilde{E}_{KL}\partial \tilde{E}_{MN}}\right|_0 \tag{42}$$

Due to the symmetry of the $\tilde{E}_{KL}$ tensor and non-dependence on order of the derivatives in the definitions in the expressions (42), these coefficients bear the symmetry characteristics indicated below:

$$\Sigma_{KL} = \Sigma_{LK}, \qquad \Sigma_{KLMN} = \Sigma_{LKMN} = \Sigma_{KLNM} = \Sigma_{MNKL}, \tag{43}$$

The following relations can be written down for the linear theory in continuum mechanics [4,6]:

$$E_{KL} \cong \tilde{E}_{KL} \equiv \frac{1}{2}(U_{K,L} + U_{L,K}), \quad e_{kl} \cong \tilde{e}_{kl} = \in_{kl} \equiv \frac{1}{2}(u_{k,l} + u_{l,k}), \quad \in_{kl} \cong \lambda_{kK}\lambda_{lL}\tilde{E}_{KL},$$

$$\tilde{E}_{KL} \cong \lambda_{kK}\lambda_{lL}\tilde{e}_{kl}, \quad x_{k,K} = \lambda_{kK} + u_{k,K}, \quad X_{K,k} = \Lambda_{Kk} - U_{K,k}, \quad x_{k,K}x_{l,L} = \lambda_{kK}\lambda_{lL},$$

$$X_{K,k}X_{L,l} = \lambda_{kK}\lambda_{lL}, \quad E_{KL} \cong \tilde{E}_{KL} \equiv \lambda_{kK}\lambda_{lL}\tilde{e}_{kl} = \frac{1}{2}\lambda_{kK}\lambda_{lL}(u_{k,l} + u_{l,k}),$$

$$d_{pr} = \frac{\partial E_{PR}}{\partial t}X_{P,r}X_{R,r} = \frac{\partial \in_{pr}}{\partial t}, \quad d_{pr} = \frac{\partial (u_{p,r})}{\partial t} = \dot{u}_{p,r}, \qquad \dot{\varepsilon} \approx \frac{\partial \varepsilon}{\partial t} \tag{44}$$

For incompressible medium, the spatial form of elastic stress can be written as follows.

$$ {}_E t_{pr} = -p\,\delta_{pr} + \frac{\partial \Sigma}{\partial \in_{pr}} \tag{45} $$

In the linear theory, arguments on which Σ depends can be expressed in spatial form as follows:

$$ \Sigma = \Sigma(\in_{kl}, \theta) \tag{46} $$

Assuming this function is analytic in terms of $\in_{kl}$ and expanding it in the Taylor series around $\in_{kl} = 0$ will give us the following expression:

$$ \Sigma(\in_{kl}, \theta) = \Sigma_0(\theta, \mathbf{X}) + \Sigma_{kl}(\theta, \mathbf{X}) \in_{kl} + \frac{1}{2}\Sigma_{klmn}(\theta, \mathbf{X}) \in_{kl} \in_{mn} + \ldots \tag{47} $$

The spatial material tensors Σ_{kl} and Σ_{klmn} in the equation (47) bear the same properties as the material tensors of the material Σ_{KL} and Σ_{KLMN}, and are defined as follows:

$$ \Sigma_{kl} = \lambda_{kK}\,\lambda_{lL}\,\Sigma_{KL}, \qquad \Sigma_{klmn} \equiv \lambda_{kK}\,\lambda_{lL}\,\lambda_{mM}\,\lambda_{nN}\,\Sigma_{KLMN} \tag{48} $$

In order to reach a real linear theory, the expression (47) should be quadratic at most in terms of the endlessly small expansion tensor $\in_{kl}$ and temperature change T. For this purpose, the coefficients dependent on θ in the expression (47) have been defined as follows, respectively:

$$ \Sigma_0(\theta, \mathbf{X}) = \Sigma_0(T_0 + T, \mathbf{X}) = \rho_0(\mathbf{X})\psi_0(T_0, \mathbf{X}) - \rho_0(\mathbf{X})\eta_0(T_0, \mathbf{X})T - \frac{1}{2}\rho_0(\mathbf{X})\frac{1}{T_0}C(T_0, \mathbf{X})T^2 + \ldots $$

$$ \Sigma_{kl}(\theta, \mathbf{X}) = \gamma_{kl}(T_0, \mathbf{X}) - \beta_{kl}(T_0, \mathbf{X})T + \ldots $$

$$ \Sigma_{klmn}(\theta, \mathbf{X}) = \Sigma_{klmn}(T_0 + T, \mathbf{X}) = \Sigma_{klmn}(T_0, \mathbf{X}) \tag{49} $$

Coefficients in this equations have been defined as follows:

$$ \left.\frac{\partial \psi_0(T, \mathbf{X})}{\partial T}\right|_{T=T_0} \equiv -\eta_0(T_0, \mathbf{X}), \qquad \left.\frac{\partial^2 \psi_0(T, \mathbf{X})}{\partial T^2}\right|_{T=T_0} \equiv -\frac{1}{T_0}C(T_0, \mathbf{X}), $$

$$ \gamma_{kl}(T_0, \mathbf{X}) \equiv \Sigma_{kl}(T_0, \mathbf{X}) = \gamma_{lk}(T_0, \mathbf{X}), \qquad \beta_{kl}(T_0, \mathbf{X}) \equiv -\left.\frac{\partial \Sigma_{kl}(T, \mathbf{X})}{\partial T}\right|_{T=T_0} = \beta_{lk}(T_0, \mathbf{X}) \tag{50} $$

In these expressions, $\psi_0(T_0, \mathbf{X})$, $\eta_0(T_0, \mathbf{X})$, and $C(T_0, \mathbf{X})$ are scalar; $\gamma_{kl}(T_0, \mathbf{X})$, $\beta_{kl}(T_0, \mathbf{X})$ and $\Sigma_{klmn}(T_0, \mathbf{X})$ are tensorial material constants and these coefficients depend on the initial temperature T_0 of the medium and medium particles in heterogeneous materials. In homogenous materials, the dependence on $\mathbf{X}$ is eliminated. In order to simplify notation, we will omit indicating the arguments $(T_0, \mathbf{X})$ of such coefficients. Substituting the expressions (50) and (49) in equation (47) gives us the following expression:

$$\Sigma(\in_{kl}, T_0 + T, \mathbf{X}) = \rho_0 \psi_0 - \rho_0 \eta_0 T - \frac{\rho_0 c}{2T_0} T^2 + \gamma_{kl} \in_{kl} - \beta_{kl} T \in_{kl} + \frac{1}{2} \Sigma_{klmn} \in_{kl} \in_{mn} + \ldots \quad (51)$$

If derivatives in expression (45) is taken from (51) and used in substitution, the following expressions are obtained:

$${}_E t_{pr} = -p\delta_{pr} - \beta_{pr} T + \Sigma_{prmn} \in_{mn} \quad (52)$$

Due to $\Sigma_{prmn} = \Sigma_{prnm}$ symmetry property of the coefficient Σ_{prmn} in this expression, the constitutive equation of elastic stress given by expression (52) can be converted into the following form in terms of linear constituents of displacement gradient.

$${}_E t_{pr} = -p\delta_{pr} - \beta_{pr} T + \Sigma_{prmn} u_{m,n} \quad (53)$$

In a thermo-viscoelastic material, assuming the medium is to be anisotropic, incompressible, homogeneous, dependent on temperature gradient and showed linear visco-elastic behavior, the equation (53) is the linear constitutive equation of elastic stress. First term on the right part of equation (53) is caused by the incompressible of the medium. The second term expresses the temperature effect and the fourth term expresses the contribution of the elastic deformation to the elastic stress tensor.

Here, the approach assumed for the stress potential has been assumed for the dissipative tensor and the heat flux vector. Accordingly, the dissipative tensor and the heat flux vector can be found through a power series expansion in terms of components of the arguments on which it depends, around a reference location selected as the natural condition. Considering that $\mathbf{E}$ can be substituted by $\tilde{\mathbf{E}}$ and $\dot{\mathbf{E}}$ can be substituted by $\dot{\tilde{\mathbf{E}}}$ in the linear theory, arguments on which the dissipative tensor and the heat flux vector depend, entropy inequality and constraint caused by this inequality have been found as follows:

$${}_D T_{PR} = {}_D T_{PR}(\tilde{E}_{KL}, \dot{\tilde{E}}_{KL}, G_K, \theta) \quad (54)$$

$$Q_R = Q_R(\tilde{E}_{KL}, \dot{\tilde{E}}_{KL}, G_K, \theta) \quad (55)$$

$$\frac{1}{2} {}_D T_{KL} \dot{C}_{KL} + \frac{1}{\theta} G_K Q_K \geq 0 \quad (56)$$

$${}_D T_{PR} = {}_D T_{PR}(\tilde{\mathbf{E}}, 0, 0, \theta) = 0 \quad (57)$$

$$Q_R = Q_R(\tilde{\mathbf{E}}, 0, 0, \theta) = 0 \quad (58)$$

Opening the functions (54) and (55) in a Taylor series around $\tilde{\mathbf{E}} = \mathbf{0}$, $\dot{\tilde{\mathbf{E}}} = \mathbf{0}$, $\mathbf{G} = \mathbf{0}$ will give us the following expression:

$${}_{D}T_{PR}(\tilde{\mathbf{E}},\dot{\tilde{\mathbf{E}}},\mathbf{G},\theta)=K_{PRKL}\tilde{E}_{KL}+\Gamma_{PRMN}\dot{\tilde{E}}_{MN}+H_{PRS}G_{S}+\ldots \quad (59)$$

$$Q_{R}(\tilde{\mathbf{E}},\dot{\tilde{\mathbf{E}}},\mathbf{G},\theta)=D_{RLM}\tilde{E}_{LM}+N_{RLM}\dot{\tilde{E}}_{LM}+B_{RL}G_{L}+\ldots \quad (60)$$

The coefficients in these equations have certain symmetry properties and only depend on T_0 and **X**. According to the equations (57) and (58), since ${}_{D}T_{PR}={}_{D}T_{PR}(\tilde{\mathbf{E}},0,0,\theta)=0$ and $Q_R=Q_R(\tilde{\mathbf{E}},0,0,\theta)=0$, K_{PRKL} and D_{RLM} coefficients must be equal to zero. ($K_{PRKL}=0$ and $D_{RLM}=0$). In addition, the term $G_L=\theta_{,L}$ can be written as $\theta_{,R}=(T_0+T)_{,R}=T_{,R}$. In this case, the linear material constitutive equations, of the dissipative stress tensor and the heat flux vector are expressed as follows.

$${}_{D}T_{PR}(\tilde{\mathbf{E}},\dot{\tilde{\mathbf{E}}},\mathbf{G},\theta)=\Gamma_{PRMN}\dot{\tilde{E}}_{MN}+H_{PRS}T_{,S} \quad (61)$$

$$Q_{R}(\tilde{\mathbf{E}},\dot{\tilde{\mathbf{E}}},\mathbf{G},\theta)=N_{RLM}\dot{\tilde{E}}_{LM}+B_{RL}T_{,L} \quad (62)$$

Due to the symmetry of tensors ${}_{D}T_{PR}$ and $\dot{\tilde{E}}_{MN}$ and independence of the derivatives in the expansion terms from the order, these coefficients bear symmetry characteristics as below.

$$\Gamma_{PRMN}=\Gamma_{RPMN}=\Gamma_{PRNM},\quad N_{RLM}=N_{RML},\quad H_{PRS}=H_{RPS} \quad (63)$$

If the equations 61) and (62) are substituted in the equations of (38) and (39), the spatial forms of the dissipative stress tensor and heat flux vector are obtained as follows.

$${}_{D}t_{pr}=\Gamma_{prmn}\dot{u}_{m,n}+h_{prl}T_{,l} \quad (64)$$

$$q_r=n_{rlm}\dot{u}_{l,m}+B_{rl}T_{,l} \quad (65)$$

Spatial material tensors B_{rl}, n_{rlm}, h_{prs} and Γ_{prmn} in these equations have the certain symmetry characteristics and they only depend on T_0 and **X.**

$$B_{rl}\equiv\lambda_{rR}\lambda_{lL}B_{RL}$$

$$n_{rlm}\equiv\lambda_{rR}\lambda_{lL}N_{RLM}$$

$$h_{prs}\equiv\lambda_{pP}\lambda_{rR}\lambda_{sS}H_{PRS}$$

$$\Gamma_{prmn}\equiv\lambda_{pP}\lambda_{rR}\lambda_{mM}\lambda_{nN}\Gamma_{PRMN} \quad (66)$$

The equations (63) and (64) are the linear constitutive equations of of dissipative stress tensor and heat flux vector in a thermo-viscoelastic material, assuming the medium is to be anisotropic, incompressible, homogeneous, dependent on temperature gradient and showed linear visco-elastic behavior. Considering

these equations, terms contributing to the dissipative stress tensor and heat flux vector are created by the material time derivative of displacemet gradient and the temperature gradient.

Substituting equations (53) and (64) into the expression $(28)_2$, linear spatial stress tensor occurring symmetrically in the considered anisotropic material has been obtained as follows, based on the assumptions previously mentioned.

$$t_{pr} = -p\delta_{pr} - \beta_{pr} T + \Sigma_{prmn} u_{m,n} + \Gamma_{prmn} \dot{u}_{m,n} + h_{prl} T_{,l} \qquad (67)$$

By the equation (67), symmetric stress on spatial coordinates has been expressed in terms of displacement vector gradients, the material time derivative of displacemet gradient and the temperature gradient.

4. CONCLUSION

In this study, based on the expectation that it will allow to model the linear behavior of a heat-conducting viscoelastic material, a route has been followed in the context of modern continuum mechanics. In performing this modeling; general thermodynamic balance equations, Clausius-Duhem inequality, constitutive axioms, concepts pertaining to the symmetry group of the material and obtaining the constitutive functionals, the theoretical basis of modeling of the thermo-viscoelastic behavior of the material has formed. Viscoelastic materials are both elastic and show a fluid behavior depending on time. Viscoelastic materials are also called time-dependent materials because time plays a very important role in determining the behavior of the medium. Two major models for viscoelastic materials are known as Kelvin-Voigt body and Maxwell body. In this study, the model of viscoelastic medium has been chosen as the Kelvin-Voigt body. In order to take into account the heat conduction, the material temperature gradient vector defined as $\mathbf{G} \equiv \theta_{,K} \mathbf{I}_K$ is included in the constitutive variables. For constitutive functions in a heat-conducting viscoelastic materal, it has been observed that, as a result of thermodynamic constraints, the stress potential function is dependent on the deformation tensor and the temperature, whereas the heat flux vector and the dissipative stress functions are dependent on he deformation tensor, the rates of deformation tensor, the temperature and the temperature gradient. Consisted under thermo-mechanical loads arising of the external in a heat-conducting viscoelastic material, The elastic stress tensor, the dissipative stress tensor and the heat flux vector are obtained by means of these constitutive functions. The elastic stres tensor is derived from the stress potential function whose arguments are known. Because the dissociative stress tensor and heat flux vector are not derived from a potential, they have shown up as an analytical function of their arguments. The viscoelastic medium is considered incompressible, as incompressibility of the

medium is broadly accepted in practice for formulation. The reference position of the viscoelastic medium has been selected at the $T_0 > 0$ temperature in a stress free natural condition and it has been assumed that the medium moves away from that position by small displacements, deformations, rates of deformations, and small changes in temperature. Finally, in linear thermo-viscoelasticity incompressible medium, the forms in spatial coordinates of the constitutive equations which of the elastic stress tensor, the dissipative stress tensor, the heat flux vector and the symmetric stress tensor are presented by the equations (53), (63), (64) and (67).

REFERENCES

[1] Holzapfel, A.G., Nonlinear Solid Mechanics, John Wiley and Sons Ltd, Chichester, 455p, 2000.

[2] Timoshenko, S.P., and Goodier, J.N., Theory of Elasticitiy, Mcgraw Hill, 567p, 1970.

[3] Hamamcı, B., A mathematical model for fiber reinforced thermoelastic materials, Master Thesis, Süleyman Demirel University, Institute of Science and Technology, Isparta, Turkey, pp: 93. 2006.

[4] Şuhubi, E.S., Continuum mechanics–Introduction, İ.T.U., Faculty of Arts and Sciences Publication. İstanbul, Turkey, 243 p, 1994.

[5] Usal, M., A mathematical model for a biological construction element, Ph. D Thesis, Süleyman Demirel University, Institute of Science and Technology, Isparta, Turkey, pp: 232. 2001.

[6] Eringen, A.C., Mechanics of Continua, Robert E. Krieger Pub. Co., Hungtington, 590 p, New York, 1980.

[7] Usal, M.R., A mathematical model for the electro-thermomechanical behaviour of fiber reinforced elastic dielectric media, Ph. D. Thesis, Erciyes University, Institute of Science and Technology, Kayseri, Turkey, pp: 108, 1994.

SURVEILLANCE FOR NUCLEAR ELECTRONICS AT A GLANCE

M. E. TURGAY

Department of Electrical&Electronics, Engineering Faculty, Yalova University, 77200, Yalova, TURKEY

E-mail: eturgay20@hotmail.com

Abstract

Nuclear Electronics is an important discipline of ELECTRONICS Science. Besides after radiation interacts to the detector material, electron which handled direct or indirect, is important to determine the energy level and intensity of incident radiation. There are a few solutions for these determinations. Since 1969, that's were applied by modular devices such as high voltage supplier, amplifier, discriminator and scaler, etc due to NIM standards. 1971, CAMAC was standardized. Last in 1979, VERSA was definated. Nowadays, all in one technology is preferred especially for NIM versions stated in detector systems.

Keywords: Radiation, Electron, Signal Processing, NIM, CAMAC, Detector

1. INTRODUCTION

This paper includes interdisciplinary -briefly sum up- concerning to radiation detection and its electronic's front-end structures. Essentially all of the nuclear radiation detectors produce electronic pulses in response to the interaction of some ionizing radiation. These signals are processed by standardized nuclear instrumentation modules (NIM) electronics to count the number of pulses or to more fully analyze the size or even the shape of the signal. In addition, computer-based electronics in the CAMAC (Computer Automated Measurement and Control) system are used to measure the time relationships of pulses, the pulse heights, and the signal shapes. The signals are recorded and stored by computers for later analysis. An important feature of scientific studies with radioactivities and with nuclear beams is that the data must be collected as rapidly as possible usually during a very limited time [1]. Nuclear electronics is a subfield of electronics concerned with the design and use of high-speed electronic systems for nuclear physics and elementary particle physics research, and for industrial and medical usage. Essential elements of such systems include fast detectors for charged particles, discriminators for separating them by energy, counters for counting the pulses produced by individual particles, fast logic circuits which includes coincidence and veto gates, for identification of particular types of complex particle events, and pulse height analyzers (PHAs) for sorting and counting gamma rays or particle interactions by energy, for spectral analysis. These sub-structures are originally developed and built in the laboratories, besides designed, developed, and manufactured by a specialized vendors as Apantec LLC., Berkeley Nucleonics Corporation, Wiener Plein & Baus GmbH, Canberra, EG&G Ortec, Oxford Instruments, Stanford Research Systems, Tennelec [2]. These structures should have to regulations regarding the standards like NIM, CAMAC like that [3].

2. MATERIAL AND METHODS (Theory)

2.1. RADIATION

In physics, *radiation* is a process in which energetic particles or transferred energy by *waves*, travel through a medium or space. In this paper, will be refered the gamma-ray radiation (wave) especially. It would be detected and measured by some instruments which named spectrometers, some of ones run by scintillation and others run by semiconductor materials. For scintillation detector, commonly used doped materials like NaI (Tl), it runs by high efficiently. Near by its resolution is not so good. A spectrogram is shown in Figure 1 [Resolution R is equal to ratio of $(E_U - E_L)/W$ in here]. For resolution term, could be referred further information and visuals, to reference [4], too.

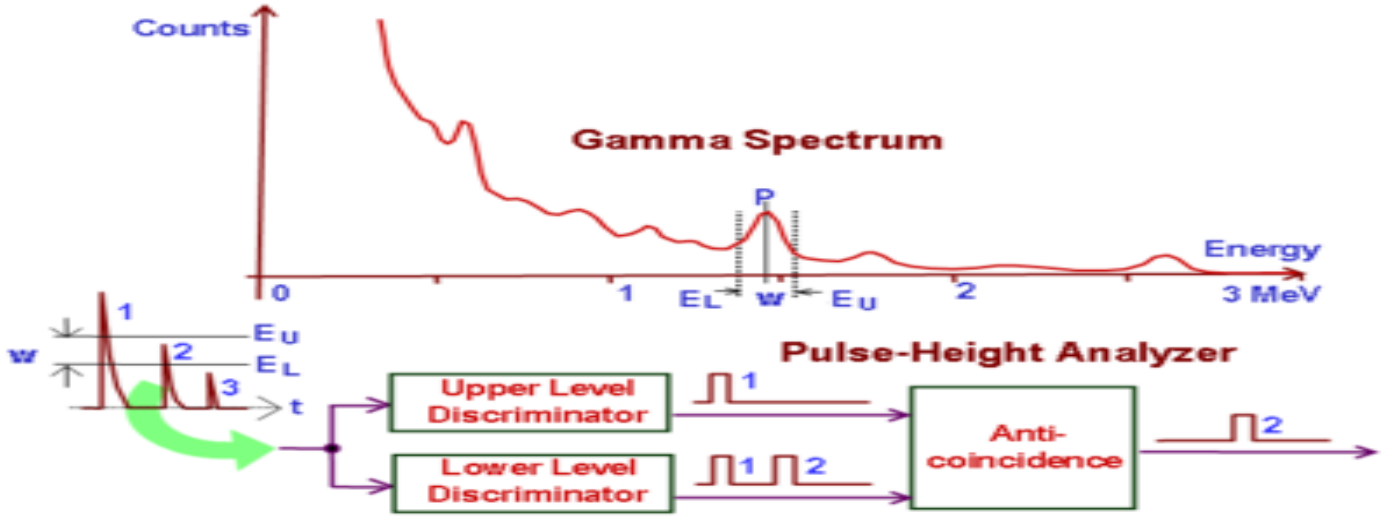

Figure 1. Spectrogram which taken by Scintillation detector system [1].

2.2. MEASUREMENT

Radiation detecting systems have two basic part. One of them is detector, another one is counter (electronic parts). There are different type of detector systems existed. Besides whenever want to learn the source of radiation near by the intensity, we need the spectrometers (Table 1). Incident radiation interacts to detector, it is important to handle the electron direct or indirect. After that, its conventional -signal processing- succeed by these units consequently: Pre-amplifier, Linear amplifier, Biased amplifier, Pulse stretcher, Sum-amplifier, Delay, Linear gate, >> Integral discriminator, Differential discriminator (SCA), Time pick-off (trigger), >> Time amplitude converter, >> Coincidence, Anti-coincidence, Scaler [4].

Table 1. Measuring Devices of Radiation

	Dosimeters	Counters	Spectrometers
Detection of Radiation	Film	Ion Chamber	Scintillator
	TLD	Proportional Counter	Semiconductor
	OSL	GM Tube	--

3. RESULTS AND DISCUSSION (Discussion)

In order to get spectrogram by higher resolution, it should be used the semiconductor detectors like high purity Germanyum (HpGe). In this case low efficiency had to be acceptable for this kind of studies in advance. Block diagram for solid state detector is shown in Figure 2.

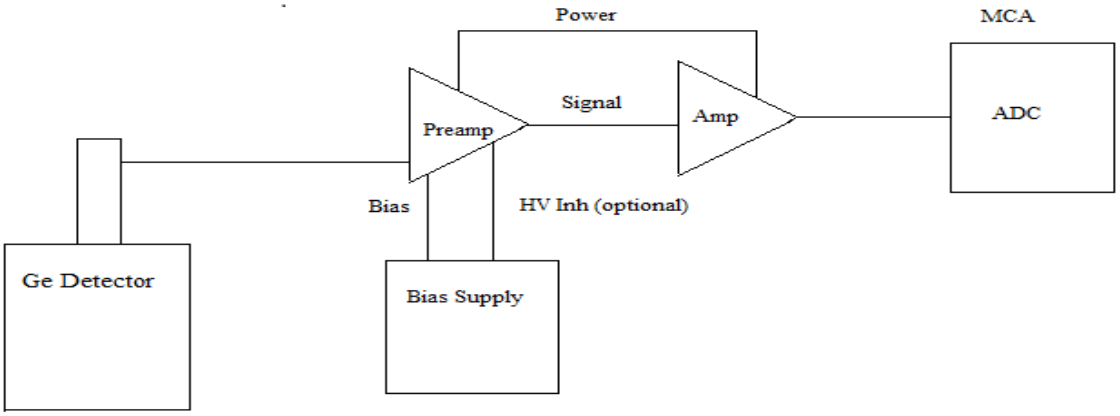

Figure 2. Block Diagram for solid state (Germanyum) detector system [5].

4. CONCLUSION

This study would be rather useful for beginners and also researchers about Nuclear Electronics and its classification. Further more could be had by following the detailed publications and books, too. Földiak's [6] and Gilmore's [7] book are useful sources for nuclear techniques, too.

ACKNOWLEDGMENTS

Dr. TURGAY appreciates to Cevdet IŞIK who is an outstanding professor of Istanbul Technical University (I.T.U.) for his kind supports to author during Microwave Lab and Graduation Project at faculty of EE. ***In memory of 'Inci AKKAYA' and 'Mehmet KORUREK'*** **(both dead)** ***who outstanding professors in Electrical&Electronics (EE) Faculty of ITU.***

REFERENCES

[1] Course Notes, Radiation Detectors, Chapter 18, Oregon State University.

[2] www.wikipedia.org/ nuclear electronics.

[3] T. Hoagland A Brief Discussion of NIM, CAMAC and VME Standards. Holland, 2004.

[4] Knoll, G.F., Radiation Detection and Measurement, C.17, P.609, (NY) 2000.

[5] http://www.canberra.com/products/detectors/germanium-detectors.asp

[6] Földiak, G., Industrial Applications of Radioisotopes, 1986.

[7] Gilmore, G.R., Practical Gamma-Ray Spectrometry, April- 2008.

SYNTHESIS, CRYSTAL STRUCTURE, SPECTRAL CHARACTERIZATION, α–GLUCOSIDASE INHIBITION AND TD/DFT STUDY OF THE Cu (II) COMPLEX

S. Altürk[1], D. Avcı[1], F. Sönmez[2], Ö. Tamer[1], A. Başoğlu[1], Y. Atalay[1], and B. Zengin Kurt[3]

[1]*Sakarya University, Faculty of Arts and Sciences, Department of Physics, 54187, Sakarya, Turkey*
[2]*Sakarya University, Faculty of Arts and Sciences, Department of Chemistry, 54187, Sakarya, Turkey*
[3]*Bezmialem Vakif University, Faculty of Pharmacy, Department of Pharmaceutical Chemistry, 34093 Istanbul, Turkey*

E-mail: sumeyye-alturk@hotmail.com

Abstract

The Cu (II) complex of 6–methylpyridine–2–carboxylic acid was synthesized and its structure was characterized by XRD, FT–IR and UV–Vis spectroscopic techniques. The α–glucosidase inhibition activity of the synthesized complex was determined by IC_{50} values. Furthermore, the optimized molecular structure and vibrational frequencies were obtained by using Density Functional Theory (DFT) with HSEh1PBE/6–311G (d, p)/LanL2DZ level. In order to investigate electronic spectral properties, TD–DFT calculations in ethanol solvent and gas phase were fulfilled. The NLO parameters and FMO energies of the complex was calculated by using HSEh1PBE/6–311G (d, p) level. Lastly, to show the binding site of the target protein (the template structure S. cerevisiae isomaltase), the docking study of complex was carried out.

Keywords: 6–methylpyridine–2–carboxylic acid, XRD, FT–IR and UV–Vis; α–Glucosidase; Docking; TD/DFT–HSEh1PBE level.

1. INTRODUCTION

Picolinic acid and its derivatives have largely studied because of their major coordination elasticity and versatility [1–7]. These ligand having one or more carboxylic acid groups have provide to coordinate with many metal centers in different modes [4]. Many transition metal complexes of these ligands have been extensively studied because of great coordination potential, biological and pharmaceutical properties [6,8,9]. α−Glucosidase, a critical enzyme for the digestion of carbohydrates, catalyzes the cleavage of absorbable monosaccharides, beginning from disaccharides and oligosaccharides [10,11]. The functions of α−glucosidase for mammals contain intestinal digestion of dietary carbohydrates, glycogen degradation, and glycoprotein folding and maturation [12,13]. Synthesis, crystal structure and spectroscopic characterization for 6−mpa and its metal complexes have been reported [4,6,9,13]. The synthesis of Cu (II) complex of 6−mpa, its crystal structure, IR and EPR spectra were experimentally investigated. Previously, we studied the experimental and theoretical analysis of the Cu (II) complex [6], but α−Glucosidase enzyme activity and molecular docking was not studied. In this work, the crystal structure characterization of the synthesized Cu (II) complex was performed by XRD method. Spectroscopic and electronic properties and α–glucosidase enzyme activity study were also carried out. The experimentally obtained structural, spectroscopic and electronic properties for the Cu (II) complex have been theoretically supported by using DFT/HSEh1PBE/6–311G (d,p)/LanL2DZ level.

2. MATERIAL AND METHODS

To an ethanol/water solution (40 mL, in molar ratio 1:1) containing copper (II) acetate monohydrate ($(CH_3COO)_2Cu{\cdot}H_2O$) (1 mmol), 6–methylpicolinic acid (6−mpa) (2 mmol) was added slowly. The obtained solution was allowed to evaporate for 10 day at room temperature after being stirred at the proper temperature. After 10 days the blue crystals adequate for X–ray diffraction analysis were obtained.

The calculations of Cu (II) complex was performed by using the Gaussian 09, Revision D01 program [14] and the output files were visualized by GaussView 5 software [15]. The optimized molecular geometry and vibrational frequencies of Cu (II) complex were calculated through performing density functional theory (DFT) with HSEh1PBE method [16–20] at 6–311G (d,p)/LanL2DZ basis set [21–24]. The electronic transition and oscillator strength were computed by using time dependent DFT (TD–HSEh1PBE) [25] and 6–311G (d,p)/LanL2DZ basis set with polarizable continuum model (PCM) [26] in ethanol solvent and gas phase. Frontier molecular orbital energies were calculated by using HSEh1PBE/6–311G (d,p)/LanL2DZ level. The second– and third– order nonlinear optical (NLO) parameters were

calculated at the same level in ethanol solvent and gas phase. NBO (natural bond orbital) analysis [27] has been fulfilled to understand the hydrogen bonding interaction and coordination around the Cu center.

3. RESULTS AND DISCUSSION

The molecular structure of the Cu (II) complex crystallizes in the triclinic P–1 space group. The crystal structure data of the complex are established to be a= 8.0581(9) Å, b= 9.4965(9) Å, c= 11.0973(12) Å, α= 96.332(8)°, β= 100.026(9)°, γ= 107.910(8)°, V= 783.46(15) Å^3. Figure 1 shows the crystal structure and theoretical geometry of the Cu (II) complex. Selected theoretical bond lengths and angles are listed in Table 1 and compared with XRD results.

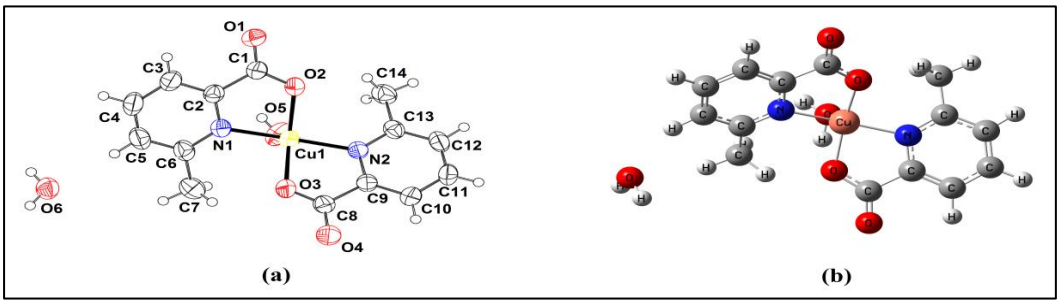

Figure 1. a) The experimental molecular structure b) the optimized molecular structure of the Cu (II) complex at HSEh1PBE/6–31G (d,p)/LanL2DZ.

Table 1. Selected experimental and theoretical bond length and angles for the Cu (II) complex.

Parameters	XRD	HSEh1PBE	Parameters	XRD	HSEh1PBE
Cu1–O2	1.962(18) Å	1.895 Å	O2–Cu1–O3	141.2 (9)º	164.6º
Cu1–O3	1.961(19) Å	1.930 Å	O2–Cu1–N1	82.5 (8)º	82.8º
Cu1–O5	2.153(2) Å	2.380 Å	O3–Cu1–N1	94.6 (8)º	98.3º
Cu1–N1	2.014(2) Å	2.055 Å	O2–Cu1–N2	96.8 (8)º	95.9º
Cu1–N2	2.031(2) Å	2.044 Å	O3–Cu1–N2	81.9 (8)º	81.7º
			N1–Cu1–N2	173.5 (8)º	175.5º
			O2–Cu1–O5	115.9 (9)º	115.1º
			O3–Cu1–O5	102.8 (9)º	80.2º
			N1–Cu1–O5	88.3 (9)º	93.8º
			N2–Cu1–O5	98.2 (9)º	90.7º

Vibrational properties have been investigated to determine fundamental modes connected with molecular structure of the Cu (II) complex using FT–IR spectra. The comparison of FT–IR and theoretical IR spectra for the Cu (II) complex are shown in Figure 2 and summarized in Table 2.

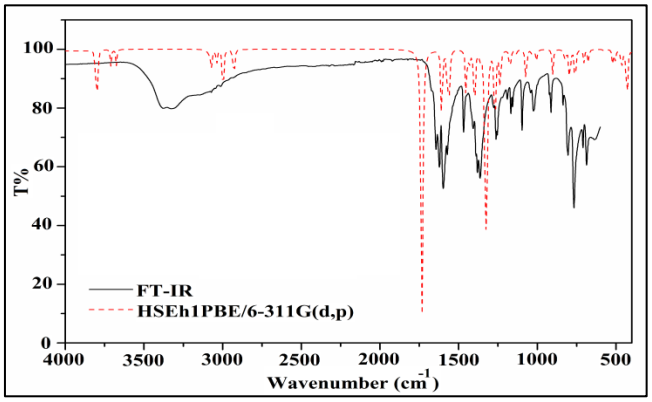

Figure 2. The comparison of experimental and theoretical IR spectra of the Cu (II) complex

Table 2. Comparison of the FT–IR and calculated vibration frequencies for complex

Assignments	FT–IR	HSEh1PBE
		Scaled freq.[a]
υ_{as} OH	3376	3794
υ_{s} OH	3318	3676
υ CH ring	3071	3071
υ CH_3	3041	3040
υ OC	1645	1740
υ CC ring	1601	1608
β H_2O	1570	1566
β CH_3	1383	1364
υ OC	1366	1329
υ NC	1264	1270
γ HCCC	1026	990
β CNCu	635	468
γ CuCCN		443
β HOCu		430

[a] Scaled frequencies are in unit of cm^{-1}. υ: Stretching; β: in plane bending; γ: out–of plane bending.

The electronic excitation energies and oscillator strengths in ethanol solvent and gas phase were calculated by using the TD–HSEh1PBE/6–311G (d,p)/LanL2DZ level with PCM [26]. The remarkable contributions of the electronic transitions were appointed via SWizard program [28]. Obtained electronic results are compared with the experimental ones and summarized in Table 3.

Table 3. Experimental and theoretical electronic transition, oscillator strength and major contributions for Cu (II) complex.

Solvent	Experimental	HSEh1PBE/6–311G(d,p)			
	λ (nm)	λ (nm)	Osc. Strength	Major contribution	
Ethanol	–	737	0.0016	H–14→L β(33%)	H–4→L β(17%)
	447.59	597	0.0001	H–8→L β(28%)	H–13→L β(18%)
	–	328	0.0003	H→L α(68%)	H–1→L+1 α(8%)
	290.77	323	0.0002	H→L+1 α(56%)	H–1→L α(12%)
Gas phase		721	0.0002	H–3→L β(20%)	H–7→L β(18%)
		355	0.0002	H→L α(44%)	H→L+1 α(13%)
		331	0.0133	H→L β(75%)	H→L+1 α(9%)
		322	0.0073	H–1→L β(27%)	H–1→L+1 β(19%)

The frontier molecular orbitals (FMO) play an important role in optical and electronic properties of molecular systems. FMO energies of Cu (II) complex are calculated by using the DFT/HSEh1PBE method and 6–311G(d,p)/LanL2DZ basis set. Energy gap between HOMO and LUMO characterizes the molecular chemical stability, chemical reactivity and hardness of the molecule. The designs of FMO and energy gap between them are given in Figure 3.

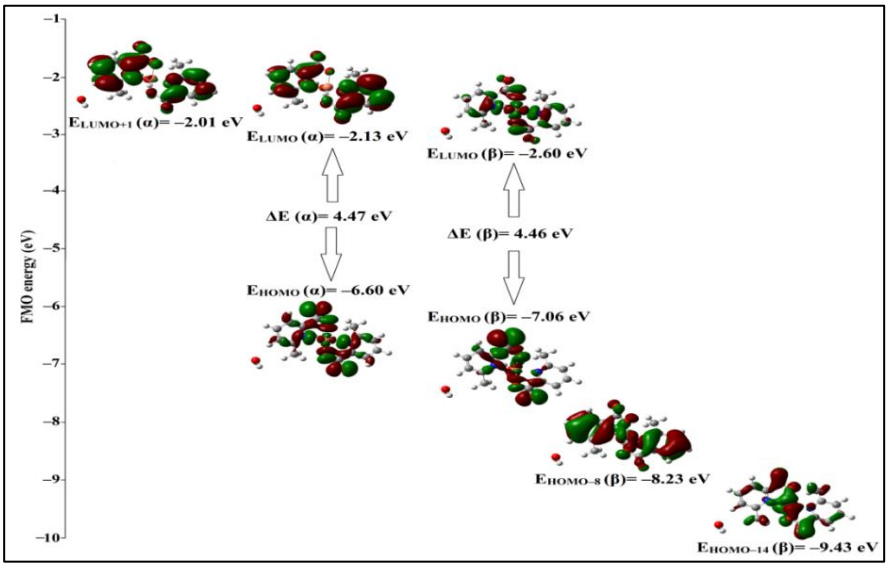

Figure 3. The occupied and unoccupied molecular orbitals being the most active in electronic transition for the Cu (II) complex.

The nonlinear optics (NLO) have been investigated by several research groups for the arising technologies in the areas such as signal processing, telecommunications and optical inter connections [29,30]. The higher values of second– and third– order nonlinear optical (NLO) parameters are important

for more active NLO properties. NLO parameters are calculated by using HSEh1PBE/6–311G (d,p)/LanL2DZ level in ethanol solvent and gas phase. In comparison of NLO parameters for molecular systems without experimental measurements, p–Nitroaniline (pNA) [31,32] and urea [33] which is a typical NLO materials are used (see Table 4).

Table 4. Electric dipole moment (μ, in Debye), the average and anisotropic static polarizabilities (‹α› and Δα, in10^{-24} esu), the first– and second– order static hyperpolarizabilities (‹β›, in10^{-30} esu and ‹γ›, in10^{-36} esu) for Cu (II) complex.

Property	HSEh1PBE/6–311G(d,p)		pNA[a] [31,32] and urea[b] [33] results
	Ethanol	Gas phase	
μ	10.06	5.07	2.44[a]
<α>	39.40	30.40	22[a]
Δα	23.66	20.1	
<β>	3.21	1.57	8[a], 0.13[b]
<γ>	50.82	21.06	15[a]

The NBO (natural bond orbital) analysis is used to investigate inter and intramolecular bonding and interaction among bonds [34]. Furthermore, it provides a basis for investigating charge transfer or conjugative interaction in molecular system. It is stated that the larger the $E^{(2)}$ value indicates the more donating tendency between electron–donating and accepting groups as well as the greater the extent of conjugation of the whole system.

Table 5. Second –order perturbation theory analysis of Fock matrix on NBO basis for complex

Donor (*i*)	Acceptor (*j*)	E(2) (kcal/mol)
π(C4–C5)	π*(N1–C2)	15.92
π(C12–C11)	π*(N2–C13)	15.58
LP(1) N1	LP*(6) Cu1	20.33
LP(1) N2	LP*(6) Cu1	20.23
LP(2) O2	LP*(6) Cu1	21.34
LP(3) O2	π*(O1–C1)	30.98
LP(2) O3	LP*(6) Cu1	15.66
LP(3) O3	π*(O4–C8)	28.10

The inhibitory activities of the synthesized complexes on α–glucosidase were carried out with small changes as given by Sun's protocol [35] using genistein as the reference compound. Complex exhibited the strongest inhibition against α–glucosidase with an IC_{50} value of 2.95 μM. This value is also higher than that of genistein (IC_{50}= 16.58 μM), used as a standard in this study.

Table 6. In vitro inhibition IC_{50} values (μM) of the Cu (II) complex for α–glucosidase, protein–ligand interactions and theirs energy values.

Compound	**IC_{50} (μM)[a]**	**Cu complex–protein interaction**	**Energy[b] (kcal/mol)**
6–Methylpicolinic acid (6–mpa)	not active	Van der Waals interactions	
$[Cu(6–mpa)_2·H_2O]·H_2O$	2.95±0.55	M–ALA–331	–4.9
Genistein	16.58±0.23	M–GLU–332	–4.2
Acarbose [36,37]	906	M–ARG–335	–12.1
Resveratrol [38,39]	12.70	S–ARG–335	–15.1
		M–ASN–338	–4.0
		Hydrogen bonding interactions	
		S–ASP–283	–7.5
		S–ARG–335	–8.4
		M–TYR–336	–6.7
		E_{total}	–90.7

[a] IC_{50} values represent the means ± S.E.M. of three parallel measurements ($p < 0.05$).
[b] The values of VDW and H–Bond energy are taken as lower than –4.0 and –2.5 kcal/mol, respectively. M and S indicate the main and side chain of the interacting residue, respectively.

To understand ligand binding mechanisms of a therapeutic target, we investigated pharmacological interactions by molecular docking. All stages (binding–site and ligand preparations, virtual screening, and post–screening analysis) of structure–based virtual screening (VS) for docking with the mode of accurate docking (very slow) were performed by using iGEMDOCK program [40–42]. The results of the protein–complex interaction profiles for electrostatic (E), hydrogen–bonding (H), and van der Waals (V) interactions were calculated. Based on these profiles, estimated interactions and their energy values are given in Table 6. It is clear that the protein–complex interaction was stabilized by different interacting amino–acid residues through some hydrogen–bonding and van der Waals interactions.

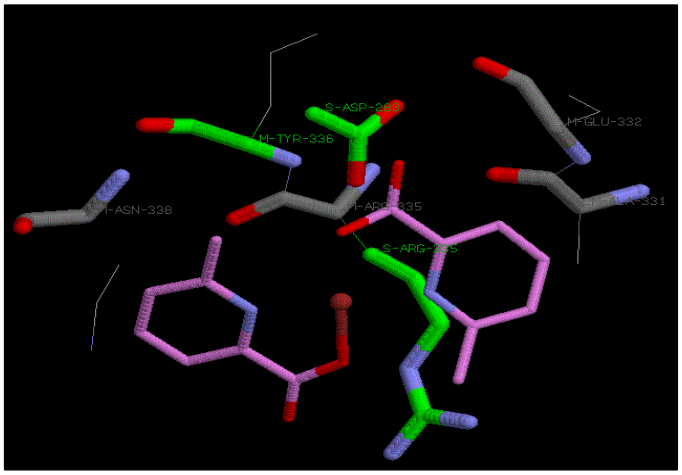

Figure 4. The plot of active interactions between protein and ligand for the Cu (II) complex

4. CONCLUSION

The Cu (II) complex with 6–methylpyridine–2–carboxylic acid was synthesized and its structure elucidation was performed by XRD, FT–IR and UV–Vis spectra. Furthermore, the geometry optimization and vibrational parameters were obtained by using DFT calculations with HSEh1PBE method and 6–311G (d,p)/LanL2DZ basis set. Additionally, electronic properties in gas phase and ethanol solvent were investigated at TD–HSEh1PBE/6–311G (d,p)/LanL2DZ level. Obtained results were compared to theoretical values. It can be said that there is a good agreement between the theoretical and corresponding experimental results. The UV–Vis spectrum displays the peaks originated from n→π and π → π transitions. It is concluded that the ILCT transitions appear because of the destabilizing effect of the electron with drawing/donating carboxylate O atoms/methyl group. The C–H···O and O–H···O types of intermolecular interactions are verified by NBO analysis. Furthermore, these parameters for the future works including particularly 6–mpa complexes could be evaluated. The third–NLO parameters show that the Cu (II) complex is a good nominate for NLO materials.

ACKNOWLEDGMENTS

This work was supported by the Scientific and Technological Research Council of Turkey (TÜBİTAK) (Project Number: MFAG–117F235).

REFERENCES

[1] Popovic´, Z., Pavlovic´, G., Vinkovic´, M., Vikic´–Topic´, D., Rajic´ Linaric´,M., Coordination modes of 3–hydroxypicolinic acid (OH–picH): Synthesis and characterization of cadmium(II) complexes: Crystal and molecular structures of $[CdX(OH–pic)(OH–picH)(H_2O)]_2$ X = Cl−, Br−, Polyhedron, 25, 2353–2362, 2006.

[2] Kukovec, B. –M., Popović, Z., Komorsky–Lovrić, Š., Vojković, V., Vinković, M., Synthesis, structural, spectroscopic and thermal characterization of cobalt complexes with 3– and 6–methylpicolinic acid, Voltammetric and spectrophotometric study in solution, Inorganica Chimica Acta, 362, 2704–2714, 2009.

[3] Kukovec, B.–M., Vaz, P.D., Popović, Z., Calhorda, M.J., Furić, K., Pavlović, G., Linarić, M.R., Pseudopolymorphism in nickel(II) complexes with 6–methylpicolinic acid. Synthesis, structural, spectroscopic, thermal and DFT study, Crystal Growth and Design, 8, 3465–3473, 2008.

[4] Kukovec, B.–M., Popović, Z., Kozlevčar, B., Jagličić, Z.,3D supramolecular architectures of copper(II) complexes with 6–methylpicolinic and 6–bromopicolinic acid: Synthesis, spectroscopic, thermal and magnetic properties, Polyhedron, 27, 3631–3638, 2008.

[5] Altürk, S., Avcı, D., Tamer, Ö., Atalay, Y., Şahin, O., A cobalt (II) complex with 6–methylpicolinate: Synthesis, characterization, second– and third–order nonlinear optical properties, and DFT calculations, Journal of Physics and Chemistry Solids, 98, 71–80, 2016.

[6] Altürk, S., Avcı, D., Başoğlu, A., Tamer, Ö., Atalay, Y., Dege, N., Copper(II) complex with 6–methylpyridine–2–carboxyclic acid: Experimental and computational study on the XRD, FT–IR and UV–Vis spectra, refractive index, band gap and NLO parameters, Spectrochimica Acta, Part A: Mol Biomol Spectroscopy, 190, 220–230, 2018.

[7] García, F., Perles, J., Zamora, F., Amo–Ocho, P., Rhodium and copper 6–methylpicolinate complexes. Structural diversity and supramolecular interaction study, Inorganic Chimica Acta, 453, 574–582, 2016.

[8] Sakurai, H., Fujii, K., Watanabe, H., Tamura, H., Orally active and long–term acting insulin–mimetic vanadyl complex:bis(picolinato)oxovanadium (IV), Biochemical and Biophysical Research Communications, 214, 1095–1101, 1995.

[9] Nakai, M., Sekiguchi, F., Obata, M., Ohtsuki, C., Adachi, Y., Sakurai, H., Orvig, C., Rehder, D., Yano, S., Synthesis and insulin–mimetic activities of metal complexes with 3–hydroxypyridine–2–carboxylic acid, Journal of Inorganic Biochemistry, 99, 1275–1282, 2005.

[10] Chaudhry, F., Naureen, S., Huma, R., Shaukat, A., al–Rashida, M., Asif, N., Ashraf, M., Munawar, M.A., Khan, M.A., In search of new alpha–glucosidase inhibitors: Imidazolylpyrazole derivatives, Bioorganic Chemistry, 71, 102–109, 2017.

[11] Sun, H., Zhang, Y.Z., Ding, W.N., Zhao, X., Song,X.T., Wang,D., Li,Y.S., Han,K.L., Yang,Y., Ma, Y., Wang,R.L., Wang,D., Yu,P., Inhibitory activity evaluation and mechanistic studies of tetracyclic oxindole derivatives as alpha–glucosidase inhibitors, European Journal of Medical Chemistry, 123, 365–378, 2016.

[12] Ma, J., Zhang, X., Soloveva, V., Warren, T., Guo, F., Wu, S., Lu, H., Guo, J., Su, Q., Shen, H., Solon, E., Comunale, M.A., Mehta, A., Guo, J.T., Bavari, S., Du, Y., Block, T.M., Chang, J., Enhancing the antiviral potency of ER alpha–glucosidase inhibitor IHVR–19029 against hemorrhagic fever viruses in vitro and in vivo, Antiviral Research, 150, 112–122, 2018.

[13] Barakat, A., Islam, M.S., Al–Majid, A.M., Ghabbour, H.A., Yousuf, S., Ashraf, M., Shaikh, N.N., Choudhary, M.I., Khalil, R., Ul–Haq, Z., Synthesis of pyrimidine–2,4,6–trione derivatives: Anti–oxidant, anti–cancer, alpha–glucosidase, beta–glucuronidase inhibition and their molecular docking studies, Bioorganic Chemistry, 68, 72–79, 2016.

[14] Frisch, M.J., et al., Gaussian 09, Rev D.1, Gaussian, Inc., Wallingford CT, 2013.

[15] Dennington,R., Keith,T., Millam,J., Semichem Inc., Shawnee Mission KS, GaussView, Version5, 2009.

[16] Heyd, J., Scuseria, G.E., Efficient hybrid density functional calculations in solids: assessment of the Heyd–Scuseria–Ernzerhof screened Coulomb hybrid functional, Journal of Chemical Physics, 121, 1187–1192, 2004.

[17] Heyd, J., Scuseria, G.E., Assessment and validation of a screened Coulomb hybrid density functional, Journal of Chemical Physics, 120, 7274–7280, 2004.

[18] Heyd, J., Peralta, J.E., Scuseria, G.E., Martin, R.L., Energy band gaps and lattice parameters evaluated with the Heyd–Scuseria–Ernzerhof screened hybrid functional, Journal of Chemical Physics, 123, 1–8, 174101, 2005.

[19] Heyd, J., Scuseria, G.E., Ernzerhof, M., Erratum: “Hybrid functionals based on a screened Coulomb potential”,[Journal of Chemical Physics, 118, 8207, 2003], Journal of Chemical Physics, 124, 219906, 2006.

[20] Krukau, A.V., Vydrov, O.A., Izmaylov, A.F., Scuseria, G.E., Influence of the exchange screening parameter on the performance of screened hybrid functional,Journal of Chemical Physics,125,224106, 2006.

[21] Frisch, M.J., Pople, J.A., Binkley, J.S., Self–consistent molecular orbital methods 25. Supplementary functions for Gaussian basis set, Journal of Chemical Physics, 80, 3265–3269, 1984.

[22] Hay, P.J., Wadt, W.R., Ab initio effective core potentials for molecular calculations. Potentials for the transition metal atoms Sc to Hg, Journal of Chemical Physics, 82, 270–283, 1985.

[23] Wadt, W.R., Hay, P.J., Ab initio effective core potentials for molecular calculations. Potentials for main group elements Na to Bi, Journal of Chemical Physics, 82, 284–298, 1985.

[24] Hay, P.J., Wadt, W.R., Ab initio effective core potentials for molecular calculations. Potentials for K to Au including the outermost core orbitals, Journal of Chemical Physics, 82, 299–310, 1985.

[25] Runge, E., Gross, E.K.U., Density–Functional Theory for Time–Dependent Systems, Physical Review Letters, 52, 997–1000, 1984.

[26] Miertus, S., Scrocco, E., Tomasi, J., Electrostatic interaction of a solute with a continuum. A direct utilizaion of Ab initio molecular potentials for the prevision of solvent effects, Journal of Chemical Physics, 55, 117–129, 1981.

[27] Glendening, E.D., Reed, A.E., Carpenter, J.E., Weinhold, F., NBO Version3.1, TCI, University of Wisconsin, Madison, 1998.

[28] Gorelsky, S.I., SWizard Program Revision 4.5, University of Ottawa, Ottawa, Canada, 2010.

[29] Kanis, D.R., Ratner, M.A., Marks, T.J., Design and construction of molecular assemblies with large second–order optical nonlinearities. Quantum chemical aspects, Chemical Reviews, 94, 195–242, 1994.

[30] Prasad, P.N., Williams, D.J., Introduction to Nonlinear Optical Effects in Molecules and Polymers, Wiley, New York, 1991.

[31] Cheng, L.T., Tam, W., Stevenson, S.H., Meredith, G.R., Rikken, G., Marder, S.R., Experimental investigations of organic molecular nonlinear optical polarizabilities. 1. Methods and results on benzene and stilbene derivatives, Journal of Physical Chemistry, 95, 10631–10643, 1991.

[32] Kaatz, P., Donley, E.A., Shelton, D.P., A comparison of molecular hyperpolarizabilities from gas and liquid phase measurements, Journal of Chemical Physics, 108, 849–856, 1998.

[33] Adant, C., Dupuis, M., Bredas, J.L., Ab initio study of the nonlinear optical properties of urea: Electron correlation and dispersion effects, International Journal of Quantum Chemistry, 56, 497–507, 2004.

[34] Weinhold, F., Landis, C., Valency and Bonding: A Natural Bond Orbital Donor– Acceptor Perspective, Cambridge University Press, Cambridge, 2005.

[35] Sun, H., Ding, W.N., Song, X.T., Wang, D., Chen, M.Z., Wang, K.L., Zhang, Y.Z., Yuan, P., Ma, Y., Wang, R.L., Dodd, R.H., Zhang, Y.M., Lu, K., Yu, P., Synthesis of 6–hydroxyaurone analogues and evaluation of their α–glucosidase inhibitory and glucose consumption–promoting activity:Development of highly active 5,6–disubstituted derivatives,Bioorganic and Medicinal Chemistry Letters,27,3226–3230,2017.

[36] Taha, M., Hadiani Ismail, N., Lalani, S., Qaiser Fatmi, M., Wahab, A., Siddiqui, S., Khan, K.M., Imran, S., Iqbal Choudhary, M., Synthesis of novel inhibitors of α–glucosidase based on the benzothiazole skeleton containing benzohydrazide moiety and their molecular docking studies, European Journal of Medicinal Chemistry 92, 387–400, 2015.

[37] Taha, M., Hadiani Ismail, N., Syukri Baharudin, M., Lalani, S., Mehboob, S., Khan, K.M., Yousuf, S., Siddiqui, S., Rahim, F., Choudhary, M.I., Synthesis crystal structure of 2–methoxybenzoylhydrazones and evaluation of their α–glucosidase and urease inhibition potential, Medicinal Chemistry Research, 24, 1310–1324, 2015.

[38] Zheng, J.–W., Ma, L., Silver(I) complexes of 2,4–dihydroxybenzaldehyde–amino acid Schiff bases–Novel noncompetitive α–glucosidase inhibitors,Bioorganic Medicinal Chemistry Letters,25,2156–216,2015.

[39] Zheng, J.–W., Ma, L., Metal complexes of anthranilic acid derivatives: A new class of non–competitive α–glucosidase inhibitors, Chinese Chemical Letters 27 (2016) 627–630.

[40] Yang, J.–M., Chen, C.–C., GEMDOCK: a generic evolutionary method for molecular docking, Proteins, 55, 288–304, 2004.

[41] Yang, J.–M., Shen, T.W., A pharmacophore–based evolutionary approach for screening selective estrogen receptor modulators. Proteins. 59(2), 205–220, 2005.

[42] Hsu, K.–C., Chen, Y.–F., Lin, S.–R., Yang, J.–M., iGEMDOCK: a graphical environment of enhancing GEMDOCK using pharmacological interactions and post–screening analysis,BMC Bioinformatics,12,S33, 2011.

SYNTHESIS, CRYSTAL STRUCTURE, DFT CALCULATIONS, MOLECULAR DOCKING AND α–GLUCOSIDASE INHIBITION STUDY OF THE Zn (II) COMPLEX

S. Altürk[1], D. Avcı[1], F. Sönmez[2], Ö. Tamer[1], A. Başoğlu[1], Y. Atalay[1], B. Zengin Kurt[3], and N. Dege[4]

[1]*Sakarya University, Faculty of Arts and Sciences, Department of Physics, 54187, Sakarya, Turkey*

[2]*Sakarya University, Faculty of Arts and Sciences, Department of Chemistry, 54187, Sakarya, Turkey*

[3]*Bezmialem Vakif University, Faculty of Pharmacy, Department of Pharmaceutical Chemistry, 34093 Istanbul, Turkey*

[4]*Ondokuz Mayıs University, Faculty of Arts and Sciences, Department of Physics, 55139, Samsun, Turkey*

E-mail: sumeyye-alturk@hotmail.com

Abstract

The synthesized Zn (II) complex of 6–methylpyridine–2–carboxylic acid [Zn (6–mpa)$_2$·H$_2$O]·H$_2$O was characterized by XRD, FT–IR and UV–Vis spectroscopies. The α–glucosidase inhibition activity of the synthesized complex was predicted by IC_{50} values. Moreover, the optimized geometry and vibrational frequencies were obtained by using Density Functional Theory (DFT) with HSEh1PBE method and 6–311G(d,p)/LanL2DZ basis set. Electronic spectral properties were studied by using TD–DFT/HSEh1PBE/6–311G (d,p)/LanL2DZ level with CPCM in ethanol solvent and gas phase. The NLO parameters and FMO energies of the Zn (II) complex were calculated by using HSEh1PBE/6–311G (d,p) level. Finally, the docking study of the Zn (II) complex to the binding site of the target protein (the template structure S. cerevisiae isomaltase) is fulfilled.

Keywords: 6–methylpyridine–2–carboxylic acid, XRD, FT–IR and UV–Vis; α–Glucosidase; Docking; TD/DFT–HSEh1PBE level

1. INTRODUCTION

6−methylpicolinic acid (6−mpa), known as a picolinic acid derivative, and its complexes have been largely studied in coordination chemistry because of its major coordination elasticity and versatility with many metal centers in different modes [1–7]. Due to great coordination potential, biological and pharmaceutical properties of these ligands commonly specified as insulinomimetic activity studies, their a number of transition metal complexes have been extensively surveyed [8,9]. α−Glucosidase, a critical enzyme for the digestion of carbohydrates, catalyzes the cleavage of absorbable monosaccharides, beginning from disaccharides and oligosaccharides [10,11]. The functions of α−glucosidase for mammals contain intestinal digestion of dietary carbohydrates, glycogen degradation, and glycoprotein folding and maturation [12,13]. Synthesis crystal structure and spectroscopic characterization for 6−mpa and its metal complexes have been reported [4,6,9,13,14]. The synthesis, crystal structure, IR and NMR spectra and elemental analysis of Zn(II) complex were experimentally investigated, but theoretically not studied. In this study the crystal structure characterization of the synthesized Zn(II) complex was performed by XRD method. Spectroscopic and electronic properties and α–glucosidase enzyme activity study for Zn(II) complex were performed. The obtained experimental structural, spectroscopic and electronic properties for the Zn(II) complex have been theoretically supported by using DFT/HSEh1PBE/6–311G(d,p)/LanL2DZ level.

2. MATERIAL AND METHODS

To an ethanol/water solution (40 mL, in molar ratio 1:1) containing zinc(II) acetate dihydrate ($(CH_3COO)_2Zn{\cdot}2H_2O$) (1 mmol), 6–methylpicolinic acid (6–mpa) (2 mmol) was slowly added with continuous stirring. Obtained solution was allowed to evaporate for 10 day at room temperature after being stirred at the proper temperature. After the 10 days, the crystal adequate for X–ray diffraction analysis were obtained.

The calculations of Zn(II) complex was performed by using the Gaussian 09, Revision D01 program [15] and the output files were visualized by GaussView 5 software [16]. The optimized molecular geometry and vibrational frequencies of Zn(II) complex were calculated through performing density functional theory (DFT) with HSEh1PBE method [17–21] at 6–311G(d,p)/LanL2DZ basis set [22–25]. The electronic transition and oscillator strength were computed by using time dependent DFT (TD–HSEh1PBE) [26] and 6–311G(d,p)/LanL2DZ basis set with polarizable continuum model (PCM) [27] in ethanol solvent and gas phase. Frontier molecular orbital energies were calculated by using HSEh1PBE/6–311G(d,p)/LanL2DZ

level. The second– and third– order nonlinear optical (NLO) parameters were calculated at the same level in ethanol solvent and gas phase. NBO (natural bond orbital) analysis [28] has been fulfilled to understand the coordination around Zn center and hydrogen bonding interaction.

3. RESULTS AND DISCUSSION

The molecular structure of the Zn(II) complex crystallizes in the triclinic space group P–1. The crystal structure data of the complex are established to be a= 7.9970 (4) Å, b= 9.4285 (5) Å, c= 11.1588 (6) Å, α= 96.824 (4)°, β= 98.744 (4)°, γ= 106.945 (4), V= 783.56 (7) $Å^3$. Figure 1 shows the crystal structure and theoretical geometry of the Zn(II) complex. Selected theoretical bond lengths and angles are listed in Table 1 and compared with XRD results.

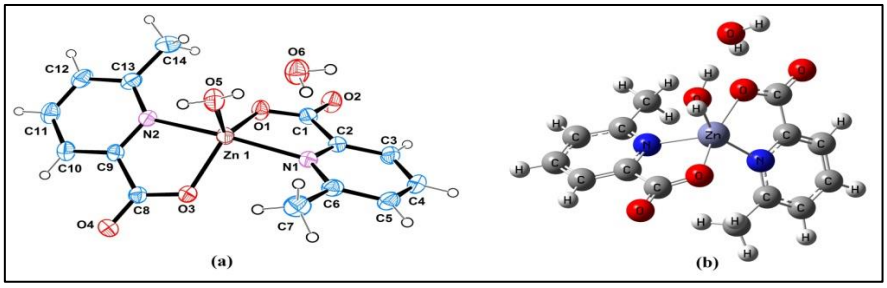

Figure 3. a) The experimental molecular structure b) the optimized molecular structure of the Zn(II) complex at HSEh1PBE/6–31G(d,p)/LanL2DZ

Table 1. Selected experimental and theoretical bond length and angles for the Zn(II) complex.

Parameters	XRD	HSEh1PBE	Parameters	XRD	HSEh1PBE
Zn1–O3	*1.983 (13)* Å	1.978 Å	O3–Zn1–O5	109.6 (7)°	85.7°
Zn1–O5	*1.992 (15)* Å	2.094 Å	O3–Zn1–O1	128.8 (6)°	160.0°
Zn1–O1	2.002 (14) Å	1.992 Å	O5–Zn1–O1	121.3 (7)°	84.0°
Zn1–N2	2.146 (14) Å	2.072 Å	O3–Zn1–N2	79.9 (5)°	82.9°
Zn1–N1	2.156 (14) Å	2.142 Å	O5–Zn1–N2	92.1 (6)°	97.3°
			O1–Zn1–N2	92.6 (6)°	115.4°
			O3–Zn1–N1	98.0 (5)°	102.9°
			O5–Zn1–N1	100.3 (6)°	152.9°
			O1–Zn1–N1	79.0 (5)°	79.5°
			N2–Zn1–N1	167.4 (6)°	109.2°

Vibrational properties have been investigated to determine vibrational modes connected with molecular structure of the Zn(II) complex using FT–IR spectra. The comparison of FT–IR and theoretical IR spectra for the Zn(II) complex are shown in Figure 2 and summarized in Table 2.

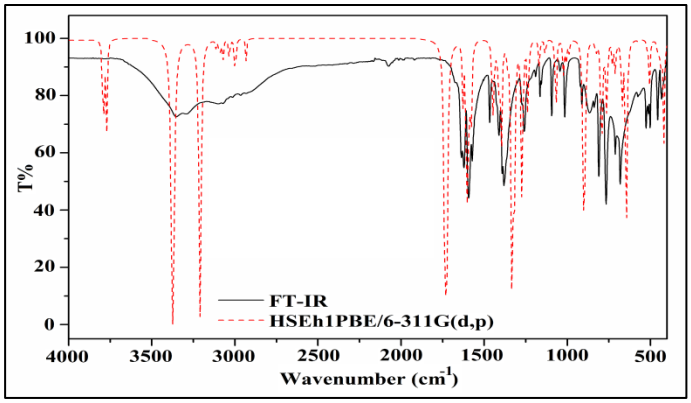

Figure 4. The comparison of experimental and theoretical IR spectra of the Zn(II) complex.

Table 2. Comparison of the FT–IR and calculated vibration frequencies for complex.

Assignments	FT–IR	HSEh1PBE
		Scaled freq.[a]
υ OH	3355	3772
υ OH	3287	3209
υ CH ring	3101	3113
υ CH_3	3011	3034
υ OC	2014	1738
β H_2O	1636	1628
υ CC ring	1621	1605
β H_2O	1593	1590
β HCC	1466	1451
β CH_3		1435
υ OC	1381	1333
υ NC	1260	1270
γ HCCC	1014	996
γ CZnCN	713	709
γ OHOZn		646
γ CNCC	501	504
γ CCCC	434	434

[a] Scaled frequencies are in unit of cm^{-1}. υ: Stretching; β: in plane bending; γ: out−of plane bending.

The electronic excitation energies and oscillator strengths in ethanol solvent and gas phase were computed by using the TD–HSEh1PBE method at 6–311G(d,p)/LanL2DZ basis set with PCM [27]. The remarkable contributions of the electronic transitions were appointed via SWizard program [29]. Obtained electronic results are compared with the experimental ones and summarized in Table 3.

Table 3. Experimental and theoretical electronic transitions, oscillator strength for Zn(II) complex.

Solvent	Experimental	HSEH1PBE/6–311G(d,p)			
	λ (nm)	λ (nm)	Osc. Strength	Major contribution	
Ethanol	–	295	0.0002	H→L+1 (88%)	H–1→L+1 (6%)
	272	291	0.0004	H–1→L (69%)	H→L (22%)
	–	263	0.0060	H→L (76%)	H–1→L (19%)
	217	246	0.0798	H–3→L (59%)	H–5→L (17%)
Gas phase		314	0.0004	H–1→L (71%)	H→L (21%)
		297	0.0035	H→L (78%)	H–1→L (18%)
		272	0.0013	H–1→L+1 (60%)	H–3→L+1 (34%)
		265	0.0018	H–2→L (85%)	H–3→L (6%)

The frontier molecular orbitals (FMO) play an important role in optical and electronic properties of molecular systems. FMO energies are calculated by using the DFT/HSEh1PBE6–311G(d,p)/LanL2DZ level. Energy gap between HOMO and LUMO characterizes the molecular chemical stability, chemical reactivity and hardness of the molecule. The designs of FMO and energy gap between them are given in Figure 3.

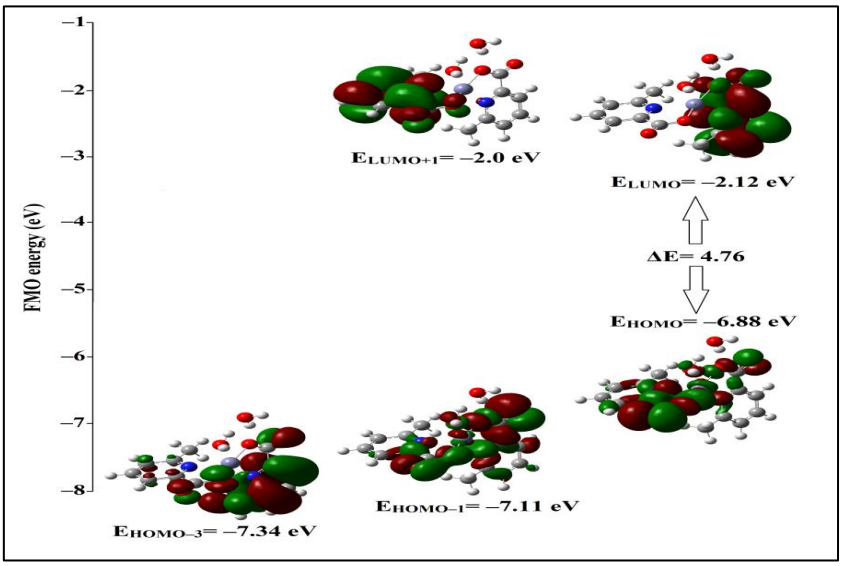

Figure 5. The occupied and unoccupied molecular orbitals being the most active in electronic transition for the Zn(II) complex.

The nonlinear optics (NLO) have been investigated by several research groups for the arising technologies in the areas such as signal processing, telecommunications and optical inter connections [30,31]. The higher values of second– and third– order nonlinear optical (NLO) parametres are important for more active NLO properties. NLO parametres are computed by using HSEh1PBE method and 6–311G(d,p)/LanL2DZ basis set in ethanol solvent and gas phase. In comparison of NLO parameters for molecular systems without experimental measurements, p–Nitroaniline (pNA) [32,33] and urea [34] which is a typical NLO materials are used (see Table 4).

Table 4. Electric dipole moment (μ, in Debye), the average and anisotropic static polarizabilities (‹α› and Δα, in10^{-24} esu), the first– and second– order static hyperpolarizabilities (‹β›, in10^{-30} esu and ‹γ›, in10^{-36} esu) for Zn(II) complex.

Property	HSEh1PBE/6–311G(d,p)		pNA[a] [32,33] and urea[b] [34] results
	Ethanol	Gas phase	
μ	6.3	4.4	2.44[a]
<α>	37.5	28.7	22[a]
Δα	10.9	10.0	
<β>	1.9	2.0	8[a], 0.13[b]
<γ>	33.3	14.2	15[a]

The NBO (natural bond orbital) analysis is used to investigate inter and intramolecular bonding and interaction among bonds [35]. Furthermore, it provides a basis for investigating charge transfer or conjugative interaction in molecular system. It is stated that the larger $E^{(2)}$ value indicates the more donating tendency between electron–donating and accepting groups as well as the greater extent of conjugation for the whole system.

Table 5. Second –order perturbation theory analysis of Fock matrix on NBO basis for complex.

Donor (*i*)	Acceptor (*j*)	E(2) (kcal/mol)
π(C4–C5)	π*(N1–C6)	31.82
π(C10–C11)	π*(N2–C9)	32.49
LP(1) N1	LP*(6) Zn1	30.83
LP(1) N2	LP*(6) Zn1	31.52
LP(2) O1	LP*(6) Zn1	29.51
LP(2) O3	LP*(6) Zn1	36.61
LP(2) O5	LP*(6) Zn1	27.05

The inhibitory activities of the synthesized complexes on α–glucosidase were carried out with small changes as given by Sun's protocol [36] using genistein as the reference compound. Complex exhibited the

strongest inhibition against α–glucosidase with an IC_{50} value of 456.04 μM. This value is also lower to that of genistein (IC_{50}= 16.58 μM), used as a standard in this study.

Table 6. In vitro inhibition IC_{50} values (μM) of the Zn(II) complex for α–glucosidase, protein–ligand inetractions and theirs energy values.

Compound	**IC_{50} (μM)[a]**	**Zn complex–protein interaction**	**Energy[b] (kcal/mol)**
6–Methylpicolinic acid (6–mpa)	not active	Van der Waals interactions	
$[Zn(6–mpa)_2·H_2O]·H_2O$	456.04±1.01	S–LYS–156	–4.6
Genistein	16.58±0.23	M–TYR–158	–8.4
Acarbose [37,38]	906	S–TYR–158	–17.9
Resveratrol [39,40]	12.70	S–HIS–280	–4.0
		S–ARG–315	–5.9
		Hydrogen bonding interactions	
		S–HIS–280	–3.5
		E_{total}	–88.4

[a] IC_{50} values represent the means ± S.E.M. of three parallel measurements ($p < 0.05$).

[b] The values of VDW and H–Bond energy are taken as lower than –4.0 and –2.5 kcal/mol, respectively. M and S indicate the main and side chain of the interacting residue, respectively.

To understand ligand binding mechanisms of a therapeutic target, we investigated pharmacological interactions by molecular docking. All stages (binding–site and ligand preparations, virtual screening, and post–screening analysis) of structure–based virtual screening (VS) for docking with the mode of accurate docking (very slow) were performed by using iGEMDOCK program [41–43]. The results of the protein–complex interaction profiles for electrostatic (E), hydrogen–bonding (H), and van der Waals (V) interactions were calculated. Based on these profiles, estimated interactions and theirs energy values are given in the Table 6. It is clear that the protein–complex interaction was stabilized by different interacting amino–acid residues through some hydrogen–bonding and van der Waals interactions.

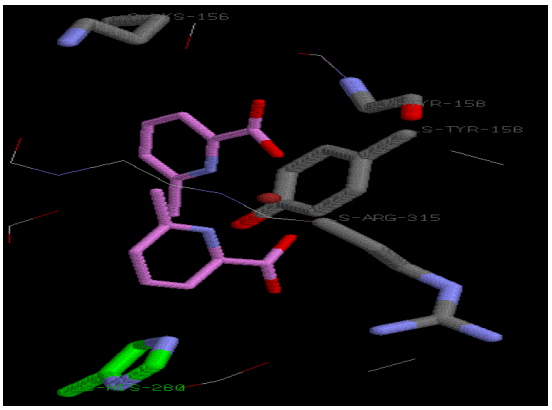

Figure 6. The plot of active interactions between protein and ligand for the Zn (II) complex

4. CONCLUSION

The Zn (II) complex with 6–methylpyridine–2–carboxylic acid was synthesized and its structure elucidation was performed by XRD, FT–IR and UV–Vis spectra. Furthermore, the geometry optimization and vibrational parameters were obtained by using DFT calculations with HSEh1PBE method and 6–311G(d,p)/LanL2DZ basis set. Additionally, electronic properties in gas phase and ethanol solvent were investigated at TD–HSEh1PBE/6–311G(d,p)/LanL2DZ level. Obtained experimental results were compared to theoretical values. It can be said that there is a good agreement between the theoretical and corresponding experimental results. It is concluded that the ILCT transitions appear because of the destabilizing effect of the electron withdrawing/donating carboxylate O atoms/methyl group. The C–H···O and O–H···O types of intermolecular hydrogen bonding interactions are verified by NBO analysis. Furthermore, these parameters for the future works including particularly 6–mpa complexes could be evaluated. The third–NLO parameters show that the Zn (II) complex is a good nominate for NLO materials.

ACKNOWLEDGMENTS

This work was supported by the Scientific and Technological Research Council of Turkey (TÜBİTAK) (Project Number: MFAG–117F235).

REFERENCES

[1] Popovic´, Z., Pavlovic´, G., Vinkovic´, M., Vikic´–Topic´, D., Rajic´ Linaric´,M., Coordination modes of 3–hydroxypicolinic acid (OH–picH): Synthesis and characterization of cadmium(II) complexes: Crystal and molecular structures of $[CdX(OH–pic)(OH–picH)(H_2O)]_2$ X = $Cl^–$, $Br^–$, Polyhedron, 25, 2353–2362, 2006.

[2] Kukovec, B. –M., Popović, Z., Komorsky–Lovrić, Š., Vojković, V., Vinković, M., Synthesis, structural, spectroscopic and thermal characterization of cobalt complexes with 3– and 6–methylpicolinic acid, Voltammetric and spectrophotometric study in solution, Inorganica Chimica Acta, 362, 2704–2714, 2009.

[3] Kukovec, B.–M., Vaz, P.D., Popović, Z., Calhorda, M.J., Furić, K., Pavlović, G., Linarić, M.R., Pseudopolymorphism in nickel(II) complexes with 6–methylpicolinic acid. Synthesis, structural, spectroscopic, thermal and DFT study, Crystal Growth and Design, 8, 3465–3473, 2008.

[4] Kukovec, B.–M., Popović, Z., Kozlevčar, B., Jagličić, Z.,3D supramolecular architectures of copper(II) complexes with 6–methylpicolinic and 6–bromopicolinic acid: Synthesis, spectroscopic, thermal and magnetic properties, Polyhedron, 27, 3631–3638, 2008.

[5] Altürk, S., Avcı, D., Tamer, Ö., Atalay, Y., Şahin, O., A cobalt (II) complex with 6–methylpicolinate: Synthesis, characterization, second– and third–order nonlinear optical properties, and DFT calculations, Journal of Physics and Chemistry Solids, 98, 71–80, 2016.

[6] Altürk, S., Avcı, D., Başoğlu, A., Tamer, Ö., Atalay, Y., Dege, N., Copper(II) complex with 6–methylpyridine–2–carboxyclic acid: Experimental and computational study on the XRD, FT–IR and UV–Vis spectra, refractive index, band gap and NLO parameters, Spectrochimica Acta, Part A: Mol Biomol Spectroscopy, 190, 220–230, 2018.

[7] García, F., Perles, J., Zamora, F., Amo–Ocho, P., Rhodium and copper 6–methylpicolinate complexes. Structural diversity and supramolecular interaction study, Inorganic Chimica Acta, 453, 574–582, 2016.

[8] Sakurai, H., Fujii, K., Watanabe, H., Tamura, H., Orally active and long–term acting insulin–mimetic vanadyl complex:bis(picolinato)oxovanadium (IV), Biochemical and Biophysical Research Communications, 214, 1095–1101, 1995.

[9] Nakai, M., Sekiguchi, F., Obata, M., Ohtsuki, C., Adachi, Y., Sakurai, H., Orvig, C., Rehder, D., Yano, S., Synthesis and insulin–mimetic activities of metal complexes with 3–hydroxypyridine–2–carboxylic acid, Journal of Inorganic Biochemistry, 99, 1275–1282, 2005.

[10] Chaudhry, F., Naureen, S., Huma, R., Shaukat, A., al–Rashida, M., Asif, N., Ashraf, M., Munawar, M.A., Khan, M.A., In search of new alpha–glucosidase inhibitors: Imidazolylpyrazole derivatives, Bioorganic Chemistry, 71, 102–109, 2017.

[11] Sun, H., Zhang, Y.Z., Ding, W.N., Zhao, X., Song,X.T., Wang,D., Li,Y.S., Han,K.L., Yang,Y., Ma, Y., Wang,R.L., Wang,D., Yu,P., Inhibitory activity evaluation and mechanistic studies of tetracyclic oxindole derivatives as alpha–glucosidase inhibitors, European Journal of Medical Chemistry, 123, 365–378, 2016.

[12] Ma, J., Zhang, X., Soloveva, V., Warren, T., Guo, F., Wu, S., Lu, H., Guo, J., Su, Q., Shen, H., Solon, E., Comunale, M.A., Mehta, A., Guo, J.T., Bavari, S., Du, Y., Block, T.M., Chang, J., Enhancing the antiviral potency of ER alpha–glucosidase inhibitor IHVR–19029 against hemorrhagic fever viruses in vitro and in vivo, Antiviral Research, 150, 112–122, 2018.

[13] Barakat, A., Islam, M.S., Al–Majid, A.M., Ghabbour, H.A., Yousuf, S., Ashraf, M., Shaikh, N.N., Choudhary, M.I., Khalil, R., Ul–Haq, Z., Synthesis of pyrimidine–2,4,6–trione derivatives: Anti–oxidant, anti–cancer, alpha–glucosidase, beta–glucuronidase inhibition and their molecular docking studies, Bioorganic Chemistry, 68, 72–79, 2016.

[14] Chaudhry, F., Naureen, S., Huma, R., Shaukat, A., al–Rashida, M., Asif, N., Ashraf, M., Munawar, M.A., Khan, M.A., In search of new alpha–glucosidase inhibitors: Imidazolylpyrazole derivatives, Bioorganic Chemistry, 71, 102–109, 2017.

[15] Frisch, M.J., et al., Gaussian 09, Rev D.1, Gaussian, Inc., Wallingford CT, 2013.

[16] Dennington,R., Keith,T., Millam,J., Semichem Inc., Shawnee Mission KS, GaussView, Version5, 2009.

[17] Heyd, J., Scuseria, G.E., Efficient hybrid density functional calculations in solids: assessment of the Heyd–Scuseria–Ernzerhof screened Coulomb hybrid functional, Journal of Chemical Physics, 121, 1187–1192, 2004.

[18] Heyd, J., Scuseria, G.E., Assessment and validation of a screened Coulomb hybrid density functional, Journal of Chemical Physics, 120, 7274–7280, 2004.

[19] Heyd, J., Peralta, J.E., Scuseria, G.E., Martin, R.L., Energy band gaps and lattice parameters evaluated with the Heyd–Scuseria–Ernzerhof screened hybrid functional, Journal of Chemical Physics, 123, 1–8, 174101, 2005.

[20] Heyd, J., Scuseria, G.E., Ernzerhof, M., Erratum: "Hybrid functionals based on a screened Coulomb potential",[Journal of Chemical Physics, 118, 8207, 2003], Journal of Chemical Physics,124, 219906, 2006.

[21] Krukau, A.V., Vydrov, O.A., Izmaylov, A.F., Scuseria, G.E., Influence of the exchange screening parameter on the performance of screened hybrid functional,Journal of Chemical Physics,125,224106, 2006.

[22] Frisch, M.J., Pople, J.A., Binkley, J.S., Self–consistent molecular orbital methods 25. Supplementary functions for Gaussian basis set, Journal of Chemical Physics, 80, 3265–3269, 1984.

[23] Hay, P.J., Wadt, W.R., Ab initio effective core potentials for molecular calculations. Potentials for the transition metal atoms Sc to Hg, Journal of Chemical Physics, 82, 270–283, 1985.

[24] Wadt, W.R., Hay, P.J., Ab initio effective core potentials for molecular calculations. Potentials for main group elements Na to Bi, Journal of Chemical Physics, 82, 284–298, 1985.

[25] Hay, P.J., Wadt, W.R., Ab initio effective core potentials for molecular calculations. Potentials for K to Au including the outermost core orbitals, Journal of Chemical Physics, 82, 299–310, 1985.

[26] Runge, E., Gross, E.K.U., Density–Functional Theory for Time–Dependent Systems, Physical Review Letters, 52, 997–1000, 1984.

[27] Miertus, S., Scrocco, E., Tomasi, J., Electrostatic interaction of a solute with a continuum. A direct utilizaion of Ab initio molecular potentials for the prevision of solvent effects, Journal of Chemical Physics, 55, 117–129, 1981.

[28] Glendening, E.D., Reed, A.E., Carpenter, J.E., Weinhold, F., NBO Version3.1, TCI, University of Wisconsin, Madison, 1998.

[29] Gorelsky, S.I., SWizard Program Revision 4.5, University of Ottawa, Ottawa, Canada, 2010.

[30] Kanis, D.R., Ratner, M.A., Marks, T.J., Design and construction of molecular assemblies with large second–order optical nonlinearities. Quantum chemical aspects, Chemical Reviews, 94, 195–242, 1994.

[31] Prasad, P.N., Williams, D.J., Introduction to Nonlinear Optical Effects in Molecules and Polymers, Wiley, New York, 1991.

[32] Cheng, L.T., Tam, W., Stevenson, S.H., Meredith, G.R., Rikken, G., Marder, S.R., Experimental investigations of organic molecular nonlinear optical polarizabilities. 1. Methods and results on benzene and stilbene derivatives, Journal of Physical Chemistry, 95, 10631–10643, 1991.

[33] Kaatz, P., Donley, E.A., Shelton, D.P., A comparison of molecular hyperpolarizabilities from gas and liquid phase measurements, Journal of Chemical Physics, 108, 849–856, 1998.

[34] Adant, C., Dupuis, M., Bredas, J.L., Ab initio study of the nonlinear optical properties of urea: Electron correlation and dispersion effects, International Journal of Quantum Chemistry, 56, 497–507, 2004.

[35] Weinhold, F., Landis, C., Valency and Bonding: A Natural Bond Orbital Donor– Acceptor Perspective, Cambridge University Press, Cambridge, 2005.

[36] Sun, H., Ding, W.N., Song, X.T., Wang, D., Chen, M.Z., Wang, K.L., Zhang, Y.Z., Yuan, P., Ma, Y., Wang, R.L., Dodd, R.H., Zhang, Y.M., Lu, K., Yu, P., Synthesis of 6–hydroxyaurone analogues and evaluation of their α–glucosidase inhibitory and glucose consumption–promoting activity:Development of

highly active 5,6–disubstituted derivatives,Bioorganic and Medicinal Chemistry Letters,27,3226–3230,2017.

[37] Taha, M., Hadiani Ismail, N., Lalani, S., Qaiser Fatmi, M., Wahab, A., Siddiqui, S., Khan, K.M., Imran, S., Iqbal Choudhary, M., Synthesis of novel inhibitors of α–glucosidase based on the benzothiazole skeleton containing benzohydrazide moiety and their molecular docking studies, European Journal of Medicinal Chemistry 92, 387–400, 2015.

[38] Taha, M., Hadiani Ismail, N., Syukri Baharudin, M., Lalani, S., Mehboob, S., Khan, K.M., Yousuf, S., Siddiqui, S., Rahim, F., Choudhary, M.I., Synthesis crystal structure of 2–methoxybenzoylhydrazones and evaluation of their α–glucosidase and urease inhibition potential, Medicinal Chemistry Research, 24, 1310–1324, 2015.

[39] Zheng, J.–W., Ma, L., Silver(I) complexes of 2,4–dihydroxybenzaldehyde–amino acid Schiff bases–Novel noncompetitive α–glucosidase inhibitors,Bioorganic Medicinal Chemistry Letters,25,2156–216,2015.

[40] Zheng, J.–W., Ma, L., Metal complexes of anthranilic acid derivatives: A new class of non–competitive α–glucosidase inhibitors, Chinese Chemical Letters 27 (2016) 627–630.

[41] Yang, J.–M., Chen, C.–C., GEMDOCK: a generic evolutionary method for molecular docking, Proteins, 55, 288–304, 2004.

[42] Yang, J.–M., Shen, T.W., A pharmacophore–based evolutionary approach for screening selective estrogen receptor modulators. Proteins. 59(2), 205–220, 2005.

[43] Hsu, K.–C., Chen, Y.–F., Lin, S.–R., Yang, J.–M., iGEMDOCK: a graphical environment of enhancing GEMDOCK using pharmacological interactions and post–screening analysis, BMC Bioinformatics, 12, S33, 2011.

A RESEARCH ON GEOTHERMAL ENERGY POTENTIAL IN KIRKLARELİ CITY OF TURKEY: IS IT ACTUALLY SUSTAINABLE?

B.Özer[1,2] and S. Kızılay[1]

[1]*Department of Energy Systems Engineering, Institute of Science, Kırklareli, Turkey*
[2]*Department of Energy Systems Engineering, Faculty of Technology, Kırklareli, Turkey*

E-mail: betulozer@klu.edu.tr

Abstract

Geothermal energy is one of the important renewable energy sources which provides massive contribution to the region by direct usage and/or indirectly usage which is electric production. It is very critical resource for our country and the region by providing the return on investment in a relatively short time and relatively less environmental damage. For direct usage applications such as household heating, green housing relatively low-enthalpy resource which are around 50^0C is enough to use this energy with the help of current technology. Direct usage applications can be critical for the local communities' basic needs such as heating, nourishment etc. In this study, newly discovered low-enthalpy resource at Thrace Region will be investigated for potential applications according the geothermal drilling researches done by Mineral Research and Exploration (MTA) at Kırklareli. Besides geothermal energy is clean and renewable resource, its developments may result in both positive and negative environmental, economic and social impacts. These impacts must be managed delicately so as to result in positive outcomes. So, sustainability of this potential will be discussed under sustainable development goals. If precautions are taken, negative impacts of geothermal energy could be minimized before even utilize it.

Keywords: sustainable development, geothermal energy, Thrace Region

1. INTRODUCTION

Thrace region is located European part of Turkey and includes 3 cities named Tekirdağ, Kırklareli and Edirne and partially 2 citied named Istanbul and Çanakkale. Tekirdağ's towns named Çorlu and Çerkezköy has high capacity industrial zones and takes a big burden of İstanbul's needs. Hence as city it need larger amount of electricity. Like as Tekirdağ, Kırklareli's biggest town named Lüleburgaz has lots of fabrics that provides variety of goods to all over Turkey and Edirne has a town named Keşan likewise. Even though these industrial establishments promote region's economic growth it also causes high population increase. And these two main causes elevate energy needs of Thrace region excessively. So, there are lots of investment of plants from fossil (Natural Gas) and renewable sources (Wind and Solar).

Worldwide known fact that at energy crisis exists globally. So, energy sources usage should be sustainable. Best way to execute that lead the way to the renewable sources. But, an energy source being renewable do not require to be sustainable. In order to use sustainable and renewable energy source, sustainable development steps should be followed before even use that renewable energy. This path leads the way to 17 goals that United Nation set globally. In order to reach these goals, an individual framework is needed for every project and this framework consists of themes for the goals to point out possible problems and under the themes, there are indicators to measure and calibrate progress towards sustainable development goals.

Geothermal energy is one of the important renewable and clean energy sources which can provide massive contribution to the region by direct usage and/or indirectly usage which is electric production. It can be very critical resource for the region by providing the return on investment in a relatively short time and relatively less environmental damage.

Low-enthalpy geothermal resource at Thrace Region newly discovered by drilling researches done by Mineral Research and Exploration (MTA). Wells have around 50^0C surface artesian flow which might be enough for direct usage applications such as household heating, green housing with the help of current technology. Direct usage applications can be critical for the local communities of Kırklareli's basic needs like heating, nourishment and such.

With this discovery, execution of any geothermal project should follow the logic of sustainable development in order to save the environment for the future and obtain its ground and underground richness. Geothermal resources considered as renewable but it may not sustainable if it is not properly used. So, it is important that geothermal resources are developed in a sustainable manner but its developments may result

in both positive and negative impacts. Impacts are classified into dimensions can be implanted to this case as social, economic, environmental, renewable & efficiency and equitable (readily accessible, available and affordable).

The social impacts cover aspects of providing a local source of energy.

The economic impacts cover energy use and production patterns.

The environmental impacts cover impacts on atmosphere, water and land as well as waste issues.

Renewable & efficiency, are based on re-injection and usage.

Equitable, energy should be accessible affordable and available. The environmental impacts cover impacts on atmosphere, water and land as well as waste issues.

Clearly, these impacts can shift the future of the Kırklareli region. So, action has to be made to create positive impact direction while utilization of the potential. That is the reason why before even starting to use this source at the region, precautions and decisions have to be made within sustainable development framework. In order to do so, goals to success has to be determined. Shortall et. al., at 2015 established goals, themes and indicators that suits geothermal energy in their 3 articles for 3 project including Iceland, New Zealand and Kenya.

Goals that used mentioned projects are listed below.

Goal1 – Renewability: In order to ensure that a geothermal resource remains replenishable, sustainable production should be the goal in all geothermal projects. For each geothermal area and each mode of production there exists a certain maximum level of production, E0, so that with production below E0 it is possible to sustain steady energy production from the system for at least 100–300 years. If the level of production exceeds E0 it is not possible to sustain steady production from the system for so long. Geothermal production that is less than or equal to E0 is defined as sustainable production but production exceeding E0 is not sustainable.

Goal2 – Water resource usage: Water usage of a geothermal project must not reduce supply of cold fresh water to communities nearby.

Goal3 – Environmental management: A geothermal resource should be managed in such a way as to avoid remedy or mitigate adverse environmental effects.

Goal4 – Efficiency: Geothermal utilization shall be managed in such a way as to maximize the utilization of energy available where practical at sustainable production levels.

Goal5 – Economic management & profitability: Energy use from geothermal projects must be competitive, cost effective and financially viable. The financial risk of the project shall be minimized. The project should carry positive net national and community economic benefits.

Goal6 – Energy equity: The energy supplied by the geothermal resource is readily available, accessible and affordable to the public.

Goal7 – Energy security & reliability: The operation of geothermal projects shall be reliable and prioritize the security of supply.

Goal8 – Community Responsibility: The geothermal companies should be responsible toward the community and the effect of the utilization of the geothermal resource shall be as positive for the community as possible and yield net positive social impact.

Goal9 – Research and innovation: Geothermal companies shall encourage research that improves the knowledge of the geothermal resource as well as technical developments that improve efficiency, increase profitability and reduce environmental effects.

Goal10 – Dissemination of knowledge: Information and experience gained through geothermal utilization shall be accessible and transparent to the public and the academic community a like while respecting confidential intellectual property rights.

This produced guidelines for the creation of sustainability themes for sustainable geothermal development which narrowed done by Shortall et.al.;

1. Poverty
2. Health
3. Education
4. Natural hazards
5. Demographics
6. Atmosphere
7. Land
8. Fresh water
9. Biodiversity

10. Economic development: including macroeconomic performance, employment and tourism, research and development.
11. Consumption and production patterns including energy use

This paper aims to show Kırklareli region has another renewable energy source alternative for its energy consumption and to indicate that geothermal energy can be sustainable if it is used properly within sustainable development framework.

2. MATERIAL AND METHODS

The data obtained from the first drilled geothermal well by MTA at Kırklareli is used for the determination of the resource potential. Possible energy income from this well is taken from MTA's report and compared with Kırklareli's annual consumption so, possible impact of geothermal energy usage is calculated.

And, while setting goals for sustainability for the region, Shortall et.al. 's published 3 articles at 2015 were analyzed. They created sustainable development framework for geothermal projects at Iceland, New Zealand and Kenya. At these studies first, they determined 10 goals towards to sustainable geothermal energy and chose 11 themes among the themes of UN. And then the choose 21 indicators under those topics. Then they gave this information to stakeholders of these projects and asked to order them in manner of relativeness to their projects. And then, researchers use a program called Delphi to run these data and made 3 iterations according relativeness to the goals of sustainable development with interests of the stakeholders. As a result, they are established top indicators to reach these goals.

Data from wells puts the fact that our region does not have a potential to have power plant for electricity generation. So, in this study, only "fresh water", and "economic development" and "energy use" themes are chosen within compatibility of these works with Kırklareli Region and the most related indicators; Percentage of renewables in total energy supply regionally, resource reserve capacity ratio of the geothermal resource and water quality of water bodies impacted by geothermal operations are chosen indicators for this case.

2.1. GEOTHERMAL ENERGY POTENTIAL

Low-enthalpy geothermal resource at Thrace Region newly discovered by drilling researches done by Mineral Research and Exploration (MTA) at Kırklareli Asimbeyli location which has reservoir with quantities 57^0C and 4 lt/sec artesian flow. This well has potential of 2,38 MWt (MW thermal) energy income and possibility to utilize green housing area of 12.500m^2 and heating of 340 houses and potential of thermal tourism for the 2,600 people.

Also, at Tekirdağ/Saray second well had been drilled to 1500m and has similar production values and at 2016 at Kırklareli/Vize third well had been drilled to 2200m and has reservoir with quantities 43^0C and 5 lt/sec artesian flow. Forth one is drilled at Istanbul/Silivri to 1500m depth and has a reservoir with quantities of 60^0C and 10lt/sec flow with compression. If an extrapolation has to be made, one well is calculated 2,38 MWt energy production capacity so, there is 4 more wells than approximately 10 MWt energy production for all The Thrace Region potential can be predicted.

So, in order to understand this energy potential's importance numerically, we compared as a ratio this energy income with annual energy consumption data of Kırklareli City which is taken from Republic of Turkey Energy Market Regulatory Authority

- 2,016,467.31 MWh is annual energy consumption of Kırklareli City
- 2,38 MWt (MW thermal) energy income of a one geothermal well

But first a conversion has to be made for, 2,38 MWt to MWh. According to Zarrouk S. article called "Efficiency of geothermal power plants: A worldwide review", at 2014 worldwide average efficiency of geothermal conversion power plants is around 12%.

So, potential annual energy production from geothermal can be calculated as

- 2,38 MWt x 0,12 (efficiency) x 365 (days) x 24 (hours) = 2,501.856 MWh
  (Production MWh/ Consumption MWh) x 100 =>
- (2,501.856 MWh/ 2,016,467.31 MWh)x 100 = 0,124

So, one well of geothermal source can utilize 0,124% of Kırklareli's needs with suitable investment to geothermal substructure.

Potential of Kırklareli of geothermal energy is not suitable for indirect usage as electricity production. It is more likely suitable for direct usage like household heating, green housing and thermal tourism. Direct use of geothermal energy can be more suitable and beneficial for our region, and tends to provide more local employment opportunities. If this resource is used as house heating the effect of it to society may be significant because only from a one well can be capable to heat 340 houses. According to master thesis of Altaş, S. at 2010, benefits and limitations (due to wells) of house heating with geothermal energy source is listed below.

Benefits of House heating	**Limitations during house heating by source usage**
1. National and Clean Energy	1.Geothermal Fluid composition
2. Diversity of sage	2.Well head flow
3. Modularity	3.Source temperature
4. High Efficiency	4.Usage density
5. Easy to use	5.Well depth
6. Lower transportation and maintenance cost	6.Distance btw wells and usage area
7. Alternative energy cost	

Kırklareli City has substructure of natural gas for heating houses in center but not all villages have this substructure. So, 340 houses may cover some number of villages which are already using coal for heating. And, this geothermal energy may promote region economically, socially and environmentally.

Also, if this potential is used for 12.500m^2 area of green housing, there would be many advantages with environmental and economic benefits to the agriculture. Madencilik Politikaları Özel İhtisas Komisyonu under the authority of the Presidency of the Republic of Turkey is published a report about green housing with geothermal energy source and benefits are mentioned below.

1. Geothermal heating increases efficiency up to 60%.
2. Pumping geothermal carbon dioxide to green housing atmosphere increases efficiency 40%
3. Temperature within greenhouse is higher than insemination temperature which is also increasing the efficiency.
4. Ideal temperature gives the opportunity of production without hormones.
5. It is cheaper relatively fossil and other alternative energy sources.
6. Reliable no risks of fire or explosion.
7. Minimum space needs compared to hydro or photovoltaic.
8. Easy and fast installation, operation and maintenance. (6months to 1year)
9. Long facility life.

Thrace region is known as its agriculture production. Green housing running by geothermal source can contribute region's sustainable agriculture production.

The third possibility is potential of thermal tourism for the 2,600 individuals. After, exploration of geothermal energy at Saray/Tekirdağ there is ongoing Thermal Hotel project for 3,000 individuals. If that project becomes successful, potential of Kırklareli can be considered to be assessed too.

2.2. SUSTAINABLE GEOTHERMAL ENERGY

As United Nation's description, sustainable energy can be described basically, economic, social and environmental needs of developmental context of the society should be provided by affordable, accessible and reliable energy services while recognizing equitable distribution in meeting those needs. There are 17 goals that United Nations set for better future. To reach these goals there are set themes and subthemes to create a framework for action. In order to apply the correct framework, The Commission for Sustainable Development (CSD) has called for the development core indicators under the themes and subthemes to measure and calibrate progress towards sustainable development goals. The indicators also provide an overview of the progress towards a more sustainable economy, society and environment.

In order to apply the correct framework, The Commission for Sustainable Development (CSD) has called for the development core indicators under the themes and subthemes to measure and calibrate progress towards sustainable development goals. A sustainable development indicator (SDI) can be explained as a quantitative tool that analyses alterations, while evaluating and communicating progress towards the sustainable use and management of economic, social, institutional and environmental resources. At 2007 revised CSD indicators has been published which contain a core set of 50 indicators within 92 indicators under the themes. Indicator framework can serve as a starting point for decision makers for any project that uses sustainable energy. So, according to Shortall et.al. 's article, common indicators are given to the stakeholders to relate importance under the themes for goals listed above on study called "A sustainability assessment framework for geothermal energy projects: Development in Iceland, New Zealand and Kenya". After that they made 3 rounds of iterations by the program called Delphi with the data to point out the most related indicators for their projects.

All indicators are listed below.

1. Air quality in the surrounds of the geothermal power plant
2. Average Income Levels in Project-Affected Communities

3. Direct and indirect local job creation over lifetime of project
4. Duration of Plant Power Outages per year
5. Estimated productive life time of geothermal resource
6. Expenditure on heat and electricity as a percentage of household income
7. Impact on important or vulnerable geothermal features
8. Imported energy as a percentage of total (national level)
9. Income-to-expenditure ratio for project-affected municipalities
10. Level of induced seismicity per year
11. Noise levels in working, recreation and residential areas in the surrounds of the geothermal powerplant.
12. Number of accidents leading to work absence in the energy company per year
13. Percentage of community residents that must be relocated due to energy project
14. Percentage of energy company expenditure given to R&D per year
15. Percentage of renewables in total energy supply nationally
16. Project internal rate of return (IRR)
17. Rate of subsidence in the geothermal field
18. Resource reserve capacity ratio of the geothermal resource
19. Tons of greenhouse gas emissions resulting from geothermal operations
20. Utilization efficiency for the geothermal power plant
21. Water Quality of water bodies impacted by geothermal power plant operations

There are top3 results for each project but since Kırklareli's potential is not enough for electricity generation there no need to state power plants related indicators so, the most related 3 indicators are chosen for this case. Which are;

1. **Percentage of renewables in total energy supply regionally** under the theme of "Consumption and production patterns including energy use" to the Goal 5 – Economic Management & Profitability.

As it calculated above one well of geothermal source can potentially utilize some amount Kırklareli's needs with suitable investment to geothermal substructure. But evaluation has to be made on household scale, it is possible to use for household heating and net positive profit of heating expenses over a certain period should be compared to fossil fuels. That is why first investment should be deeply investigated. Also, farming (green housing) and tourism activities may have positive impact to the region's economy. Also,

Increasing the efficiency is key of sustainability. Waste energy, water and gas and efficiency have reverse proportion relation.

2. **Resource reserve capacity ratio of the geothermal resource** under the theme of "Economic development: including macroeconomic performance, employment and tourism, research and development." to the Goal 1 – Renewability.

In order to understand reserve, other well's reports from the field must be analyzed to discussed reservoir capacity whenever they are ready. Production rate should be balanced according to purpose of usage. But no matter what, geothermal energy is renewable and it is only possible with re-injection. Re-injected water should be clean to preserve reservoir down below.

3. **Water Quality of water bodies impacted by geothermal operations** under the theme of "Fresh Water" to the Goal 3 – Environmental Management.

Geothermal operations even drilling process can cause gases emission and waste water which may have heavy metals at different levels. Higher concentrations of heavy metals like arsenic, mercury, ammonia, boron can be toxic on living bodies. It may contaminate ground water, soil and water sources for agricultural purposes. According to Yilmaz, E., & Mustafa Ali, K. 's study about environmental impact of Germencik Geothermal Field in Aydın downhole fluid which generated during the drilling, stimulation and production phases contains dissolved toxic minerals especially boron, which poisons surface or groundwater and harm local vegetation.

But unlike this case, according to analysis from end of the well report of Kırklareli's well, water samples taken from reservoir does not contain any boron and all other minerals (Na, Cl, Fe, Mn, Pb, Zn, Cu, Ni) are within the limits of direct usage for agricultural purposes. But, only fluoride mineral is higher than drinkable water limits that World Health Organization (WHO) set. Fortunately, this well does not have any dangerous heavy metal risks to environment, but all new wells' analyses should be taken under consideration before usage.

Bottom line under this topic is, water sources should not be contaminated by underground water so filtration should be applied to avoid heavy metal contamination. Also, emissions during drilling process should be lowered as possible and it should be auctioned.

3. RESULTS

Kırklareli has a potential of sourcing its needs from geothermal energy from even one well is calculated as 0,124%. Higher effect can be seen by using it for house heating. Only from a one well can be capable to heat 340 household. It would be higher benefits for environment and society if it is used for green housing area of 12.500m^2. Sustainable geothermal energy is possible if precautions can be applied. Precautions has to be taken by following the indicators of sustainable development, in order to avoid negative impacts of geothermal energy before even utilize it. In this study, we chose 3 indicators to obtain 3 goals within circumstances of the reserve data of one well.

To achieve 5th goal of CSD Economic Management & Profitability, we choose "Percentage of renewables in total energy supply regionally" as an indicator. Which will indicate growth of the usage of renewable sources for energy need over the time. Increase of this data will reduce fossil fuel consumption hence it will be more economical and environment friendly.

To achieve 1st goal of CSD Renewability, we choose "Resource reserve capacity ratio of the geothermal resource" as an indicator. Which will show us most efficient production/induction rates to sustain the potential longer. Balance of this rate should be calculated with new well's reports for future work.

To achieve 3rd goal of CSD Environmental Management, we choose "Water Quality of water bodies impacted by geothermal operations" as an indicator. Which will give us the opportunity of keeping track of heavy metal ratio of water or vapor for all living habitat which uses reservoir water or contaminated ground water. Unlike, Aydın case, these precautions have to be made before even geothermal projects starts and sustains for centuries. For all stages of usage of geothermal energy should be organized to controlled by laws, directives, articles, etc. for cover future of earth and life.

4. ACKNOWLEDGEMENT

The authors are grateful for the support and data provided for this paper by Lütfi TAŞKIRAN from Thrace Geothermal Survey Studies, Turkish General Directorate of Mineral Research and Exploration (MTA).

REFERENCES

1. Altaş, S. (2010). Kızılcahamam Jeotermal Merkezi Isıtma Sistemi ile Klasik Merkezi Isıtma Sisteminin Karşılaştırılması (Master's thesis, Gazi Üniversitesi, 2010) (pp. 61-62). Ankara. doi:708.1.038

2. ANONİM, 2013b. Onuncu Kalkınma Planı (2014-2018) Madencilik Politikaları Özel İhtisas Komisyonu, Enerji Hammaddeleri Grubu Jeotermal Çalışma Alt Grubu Raporu. Kalkınma Bakanlığı, Ankara.
3. Elektrik Piyasası 2017 Yili Piyasa Gelişim Raporu (pp. 7-22, Rep.). (2018). Ankara: T.C. Enerji Piyasası Düzenleme Kurumu Strateji Geliştirme Dairesi Başkanlığı.
4. Shortall, R., Davidsdottir, B., & Axelsson, G. (2015). A sustainability assessment framework for geothermal energy projects: Development in Iceland, New Zealand and Kenya. Renewable and Sustainable Energy Reviews, 50, 372-407. doi:10.1016/j.rser.2015.04.175
5. Shortall, R., Davidsdottir, B., & Axelsson, G. (2015). Development of a sustainability assessment framework for geothermal energy projects. Energy for Sustainable Development, 27, 28-45. doi:10.1016/j.esd.2015.02.004.
6. Shortall R., Davidsdottir, B., & Axelsson, G. (2015). Geothermal energy for sustainable development: A review of sustainability impacts and assessment frameworks. *Renewable and Sustainable Energy Reviews*,*44*, 391-406. doi:10.1016/j.rser.2014.12.020
7. Taşkıran, L., Arslan, G., Turalı, Ü, Güven, A., Abdi, A., & Akar, A. (2017). Kirklareli-Merkez Ar: 201339002, Ar: 201339003 ve Ar: 201339004 No.lu Jeotermal Kaynak Arama Ruhsat Sahalari Jeotermal Etüt (Jeoloji-Jeofizik) ve Kma- 2014/2 Jeotermal Gradyan, Kma-2014/7 Jeotermal Araştirma Sondajlari Kuyu Bitirme Raporu(Pp. 92-98, Rep.). Ankara: Maden Tetkik Ve Arama Genel Müdürlüğü.
8. Turkish General Directorate of Mineral Research and Exploration (MTA), Geothermal Energy Potential Research and Research Works in Turkey, in Turkish, November 2017, Thrace Geothermal Survey Studies, Lütfi TAŞKIRAN, Ph. D. et. al. Retrieved from http://www.mta.gov.tr/v3.0/arastirmalar/jeotermal-enerji-arastirmalari
9. United Nations. Indicators of sustainable development: guidelines and methodologies. 3rd ed.. New York: United Nations; 2007.
10. Yilmaz, E., & Mustafa Ali, K. (n.d.). EEMS 2017. In *Environmental impact of geothermal power plants in Aydın, Turkey*. E3S Web of Conferences 19, 02028 (2017). doi:10.1051/e3sconf/20171902028
11. Zarrouk, S. J., & Moon, H. (2014). Efficiency of geothermal power plants: A worldwide review. Geothermics,*51*, 142-153. doi:10.1016/j.geothermics.2013.11.001

THE ANALYSIS OF THE ELECTRICAL PROPERTIES OF THE Cu//n-TYPE Si STRUCTURES AT ROOM TEMPERATURE

Şükrü Karataş

Department of Physics, Faculty of Sciences and Arts, Kahramanmaraş Sütçü İmam University, 46100-Kahramanmaraş, Turkey

E-mail: skaratas@ksu.edu.tr

Abstract

We investigated the main electrical characteristics of Cu/n-type Si structures at room temperature (300 K). The electrical characteristics such as ideality factors (n), barrier heights (Φ_{bo}), series resistances (R_S), and reverse-saturation currents were investigated using the forward bias current–voltage (I–V) and capacitance–voltage (C–V) dates. The current–voltage (I–V) characteristics of the Sn/p-Si structures were analyzed by the thermionic emission theory. Also, the energy distribution of interface states density (N_{SS}) as a function of energy distribution (E_C-E_{SS}) were determined from the forward bias I–V characteristics by taking into account the bias dependence of the effective barrier height. The results show that the interface states densities obtained taking into account the series resistance are lower than those obtained without taking into account the series resistance.

1. INTRODUCTION

The metal-oxide-semiconductor (MOS) type Schottky barrier diodes (SBDs), metal and semiconductor structure remain separated by an oxide layer. As known, it is extremely significant to obtain high quality Schottky barrier diodes for improve device performance and reliability. Si is extensively used in the fabrication of electronic devices such as diodes, integrated circuits, and transistors [1-3]. Copper (Cu) is a remarkable metal in recent years due to high conductivity. Thus, Cu are increasingly used in different devices such as in catalysis, batteries, gas sensors, heat transfer fluids, and solar energy owing to its suitable band gap [4-9].

In this study, we examined the electronic properties of main parameters obtained from current-voltage (*I-V*) and capacitance-voltage (*C-V*) measurements and interface state density distribution properties of interface states of Cu/*n*-type Si structures at the room temperature. Also, as function of energy distribution (E_{CC}- E_S) of interface state densities (N_{SS}) with and without taking into account series resistance obtained from the forward-bias *I–V* characteristics of the Cu/n-type Si (MS) Schottky diodes at room temperature.

2. MATERIAL AND METHODS

The *n*-type Si wafer used in this study has <100> orientation and was 0.10 Ω-cm in resistivity. The Schottky structures were formed on the polished side of the n-Si substrate as dots with diameter of about 1 mm (the Contact area = 7.85×10^{-3} cm^2) by the electroless deposition of Cu. The current–voltage (*I–V*) measurements carried out by the use of a Keithley 2400 source meter. The capacitance–voltage (*C–V*) measurements were performed using an HP 4192A LF impedance analyzer (5 Hz–13 MHz). The wafer was chemically cleaned using the RCA cleaning procedure [10].

3. RESULTS AND DISCUSSION

The current-voltage plots of Cu/n-type Si structures obtained at room temperature are showed in Fig. 1. The experimental forward bias *I–V* characteristics of Cu/n-type Si structures at room temperature can be analyzed by thermionic emission (TE) theory [1-8]:

$$I = I_o \exp\left(\frac{qV}{nkT}\right)\left[1-\exp\left(-\frac{qV}{kT}\right)\right] \quad (1)$$

where *n* is the ideality factor, *q* is the elementary charge, *k* is the Boltzmann constant, T is the absolute temperature and *V* is the applied voltage. Furthermore, where the saturation current I_o in Eq. (1) is given by

$$I_o = AA^*T^2 \exp\left(-\frac{q\Phi_b}{kT}\right) \quad (2)$$

where Φ_b is the Schottky barrier height (SBH) at zero bias, A^* is the effective Richardson constant for *p*-type Si (A^*=112 $Acm^{-2}K^{-2}$), and A is the effective diode area (=7.85x10^{-3} cm^2). The ideality factor is determined from forward bias *lnI-V* characteristics through the relation:

$$n = \frac{q}{kT}\left(\frac{dV}{d\ln I}\right) \quad (3)$$

On the other hand, barrier height, Φ_b, can be obtained from the eq. (2),

$$\Phi_b = \frac{kT}{q}\ln\left(\frac{A^*AT^2}{I_0}\right) \quad (4)$$

The values of the ideality factor (*n*) and the barrier height (Φ_b) were found to be 4.38 and 0.741 eV, respectively, by using Eqs (3) and (4), respectively. The high values of n can be attributed to effects of the bias voltage drop across the interfacial native oxide layer and series resistance. Basically, the value of ideal factor should be n =1 for an ideal contact.

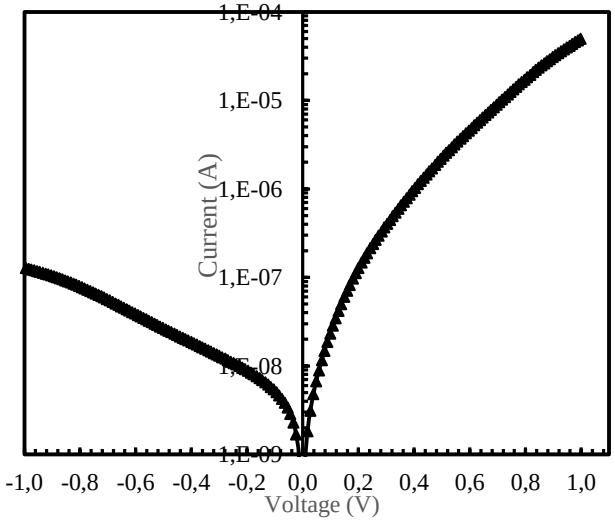

Figure 1. The I-V curves of the Cu/n-Si Schottky structure

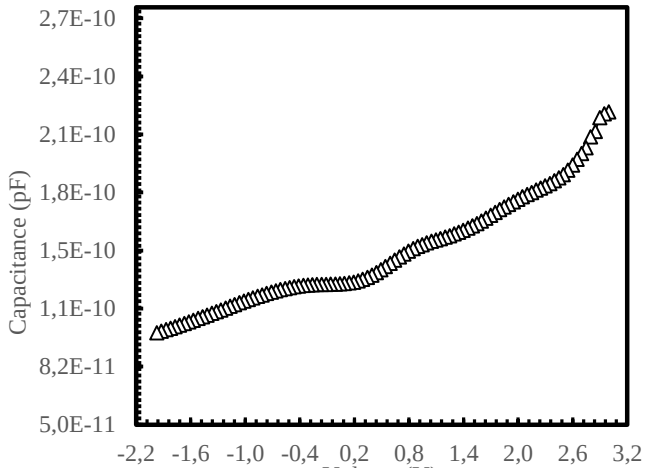

Figure 2. The C-V plot of Cu/n-type Si strtucture

Furthermore, the capacitance-voltage (*C-V*) measurements are one of another most important to determine of the fundamental properties of the metal-semiconductor (MS) or metal–oxide-semiconductor (MOS) structures.

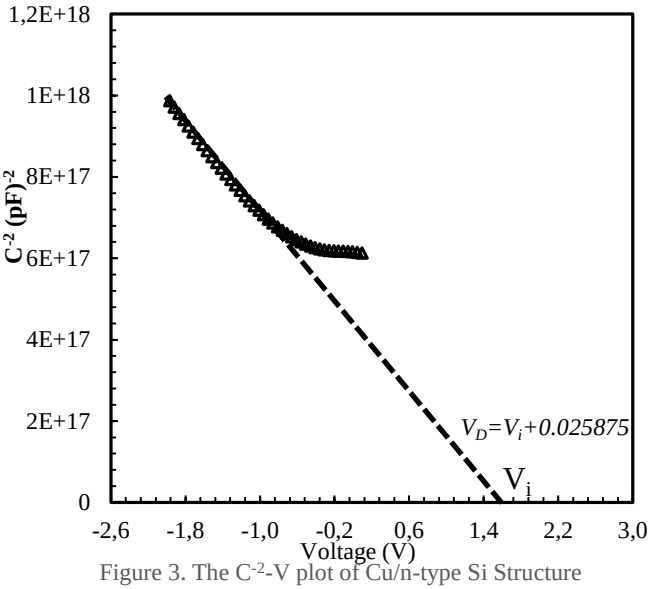

Figure 3. The C^{-2}-V plot of Cu/n-type Si Structure

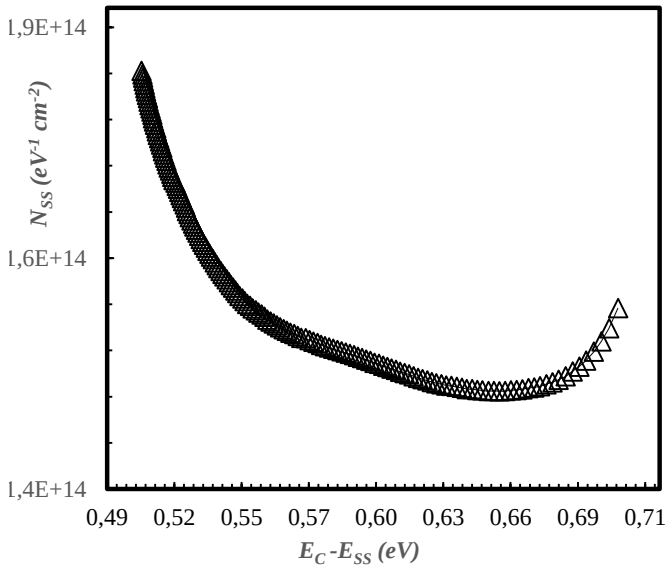

Figure 4. The interface states N_{SS} as a functions of E_C-E_{SS}

The *C-V* measurements can provide information about the diffusion potential, fermi energy, carrier/ donor density, image force lowering and barrier height of SBDs. Fig. 2 shows the *C-V* characteristic at room temperature (T=300 K) measured at frequency of 500 kHz by using HP 4192 A Impedence Analyzer. As can be seen in Fig 2 that while *C-V* characteristic in the idealized Cu/n-type Si structures case shows an increase in capacitance with increasing forward voltage. The C^{-2}–*V* characteristic illustrated in Fig. 4 is linear over the range of -2.6 V- 3.0 V at 500 kHz. The diffusion potential or built-in potential is usually measured by extrapolating C^{-2}-V plot to the V-axis. The barrier height, Φ_{CV}, from *C-V* measurement is defined by;

$$\Phi_{CV} = V_i + \frac{kT}{q} + kT\ln\left(\frac{N_C}{N_D}\right) - \Delta\Phi_b = V_a + E_F - \Delta\Phi_b \qquad (5)$$

where $\Delta\Phi_b$ is the image force correction and E_F is the Fermi energy measured from the conduction band edge in the neutral region of Cu/n-type Si structures and can be calculated knowing the carrier concentration. According to Eq. (5), the measured barrier height Φ_{CV} is 1.503 eV. The difference between barrier heights obtained from *I-V* and *C-V* measurements is mainly due to in homogeneities. Furthermore, as explained in refs [1, 3, and 10], this difference is explained due to an interface layer or to trap states in the substrate, the effect of the image force and the barrier in homogeneities.

The interface state energy distribution (N_{SS}) curve of the Cu/n-type Si structures is given in Fig. 4. As can be seen from Fig. 4, the interface state density N_{SS} has an exponential drop with bias from the midgap towards the top of the conduction band for Cu/n-type Si structures. As can be seen in Fig. 4, the exponential growth of the interface state density from midgap towards the bottom of the conduction band is very apparent, and the N_{SS} values obtained decrease with applied voltages.

4. CONCLUSION

In this study, we examined the electronic properties of main parameters obtained from *I-V* and *C-V* measurements and interface state density distribution properties of interface states of Cu/n-type Si structures at the room temperature. The experimental results show that the main parameters, such as ideality factors (n), series resistances (R_S), and barrier heights (Φ_b) were found to be strongly depending on the voltage. The second goal is to investigate as a function of energy distribution (E_{CC}- E_S) of interface state densities (N_{SS}) with and without taking into account series resistance obtained from the forward-bias *I–V* characteristics of the Cu/*n*-type Si (MS) Schottky diodes at room temperature.

REFERENCES

[1] Sze,S.M., Physics of Semiconductor Devices, 2nd ed., Wiley, New York, 1981, p. 850.

[2] Schultz, M.L., Silicon: Semiconductor Properties, Infrared Physics, 4, 93-112, 1964.

[3] Brillson, L.J., The structure and properties of metal-semiconductor interfaces, Surface Science Reports, 2, 123-326, 1982.

[4] Li, J., Sun, F.,Gu, K.,Wu,T.,Zhai,W., Li,W.,Preparation of spindly CuO micro-particles for photodegradation of dye pollutants under a halogen tungsten lamp,Applied CatalysisA,406,51–58, 2011

[5] Oral, A.Y., Mensur, E., Aslan, M.H., Basaran, E.,The preparation of copper(II) oxide thin films and the study of their microstructures and optical properties,Materials Chemistry Physics.,83,140–144, 2004.

[6] Erdogan, İ.Y., Güllü, Ö., Silicon MIS diodes with Cr_2O_3 nanofilm: Optical, morphological/structural and electronic transport properties., Applied Surface Science 256, 4185–4191, 2010.

[7] Çetinkaya, H.G., Altındal, Ş., Orak, İ., Uslu, İ., Electrical characteristics of Au/n-Si (MS) Schottky Diodes (SDs) with and without different rates (graphene + Ca1.9Pr0.1Co4Ox-doped poly(vinyl alcohol, Journal of Materials Science: Materials in Electronics 28, 7905-7911, 2017

[8] Çetin, H., Ayyildiz, E., Temperature dependence of electrical parameters of the Au/n-InP Schottky barrier diodes, Semiconductor Science and Technology, 20, 625-630, 2005.

[9] Uluşan, A. B., Tataroğlu, A., Kalandaragh, Y. A., Altındal, Ş, On the conduction mechanisms of Au/(Cu2O–CuO–PVA)/n-Si (MPS) Schottky barrier diodes (SBDs) using current–voltage–temperature (I–V–T) characteristics, Journal of Materials Science: Materials in Electronics, 29, 159-170, 2018

[10] Karataş¸ Ş., Altındal¸Ş., Türüt, A. Özmen,A., Temperature dependence of characteristic parameters of the H-terminated Sn/p-Si (1 0 0) Schottky contacts, Applied Surface Science, 217, 250 (2003).

[11] Rhoderick, E.H., Williams, R.H., Metal–Semiconductor Contacts, 2nd ed., Clarendon Press, Oxford, 1988.

ON THE ELECTRICAL PROPERTIES OF Ag/GRAPHENE OXIDE/p-Sİ STRUCTURES AT ROOM TEMPERATURE

Şükrü Karataş[1], Halil Özerli[2]

[1]*Kahramanmaraş Sütçü İmam University, Faculty of Sciences and Arts, Department of Physics, 46100-Kahramanmaraş, Turkey*

[2]*Department of Materials Science and Engineering, Kahramanmaras Sutcu Imam University, Kahramanmaraş, Turkey*

E-mail: skaratas@ksu.edu.tr

Abstract

In this study, we investigated the current-voltage (*I-V*) and capacitance–voltage (*C–V*) characteristics of Ag/GO/*p*-type Si structure at the room temperatures. The main parameters such as ideality factors (*n*), barrier heights (Φ_{b0}), series resistances (R_S), and the density of interface states (N_{SS}) have been investigated using current–voltage measurements at room temperature. The barrier height, ideality factor and series resistance of the Ag/GO/*p*-Si Schottky heterojunction have been also determined using different methods. The energy distribution of interface states density (N_{SS}) as a function of energy distribution (E_{SS}-E_V) were determined from the forward bias current–voltage (*I-V*) characteristics.

1. INTRODUCTION

The silicon (Si) based Schottky barrier diodes play an important role in integrated circuit technology. Thus, a thorough knowledge of their fundamental characteristics is critical for their rational design. Many experimental and theoretical studies on the current flow mechanism of the metal-Si Schottky barriers have been reported [1, 2]. Furthermore, it is well known that Schottky diodes with organic components have many advantages over inorganic semiconductors in electronic devices such as easy fabrication, low cost, and applicability to rigid-flexible substrates [3-6]. Many organic interfacial layers between metal and semiconductors can be prepared with simple techniques such as electrostatic spraying, spin coating, dip coating, the sol-gel technique, etc. [5]. The electrical parameters of Schottky diodes are mainly affected by the interfacial organic layer [6]. In this paper, our aim is to investigate the I–V characteristics of Ag/GO/*p*-type Si structure at room temperature. The barrier height and series resistance obtained from Norde's function was compared with those from Cheung functions. It was seen that there was a good agreement between the BH values and series resistances from both methods. As a function of energy distribution (E_{SS}-E_V) of interface state densities (N_{SS}) obtained from the forward-bias *I–V* characteristics of the Ag/GO/*p*-type Si structure at room temperature. It is seen that the series resistance value should be taken into account in determining the interface-state density distribution curves.

2. MATERIAL AND METHODS

The samples were prepared using cleaned and polished p-type Si wafers with (100) orientation and 10 Ω-cm resistivity. The wafer was chemically cleaned using the RCA cleaning procedure [3]. The *I-V* characteristics of the Ag/GO/p-Si Schottky structures were measured using a Keithly 220 programmable constant current source and a Keithly 199 dmm/scanner under dark conditions. The Schottky contacts were formed by evaporation of Ag dots with diameter of about 1 mm (diode area =7.83x10^{-3} cm^2).

3. RESULTS AND DISCUSSION

The current-voltage (*I-V*) plot of Ag/GO/*p*-type Si structure at the room temperature are showed in Fig. 1. The experimental forward bias *I–V* characteristics of structure can be analyzed by thermionic emission (TE) theory [1-5]:

$$I = I_o \exp\left(\frac{qV}{nkT}\right)\left[1-\exp\left(-\frac{qV}{kT}\right)\right] \quad (1)$$

where *n* is the ideality factor, *q* is the elementary charge, *k* is the Boltzmann constant, T is the absolute temperature and *V* is the applied voltage. Furthermore, where the saturation current I_o in Eq. (1) is given by

$$I_o = AA^* T^2 \exp\left(-\frac{q\Phi_b}{kT}\right) \quad (2)$$

where Φ_b is the Schottky barrier height (SBH) at zero bias, *A** is the effective Richardson constant for *p*-type Si (A*=32 $Acm^{-2}K^{-2}$), and A is the effective diode area (=7.8310^{-3} cm^2). The values of the ideality factor (n) and the barrier height (Φb) were found to be 2.46 and 0.762 eV at room temperature, by using Eqs (1) and (2), respectively. The high values of n can be attributed to effects of the bias voltage drop across the interfacial native oxide layer and series resistance. Basically, the value of ideal factor should be n =1 for an ideal contact.

Thus, ideality factor and the series resistance were evaluated using a method developed by Cheung et al. [28]. The Cheung's method is achieved by using the functions;

$$\frac{dV}{d(\ln I)} = R_s I + n\frac{kT}{q} \quad (3)$$

$$H(I) = V - n\left(\frac{kT}{q}\right)\ln\left(\frac{I}{AA^* T^2}\right) \quad (4)$$

and

$$H(I) = IR_S + n\Phi_{bo} \quad (5)$$

The plots associated with these functions are given in Fig. 2. Using the n value 3.16 determined from Eq. (3) and the data of downward curvature region in Eq. (4), a plot of H(I) versus I according to Eq. (5) will also give a straight line with y-axis intercept equal to $n\Phi_b$. From dV/dln(I) versus I plot by means of Eq. (3), the values of 207684 Ω and 3.16 for R_S and n of the device were obtained, respectively. The values of 245289 Ω and 0.303 eV for R_S and Φ_b were also obtained from H(I)-I plot according to Eq. (5), respectively.

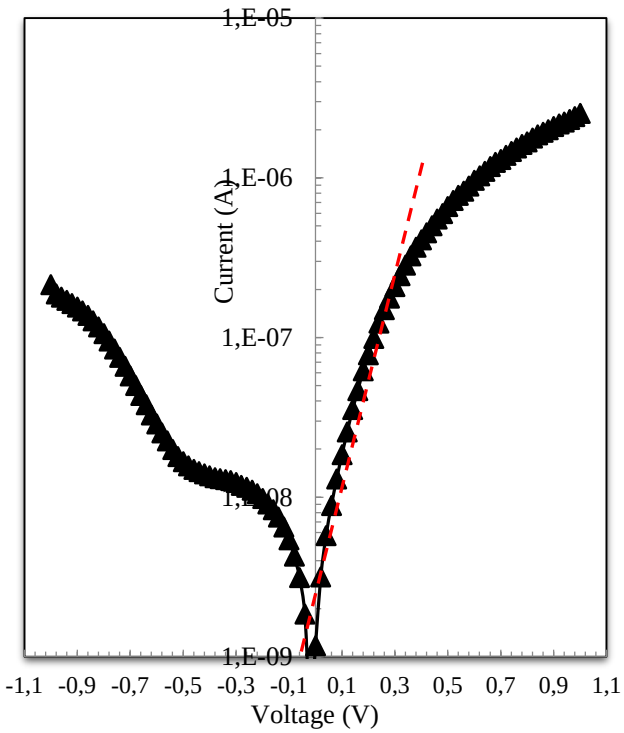

Figure 1. The current-voltage (*I-V*) plot of structure

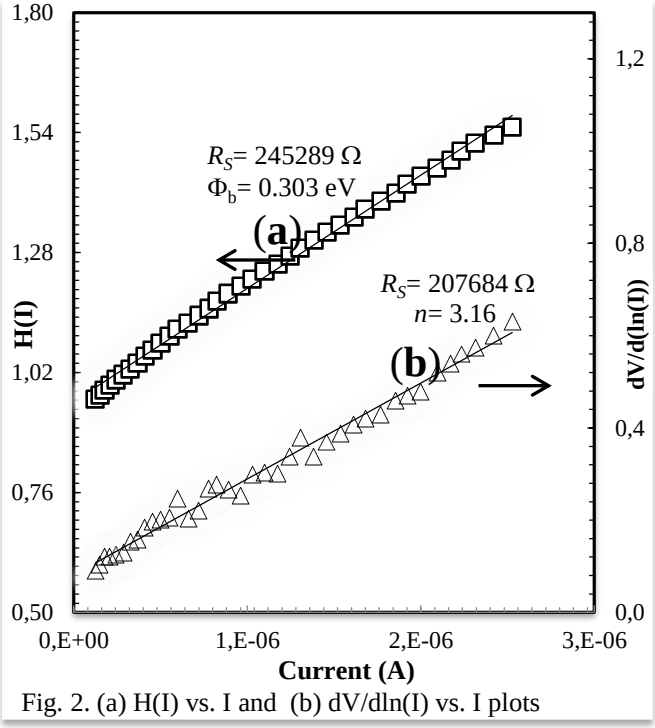

Fig. 2. (a) H(I) vs. I and (b) dV/dln(I) vs. I plots

Furthermore, Norde proposed an alternative method to determine the value of the series resistance. The following function has been defined in the modified Norde method [13, 29]:

$$\Phi_b = F(V_0) + \frac{V_0}{\gamma} - \frac{kT}{q} \tag{6}$$

where γ is an arbitrary integer greater than n (γ >n). Once the minimum of the F(V) versus V plot is determined, the value of barrier height (Φb) can be obtained from Eq.(6), where $F(V_0)$ is the minimum point of F(V), and V_0 is the corresponding voltage. Figure 3 shows the F(V)-V plots of the diodes. The value of the series resistance (R_S) was obtained from Norde's method for Ag/GO/*p*-type Si structure. Furthermore, Norde's functions R_S value is determined as

$$R_S = \frac{\gamma - n}{I} \quad \frac{kT}{q} \tag{7}$$

From the F(V)–V plot the values of Φ_b and R_S of the structure have been determined as 0.441 eV and 271818 Ω, respectively. It can be seen that there is a good agreement the values of series resistance obtained from the forward bias lnI–V, Cheung functions and Norde functions.

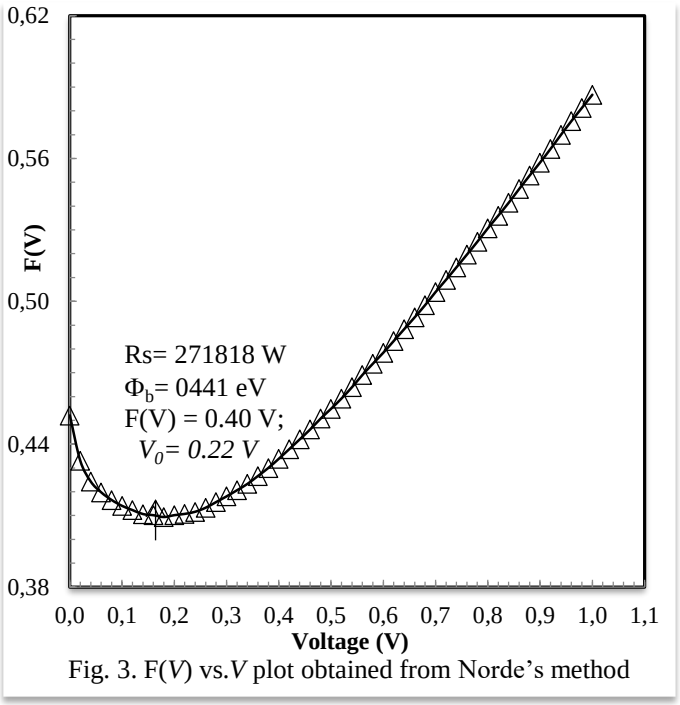

Fig. 3. F(*V*) vs.*V* plot obtained from Norde's method

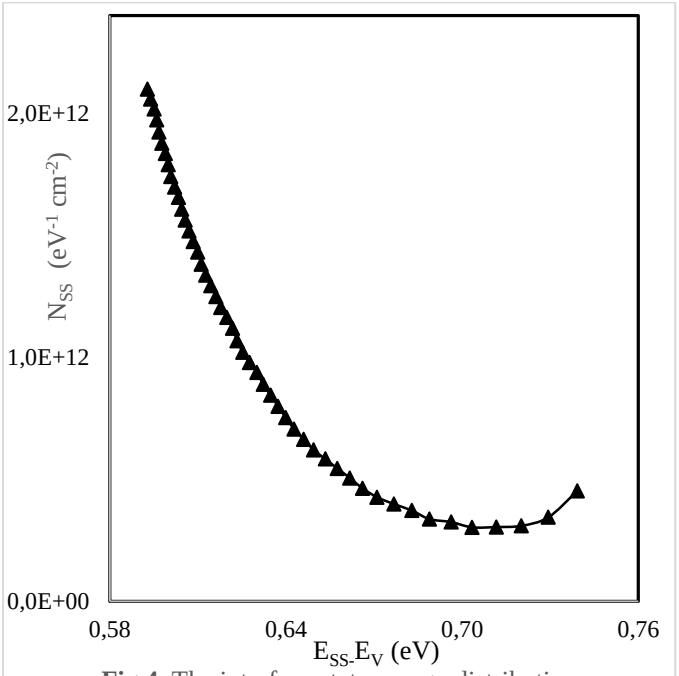

Fig 4. The interface state energy distributions

Interface states can be written as below;

$$N_{SS}(V)=\frac{1}{q}\left[\frac{\varepsilon_i}{\delta}\left(n(V)-1\right)-\frac{\varepsilon_s}{W_D}\right] \tag{8}$$

Furthermore, in *p*-type semiconductors, the energy of the interface states, E_{SS}, with respect to the top of the valance band, E_V, at the surface of the semiconductor is given by [35, 40, and 41].

$$E_{SS}-E_V=q\Phi_e-qV \tag{9}$$

Thus, we can use Eqs. (8) and (18) together with Eqs in the calculation of the interface state density distribution. N_{SS} vs. E_{SS}-E_V plots of the Ag/GO/*p*-Si Schottky structure is shown in Fig.4. As can be Fig. 4, the interface state density (N_{SS}) calculated without taking into account series resistance (R_S) has increased exponentially with bias from 4.52x10^{11} cm^{-2}eV^{-1} in (0.739- E_V) eV to 2.09910^{12} cm^{-2}eV^{-1} in (0.593- E_V) eV of *p*-Si. This case may be ascribed to the chemical reactivity of Schottky metal. That is, chemical reactions involving oxygen could also change the distribution of states at the interface.

4. CONCLUSION

The electrical and interface state density distribution properties of Ag/nGO-PVA/*p*-Si/Ag structure have been investigated from current-voltage measurement at room temperature. The ideality factor and barrier height values calculated from Cheung functions and Norde's functions. Furthermore, the interface states in equilibrium with the semiconductor were calculated from the downward curvature region caused by the presence of series resistance and interface states in the current–voltage plots. The interface state density obtained from the forward bias *I–V* ranges from 4.52×10^{11} $cm^{-2}eV^{-1}$ in (E_{SS}–0.739) eV to 2.099×10^{12} $cm^{-2}eV^{-1}$ in (E_{SS}-*0.593*) eV, of the Ag/nGO-PVA/*p*-Si hetero structure.

Acknowledgement:

This work was supported by Kahramanmaras Sütçü Imam University Scientific Research Project (Project number: 2015/3-90M). We would like to thank Kahramanmaraş Sütcü Imam University for financial support of the research program.

REFERENCES

[1] Sze,S.M., Physics of Semiconductor Devices, 2nd ed., Wiley, New York, 1981, p. 850.

[2] Rhoderick, E.H., Williams, R.H., Metal–Semiconductor Contacts, 2nd ed., Clarendon Press, Oxford, 1988.

[3] Kılıçoğlu, T., Aydın, M.E., Ocak, Y.S, The determination of the interface state density distribution of the Al/methyl red/p-Si Schottky barrier diode by using a capacitance method, Physica B: Condensed Matter, 388, 244-248, 2007.

[4] Kılıçoğlu, T., Effect of an organic compound (Methyl Red) interfacial layer on the calculation of characteristic parameters of an Al/Methyl Red/p-Si sandwich Schottky barrier diode, Thin Solid Films, 516, 967-970, 2008

[5] Ocak, Y.S., Kulakçı, M., Kılıçoğlu, T., Turan, R.,Akkılıç, K., Current–voltage and capacitance–voltage characteristics of a Sn/Methylene Blue/p-Si Schottky diode, Synthetic Metals, 159, 1603-1607, 2009.

[6] Soylu, M., Al-Hartomy, O.A., Al Said, S.A.F., Al-Ghamdi, A.A., Yahia, I.S. and Yakuphanoglu, F., Interface control and photovoltaic properties of n-type silicon/metal junction by organic dye, Microelectronics Reliability, 53, 1901-1906, 2013.

TEMPERATURE DEPENDENCE OF C–V AND G/ω–V CHARACTERISTICS OF Sn/p-TYPE Si SCHOTTKY STRUCTURES

Şükrü Karataş

Department of Physics, Faculty of Sciences and Arts, Kahramanmaraş Sütçü İmam University, 46100-Kahramanmaraş, Turkey

E-mail: skaratas@ksu.edu.tr

Abstract

In this study, the forward and reverse-bias current–voltage (*I–V*) and capacitance–voltage (*C–V*) characteristics of Sn/p-Si Schottky structures were measured for two different temperature (280 and 310 K). The main parameters such as ideality factors (*n*), series resistances (R_S) and barrier heights (Φ_b) obtained from Cheung's and Norde's functions. Also, the temperature dependence of energy distribution of interface state density (N_{SS}) profiles has been determined from *I–V* measurements by taking into account the bias dependence of the effective barrier height and ideality factor. The ideality factors (*n*), series resistances (R_S) and interface state densities (N_{SS}) decreased with increasing temperature for Sn/*p*-Si Schottky structures. The higher values of n and R_S were attributed to the presence of a native insulator on Si surface and to high density of interface states localized at semiconductor–native oxide layer (Si/SiO_2) interface.

1. INTRODUCTION

Silicon (Si) is a chemical element with symbol Si and atomic number 14. Si as a semiconductor material is important for a variety of reasons. It is extensively used in the fabrication of electronic devices such as diodes, integrated circuits, and transistors [1-3]. Furthermore, silicon solar cells are important in the space program for the conversion of photon radiation to electrical power [2, 3, and 4]. Thus, due to the technological importance of Sn/p-type Si Schottky structures (SSs) which are of the most simple of the metal-semiconductor (MS) contact devices, a full understanding of the nature of their electrical characteristics is of greater interest [1–5].

In this study, the forward and reverse-bias current–voltage (*I–V*) and capacitance–voltage (*C–V*) characteristics of Sn/p-type Si Schottky structures were measured for two different temperature. The experimental results show that the main parameters, such as ideality factors (*n*), series resistances (R_S), saturation currents (I_0) and barrier heights (Φ_b) were found to be strongly depending on the temperature.

2. MATERIAL AND METHODS

The samples were prepared using cleaned and polished p-type Si wafers with (100) orientation and 6.24 Ω-cm resistivity. The wafer was chemically cleaned using the RCA cleaning procedure [3]. The detail of experimental section can be seen elsewhere [3]. The *I-V* characteristics of the Sn/p-Si Schottky structures were measured for two different temperature using a temperature controlled janes vpf-475 cryostat, and a Keithly 220 programmable constant current source and a Keithly 199 dmm/scanner under dark conditions. The capacitance-voltage (*C–V*) and conductance-voltage (*G/ω–V*) measurements were performed in by using a HP 4192A LF impedance analyzer (in the range of 5 Hz-13 MHz) and the test signal of 40 mVrms. The Schottky contacts were formed by evaporation of Sn dots with diameter of about 1.5 mm (diode area =$1.76\text{x}10^{-2}$ cm^2).

3. RESULTS AND DISCUSSION

The current-voltage plots of Sn/*p*-type-Si Schottky structures obtained from different temperatures are showed in Fig. 1. The experimental forward bias I–V characteristics of Sn/*p*-type-Si Schottky structures can be analyzed by thermionic emission (TE) theory [2-5]:

$$I = I_o \exp\left(\frac{qV}{nkT}\right)\left[1-\exp\left(-\frac{qV}{kT}\right)\right] \quad (1)$$

where *n* is the ideality factor, *q* is the elementary charge, *k* is the Boltzmann constant, T is the absolute temperature and *V* is the applied voltage. Furthermore, where the saturation current I_o in Eq. (1) is given by

$$I_o = AA^* T^2 \exp\left(-\frac{q\Phi_b}{kT}\right) \quad (2)$$

where Φ_b is the Schottky barrier height (SBH) at zero bias, *A** is the effective Richardson constant for *p*-type Si (A*=32 $Acm^{-2}K^{-2}$), and A is the effective diode area (=1.76x10^{-2} cm^2). The values of the ideality factor (n) and the barrier height (Φb) were found to be 1.242; 0.783 eV (at 280 K), and 1.210; 0.813 eV (at 310 K), by using Eqs (1) and (2), respectively. The high values of n can be attributed to effects of the bias voltage drop across the interfacial native oxide layer and series resistance. Basically, the value of ideal factor should be n =1 for an ideal contact.

The capacitance (*C*-*V*) and conductance-voltage (*G*/*ω*-*V*) measurements are one of another most important to determine of the fundamental properties of the metal-semiconductor structures (*MSS*). Figs. 2 and 3 show the measured capacitance and conductance as function of the voltage for 280 K and 310 K temperatures. As can be seen from Fig.2 and Fig. 3, the capacitance (C_m) and conductance (G/ω) plots are dependent on both the bias voltage and temperature.

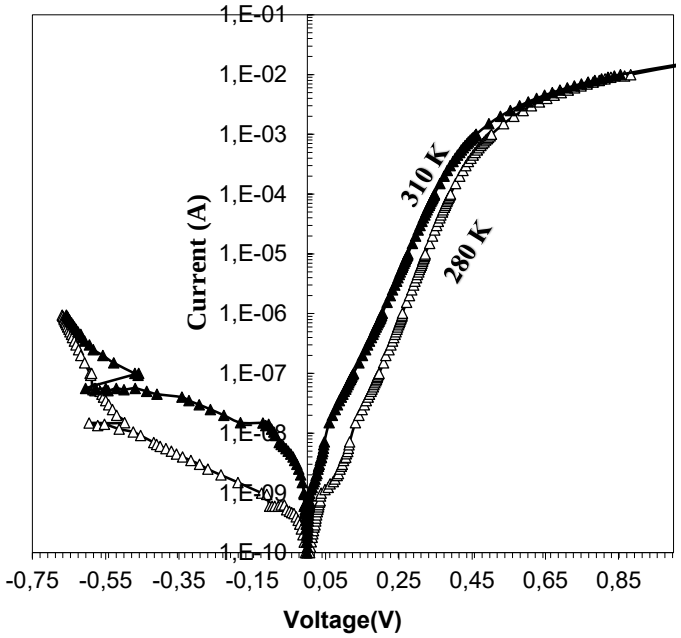

Figure 1. The I-V curves of the Sn/p type Si Schottky structure

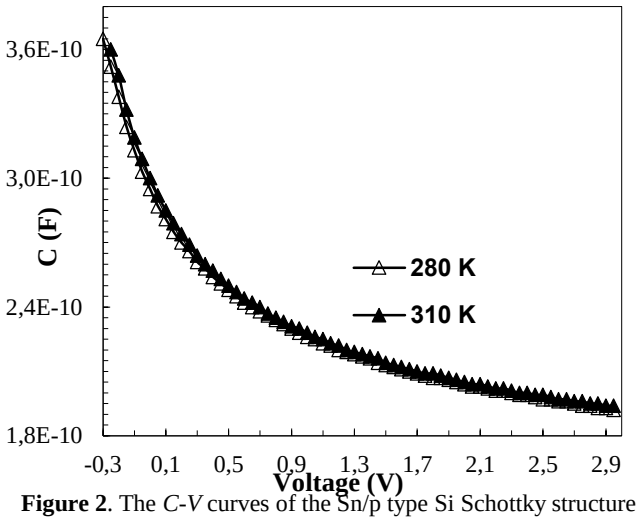

Figure 2. The *C-V* curves of the Sn/p type Si Schottky structure

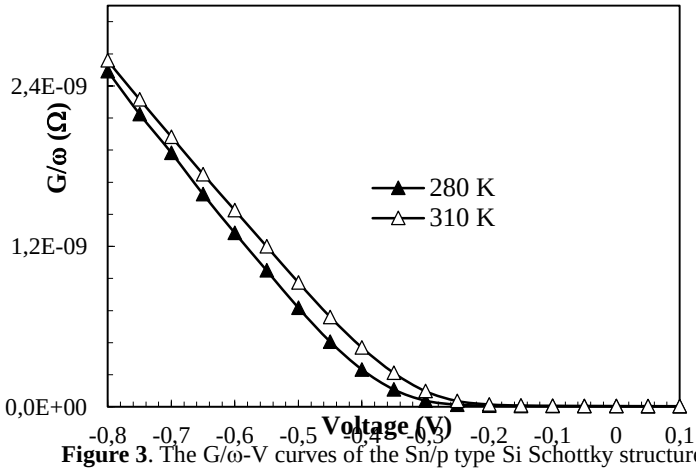

Figure 3. The G/ω-V curves of the Sn/p type Si Schottky structure

4. CONCLUSION

In this study, the forward and reverse-bias current–voltage (*I–V*) and capacitance–voltage (*C–V*) characteristics of Sn/p-Si Schottky structures were measured for two different temperature (280 and 310 K). The ideality factors (*n*), series resistances (R_S) and interface state densities (N_{SS}) decreased with increasing temperature for Sn/*p*-Si Schottky structures. The higher values of n and R_S were attributed to the presence of a native insulator on Si surface and to high density of interface states localized at semiconductor–native oxide layer interface.

REFERENCES

[1] Schultz, M.L., Silicon: Semiconductor Properties, Infrared Physics, 4, 93-112, 1964.

[2] Brillson, L.J., The structure and properties of metal-semiconductor interfaces, Surface Science Reports, 2, 123-326, 1982.

[3] Karataş¸ Ş., Altındal¸Ş., Türüt, A. Özmen,A., Temperature dependence of characteristic parameters of the H-terminated Sn/p-Si (1 0 0) Schottky contacts, Applied Surface Science, 217, 250-260, 2003.

[4] Sze,S.M., Physics of Semiconductor Devices, 2nd ed., Wiley, New York, 1981, p. 850.

[5] Rhoderick, E.H., Williams, R.H., Metal–Semiconductor Contacts, 2nd ed., Clarendon Press, Oxford, 1988.

ELECTRICAL AND OPTICAL PROPERTIES OF PHOTODIODE STRUCTURES FORMED BY SURFACE POLYMERIZATION OF P(EGDMA-VPCA)/SWCNT FILMS ON n-GaAs

B. Kirezli[1], M. Ahmetoglu (Afrailov)[1*], A. Kara[2*]

[1]*Department of Physics, Uludağ University, 16059, Görükle, Bursa, Turkey*
[2] *Department of Chemistry, Uludağ University, 16059, Görükle, Bursa, Turkey*

E-mail: burcukirezli@gmail.com

*Corresponding author's e-mail address: afrailov@uludag.edu.tr; akara@uludag.edu.tr

Abstract

Poly (ethylene glycol dimethacrylate-1-vinyl-1H-pyrrole-2-carboxylic acid) /carbon nanotube, single-walled)/n-GaAs [P(EGDMA-VPCA)/SWCNT]/n-GaAs photodiode structures was fabricated by using surface polymerization method. Electrical and optical properties were carried out at several temperatures. Dark and light current characteristics were investigated. Spectral photoresponse measurements of the structure are carried out at room temperature. The maximum open circuit voltage V_{OC} and short-circuit current I_{SC} values for the diode under 20 mW/cm^2 were found to be 0,52 V and 54,63 μA, respectively. Those were shown that the fabricated structure exhibited rectification behavior that makes it a good candidate for optoelectronic device applications.

1. Introduction

The Schottky barrier diodes are widely used in extremely important applications in electronic industry, such as microwave mixer, high-current power supplies, varistor, varactor, solar cell, photodetector, metal-based transistor, MESFET, etc. [1, 2]. Also, the Schottky diodes are often used for complicated applications in telecommunication systems, radioastronomy, radar technology, and plasma diagnostics [3].

In recent years, electrical properties of the polymer-carbon nanotube, the homogeneous dispersion of the carbon nanotubes in the polymer matrix, Schottky diodes the are intensively investigated due to their valuable properties and perspectives of the application for the research purposes [4, 5, 6].
In the present paper, [P(EGDMA-VPCA)/SWCNT]/n-GaAs structure has been fabricated using surface polymerization [7], and the electrical properties of the device have been reported. Current-voltage (I-V) characteristics were analyzed at a temperature range between 230 -330 K, and several parameters are investigated depending on temperature. Dark and light current characteristics were investigated. Spectral photoresponse measurements of the structure are carried out at room temperature.

The energy gap values of the GaAs semiconductor layer were obtained from both spectral distributions of sensitivity and the dependence of the root of photocurrent on photon energy.

2. Experimental Procedure

2.1 Materials

Ethylene glycol dimethacrylate (EGDMA) was obtained from Merck (Darmstadt, Germany), purified by passing through active alumina and stored at 4 ^{o}C until use. 1-vinyl-1H-pyrrole-2-carboxylic acid (VPCA) was obtained Aldrich (Steinheim, Germany). 2,2-Azobisisobutyronitrile (AIBN) was obtained from Fluka A.G. (Buchs, Switzerland). All other chemicals were of reagent grade and were purchased from Merck AG (Darmstadt, Germany). Single-Walled Carbon Nanotubes [SWCNT] was obtained from TUBALL (Luxembourg).

2.2 *Surface polymerization of poly (ethylene glycol dimethacrylate-1-vinyl-1H-pyrrole-2-carboxylic acid) [P(EGDMA-VPCA)/SWCNT] films on n-GaAs*

The feed composition menu for the preparation of the [P(EGDMA-VPCA)/SWCNT] films were showed in Table 1.

About 3.5 mL of each solution consisting of toluene, EGDMA, VPCA, AIBN, and SWCNT were used to prepare the Poly(ethylene glycol dimethacrylate-1-vinyl-1H-pyrrole-2-carboxylic acid) [P(EGDMA-VPCA)/SWCNT] films. The mixture was degassed 40 min by nitrogen purging before the addition of the initiator, AIBN. Then the polymerization was standing 2 h at 25 ^{o}C under stirring and nitrogen atmosphere. At room temperature, after 2 h the solution was transferred to a known area (p-type Petri dishes), and the polymerization was standing for 15 h at 70 ^{o}C in an oven.

Table 1. Feed composition used for the polymerization.

EGDMA	VPCA	AIBN	Toluene	SWCNT
1.0 mL	3.0 ml	0.050 g	3.5mL	0.010 g

N-Type GaAs wafer used for the fabrication of the [P(EGDMA-VPCA)/SWCNT]/n-GaAs structure has (100) orientation, 400 μm thickness and 508 mm diameter. Before making contacts, the wafer was chemically cleaned using RCA cleaning procedure (i.e., 10 min boiling in H_2 SO_4 +H_2 O_2 followed by a 10 min HCl + H_2O_2 + 6H_2O at 60°C). It was immersed in diluted 20% HF for 60 s. The wafer was rinsed in deionized water of resistivity 18 MΩ cm with ultrasonic cleaning in each step. After that, the sample was dried in the high-purity nitrogen stream and inserted into the deposition chamber. Au (88%) and Ge (12%) were used for ohmic contact [1, 8]. The ohmic contact with a thickness of≈1875 Å was made by evaporating 99.995% purity Au metal and germanium on the back of the surface wafer in a thermal evaporator unit at 10^{-6} Torr. Then it was annealed at 450°C for 5 min in flowing N_2 in a quartz tube furnace. The top ohmic contact on the P(EGDMA-VPCA)/SWCNT was formed by silver contact paste.

The current-voltage (I–V) measurements were performed by the use of KEITHLEY 6487 picoammetre/voltage source using a temperature controlled Janis CCS-150 cryostat, which enables us to make measurements in the temperature range of 77K-380K.

Photoresponse spectra of the [P(EGDMA-VPCA)/SWCNT]/n-GaAs structure were measured in the range of 860-1160 nm with a setup of Oriel Apex2 100 W quartz tungsten halogen lamb, Cornerstone 260

monochromator and SR830 DSP Lock-In-Amplifier at two several temperatures. The light-current-voltage measurements were performed by using of He-Ne Laser with 633 nm. The Intensity of incident light was measured using THORLABS P100D – Compact Power and Energy Meter Console with S401 Thermal power sensor head. The results of the measurements were fed via an IEEE-488 interface into a computer for storage and processing.

3. Results and discussion

3.1 *Surface Morphology of SWCNTs and SWCNTs embedded in P(EGDMA-VPCA).*

The surface morphology of the SWCNT was observed by scanning electron microscopy (SEM) as shown in Fig 1. Fig 1a shows a SEM image of the SWCNT prepared after the polymerization. From Fig 1b, it can be seen that the SWCNT were fully covered by the polymer.

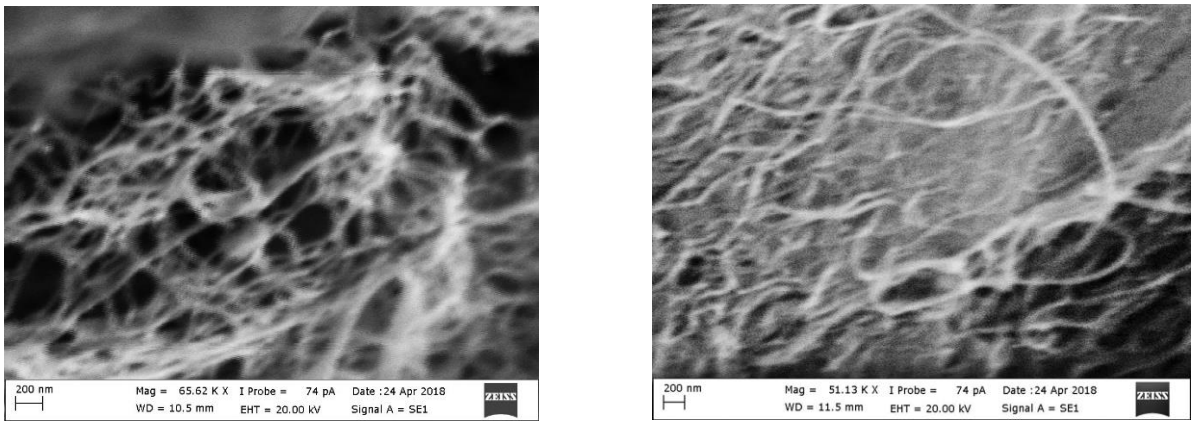

(a) **(b)**

Fig 1. *SEM images of (a) SWCNTs and (b) SWCNTs embedded in P(EGDMA-VPCA).*

3.2 *Electrical Properties*

According to the thermionic emission theory, the current-voltage (I-V) characteristics of a Schottky diode are given as follows [3],

$$I = I_0 \exp\left(\frac{qV}{nkT}\right)\left[1 - exp\left(-\frac{qV}{kT}\right)\right] \quad (1)$$

Where I is the current, n is the ideality factor, q is the electron charge, V is the voltage, k is the Boltzmann constant, T is the temperature in Kelvin, and I_0 is the saturation current.

$$I_0 = AA^*T^2 exp\left(-\frac{q\emptyset_b}{kT}\right) \quad (2)$$

Here, A is the diode area, A^* Richardson constant and the value is 1,1x10^5 A.m^{-2}K^{-2} [12], m* effective mass, h Planck constant, ϕ_b barrier height. From equations (1) and (2) we can calculate the ideality factor and (ϕ_b) barrier height (n) as follows.

$$n = \frac{q}{kT}\left(\frac{dV}{dIn(I)}\right) \quad (3)$$

$$\emptyset_b = \frac{kT}{q} In\left(\frac{AA^*T^2}{I_0}\right) \quad (4)$$

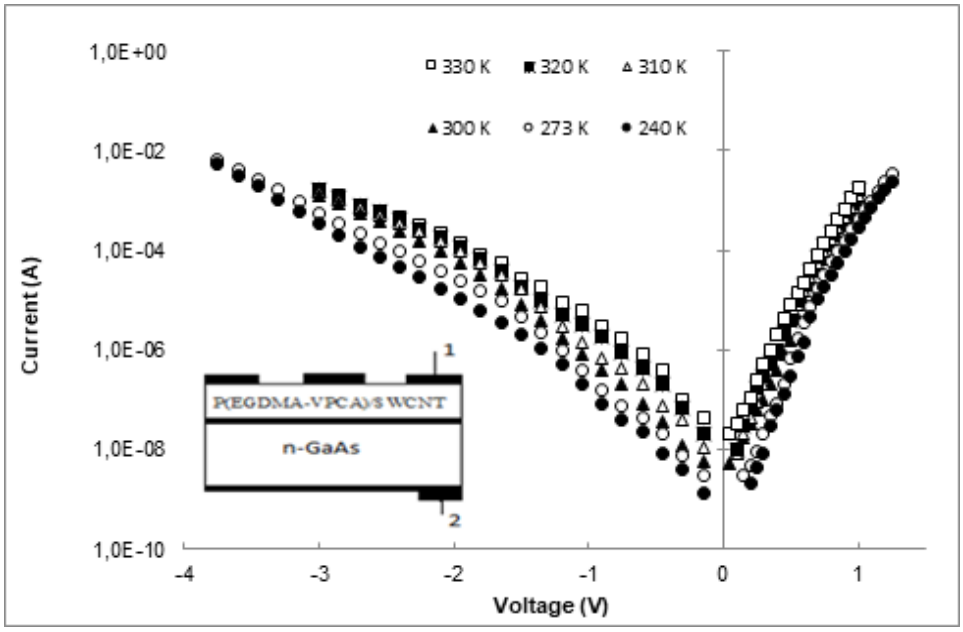

Fig 2. *The forward and backward I-V characteristics of the [P(EGDMA-VPCA)/SWCNT]/n-GaAs structure at different temperatures. In the inset showing the cross-section of the diode structure: 1,2 — ohmic contacts.*

In Fig 2, the [P(EGDMA-VPCA)/SWCNT]/n-GaAs structure shows forward and reverse current-voltage measurements in the range of 240-330 K. The ideality factor and barrier height values were obtained from the intersection and slope of the linear section of line V versus In (I) at each temperature. At room temperature and barrier height ϕ_b = 0,9 eV and ideal factor n = 1,64.

As shown in Fig 3, the values obtained for and ϕ_b for the structure are the functions of the warmth. As the temperature increases, the barrier height rises to 0,77 degrees 0,99. The ideality factor goes down to 2,01 and 1,36 in proportion to the temperature. The large ideality factor values may be attributed to the presence of a native oxide layer, inhomogeneities of [P(EGDMA-VPCA)/SWCNT]/n-GaAs film thickness and

series resistance [3,8,9].

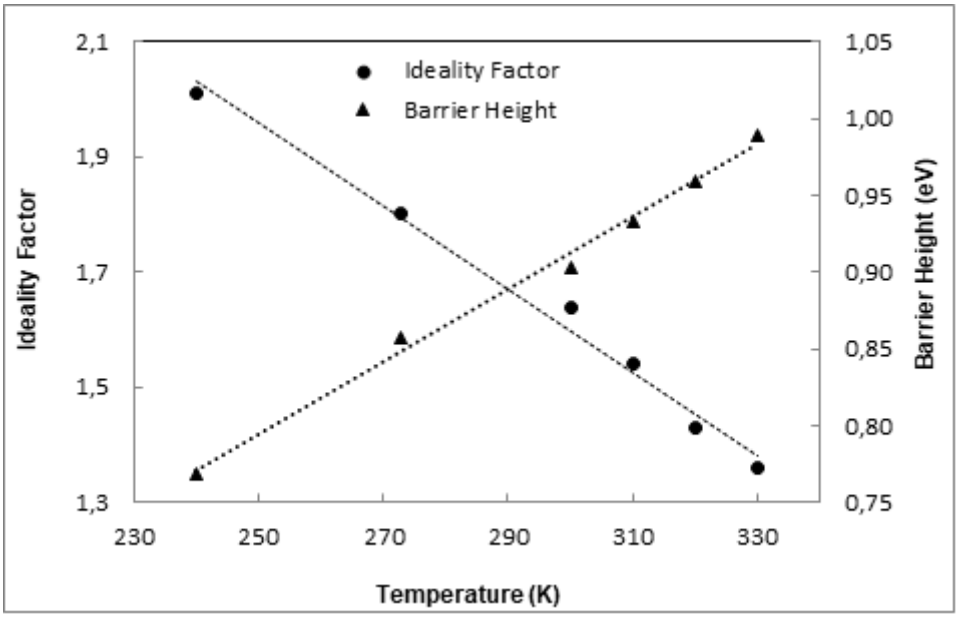

Fig 3. *Temperature-dependent barrier height and factor for the [P(EGDMA-VPCA)/SWCNT]/n-GaAs structure.*

The Norde method is used to determine the value of series resistance. Norde method;

$$F(V) = \frac{V}{\gamma} - \left(\frac{kT}{q}\right) \ln\left(\frac{I}{AA^{*}T^{2}}\right) \qquad (5)$$

γ is a constant parameter. When the minimum value of the V graph against $F(V)$ is determined, the value of the barrier height is obtained from the equation.

$$\emptyset_b = F(V_0) + \frac{V_0}{\gamma} - \frac{kT}{q} \qquad (6)$$

$F(V_0)$ is the minimum point of $F(V)$ and is the voltage corresponding to V_0.

Graph 4 is calculated as follows: V_0=0,45 V, $F(V_0)$=0,56 V and ϕ_b=0,91 eV

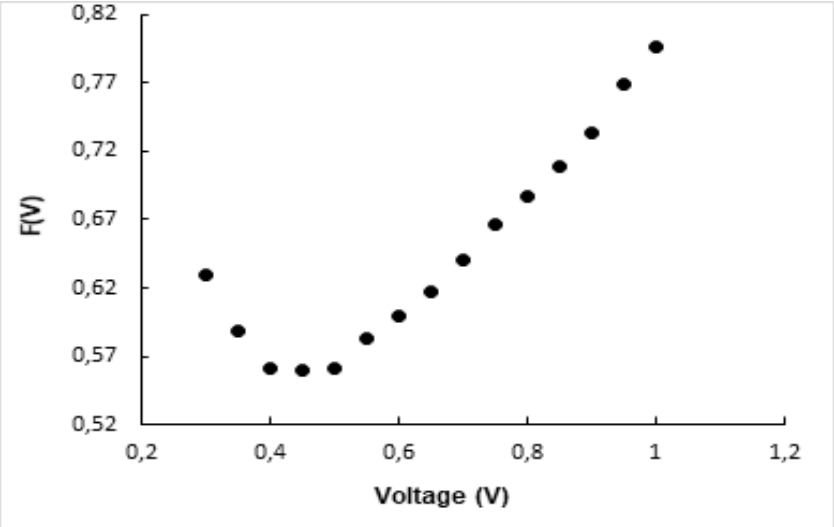

Fig 4. *Experimental determination of [P(EGDMA-VPCA)/SWCNT]/n-GaAs diode F (V) -V*

One of the parameters enabling the formation of the [P(EGDMA-VPCA)/SWCNT]/n-GaAs structure is the interface state density. If the density of the interface state density of the sample varies depending on the ideality factor, the density of the interface state can be expressed as [9]

$$N_{SS}(V) = \frac{1}{q}\left\{\frac{\varepsilon_i}{\delta}[n(V) - 1] - \frac{\varepsilon_S}{W_D}\right\} \quad (7)$$

Where ε_i and ε_s are the dielectric constant of the insulating layer and the semiconductor, respectively. ε_i = 3 and ε_s = 12,9 for n-type GaAs. ε_0 = 8,85 x 10^{-2} pF/m. δ is the thickness of the insulating layer and is calculated as δ = 11 Aº at room temperature measurements. W_D is the thickness of the consumption layer.

$$W_D = \sqrt{\frac{2\varepsilon_S\varepsilon_0 V_d}{qN_d}} \quad (8)$$

Using the equality, the tension-dependent expression of the ideality factor,

$$n(V) = \frac{q}{kT}\frac{V}{In\left(I/I_0\right)} \quad (9)$$

V is the applied voltage. The voltage dependence [P(EGDMA-VPCA)/SWCNT]/n-GaAs structures of the *Nss* and *n(V)* values obtained from the correct prestress were applied with negligible series resistance at 300 K temperature.

The ideal factor should also be dependent on the interface parameters, since the larger the ideality factor is the result of the insulating interface layer [13].

The energy of the interface states of a metal n-type semiconductor depends on the base of the conduction band of *Ess*,

$$E_C - E_{SS} = q(\emptyset_e - V) \tag{10}$$

ϕ_e is the effective barrier height. Due to the presence of an interfacial layer and the interface states, it was assumed that the effective barrier height depends on the voltage. Accordingly, the effective obstacle height,

$$\emptyset_e = \emptyset_b + \left(1 - \frac{1}{n(V)}\right)V \tag{11}$$

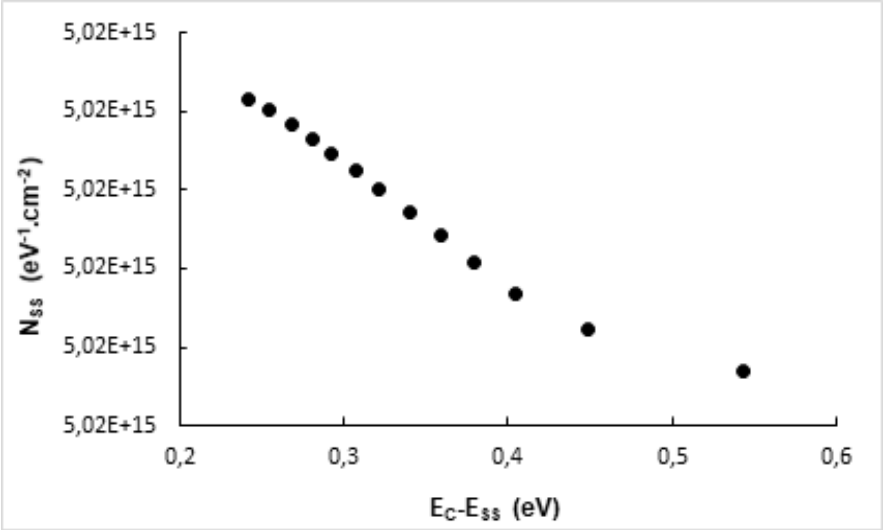

Fig 5. *The curve of the interface state intensity distribution of [P(EGDMA-VPCA)/SWCNT]/n-GaAs Schottky diode.*

The energy distribution of the interface states is determined from experimental data of this region of the forward bias *I–V,* and this is shown in Fig 5. The energy state densities decrease from the conductivity band towards the middle of the forbidden band gap. That confirms that the energy state densities vary depending on the applied supply voltage and that each voltage corresponds to a different state in the band gap.

The interface states and interfacial layer between the polymeric organic compound/semiconductor structures play an important role in the determination of the characteristic parameters of the devices. The

presence of the interface layer, interface states, and fixed surface charge causes the reverse bias and forward bias characteristics of Schottky devices not to obey the ideal Schottky diode characteristics. Therefore, it can be said that the performance and reliability of Schottky devices depend on the interface layer and a fixed surface charge. Briefly, polymeric organic/inorganic semiconductor diodes may be useful to increase the quality of devices fabricated by using the semiconductor in establishing processes for minimizing surface states [14].

3.3 *Optical Properties*

The spectral distribution of sensitivity for a [P(EGDMA-VPCA)/SWCNT]/n-GaAs Schottky diode at two several temperatures is shown in Fig 6. From the shift of the long-wavelength edge of the photoresponse, we estimated the temperature coefficient of the gap with of GaAs layer. The temperature coefficient of the energy gap of the narrow-gap GaAs layer was found to be $\Delta E_g/\Delta T$ = 4,38x10^{-4} eV/K. This value very close to the temperature coefficient obtained from the temperature dependence of the energy gap of GaAs [16]:

$$E_g = 1{,}519 - (5{,}405 \times 10^{-4})\frac{T^2}{T+204} \qquad (12)$$

The value obtained at two several temperatures is $\Delta E_g/\Delta T$ = 4,24x10^{-4} eV/K.

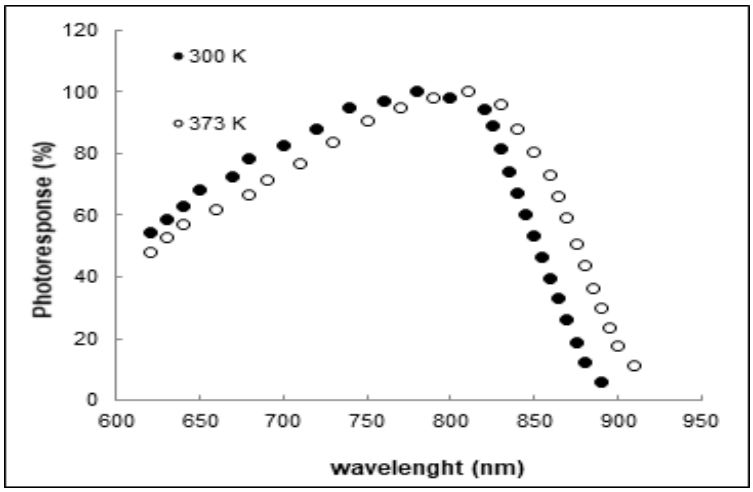

Fig 6. *The spectral distribution of sensitivity of the [P(EGDMA-VPCA)/SWCNT]/n-GaAs that Schottky diode at two different temperatures.*

The energy gap of the narrow-gap GaAs layers determined from the wavelength corresponding to a twofold decrease in sensitivity is 1,42 ± 0,02 eV at T = 300 K. This value is very close to the energy gap values of

the GaAs at room temperature. The short wavelength cut-off of the photosensitivity is due to strong absorption of the short-wavelength radiation in the wide-gap [P(EGDMA-VPCA)/SWCNT] window layer. Also, the type of band gap of GaAs can be determined from the experimental results of Fig 7 near the cutoff. The amount of the photocurrent produced during absorption of a photon depends on the excess energy produced from the difference of the photon energy *hv* and the bandgap energy, E_g. Near the bandgap edge of the semiconductor, the proportionality of the photocurrent about the excess energy determines the type of the bandgap as shown in the following equations:

Direct Bandgap:

$$I \ \alpha \ (hv - E_g)^2 \tag{13}$$

$$I^2 \ \alpha \ (hv - E_g) \tag{14}$$

Plotting the values of the photocurrent near the cut-off wavelength of 870 nm as a function of the photon energy about Eq (14) it is possible to determine the value of the GaAs band gap. The intercept of the line at x-axis gives the band gap of GaAs, found to be about 1,42 eV (300 K) and 1,38 eV (373 K).

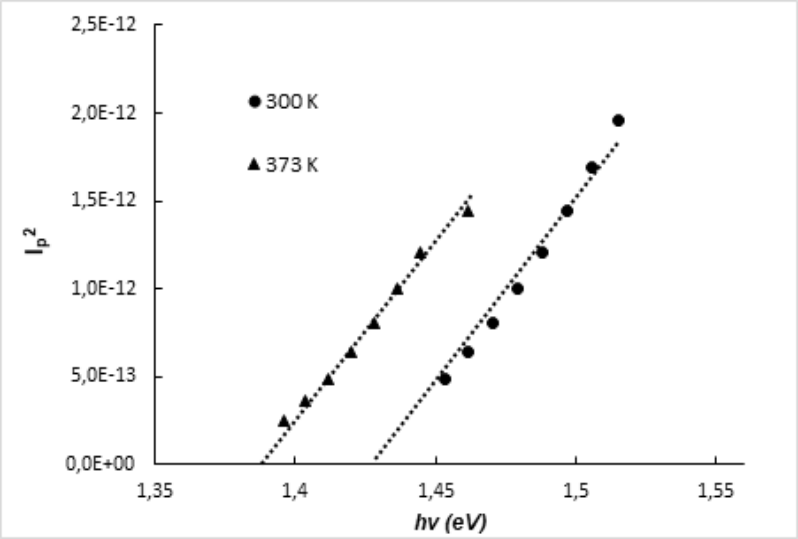

Fig 7. *The plot of the root of photocurrent versus photon energy near the band edge*

Fig 8 shows the light current-voltage characteristics of the investigated structures under different illumination intensities by photons with a wavelength of 633nm. Illuminating the Schottky diode with optical radiation, shifts the *I–V* curve by the amount of photocurrent Ip. Thus:

$$I = I_0\left(\frac{eV}{nkT}\right) - I_P \tag{15}$$

I_P is the photocurrent.

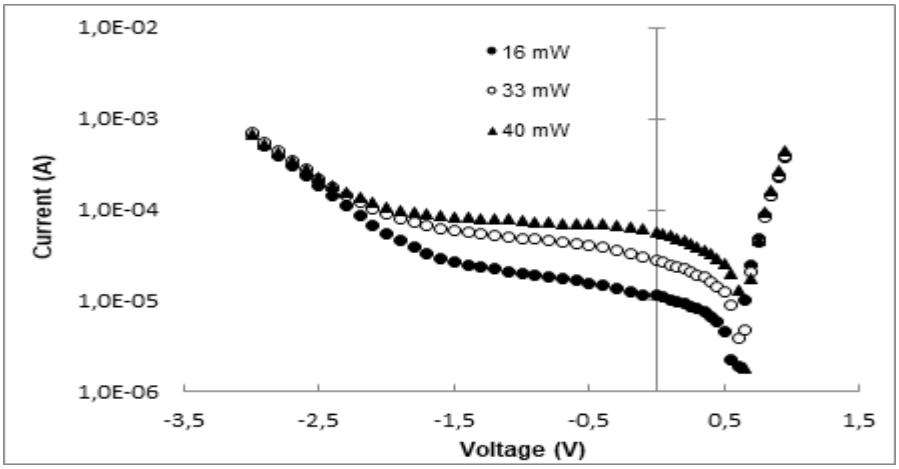

Fig 8. *Room temperature current-voltage characteristics under various illumination intensities by 633 nm wavelength photons (He-Ne Laser).*

As seen in Fig 8, the light on the reverse I–V characteristic under various illumination intensities were translated upward moved in the I direction along the current axis, giving an open circuit voltage (*Voc*) along with a short-circuit current (Isc). The maximum open circuit voltage Voc value for the diode under 20 mW/cm^2 illumination was found to be 0,52 V [15].

In the photovoltaic regime, energy characteristics depend on either of short-circuit current or open circuit voltage from the intensity of incident light. Fig 8 shows the variation of the short-circuit current with light intensity for the Schottky diode. As seen in Fig 9, the law of variation in these dependences linear in the range of incident light intensity.

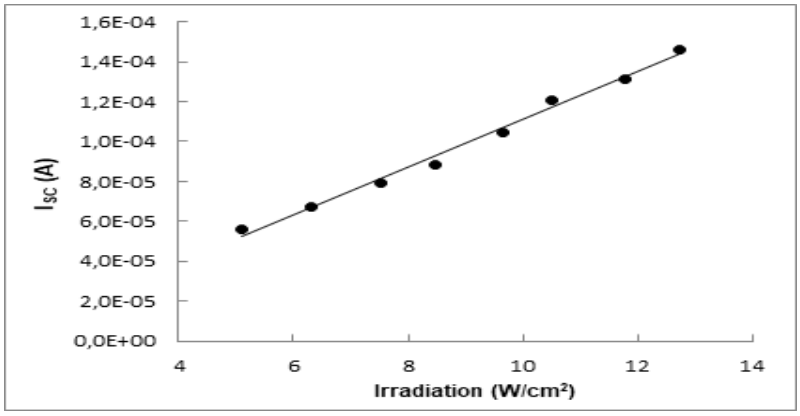

Fig 9. *Variation of the short-circuit current with a light intensity*

4. Conclusion

P(EGDMA-VPCA)/SWCNT/n-GaAs Schottky diode structures were fabricated using a surface polymerization method, and the surface morphology was observed by scanning electron microscopy (SEM). Before making contacts, the wafer was chemically cleaned using RCA cleaning procedure. Electrical and optical properties were achieved at various temperatures. Barrier height of the structure was obtained from I-V measurements. The barrier height was obtained as 1,64 *eV* and the ideality factor as 0,9 respectively.

Light volt-current characteristics under various illumination light intensities were investigated. Spectral photoresponse measurements of the structure were carried out at two several temperatures. The energy gap values of the GaAs semiconductor layer were obtained from both spectral distributions of sensitivity and the dependence of the root of photocurrent on photon energy. It is shown that the fabricated structure by surface polymerization technique exhibits rectification behavior that makes it a good candidate for electronic device applications.

Acknowledgment

Uludag University supported this work; Scientific Research Project Unit grant No. OUAP(F)-2016/11. The authors would like to thank for this support.

References

[1] K.Ng. Kwok, Complete Guide To Semiconductor Devices, McGraw-Hill, New York 1995.

[2] J. Singh, Semiconductor Optoelectronics Physics and Technology, McGraw-Hill, New York 1995.

[3] M.E. Aydın, M. Soylu, F. Yakuphanoglu, W.A. Farooq, Microelectron. Eng. 88, 867 (2011).

[4] Ahmetoglu, M.; Kara, A.; Kucur B., Poly(ethylene glycol dimethacrylate-co-1-vinyl-1,2,4-triazole/ carbon nanotube, single-walled)/n-GaAs Diode Formed by Surface Polymerization. Conference: 2nd International Conference on Computational and Experimental Science and Engineering (ICCESEN)Location: Kemer, Turkey Date: OCT 14-19, 2015 ACTA PHYSICA POLONICA A Volume: 130 Issue: 1 Page: 206-208 Published: JUL 2016

[5] Tekin, Nalan; Kara, A; Beyaz, Saadet Kayiran; et al., Preparation, Solubility, and Electrical Properties of Multiwalled Carbon Nanotubes/Poly(1-vinyl-1,2,4-triazole) Composites via in situ Functionalization. POLYMER-PLASTICS TECHNOLOGY ENGINEERING Volume: 53 Issue: 8 Pages: 840-850

[6] Ahmetoglu (Afrailov), Muhitdin; Kara, Ali; Tekin, Nalan; et al., Electrical properties of Poly(ethylene glycol dimethacrylate-n-vinyl imidazole)/Single Walled Carbon Nanotubes/n-Si Schottky diodes formed by surface polymerization of Single-Walled Carbon Nanotubes. THIN SOLID FILMS Volume: 520 Issue: 6 Pages: 2106-2109 Published: JAN 1 2012

[7] M. Ahmetoglu (Afrailov), A. Kara, N. Tekin, S. Beyaz, H. Köçkar, Electrical properties of Poly(ethylene glycol dimethacrylate-n-vinyl imidazole)/Single Walled Carbon Nanotubes/n-Si Schottky diodes formed by surface polymerization of Single-Walled Carbon Nanotubes, Thin Solid Films 520 (2012) 2106-2109. *DOI:10.1016/j.tsf.2011.08.066*

[8] A. Kırsoy, M. Ahmetoglu (Afrailov), A. Asimov, B. Kucur, The electrical properties of Au/P3HT/n-GaAs Schottky barrier diode, Acta Physica Polonica A 128 (2015) 170-173. DOI:10.12693/APhysPolA.128.B-170

[9] E. H. Rhoderick, R. H. Williams, Metal-Semiconductor Contacts, Clarendon Press, Oxford, 1988.

[10] S. M. Sze, Physics of Semiconductor Devices, 2nd ed., Wiley, New York, 1981.

[11] S. Kasap, P. Capper, Handbook of Electronic and Photonic Materials, Springer, 2006.

[12] Ş. Karataş, A. Türüt, The determination of electronic and interface state density distributions of Au/n-type GaAs Schottky barrier diodes, Physica B 381 (2006) 199-203. DOI:10.1016/j.physb.2006.01.412

[13] Singh A., "Characterization of Interface States at Ni/n-CdF2 Schottky Barrier Type Diodes and the Effect of CdF2 Surface Preparation", *Solid State Electronics*, 28 (3): 223-232 (1985).

[14] F. F. So, S. R. Forrest, J. Appl. Phys. 63(2), 442 (1988).

[15] Afrailov M. Ahmetoglu, "Photoelectrical characteristics of GaSb/GaInAsSb/GaAlAsSb heterojunction photodiodes under illumination by photons with wavelength of 0.95–1.0 μm", Thin Solid Films 520 (2012) 5014–5017

[16] M Levinshtein, Michail Shur and S. Rumyantsev, Handbook Series on Semiconductor Parameters, Vol.1. World Scientific, 1996, p. 3.

ELECTRICAL AND OPTICAL PROPERTIES OF PHOTODIODE STRUCTURES FORMED BY SURFACE POLYMERIZATION OF P (EGDMA-VPCA)/SWCNT FILMS ON n-Si

B. Kirezli[1*], I. Gucuyener[3], A. Kara[2*], M. Ahmetoglu (Afrailov)[1]

[1]*Department of Physics, Uludağ University, 16059, Görükle, Bursa, Turkey*
[2] *Department of Chemistry, Uludağ University, 16059, Görükle, Bursa, Turkey*
[3]*Department of Mechatronic Program, Vocational School of Technical Sciences, Uludağ University, 16059, Görükle, Bursa, Turkey*

E-mail: burcukirezli@gmail.com

Abstract

Poly (ethylene glycol dimethacrylate-1-vinyl-1H-pyrole-2-carboxylic acid) /carbon nanotube, single-walled)/n-Si ([P(EGDMA-VPCA)/SWCNT]/n-Si) photodiode structures was fabricated by using surface polymerization method. Electrical and optical properties were carried out at several temperatures. Dark and light current characteristics were investigated. Spectral photo response measurements of the structure were carried out at room temperature. Those were shown that the fabricated structure exhibited rectification behavior that makes it a good candidate for optoelectronic device applications.

1. Introduction

Interfaces between thin metal layers and semiconductors e used in optical detectors, solar cells [1] and chemical sensors [2,3]. The transport properties of such Schottky diodes and the dependence of the transport parameters on preparation are of essential importance for the device performance. Metal-semiconductor interfaces may be characterized by photoelectrical and current-voltage measurements [4,5]. The metallization of semiconductor surfaces is still mostly performed in vacuum by evaporation or sputtering. The process, itself, is of great technological importance for preparing Schottky barriers and ohmic contacts in electronic devices.

Compared with conventional electronic materials, Polymer/Single Wall Carbon Nanotubes with outstanding electrical conductive and optical properties are ideal materials for many applications [6-14]. Due to the electrical conductivity and optical properties between the polymer matrix and SWCNT, Poly(ethylene glycol dimethacrylate-1-vinyl-1H-pyrole-2-carboxylic acid) /carbon nanotube, single-walled)/n-Si ([P(EGDMA-VPCA)/SWCNT]/n-Si) could be chosen for optoelectronic device applications.

In the present paper, ([P(EGDMA-VPCA)/SWCNT]/n-Si) structure has been fabricated using surface polymerization and electrical properties of the device has been reported. Current-voltage *(I–V)* characteristics are analyzed at a temperature range between 300 K and 360 K, and several parameters are investigated depending on temperature. Also, capacitance-voltage *(C–V)* measurement of the structure is carried out at room temperature. It is shown that the fabricated structure by surface polymerization technique exhibits rectification behavior that makes it a good candidate for electronic device applications.

2. Experimental procedure

2.1 *Materials*

Ethylene glycol dimethacrylate (EGDMA) was obtained from Merck (Darmstadt, Germany), purified by passing through active alumina and stored at 4 ºC until use. 1-vinyl-1H-pyrole-2-carboxylic acid (VPCA) was obtained Aldrich (Steinheim, Germany). 2,2-Azobisisobutyronitrile (AIBN) was obtained from Fluka A.G. (Buchs, Switzerland). All other chemicals were of reagent grade and were purchased from Merck AG (Darmstadt, Germany). Single-Walled Carbon Nanotubes [SWCNT] was obtained TUBALL (Luxembourg) nanomodifier of materials.

2.2 *Poly (ethylene glycol dimethacrylate-1-vinyl-1H-pyrole-2-carboxylic acid) [P(EGDMA-VPCA)/SWCNT]/ Single-Walled Carbon Nanotubes/n-Si films*

The feed composition menu for the preparation of the [P(EGDMA-VPCA)/SWCNT] films were showed in Table I. About 3.5 mL of each solution consisting of toluen, EGDMA, VPCA, AIBN, and SWCNT were used to prepare the Poly(ethylene glycol dimethacrylate-1-vinyl-1H-pyrole-2-carboxylic acid) [P(EGDMA-VPCA)/SWCNT] films. The mixture was degassed 40 min by nitrogen purging before the addition of the initiator, AIBN. Then the polymerization was standing 2 h at 25 ºC under stirring and nitrogen atmosphere. At room temperature, after 2 h the solution was transferred to a known area (p-type petri dishes), and the polymerization was standing for 15 h at 70 ºC in an oven.

Table 1. Feed composition used for the polymerization.

EGDMA	VPCA	AIBN	Toluen	SWCNT
1.0 mL	3.0 ml	0.050 g	3.5 mL	0.010 g

One-sided polished n-Si (111) samples, phosphorus-doped, 1– 20 Ω cm plates were used as the substrate. They were cleaned following the cleaning procedure in ref.[13], i.e., degreasing in 2-propanol under reflux for 2 h and then boiling alternatively several times for 15 min in basic and acidic H_2O_2 solutions. Before each experiment, the substrates were etched for 1 min in 20% HF (Merck, VLSI Selectipur) to remove the oxide layer. An ohmic contact was formed by vacuum evaporation of an Au layer on the back of the n-Si after the standard etching procedure. [P(EGDMA-VPCA)/SWCNT] was polymerized on n-Si semiconductor, a surface of 1% Sb-doped Au, made ohmic contact. Top ohmic contacts on the [P(EGDMA-VPCA)/SWCNT] were formed by silver contact paste.

The current-voltage *(I–V)* measurements were performed by the use of KEITHLEY 6487 picoammetre/voltage source and capacitance-voltage *(C–V)* measurements were performed by the use of KEITHLEY 590/1M *C–V* Analyzer using a temperature controlled Janis CCS-150 cryostat, which enables us to make measurements in the temperature range of 77K-380K.

Photoresponse spectra of the [P(EGDMA-VPCA)/SWCNT]/n-Si structure were measured in the range of 860-1160 nm with a setup of Oriel Apex2 100 W quartz tungsten halogen lamb,

Cornerstone 260 monochromator and SR830 DSP Lock-In-Amplifier at two several temperatures. The light current-voltage measurements were performed by using of Diode Laser with 976 nm. The Intensity of incident light was measured using THORLABS P100D – Compact Power and Energy Meter Console with S401 Thermal power sensor head. The results of measurements were fed via an IEEE-488 interface into a computer for storage and processing.

3. Results and discussion

3.1 Surface Morphology of the SWCNTs distribution in the P(EGDMA-VPCA).

The surface morphology of the SWCNTs distribution in the P(EGDMA-VPCA) was observed by scanning electron microscopy (SEM) as shown in Fig 1. Fig 1a shows SEM image at low magnification (2135×), Fig 1b shows SEM image at high magnification (47 050×).

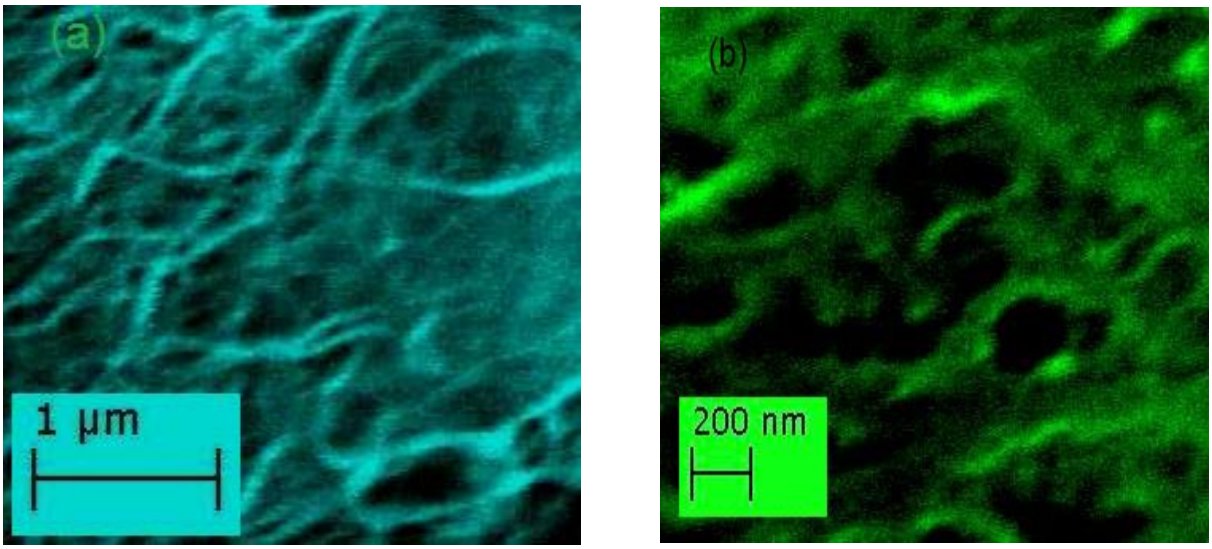

(a) **(b)**

Fig 1*. SWCNTs distribution in the P(EGDMA-VPCA).: (a) SEM image at low magnification (2135×), and (b) SEM image at high magnification (47 050×).*

3.2 *Electrical Properties*

According to the thermionic emission theory, the current-voltage *(I-V)* characteristics of the Schottky diode are given as follows [15]:

$$I = I_0 \exp\left(\frac{qV}{nkT}\right)\left[1 - \exp\left(-\frac{qV}{kT}\right)\right] \quad (1)$$

n is the ideality factor, *I* is the current, *q* is the electron charge, *V* is the voltage, *k* is the Boltzmann constant, *T* is the temperature in Kelvin, and I_0 is the saturation current.

$$I_0 = AA^*T^2 \exp\left(-\frac{q\emptyset_b}{kT}\right) \quad (2)$$

Where *A* is the diode area, A^* Richardson constant and the value is 1,1x10^5 A.m^{-2}K^{-2}, m* effective mass, h Planck constant, ϕ_b Schottky diode barrier height. From equations (1) and (2) we can calculate the idealtite factor and (ϕ_b) barrier height (*n*) as follows.

$$n = \frac{q}{kT}\left(\frac{dV}{dIn(I)}\right) \quad (3)$$

$$\emptyset_b = \frac{kT}{q} In\left(\frac{AA^*T^2}{I_0}\right) \quad (4)$$

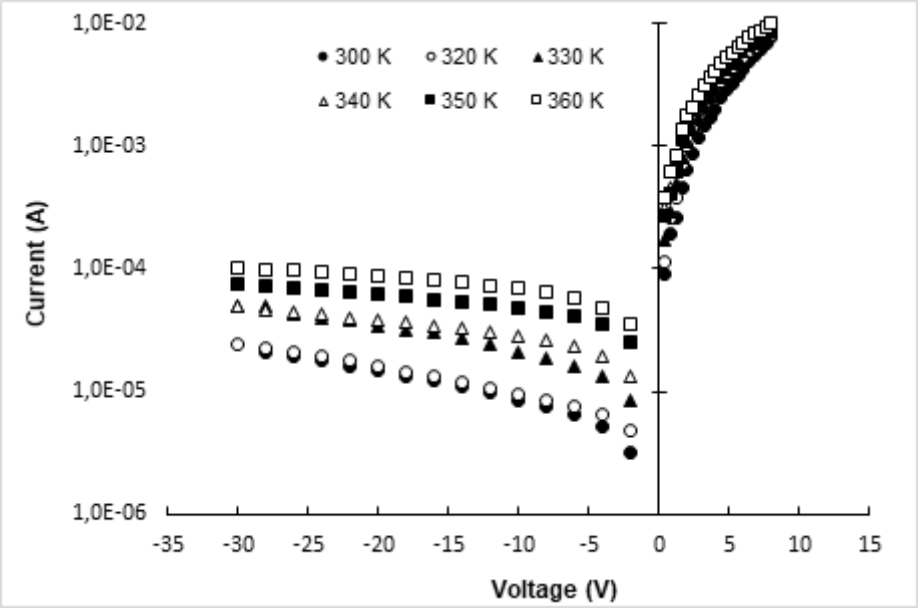

Fig 2. *[P(EGDMA-VPCA) / SWCNT] /n-Si forward and backward I-V properties of the n-Si structure at different temperatures.*

Fig 2 shows the forward and reverse current-voltage measurements of [P(EGDMA-VPCA)/SWCNT] /n-Si structure in the range of 300-360 K. The ideality factor and barrier height values were obtained from the intersection and slope of the linear section of line *V* versus *In(I)* at each temperature. The experimental values of ϕ_{b0} and *n* for the device range from 1,01 eV and 4,94 (at 300 K) to 1,1 eV and 2,81 (at 360 K), respectively. The values of *n* and ϕ_{b0}

obtained depending on the temperature are given in Fig 3. The experimental value of *n* increased with a decrease in temperature, and the experimental value of ϕ_{b0} decreased with a decrease in temperature as can see in Fig 3. Since current transport across the MS interface is a temperature activated process, electrons at low temperatures can surmount the lower barriers, and therefore current transport will be dominated by current flowing through patches of the lower Schottky barrier height (SBH) and a larger ideality factor. As the temperature increases, more and more electrons have sufficient energy to surmount the higher barrier. As a result, the dominant barrier height will increase with the temperature and bias voltage [16].

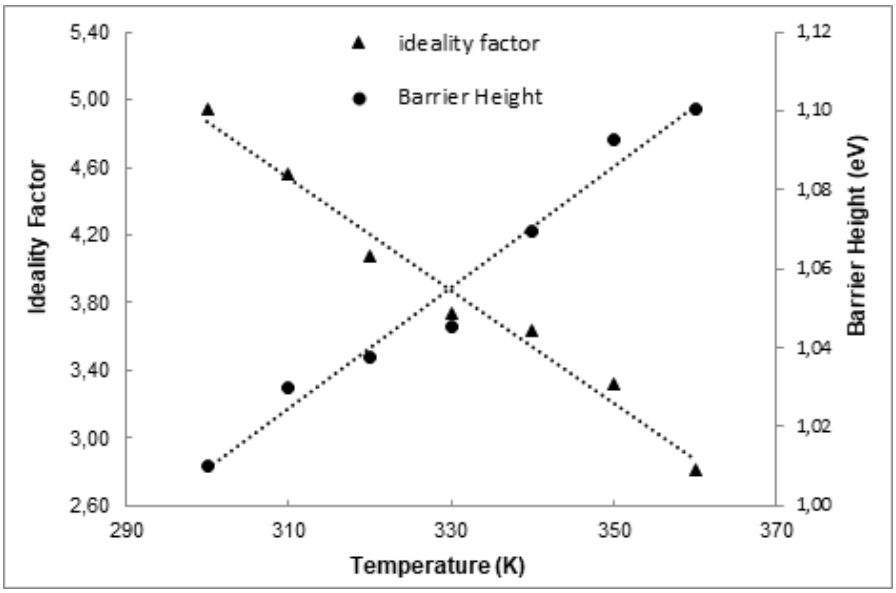

Fig 3. *Temperature dependence of the barrier height and the ideality factor of the [P(EGDMA-VPCA) / SWCNT] /n-Si Schottky diode*

Capacitance-voltage *(C–V)* measurement is one of the fundamental electrical measurement techniques used to investigate the properties of the Schottky barrier structure. Fig. 4 shows $1/C^2$ dependence on *V* taken at temperature T = 300 K and frequency f = 1 MHz. The *C–V* dependence can be interpreted by the law,

$$\frac{1}{C^2} = \frac{2(V_R + V_B)}{q\varepsilon_S N_d A^2} \tag{5}$$

where *A* is the device area, V_R is the reverse bias voltage, V_B is the built-in potential at zero bias and is determined from the extrapolation of the $1/C^2$ plot to the *V*-axis, ε_S is the dielectric constant of the Si and N_d is the doping concentration. The gradient of the C^{-2}–*V* curve leads to a carrier concentration in the Si of $N_d = 3.95 \times 10^{16}$ cm^{-3}.

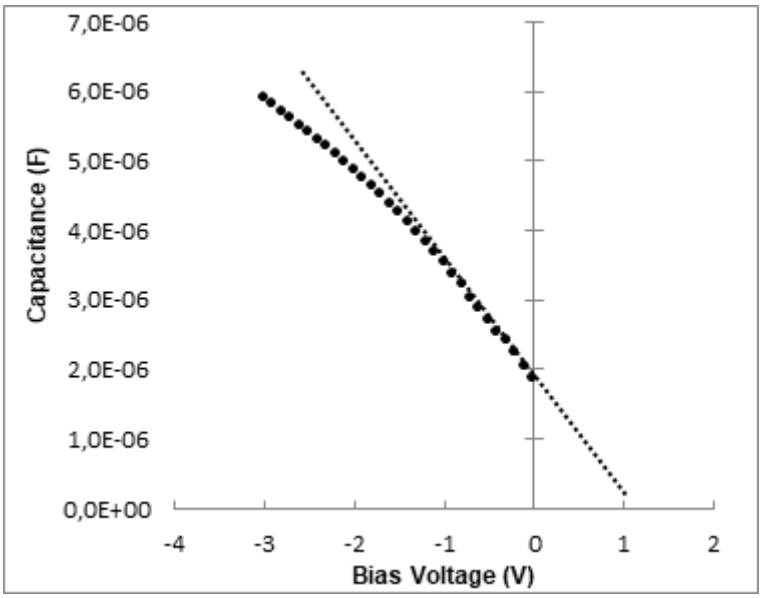

Fig 4. *C–V characteristics of the [P(EGDMA-VPCA) / SWCNT] /n-Si Schottky diode structure at room temperature at f = 1 MHz*

Fig 5 shows a conventional activation energy $ln(J_0/T^2)$ vs. $1/T$ plot. According to Eq. (2), one obtains.

$$\ln\left(\frac{J_0}{T^2}\right) = \ln(AA^*) - \frac{q\emptyset_{b0}}{kT} \tag{6}$$

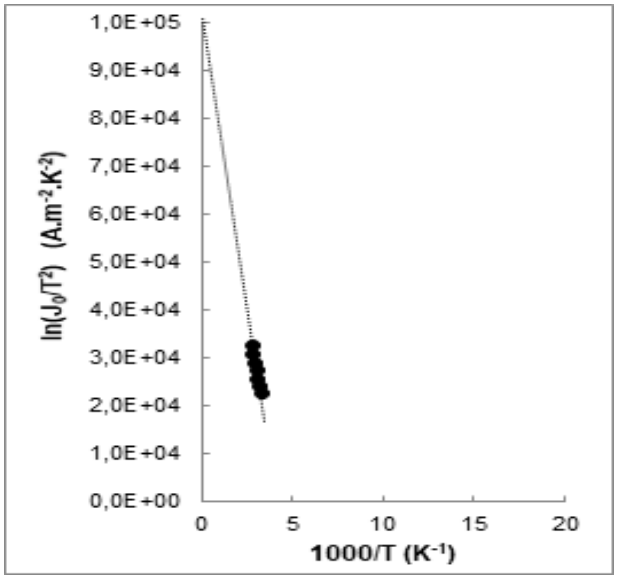

Fig 5. *Richardson plots of $ln(J_0/T^2)$ - 1/T for the [P(EGDMA-VPCA)/SWCNT] /n-Si Schottky diode.*

Bowing of the experimental $ln(J_0/T^2)$ vs. $1/T$ plot in Fig 5 demonstrates that it is impossible to fit the experimental data with ϕ_{b0}. The experimental data are seen to fit asymptotically to a straight line at higher temperatures only. An activation energy value of 1,02 eV from the slope of this straight line was obtained for the device. Bowing of the experimental $ln\ (J_0/T^2)$ vs. $1/T$ curve is caused by the temperature dependence of the barrier height and ideality factor. As will be discussed below, the deviation in the Richardson plots may be due to the spatially inhomogeneous barrier heights and potential fluctuations at the interface that consist of low and high barrier areas [17], that is, the current through the diode will flow preferentially through the lower barriers in the potential distribution [18]. Likewise, a Richardson constant value of $1{,}07x10^5$ $A.K^{-2}m^{-2}$ for the [P(EGDMA-VPCA)/SWCNT] /n-Si SBD was determined from the intercept at the ordinate of the experimental $ln(J_0/T^2)$ vs. $1/T$ plot in Fig 5 the theoretical value of $1{,}1x10^5$ $A.K^{-2}.m^{-2}$ for electrons in n-type Si. As known that, the A^* value obtained from the temperature dependence of the I–V characteristics may be affected by lateral inhomogeneity of the barrier, and the fact that it is different from the theoretical value may be connected to a value of the real effective mass that is different from the calculated one.

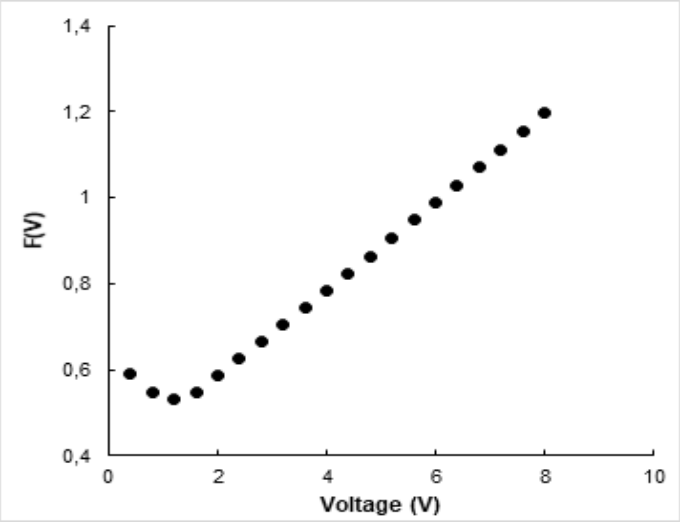

Fig 6. *Experimental determination of [P(EGDMA-VPCA)/SWCNT] /n-Si Schottky diode F (V) -V*

Furthermore, the values of barrier height and series resistance of the device has been evaluated by the analysis of Norde's method [19]. The following function has been defined in the modified Norde's method:

$$F(V) = \frac{V}{\gamma} - \left(\frac{kT}{q}\right) In\left(\frac{I}{AA^{*}T^{2}}\right) \quad (7)$$

γ is a constant parameter. *I* is currently obtained from the *I–V* curve. Once the minimum of the *F* versus *V* plot is determined, the value of barrier height can be obtained from Eq (6),

$$\emptyset_b = F(V_0) + \frac{V_0}{\gamma} - \frac{kT}{q} \quad (8)$$

F(V₀) is the minimum point of *F(V)* and is the voltage corresponding to *V₀*. Fig 6 is calculated as follows: *V₀* =1,1 V, *F(V₀)* = 0,52 V and ϕ_b=1,04 eV.

One of the parameters enabling the formation of the structure is the interface state density. If the density of the interface state density of the sample varies depending on the ideality factor, the density of the interface state can be expressed as:

$$N_{SS}(V) = \frac{1}{q}\left\{\frac{\varepsilon_i}{\delta}[n(V) - 1] - \frac{\varepsilon_S}{W_D}\right\} \quad (9)$$

Where ε_i and ε_s are the dielectric constants of the insulating layer and the [P(EGDMA-VPCA)/SWCNT] /n-Si semiconductor, respectively. ε_i = 5 and ε_S = 12 for *n*-type Si. ε_0 = 8.85 x 10^{-2} pF/m. δ is the thickness of the insulating layer and is calculated as δ=11 A° at room temperature measurements. W_D is the thickness of the consumption layer.

$$W_D = \sqrt{\frac{2\varepsilon_S\varepsilon_0 V_d}{qN_d}} \quad (10)$$

Using the equality, the tension-dependent expression of the ideality factor,

$$n(V) = \frac{q}{kT}\frac{V}{In\left(I/I_0\right)} \quad (11)$$

V is the applied voltage. The strain dependence of the N_{SS} and *n(V)* values obtained from the correct prestress *I-V* data at the 300 K temperature of the [P(EGDMA-VPCA)/SWCNT]/n-Si structure is shown in Fig 6, neglecting the series resistance. The ideal factor should also be dependent on the interface parameters, since the larger the ideality factor is the result of the

insulating interface layer [21].

The energy of the interface states of a metal n-type semiconductor depends on the base of the conduction band of Ess,

$$E_C - E_{SS} = q(\emptyset_e - V) \tag{12}$$

ϕ_e is the effective obstacle height. Due to the presence of an interfacial layer and the interface states, it is assumed that the effective barrier height depends on the voltage. Accordingly, the effective obstacle height,

$$\emptyset_e = \emptyset_b + \left(1 - \frac{1}{n(V)}\right)V \tag{13}$$

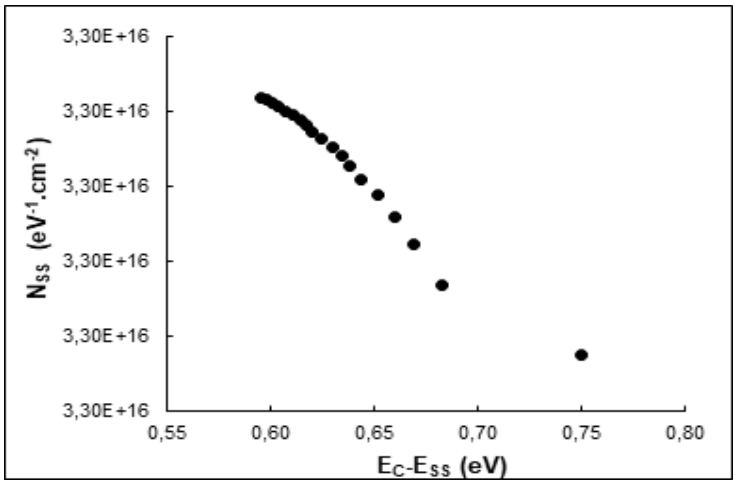

Fig 7. *[P(EGDMA-VPCA)/SWCNT] /n-Si Schottky diode interface state intensity distribution curve.*

As shown in Figure 7, the distribution profile of the interface state density (N_{ss}) was obtained as a function of energy *(E_c-E_{ss})* from the *C-V* measurements at 1 MHz frequency, without considering the presence of series resistance. The energy state densities decrease from the conductivity band towards the middle of the forbidden band gap. This confirms that the energy state densities vary depending on the applied supply voltage and that each voltage corresponds to a different state in the band gap.

3.2 *Optical Properties*

Fig 8 shows the light current-voltage characteristics of the investigated photodiodes under different illumination intensities by photons with a wavelength of 976 nm. Illuminating the Schottky diode with optical radiation, shifts the *I–V* curve by the amount of photocurrent Ip. Thus:

$$I = I_0\left(\frac{eV}{nkT}\right) - I_P \tag{14}$$

I_P is the photocurrent.

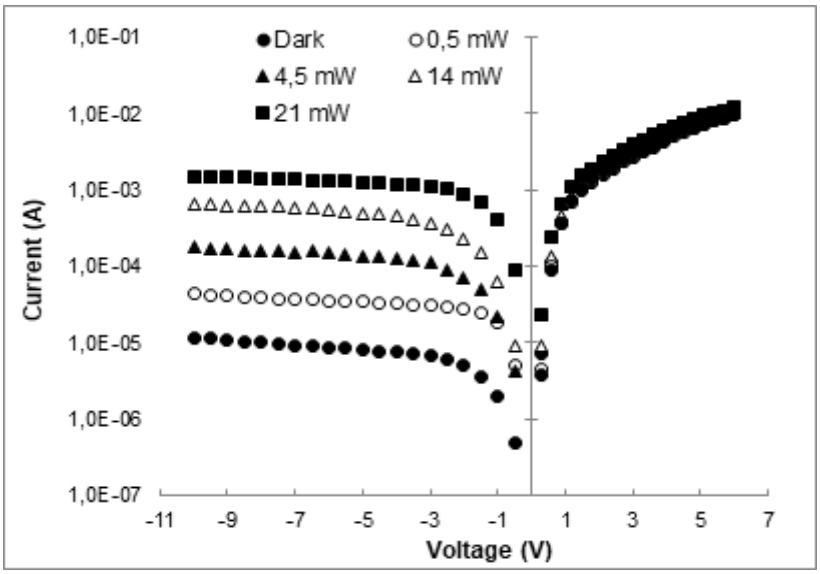

Fig 8. *Room temperature current-voltage characteristics under various illumination intensities by 976 nm wavelength photons.*

As seen in Fig 8, the light on the reverse *I–V* characteristic under various illumination intensities is translated upward moved in the I direction along the current axis with a short-circuit current (Isc). The short circuit current Isc values for the diode under 20 mW/cm^2 of the incident light intensity were found to be 720 μA.

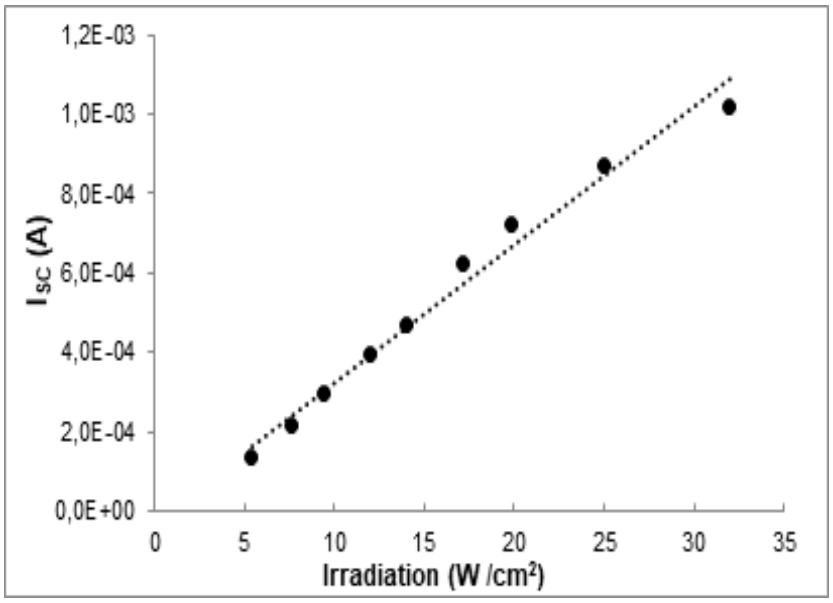

Fig 9. *Variation of the short-circuit current with a light intensity*

In the photovoltaic regime, energy characteristics are the dependencies either of short-circuit current or open circuit voltage from the intensity of incident light. In Fig 9 showing a variation of the short-circuit current with light intensity for the Schottky diode. As seen in Fig 9, with the intensity of the incident light the law of variation in these dependencies is linear. At a high intensity of the incident light in the dependence of the photocurrent on the intensity, we observed a light deviation from linearity. The appearance of this nonlinearity is connected, first of all, with the increase of voltage drop across the serial resistance of the base of a Si semiconductor layer.

Fig 10 shows the reverse light current-voltage characteristics of the investigated photodiodes under fixed (15 mW) illumination power by photons with a wavelength of 405 and 976 nm.

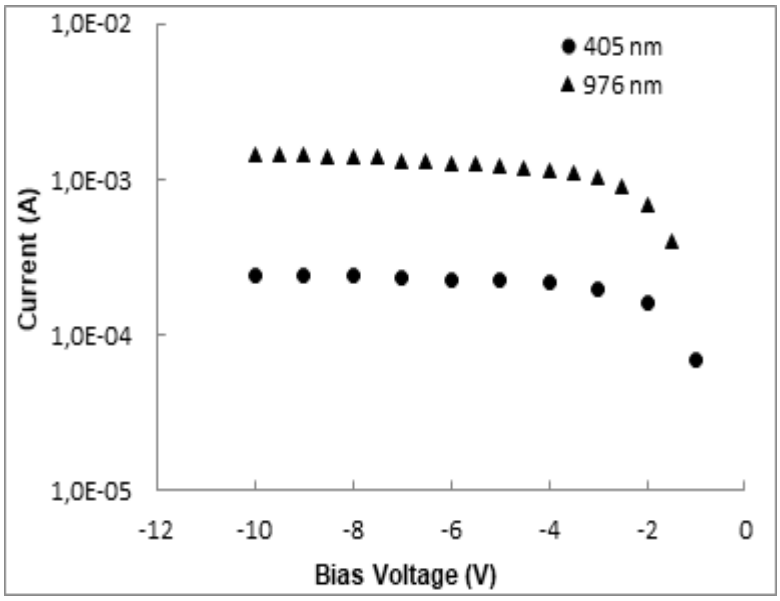

Fig 10. *Room temperature current-voltage characteristics under fixed illumination power (15 mW) by two different wavelength photons.*

As seen in Fig 10, a photocurrent created with 976 nm photons is larger than a photocurrent created by 405 nm photons. The excellent IR (Infrared) response of the Si based Schottky photodiodes may be attributed to the absorption of most photons in the region of silicon. Since short wavelength photons are absorbed in the surface polymer layer, this result is quite expected.

4. Conclusion

[P(EGDMA-VPCA)/SWCNT]/n-Si Schottky diode structures were fabricated using a surface polymerization method, and the surface morphology was observed by scanning electron microscopy (SEM). Before making contacts, the wafer was chemically cleaned using RCA cleaning procedure. Electrical and optical properties were achieved at various temperatures. Barrier height of the structure was obtained from I-V measurements. The barrier height was obtained as 1.04 eV. Light volt-current characteristics under various illumination light intensities were investigated. The short circuit current values for the investigated diodes under 20 mW/cm^2 of the incident light intensity were found to be 720 μA. The light current-voltage characteristics under fixed illumination power (15 mW) by 405 nm and 976 nm wavelength photons were studied at room temperature. It is shown that the fabricated structure by surface

polymerization technique exhibits rectification behavior that makes it a good candidate for VIS (Visible) and NIR (Near Infrared) photodetector applications.

Acknowledgment

Uludag University supported this work; Scientific Research Project Unit grant No. OUAP(F)-2016/11. The authors would like to thank for this support.

References

[1] S.M. Sze, Physics of Semiconductor Devices, 2nd ed., Wiley, New York, 1981.

[2] H. Nienhaus, H.S. Bergh, B. Gergen, A. Majumdar, W.H. Weinberg, E.W. McFarland, Phys. Rev. Lett. 82 (1999) 446.

[3] X.J. Huang, Y.K. Choi, Sens. Actuators B-Chem. 122 (2007) 659.

[4] A.I. Prokopyev, S.A. Mesheryakov, Measurement 33 (2003) 135. [5] M. Prietsch, Phys. Rep. 253 (1995) 163.

[5] M. Prietsch, Phys. Rep. **253**,163 (1995).

[6] Z. Yasser, R.Kyong Yop, Composites Science and Technology, 155 (2018) 252-260

[7] X. Wang, J. Sparkman, J. Gou, Composites Science and Technology 141 (2017) 8-15

[8] C. Feng, L. Jiang composites: Part A 47 (2013) 143–149

[9] N.Hu, Z. Masuda, C. Yan, G.Yamamoto, H. Fukunaga1, and T. Hashida, Nanotechnology 19 (2008) 215701 (10pp)

[10] D. Thuau, V. Koutsos, and R. Cheung, Journal of Vacuum Science & Technology B: Microelectronics and Nanometer Structures Processing, Measurement, and Phenomena 27, 3139 (2009)

[11] N. Tekin, A. Kara, S. K. Beyaz, E. Simşek, G. Çakmak, H. Güney, F. D. Lamari, Polymer-Plastics Technology and Engineering, 53: 840–850, 2014

[12] N. Tekin, A. Kara, S. K. Beyaz, E. Simşek, G. Çakmak, H. Güney, F. D. Lamari, Polymer Composites 33(8) · August 2012

[13] M. Ahmetoglu (Afrailov), A. Kara, N. Tekin, S. Beyaz, H. Köçkar Thin Solid Films 520 (2012) 2106–2109

[14] S.K. Beyaz, N. Tekin, A. Kara, E. Şimşek, G. Çakmak, H. Güney, F. D. Lamari, Journal of Composite Materials 45(14) 1523–1531

[15] E. H. Rhoderick, R. H. Williams, Metal-Semiconductor Contacts, Clarendon Press, Oxford, 1988.

[16] A. Kırsoy, M. Ahmetoglu (Afrailov), A. Asimov, B. Kucur, Acta Phys. Pol. A 128, B-170 (2015).

[17] Y. P. Song, R. L. Van Meirhaeghe, W. H. Lafle´re, and F. Cardon, SolidState Electron. 29, 633 (1986).

[18] C. A. Dimitriadis, S. Logothetidis, and I. Alexandrou, Appl. Phys. Lett. 66, 502 (1995).

[19] H. Norde, J. Appl. Phys. 50, 5052 (1979).

[20] A. Büyükbas Uluşan, A. Tataroglu, Y. Azizian-Kalandaragh, S. Altındal. J Mater Sci: Mater Electron (2018) 29:159–170

[21] Singh A., "Characterization of Interface States at Ni/n-CdF_2 Schottky Barrier Type Diodes and the Effect of CdF2 Surface Preparation", *Solid State Electronics*, 28 (3): 223-232 (1985).

THE EFFECT OF BINDER RATIO ON MECHANICAL PROPERTIES OF KHORASAN MORTAR

I.Kilic[1] and S. G. Gok[2]

[1,2]*Department of Civil Engineering, Faculty of Engineering, Kirklareli, Turkey*

E-mail: ismail.kilic@klu.edu.tr

Abstract

In this study, the effect of binder ratio on compressive and flexural strengths of Khorasan mortars was investigated. Crushed brick with the size of 0-4 mm was used as aggregate in mortar design. Hydrated lime dust was used as binder in mortar mixtures, in proportions of 20, 30, 40, 50 and 60 percents, respectively. 40 mm×40 mm×160 mm sized mortar specimens were produced. Weight per unit volume, compressive strength and flexural strength of mortar specimens at the age of 9 years were determined. As a result, it was found that the increased amounts of lime in mortar mixtures linearly increased the specific weight of mortar, flexural strength and compressive strength values.

Keywords: Khorasan mortar, Lime, Crushed brick, Flexural strength, Compressive strength.

1. INTRODUCTION

"Khorasan" term comes from the Khorasan region that is situated in eastern Iran, and also known as "homra" in Arab countries while it is known as "korassani" in Greece [1]. Khorasan, which is quite common in the Seljuk and Ottoman periods in Anatolia, has been successfully used as a binding material and as an artificial stone [2].

It is natural to have the knowledge of adding brick dust to lime mortar in Europe since it is in interaction with the East. The word "korassani" that was adopted in Greek can be shown as a proof of the fact that its origins in practice are West Asia and the Middle East. As brick structures and pottery techniques are in an advanced state in the Middle Eastern and Anatolian civilizations, it is not surprising that Khorasan mortar was invented and successfully used in these regions [1]. The historical "Zeynel Bey" tomb is shown as an example in Figure 1.

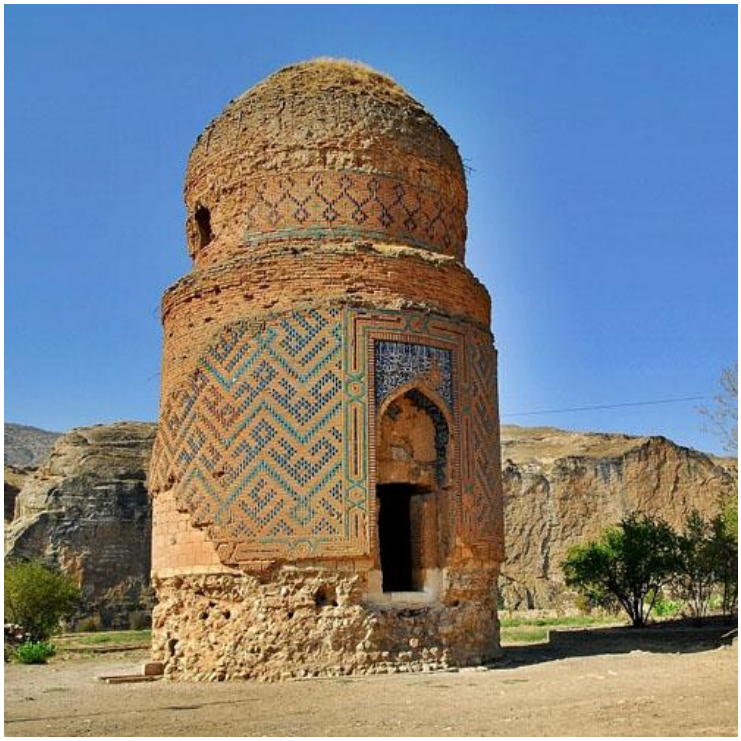

Figure 1. "Zeynel Bey" Tomb, Hasankeyf-Batman [3].

Khorasan is broken, ground and powdered baked clay such as brick, tile, pottery, etc. The mortar obtained by mixing the Khorasan with certain amounts of lime and water is defined as Khorasan mortar. In some applications sand is added to the mortar, while others involved the pea-sized broken brick or tile fragments [2].

In Khorasan mortars, lime/crushed brick is used in a ratio of 1 to 3 by weight, approximately. In Khorasan plasters, lime is used in larger amounts. It can be said that more than 50% of lime by weight is used in the preparation of plasters [4].

In some historical artifacts, it is known that the materials such as egg white, sand, flax fiber, animal hair, oak ash and straw are used as additive materials in the Khorasan mortar [5].

Just as all other traditional construction materials, materials composing the mortar and plaster vary according to the region in which the structure is built, the construction period, the construction technique, the function of the structure and the location of the material that used in the building. The main purpose of using mortar in construction is to create a unity by connecting the elements of the building components to each other. Another reason for the use of mortar is to protect structural elements from environmental factors [6].

Although various types of mortars were tried in various periods, it is possible to understand the power of Khorasan mortar from many historical works that are still standing today [2]. Khorasan mortar in the walls and domes of “Edirne Gazi Mihal Hammam” contributes to the survival of the historical monument despite it is not used today (Figure 2 and Figure 3).

Fig. 2, 3. Khorasan mortar and plaster in the walls and domes of “Edirne, Gazi Mihal Hammam” [7].

The lime mortar has a porous structure and in practice, the conditions in the mortar may differ significantly from the external environment [8]. The hardening of lime mortars is slow and the external surface of the mortar can harden more rapidly with environmental effects [9]. Hydraulic lime mortars reach their strength through hydration and carbonation [10, 11].

Although lime mortars have lower strengths in comparison with modern Portland cement mortars, they show high ductility and energy absorption capability under load [12].

2. MATERIAL AND METHODS

There is no standard available for the mixture of Khorasan mortar. Different mixing proportions and additives were used in different periods. In this research, broken tile fragments, hydrated lime powder and water were used for the production of Khorasan mortar as shown in the Figure 4, 5, 6 and 7. Lime was used in the proportions of 20-30-40-50-60% by weight of the broken tile fragments as it is indicated in Table 1. The amount of water in the mixture is 1/3 of the total weight of the lime and broken tile fragments. Five different types of mortar were produced: H1, H2, H3, H4 and H5.

Table 1. Khorasan mortar mix design.

	H1	**H2**	**H3**	**H4**	**H5**
Lime (%)	20	30	40	50	60
Broken Tile Fragments (g)	900	900	900	900	900
Lime Amount (g)	180	270	360	450	540
Water (g)	360	390	420	450	480

The amounts of broken tile fragments used in the range between 0-4 mm for the production of mortar are given in Table 2 together with sieve sizes and material weights.

Table 2. The amounts of different sized broken tile fragments.

Sieve Sizes (mm)	Broken Tile Fragments (g)
2-4	390
1-2	190
0.50-1	100
0.25-0.50	60
0.125-0.250	55
0.063-0.125	80
0-0.063	25

Fig. 4, 5, 6, 7. Broken tile fragments used in experimental study.

Khorasan mortars were produced in accordance with TS EN 1015-11 standard and were removed from the molds one day after casting [13]. The mortar specimens were kept in laboratory conditions until

the experimental stage (Figure 8 and 9). For some reasons, studies on Khorasan mortar could not be continued and the experiments on the specimens were carried out about nine years later.

Fig. 8 and 9. Khorasan mortar samples that removed from the molds.

3. RESULTS AND DISCUSSION

The images of the tests performed on specimens for determining the specific weight, flexural strength and compressive strength are given in Fig. 10 and 11, and the data obtained from the experiments are given in Table 3.

Fig. 10 and 11. Flexural and compressive strength tests.

As the numerical data obtained from the experiments were examined, it was determined that the unit weight, bending strength and compressive strength values increased in parallel with the increase in lime content in the mortar. It was found that Khorasan mortar with lime proportion of 60% had 6.94%

higher specific weight, 33.3% higher flexural strength and 168.5% higher compressive strength values than Khorasan mortar with lime proportion of 20%.

Table 3. Specific weight, flexural strength and compressive strength test results.

Mixture	Lime (%)	Specific Weight (g/cm^3)	Flexural Strength (MPa)	Compressive Strength (MPa)
H1	20	1.44	1.14	1.43
H2	30	1.52	1.35	2.46
H3	40	1.52	1.42	3.28
H4	50	1.54	1.49	3.51
H5	60	1.54	1.52	3.84

4. CONCLUSION

In this research conducted on Khorasan mortar, it was found that the mortar strength linearly increased with the increase of the amount of lime, which is the binding agent in the mortar.

In the restoration phase of historical monuments, it is seen that different mixtures are applied in the production of Khorasan mortar. In order to preserve the authenticity of historical monuments, it is necessary to determine the materials and the proportions to be used in the mixture according to the data obtained from the analysis of the mortar samples before restoration.

In today's buildings, it is necessary to establish a standard by determining the mixture proportions that would be ideal for the use of Khorasan mortars and plasters.

REFERENCES

[1] Akinci, S., "İstanbul'un Fethinden Lale Devrine Kadar Osmanlı Kagir Mimarisinde Yapım Teknikleri", İTÜ, Fen Bilimleri Enstitüsü, Yayımlanmamış Doktora Tezi, İstanbul, 1998.

[2] Akman, S., "Horasan Harcı ve Betonunun Tarihi ve Teknik Özellikleri", II. Uluslararası Türk İslam Bilim ve Teknoloji Tarihi Kongresi, İstanbul, 1986.

[3] Url 1- Retrieved from <https://www.google.com/search?q=zeynelbey+t%C3%BCrbesi&tbm=isch&tbo=u&source=univ&sa=X

&ved=2ahUKEwizgavD8oDeAhXDiCwKHf5BCe4QsAR6BAgAEAE&biw=1440&bih=789#imgrc=3sQWqhlI-FYocM:>, 12.10.2018.

[4] Böke H., Akkurt S., "Onarım Amaçlı Horasan Harç ve Sıvaların Hazırlanması", Mimarlıkta Malzeme Dergisi, sayı 1, 2007.

[5] Satongar, S., "İstanbul Şehir Surları Horasan Harçları Üzerine Bir Araştırma", İTÜ, Fen Bilimleri Enstitüsü, Yüksek Lisans Tezi, İstanbul, 1994.

[6] Sabbioni, C., Zappia, G., "Sulphur and Carbon Compounds on Damaged Mortars in Ancient Masonry", 4th International Symposium on the Conservation of Monuments in the Mediterranean, C-1, Rodos, 1997.

[7] Kilic, I., "Horasan Harç ve Sıvaları", Tarihi Eserlerin Güçlendirilmesi ve Geleceğe Güvenle Devredilmesi Sempozyumu-I, TMMOB İMO Ankara Şubesi, sayfa: 277-285, 27-29 Eylül 2007, Ankara.

[8] Ball, R. J. and Allen G. C., "The measurement of water transport in porous materials using impedance spectroscopy", J Phys D, 2010.

[9] El-Turki, A., Ball, R. J., Holmes, S., Allen, W. J., Allen, G. C. "Environmental Cycling and Laboratory Testing to Evaluate The Significance of Moisture Control for Lime Mortars", Construction and Building Materials 24 (2010), pp. 1392–1397.

[10] Martinez-Ramirez S., Sanchez-Cortes S., Garcia-Ramos JV. "Micro-Raman Spectroscopy Applied to Depth Profiles of Carbonates Formed in Lime Mortar", Cement and Concrete Research 2003; 33(12):2063–8.

[11] Balen K. "Carbonation Reaction of Lime, Kinetics at Ambient Temperature". Cement and Concrete Research 2005; 35(4), pp. 647–57.

[12] Rosson, B. T. and Suelter J. L. "Closed-Form Equations for Hardening of Sand-Lime Mortar Joints", Journal of Engineering Mechanics, 2001, pp. 574-581.

[13] TS EN 1015-11, "Kagir Harcı - Deney Metotları - Bölüm 11: Sertleşmiş Harcın Basınç ve Eğilme Dayanımının Tayini", Türk Standartları Enstitüsü, Ankara, 2000.

INVESTIGATION OF EFFECTS OF SOME DIE MATERIALS ON COATING THICKNESS BY CHANGING THE TIME OF GALVANIZING

S.S. KARABEYOĞLU[1], O. EKŞİ[1], and F.YILDIZ[1]

[1]*Department of Mechanical Engineering, Faculty of Engineering, Kırklareli, Turkey*

E-mail: sencerkarabeyoglu@klu.edu.tr

Abstract

One of the most effective methods for preventing surface corrosion of metal materials is galvanizing, also called zinc coating. In the galvanizing method, the layer thickness to be formed on the material surface changes depending on the time and it affects the surface characteristics. Depending on the time and material characteristics, the coating thickness changes during the surface modification and affects the mechanical properties of the material. In this study, CK45, Sverker 21 and 1.2379 which is used in the molding technology, were galvanized for various periods of time using the material galvanizing method. Surface characteristics of coated materials were investigated.

Keywords: Galvanizing, temperature, coating time, surface coating, surface characterization.

1. INTRODUCTION

Corrosion of metallic materials due to environmental conditions causes electrochemical reactions [1,2]. They can cause immediate fractures in machine parts under dynamic or static loads [3,4]. Hereby, machine parts become unusable and economically badly affected [5]. It also prevents the necessary process for the reuse of materials. The oxide layer breaks the surface structure and creates brittle, low-strength structures on the surface of the materials and causes cavities that may create notch effect on the surface [6]. According to the corrosion platform, the surface characteristics of the metallic structure has been defined by various studies. These are chemical and electro chemical corrosion types. The coating method, environmental conditions control, electrical protection procedures and the appropriate material selections must be done carefully to eliminate the factors that may form corrosion.

Many methods are available for protection from corrosion [7]. These are surface modifications. Among these, galvanization has an important position [8]. Through the galvanizing process, the material character is kept constant by forming an electrochemical reduction mechanism by disconnecting the material with the factors that can create corrosion [9]. Zinc, which is prone to electrical bonding in galvanizing method, is used as coating material. The fact that zinc reacts more with the environment than steel indicates that it is more active. Because of this properties, it reacts the external factor before the steel material and becomes corrosive and provides a protective layer. Many methods are available for the galvanizing coating too[10]. One of them is electro galvanizing. This method is actualized by transferring parts from anode point to cathode point.

In this study, Ck 45, Sverker 21, 1.2379 metal materials that used in mold manufacture, were coated with electro galvanizing method. The materials were kept in the cyanide-containing pool along 7.5, 10 minutes and coated with zinc. After the coating process, surface coating thicknesses and hardness were investigated. The effects of the coating time on the material were compared.

2. MATERIAL AND METHODS

The properties of the CK45 mold material used in the experiment are shown in Table 1.

Table 1. Characteristic of CK45 material

Chemical Composition(%)			**Hot forming and heat treatment**		**Mechanical Properties**	
Steel	**C45E**	**C45R**	Forging or hot rolling	1100-850 °C	Treated for cold shearability +S	max. 225 HB
C	0,45	0,45				
Si	0,25	0,25	Normalising	840-880 °C/air		
Mn	0,65	0,65	Soft annealing	680-710 °C/furnace	Soft annealed +A	max. 207 HB
S	<0,030	0,020-0,035	Hardening	820-860 °C/water,oil		
Other	(Pb)	(Pb)	Tempering	550-600 °C		

The properties of the Sverker 21 mold material used in the experiment are shown in Table 2.

Table 2. Characteristic of Sverker21 material

Typical Analysis		**Standart Specification**	**Delivery Condition**
C	1,55	AISI D2, W.-Nr. 1.2379	Soft annealed to approx. 210 HB
Si	0,3		
Mn	0,4		
Cr	11,3		
Mo	0,8		
V	0,8		

The properties of the 1,2379 mold material used in the experiment are shown in Table 3.

Table 3. Characteristic of 1,2379 material

Chemical Composition (%)		**Heat Treatment**	
C	1,55	Soft annealing	
Cr	12	Temperature	820 - 850 °C
Mo	0,8	Cooling	Furnace
V	0,9	Hardness	max. 255 HB

The content of the solution used in the electro galvanizing process is given in Table 4.

Table 4. Solution of galvanizing process

Metal	Anode	Electrolyte	Application
Zn	Zn	$6\%Zn(CN)_2, 5\%\ NaCN, 4\%\ NaOH, 1\%Na_2CO_3, 0{,}5\%Al_2(SO_4)_3$	Galvanized steel

SEM images of the test samples were taken with the EVO ls10 trademark microscope.

Before the coating process the materials should be cleaned from dirt, rust and oil. For this, degreasing and surface cleaning operations were performed in the cleaning pool. They were washed with clean water after cleaning pool operation. Water and acid pool are shown in Figure 1.

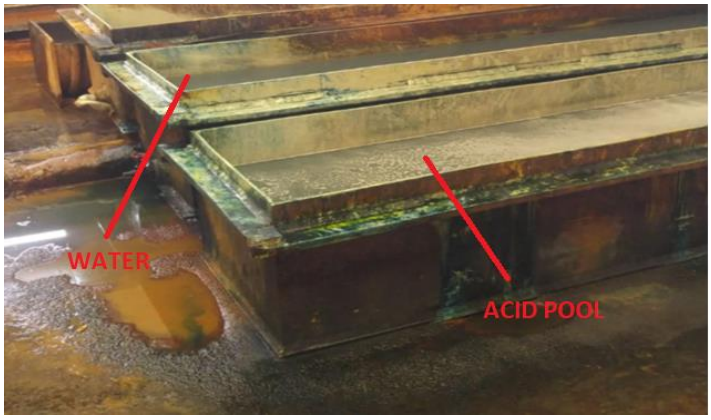

Figure 1. Acid pool and clean water pool

After the cleaning process, materials are coated by electro galvanizing method. Electro galvanizing pool is shown in Figure 2. The coated materials were washed in a clean water bath after the coating process and passivated. The moisture was removed from the material quickly. So there is no trace of rust or residue on the material.

Figure 2. Electro galvanizing pool

3. RESULTS AND DISCUSSION

SEM images and EDX analyzes were taken after the CK45 material was coated for 7.5 and 10 minutes. The SEM images of the test samples are given in Figure 3. Green parts on SEM images show the amount of coated zinc.

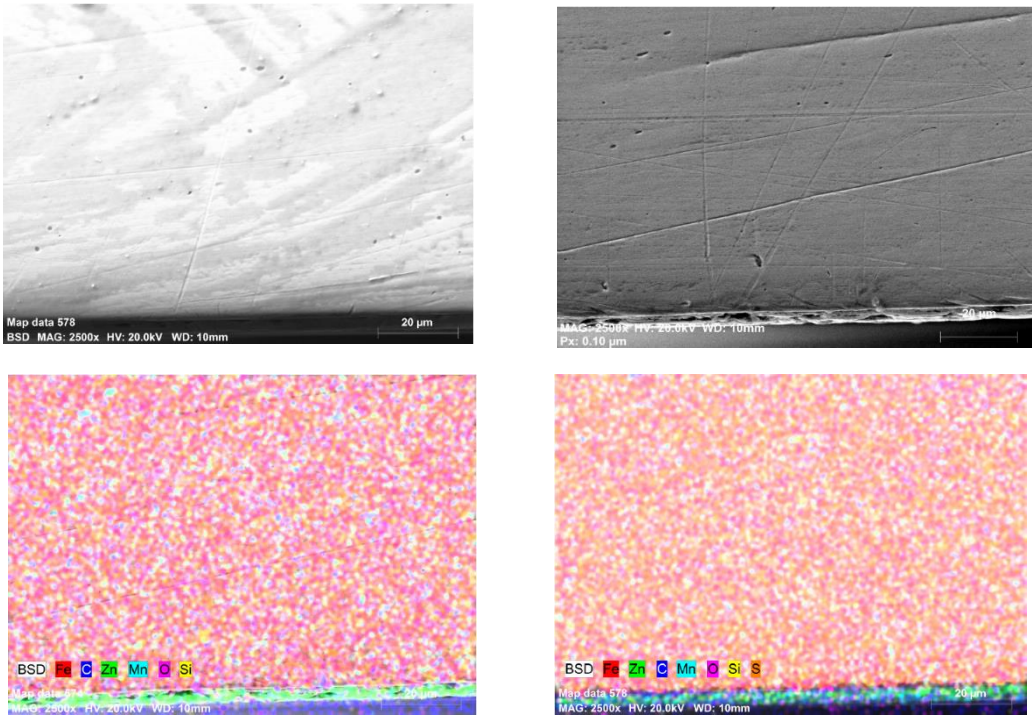

(a) (b)

Figure 3. (a) 7,5 minutes zinc coated test specimens .(b) 10 minutes zinc coated test specimens

Material content were determined from the test samples the weight percent in the image area by the EDX analysis. The EDX analysis results are shown in Figure 4 for 7.5 min and 10 min coated samples.

El	AN	Series	Net unn. C [wt.%]	norm. C [wt.%]	Atom. C [at.%]	Error (1 Sigma) [wt.%]
Fe	26	K-series	362834	78.33	83.69	57.01	2.10
C	6	K-series	12113	11.76	12.57	39.81	1.63
Zn	30	K-series	3400	1.53	1.63	0.95	0.08
Mn	25	K-series	8482	1.43	1.52	1.05	0.07
O	8	K-series	952	0.36	0.38	0.91	0.11
Si	14	K-series	1447	0.14	0.15	0.21	0.03
S	16	K-series	574	0.05	0.06	0.07	0.03

(a)

El	AN	Series	Net unn. C [wt.%]	norm. C [wt.%]	Atom. C [at.%]	Error (1 Sigma) [wt.%]
Fe	26	K-series	363992	82.22	89.31	71.60	2.20
C	6	K-series	5759	6.15	6.68	24.90	0.96
Zn	30	K-series	4131	1.88	2.05	1.40	0.09
Mn	25	K-series	8358	1.47	1.60	1.30	0.07
O	8	K-series	480	0.17	0.19	0.52	0.07
Si	14	K-series	1529	0.16	0.18	0.28	0.03

(b)

Figure 4. (a) 7,5 minutes zinc coated test specimens EDX analysis .(b) 10 minutes zinc coated test specimens EDX analysis.

SEM images and EDX analyzes were taken after the SV 21 material was coated for 7.5 and 10 minutes. The SEM images of the test samples are given in Figure 5. Green parts on SEM images show the amount of coated zinc.

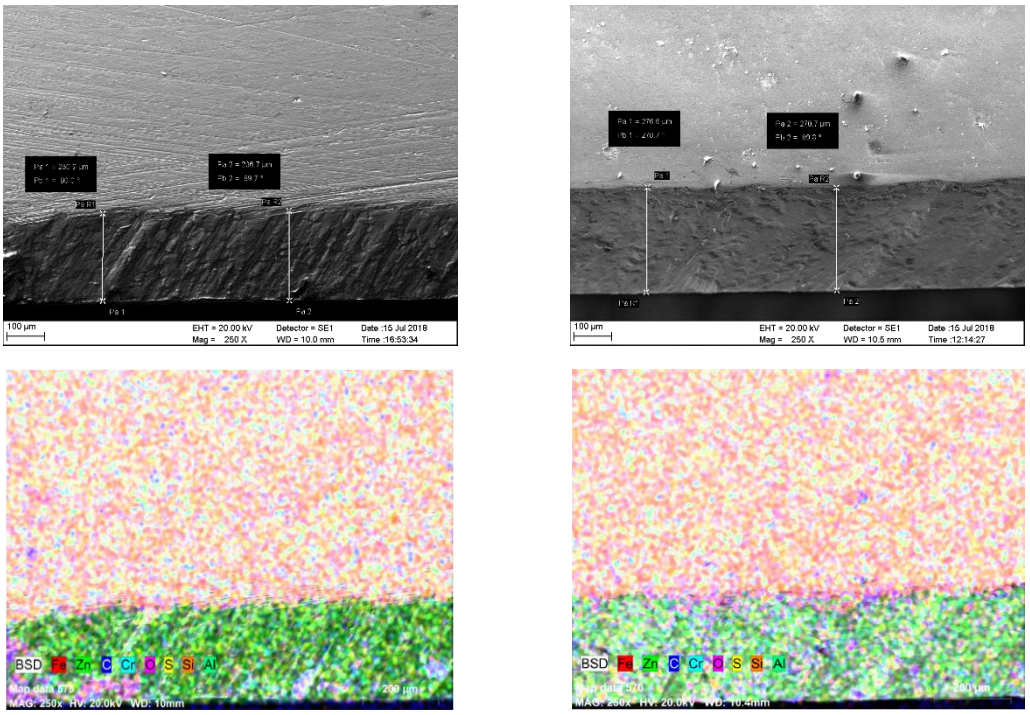

(a) (b)

Figure 5. (a) 7,5 minutes zinc coated test specimens .(b) 10 minutes zinc coated test specimens

The EDX analysis results are shown in Figure 6 for 7.5 min and 10 min coated samples.

El	AN	Series	Net unn. C [wt.%]	norm. C [wt.%]	Atom. C [at.%]	Error (1 Sigma) [wt.%]
Fe	26	K-series	231631	51.62	55.87	38.77	1.40
Zn	30	K-series	45241	19.61	21.23	12.58	0.56
C	6	K-series	8888	9.51	10.29	33.20	1.38
Cr	24	K-series	56525	7.87	8.52	6.35	0.24
O	8	K-series	8312	3.11	3.36	8.14	0.47
S	16	K-series	3353	0.34	0.37	0.45	0.04
Si	14	K-series	2101	0.22	0.24	0.33	0.04
Al	13	K-series	701	0.11	0.12	0.18	0.03

(a)

El	AN	Series	Net unn. C [wt.%]	norm. C [wt.%]	Atom. C [at.%]	Error (1 Sigma) [wt.%]
Fe	26	K-series	212916	48.72	54.60	39.32	1.32
Zn	30	K-series	44634	20.46	22.92	14.10	0.59
Cr	24	K-series	56175	8.19	9.18	7.10	0.25
C	6	K-series	6798	7.66	8.59	28.75	1.16
O	8	K-series	8810	3.33	3.73	9.37	0.50
Si	14	K-series	3386	0.37	0.41	0.59	0.04
S	16	K-series	3217	0.33	0.37	0.46	0.04
Al	13	K-series	1088	0.18	0.21	0.31	0.04

(b)

Figure 6. (a) 7,5 minutes zinc coated SV 21 test specimens EDX analysis .(b) 10 minutes zinc coated SV 21 test specimens EDX analysis.

SEM images and EDX analyzes were taken after the 1,2379 material was coated for 7.5 and 10 minutes. The SEM images of the test samples are given in Figure 7. Green part of figures are shown that amount of coated zinc.

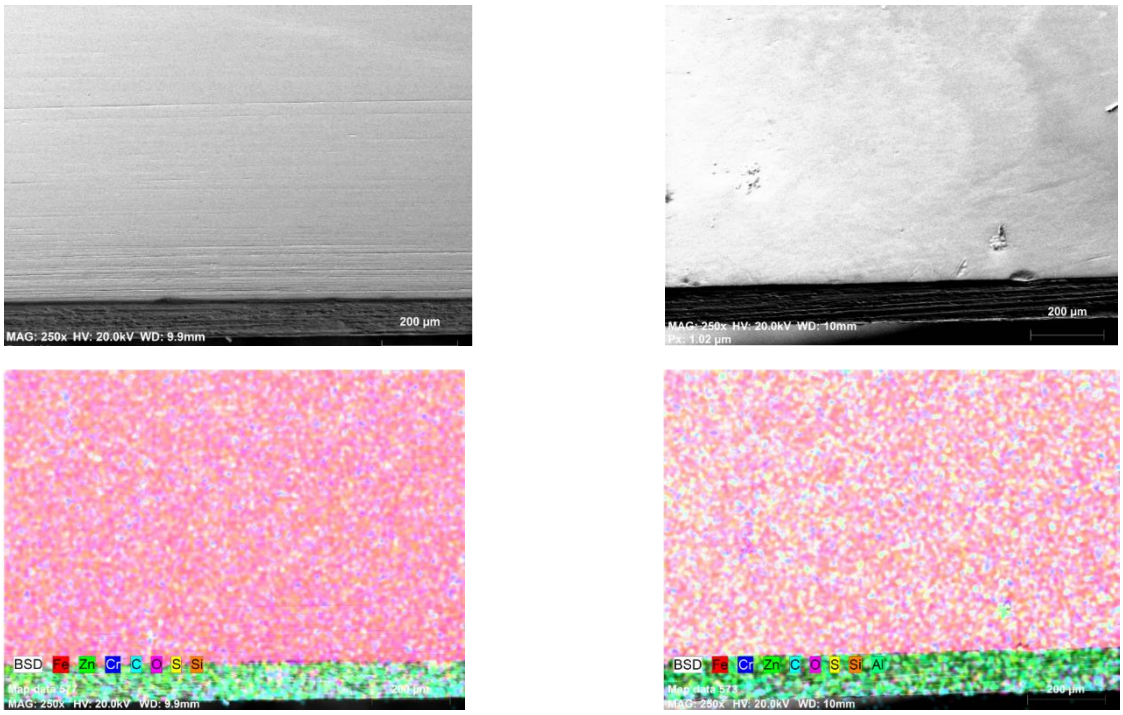

Figure 7. (a) 7,5 minutes zinc coated 1,2379 test specimens .(b) 10 minutes zinc coated 1,2379 test specimens

The EDX analysis of 1,2379 results are shown in Figure 8 for 7.5 min and 10 min coated samples.

El	AN	Series	Net unn. C [wt.%]	norm. C [wt.%]	Atom. C [at.%]	Error (1 Sigma) [wt.%]
Fe	26	K-series	300527	67.54	74.40	59.23	1.82
Cr	24	K-series	74321	9.94	10.95	9.36	0.29
Zn	30	K-series	13473	6.04	6.65	4.52	0.20
C	6	K-series	5271	5.41	5.96	22.05	0.86
O	8	K-series	3849	1.28	1.41	3.92	0.24
S	16	K-series	3676	0.34	0.38	0.52	0.04
Si	14	K-series	2331	0.23	0.25	0.40	0.04

(a)

El	AN	Series	Net unn. C [wt.%]	norm. C [wt.%]	Atom. C [at.%]	Error (1 Sigma) [wt.%]
Fe	26	K-series	292780	65.00	71.22	55.04	1.75
Cr	24	K-series	69621	9.31	10.21	8.47	0.28
Zn	30	K-series	18406	8.42	9.23	6.09	0.26
C	6	K-series	6071	6.25	6.84	24.59	0.97
O	8	K-series	4704	1.60	1.75	4.72	0.28
S	16	K-series	3991	0.39	0.43	0.58	0.04
Si	14	K-series	2085	0.21	0.23	0.35	0.04
Al	13	K-series	549	0.09	0.09	0.15	0.03

(b)

Figure 8. (a) 7,5 minutes zinc coated 1,2379 test specimens EDX analysis .(b) 10 minutes zinc coated 1,2379 test specimens EDX analysis.

The average hardness values were determined by taking measurements from the different points from the coated samples. Depending on the coating time of the test samples measured values are given in Table 5.

Table 5. Average hardness values from coated materials

7,5 min. Coated Materials		
CK45	**Sverker21**	**1,2379**
162HV	201HV	162HV
10 min. Coated Materials		
CK45	**Sverker21**	**1,2379**
186HV	227HV	210HV

4. CONCLUSION

The galvanization was carried out for 7.5 minutes and 10 minutes for each mold material. Galvanized coating thickness was increased with the change in coating time and determined by electron microscope images.

When the samples which have been galvanized for 7.5 minutes were compared among themselves, it was determined that the amount of coating per unit area was in the highest SV21 test sample. The reason for the high coating thickness of the sv21 material is explained by the fact that the surface morphology is more susceptible to the coating than the other samples and is due to the surface compatibility of the anion and cation passages to the zinc particles in the coating solution.

After hardness test, it was determined that the highest surface hardness change was observed in the sample numbered 1,2379. This situation has been associated with material morphology.

REFERENCES

[1] R.W. Revie, H.H. Uhlig (Eds.), Corrosion and Corrosion Control: An Introduction to Corrosion Science and Engineering (fourth edition), Wiley-Interscience (2008), A. R.Marder, The metallurgy of zinc – coated steel, Progress in Materials Science 45 (2000) 191-271.

[2] A.W. Momber, T. Marquardt,Protective coatings for offshore wind energy devices (OWEAs): a review J. Coat. Technol. Res., 15 (2018), pp. 13-40, 10.1007/s11998-017-9979-5.

[3] Winston Revie, R., 2000. Uhlig‘s Corrosion Handbook, Second Edition, John Wiley & Sons Inc.

[4] Schweitzer, P.E., P. (2006). Fundamentals of Metallic Corrosion. Boca Raton: CRC Press.

[5] ASM HANDBOOK, Volume 13B, Corrosion: Materials. 2005.

[6] H. Young Lee, S. Gyu Kim, Surface and Coatings Technology 135 (2000) 69.

[7] J. Giridhar, W.J. Ooji, Surface and Coatings Technology 52 (1992) 17.

[8] J.W. Dini, Electrodeposition: the Materials Science of Coatings and Substrates, Noyes Publications, Westwood, New Jersey (1992), p. 314.

[9] Smith, W.F., Principles of Materials Science and Engineering, 2.edition, McGraw-Hill International Editions, Singapore, 1990.

[10] Yu.S. Bubyalis, N.I. Mozolene, Studies in Field of Electrodeposition of Metals. Materials of XIII Republican Conference of electrochemists of Lithuanian SSR, Institute of chemistry and chemical technology of Academy of Sciences of LSSR, Vilnius, 1974, pp. 195–200.

CdTe THIN FILMS FOR INFRARED DETECTOR APPLICATIONS

S. ÖZDEN[1] and M. M. KOÇ[1, 2]

[1]*Department of Physics, Kirklareli University, Kirklareli, Turkey*

[2]*School of Engineering, University of Portsmouth, Portsmouth, United Kingdom*

E-mail: selinozden@klu.edu.tr

Abstract

Mercury Cadmium Telluride (HgCdTe) is widely used material in infrared detectors for electric, electronic and photonic properties [1]. HgCdTe films were mostly grown on GaAs substrates due to its commercially availability as epi-ready wafers [2]. However, the large lattice mismatches between HgCdTe thin films and GaAs substrates and Ga diffusion into HgCdTe layers limit the detector performance. Therefore, growth of a buffer layer consist of CdTe material is proposed to reduce detrimental effect of lattice mismatches and prevent Ga diffusion [3]. In the present work, CdTe (211)B epitaxial thin films were grown on (211)B oriented GaAs substrates by Molecular Beam Epitaxy (MBE) for use as buffer layer for HgCdTe thin films used in infrared detectors [4]. Produced CdTe thin films were surface characterized by atomic force microscopy and scanning electron microscopy. Surface roughness of thin films was determined and the thickness of the films was compared via cross-sectional scanning electron microscope, fourier transform infrared spectroscopy and spectroscopic ellipsometry. Atomic compositions of the thin films were obtained by energy dispersive X-ray apparatus of scanning electron microscope. Temperature dependent Raman spectroscopy investigations were performed to understand the behavior of Raman active modes of thin films. Lastly, Everson method were applied to the thin films to reveal lattice mismatch-induced dislocations. Decorations obtained after the Everson etching confirmed the (211) B type structure of CdTe thin films deposited on GaAs (211)B surface and dislocation densities were determined.

Keywords: Mercury Cadmium Telluride, Infrared Detectors, Molecular Beam Epitaxy, Buffer Layer, Eching, Temperature Dependent Raman Spectroscopy

1. INTRODUCTION

Infrared detector technology was developed primarily for military applications and then it has expanded rapidly to science, medical and industrial applications such as astronomy, meteorology, chemical detection and spectroscopy. Infrared technology first began with Herschel and he discovered infrared radiation in 1800. After that infrared technology was developed rapidly and in 1942 the first film sensitive to the infrared by Eastman [5]. Today, there are infrared detector materials such as HgCdTe, PbSnTe, InGaAs, etc. Among these materials, HgCdTe is most popular infrared detector material. There are several properties of HgCdTe makes it suitable for infrared detection such as adjustable bandgap, direct bandgap with a high absorption coefficient, moderate dielectric constant and index of refraction and moderate thermal expansion coefficient. The band gap energy tunability depends on Cd composition makes the HgCdTe useful for infrared detection [6]. HgCdTe can be developed by liquid phase epitaxy, vapor phase epitaxy, metalorganic chemical vapor deposition and molecular beam epitaxy. In this study, molecular beam epitaxial growth method was used.

Various substrates can be used for the growth of HgCdTe by molecular beam epitaxy (MBE) such as CdZnTe, InSb, Ge, Si and GaAs. Among these materials, GaAs has been found more advantages other substrates due to being commercially epi-ready, its low cost and it is easy to remove protective oxide layer at low temperatures. However, Ga and As atoms diffuse to growing layer. In addition, high lattice mismatch of GaAs with HgCdTe causes the dislocations [7]. To minimize these detrimental effects, a CdTe buffer layer between GaAs substrate and HgCdTe film was proposed. In this study, CdTe buffer layers were grown on (211)B oriented GaAs substrates by MBE method for HgCdTe detector materials.

2. MATERIAL AND METHODS

CdTe epitaxial films were grown on (211) B oriented epi-ready GaAs substrates by Molecular Beam Epitaxial (MBE) growth method for the use as a buffer layer for HgCdTe detector material. MBE growth of CdTe buffer layer on epi-ready GaAs substrates includes two main steps. Firstly, the protective oxide layer of GaAs substrate should be removed. To remove protective oxide layer, the substrates were heated into the growth chamber prior to growth. Removal process was performed under As_4 flux to prevent the loss of arsenic from the substrate surface. The temperature of As cracker cell bulk module was increased to 325^{o}C and crack module increased to 600^{o}C to remove oxide layer. After desorption, the substrate temperature was cooled down to 250^{o}C to grow a CdTe nucleation layer and then it was increased to 300^{o}C under Te_2 flux to grow CdTe layer. The growth was performed at a rate of about 1 μm/h. After the growth,

the surface morphologies of CdTe epitaxial layers were investigated by Atomic Force Microscopy (AFM) and Scanning Electron Microscopy (SEM).

Energy dispersive X-ray apparatus of Scanning Electron Microscope was used to assess the chemical composition and distribution of Cd, Te, Ga and As on CdTe layers. The temperature dependent Raman measurements were performed to characterize Te precipitates in CdTe and to investigate the quality of MBE grown CdTe epitaxial films. The thicknesses of films were determined by Fourier Transform Infrared Spectroscopy and Ex-situ Spectroscopic Ellipsometry. Finally, Everson defect decoration method was used to obtain an estimate for the density of defects originating from dislocations.

4. RESULTS AND DISCUSSION

The surface morphologies of MBE-grown (211)B CdTe buffer layers were investigated by AFM in tapping mode. The roughness values were found as 3.89 and 1.18 nm for samples CdTe 1 and CdTe 2, respectively. To assess the distribution of Cd, Te, Ga and As atoms on the surface, SEM-EDX analyses were performed. Atomic composition of CdTe 1 and CdTe 2 samples were given in Table 1. As given in the table, the atomic percentage of Cd was higher than the Te and also Ga contaminations were observed for some scanned areas.

The thicknesses of films were determined by ex-situ spectroscopic spectrometry and fourier transform infrared spectroscopy. Ex-situ spectroscopic ellipsometry and room temperature IR transmission curves for CdTe 1 and CdTe 2 samples were given in Figure 2. The CdTe 1 and CdTe 2 layer thicknesses were found as 1.074 and 1.088 μm by ex situ spectroscopic ellipsometry, respectively. According to the FTIR IR transmittance curves, the thicknesses of CdTe layers were found to be 1.078 and 1.085 μm for the CdTe 1 and CdTe 2 samples, respectively. These results are consistent with ex-situ spectroscopic ellipsometry results. In addition, cross-sectional SEM images were also recorded in BSE mode to estimate film thicknesses. The CdTe layer thicknesses were found to be approximately 1 μm.

Table 1. Atomic composition of CdTe 1 and CdTe 2 samples.

Sample #	Element	Atomic %
CdTe 1	Cd	51
	Te	48
	Ga	Negligible (0.3)
	As	0
CdTe 2	Cd	51
	Te	49
	Ga	Negligible (0.02)
	As	Negligible (0.03)

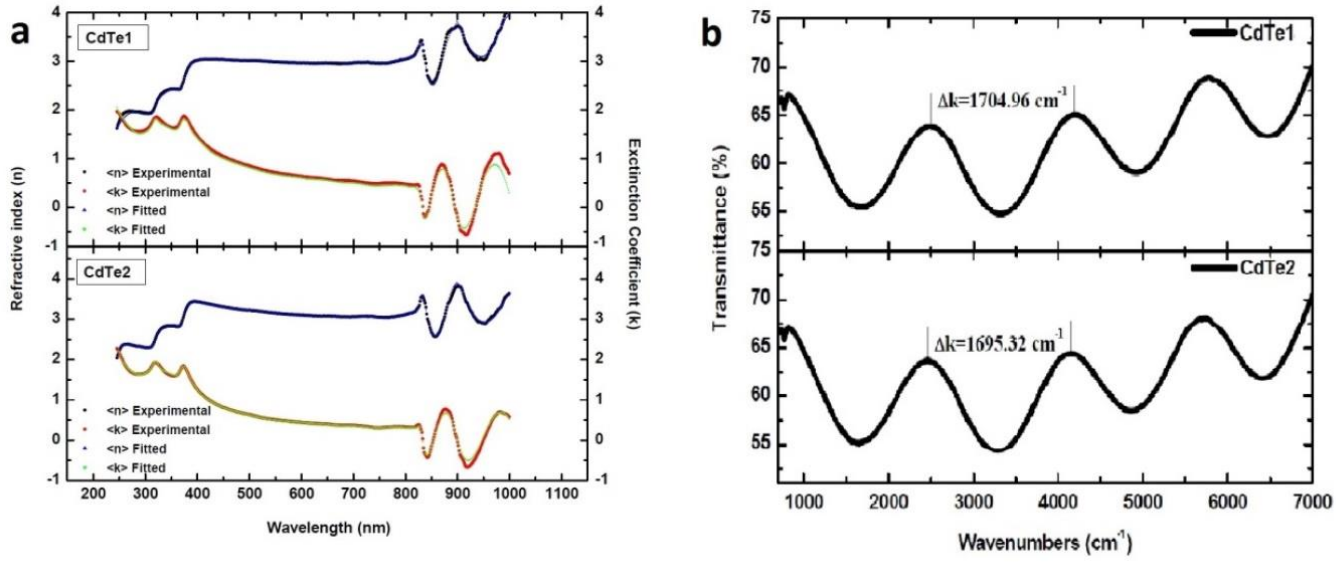

Figure 2. a Ex-situ spectroscopic ellipsometry data. **b** Room temperature IR transmission curves for MBE-grown CdTe 1 and CdTe 2 epitaxial films.

To characterize the quality of CdTe buffer layers, to investigate the change of Raman peak positions and intensity ratios, temperature dependent Raman measurements were performed. Temperature dependent Raman spectra were given in Figure 3 and Figure 4 for CdTe 1 and CdTe 2, respectively. As measurement temperature decreases from room temperature to 80 K, Te-related defect modes and the Raman active TO phonon mode of CdTe become more prominent for both samples. To study Raman peaks in more detail, peaks were fitted by Lorentzian functions. After fitting, it was seen that Te-specific A1 and E symmetry

modes and TO phonon mode of CdTe formed a broad peak as the measurement temperature decreases for both samples. Comparison of Raman peak positions and intensity ratios for CdTe 1 and CdTe 2 were given in Figure 5. The peak positions and also intensity ratios showed similar behaviour in both samples. Second order longitudinal and first order longitudinal phonon mode ratio (2LO/LO) gives information about the quality of CdTe layers. If this ratio close the unity, CdTe layer shows perfect crystal quality [8]. 2LO/LO changes non-linearly with measurement temperature. 2LO/LO had a maximum at 150 K and had a minimum at 300 K for both samples. However, the peak positions of the A1 symmetry mode of Te shifted to lower frequencies at 120 and 250 K for CdTe 2, but to higher frequencies for CdTe 1.

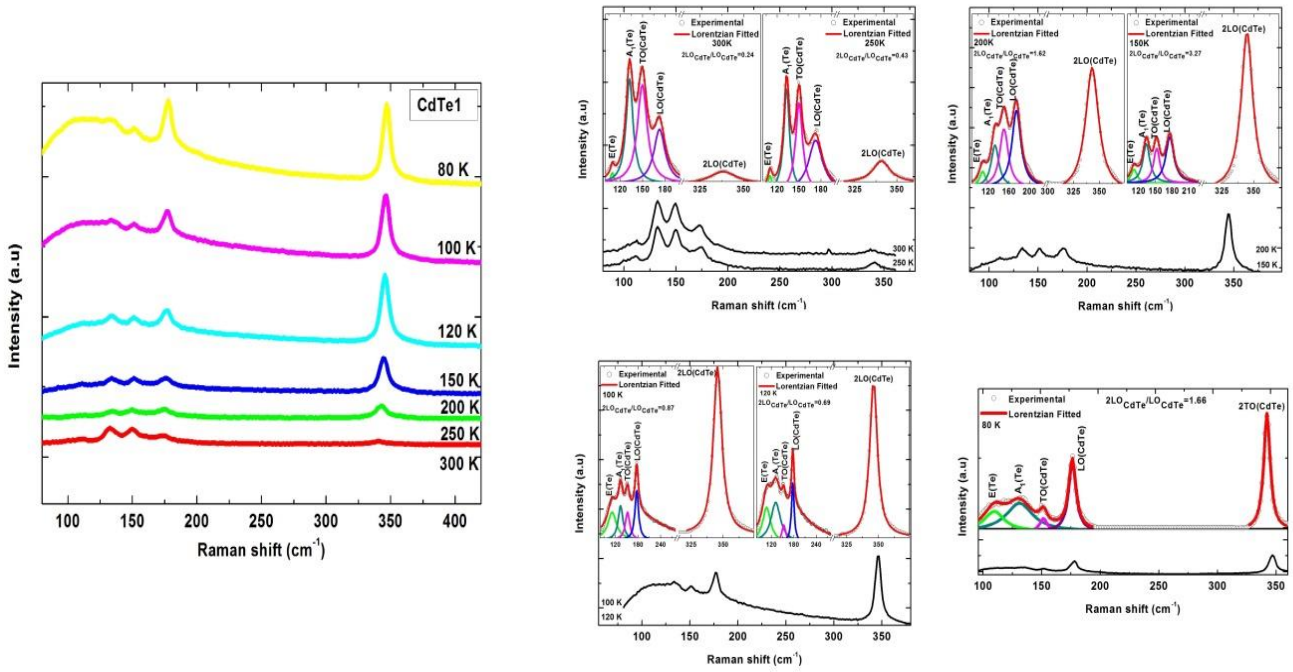

Figure 3. Temperature dependent Raman spectra of CdTe 1.

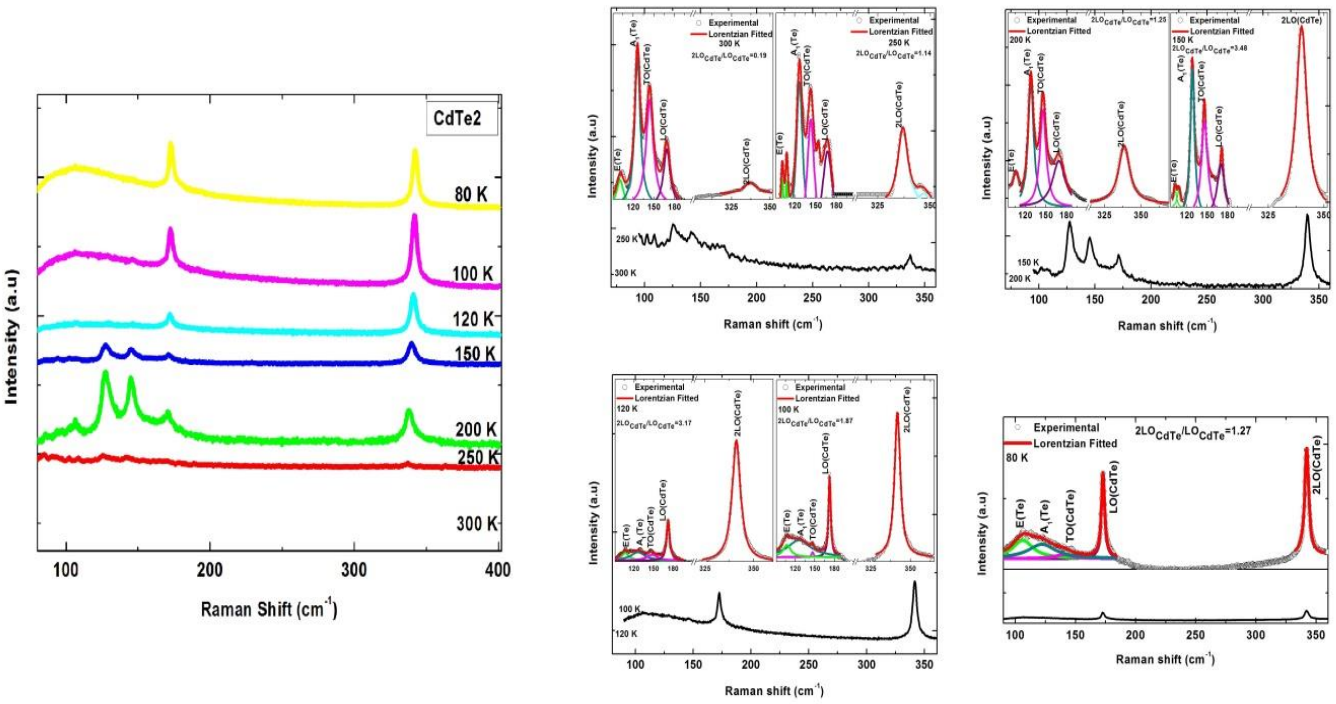

Figure 4. Temperature dependent Raman spectra of CdTe 2.

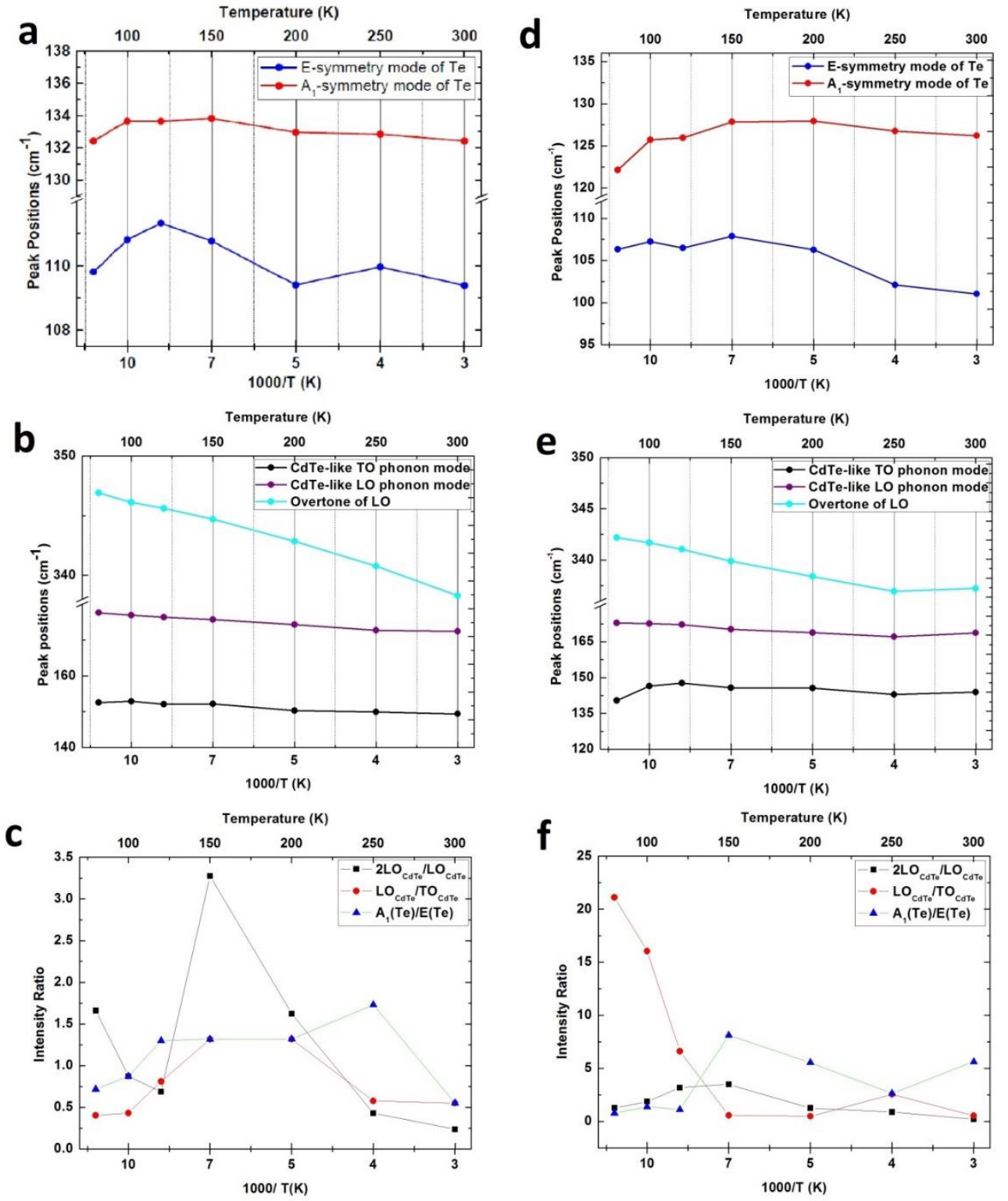

Figure 5. a, b, c Comparison of Raman peak positions and intensity ratios for CdTe 1 **d, e, f** Comparison of Raman peak positions and intensity ratios for CdTe 2.

Etch pit process gives a clear identification of dislocations per unit area. There are various etching methods to calculate etch pit densities such as Everson, Benson, Chen, Nakagawa and Inoue. However, all these etching methods do not give effective results for entire crystal orientations. Only, Everson method forms successful defect decorations for (211)B oriented layers. To obtain an estimate fort he density of defects originating from dislocations across MBE-grown (211)B oriented CdTe layers, Everson defect decoration method was used. Everson solution includes the mixture of hydrofluoric acid, nitric acid and lactic acid. Performed volume ratios and implementation times were given in Table 2. Etch pit densities (EPD) were calculated manually by SEM images. EPD was found 1.2-9.2*10^8 cm^{-2} and pits were found with 0.15 µm-0.71 µm size and 2 nm-80 nm depth. The variation of EPD, roughness, pit width and pit height against volume ratio and etching time of Everson etched CdTe samples were summarized in Table 2.

Table 2. The variation of EPD, roughness, pit width and pit height against volume ratio and implementation time of Everson etched CdTe samples.

Sample #	Volume Ratio	Etch Time (s)	Etch Pit Density (*$10^8$$cm^{-2}$)	Pit Width (µm)	Pit Height (nm)	Roughness (nm)
CdTe 1-1	0.5:4:25	30	8.8	0.15	12	2.05
CdTe 1-2	1:4:50	40	9.2	0.16	18	3.47
CdTe 1-3	1:4:25	30	N.A.	N.A	6	1.56
CdTe 2-1	0.5:4:25	30	1.7	0.24	18	2.11
CdTe 2-2	1:4:50	40	1.7	0.24	20	2.25
CdTe 2-3	1:4:25	20	1.2	0.71	80	26.1

4. CONCLUSION

AFM investigations of CdTe films showed that films showed smooth morphological character. The roughness of the films were found between 1.18 and 3.89. SEM-EDX analyses showed that the atomic percentage of Cd was higher than the Te and Ga contaminations were observed for some scanned areas. FTIR spectrometry and spectroscopic ellipsometry system were used to obtain the thickness of CdTe samples. It was calculated that the thickness of the samples varies 1.074 µm to 1.088 µm for CdTe 1 and 1.078 µm to 1.085 µm CdTe 2 samples. Raman spectroscopy results indicate that the intensity ratios changes non-linearly with measurement temperature. This non-linear change of 2LO and LO phonon mode intensity ratios indicate these ratios do not change depend on measurement temperature. GaAs related

phonon modes could not observed which showed CdTe films were grown successfully. However, Te related defect modes were observed for the samples. Te related A1 and E symmetry modes indicate the formation of Te precipitates on the MBE grown CdTe films. EPD values were calculated for both samples after Everson decoration method was performed. EPD values were found approximately 10^8 cm^{-2} which is a proper value for MBE grown CdTe epitaxial films.

ACKNOWLEDGMENTS

The authors would like to thank all supporters for their assistance with the study. Use of facilities at the IZTECH Material Research Center for scanning electron microscopy is acknowledged.

REFERENCES

[1] J. T. Cheung, M. Khoshnevisan, and T. Magee, “Heteroepitaxial growth of CdTe on GaAs by laser assisted deposition,” Appl. Phys. Lett., vol. 43, no. 5, pp. 462–464, 1983.

[2] T. Nishitani, K., Ohkata, R., & Murotani, “Molecular beam epitaxy of CdTe and Hg1-xCdxTe ON GaAs (100),” J. Electron. Mater., vol. (3), no. 12, p. 619–635., 1983.

[3] E. Bilgilisoy, S. Özden, E. Bakali, M. Karakaya, and Y. Selamet, “Characterization of CdTe Growth on GaAs Using Different Etching Techniques,” J. Electron. Mater., vol. 44, no. 9, pp. 3124–3133, 2015.

[4] S. Özden and M. M. Koc, “Spectroscopic and microscopic investigation of MBE-grown CdTe (211)B epitaxial thin films on GaAs (211)B substrates,” Appl. Nanosci., Mar. 2018.

[5] ROGALSKI, A. History of infrared detectors. Opto-Electronics Review, 2012, 20.3: 279-308.

[6]Cockrum, Charles A. "HgCdTe material properties and their influence on IR FPA performance." Photodetectors: Materials and Devices. Vol. 2685. International Society for Optics and Photonics, 1996.

[7] ROGALSKI, Antony. HgCdTe infrared detector material: history, status and outlook. Reports on Progress in Physics, 2005, 68.10: 2267.

[8] GUO, Shi-ping, et al. Study of molecular beam epitaxial growth and optical characteristics of HgCdTe. Acta Physica Sinica (Overseas Edition), 1996, 5.5: 370.

INVESTIGATION AND IMPROVEMENT OF MECHANICAL DEFORMATION BEHAVIORS AND DEPRESSION RESISTANCE OF CONCRETE STEEL BARS

C. Karpuzoglu[1], U. Cengiz[2*]

[1]*Department of Bioengineering & Materials Science Engineering, Canakkale Onsekiz Mart University, Canakkale, Turkey*

[2] *Chemical Engineering Department, Canakkale Onsekiz Mart University, Canakkale, Turkey*

E-mail: ceyhunkarpuzoglu@hotmail.com

Abstract

The main factors affecting the mechanical properties of ribbed concrete steel (RCS) bars are chemical structure and production techniques. Standards have been characterized depending on chemical structure and production techniques for many different types of depression resistant ribbed concrete throughout the world. However, there is a certain uncertainty for the depression resistant ribbed concrete steel. The purpose of this study is investigation of the production techniques and steel chemical structure effect on steel bars resistant to earthquakes. In addition, a new standard about depression resistant ribbed concrete steel production is also be reported in this study. Steel logs having different type chemical structure were provided from ICDAS steel hanes. Ribbed concrete steel bars with a diameter of 16 mm were produced by 3 different production technique (hot rolling, thermex process and alloying method with vanadium). Thus the effect of different production techniques on the resistance to depression is investigated. In addition, chemical structure differences of steel logs was also investigated to produce ribbed concrete steel bars with a diameter of 16 mm by hot rolling method. The mechanical test of steel bars were characterized by tensile strength, elongation at break, fatigue test. As a results of chemical analyses and mechanical test is showed that the mechanically more robust steel bars having 0.19 C % and 0.57 Mn % were produced by the hot rolling method. The best standard range for steel bars against depression resistance of concrete steel bars is found as min yield strength 320 MPa, min tensile strength 500 MPa and chemical content 0.18-0.22 C % and 0.55-0.70 Mn %.

Keywords: Mechanical Deformation, Depression Resistance, Concrete Steel Bars

1. INTRODUCTION

As construction sector is developing day by day, low-carbon ribbed concrete steel (RCS) to be used, specify the quality of buildings durable to natural disasters. These steels establish the strength of the building by acting as the main framework within the steel blocks. This requires the RCS within the structure to be high mechanical competent. [1] According to the earthquake regulations for the structures to be built in disaster areas, it is indicated that the RCS's tensile unit elongation is required not to be less than 10% and the average yield strength is required not to be more than 1,3 times according to the projected characteristic yield strength concerning to the steel standard. [2]. In addition, it is indicated that the tested average tensile strength is required to be 1,25 times greater than the tested average yield strength. [2] Today, steel is produced from ore and scrap steel. Producing steel from ore materializes in two stages. In the first stage, liquid raw iron obtained from blast furnace, converts to liquid raw steel in the basic oxygen converter. In the second stage; it is required to be formed into its steel chemical structure by secondary metallurgical methods. Producing steel from scrap, involves electrical arc furnace and secondary metallurgical stages. Liquid raw steel produced from ore and scrap is transformed into billets at single stage with by continuous casting. Later, the billets are rolled. [3] During rolling or thermal processes after then, RCS bars having different mechanical features are produced. [4] Production methods are classified according to their temperature difference as rolling, replenished alloying and Thermes processing.

From 1100 to 1200^{o}C tempered billets in producing RCS bars by hot rolling are provided for reaching the required size and density by applying pressure through rotatory cylinders. By applying pressure on them, the required sizes and densities are obtained. After reaching the required density, the average rolling exit temperature differs from 800 to 1000^{o}C and the micro structure of the formed steel consists of ferrite + perlite. [5] If the RCS is producing bars by using replenished alloying, the rolling exit temperature must be restored at a temperature from 750-850^{o}C by reducing the speed of rolling. Within the process, during casting, trace amount of alloying elements such as Niobium, Vanadium and Cobalt are added and the RCS mechanical forces are enhanced. [6] Producing RCS bars with Thermex Process method is the 1972 Belgium patented Tempcore Process's improved state with today's technology. Within this process, hot rolled RCS's mechanical resistance is increased by controlled cooling water and iodized water. The most important feature of this process is increasing the mechanical resistance and weldability of materials without the necessity of adding replenished alloying elements by keeping the carbon and manganese values at a low rate. [7] Across the world, there are many specified standards for many different

earthquake-resistant RCS's which are produced with different methods and between the ranges of chemical values. [8] In Table 1, there is a summary of these standards.

Table 1. International RCS Standards

Standard Country	Standard Title	Date of Issue	Yield Strength	Tensile Strength	RM/RE Ratio	C %	S-P %	Cu %	N %
TURKEY	S 220	TS728/2010	220	300	1.20	0.25	0.050	-	0.012
	S 420		420	500	1.15	0.45	0.050	-	0.012
	B 420 B		420	-	1.08	0.22	0.050	0.80	0.012
	B 420 C		420	-	1.15-1.35	0.22	0.050	0.80	0.012
	B 500 B		500	-	1.08	0.22	0.050	0.80	0.012
	B 500 C		500	-	1.15-1.35	0.22	0.050	0.80	0.012
ENGLAND	GR500B	BS4449/2005	500-650	1.06*Re	1.08	0.22	0.050		0.012
	GRB500C		500-650	1.15*Re	1.15-1.35	0.22	0.050		0.012
GERMANY	DIN B 500 B	DIN 488/ 2009	500-650	550	1.05	0.22	0.050	0.60	0.012
FRANCE	NF B 500 B	NF/2007	500	540	1.08	0.22	0.050	0.80	0.012
PORTUGAL	A 400 NR	2008	400	460	1.08	0.22	0.050	0.80	0.012
	A 500 NR		500	550	1.08	0.22	0.050		0.012
SPAIN	B 500 S	1996	500	550	1.05	0.22	0.050		0.012
	B 400 S		400	440	1.05	0.22	0.050		0.012
	B 500 SD	2000	500	575	1.25	0.22	0.050		0.012
	B 400 SD		400	480		0.22	0.050		0.012
ITALY	B450C	1966	450	540	1.15-1.35	0.22	0.050	0.80	0.012
THE UNITED STATES	GR 40	2004	300	500			0.060		
	GR 60		420	620			0.060		
ISRAEL	S 400	2000	400	500	1.25	0.38	0.05-0.055		
	S 400 W		400	500	1.25-1.45	0.22	0.05-0.060		
	S 500 W-C		500	600	1.15-1.35	0.26	0.05-0.06		
ROMANIA	PC 52	1989	355	510		0.22	0.045		
	PC 60		420	590		0.27	0.045		
	OB 37		255	360		0.23	0.045		
THE NETHERLANDS	BRL B 500B	2010	500	540	1.08	0.22	0.050	0.80	0.012
CANADA	400 R	2009	400	540	1.15	0.33	0.060		
	500 R		500	675	1.15	0.33	0.060		
	400 W		400	540	1.15	0.30	0.053-0.043		
	500 W		500	625	1.15	0.30	0.053-0.043		
PARAGUAY	AP 500 DN	2009	500	550	1.10	0.35	0.050		
	AP 400 DN		400	462	1.10	0.35	0.050		
BRAZIL	CA 50	2007	500	540	1.08				
	CA 60		600	660	1.08				
CHILE	A 440-280H	2006	280	440	1.25				
	A 560-350H		350	560	1.25				
	A 630-520H		420	630	1.25				

If we examine the International RCS standards, we will see that the yield strength (Re) between the range of 220-500 MPa, the tensile strength (Rm) between 300-675 MPa and the tensile strength according to the yield strength (Rm/Re) changes at a ratio of 1,08 to 1,45 (Table 1). When the chemical structure values are examined, it occurs that the amount of C% changes between the range of 0,22-0,35 by weight, the S% and P% amounts change between the range of 0,043-0,063 by weight, the amount of N% is 0,012 by weight, the Cu% amount changes between the range of 0,60-0,80 by weight and the carbon %

equivalence (CEQ) ratio changes between the range of 0,50-0,60. The CEQ value is calculated according to equivalence 1.

$$CEQ = C\% + Mn\%/6 + (Cr\% + Mo\% + V\%)/5 + (Ni\% + Cu\%)/15 \quad .....(1)$$

When the international standards consisting strength and chemical ratios that different from each other are examined, there is no obvious information on what kind of chemical structure and mechanical resistances (based on production techniques) of earthquake-resistant RCS bars should be. Therefore, this study is set up on which ranges the steel chemical structure and mechanical features should be in producing earthquake-resistant RCS bars. As a result of this study, a new standard has been suggested for earthquake-resistant RCS bars.

2. MATERIAL AND METHODS

2.1. Material

Within this study, 4 different billets -including 2 billets having the chemical structure but with different production techniques and 2 billets having the same production techniques but chemical structure different- have been used (Table 2). 5 different RCS bars have been produced from these billets in different techniques (Table 3).

Table 2. Production techniques of billets to be rolled

Billet No	Remarks
K-1	The billet to be used in RCS production by hot rolling and Thermex Process.
K-2	The billet to be used in RCS production by Vanadium alloys.
K-3	The billet with dissimilar chemical structure to be used in RCS production by hot rolling process.
K-4	The billet with dissimilar chemical structure to be used in RCS production by hot rolling process.

Table 3. The produced billets and methods of the produced RCS bars

RCS No	Remarks
RCS-1	RCS bars produced from K-1 by hot rolling method.
RCS-2	RCS bars produced from K-1 by Thermex method.
RCS-3	RCS bars produced from K-2 by Vanadium alloy method.
RCS-4	RCS bars produced from K-3 by hot rolling method.
RCS-5	RCS bars produced from K-4 by hot rolling method.

2.2. Method

2.2.1. Chemical Analysis with XRF Technique:

Chemical structures of both billets and RCS samples has been defined by Panalytical brand XRF (Axios max model) device appropriate to the TS 2162 EN 10025 standard [9]. During the chemical analysis of the billets, the sample is carried out by taking liquid steel from the last tank (tundish) where the billets proceed at a temperature of 1600°C. Carrying out a chemical analysis of the RCS's is done by taking a smooth cylindrical cross section with lathed deformed bulges at a size of 100 mm. The chemical analyses have been repeated by taking samples from 3 different parts of the samples and the results have been indicated on the average.

2.2.2. Strength Tests:

2.2.2.1. Tensile Test:

The tensile tests of RCS samples in 16mm diameter and at a size of 60 cm has been carried out with by Walter Bai brand tensile device (W+B 200 model) appropriate to the EN ISO 6892-1 2014 standard [10]. The device views the results of the yield and tensile strengths with a ± 20 kN sensitivity. The tests have been repeated at least 3 times for each RCS sample and the average results have been obtained. The yield strengths of the RCS bars have been calculated by the formula (R_e), $R_e = {}^{P_a}/_{f_0}$ and the tensile strengths have been calculated by the formula (R_m), $R_m = {}^{P_k}/_{f_0}$. The P_a and P_k symbolises the yield and tensile strengths (N), and the f_0 symbolises the first cross sectional area (mm^2) calculated by the elongation weight of the sample. On the other hand, the RCS bars' elongation at Rupture is calculated by the formula $A_t = \left[\frac{(Lu - Lo)}{Lo}\right].100$ and the Real elongation is calculated by $A_{gt} = \left[\frac{(Lu - Lo)}{Lo}\right].100$ +0,3. In formulas, L_u expresses the length (mm) of the sample between two points which is marked after the rupture, and L_0 expresses the first gage length (mm) of the sample. According to the Agt calculation, the L_u has been calculated 50 mm far from the rupture point. [10]

2.2.2.2. Fatigue Test:

The fatigue tests of RCS samples at a diameter of 16 mm and a size of 60 cm with both ends flattened have been carried out by Zwick brand axial fatigue device (Amsler-500 model) appropriate to the EN ISO

15630-1 standard [11]. The device views the fatigue results of the samples with a 0,1% sensitivity. The tests for each RCS sample have been repeated 3 times and the average results have been obtained.

3. **Results and Discussions**

3.1. Chemical Compositions (Spectral Analysis)

The XRF results of the RCS bars produced by billets to be used in tests are viewed in Table 4, and the XRF results of RCS bars' post-production are viewed in Table 5. According to the chemical analysis results carried out, it has been viewed that the amount of carbon in the RCS bars produced by hot rolling method has decreased at a ratio of 0,01%, and the amount of carbon in the RCS bars produced by Thermex Process has increased at a ratio of 0,01% (Table 4 and 5). No chemical changes have been detected in RCS bars produced by Vanadium alloys. As viewed in Table 5, the carbon equivalences of Bar No. 1, 2 and 3 have been resulted under 50%, and the carbon equivalences of Bar No. 4 and 5 have been resulted over 50%. According to the TS 2126 standard, the steels with a carbon equivalent under 50% can be used as construction materials due to their weldability. [9] Accordingly, while the RCS bars No. 1, 2 and 3 are appropriate to be used in construction steels, No. 4 and 5 are inappropriate due to not being weldable.

Table 4. XRF results of billets to be rolled

Billet No	C%	Mn%	Si%	P%	S%	Ni%	Cr%	Mo%	V%	Cu%	Sn%	N%	B%	Fe%	CEQ %
1	0.19	0.57	0.17	0.016	0.007	0.10	0.13	0.02	0.002	0.34	0.013	0.010	0.011	<98.10	34.47
2	0.19	0.57	0.17	0.016	0.007	0.10	0.13	0.02	0.075	0.34	0.013	0.010	0.011	<98.08	35.93
3	0.29	1.26	0.21	0.024	0.022	0.11	0.13	0.02	0.082	0.33	0.07	0.014	0.009	<98.05	56.12
4	0.45	0.96	0.20	0.037	0.017	0.10	0.14	0.02	0.003	0.46	0.014	0.011	0.010	<98.02	67.99

Table 5. XRF results of RCS bars used in post-production tests

Bar No	C%	Mn%	Si%	P%	S%	Ni%	Cr%	Mo%	V%	Cu%	Sn%	N%	B%	Fe%	CEQ %
1	0.18	0.56	0.17	0.016	0.007	0.10	0.13	0.02	0.002	0.34	0.013	0.010	0.011	<98.10	.
2	0.20	0.57	0.17	0.016	0.007	0.10	0.13	0.02	0.002	0.34	0.013	0.010	0.011	<98.10	**%34.47**
3	0.19	0.58	0.17	0.016	0.007	0.10	0.13	0.02	0.075	0.34	0.013	0.010	0.011	<98.08	**%35.93**
4	0.28	1.25	0.21	0.024	0.022	0.11	0.13	0.02	0.082	0.33	0.007	0.014	0.009	<98.05	**%56.12**
5	0.44	0.98	0.20	0.037	0.017	0.10	0.14	0.02	0.003	0.46	0.014	0.011	0.010	<98.,02	**%67.99**

3.2 Tensile Test

The tensile strength test applied on RCS bars include the tensile strength, yield strength, elongation at rupture and the real elongation results. These results have been repeated 3 times and their average values have been summarized in Table 6. As can be seen in this table, it is also seen that the chemical structures of materials and the variations in production managements directly affect the yield, tensile strength and elongation-real elongation % ratios. As shown in this table, the first 3 RCS bars have been produced by different techniques from billets having the same chemical analysis values. According to the tensile test results, the yield strength of the RCS bar (Bar No. 2) produced by Thermex Process method has been viewed

as the RCS bar having the highest yield strength at a value of 575,3 MPa. According to the Thermex Process, the yield strength of the RCS bar (Bar No. 3) produced by Vanadium alloy method has been detected 5% lower and the yield strength of the RCS bar (Bar No. 1) produced by hot rolling method has been detected 40% lower (Table 6). When the yield strength of RCS bars produced by hot rolling techniques are compared, the RCS bar (Bar No. 5) having the highest yield strength as C% at a ratio of 0,44 has been detected at a value of 487,1 MPa. This value is 5% higher according to the RCS bar (Bar No. 4) containing 0,28 of C% and is also 32% higher according to the RCS bar (Bar No. 1) containing 0,18 of C% (Table 6).

According to the tensile test results, the tensile strength of the RCS bar (Bar No. 2) produced by Thermex Process method has been viewed as the RCS bar having the highest tensile strength at a value of 743,1 MPa. According to the Thermex Process, the tensile strength of the RCS bar (Bar No. 3) produced by Vanadium alloy method has been detected 8% lower and the tensile strength of the RCS bar (Bar No. 1) produced by hot rolling method has been detected 32% lower (Table 6). When the tensile strength of RCS bars produced by hot rolling techniques are compared, the RCS bar (Bar No. 5) having the highest tensile strength as C% at a ratio of 0,44 has been detected at a value of 719,7,1 MPa. This value is 2% higher according to the RCS bar (Bar No. 4) containing 0,28 of C% and is also 28% higher according to the RCS bar (Bar No. 1) containing 0,18 of C% (Table 6).

According to the percentage elongation measuring results, the percentage elongation value of the RCS bar (Bar No. 1) produced by hot rolling method has been detected at an average of 28,4%. This value is 40% higher according to the RCS bar (Bar No. 3) produced by vanadium alloys, 25% higher according to RCS bar (Bar No. 2) produced by Thermex Process (Table 6). As can be seen, in RCS bars produced by hot rolling method, the RCS bar (Bar No. 1) containing a C% amount of 0,18 has a higher elongation ratio of 28,4%, the RCS bars (Bar No. 5) containing a C% amount of 0,44 has a 64% higher ratio and the RCS bars (Bar No. 1) containing a C% amount of 0,28 has a higher ratio of 50% (Table 6).

According to the percentage real elongation measuring results, the percentage real elongation value of the RCS bar (Bar No. 1) produced by hot rolling methods has been detected at an average of 19,4%. This value is 52% higher according to the RCS bar (Bar No. 3) produced by vanadium alloying method, 37% higher according to the RCS bar (Bar No. 2) produced by Thermex Process (Table 6). As can be seen, in RCS bars produced by hot rolling method, the RCS bar (Bar No. 1) containing a C% amount of 0,18 has a higher real elongation ratio of 19,4%, the RCS bars (Bar No. 5) containing a C% amount of 0,44 has a 36% higher ratio and the RCS bars (Bar No. 1) containing a C% amount of 0,28 has a higher ratio of 43% (Table 6).

Table 6. The tensile test results of the produced RCS bars

Bar No	Unit Weight (g/mm)	Yield Strength (Re-MPa)	Tensile Strength (Rm-MPa)	Rm/Re Ratio	Elongation Amount %	Agt Amount %
1	1526	340.9	520.4	1.58	28.4	19.4
2	1588	575.3	743.1	1.29	21.1	12.7
3	1582	554.4	687.7	1.24	17.8	10.9
4	1578	466.3	727.1	1.55	14.7	12.1
5	1569	487.1	719.7	1.63	13.2	11.5

3.3 Fatigue Test

The axial fatigue strength test applied on RCS bars according to the EN ISO 15630-1 method include the results of fatigue number of cycles. These results have been repeated 3 times and their average values have been summarized in Table 7. As shown in this table, the first 3 RCS bars have been produced by different techniques from billets having the same chemical analysis values. It is also seen that the chemical structures of materials and the variations in production managements directly affect the fatigue strength (Table 7). According to the axial fatigue strength test, the bar (Bar No. 1) produced by hot rolling method has obtained the highest fatigue strength with an amount of 4 400 086 cycles. The bar (Bar No. 1) produced by hot rolling method is 52% higher of axial fatigue strength than a bar (Bar No. 2) produced by Thermex Process and is 58% higher than a bar produced by Vanadiaum alloy method. (Table 7). When the axial fatigue strength of RCS bars produced by hot rolling techniques are compared, the RCS bar (Bar No. 1) having the highest axial fatigue strength as C% at a ratio of 0,18 has been detected as 4 400 086 cycles. In bars produced by hot rolling methods, the bar (Bar No. 1) containing 0,18 of C% has been detected 56% higher than the bar (Bar No. 5) containing 0,44 of C% and 51% higher than the bar (Bar No. 4) containing 0,28 of C% (Table 7).

Table 7. The fatigue test results of the produced deformed concrete steel bars.

Bar No	Maximum Load (KN)	Minimum Load(KN)	Number of Standard Cycles	Number of Cycle Rupture	Frequency (cycle/per sec.)
1	60,30	23,13	$2x10^6$	4 400 086	54,2
2	60,30	23,13	$2x10^6$	2 120 436	52,8
3	60,30	23,13	$2x10^6$	2 009 073	53,2
4	60,30	23,13	$2x10^6$	2 150 905	52,9
5	60,30	23,13	$2x10^6$	2 084 753	53,0

4. CONCLUSION

Within this study, the earthquake resistances of 3 different deformed concrete steel bars produced by billets having the same chemical analysis and billets having different chemicals have been compared. In consequence of these experimental studies;

1) According to the chemical analysis results, while the C% ratio of the RCS bars produced by hot rolling method decreases at an amount of 0,01, it has been detected that the C% ratio of steel bars produced by Thermex Process increases at an amount of 0,01. As weldability (according to TS 2162 standards), while Bar No 1, 2 and 3 are weldable bars, Bar No 4 and 5 are included in the nonweldable status.

2) The tensile results show that the yield and tensile strengths of RCS bars produced by Thermex Process have increased according to RCS bars produced by hot rolling and vanadium alloy methods. While the increase of the amount of C% in weight in RCS bars produced by billets having different chemical analyses increase the yield and tensile strengths in bars, it decreases the elongation % and the Agt %. It has been detected that the increase of the amount of Mn% in weight has increased the tensile strength in bars. An increase of the amount of V% in weight having increased the tensile strength in bars and a positive affect in the elongation percentage has been detected. According to the earthquake regulations prepared for buildings to be constructed on disaster areas, the importance of ductility in RCS bars is emphasized. When the ratio of the tensile strength according to the tensile strength and the real elongation percentage values are considered on this basis, it has been detected that the RCS bar (Bar No. 1) produced by hot rolling is 37% more earthquake-resistant than the RCS bar (Bar No. 2) produced by Thermex Process and is 52% more resistant than the RCS bar (Bar No. 3) produced by Vanadium alloy method. When the ductility features of billets with different chemical structures and RCS bars produced by hot rolling are compared; it has been detected that the RCS (Bar 1) with C - Mn ratios percentage at a weight of 0,19-0,57 is 36% more earthquake-resistant than the RCS bar (Bar 5) with a percentage at a weight of 0,44-0,9 and 43% more resistant than the RCS bar (Bar 4) with a percentage at weight of 0,28-1,26.

3) According to the fatigue test results, the RCS bars provide us information about their strengths in abrasion after years and vibrations during earthquakes or during daily vibrations (such as in major bridges). According to this, it has been detected that hot rolled RCS bar (Bar No. 1) has 52% higher axial fatigue strength than the RCS bar (Bar No. 2) produced by Thermex method and 58% higher than the RCS bar produced by Vanadium alloy method.

In consequence of the tests, a new standard has been formed for an earthquake-resistant RCS bar. The standard values have been summarized in the following table.

C%	Mn%	S-P% (max)	Cu% (max)	N% (max)	CEQ% (max)	Min. Yield Strength (MPa)	Min. Tensile Strength (MPa)	AGT% (min)
0.18-0.22	0.5-0.8	0.5	0.5	0.5	45	320	500	15

It has been considered that a RCS bar appropriate to this table would be more resistant especially in earthquake areas and on bridges where there is high vibration

REFERENCES

[1] Badem, M.T., The Mechanical Features of Concrete Steel and The Concrete Steel Used in Denizli, Master's Thesis, Pamukkale University Institute of Science and Technology, Denizli, 2001.
[2] The Regulation Concerning Structures to be Constructed on Disaster Areas, Earthquake Regulations of Ministry of Public Works and Settlement, 14.07.2007
[3] Schulz, E., Ameling, D., Gerstenberg, B., Hüffken, E., Peters, K.H., Simon, R.W, "State of the Flit and Development Potential of the Currently Applied Metallurgical Production Processes", Metallurgical Plant on Technology, Volume 5, 32-49, 1990.
[4] Simon, P., Economopoulos, M., Nilles, P., 1984, Tempcore, an Economical Process for the Production, Metallurgical Plant and Technology, 3/84, 80 –93.
[5] Studying the cyclic deformation actions of concrete steel bars, Master's Thesis, Engineer Abdulkadir UYSAL/2015
[6] Kankam, C.K., "Bond Strength of Reinforcing Steel Bars Milled from Scrap Metals", Materials and Design, Volume 25, 231-238, 2004.
[7] Kankam, C.K., Asamoah, M., "Shear Strength of Concrete Beams Reinforced with Steel Bars Milled from Scrap Metals", Materials and Design, Article in press, 2005
[8] EN 10080-24 2008 "Rolling Mill Products Manufactured by Constructional Steels-Technical Conditions of Delivery", ISO 9001 2008.
[9] TS 2162 EN 10025, "Hot Rolling Products Manufactured by Unalloyed Constructional Steels-Technical Conditions of Delivery", Turkish Standards Institute, Ankara, 1996.
[10] EN ISO 6892-1 2014 "Metallic Materials–Tensile Test–Test Method at Ambient Temperature" ISO 9001 2014.
[11] EN ISO 15630-1 2011 "Metallic Materials–Fatigue Test–Ambient Method" ISO 9001 2011.
[12] ASTM –E45 American Standard for Use with Plain Carbon Steel Bars for Concrete Reinforcement
[13] TS 282- EN 910 "Rolling mill Products Manufactured by Unalloyed Constructional Steels-Fold Test", Turkish Standards Institute, Ankara, 2014.
[14] EN ISO 10002-1 2010 Contract of Rib Design of Constructional Steels ISO 9001 2010

PRODUCTION OF POLYMERIC FIBER REINFORCED GEOPOLYMER COMPOSITE MATERIAL

B. Kartal[1], U. Cengiz[2]

[1] *Department of Energy Resources and Management, Canakkale Onsekiz Mart University, Canakkale, Turkey*
[2] *Chemical Engineering Department, Canakkale Onsekiz Mart University, Canakkale, Turkey*
E-mail: burcukartal17@gmail.com

Abstract

In this study, the structural and material characteristics of synthetic fiber reinforced geopolymer concrete is investigated. Polymer-fiber composite process has developed as the most cost-effective method of choice for producing pressure-retaining structures from fiber-reinforced polymeric composites such as pipes and tanks for the transport / storage of fluids in the industry. Fiber reinforced polymer, which is produced in the form of fabric and laminate and widely used in many different areas, must be an excellent adherence between Fiber-reinforced polymer wrapped material interface to exhibit composite and monolithic behavior. Geopolymers are noncrystal alumina silicate polymers formed by the polycondensation reaction of reactive alumina silicate materials and silicate solutions at normal temperature conditions. The mechanism is based on the reaction of different SiO_2 - Al_2O_3 - Na_2O or K_2O and H_2O ratios.

Materials such as metakaolin, fly ash, volcanic glass and perlite are used as reactive alumina silicate materials. Alkaline active geopolymers produced from waste materials such as fly ash or blast furnace slag are particularly advantageous due to environmental sustainability and low cost, but their durability and functionality remain a matter of further study. Geopolymer and reinforced composite materials are promising from this point of view due to their advantages. Depending on the chemical composition of the fiber reinforced geopolymer materials, source materials and activators, can be used in a variety of applications such as sewer piping products fire and chemical resistant wall panels, wall units, protective coatings and repair materials, shotcrete and high performance fiber reinforced laminates.

This study focused on the effect of fibres on mechanical and flexural performance of metakaolin based geopolymer concrete. SiO_2/Al_2O_3: 4 moles, Na_2O /SiO_2: 0.35 moles, H_2O/Na_2O: 18 moles ratio was fixed. Thermal and mechanical characterization studies was carried out by TGA and compressive and flexural strength tests. The structure analyses of geopolymer and its starting materials were also investigated by XRD, XRF and FTIR. The fiber ratio was arranged from 0 to 1 % wt. The mechanical properties of fiber reinforced geopolymer materials were also investigated.

Keywords: Geopolymer, Fiber, Composite, Reinforced

1. INTRODUCTION

With today's rapidly developing industry, population growth and the increasing consumption demand it brings, environmental protection and sustainable design work are expanding widely. One of the most important problems in industrial activities to improve the quality of human life is global warming. The need for ordinary portland cement (OPC), which has an annual consumption of 130 million tonnes in the world, is increasing every year, and studies [16-21] show that producing 1 tonne of OPC requires about a ton of CO_2 emissions. When 5% of global CO_2 emissions originate from OPC production [16] and when environmental damage is assessed, an alternative "green" material needs to be sought to increase awareness of greenhouse emissions from Portland cement production [1]. Although it has good mechanical properties ordinary cement is insufficient in some applications in the field of construction like flammability and a surface degradation. However, along with the expected performance of engineering applications in parallel with developing world standards, OPC have become unable to respond to needs.

Geopolymers are alternative new materials with no such disadvantages [2-16-21]. Their advantages are the low energy cost of materials, less greenhouse gas release, pressure resistance, high temperature stability, low thermal conductivity, resistance to fire and high strength in early ages compared to concrete and similar products material industry. Geopolymers are produced at low temperatures because they require a lower CO_2 release in about 62-66% of OPC [4]. and are considered green cement [7-8], as a matrix for a wide variety of fibers [17]. If the produced geopolymer is to work against the force, this situation must be clearly defined and strengthened. This goal can be achieved by developing "green materials" through the use of a fiber-reinforced geopolymer composite natural fiber [18]. The advantages of natural fibers in composites with high mechanical performance, which have attracted much attention in recent years, are low density, high bending strength, bendability and flexibility [3-6-10]. Other advantages result from the biodegradable, renewable and recyclable nature of natural fibers [16]. Based on these properties, homogeneously dispersed fibers in concrete become an attractive reinforcement for these composite systems.

In this study, high CO_2 emission and high energy requirement of the changing industry can be met by replacing cement with a more robust, environmentally friendly construction material; studies on the importance of polymeric fiber reinforced geopolymer composite material production have been investigated in order to overcome the problems of global warming caused by greenhouse gases.

2. MATERIAL AND METHODS

Metakaolin was purchased from Kaolin Industrial and Minerals A.S. (Istanbul). The composition of the metakaolin, as determined by using X-RAY fluorescence (XRF) spectrophotometer is listed in Table 1. Sodium hydroxide pellets was used as the alkaline source and was purchased from ISOLAB chemicals. Sodium silicate used in experimental studies was supplied by Sodel Silicate Chemistry A.S. The product is obtained by reacting the silica source with sodium hydroxide under heat and pressure. The resulting liquid product is filtered. Alkaline glass water, known as 2 modules, was used in the studies. MODULE for silicate: % SiO_2 / Na_2O ratio. The density of the product is 1.50 gr / lt.

Table-1. Chemical composition of metakaolin using XRF

Compound*	% Weight	Standard Deviation	Element	% Weight	Standard Deviation
SiO_2	51.97	0.25	Si	24.30	0.12
Al_2O_3	43.52	0.25	Al	23.03	0.13
Na_2O	0.969	0.048	Na	0.719	0.036
MgO	0.917	0.046	Mg	0.553	0.028
Fe_2O_3	0.842	0.042	Fe	0.589	0.029
TiO_2	0.563	0.028	Ti	0.338	0.017
Cl	0.502	0.025	Cl	0.502	0.025
K_2O	0.433	0.022	K	0.360	0.018
CaO	0.146	0.007	Ca	0.104	0.005

* The percent that was under the % 0.1 didn't added this table.

The prescriptions of geopolymers are shown in Table 2. In accordance with the recipe ratios, the NaOH were homogenized by mixing in a magnetic stirrer until dissolved in (Na_2SiO_3) glass water. When completely dissolved, water was added and stirring continued for 15 minutes. Thus, the alkali solution of the geopolymer mortar was prepared. Since the mixture of NaOH and Na_2SiO_3 brings an exothermic reaction to the temperature rising up to 90 ^oC, the cooling of the prepared alkali solution is important for controlling the geopolymerization. The solution cooled to room temperature is added to the powdered metakaolen and mixed. The obtained mortar is poured into a steel mold of 4x4x16 cm^3. Geopolymerization is a condensation polymerization and the added water facilitates the process and exits at the end of geopolymerization. For this reason, during the geopolymerization caused by air-related water loss is prevented by a plastic cover as it causes cracks and dryness. For production of fiber reinforced geopolymer composites proper amount of fiber added into the metakaolin powder. In 7. Curing day geopolymer bricks sent for a mechanical test to Ak-Kim Chemical Company in Yalova. Compressive and flexural strengths measured by ELE International machine.

Table-2. Geopolymer recipe and trial codes

Trial Codes	INPUT MATERIALS (GRAMS)					MOLAR RATIOS			
	Metakaolin	Sodium Silicate	NaOH	KOH	H_2O	Si/Al_2	Na_2/Si	H_2O/Na_2O	Na_2/Al_2
G1	10	2.7	1	1.3	5.0	2.36	0.19	20.5	0.45
G6	10	2.7	2.3	-	5.0	2.36	0.36	11.3	0.85
B2	10	3.5	2.2	-	4.5	2.46	0.36	11.0	0.88
B4	10	8.2	1.8	-	2.9	3.00	0.33	11.0	1.00
B6	10	-	3.3	-	7.5	2.05	0.49	11.1	1.01
B7	10	3.9	2.6	-	5.3	2.50	0.40	11.0	1.00
B8	10	12.5	1.1	-	0.6	3.50	0.29	11.0	1.01

3. RESULTS AND DISCUSSION

The mechanical test results were given in Table 3. In this table was shown that the SiO_2/Al_2O_3 ratio as arranged between 2 to 3 and their Flexural and compressive strength results.

Table-3. Geopolymer bricks mechanical test results

Samples	SiO_2/Al_2O_3:	M/Al:	Flexural Strength (MPa)		Compressive Strength (Mpa)	
			maksimum	stress	maksimum	Stress
B2	2.5	0.88	8.0	18.8	16.5 – 25.1	10.3 – 15.6
B2 F12	2.5	0.88	16.1	37.8	36.7 – 37.0	23.0
B4 m54	3.0	1.0	9.2	21.6	66.3 – 64.7	41.5 – 40.4
B6	3.5	1.0	20.5	48.1	86.5 – 82.2	54.0 – 51.3
B4	3.0	1.0	16,5	26,9	76.6 – 72.9	47.8 – 45.6
B7	2.5	1.0	12.3	28.9	37.1 – 33.2	23.2 – 20.7
B8	2.0	1.0	8.8	20.6	29.1 –21.2	18.2 – 13.2
G1	2.4	0.85	8.3	19.5	36.1 - 38.6	22.6 – 24.1
G1 (ac)	2.4	0.85	N/A	N/A	12.9 – 11.6	7.9 – 7.3
G1 m54	2.4	0.85	N/A	N/A	15.7	9.8
G6 (ac)	2.4	0.85	7.0	16.4	15.8 – 19	9.8 – 11.8

The addition of polypropylene fibers F12 increased the compressive strength and the flexural strength of the geopolymer composite 50% respectively to control sample. Despite the decrease in compressive strength in other fiber-reinforced geopolymer samples, it is considered that the selected F12

fiber is well bonded to the geopolymer because of the high fiber amount in this sample [22]. The M54 fiber caused a 50 % decrease in the compressive strength of the geopolymer for the B4 sample and 12% for the G1 sample. The small amount of air pockets around the fibres could be the main reason for the observed strength decrease [18].

To observe the strength effect of the ambient condition of curing in the geopolymers, the G1 sample was left to the open environment. The bending strength of the G1 sample, which is open to the surface, is so small that it can't be read on the device, while the compressive strength is also decreased by 60 %. G6 is containing only NaOH and G1 containing NaOH and KOH as alkali in the mixture in order to see the change of the environment conditions on curing depending on the used alkali substance they were left to harden in the open environment the potassium effect on the geopolymer structure was observed [16]. This phenomenon may be attributed to the bigger hydration energy of sodium than potassium, which induces a lower amount of free water in the mixture and explains why sodium-containing G6 has higher pressure resistance [20]. It is understood that the compressive strength of geopolymers varies under different hardening conditions. At the same time, the presence of unreacted raw materials may weaken the solid structure of geopolymers, for example, large pores and cracks occur in the presence of excess water [22].

In order to determine the importance of SiO_2 concentration, recipe was prepared by keeping H_2O / Na_2O: 11 and Na/Al: 1 ratios constant according to different SiO_2 / Al_2O_3 ratios and the results showed that in high SiO_2 concentrations the compressive strength increased as seen in (Fig 1.), (Fig. 2.). As the amount of Na_2SiO_3 within the sample rises, it provides more Si content to the geopolymer mortar thus improving the strength results corresponding to the literature.

Chen et al. have studied the effect of SiO_2/Al_2O_3 in the range of 2.0, 2.5, 3.0, 3.5 and 4.0 by adding silica fume in mixture on the mechanical properties and microstructure of metakaolin-based geopolymer. It was found that high aluminum content has low mechanical properties [4]. Similar increase in ambient temperature mechanical strength of geopolymer samples with increase in Si/Al molar ratio has also been observed in other literatures [11-14-23].

Lahoti et al. investigated the effect of variation in Si/Al molar ratio of metakaolin geopolymers and the compressive strength of samples increased with increasing Si/Al molar ratio from 1.03 to 2.0 show the same trend with our mechanical strength test results [15].

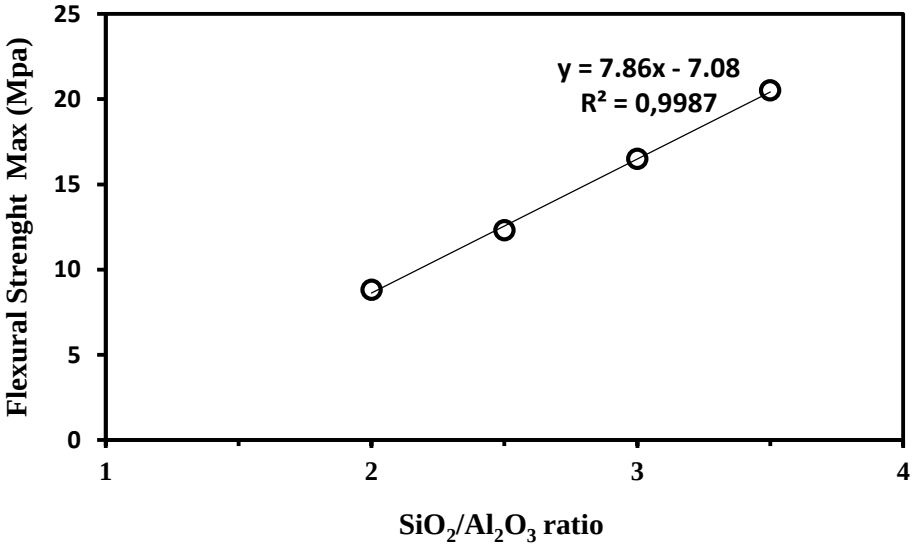

Fig. 1. Geopolymer bricks mechanical flexural strength

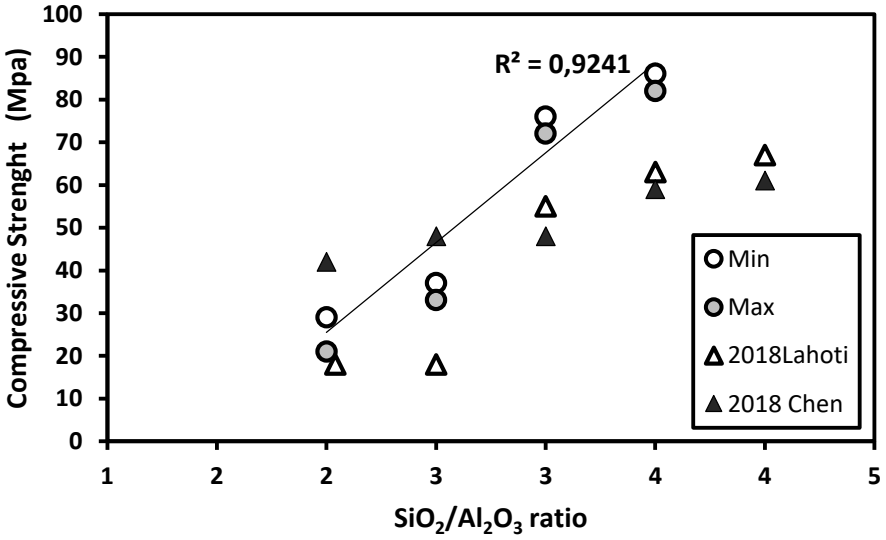

Fig. 2. Geopolymer bricks mechanical compressive strength

Both of the figure were indicated that increase in the SiO_2/Al_2O_3 ratio resulted in increase in the Flexural Strength (Fig 1) and Compressive strength (Fig. 2.)

4. CONCLUSION

Results showed that the addition of fibers decreased the flexural strength and the compressive strength due to small amount of air pockets around the fibers with respect to control samples. Sodium-containing geopolymers has higher pressure resistance than potasium-containing geopolymers as alkali hardener in the mixture due to the lower amount of free water in the mixture. High SiO_2/Al_2O_3 ratios; decreasing the viscosity while increasing the compressive strength and flexural strength of the bricks.

ACKNOWLEDGMENTS

This work was supported by Çanakkale Onsekiz Mart University the Scientific Research Coordination Unit, Project number: FYL-2018-2469. The authors would like to thank AK-Kim chemical industry and Mr. Kamil Özgür and Miss. Şeyma Yılmaz to providing the mechanical test of geopolymer materials

REFERENCES

[1] Ali, H., Lynn, P., Elina, L., Emerging Energy-Efficiency and CO2 Emission-Reduction Technologies for Cement and Concrete Production: A Technical Review, Renewable and Sustainable Energy Reviews, 16, 6220–6238, 2012.

[2] Barbosa, V.F.F., MacKenzie, K.J.D., Thaumaturgo, C., Synthesis and characterisation of materials based on inorganic polymers of alumina and silica: sodium polysialate polymers, Int. J. Inorg. Mater., 2, 4, 309-317, 2000.

[3] Bohlooli, H., Nazari, A., Khalaj, G., Kaykha, M.M., Riahi, S., Experimental Investigations and Fuzzy Logic Modeling of Compressive Strength of Geopolymers with Seeded Fly Ash and Rice Husk Bark Ash, Compos. Part B, 43, 3, 1293-1301, 2012.

[4] Chen, X., Niua, Z., Wanga, J., Zhua, G.R., Zhoua, M., Effect of Sodium Polyacrylate on Mechanical Properties and Microstructure of Metakaolin-Based Geopolymer with Different SiO2/Al2O3 ratio, Ceramics International, 44, 18173–18180, 2018.

[5] Davidovits J., False Values on CO2 Emission for Geopolymer Cement/Concrete Published in Scientific Papers, Technical Paper #24, Geopolymer Institute Library,2015.

[6] Davidovits J., Geopolymer Chemistry and Applications, 3rd edn. Institut Ge´opolyme´re, Saint-Quentin, France, 2011.

[7] Duxson P., A. Fernandez-Jimenez, Provis, J.L., Luckey, G.C., Palomo, A., van Deventer, J.S.J., Geopolymer Technology: The Current State of the Art, Mater. Sci., 42, 2917-2933, 2007.

[8] Essaidi, N., Samet, B., Baklouti, S., Rossignol, S., Feasibility of producing geopolymers from two different Tunisian clays before and after calcination at various temperatures, Appl. Clay Sci., 88–89, 221-227, 2014.

[9] Ferreira, J.A.M., Capela, C., Costa, J.D., A Study of the Mechanical Properties of Natural Fiber Reinforced Composites, Fibers Polym., 11, 8, 1181-1186, 2010.

[10] Hammell, J.A., Balaguru, P.N., Lyon, R.E., Strength Retention of Fire Resistant Aluminosilicate–Carbon Composites Under Wet–Dry Conditions, Compos. Part B, 31, 107-111, 2000.

[11] He, P., Wang, M., Fu, S., Jia, D., Yan, S., Yuan, J., Xu, J., Wang, P., Zhou, Y., Effects of Si/Al Ratio on the Structure and Properties of Metakaolin Based Geopolymer Ceramics International, 42, 14416–14422, 2016.

[12] Huntzinger, D.N., Eatmon., T.D., A Life-cycle Assessment of Portland Cement Manufacturing: Comparing the Traditional Process with Alternative Technologies, J. Clean. Prod., 17, 7, 668-675, 2009.

[13] Kriven, W.M., Bell, J.L., Gordon, M., Microstructure and Microchemistry of Fully-reacted Geopolymers and Geopolymer Matrix Composites, Ceram. Trans., 153, 4, 227-250, 2003.

[14] Lahoti, M., Yang, E., Tan, K.H, Narang, P., Mix Design Factors and Strength Prediction of Metakaolin-Based Geopolymer, Ceramics International, 43, 11433–11441, 2017.

[15] Lahoti, M., Wong, K.K., Yang, E., Tan, K.H., Effects of Si/Al Molar Ratio on Strength Endurance and Volume Stability of Metakaolin Geopolymers Subject to Elevated Temperature, Ceramics International, 44, 5726–5734, 2018.

[16] Leong, H.Y., Ong, D.E.L., Sanjayan, J.G., Nazari, A., The Effect of Different Na2O and K2O Ratios of Alkali Activator on Compressive Strength of Fly Ash Based-Geopolymer, Construction and Building Materials, 106, 500–511, 2016.

[17] MacKenzie, K.J.D., Alzeer, M., Synthesis and Mechanical Properties of Novel Composites of Inorganic Polymers (Geopolymers) With Unidirectional Natural Flax Fibres, Appl. Clay Sci., 75, 6, 148-152, 2013.

[18] Nematollahi, B., Sanjayan, J., Shaikh, F.U.A., Comparative Deflection Hardening Behavior of Short Fiber Reinforced Geopolymer Composites, Constr. Build. Mater., 70, 54-64, 2014.

[19] Ozer, I., Soyer-Uzun, S., Relations Between The Structural Characteristics And Compressive Strength In Metakaolin Based Geopolymers With Different Molar Si/Al Ratios, Ceramics International, 41, 10192–10198, 2015.

[20] Ricc, M.A., Mancinelli, R., Botti, A., Bruni, F., Hydration of Sodium, Potassium, and Chloride Ions in Solution and the Concept of Structure Maker/Breaker, The Journal of Physical Chemistry B., American Chemical Society, 2007.

[21] Roy, D.M., Alkali-activated Cements, Opportunities and Challenges, Cem. Concr. Res., 29, 2, 249-254, 1999.

[22] Sabbatini, A., Vidal, L., Pettinari, C., Sobrados, I., Rossignol, S., Control of Shaping and Thermal Resistance of Metakaolin-Based Geopolymers, Materials and Design, 116, 374–385, 2017.

[23] Wan, Q., Rao, F., Song, S., García, R. E., Estrella, R. M., Zhang, Y., Geopolymerization Reaction, Microstructure and Simulation of Metakaolin-Based Geopolymers at Extended Si/Al Ratios, Cement and Concrete Composites, 79, 45-52, 2017.

FABRICATION OF SUPERHYDROPHOBIC SURFACE USING FLUORO-STYRENE COPOLYMERS BY SPRAYING METHOD

B. Kartal[1], Ö.Ünzal[2],U. Cengiz[1,2]

[1]*Department of Energy Resources and Management, Canakkale Onsekiz Mart University, Canakkale, Turkey*

[2]*Department of Bioengineering & Materials Science Engineering, Canakkale Onsekiz Mart University, Canakkale, Turkey*

E-mail: burcukartal7@gmail.com

Abstract

The control of the surface wettability is crucial in many industrial applications and is expressed directly by the contact angle (θ) of a liquid droplet on these surfaces**.** Superhydrophobic surfaces are defined as having water contact angles (WCA) greater than 150° with a low contact angle hysteresis (CAH) value (the difference between advancing *(θ_a)* and receding *(θ_r)* contact angles). CAH value of ideal, flat monolayer surface is equal to zero; however, every surfaces have a CAH value due to the surface roughness, surface chemical heterogeneity or contamination. Superhydrophobic surfaces are used as antifouling surfaces under air or water in many practical applications. Two important principles is valid to synthesis these surfaces: Firstly, a solid surface having low surface free energy must be formed and secondly the roughness of these surfaces must be high to accommodate the air pockets within them.

In the first part of this study, we synthesized fluoroacrylate-styrene (PS-F) copolymers that styrene content is 50 wt % in CO_2-expanded monomer phase [3]. The PS-F polymer was characterized by NMR, FTIR and GPC. In the second part, we prepared superhydrophobic surfaces by applying the spray coating methods using PS and PS-F polymer solution in toluene, and their silica blends. It is found that the superhydrophobic PS-F-silica composite surface contact angle was changed from 100 to 170^o depending on floracrylate content, silica content and spraying time.

Keywords: Superhydrophobic, Fluoro-Styrene, Copolymer, Fiber, Spray coating

1. INTRODUCTION

Superhydrophobic surfaces are defined as the surfaces where water forms a contact angle of larger than 150° and have low contact angle hysteresis [1-3]. These surfaces are used as self-cleaning, water-oil repellent fabrics and biological applications [1-6]. It is well-known that wettability of a surface can be altered by increasing surface roughness and chemical heterogeneity in terms of liquid/solid interfacial area [1-10]. Two important principles are valid for the synthesis of these surfaces: Firstly, a solid surface having low surface free energy must be formed and secondly the roughness of these surfaces must be high to accommodate the air pockets within them [3-5]. Surface morphology alteration at the micro- and/or nanoscale can allow for an air layer to be maintained in the space between the asperities during liquid contact. Known as the lotus effect this result can significantly reduce droplet and fluid flow resistance and it has been successfully employed in creating an array of superhydrophobic surfaces [1-7]. Synthesis of an artificial superhydrophobic surface was first reported by using alkylketene dimer wax [8] in 1996, and later superhydrophobic surfaces were obtained by a phase separation method [11], electrospinning [12], lithographic methods [13], sol-gel method [14], chemical vapor deposition [15], etching [16] and spraying [17].

The objective of this study is the synthesis of a superhydrophobic surface by coating the fluoro (meth) acrylate-styrene (TMS) copolymers and polystyrene (PS) onto glass slide in a spray process. Hierarchical and heterogeneous polymeric surfaces having high water repellent properties were formed using previously synthesized TMS copolymers [18] with PS at room temperature. These hierarchical surfaces were prepared by a spray coating process where toluene was used as the solvent. Hierarchical heterogeneous surfaces were imaged by SEM. Contact angle of these surface was performed by using Theta attention contact angle meter. The wettability performance of these surfaces were investigated depending on silica particles content in composite solution in the text.

2. MATERIAL AND METHODS

PS, toluene and methanol were purchased from Aldrich. Ultrapure water was obtained from Merck and used as received. Pyrogenic silica (HDK-H18) was kindly supplied by Wacker Silicones-Turkey. The random copolymer of perfluoro acrylate-ran-styrene was used as a previously synthesized [18]. TMS copolymers were dissolved in toluene with a concentration of 50 mg/ml and PS homopolymer was also dissolved in toluene with a concentration of 50 mg/ml at room temperature. The polymer solution was mixed homogenously. Different rates of silica particles added the polymer blend solution after a preparation

of silica dispersion in toluene. The moisture was firstly removed from the silica structure at 105°C, 1.5 h and then the silica particles were waited to come to room temperature in desiccators. Dried silica nano particles were dispersed in MeOH by using ultrasonic probe (Hielscher Ultrasonics GmbH, Germany, Probe Code: BS2d18) at 150 watt for 10 second. The composite solution having TMS copolymer, PS homopolymer and different rate of the silica were coated the glass slide that were cleaned with warm chromic acid solution, washed with deionized water and dried at 100◦C in an oven by spray coating with pen spray gun as given in Fig 1.

Figure 1. The schematic illustration of spray coating process

The apparent (θ^{app}), advancing (θ_{adv}) and receding (θ_{rec}) contact angles under air were measured by using attension theta contact angle meter with a PC controlled motorized syringe within ±1° precision, and the details of the measurement was clearly given in a previous study [11].

3. RESULTS AND DISCUSSION

In figure 2 shown that increase in the PS % (wt) content of the TMS-PS blend solution resulted in increase in the apparent contact angle sharply from 90° to 110°, however, a plateau was happened when the PS % (wt) reached at 30.

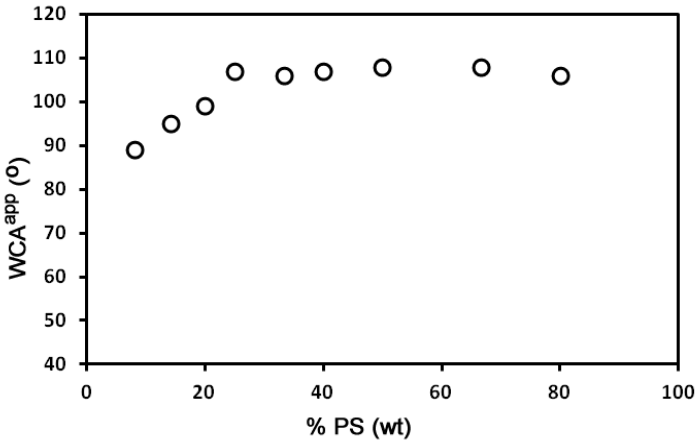

Figure 2. Change of apparent contact angle values with the change in weight fraction of PS (%) in the blend solution

In this figure indicated the limit PS (%) content of the TMS-PS blend solution as 50 % (wt), due to the having higher apparent WCA values. Thus, we choose the 3 different PS content in blend solution at this plateau region as given in Table 1.

Table 1. The weight percent of polymer content of the blend solution

Code	PS % (wt)	TMS % (wt)
TMS-PS_{22}	22.5	77.5
TMS-PS_{33}	33.0	67.0
TMS-PS_{50}	50.0	50.0

The TMS-PS composite solution with silica was prepared by adding the different weight of the silica particles in the blend solution. TMS-PS + silica content of the blend solution was given in Table 2.

Table 2. The weight percent of polymer and silica content of the blend solution

Kod	% PS (Wt)	% Silika (Wt)	WCA^{app} (º)
TMS-$PS_{22}NP_{2,5}$	22.5	2.5	100
TMS-$PS_{22}NP_{5,0}$	22.5	5.0	117
TMS-$PS_{22}NP_{7,5}$	22.5	7.5	115
TMS-$PS_{22}NP_{10}$	22.5	10.0	112
TMS-$PS_{22}NP_{12,5}$	22.5	12.5	129
TMS-$PS_{33}NP_{2,5}$	33.0	2.5	104
TMS-$PS_{33}NP_{5,0}$	33.0	5.0	108
TMS-$PS_{33}NP_{7,5}$	33.0	7.5	120
TMS-$PS_{33}NP_{10}$	33.0	10.0	135
TMS-$PS_{33}NP_{12,5}$	**33.0**	**12.5**	**164**
TMS-$PS_{50}NP_{2,5}$	50.0	2.5	114
TMS-$PS_{50}NP_{5,0}$	50.0	5.0	107
TMS-$PS_{50}NP_{7,5}$	50.0	7.5	110
TMS-$PS_{50}NP_{10}$	50.0	10.0	113
TMS-$PS_{50}NP_{12,5}$	**50.0**	**12.5**	**167**

In this table is shown that increase in the silica weight content of the blend solution from 2.5 to 12.5 % resulted in increase in the apparent WCA from 100º to 129º at the 22.5 (wt) PS content, from 104º to 164º at the 33.0 (wt) PS content, from 114º to 167º at the 50.0 (wt) PS content. The apparent WCA results indicated that TMS-PS_{33}NPx (different weight percent of the silica particles in TMS-PS_{33} blend solution) is shown the more linearly increases by adding the silica particles as given in Fig 3.

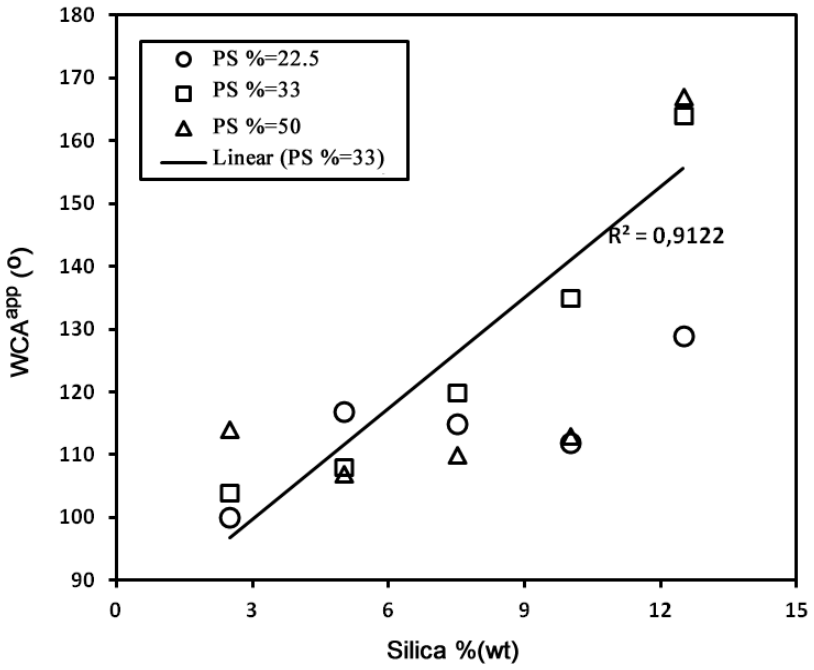

Figure 3. Change of apparent contact angle values with the change in weight fraction of silica (%) in the TMS-PS blend solution

The SEM images of the TMS-PS_{33}NPx was given in Figure 4.

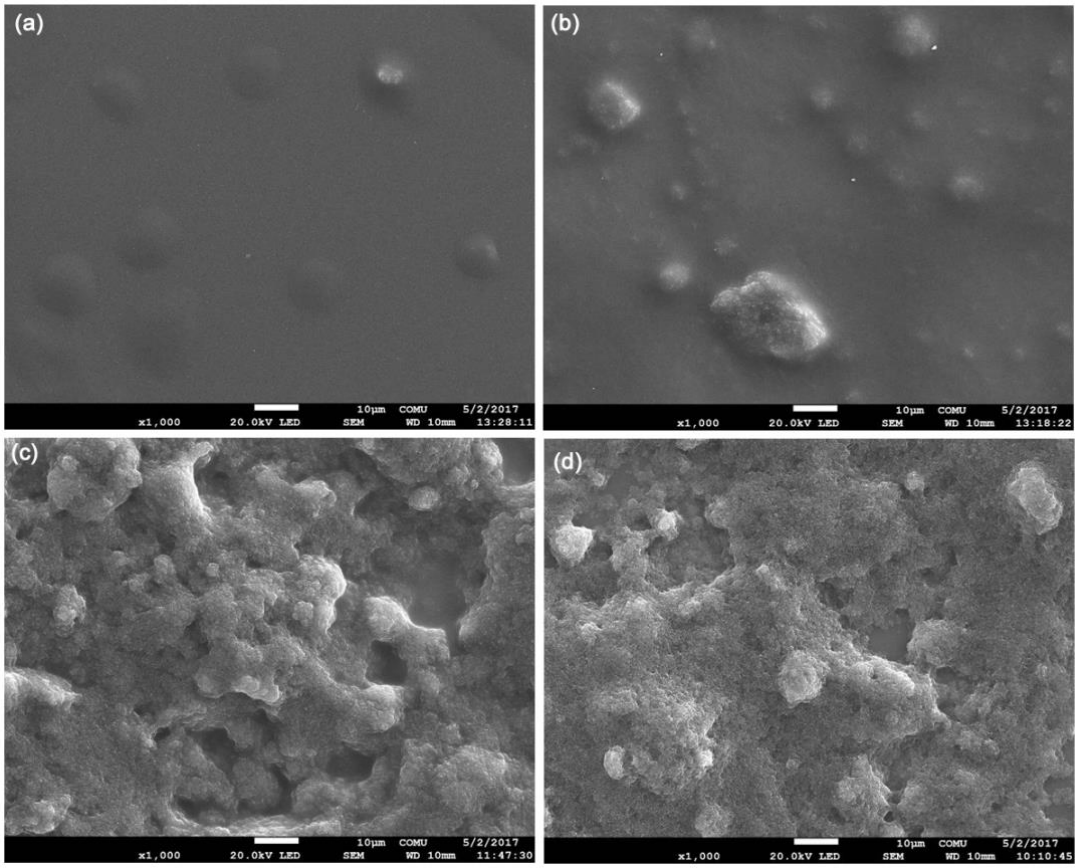

Figure 4. The SEM images (1000X) of the TMS-PS_{33} at the different weight fraction of silica a)$TMS_{33}NP_{2,5}$ b)$TMS_{33}NP_5$ c)$TMS_{33}NP_{10}$ d)$TMS_{33}NP_{12,5}$

The SEM images of the blend surface indicated the increasing the roughness of the surfaces by increasing the silica weight percent from 2.5 to 12.5 % (wt) (Fig 4). When the silica content is 2.5 % (wt), the surface was almost flat due to the lower silica content (Fig 4a). In addition it's apparent contact angle values is measured as 104^o. Increasing the silica content from 2.5 to 5 %, the apparent WCA values is increased by 4^o (Table 2) and the SEM images is also shown that the surface of the TMS-$PS_{33}NP_5$ (Fig 4b) is close the TMS-$PS_{33}NP_{2.5}$ (Fig 4a). When the silica content is 10 % (wt), the rough surface was obtained (Fig 4c) and the apparent WCA values is reached as 135^o (Table 2). The superhydrophobic, self cleaning surfaces was obtained when the silica content is 12.5 % (wt) (Table 2) due to the increasing the surface roughness (Fig 4d). The PS content effect in the blend surface at the constant silica weight percent as 12.5% as given in Figure 5.

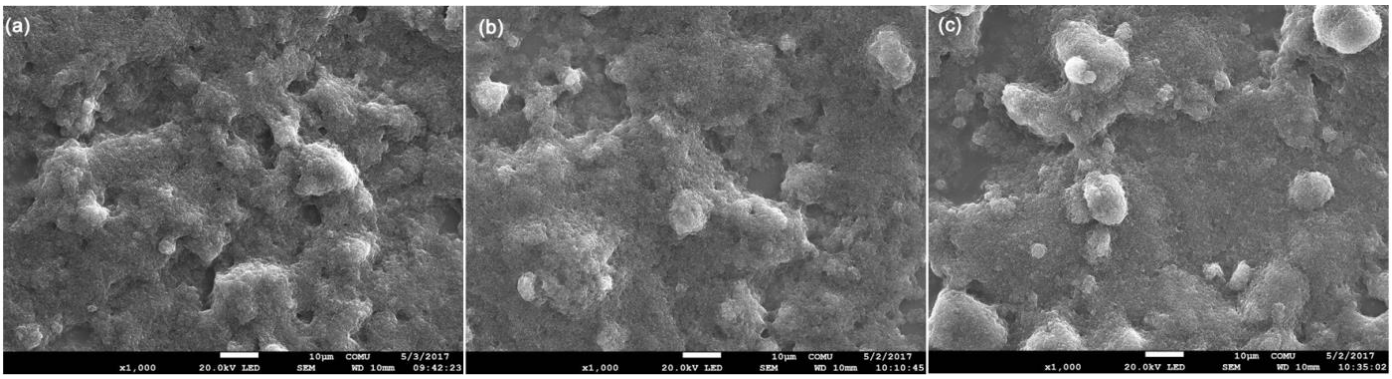

Figure 5. The SEM images (1000X) of the TMS-$PS_XNP_{12.5}$ surfaces at the different weight fraction of PS in blend solution a) TMS-$PS_{22}NP_{12,5}$ b) TMS-$PS_{33}NP_{12,5}$ c) TMS-$PS_{50}NP_{12,5}$

Increase in the PS % (wt) in blend solution resulted in increase in the apparent WCA from 129^o to 167^o as given in Table 2 and Figure 3 due to the increasing the heterogeneity of the rough surfaces.

4. CONCLUSION

In conclusion, we have created, a superhydrophobic nanocomposite coating that can be easily applied to almost any surface, in addition to the glass substrates used in the current work, similar to spraying paint. The resulting surface attains high contact angles and low contact angle hysteresis values using a precisely controlled the roughness of the surfaces, using a low surface energy polymer, and compatibilizing nano particles. The self cleaning properties was also achieved by fabrication of higher WCA rough surfaces.

ACKNOWLEDGMENTS

The authors would like to thank Central Laboratory of Canakkale Onsekiz Mart University for providing SEM.

REFERENCES

[1] Erbil, H.Y. Surface Chemistry of Solid and Liquid Interfaces, Blackwell Publishing: Oxford, 2006.

[2] de Gennes, P.G., Brochard-Wyart, F. B., Quere, D. Capillarity and Wetting Phenomena: Drops, Bubles, Pearly, Waves, Springer, Berlin, 2003.

[3] Feng, X.J., Jiang, L. Designed and Creation of Superwetting/Antiwetting Surfaces, Adv. Mater. 18, 3063-3078, 2006.

[4] Feng, L., Li, S., Li, Y., Li, H., Zhang, L., Zhai, J., Song, Y., Liu, B., Jiang, L., Zhu, D. Super-Hydrophobic Surfaces: From Matural to Artifical, Adv. Mater. 14, 1857-1860, 2002.

[5] Celia, E., Darmanin, T., de Givenchy, E.T., Amigoni, S., Guittard, F. Recent advances in designing superhydrophobic surfaces, J. Colloid Interface Sci. 402, 1–18, 2013.

[6] Marmur, A. A guide to the equilibrium contact angles maze in Contact Angle, Wettability and Adhesion Volume 6, CRC Press, Boston, 2009.

[7] Erbil, H.Y., Demirel, A.L., Avci, Y., Mert, O. Transformation of a Simple Plastic into a Superhydrophobic Surface, Science 299, 1377-1380, 2003.

[8] Onda, T., Shibuichi, S., Sato, N., Tsuji, K. Super-Water-Repellent Fractal Surfaces, Langmuir 12, 2125-2127, 1996.

[9] Drelich J., et al. Contact Angles and Wettability: Towards Common and Accurate Terminology, Surface Innovations, 5, 3–8, 2017.

[10] Bormashenko, E.Y. Wetting of Real Surfaces, Walter de Gruyter, Berlin, 2013.

[11] Cengiz, U., Erbil, H.Y. Superhydrophobic perfluoropolymer surfaces having heterogeneous roughness created by dip-coating from solutions containing a nonsolvent, Appl Surf Sci, 292, 591-597, 2014.

[12] Cengiz, U., Avci, M.Z., Erbil, H.Y., Sarac, S.A. Superhydrophobic Terpolymer nanofibers Containing Perfluoroethyl Alkyl Methacrylate by Electrospinning, Appl. Surf. Sci. 258, 5815-5821, 2012.

[13] Cansoy, C.E. Erbil, H.Y., Akar, O., Akin, T. Effect of pattern size and geometry on the use of Cassie–Baxter equation for superhydrophobic surfaces, Colloids Surf. A. Physicochem Eng. Asp. 386, 116–124, 2011.

[14] Kaya, A.S.T., Erdogan, E., Cengiz, U. Preparation of stable, transparent superhydrophobic film via one step one pot sol-gel method, Colloid Polym Sci, 296, 1523-1532, 2018.

[15] Meng, L.Y., Park, S.J. Effect of growth of graphite nanofibers on superhydrophobic and electrochemical properties of carbon fibers, Mater. Chem. Phys. 132, 324-329, 2012.

[16] Lee, E.J., Jung, C.H., Hwang, I.T., Choi, J.H., Cho, S.O., Nho, Y.C. Surface Morphology Control of Polymer Films by Electron Irradiation and Its Application to Superhydrophobic Surfaces, ACS Appl. Mater. Interfaces 3, 2988-2993, 2011.

[17] Steele, A., Bayer, I., Loth, E. Inherently Superoleophobic Nanocomposite Coatings by Spray Atomization, Nano Lett. 9, 501-505, 2009.

[18] Cengiz, U., Erbil, H.Y. Perfluoromethacrylate-Styrene Statistical Copolymers Synthesized in CO_2-Expanded Monomers, Colloid and Polymer Science 292 (9), 2207-2215, 2018.

FABRICATION AND CHARACTERIZATION OF FIRE-RESISTANCE GEOPOLYMER MATERIAL

G. Akarken[1], U. Cengiz[2*]

[1]*Department of Bioengineering & Materials Science Engineering, Canakkale Onsekiz Mart University, Canakkale, Turkey*
[2] *Chemical Engineering Department, Canakkale Onsekiz Mart University, Canakkale, Turkey*
E-mail: gurkanakarken@gmail.com

Abstract

Portland cement is one of the topmost engineering building materials in use today. It has been used as a binding agent for concrete due to its exceptional thermal performance, mechanical properties and durability. However, there is an argument in environmental issues on the enormous energy consumption and emissions of carbon dioxide (CO_2) during its manufacture. The manufacturing of concrete in industry is one of the major contributors of the global warming. For this reason, geopolymers attract attention with applications such as environment friendly fireproof building materials, sound heat insulators, encapsulation of hazardous wastes. Geopolymers have many advantages over Portland cement such as low energy cost, reduced greenhouse gas emissions, high compressive strength, high temperature stability, low thermal conductivity, high strength at early age. Protection against fire using inorganic polymer is a new application of engineering technology. Geopolymer composites materials are promising from this point of view due to their advantages. Alkali activated geopolymers made from waste materials such as fly ash or blast furnace slag are particularly advantageous because of their environmental sustainability and low cost. However, their durability and functionality continue to be the subject of further work. Geopolymer materials can be used in various applications such as fire and heat resistant composites, depending on the chemical composition of the source materials and the activators. In this study, different prescriptions will be applied to produce fire resistance geopolymers and characterization studies will be carried out. Composite structure of metakaolin based geopolymer with basalt fiber is obtained. The thermal properties, micro structures, energy efficiencies, sound insulation properties of the produced samples were tested. Samples will be invastigated with various characterization techniques such as X-ray diffraction (XRD) to investigate the nature and compositions and Thermogravimetric analysis (TGA) for thermal behavior. Thermal conductivity, strength retention after heat treatment, non combustibility was used as indicators for investigation of fire endurance of geopolymer materials.

Keywords: Geopolymer, Fire Resistance Geopolymer, Thermogravimetric analysis

1. INTRODUCTION

Global warming is being caused by increased concentration green house gases, primarily CO_2 in the atmosphere. 5 percent of CO_2 emissions come from the ordinary portland cement manufacturing industry [1,2]. Moreover %59 of the cost of manifacturing cement is energy. Concrete is the second primary consuming material after water and in 2050 cement production will be double of today. If we consider all these information we need to minimize our impact on nature. In addition we should start to use new material more eco friendly, lower cost and with similar or even better engineering properties than ordinary portland cement (Opc) for making concrete. At this point, geopolymers has been recognized as one of the most promising materials in last years.

Geopolymers are known as new kind of materials which were first developed by Joseph Davidovits and patented in the late of 70s. They are inorganic polymeric materials produced from a mixture of several aluminosilicate materials (with high contents of Si and Al) along with an alkaline-activating solution (mostly Na+ or K+ silicates and hydroxides). Geopolymers have the general formula M+n{(SiO2)z,AlO2}n, wH2O where z is the Si/Al molar ratio, M+ is the monovalent cation and n is the polymerization degree. These materials are liquid mixtures which consolidate at room temperature. They are obtained by the dissolution of an aluminosilicate source in the presence of an alkaline silicate solution [3,4].

In the last years researches has shown that geopolymers might be an logical alternative for Opc with their high compressive strength, durability, good acid resistance, good fire resistance, low cost and enviroment friendly properties. Geopolymers could be produced from low cost waste industrial materials such as fly ash, blust furnace slag, metakaolin, mine tailings which make them green material.

Geopolymer materials can be used in various applications such as fire and heat resistant composites, depending on the chemical composition of the source materials and the activators. In this study, different prescriptions will be applied to produce fire resistance geopolymers and characterization studies will be carried out.

2. MATERIAL AND METHODS

Metakaolin is used for this study for the main source of silica (SiO_2) and alumina (Al_2O_3). Its chemical composition was evaluated by XRF spectroscopy technique to know the quantity of SiO_2 and Al_2O_3 (Table 1.). The alkaline activating solutions were composed of alkaline sodium silicate (Na_2SiO_3), hydroxide (NaOH), and potassium hydroxide (KOH).

Table 1. Chemical composition of metakaolin using XRF

Compound	% Weight	Element	% Weight
SiO_2	51.97	Si	24.30
Al_2O_3	43.52	Al	23.03
Na_2O	0.969	Na	0.719
MgO	0.917	Mg	0.553
Fe_2O_3	0.842	Fe	0.589
TiO_2	0.563	Ti	0.338
Cl	0.502	Cl	0.502
K_2O	0.433	K	0.360
CaO	0.146	Ca	0.104
ZnO	0.031	Zn	0.025

All the alkaline activators are used to consider SiO_2 / Al_2O_3 raito in prescriptions. In addition to these materials we used water to make geopolymer mortars. The prescriptions of geopolymers are shown in Table 2. For the mechanical test, samples were made 20 times bigger than quantities in Table 2.

The Metakaolin-based geopolymer mortars were produced according to the following procedure. Firstly the alkaline activating solution was mixed for 15 min according to quantities in Table 2. In some samples activators were used as NaOH and Na_2SiO_3 and for others NaOH, KOH and Na_2SiO_3. After mixing 15 min solutions were let to cool down at room temperature. After cooling down solutions were gradually added to the metakaolin under continuous stirring. Samples were mixed till got homogenized. After homogenizaiton we pured the mortars into the steel molds (Figure 1.). After curing 24 hours in the room temperature samples were taken from molds (Figure 2).

Table 2. Mix proportions of geopolymers

Sample	Reaktant Material (g)					From Metakaolin (g)		From Na_2SiO_3 (g)			Molar Ratios (Mol/Mol)		
	Metakaolin	Na_2SiO_3	NaOH	KOH	H_2O	SiO_2	Al_2O_3	SiO_2	Na_2O	H_2O	SiO_2/Al_2O_3	Na_2O/SiO_2	H_2O/Na_2O
1	10	16.9	1.6		8.4	5.0	4.2	4.8	2.3	9.8	4.0	0.35	18.0
2	15	16.9	1.6		8.4	7.6	6.2	4.8	2.3	9.8	3.4	0.28	18.0
B1	10	8.7	1.8		4.1	5.0	4.2	2.5	1.2	5.0	3.0	0.33	13.0
A1	10	2.7	1.0	1.3	5.0	5.0	4.2	0.8	0.4	1.6	2.4	0.19	20.5
A2	20	12.3	4.5	5.9	22.7	10.1	8.3	3.5	1.7	7.1	2.8	0.37	20.5
B2	10	3.6	2.2		4.5	5.10	4.2	1.0	0.5	2.0	2.5	0.36	11.0
B3	10	8.2	1.4		3.0	5.0	4.2	2.3	1.1	4.8	3.0	0.29	12.5
B4	10	8.2	1.8		2.9	5.0	4.2	2.3	1.1	4.8	3.0	0.33	11.0
B5	10	8.2	1.8		4.4	5.0	4.2	2.3	1.1	4.8	3.0	0.33	13.1
A5	10	2.9	1.0	1.3	4.5	5.0	4.2	0.8	0.4	1.7	2.4	0.19	19.0
A6	10	2.7	2.3		5.0	5.0	4.2	0.8	0.4	1.6	2.4	0.36	11.4
B7	10	3.9	2.6		5.3	5.0	4.2	1.1	0.5	2.3	2.5	0.40	11.0
B8	10	12.6	1.11		0,7	5.0	4.2	3.5	1.7	7.3	3.5	0.29	11.0

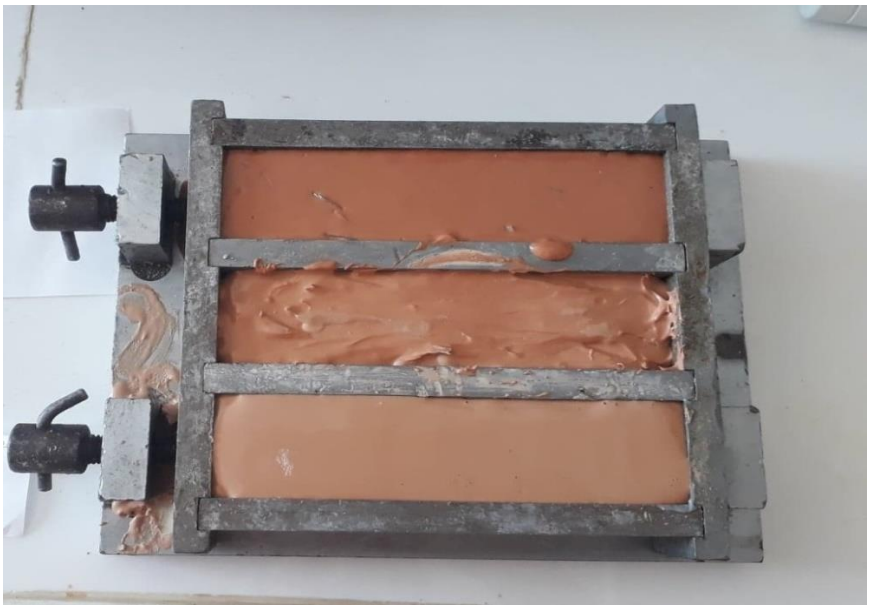

Figure 1. : Samples in steel mold for curing 24 hours.

Figure 2: Samples after 24 hours curing.

The samples were grinded to prepare geopolymer powders for TGA and X-ray diffraction (XRD) characterization after naturally dried at room temperature. Xrd analyzes were performed to investigate the nature and composition of the reaction products. Thermogravimetric analysis (TGA) were also performed to invastigate fire resistance behavior of samples. The mass loss with gradual temperature increase was measured for the geopolymer samples. TGA of the powdered samples was recorded from 30 ^{o}C to 800 ^{o}C at a heating rate of 10 ^{o}C /min in air atmosphere.

3. RESULTS AND DISCUSSION

Figure 3, 4, 5, 6 displays XRD profiles of A1, A2, B1, B2 samples. XRD analyzes were performed to investigate the nature and composition of the reaction products. The presence of a quartz-weighted structure in the samples indicates the density of SiO_2 in the structure. When the samples B2 and A2 are examined, in addition to quartz and zeolite crystal phases, another form of SiO_2 is seen as coesite. The existence of these characteristic peaks depend on type of alkali activator, type of aluminosilicate source, , their mix-design in geopolymer composite, remaining unreacted silica or alumina in geopolymer [5]. When

the crystal phases are examined, it is seen that quartz, zeolite and coesite structures are not affected by sodium silicate. The better stability and thermal stability of geopolymers were attributed to the zeolite-like structure characteristics [6]. In the continuation of the project, we will apply Xrd analysis at different temperatures and examine the differences in the crystal structures of the samples.

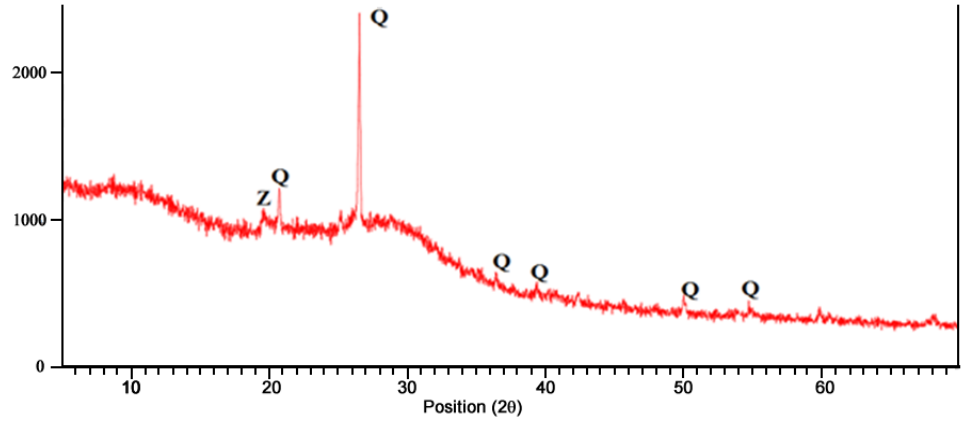

Figure 3. : XRD pattern of sample A1 (Q: Quarts, Z: Zeolite)

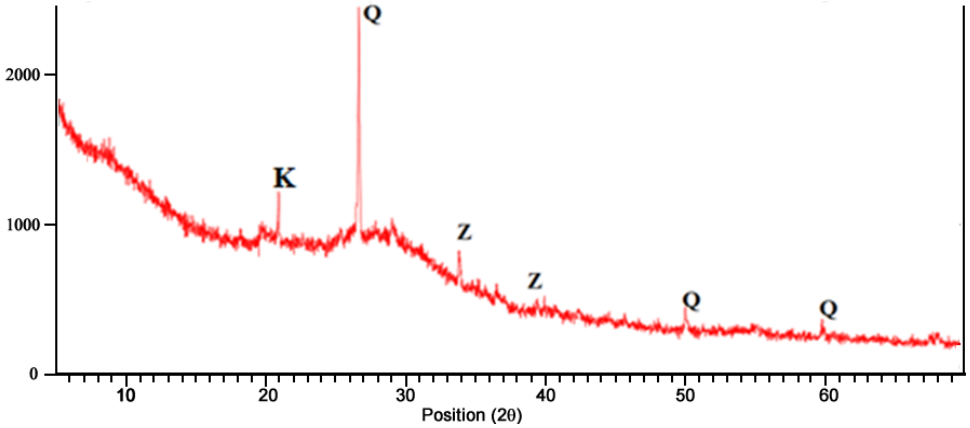

Figure 4. : XRD pattern of sample A2 (Q: Quarts, Z: Zeolite, K: Koesite)

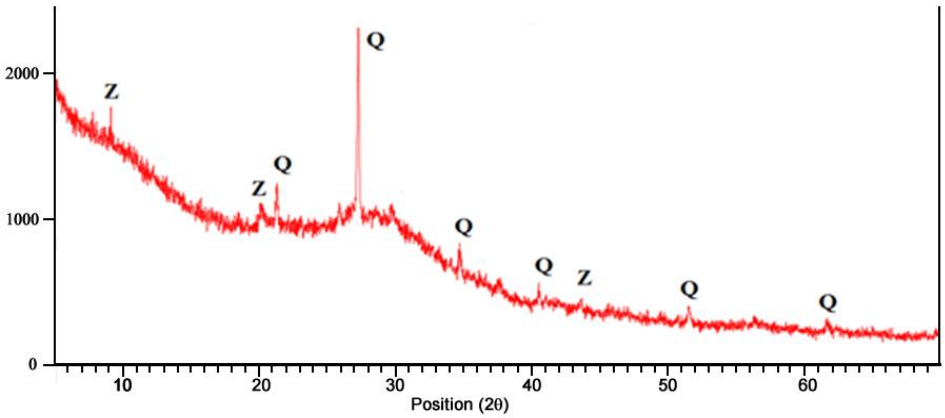

Figure 5. : XRD pattern of sample B1 (Q: Quarts, Z: Zeolite)

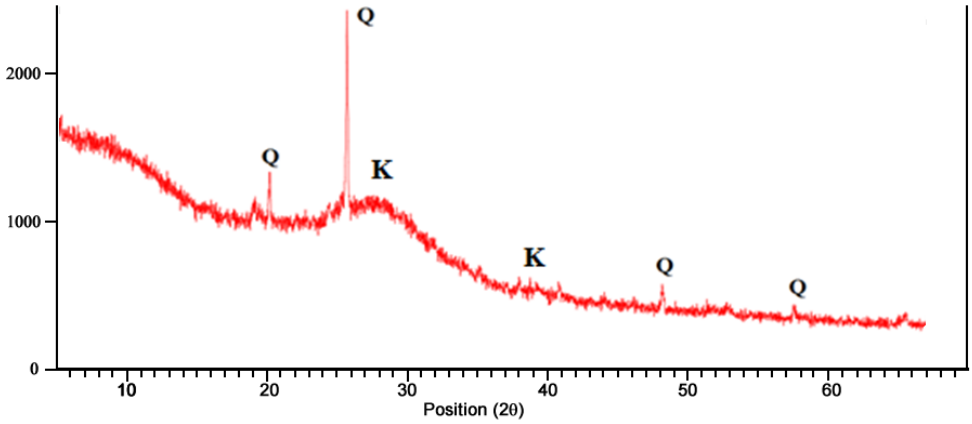

Figure 6. : XRD pattern of sample B2 (Q: Quarts, Z: Zeolite, K: Koesite)

Thermogravimetric analysis results for A1, A2, B1, B3 samples are shown in figure 7, 8, 9 and 10. Figure 7 and Figure 8 are temperature-sample % weight graphs obtained by increasing the temperature of the samples A1 and A2 by 10 °C per minute from 30 °C to 800 °C (Fig 7 and 8). A significant reduction in sample weight (about 11%) was obtained from room temperature to 200 °C. The reason for this decrease is the gradual separation of the free water from the pores in the structure of the geopolymer [7, 8]. Stable weight loss from 200 °C to 740 °C is defined as the separation of chemically bonded water and hydroxyl (OH) groups chemically bound to the structure by evaporation [9]. There is no mass loss in the range of 740 °C and 800 °C. When the temperature is reached to 800 °C, the average of the total mass is %84.85 for A1, %84.39 for A2.

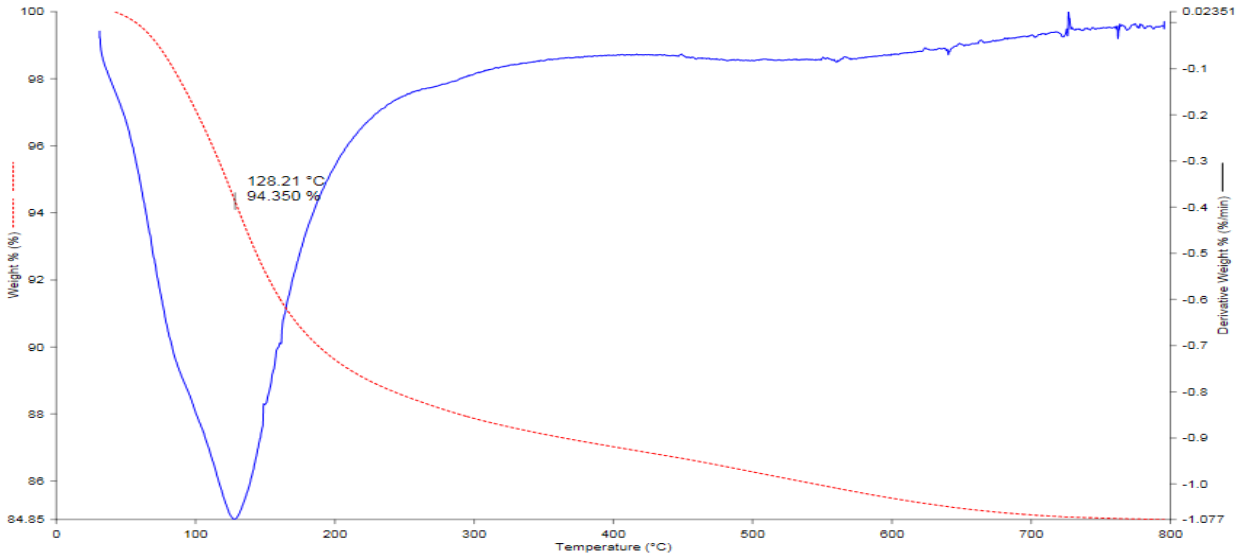

Figure 7: Tga curve of the sample A1

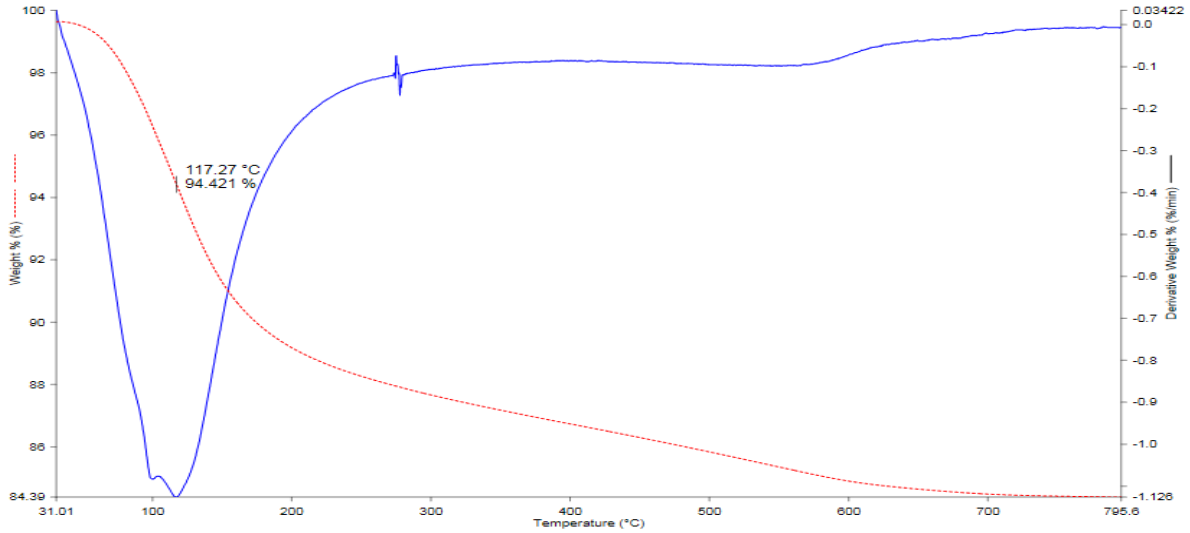

Figure 8: Tga curve of the sample A2.

For B1 and B3 samples important weight loss (about 14%) has seen from room temperature to 250 °C. This is also attributed to seperation of free water in the structure (Fig 9 and 10). The mass loss from 250 to 700 °C is explained by the dehydroxylation process and liberalization of bonden water in the internal structure of geopolymers [10, 11]. There was no loss of mass after these temperatures and when the temperature reached to 800 °C total mass was %81.77 for B1, %82.58 for B3.

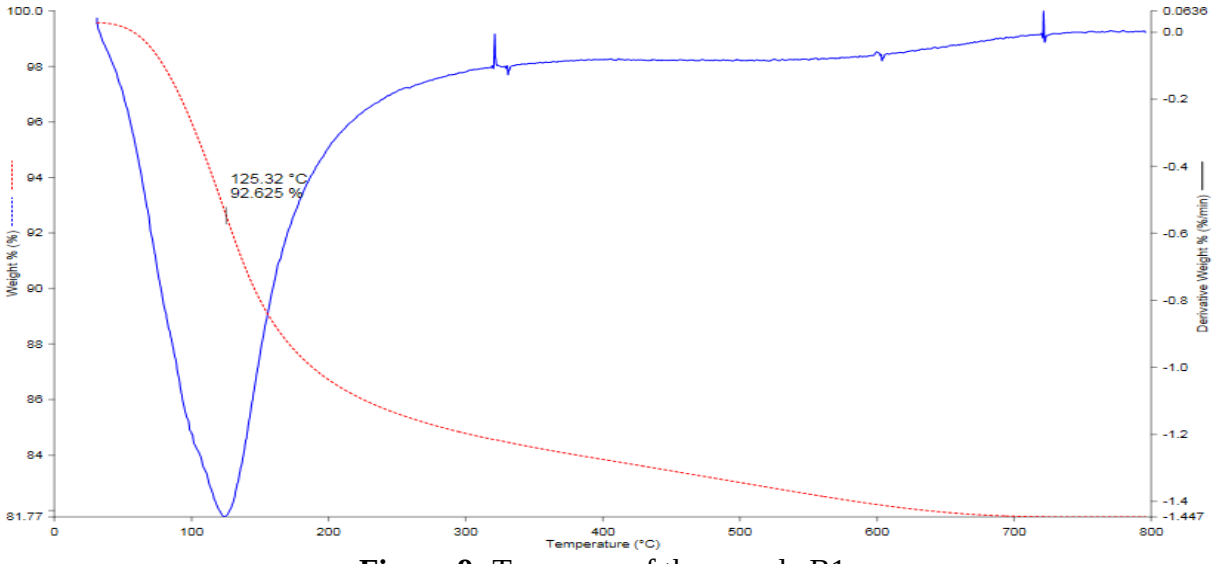

Figure 9: Tga curve of the sample B1.

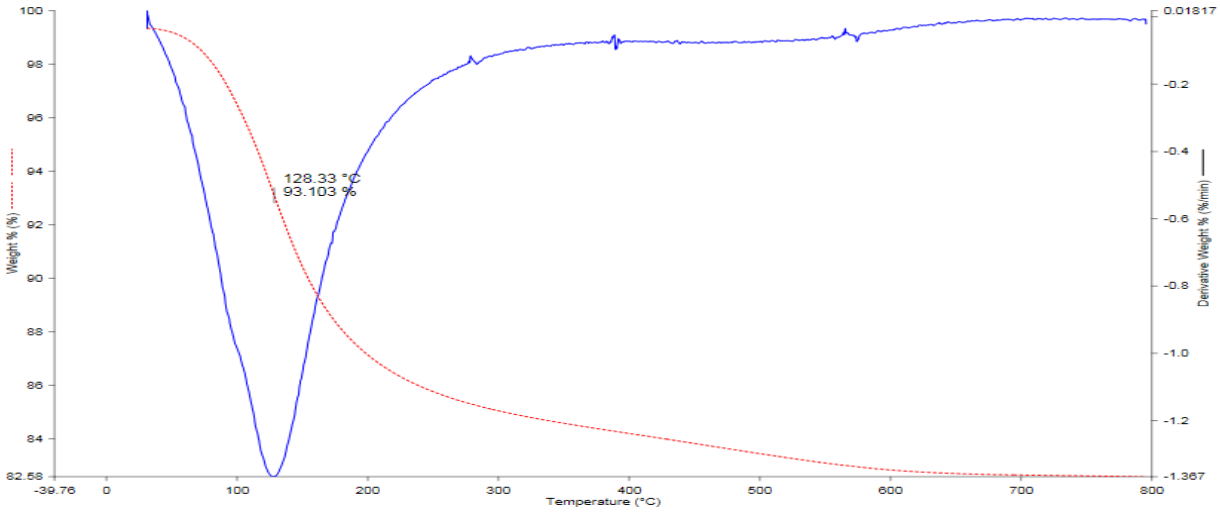

Figure 10. : Tga curve of the sample B3.

4. CONCLUSION

In this study thermal behivors of different mixed geopolymers were investigated. The results of thermal analyse (TGA) showed that mortars indicated very similar weight loss respect to mass loss. Geopolymers which have highest thermal resistance produced with using NaOH and KOH alcaline activators in same mortar. This means we can control the thermal resistance of geopolymer materials by controlling the raw materials used in their preparation. According to results of thermal analyse geopolymers invastigated in this study can be used in thermal resistance applications.

ACKNOWLEDGMENTS

This work was supported by Canakkale Onsekiz Mart University The Scientific Research Coordination Unit, Project number: FYL-2018-2465

REFERENCES

[1] P.S. Deb, P. Nath, P.K. Sarker, The effects of ground granulated blast-furnace slag blending with fly ash and activator content on the workability and strength properties of geopolymer concrete cured at ambient temperature, Mater. Des. 62 (2014) 32–39.

[2] Z. Liu, C.S. Cai, F. Liu, F. Fan, Feasibility study of loess stabilization with fly ashbased geopolymer, J. Mater. Civ. Eng. 28 (5) (2016) 04016003.

[3] V.D. Glukhovsky, Soil Silicates, Gosstroyizdat, Kiev, 1959.

[4] E. Prud'homme, Rôles du cation alcalin et des renforts minéraux et végétaux sur les mécanismes de formation de géopolymères poreux ou denses (PhD Thesis) University of Limoges, 2011.

[5] J. Ye, W. Zhang, D. Shi, Effect of elevated temperature on the properties of geopolymer synthesized from calcined ore-dressing tailing of bauxite and ground-granulated blast furnace slag, Constr. Build. Mater. 69 (2014) 41–48,

[6] Y.J. Zhang, S. Li, Y.C. Wang, D.L. Xu, Microstructural and strength evolutions of geopolymer composite reinforced by resin exposed to elevated temperature, J. Non. Cryst. Solids. 358 (2012) 620–624

[7] P. Duxson, G.C. Lukey, J.S.J. van Deventer, Physical evolution of Na-geopolymer derived from metakaolin up to, 1000 °C, J. Mater. Sci. 42 (2007) 3044–3054.

[8] D.L.Y. Kong, J.G. Sanjayan, K. Sagoe-Crentsil, Comparative performance of geopolymers made with metakaolin and fly ash after exposure to elevated temperatures, Cem. Concr. Res. 37 (2007) 1583–1589,

[9] P. Behera, V. Baheti, J. Militky, S. Naeem, Microstructure and mechanical properties of carbon microfiber reinforced geopolymers at elevated temperatures, Constr. Build. Mater. 160 (2018) 733–743.

[10] Z. Pan, J.G. Sanjayan, F. Collins, Effect of transient creep on compressive strength of geopolymer concrete for elevated temperature exposure, Cem. Concr. Res. 56 (2014) 182–189

[11] A. Sabbatini, L. Vidal, C. Pettinari, I. Sobrados, S. Rossignol "Control of shaping and thermal resistance of metakaolin-based geopolymers, Materials and Design 116 (2017) 374–385, 2016.

FABRICATION AND CHARACTERIZATION OF MAGNETIC NANOPARTICLE-POLYMER COMPOSITE MATERIALS

G. Akarken[1], U. Cengiz[2*]

[1]*Department of Bioengineering & Materials Science Engineering, Canakkale Onsekiz Mart University, Canakkale, Turkey*
[2] *Chemical Engineering Department, Canakkale Onsekiz Mart University, Canakkale, Turkey*

E-mail: gurkanakarken@gmail.com

Abstract

Nanostructures have scientific, industrial and medical importance. They are important research topic due to their wide range of application area of electric, magnetic, spintronic and biomedicine feature. Thus, many nano-particle structures have been fabricated to use technology, military, medicine and industry. Nano-composites have an important role in nanoscience and nanotechnology. Nano-composites generally consist of inorganic particles (nano size fillers) with their reinforced polymer matrix. These structures are mostly dielectric materials having different shapes and sizes filled with metallic or magnetic particle. Polymer-nano metallic composites due to its thermal, mechanic, chemical, magnetic, electric, electronic and optic properties have a very high commercial potential and excellent materials in many application areas. However, composite materials have become widely used in electromagnetic absorber technology due to its higher advantages. Electromagnetic Radiation (EMR) absorber materials are extensively studied especially their stealth aircraft feature and other stealth-like military coating. Significant progress in this regard over the world. However, this progression is unclear what the exact level is, due to keeping this project's result secret. In addition, It has been known for publicly available sources that, these material consist of different nanostructure (nanoparticle or nanowire) materials. In this study, the NP of $CuFe_2O_4$, $MnFe_2O_4$, $NiFe_2O_4$, $ZnFe_2O_4$, $CoFe_2O_4$ and $CrFe_2O_4$ will be synthesized by the bottom-up technique. The Florocopolymer - MNP composite materials will be synthesized. The copolymer and NP prepared in different media are mixed in a suitable solvent environment to produce composite material

Keywords: Magnetic Nanoparticle-Polymer, Composite, Electromagnetic Radiation

1. INTRODUCTION

Nanostructured materials having scientific, industrial and medical importance while they important research topic such as electronic, electromagnetic, spintronic and biomedical applications due to their superior properties primarily because of their high surface-to-volume ratios [1-3]. The magnetic nanoparticles exhibit quantum size effects compared to the huge materials [3,4]. In additional, the magnetic nanoparticles/powders have been steadily interesting in sensor technology, spintronics and drug delivery, industrial area because of their wide range of usage for potential application such as magnetic memory [5-10], magnetic resonance imaging [1,11], DNA recovery, gene carrier-cancer therapy [12,13].

Two general approaches are employed in making nano-structured materials: top-down and bottom-up. Typical top-down techniques start with a bulk material and obtain a nanostructure by size reduction [14-16]. The bottom-up methods, nano-materials that make up an atom or molecule itself is produced by bringing together in a controlled manner. There are some disadvantages of both techniques. For example, the top-down technique where one starts with a bulk material and obtains a nanostructure by size reduction included the some physical process such as crushing and grinding [14-16]. However, this production is not fully controlled and the desired nano materials of the bulk state must be present in nature. In addition, sometimes the nano particles structure that was fabricated by the top-down technique occur undesirable defects and impurities. On the other hand, the bottom-up approaches enable to the synthesis of nanostructured materials with fewer defects, less impurities and fabricated to be use application is by an engineering approach. Therefore, It is so important to develop the new bottom-up technique and using the applications [14-16].

In the present study, the magnetic nano particles of $CuFe_2O_4$, $MnFe_2O_4$, $NiFe_2O_4$, $ZnFe_2O_4$, $CoFe_2O_4$ and $CrFe_2O_4$ were synthesized by the bottom-up technique by ethylenediaminetetraacetic acid (EDTA) assisted hydrothermal route method. The nano-composite particles containing magnetic nano particles and perfluoroalkyl acrylate-ran-stiren copolymer were also fabricated. The magnetic nano particles and composite particles differences were examined.

2. MATERIAL AND METHODS

The used perfluoroacrylate-ran-styrene copolymer was prepared by Cengiz et al [17] and used directly. The physical properties of copolymer were given in Table 1.

Table 1. The physical properties of perfluoroacrylate-ran-stiren copolymer*

Copolymer Code	$W_{Zonly\text{-}TM}$ (%Wt)	W_{St} (%Wt)	Mw (kg/mol)	Tg (°C)
TMS	34.8	65.2	36	75.6

*The copolymer was synthesized by Cengiz and Erbil [17]

Nanoparticles of α-Fe_2O_4 spinel type ferrite have been prepared via surfactant-assisted hydrothermal process using EDTA as a surfactant. According to this method, 0.003 mol EDTA was dissolved in 35 ml deionized water to obtain a transparent solution. Then ferric chloride hexahydrate ($FeCl_3.6H_2O$) of 0.004 mol added to solution and mixed 10 min. After 10 min stirring, stoichiomeric amount of α-Cl_26H_2O was added in the homogeneous solution. Deionized water was added until the total water volume is 40 mL and pH of the solution mixture was adjusted to 11. Before being transferred to teflon lined auto clave of 50 ml capacity, the solution mixture was pretreated under an ultrasonic water bath for 40 min hydrotermal synthesis was carried out at 130 ºC for 15 h in an electric oven without shaking or stirring. Afterwards, the autoclave was allowed to cool to room temperature gradually. The black precipitate collected was washed with distilled water several times in an ultrasonic bath to remove any possible impurities. The solid was then heated at 100 ºC and dried under vacuum for 5 h. The synthesized nano particles code and yield % was collected in Table 2. The general reaction between metal and iron salt is seen in Equation-1.

$$M^{+2} + 2Fe^{+3} + 8OH^{-} \longrightarrow MFe_2O_4 + 4H_2O \qquad \textbf{(1)}$$

Table 2. Synthesized magnetic nanoparticles, input and product quantities

Sample Code	NP	The amount of metal salt added to the reaction M^{2+}	W_{MNP}* (g)
NP_1	$CuFe_2O_4$	0,010 mol (1,3445 g) $CuCl_2$	2,30
NP_2	$MnFe_2O_4$	0,010 mol (1,9797 g) $MnCl_24H_2O$	1,87
NP_3	$NiFe_2O_4$	0,010 mol (2,3763 g) $NiCl_26H_2O$	2,28
NP_4	$ZnFe_2O_4$	0,010 mol (1,3630 g) $ZnCl_2$	1,82
NP_5	$CoFe_2O_4$	0,010 mol (2,3793 g) $CoCl_26H_2O$	1,95
NP_6	$CrFe_2O_4$	0,010 mol (1,2290 g) $CrCl_2$	2,60

The composite solution was prepared by using perfoluoromethacrylate-ran-styrene copolymer (TMS) and magnetic nano particles of $CuFe_2O_4$ (NP_1). NP_1 content was arranged between 1 to 10 % wt as given in Table 3.

Table 3. The composite materials code and NP contents

Code	NP_1 (Wt, %)
TMS-NP_1	1
TMS-NP_2	3
TMS-NP_3	5
TMS-NP_4	10

The NP_1 nano particles were added in THF:Methanol (3:2, v/v) solution mixture and the solution was dispersed in ultrasound batch. 50 mg/mL of copolymer TMS was also solved in THF:Methanol mixture. Both of the solution was mixed and the composite solution was sonicated in ultrasound batch at 15 min. Then, composite solution was refluxed under condenser at 70 ^oC for 4h. The nanostructure and morphology of the composite films (150X150 μm^2) were investigated by Scanning Electron Microscopy (SEM). FT-IR spectra measurements of copolymer, nanoparticles and polymer-nano particles composite obtained by using Perkin Elmer spectroscopy in the range of 650–4000 cm^{-1}. The XRD measurements were carried out using a Rigaku D-Max Rint-2200 series X-Ray Diffractometer.

3. RESULTS AND DISCUSSION

Figure 1 displays XRD profiles of TMS and EDTA-assisted hydrothermally synthesized $CuFe_2O_4$ spinel ferrite NPs. The XRD measurements of TMS indicated that, the Zonyl-TM-ran-St copolymers are completely amorphous (2θ=18-20^o). In addition, the pattern shows diffraction peaks of $CuFe_2O_4$ is observed that the copper ferrites are cubic spinel structure. Among these peaks the reflection at (311) is the strongest intense one. The strongest reflection comes from the (311) plane that indicates the spinel phase. From XRD pattern the average ferrite NPs sizes were calculated from the Debye-Scherrer equation as below:

$$D= (0.9\lambda)/(B.Cos(\theta_B)) \quad (1)$$

$$LS= B/(4tan\theta) \quad (2)$$

where, λ, B and θ_B are the the wavelength of x-ray source used in XRD, full width at half maximum (FWHM) and the angle of Bragg diffraction, respectively [3]. As a result of this equation is shown that average diameters of nano-parietal NP_1 is found as 40.1 nm.

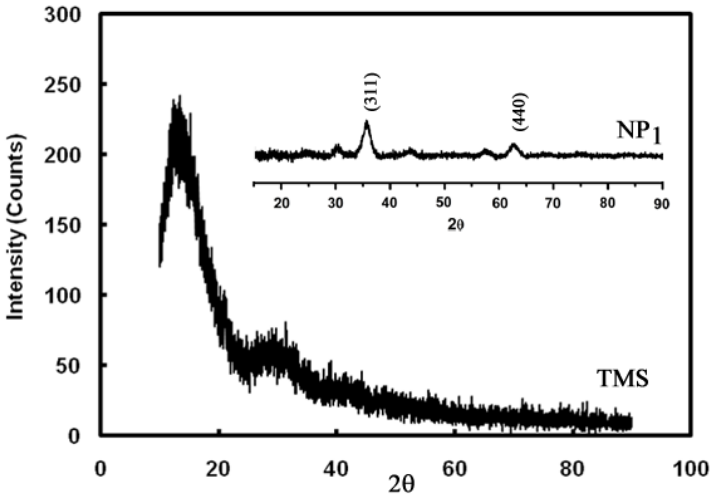

Figure 1. The XRD peak of the TMS and NP_1

The XRD peaks of TMS-NP1 composite nano particles was given in Fig. 2. In this figure indicated the both of the structure characteristic.

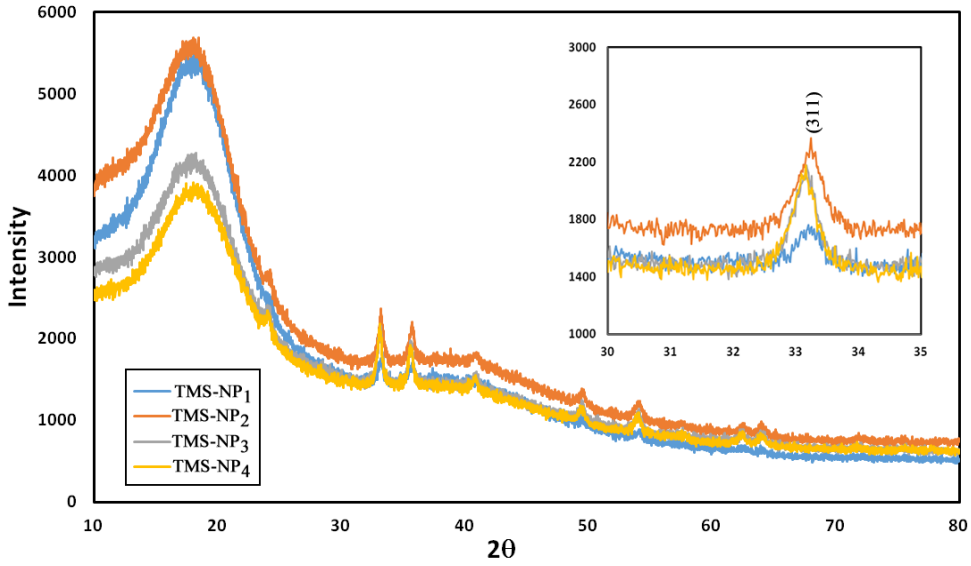

Figure 2. The XRD peak of the TMS-NP composite particles

The broad peak is about 18-20^o is due to the amorphous TMS copolymer. However, the peaks (311) having 2θ=35-37^o is about nanoparticles characteristic peaks. The composite peaks of TMS-NP reflected both of the copolymer and NP (Fig.2). In addition, increasing the NP content of the composite structure from 1 to 10 % wt resulted in increasing the characteristic NP peaks intensity of 311. The FTIR spectrum of magnetic nano particles is given in Fig.3. In this figure indicated that the vibrations of ions in the crystal lattice generally occur in the range of 100-2000 cm^{-1}. Two important peak is due to the metal-oxygen band.

One of them is seen in ν_1 = 600 cm^{-1} and other is seen about ν_2 = 1400 cm^{-1}.The most intensive peaks are due to the tetrahedral metal stress vibrations (M Octa-O).

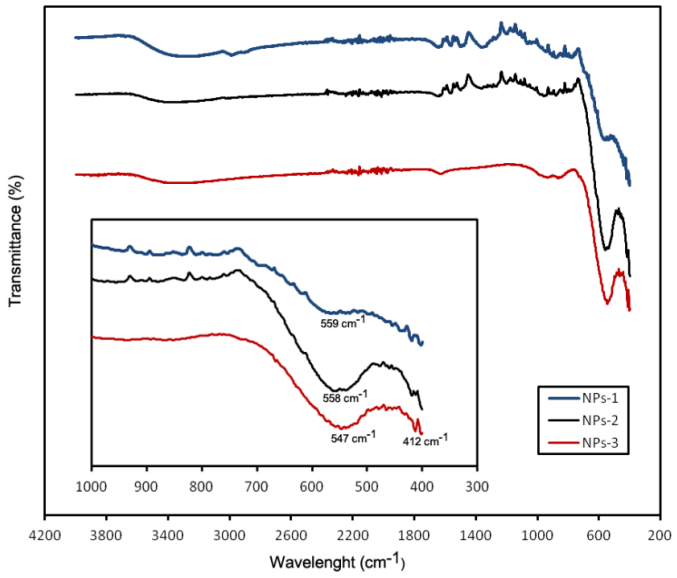

Figure 3. The FTIR spectrum of NP_1, NP_2 and NP_3 magnetic particles

The SEM images of NP_1 and TMS-NP_1 composite films that were prepared by using spray coating are given in Fig 4. The SEM EDX result is indicated the Cu content of the surface is 0.5 wt % and Fe content is 16.8 wt %.

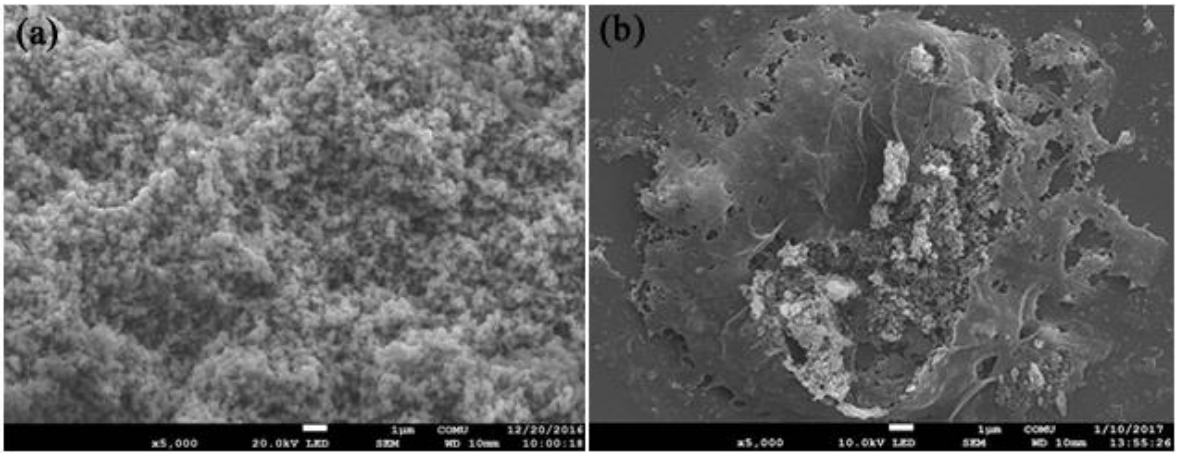

Figure 4. The SEM images of a) NP_1 b) TMS-NP_1 composite films

The TEM images of TMS-NP1 composite films are given in Fig 5.

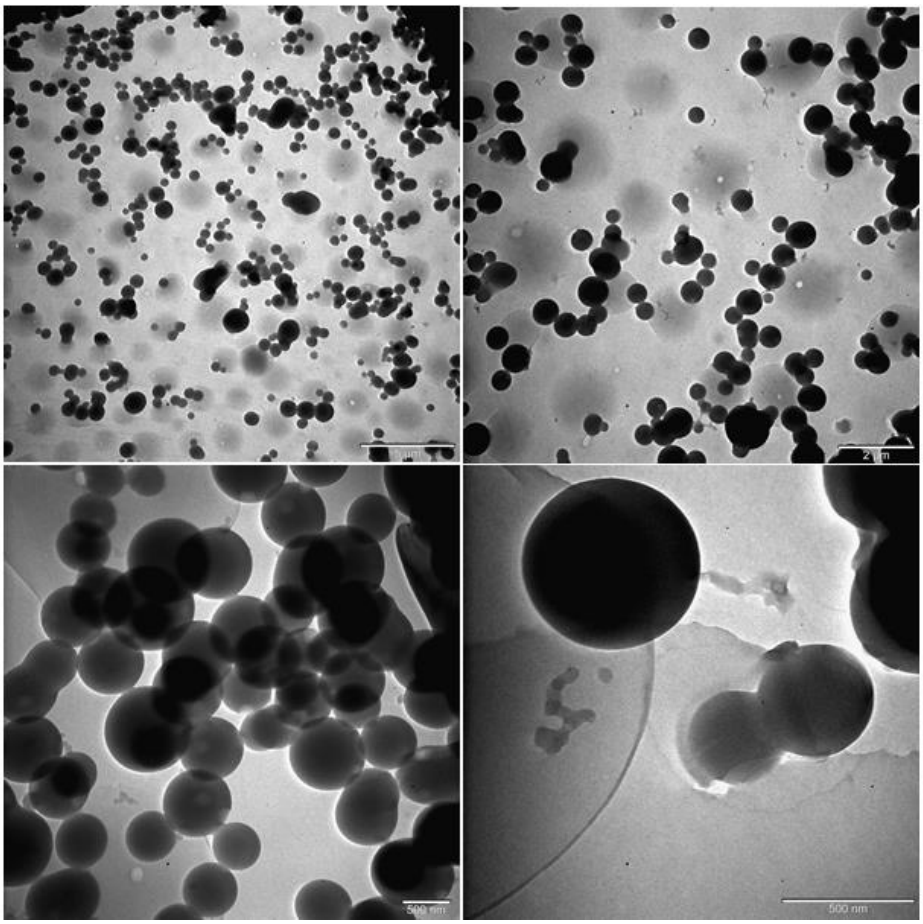

Figure 5. The TEM images of TMS-NP_1 composite films

The TEM images were indicated the linkage between polymer and nanoparticles. The ESR peaks given in Fig 6.

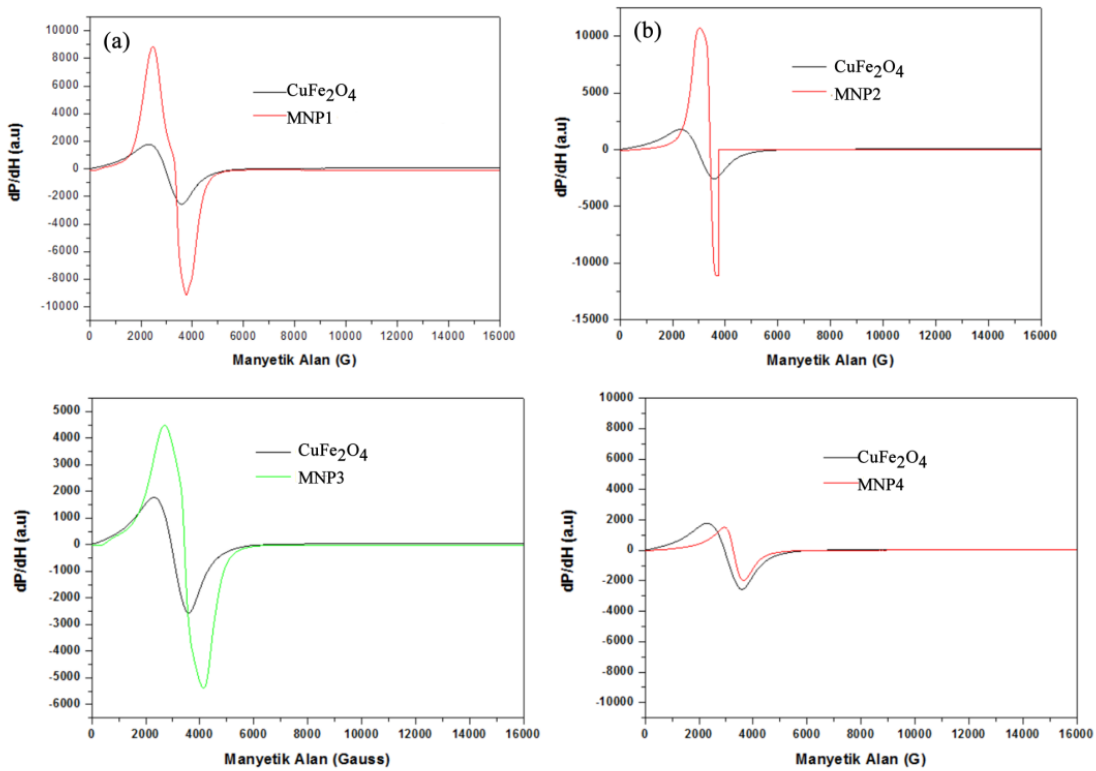

Figure6. The ESR images of TMS-NP composite particles (a) TMS-NP_1, (b) TMS-NP_2, (c) TMS-NP_3, (d) TMS-NP_4

Fig. 6 shows the evolution of the ESR spectra for TMS-NP composite nano particles. As can be seen from Figures, ESR signals are quite symmetric with respect to the resonance field values near the room temperature. The SP property of Cu doped Fe_2O_4 sample (Fig. 1d) is different from the signal of Cu doped Fe_2O_4 samples (Fig. 1a-c). The resonance field, line-width, intensity and *g*-factor for Cu doped Fe_2O_4 sample is calculated as $g_c = 2.12$, $g_a = 2.00$, $g_b = 1.88$. The ESR measurement showed that the TMS-NP particles are spinal ferrite. In addition all of the ESR peaks are same as the NP1 peaks. However, the peaks of NP and TMS-NP approached each other by increasing the NP amount of the composite particles. TMS-NP peaks and NP1 peaks were almost the same when NP1 content is 10 % wt (Fig 6d). It means the composite materials show the same behavior of NP1 nano particles.

4. CONCLUSION

The FMR spectra for these samples show brod lines and asymmetric behaviors. The broad line properties for the spectra originated from the antiferromagnetic interaction between tedrahedral and octahedral sites (Fe^{2+} ions). Because, Cu^{2+} ions occupy tetrahedral site in the spinel structures, in generally. The ESR peaks indicated that the TMS- $CuFe_2O_4$ composite particles having 10 % wt NP showed the same

behavior with $CuFe_2O_4$ nanoparticles. It is indicated the polymer-nanoparticles composite was can be used as a RADAR absorber film technology.

ACKNOWLEDGMENTS

This work was supported by Çanakkale Onsekiz Mart University The Scientific Research Coordination Unit, Project number: FYL-2014-140

REFERENCES

[1] GUPTA S C., Agrawal N K. and Chaitanya M V. Kumar, "Broad band thin sheet absorbers for S-; C-; X-; and Ku-bands.", J.IETE, 39, 197 (1993).

[2] SANCHEZ C., Julian B., Belleville P. and Popall M.,"Applications of Hybrid Organic-Inorganic Nanocomposites.", J. Mater. Chem. 15, 3559-3592, (2005).

[3] TADA M., Kanemaru T., Hara T., Nakagawa T., Handa H., Abe M., "Synthesis of hollow ferrite nanospheres for biomedical applications", Journal of Magnetism and Magnetic Materials,321, (2009), 1414.

[4] Yalçın, O., Erdem, R., Demir, Z., Magnetic properties and size effects of spin-1/2 and spin-1 models of core–surface nanoparticles in different type lattices, in: Smart Nanoparticles Technology, Abbass Hashim (Ed.), ISBN:978-953-51-0500-8,

[5] Parkin, S.S.P., Hayashi, M., Thomas, L., Magnetic domain-wall racetrack memory, Science 320, 190-194, 2008.

[6] Sunkara, B., Misra, R.D.K., Enhanced antibactericidal function of W^{4+}-doped titania-coated nickel ferrite composite nanoparticles: A biomaterial system, Acta Biomater. 4, 273-283, 2008.

[7] Venkatasubramanian, R., Srivastava, R.S., Misra, R.D.K., Comparative study of antimicrobial and photocatalytic activity in titania encapsulated composite nanoparticles with different dopants, Mater. Sci. Tech. 24, 589–595, 2008.

[8] Zhang, J., Misra, R.D.K., Magnetic drug-targeting carrier encapsulated with thermosensitive smart polymer: Core–shell nanoparticle carrier and drug release response, Acta Biomater. 3, 838-850, 2007.

[9] Zhang, J., Srivatsava, R.S., Misra, R.D.K., Core-Shell Magnetite Nanoparticles Surface Encapsulated withSmart Stimuli-Responsive Polymer: Synthesis, Characterization, and LCST of Viable Drug-Targeting Delivery System, Langmuir 23, 6342-6351, 2007.

[10] Rawat, J., Rana, S., Srivatsava, R.S., Misra, R.D.K., Anti-microbial activity of composite nanoparticles consisting of titania photocatalytic shell and nickel ferrite magnetic core, Mater. Sci. Eng. C 27, 540-545, 2007.

[11] Kim, J., Park, S., Lee, J.E., Jin, S.M., Lee, J.H., Lee, I.S., Yang, I., Kim, J.S., Kim, S.K., Cho, M.H., Hyeon, T., Designed fabrication of multifunctionalmagnetic gold nanoshells and their application tomagnetic resonance imaging and photothermal therapy, Angew. Chem. Int. Edit. 45, 7754-7758, 2006.

[12] Yalçın, O., Bayrakdar, H., Özüm, S., Spin-flop transition, magnetic and microwave absorption properties of α-Fe_2O_4 spinel type ferrite nanoparticles, J. Magn. Magn. Mater. 343, 157-162, 2013.

[13] Bayrakdar, H., Yalçın, O., Cengiz, U., Özüm, S., Anigi, E., Topel, Ö., Comparison effects and electron spin resonance studies of α-Fe2O4 spinel type ferrite nanoparticles, Spectrochimica Acta Part A: Molecular and Biomolecular Spectroscopy, 132, 160-164.

[14] Cao, G., Nanostructures & nanomaterials, 1st edn. Imperial College Press, London, 2004.

[15] Bozbag, S.E., Sanli, D., Erkey, C., Synthesis of nanostructured materials using supercritical CO_2:Part II. Chemical transformations, Journal of Materials Science, 47, 3469-3492, 2012.

[16] Sanlı, D., Bozbag, S.E., Erkey, C., Synthesis of nanostructured materials using supercritical CO_2:Part I. Physical transformations, Journal of Materials Science, 47, 2995-3025, 2012.

[17] Cengiz, U., Erbil, H.Y. Perfluoromethacrylate-styrene statistical copolymers synthesized in CO_2-expanded monomers, Colloid and Polymer Science 292 (9), 2207-2215, 2014.

THE INFLUENCE OF ACTIVATOR CONCENTRATION ON STRENGTH CHARACTERISTICS OF ALKALI-ACTIVATED SLAG MORTARS

S. G. Gok[1] and S. Gundogan[2],

[1,2]*Department of Civil Engineering, Faculty of Engineering, Kirklareli, Turkey*

E-mail: saadet.gokce.gok@klu.edu.tr

Abstract

Alkali-activated mortars and concretes are alternative construction materials to Portland cement with their advantageous properties such as having lower cost of production, lower need of energy in production and being more environmentally friendly. Conventional concrete production is a large-scale industry with some negative effects: high levels of carbon dioxide emission and the growth of energy consumption during production. Industrial by-products can be used as main binder in alkali-activated materials. By the substitution of by-products like blast furnace slag and fly ash for traditional cementitious materials, the emissions of greenhouse gases during cement production can be decreased and their environmentally hazardous effects can be eliminated. However, to produce a sustainable construction material, workability, durability and strength characteristics of alkali-activated materials should be investigated thoroughly as well as their cost of production, and the need of the development of standards for these materials become apparent.

The purpose of this study was to investigate the effect of varying molarity of alkaline activator on mechanical properties of alkali-activated slag mortars. In this experimental study, alkali-activated slag mortars were produced, and blast furnace slag was activated by alkaline activators, which were sodium hydroxide (NaOH) solution and liquid sodium silicate (Na_2SiO_3). The mortar design kept same while the molarity of sodium hydroxide solution changed. The composition of alkali-activated mortars was consisted of standard sand, alkaline activator and blast furnace slag where no cement was used. CEM I 42.5 R Portland cement was used in reference mortar sample, and all the specimens were moist cured. Flexural and compressive strength values of 40 mm×40 mm×160 mm sized mortar specimens were determined at different ages.

Keywords: Alkali activation, Blast furnace slag, Mechanical properties

1. INTRODUCTION

The construction industry has great demand for concrete. Portland cement, which is the main component of conventional concrete, causes approximately 7% of world's total CO_2 emission. Several studies were focused on decreasing the amount of CO_2 emissions and producing more durable concrete. These studies reported different types of binders such as alkali-activated slag (AAS) has a potential in replacing Portland cement.

Alkali-activated mortar and concrete can be used as construction materials alternative to conventional concrete. A large number of experiments have been conducted in order to investigate the main factors affecting the development of mechanical strengths of AAS mortars and concretes [1-4].

Al-Otaibi found that the activator type and dosage had an important effect in AAS concrete. Higher dosage and the higher silicate modulus of the activator led to higher strength [5].

Chi carried out tests on physical and mechanical properties and durability characteristics of AAS concrete with varying dosages of activator solution, and found that the dosage of activator solution and curing conditions were significantly effective in strength and durability of AAS cement. The properties and durability of AAS cement enhanced with an increased dosage of Na_2O [6].

Recent studies show that the properties and durability of AAS are significantly dependent on dosage of alkaline solution [7]. It was reported that compressive strength of the slag mortars increased as the concentration of the activator increased [8, 9].

In this study, the effects of the activator concentration on the strength characteristics of AAS mortars were investigated. For this purpose, different concentrations of NaOH and liquid sodium silicate were used in alkali activation and mechanical properties of alkali-activated mortars were tested at the ages of 3, 7, 28 and 90 days.

2. MATERIAL AND METHODS

In order to produce alkali-activated mortars, standard sand, blast furnace slag and alkaline activators were used. Blast furnace slag was activated by sodium hydroxide (NaOH) solution and liquid sodium silicate (Na_2SiO_3).

The concentrations of sodium hydroxide solutions were changed between 8 M to 14 M. Before casting, 8 M, 10 M, 12 M and 14 M NaOH solutions were prepared. The purity of NaOH in solid form was 0.99. Due to dissolving NaOH in water is an exothermic reaction, sodium hydroxide solutions were used in mortars 24 hours after preparation.

Mortars in fresh state were casted into 40 mm×40 mm×160 mm sized moulds. Reference sample with water/cement (w/c) ratio of 0.43 was produced by using Portland cement CEM I 42.5 R, water and standard sand. In alkali-activated mortar design, no cement and no additional water were used, activator/slag ratio was 0.43 and Na_2SiO_3/NaOH solution ratio was 2.5. The amount of liquid sodium silicate was kept constant. As there was no change in mortar design, water/binder (w/b) ratio was decreased with the increasing molarities of sodium hydroxide.

The specimen codes show the molarities of sodium hydroxide solution. Prismatic mortar specimens coded with 10M and 12M were produced with blast furnace slag provided from Zonguldak-Eregli region. Specimens coded with 8M and 14M were produced with a different source of blast furnace slag. For each sodium hydroxide concentration, compressive and flexural strengths of mortars were tested at the ages of 3, 7, 28 and 90 days. Three specimens were tested for each group. The average of three values for flexural strength and the average of six values for compressive strength were determined.

3. RESULTS AND DISCUSSION

The compressive strength values of water-cured mortars at the ages of 3, 7, 28 and 90 days were given in Table 1. Due to the hydration reaction of cement was faster than the pozzolanic reaction, the strength gaining rate of Portland cement mortars was higher than the alkali-activated mortars at earlier ages. However, at later ages, alkali-activated materials had higher compressive strength values than Portland cement mortars.

The compressive strength values of water-cured mortars at the ages of 3, 7, 28 and 90 days were shown graphically in Figure 1.

Table 1. Compressive strength values of mortars at different ages.

	Compressive strength (MPa)			
	3 days	7 days	28 days	90 days
Reference	28.76	42.65	43.03	54.84
8M	19.31	41.52	75.96	88.45
10M	20.81	35.66	56.50	68.42
12M	22.40	39.68	59.83	68.45
14M	46.04	73.44	76.68	91.74

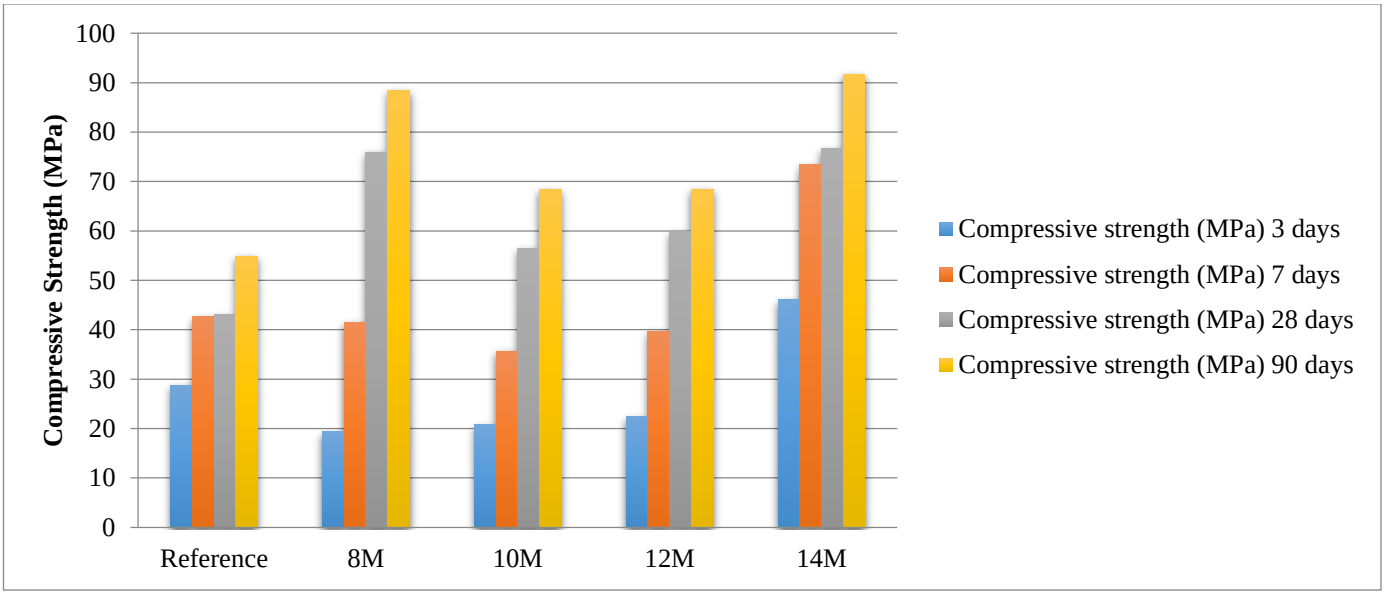

Figure 1. Compressive strength values of mortars at different ages.

The flexural strength values of water-cured mortars at the ages of 3, 7, 28 and 90 days were given in Table 2. As the NaOH concentration increased, flexural strength values of mortars increased. The decrement on flexural strength as changing the NaOH concentration to 10 M from 8 M was caused by the difference in blast furnace slag content.

Table 2. Flexural strength values of mortars at different ages.

	Flexural strength (MPa)			
	3 days	7 days	28 days	90 days
Reference	5.56	8.95	9.37	10.19
8M	3.42	5.04	6.96	9.45
10M	3.27	6.66	10.34	10.52
12M	3.46	8.94	10.55	11.83
14M	4.54	5.67	8.30	9.98

The flexural strength values of water-cured mortars at the ages of 3, 7, 28 and 90 days were shown graphically in Figure 2.

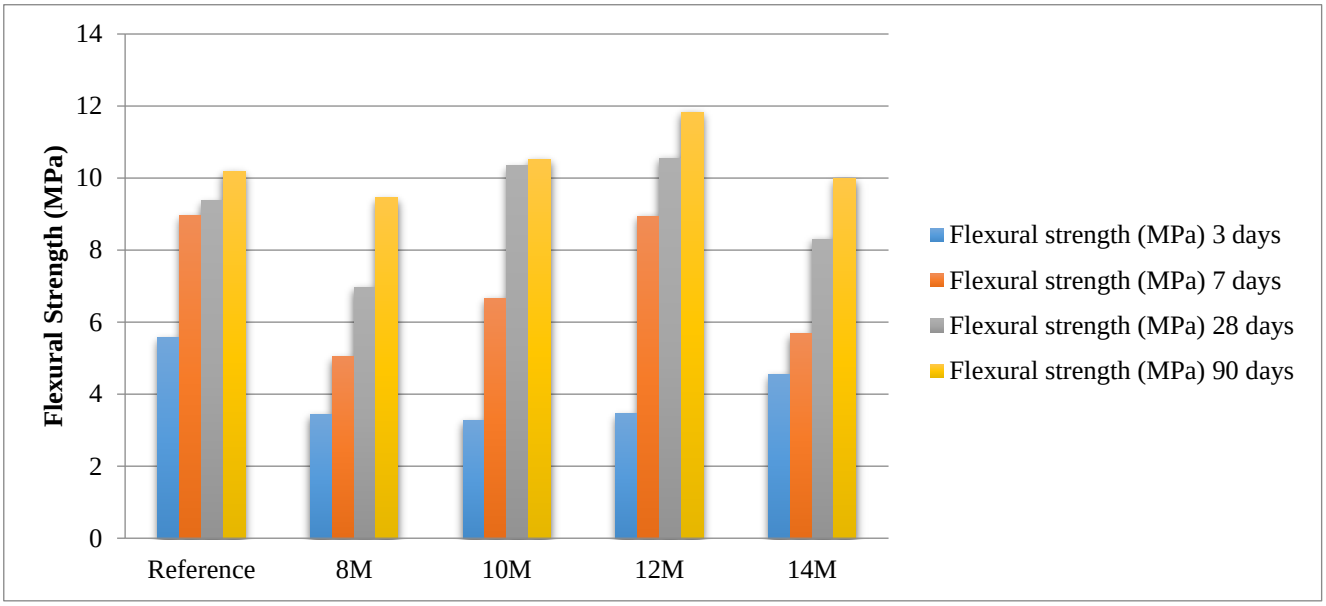

Figure 2. Flexural strength values of mortars at different ages.

4. CONCLUSION

As a result, it was found that compressive strength values of alkali-activated mortars increased at earlier ages with increasing molarities of sodium hydroxide solution.

Prismatic mortar specimens with 8 M and 14 M NaOH solutions were produced with a different source of blast furnace slag. Based on the obtained test results, it can be said that blast furnace slag content was a more effective factor on mechanical strength values than sodium hydroxide concentration.

The workability of mortars decreased with increasing concentrations of sodium hydroxide due to the weight of NaOH solution was kept constant; as the molarity of sodium hydroxide increased, the amount of solid NaOH increased and w/b ratio decreased.

As the strength test results of alkali-activated mortars was compared to Portland cement mortars, it can be reached that alkali-activated mortar can be used as an alternative material to ordinary Portland cement in prefabricated structural members with making appropriate design.

REFERENCES

[1] Aydin, S., Baradan, B. (2012). Mechanical and microstructural properties of heat cured alkali-activated slag mortars. *Materials and Design*, *35*, 374–383. https://doi.org/10.1016/j.matdes.2011.10.005

[2] Behfarnia, K., Shojaei, M., Mohebi, R. (2015). Compressive strength and flexural strength of alkali-activated slag concrete designed by Taguchi method. *Asian Journal of Civil Engineering*, *16*(4), 505–513.

[3] Fernández-Jiménez, A., Palomo, J. G., Puertas, F. (1999). Alkali-activated slag mortars: Mechanical strength behaviour. *Cement and Concrete Research*, *29*(8), 1313–1321. https://doi.org/10.1016/S0008-8846(99)00154-4

[4] Lee, N. K., Lee, H. K. (2013). Setting and mechanical properties of alkali-activated fly ash/slag concrete manufactured at room temperature. *Construction and Building Materials*, *47*, 1201–1209. https://doi.org/10.1016/j.conbuildmat.2013.05.107

[5] Al-Otaibi, S. (2008). Durability of concrete incorporating GGBS activated by water-glass. *Construction and Building Materials*, *22*(10), 2059–2067. https://doi.org/10.1016/J.CONBUILDMAT.2007.07.023

[6] Chi, M. (2012a). Effects of dosage of alkali-activated solution and curing conditions on the properties

and durability of alkali-activated slag concrete. *Construction and Building Materials*, *35*, 240–245. https://doi.org/10.1016/j.conbuildmat.2012.04.005

[7] Chi, M. (2012b). Effects of dosage of alkali-activated solution and curing conditions on the properties and durability of alkali-activated slag concrete. *Construction and Building Materials*, *35*, 240–245. https://doi.org/10.1016/j.conbuildmat.2012.04.005

[8] Duran Atis, C., Bilim, C., Celik, O., Karahan, O. (2009). Influence of activator on the strength and drying shrinkage of alkali-activated slag mortar. *Construction and Building Materials*, *23*(1), 548–555. https://doi.org/10.1016/j.conbuildmat.2007.10.011

[9] Rashad, A. M., Zeedan, S. R. (2011). The effect of activator concentration on the residual strength of alkali-activated fly ash pastes subjected to thermal load. *Construction and Building Materials*, *25*(7), 3098–3107. https://doi.org/10.1016/j.conbuildmat.2010.12.044

EFFECT OF CURING CONDITIONS ON MECHANICAL PROPERTIES OF ALKALI-ACTIVATED MORTARS

S. G. Gok[1] and S. Gundogan[2],

[1,2]*Department of Civil Engineering, Faculty of Engineering, Kirklareli, Turkey*

E-mail: saadet.gokce.gok@klu.edu.tr

Abstract

Alkali-activated materials are more environmentally-friendly and sustainable materials in comparison with conventional concrete. In concrete production, cement is used as main binder and cement production is a pollutant process due to high carbon dioxide emissions during clinker production. By taking into consideration the high levels of energy consumption in this process, the need of using alternative construction materials arise. Alkali-activated materials, in which pozzolans such as fly ash and blast furnace slag gain binding property in the presence of alkaline activators, can be alternative construction materials especially in prefabricated structural members. The use of industrial by-products in alkali-activated materials makes these materials more energy-efficient and eco-friendly.

The aim of this study was to determine the effect of curing conditions on flexural and compressive strengths of alkali-activated slag based mortars. Sodium hydroxide (NaOH) solution and liquid sodium silicate (Na_2SiO_3) were used as activator solutions in alkali-activated mortars. In mortar design, blast furnace slag, alkaline activator and standard sand were used and mortar specimens were exposed to three different curing conditions: moist curing entire-time, in laboratory air entire-time, and in laboratory air after 24 hours in 60˚C. Portland cement CEM I 42.5 R, water and standard sand were used in reference sample. For each curing condition, flexural and compressive strengths of mortars were tested at different ages.

Keywords: Alkali activation, Flexural strength, Compressive strength

1. INTRODUCTION

There is an increasing interest in investigating the usage of alkali-activated materials (AAM) as an alternative to ordinary Portland cement (OPC). Industrial waste such as blast furnace slag can be reused in an efficient way through alkali activation. Alkali-activated slag (AAS) is more environmentally-friendly material in comparison with ordinary Portland cement [1].

Alkali-activated slag is a mixture of blast furnace slag and alkaline solution. Alkali-activated slag binders have advantages by comparison with ordinary Portland cement such as lower hydration heat, the development of earlier and higher mechanical properties, better resistance to chemical attacks and freeze-thaw cycles [2].

A number of studies have investigated the factors having influence on the development of the mechanical properties. These factors include curing temperature, activator concentration and nature of alkaline activator [3]. Previous investigation showed the effect of curing temperature on microstructure, shrinkage, and compressive strength of alkali-activated slag (AAS) concrete [4]. It was found that heat treatment is effective on initial strength development but at later ages compressive strength is significantly reduced by comparison with concrete cured at room temperature.

Investigation on mechanical properties of heat cured AAS mortars showed that autoclaving is a proper curing method for the activator solution with low Na_2O concentrations and low Ms (SiO_2/Na_2O) ratios, and steam curing is preferable for the activators that have high Ms (SiO_2/Na_2O) ratios [5].

Chi carried out tests on AAS concrete with three different curing conditions and reported that the properties and durability of AAS concrete were considerably dependent on dosage of alkali-activated solution and curing conditions [6].

Bilim, Karahan, Atis and Ilkentapar observed that the best results were obtained from the AAS mortars cured at 23±2°C and 95% relative humidity during the test period [7].

Gebregziabiher, Thomas and Peethamparan investigated the compressive strength development of alkali-activated slag binders cured at ambient and elevated temperature and reported that strength development was improved with higher activator concentrations when cured at elevated temperature [8].

The aim of this study was to determine the effect of different curing conditions on flexural and compressive strengths of alkali-activated slag based mortars. For this purpose, prismatic mortar specimens

were exposed to three different curing conditions and variation in strengths were determined at different ages.

2. MATERIAL AND METHODS

In this experimental study, alkali-activated mortars composed of blast furnace slag, standard sand and activator solution were produced. Blast furnace slag provided from Zonguldak-Eregli region was activated with alkaline activator consisting of 10 M sodium hydroxide solution and liquid sodium silicate. Sodium hydroxide in solid form with purity of 99% was dissolved in water and sodium hydroxide solution was used in mortar 24 hours after preparation to provide enough cooling.

In alkali-activated slag mortar (AASM) design, no cement and no additional water were used, activator/slag ratio was 0.43 and Na_2SiO_3/NaOH ratio was 2.5. Reference sample (R) having 0.43 water/cement (w/c) ratio was produced. Portland cement CEM I 42.5 R, water and standard sand were used in reference sample.

Prismatic mortar specimens with the size of 40 mm×40 mm×160 mm were exposed to three different curing conditions: moist curing entire-time, in laboratory air entire-time, and in laboratory air after 24 hours in 60˚C. For each curing condition, flexural and compressive strengths of mortars were tested at the ages of 3, 7, 28 and 90 days. Three specimens were tested for each group. The average of three values for flexural strength and the average of six values for compressive strength were determined.

3. RESULTS AND DISCUSSION

The flexural and compressive test results of alkali-activated mortars at the ages of 3, 7, 28 and 90 days were given in the Table 1, 2, 3 and 4, respectively. As expected, heat treatment caused a decrement on flexural and compressive strengths of reference specimens, while it provided a rapid strength development at earlier ages. Curing conditions had a significant effect on earlier ages.

Table 1. Flexural and compressive strength test results of mortars at the age of 3 days.

Specimen/Curing Condition	Flexural Strength (MPa)	Compressive Strength (MPa)
Reference/laboratory air entire-time	3.98	19.71
Reference/moist curing entire-time	5.56	28.76
Reference /laboratory air after 24 hours in 60˚C	3.25	19.73
AASM/laboratory air entire-time	4.17	16.61
AASM/moist curing entire-time	3.27	20.81
AASM/laboratory air after 24 hours in 60˚C	4.79	48.23

Table 2. Flexural and compressive strength test results of mortars at the age of 7 days.

Specimen/Curing Condition	Flexural Strength (MPa)	Compressive Strength (MPa)
Reference/laboratory air entire-time	4.57	27.54
Reference/moist curing entire-time	7.36	43.04
Reference /laboratory air after 24 hours in 60˚C	4.28	21.68
AASM/laboratory air entire-time	6.36	39.31
AASM/moist curing entire-time	6.66	38.18
AASM/laboratory air after 24 hours in 60˚C	4.97	56.71

Table 3. Flexural and compressive strength test results of mortars at the age of 28 days.

Specimen/Curing Condition	Flexural Strength (MPa)	Compressive Strength (MPa)
Reference/laboratory air entire-time	5.02	28.07
Reference/moist curing entire-time	8.95	45.95
Reference /laboratory air after 24 hours in 60˚C	4.91	23.22
AASM/laboratory air entire-time	10.43	55.03
AASM/moist curing entire-time	10.52	56.50
AASM/laboratory air after 24 hours in 60˚C	10.97	66.36

Table 4. Flexural and compressive strength test results of mortars at the age of 90 days.

Specimen/Curing Condition	Flexural Strength (MPa)	Compressive Strength (MPa)
Reference/laboratory air entire-time	5.79	29.08
Reference/moist curing entire-time	9.37	54.84
Reference /laboratory air after 24 hours in 60˚C	5.45	24.30
AASM/laboratory air entire-time	11.56	62.14
AASM/moist curing entire-time	13.56	71.48
AASM/laboratory air after 24 hours in 60˚C	13.78	72.59

Flexural and compressive strengths of mortars at the ages of 3, 7, 28 and 90 days were given graphically in Figure 1 and Figure 2, respectively.

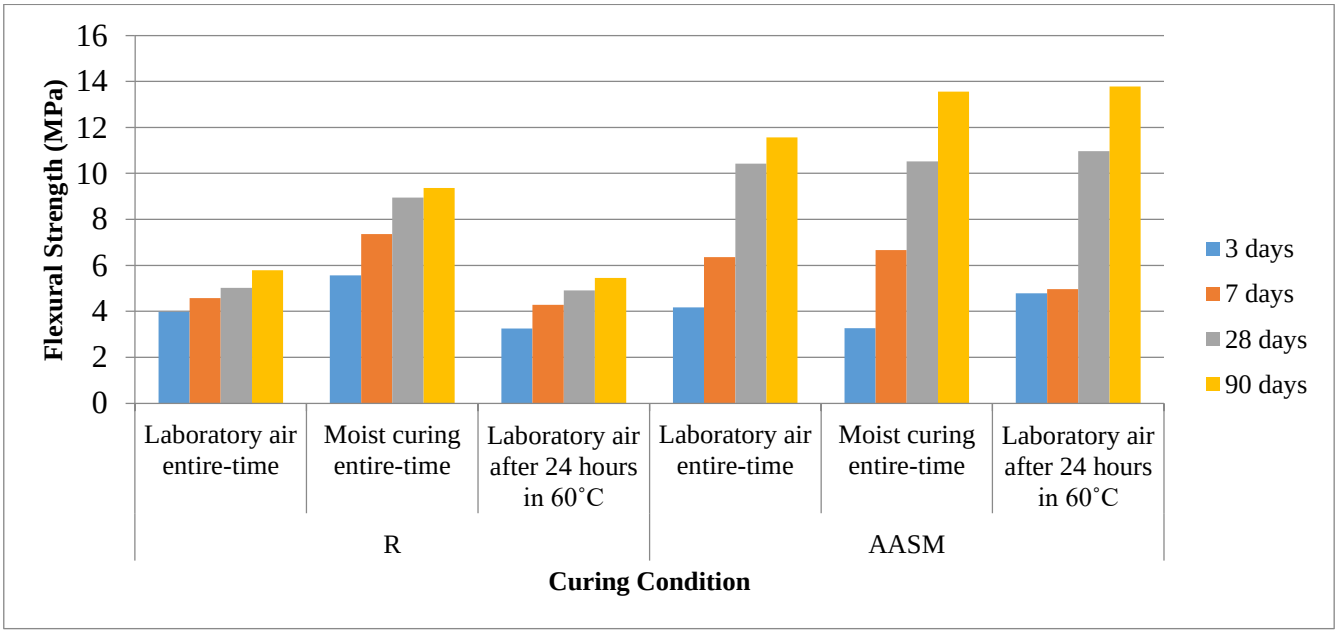

Figure 1. Flexural strength of mortars at different ages.

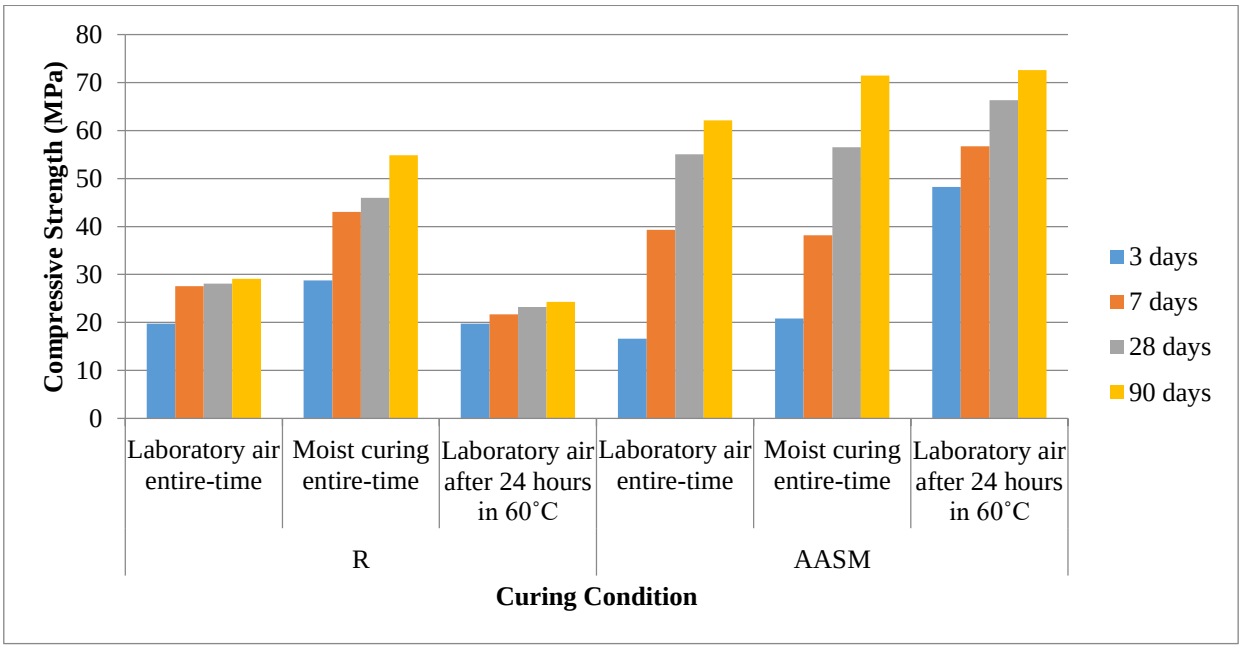

Figure 2. Compressive strength of mortars at different ages.

4. CONCLUSION

As a consequence, it was observed that curing in laboratory air after 24 hours in 60˚C gave the highest strength results in alkali-activated mortars in comparison with other curing conditions of this research. As expected, moist curing gave the best results in mortars produced by using ordinary Portland cement. At later ages, curing condition did not have a significant effect on mechanical strengths of alkali-activated mortars. With appropriate design and curing of alkali-activated mortars, high compressive strength values can be reached.

REFERENCES

[1] Ding, Y., Dai, J. G., Shi, C. J. (2018). Fracture properties of alkali-activated slag and ordinary Portland cement concrete and mortar. *Construction and Building Materials*, *165*, 310–320. https://doi.org/10.1016/j.conbuildmat.2017.12.202

[2] Wang, S. D., Scrivener, K. L., Pratt, P. L. (1994). Factors affecting the strength of alkali-activated slag. *Cement and Concrete Research*, *24*(6), 1033–1043. https://doi.org/10.1016/0008-8846(94)90026-4

[3] Fernández-Jiménez, A., Palomo, J. G., Puertas, F. (1999). Alkali-activated slag mortars: Mechanical strength behaviour. *Cement and Concrete Research*, *29*(8), 1313–1321.

https://doi.org/10.1016/S0008-8846(99)00154-4

[4] Bakharev, T., Sanjayan, J. G., Cheng, Y. B. (1999). Effect of elevated temperature curing on properties of alkali-activated slag concrete. *Cement and Concrete Research*, *29*(10), 1619–1625. https://doi.org/10.1016/S0008-8846(00)00349-5

[5] Aydin, S., Baradan, B. (2012). Mechanical and microstructural properties of heat cured alkali-activated slag mortars. *Materials and Design*, *35*, 374–383. https://doi.org/10.1016/j.matdes.2011.10.005

[6] Chi, M. (2012). Effects of dosage of alkali-activated solution and curing conditions on the properties and durability of alkali-activated slag concrete. *Construction and Building Materials*, *35*, 240–245. https://doi.org/10.1016/j.conbuildmat.2012.04.005

[7] Bilim, C., Karahan, O., Atis, C. D., Ilkentapar, S. (2013). Influence of admixtures on the properties of alkali-activated slag mortars subjected to different curing conditions. *Materials and Design*, *44*, 540–547. https://doi.org/10.1016/j.matdes.2012.08.049

[8] Gebregziabiher, B. S., Thomas, R. J., Peethamparan, S. (2016). Temperature and activator effect on early-age reaction kinetics of alkali-activated slag binders. *Construction and Building Materials*, *113*, 783–793. https://doi.org/10.1016/j.conbuildmat.2016.03.098

EFFECTS OF SODIUM CHLORIDE ON CONCRETES SUBSTITUTED ZEOLITE AND DIATOMITE

Y. Koçak[1] and M. Savaş[2]

[1]*Department of Civil Engineering, Faculty of Technology, Düzce, Turkey*
[2]*Özsoy Mimarlık, Düzce, Turkey*

E-mail: yilmazkocak@duzce.edu.tr

Abstract

Cement and pozzolans have become common building materials in today's fast developing construction sector. Due to economic and ecological factors, natural pozzolanic materials like zeolite and diatomite are intensely used in the cement and concrete technology. In this study, it is tried to state the physical and mechanic characteristics of the concrete produced with diatomite and zeolite substitution in which Turkey is quite rich. This study was designed to investigate the behavior of zeolite and diatomite under the effect of sodium chloride (NaCl). In the purpose, Portland cement, 5+5% and 10+10% diatomite and zeolite, which were substituted for Portland cement, a total of 3 different cements have been used. 15x15x15 cm cube samples have been made for each concrete group which was produced with these cements and this makes totally 54 units. While preparing the samples for the study, a mix design have been done (the amount of subsidence is between 7-10 cm). On samples of produced hardened concrete unit weight, water absorption, porosity, ultrasonic velocity, capillary water absorption and compressive strength experiments have been done. Hardened concrete tests have been done on three different types of concrete, for 28 days, in 23±2 ^{o}C water, then on the concrete samples which are cured NaCl of the media factor and in the level 2 (56 and 90 days) of concrete age factor. As a result, it was determined that the compressive strength, capillary water absorption, ultrasonic velocity, porosity, water absorption and unit weight of the cured concrete specimens were in coherent with each other.

Keywords: Zeolite, Diatomite, Sodium Chloride, Capillary water absorption, Compressive strength

1. INTRODUCTION

Concrete has been the most important building materials in the last century that is used very widely in civil engineering aplication. Impermeability is very important in concrete, and, one of the most important precautions for reducing the corrosion is to manufacture impermeability concrete. One on the most important cause of steel corrosion in concrete and concrete is the presence of chloride ions in the concrete. Chloride ions can enter the concrete with a porous structure in various ways such as sea water, sea sands or aggregates extracted from salty medium [1]. With the high concentration of sulfate ions it contains, sea water makes sulphate on the concrete. It also dissolves cement components with carbonic acid effect in sea water permeable concrete [2]. The amount of salt used and the frequency of application increases the deterioration of the concrete surface, even 2% NaCl solution can cause great damage to concrete [3]. The main damage of sea water to the concrete structure is the chlorine origin in sea waters. Chlorine in seawater accelerates the corrosion of the iron fittings in the concrete and can lead to the disintegration of the concrete [4]. It is very important to take necessary precautions in the concrete works to be done in the industry branches. If concrete is manufactured as impermeable as possible and besides the materials used in concrete production are carefully selected, the resistance against chloride effect of concrete can be increased. Therefore, finer grain pozzolans such as zeolite, diatomite, trass, pumice, blast furnace slag, rice husk ash, fly ash and silica fume are added into concrete and cement [1]. Besides, some characteristics of pozzolans such as strength, durability and low permeability expected from good concrete are closely related not only to mix proportions but also to cement properties [5–12].

Zeolite and diatomite are preferred for various characteristics structures and among the most abundant minerals in Turkey. This study was designed to investigate the performance of the concrete produced with zeolite and diatomite substitution under the effect of sodium chloride (NaCl). In the purpose, reference (Portland cement), 5+5%-10+10% zeolite and diatomite, which were substituted for Portland cement, a total of 3 different cements have been used. The properties of hardened concrete samples prepared with these cements were investigated by experiments such as compressive strength, capillary water absorption, ultrasonic velocity, porosity, water absorption and unit weight.

2. MATERIAL AND METHODS

CEM I 42.5 R type ordinary Portland cement, zeolite and diatomite were used in the study. CEM I 42.5 R Portland cement (PC) produced by Bolu Cement Factory. Diatomite was supplied by ASU Chemistry and Mining Firm and zeolite was supplied by a Turkish Zeolite Firm. The physical, mechanical

and chemical properties of the cement, zeolite and diatomite used in the study are given at the Table 1.

Table 1. The physical, mechanical and chemical properties of PC, zeolite and diatomite.

Materials		PC	Zeolite	Diatomite
Physical and mechanical properties				
Blaine, cm^2/g		4249	5740	13640
Specific gravity		3.17	2.18	2.28
Setting time, minute	Initial	118	-	-
	Final	-	-	-
Range dimension (over sieve), %	45 µm	4.08	17.60	9.80
	90 µm	-	35.80	28.60
Compressive strength, (MPa)	7 days	29.6	-	-
	28 days	52.8	-	-
Chemical composition, wt.%				
SiO_2 (S)		18.68	68.85	79.56
Al_2O_3 (A)		4.67	11.71	6.54
Fe_2O_3 (F)		3.53	1.29	2.76
CaO		64.56	3.97	2.45
MgO		0.98	1.06	0.79
SO_3		3.00	0.18	0.48
Na_2O		0.14	0.29	2.63
K_2O		0.73	2.19	0.69
S+A+F		-	81.85	88.86
Loss on ignition		3.92	10.00	3.88
Insoluble residue		0.50	37.32	75.98
Free CaO		1.74	-	-

In the study, 0–5 mm crashed sand with 1.647 specific gravity and 0.615% water absorption rate, 5–19 mm crushed stone with 1.650 specific gravity and 0.666% water absorption rate and 19–30 mm with 1.678 specific gravity and 1% water absorption rate are used. These aggregates are Asar River aggregates in Düzce region. Well water from Doğanlı village in Düzce is used as mixing water. Moreover, the type of fluid 70 produced by AYDOS Construction Chemicals Factory and new generation hyper plasticizer with solid matter content of 34.32, intensity of 1.184 (20°C), pH value of 7.26 (20°C) are applied as admixture for concrete.

In the study, three different cements which are encoded as R, 5D5Z (5+5% diatomite-zeolite) and 10D10Z (10+10% diatomite-zeolite) according to the addition rate are used. Zeolite and diatomite are substituted for Portland cement. For concrete mixture design, materials' amounts to be put into the mixture are determined according to the TS 802 standards [13]. According to the type and rate of mineral additive,

which is substituted for the concrete, three types of concrete are produced. According to TS EN 12350–2, consistency of concrete in fresh concrete is stated for each mixing group individually [14]. The materials amounts of the samples in concrete mixture of $1m^3$ and the characteristics of fresh concrete are given in the Table 2.

Table 2. Material quantity in the 1 m^3 for each concrete group.

Materials		Specific gravity	R, kg	5D5Z, kg	10D10Z, kg
Aggregate, mm	0-5	2.66	822	849	855
	5-19	2.69	586	606	611
	19-30	2.70	428	442	445
Total			1836	1897	1911
PC		3.17	400	360	320
Diatomite		2.28	-	20	40
Zeolite		2.18	-	20	40
Hyper plasticizer		1.184	4.8	4.320	3.840
Water		1	139.7	139.7	124.2

The produced concretes are poured into 150 x 150 x 150 mm cubic molds without segregation. These concretes are retained for 24 hours in the molds and harden. Hardened concrete tests have been done on three different types of concrete, for 28 hydration days, in 23±2 ^oC water. Subsequently, the concrete samples are cured in %5 sodium chloride (NaCl) and in the 56 and 90 hydration days. According to TS EN 12390–3 [15], the compressive strengths of all the concrete samples are measured at the end of 28, 56 and 90 hydration days.

3. RESULTS AND DISCUSSION

3.1. Slump test

While the samples are being prepared for the study, it is aimed to make a mixture design with a slump between 7 cm and 10 cm. In the light of the data, the slump amount is 7 cm in the concretes with R code, 7.8 cm in the concrete with 10D10Z code and 9.3 cm in the concrete 5D5Z code.

3.2. Unit Weight, Water Absorption and Porosity

Unit weight, water absorption and porosity test results of concretes according TS EN 12390-7 are given in the Figure 1, 2 and 3, respectively [16].

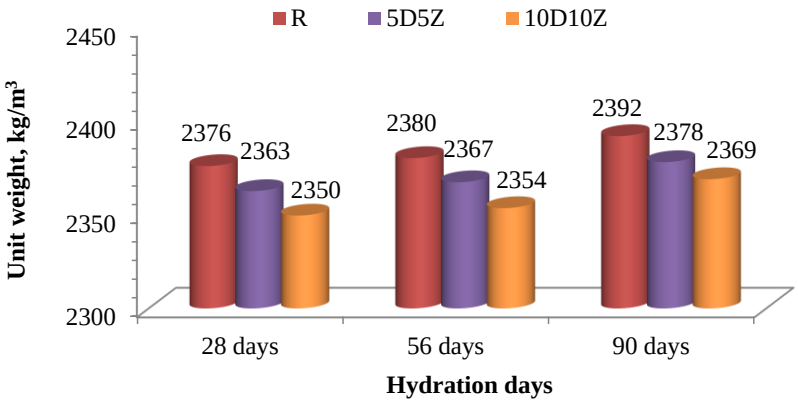

Figure 1. Unit weight results of concrete specimens.

As a result of the experiments of unit weight of concrete samples under the effect of sodium chloride (NaCl), it is found out that at the end of 28, 56 and 90 days the concrete sample with R code has the highest unit weight (2376, 2380 and 2392 kg/m^3) and the concrete sample with 10D10Z code has the lowest unit weight (2350, 2354 and 2369 kg/m^3), respectively. When the unit weight tests carried out at the end of 28, 56 and 90 days are taken as basis, according to reference concrete samples, the concrete samples with 5D5Z and 10D10Z code exhibit a unit weight decrease of 0.6-1.1%, 0.5-1.1%, and 0.6-1.0%, respectively (Figure 1).

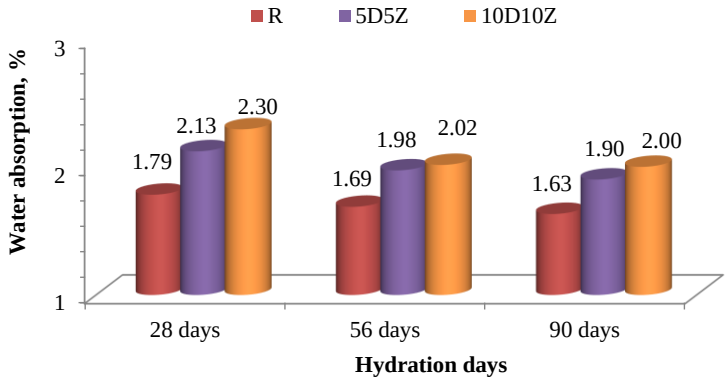

Figure 2. Water absorption results of concrete specimens.

As a result of the experiments of water absorption of concrete samples under the effect of sodium chloride (NaCl), it is found out that at the end of 28, 56 and 90 days the concrete sample with R code has the lowest water absorption (1.79%, 1.69% and 1.63%) and the concrete sample with 10D10Z code has the highest water absorption (2.30%, 2.02% and 2.00%)), respectively. When the water absorption tests carried

out at the end of 28, 56 and 90 days are taken as basis, according to reference concrete samples, the concrete samples with 5D5Z and 10D10Z code exhibit a water absorption increase of 19.1-28.7%, 16.6-19.1%, and 16.5-22.6%, respectively (Figure 2).

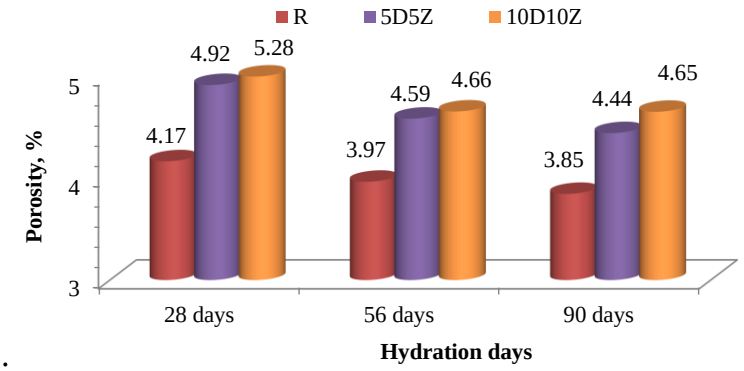

Figure 3. Porosity results of concrete specimens.

As a result of the experiments of porosity of concrete samples under the effect of sodium chloride (NaCl), it is found out that at the end of 28, 56 and 90 days the concrete sample with R code has the lowest porosity (4.17%, 3.97% and 3.85%) and the concrete sample with 10D10Z code has the highest porosity (5.28%, 4.66% and 4.65%), respectively. When the porosity tests carried out at the end of 28, 56 and 90 days are taken as basis, according to reference concrete samples, the concrete samples with 5D5Z and 10D10Z code exhibit a porosity increase of 18.0-26.7%, 15.6-17.4%, and 15.5-21.0%, respectively (Figure 3).

The results show that the unit weight, water absorption and porosity results of hardened concrete specimens are consistent.

3.5. Ultrasonic pulse velocity

Ultrasonic pulse velocity test results of the concretes are given in the Figure 4.

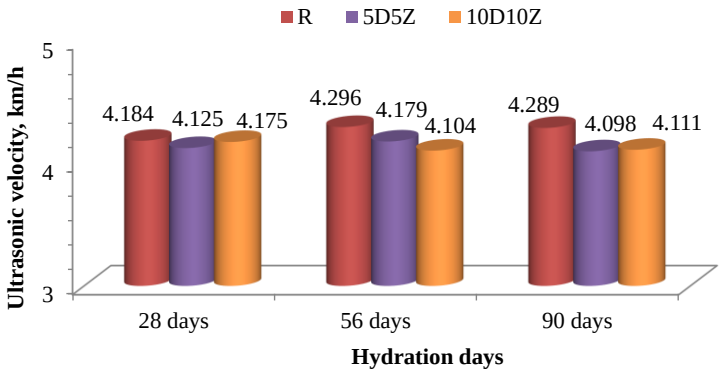

Figure 4. Ultrasonic pulse velocity of concrete specimens.

As a result of the experiments of ultrasonic pulse velocity of concrete samples under the effect of sodium chloride (NaCl), it is found out that at the end of 28, 56 and 90 days the concrete sample with R code has the highest ultrasonic pulse velocity (4.184, 4.296 and 4.289 km/h). While, the concrete sample with 5D5Z code has the lowest ultrasonic pulse velocity (4.125 and 4.098 km/h) at the end of 28 and 90 days, respectively, the concrete sample with 10D10Z code has the lowest ultrasonic pulse velocity (4.104 km/h) at the end of 56 days. When the ultrasonic pulse velocity tests carried out at the end of 28, 56 and 90 days are taken as basis, according to reference concrete samples, the concrete samples with 5D5Z and 10D10Z code exhibit a ultrasonic pulse velocity decrease of 1.4-0.2%, 2.7-4.5%, and 4.5-4.2%, respectively (Figure 4). According to the assessment of the quality of all concrete samples produced up to the ultrasonic pulse velocity values by Whitehurst (3.5–4.5 km/h), they belong to the good category of concrete [17]. The results show that the ultrasonic pulse velocity of hardened concrete specimens are consistent with the unit weight, water absorption and porosity results.

3.6. Capillary water absorption

A graphic is drawn between the averages of water amount absorbed per unit area (Q/A) and the square root of capillary water absorption durations ($t^{0.5}$). Capillarity coefficients are obtained from the curves of the graphs and the average capillary coefficients of capillary water absorption test results are given in the Figure 5.

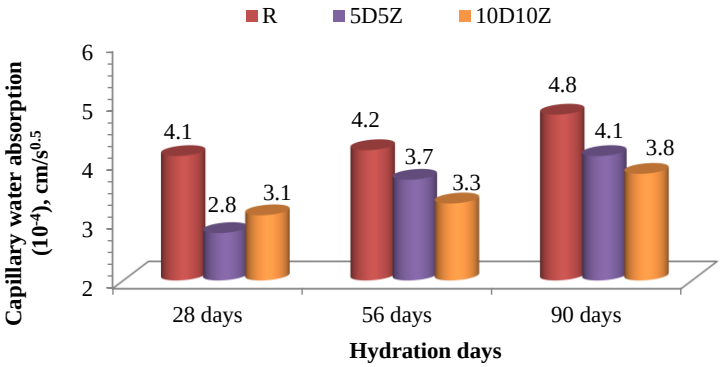

Figure 5. Capillary water absorption of concrete specimens.

As a result of the experiments of capillary water absorption of concrete samples under the effect of sodium chloride (NaCl), it is found out that at the end of 28, 56 and 90 days the concrete sample with R code has the highest capillary water absorption ($4.1x10^{-4}$, $4.2x10^{-4}$ and $4.8x10^{-4}$ $cm/s^{0.5}$). While, the concrete sample with 10D10Z code has the lowest capillary water absorption ($3.3x10^{-4}$ and $3.8x10^{-4}$

cm/s$^{0.5}$) at the end of 56 and 90 days, respectively, the concrete sample with 5D5Z code has the lowest capillary water absorption (2.8x10^{-4} cm/s$^{0.5}$) at the end of 28 days. When the capillary water absorption tests carried out at the end of 28, 56 and 90 days are taken as basis, according to reference concrete samples, the concrete samples with 5D5Z and 10D10Z code exhibit a capillary water absorption decrease of 31.7-24.4%, 11.9-21.4%, and 14.6-20.8%, respectively (Figure 5). According to the findings, there is an inverse relationship between the increase of hydration period and capillarity coefficient. The researches show that the produced concretes have a low capillary spaces and their quality of concrete is good [18–20]. The results show that the capillary water absorption of hardened concrete specimens are consistent with the unit weight, water absorption, porosity and ultrasonic pulse velocity results.

3.7. Compressive strength

Compressive strength test results of the concrete samples are given in the Figure 6.

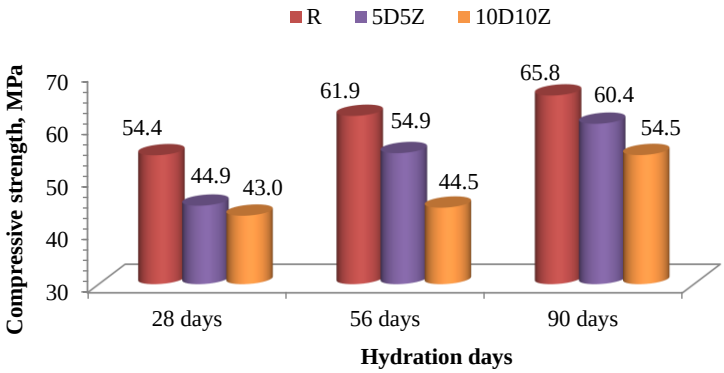

Figure 6. Compressive strength of concrete specimens.

When the test results are examined, it is obvious that compressive strength of the concrete samples depend on type of mineral additives, substitution rate, particle size, specific surface areas and hydration duration. As a result of the experiments of compressive strength of concrete samples under the effect of sodium chloride (NaCl), it is found out that at the end of 28, 56 and 90 days the concrete sample with R code has the highest compressive strength (54.4, 61.9 and 65.8 MPa) and the concrete sample with 10D10Z code has the lowest compressive strength (43.0, 44.5 and 54.5 MPa), respectively. When the compressive strength tests carried out at the end of 28, 56 and 90 days are taken as basis, according to reference concrete samples, the concrete samples with 5D5Z and 10D10Z code exhibit a compressive strength decrease of 17.5-21.0%, 11.3-28.1%, and 8.2-17.2%, respectively (Figure 6). When the rate of 5+5% is taken as basis, this fact proves that zeolite and diatomite substitution increase compressive strength in the future hydration

phases due to their pozzolanic properties, the concrete samples with zeolite and diatomite substitution acquire strength more slowly compared to the reference concrete. According to the compressive strength test results, it develops in consistency with both ultrasonic pulse velocity and capillary coefficients and at the end of 90 days, it is determined that the compressive strength of zeolite and diatomite for 5+5% substitution leaves the reference concrete behind even a little. Moreover, it is thought that more durable concretes can be produced by making no concessions to strength due to the fact that there are just a few capillary spaces (Figure 5).

4. CONCLUSION

The findings obtained from the experiments and analyses can be summarized as follows:

- As a result of the chemical analyses, it is stated that zeolite and diatomite are positive in terms of puzzolanic characteristics (S+A+F≧%70).
- According to their specific gravities, PC weighs 3.17, diatomite 2.28 and zeolite 2.18, thus, zeolite has the lowest specific gravity.
- The slump amount in the concrete mixture prepared with the reference and pozzolan substituted cements is about 7 cm, thus, the concrete of plastic consistency is produced and the cohesion in all types of concrete is fine, no disintegration is observed.
- As the hydration days are increased, water absorption and porosity of concrete samples are decreased, however unit weight of concrete samples are increased.
- Ultrasonic pulse velocity values depend on concrete type and age, as hydration day increases, ultrasonic value increases accordingly in the referance concrete samples.
- The compressive strength values of the concrete samples depend on material type, substitution rate and concrete age; the speed of strength acquirance of the zeolite and diatomite substituted concrete samples is slower than the one of reference concrete; compressive strength values develop in consistency with ultrasonic pulse velocity.
- The compressive strength, capillary water absorption, unit weight, water absorption, porosity and ultrasonic pulse velocity results of hardened concrete specimens are consistent with each other.

As the results of the tests, it is stated that zeolite and diatomite substitutions have a positive influence on the produced concrete samples and the most proper substation rate is determined to be 5+5%. During hydratation of concrete samples, CH formation is reduced due to zeolite and diatomite substitution, and therefore a lower compressive strength is obtained at the early ages when compared to referance concrete

samples. In the following hydratation days, zeolite and diatomite having pozzolanic structure bind CH in time and turn it into new (pozzolanic) C-S-H gel and cause the strength values reach that of referance concrete samples. Although Turkey is rich in zeolite and diatomite, their use is very limited. It is thought that both zeolite and diatomite may be an alternative to the materials in the artifical pozzolan category like blast furnace slag, fly ash and silica fume which are widely used in the concrete sector.

ACKNOWLEDGMENTS

In this study, the authors thank Düzce University Presidency of Scientific Research Projects that provided financial support with the project code number 2011.03.HD.009 and Düzce Yiğitler Beton that enabled the tests to be carried out.

REFERENCES

[1] Keleştemur, O., Yıldız, S., Effect of Various NaCl Concentration on Corrosion of Steel in Concrete Produced by Addition of Styrofoam, G.U. J. Sci., 19(3): 163-172, 2006.

[2] Kuyumcu, H.M., Deniz suyu ve sülfatlı suların beton dayanımına etkisi, Yüksek lisans Tezi, Sakarya Üniversitesi Fen Bilimleri Enstitüsü, Sakarya, 2006. (in Turkey)

[3] Çalişkan, Ö., Uçucu küllü harçların NaCl ve MgSO4 çözeltileri içersindeki davranışları, Yüksek Lisans Tezi, Osmangazi Üniversitesi Fen Bilimleri Enstitüsü, Eskişehir, 2005. (in Turkey)

[4] Yörükoğlları, E., Doğal Zeolitlerin Karayollarında Buz/Kar Çözücü Olarak Kullanımı, Madencilik Bülteni İnceleme, 40-42, 2005. (in Turkey)

[5] Ikotun, B.D., Ekolu, S., Strength and durability effect of modified zeolite additive on concrete properties, Construction and Building Materials, 24: 749–757, 2010.

[6] Kocak, Y., Tascı, E., Kaya, U., The effect of using natural zeolite on the properties and hydration characteristics of blended cements, Construction and Building Materials, 47: 720–727, 2013.

[7] Gerengi, H., Kocak, Y., Jażdżewska, A., Kurtay, M., Durgun, H., Electrochemical investigations on the corrosion behaviour of reinforcing steel in diatomite– and zeolite–containing concrete exposed to sulphuric acid, Construction and Building Materials, 49: 471–477, 2013.

[8] Najimi, M., Sobhani, J., Ahmadi B, Shekarchi M. An experimental study on durability properties of concrete containing Zeolite as a highly reactive natural pozzolan, Construction and Building Materials, 35: 1023–1033, 2012.

[9] Kocak, Y., A Study on the Effect of Fly Ash and Silica Fume Substituted Cement Paste and Mortars, Scientific Research and Essays, 5 (9): 990–998, 2010.

[10] Yıldız, K., Dorum, A., Koçak, Y., The investigation of the effect of minerological molecular electrokinetical and thermal compliance of pumice, zeolite and CEM I cement on high strength concrete, Journal of the Faculty of Engineering and Architecture of Gazi University, 25 (4): 867–879, 2010.

[11] Karakurt, C., Topçu, İ.B., Effect of blended cements produced with natural zeolite and industrial by–products on alkali–silica reaction and sulfate resistance of concrete, Construction and Building Materials, 25: 1789–1795, 2011.

[12] Aruntaş, H.Y., Tokyay, M., Katkılı çimento üretiminde diyatomitin puzolanik malzeme olarak kullanılabilirliği, Çimento ve Beton Dünyası, 1 (4): 3–41, 1996. (in Turkey)

[13] TS 802, Design of concrete mixes, Turkish Standards, 2009, Ankara (in Turkey).

[14] TS EN 12350–2, Testing fresh concrete – Part 2: Slump test, Turkish Standards, 2010, Ankara (in Turkey).

[15] TS EN 12390–3, Testing hardened concrete – Part 3: Compressive strength of test specimens, Turkish Standards, 2003, Ankara (in Turkey).

[16] TS EN 12390–7, Testing hardened concrete - Part 7: Density of hardened concrete, Turkish Standards, 2010, Ankara (in Turkey).

[17] Erdoğan, T.Y., Concrete, Metu Press Publishing Company, 2010, Ankara (in Turkey).

[18] Ghrici, M., Kenai, S., Said–Mansour, M., Mechanical properties and durability of mortar and concrete containing natural pozzolana and limestone blended cement, Cement & Concrete Composites, 542–549, 2007.

[19] Siddique, R., Kadri, E–H., Effect of metakaolin and foundry sand on the near surface characteristics of concrete, Construction and Building Materials, 3257–3266, 2011.

[20] Topçu, İ.B., Bilir, T., Uygunoğlu, T., Effect of waste marble dust content as filler on properties of self–compacting concrete, Construction and Building Materials, 1947–1953, 2009.

COMPRESSIVE STRENGTH OF CONCRETE CONTAINING DIATOMITE UNDER THE EFFECT OF SODIUM CHLORIDE BY ANN

G.Özcan[1], M. Akçay[2], Y. Koçak[3] and E. Gülbandılar[4]

[1]*Department of Computer Engineering, Faculty of Engineering, Bursa, Turkey*
[2]*Department of Computer Engineering, Faculty of Engineering, Kütahya, Turkey*
[3]*Department of Civil Engineering, Faculty of Technology, Düzce, Turkey*
[4]*Department of Computer Engineering, Faculty of Engineering, Eskişehir, Turkey*

E-mail: yilmazkocak@duzce.edu.tr

Abstract

In the world, concrete is an important role to play in construction technology. Different kinds of cements and pozzolans have been used in concrete technology. Diatomite, which is a natural pozzolan, is abundant in our country. Besides this, expert systems, which are Adaptive Network-based Fuzzy Inference Systems (ANFIS), fuzzy system, artificial neural network (ANN), and so on, have been used to solve a wide variety of problems in civil engineering applications by many researchers. In this study, two ANN prediction models were designed to investigate the behavior of concrete containing diatomite under the effect of sodium chloride. Three different mixes of the 28, 56 and 90 hydration days compressive strength experimental results of concrete containing diatomite used in training and testing for ANN systems was gathered from the experiments to construct this model. The data used in the ANN models are arranged in a format of six input parameters that cover the days (age of samples), Portland cement, diatomite, aggregate, water and hyper plasticizer and an output parameter which is compressive strength of concrete. In these models, results of the train and test results imply that our artificial neural network models have strong potential as a feasible tool for predicting 28, 56 and 90 hydration days' compressive strength of concrete containing diatomite under the effect of sodium chloride.

Keywords: ANN, Concrete, Sodium chloride, Diatomite, Compressive strength

1. INTRODUCTION

Concrete is an important role to play in building technology. Concrete is a composite material and concrete consists of homogenous mixtures of cement, aggregate, water, and sometime mineral and chemical admixture [1, 2].

Different kinds of cements have been used in concrete technology. In concrete, the most commonly used cement is either Portland or blended cement. In the cement and concrete technology, due to economic and ecological factors like trass, zeolite, diatomite, metakaolin, pumice, fly ash, blast furnace slag, and silica fume are intensely used [3-15]. Strength, durability and low permeability characteristics of expected from good concrete are closely related not only to mix proportions but also to cement properties. In our country, diatomite is preferred for various characteristics structures and among the most abundant minerals.

Nowadays, expert systems have been used to solve many problems in civil engineering applications by many researchers. One of the alternative approaches for predicting mechanical behavior and physical properties of concrete and cement mortars is artificial neural network (ANN) [16-20]. The purpose of this study is to build model in ANN system to evaluate the effect of compressive strength of reference concrete and concrete produced with diatomite substitution under the effect of sodium chloride (NaCl). In the purpose, %0, 10% and 20% diatomite, which were substituted for Portland cement, a total of 3 different cements have been used in the study. With these cements, 3 concrete samples were produced for each concrete type. Compressive strength experiments of concretes were carried out on the 28^{nd}, 56^{th} and 90^{th} days. The total 27 compressive strength results of concretes obtained from these experiments are used for training and test of this ANN system. Six input parameters that cover the days (age of samples), Portland cement, diatomite, aggregate, water and hyper plasticizer and an output parameter which is compressive strength of concrete had used in the ANN models. The results obtained from compressive strength of concrete were compared with predicted results.

2. EXPERIMENTAL STUDY

2.1. Materials

CEM I 42.5 R type ordinary Portland cement, diatomite, aggregate, hyper plasticizer and water were used in this study. CEM I 42.5 R Portland cement (PC) produced by Bolu Cement Factory. Diatomite was supplied by ASU Chemistry and Mining Firm. The chemical properties of the Portland cement and diatomite used in the study were given at the Table 1, and the physical and mechanical properties of the

Portland cement and diatomite were given at the Table 2. Asar River aggregates in Duzce region as aggregate (0–5 mm crashed sand, 5–19 mm and 19–30 mm crushed stone) were used. Furthermore, hyper plasticizer (type of fluid 70) produced by AYDOS Construction Chemicals Factory were used in the study. Hyper plasticizer, which is solid matter content of 34.32%, intensity of 1.184 (20°C), pH value of 7.26 (20°C), is new generation hyper plasticizer. And finally, mixing water of concrete is well water from Doganli village in Duzce.

Table 1. The chemical properties of PC and diatomite.

Chemical composition, wt.%	PC	Diatomite
SiO_2 (S)	18.68	79.56
Al_2O_3 (A)	4.67	6.54
Fe_2O_3 (F)	3.53	2.76
CaO	64.56	2.45
MgO	0.98	0.79
SO_3	3.00	0.48
Na_2O	0.14	2.63
K_2O	0.73	0.69

Table 2. The physical and mechanical properties of PC and diatomite.

Materials	Compressive strength, MPa		Setting time, minute		Blaine, cm^2/g	Specific gravity
	7 days	28 days	Initial	Final		
PC	29.6	52.8	118	-	4249	3.17
Diatomite	-	-	-	-	13640	2.28

2.2. Methods

In the study, three different cements, which were encoded as R (0% diatomite), 10D (10% diatomite) and 20D (20% diatomite) according to the addition rate of diatomite, were used. For concrete mixture design, materials' amounts to be put into the mixture were determined according to the TS 802 standards [21]. According to the type and rate of mineral additive, which was substituted for the concrete, three types of concrete were produced. According to TS EN 12350-2 [22], fresh concrete consistency was specified for each mixing group. The materials amounts of the samples in concrete mixture of $1m^3$ and the characteristics were given in the Table 3. The produced concretes were poured into 150 x 150 x 150 mm cubic molds without segregation, and were retained for 24 hours in the molds. The concrete samples were cured in 23±2 °C water until the 28 hydration days. Subsequently, the concrete samples were cured in %5

sodium chloride (NaCl) and in the 56 and 90 hydration days. According to TS EN 12390–3 [23], the compressive strengths of all the concrete samples were measured at the end of 28, 56 and 90 hydration days.

Table 3. Material quantity in the 1 m^3 for each concrete group.

Materials		Specific gravity	R, kg	10D, kg	20D, kg
Aggregate, mm	0-5	2.66	822	831	822
	5-19	2.69	586	593	586
	19-30	2.70	428	433	428
Total			1836	1857	1836
PC		3.17	400	360	320
Diatomite		2.28	-	40	80
Hyper plasticizer		1.184	4.800	4.320	4.800
Water		1	139.7	139.7	123.3

3. ARTIFICIAL NEURAL NETWORK MODELS AND EFFICIENT PARAMETERS

During the train and test phases of the ANN models, we utilize the days (age of samples), PC, diatomite, aggregate, water and hyper plasticizer as input parameters; whereas compressive strength of concrete was used as an output parameter according to Table 4.

Table 4. The input and output quantities used in ANN models.

		Data used in training and testing the model	
		Minimum	Maximum
Input variable	Age of samples, days	28	90
	PC, kg	320	400
	Diatomite, kg	0	80
	Aggregate, kg	1836	1857
	Water, kg	123.3	139.7
	Hyper plasticizer, kg	42.8	69.1
Output variable	**Compressive strength, MPa**	**43.8**	**68.7**

During the experimentation, we exploited 27 experimental data for the training phase of the model, whereas we utilized 9 data as the average of the observed results for testing the model. Various parameters are used in the design of ANN-1 model. These parameters are respectively, feed-forward back propagation, one hidden layer, the training function which utilize the Levenberg-Marquardt function, learngdm as the adaptation learning function, the transfer function which utilizes tansig, and the performance function that

computes mean squared error. We present the ANN frame in Figure 1-a. The input value of each layer in ANN-1 model is computed by the summation of multiplied weights of the outputs of all previous layers.

In terms of our second ANN model, ANN-2, we utilize a radial basis function network, which are based on linear combination of radial basis functions. The ANN-2 uses the radial basis as activation function as seen in Table 6. The radial basis function is important since it is commonly used in function approximation, time series prediction, and control. We demonstrate our ANN-2 in Figure 1-b. As can be seen in the figure, radial basis function network consists of one layer of input nodes, one hidden radial-basis function layer and one output linear layer [24].

a. ANN-1

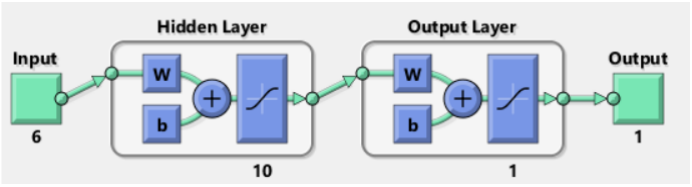

b. ANN-2

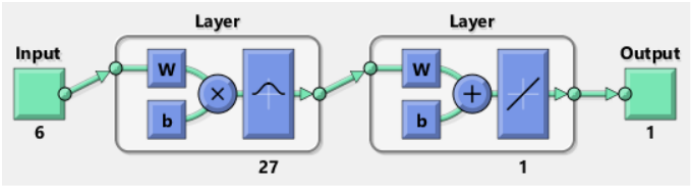

Figure 1. The architectures used in the ANN for compressive strength.

Having defined the momentum and learning rates, the model is exposed to training through neural network iterations. During the iterations we have observed the following parameters from the multilayer feed-forward neural network models were given in Table 5.

Table 5. The values of parameters used in models.

Parameters	ANN-1	ANN-2
Number of input layer neurons	6	6
Number of hidden layers	1	1
Number of layers	2	2
Number of first hidden layer neurons	10	27
Number of output layer neuron	1	1
Error after learning	$1x10^{-8}$	-
Learning cycle	5	-

The results of the trained model are compared to the input values. Observations show that predicted results are close to the experimental ones.

4. RESULTS AND DISCUSSION

In terms of ANN-1 model, firstly, we aim to achieve more reliable solutions by means of multilayer feedforward network model that contain one hidden layer. During the experimentation, it is necessary to find a design that introduces optimum number of the hidden layers' neurons that enable accurate prediction of the parameters. Initially, we start with a few neurons and we increase the number of neurons step by step to find the best model. In this respect, we aim to find a model that ensure optimum number of hidden neurons. We observed the performance of the ANN model according to the selected performance criteria during this process for each hidden neuron number. We repeated the experimentation until the error between experimental observations and predictions is sufficiently small.

At the beginning of the experimentation process, we exploit various number of neurons in the one hidden layers. During the advancement of the experimentation process, we increment the number of neurons step-by-step adding 1 neuron. We stop if neuron incrimination no more causes significant improvement.

In order to evaluate the ANN models, we utilize absolute fraction of variance (R^2), mean absolute percentage error (MAPE) and a root-mean squared (RMS) error criteria. These criteria are defined by Eqs. (1), (2) and (3), respectively [25].

$$RMS = \sqrt{\frac{1}{N}\sum_{i=1}^{N}\left|t_i - o_i\right|^2} \qquad (1)$$

$$R^2 = 1 - \left(\frac{\sum_{i=1}^{N}(t_i - o_i)^2}{\sum_{i=1}^{N}(o_i)^2}\right) \qquad (2)$$

$$MAPE = \frac{1}{N}\sum_{i=1}^{N}\left|\left(\frac{t_i - o_i}{o_i}\right)\right| * 100 \qquad (3)$$

where ***t*** is the target value, ***o*** is the network output value, and ***N*** is the total number of pattern.

In the ANN models, we collected 27 data from experimental results that are collected from laboratory experiments. These data is used for training. Furthermore, 9 data is utilized as average of these test results for testing. We present sample number and experimental results in Figure 2 and Figure 3. In the figures, reader can see the training and testing results, which are the yields of ANN models. All

experimental results and predictions by means of ANN models for 28, 56 and 90 days compressive strength are demonstrated in Figure 2 and 3, respectively.

Furthermore, we present inputs values/experimental results and predictions of ANN models were given in Table 6.

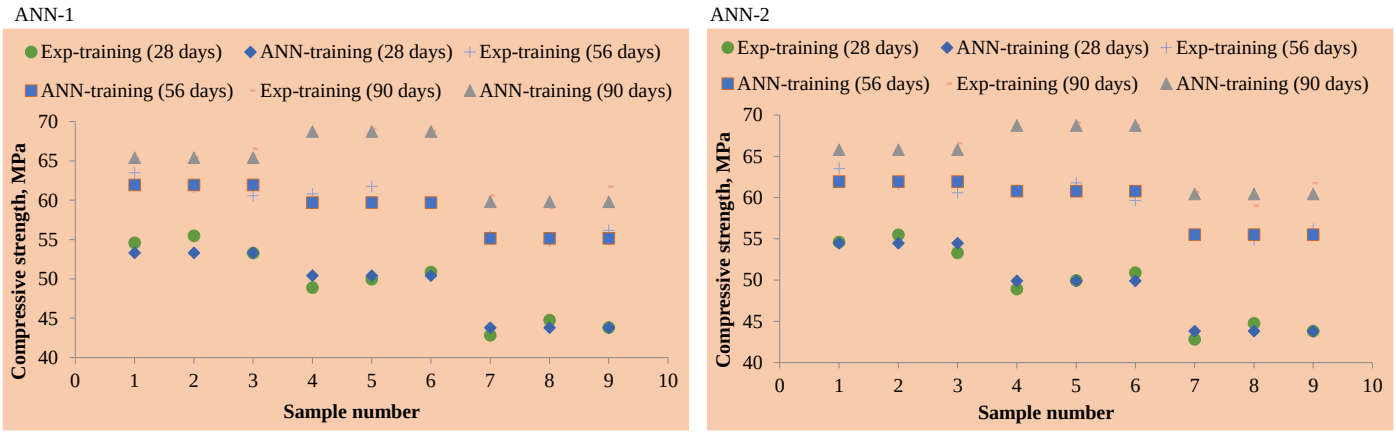

Figure 2. Comparison of compressive strength of training results.

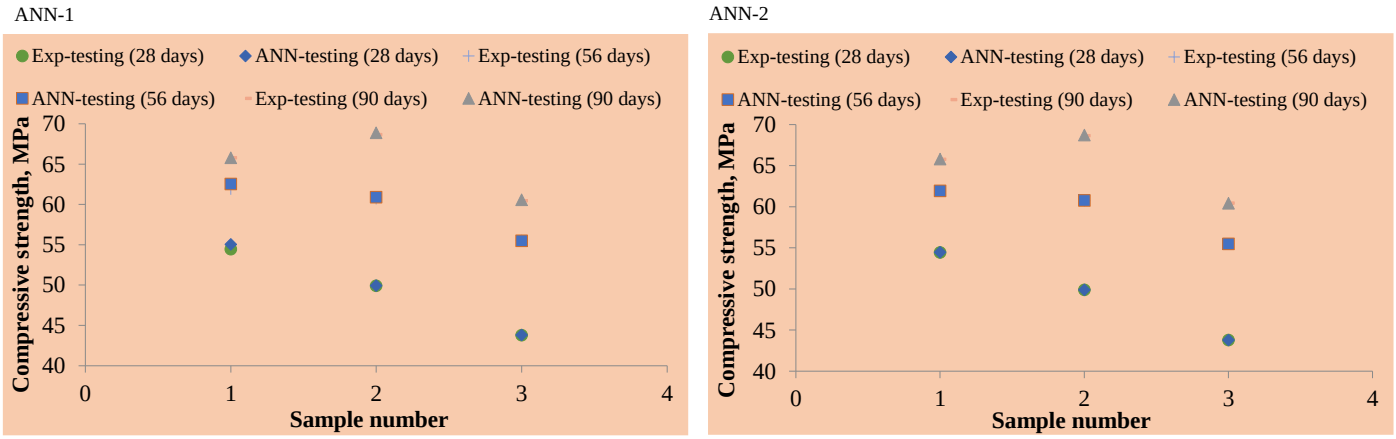

Figure 3. Comparison of compressive strength of testing results.

Table 6. Comparison of compressive strength of testing results obtained from ANN with experimental results.

Compressive strength, MPa								
Days	PC, kg	D, kg	A, kg	W, kg	HP, kg	Exp.	ANN-1	ANN-2
28	400	0	1836	139.7	4.800	54.4	55.0	54.5
28	360	40	1761	155.2	4.800	49.9	49.9	49.9
28	320	80	1712	154.0	6.000	43.8	43.8	43.8
56	400	0	1836	139.7	4.800	61.9	62.5	61.9
56	360	40	1761	155.2	4.800	60.7	60.9	60.8
56	320	80	1712	154.0	6.000	55.5	55.5	55.5
90	400	0	1836	139.7	4.800	65.8	65.8	65.8
90	360	40	1761	155.2	4.800	68.7	68.9	68.7
90	320	80	1712	154.0	6.000	60.5	60.6	60.4

In terms of the ANN models based on training and testing data; linear least square fit line, its equation and the R^2 values are shown in these figures. The results on Figure 4 and 5 shows that, the numerical values from experiments and predictions of ANN models are very closer to the experimental results.

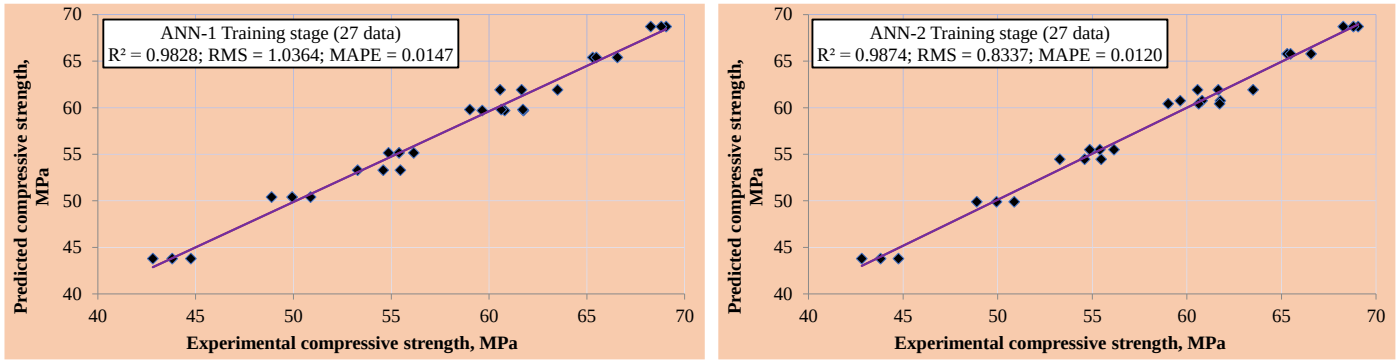

Figure 4. Comparison of compressive strength experimental results with training results of model.

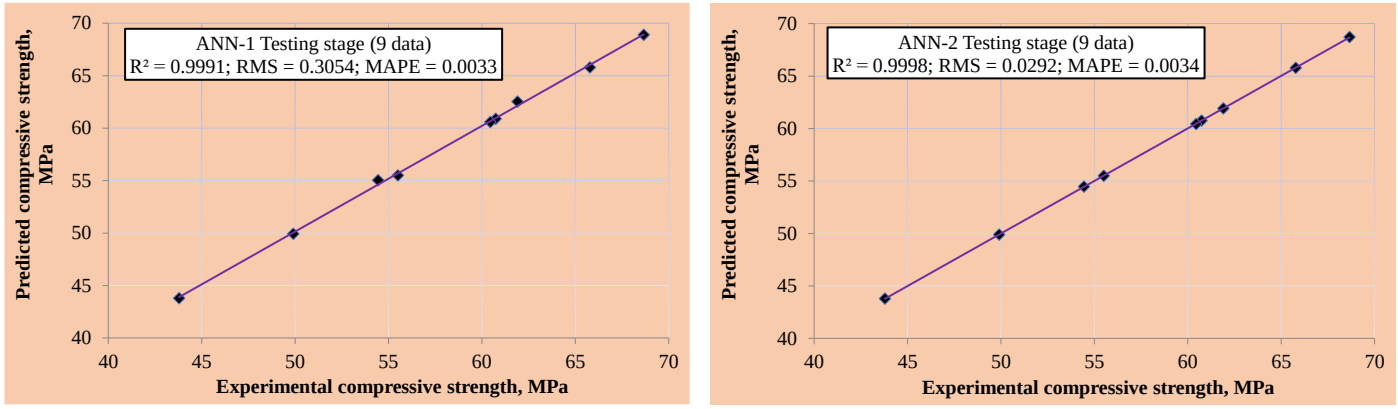

Figure 5. Comparison of compressive strength average of experimental results with testing results of model.

The results on Figure 4 and Figure 5 implies that it is possible to find an efficient ANN for our problem that can define an algorithm between input and output variables and make reasonably good predictions.

For all ANN experiments, the statistical values, R^2, RMS and MAPE, are demonstrated in Figure 4 and 5.

In summary, we did two sets of ANN based predictions and evaluated the results. Our analysis show that statistical values of R^2, RMS and MAPE from training in the ANN-1 model are founded as 0.9828, 1.0364 and 0.0147, respectively. These values were found in testing as 0.9991, 0.3054 and 0.0033, respectively (Table 8). When we analyze the training of ANN-2 model, we observed that same statistical values present 0.9874, 0.8337 and 0.0120. In terms of testing ANN, we observed 0.9998, 0.0292 and 0.0034 respectively. All the statistical values show that the proposed ANN models are suitable to predict the 28, 56 and 90 days compressive strength values and they are very close to the experimental values.

5. CONCLUSION

The findings obtained from the experiments and ANN models can be summarized as follows:

- As a result of the chemical analyses, it is stated that diatomite is positive in terms of puzzolanic characteristics (S+A+F≧%70).
- According to their specific gravities, PC weighs 3.17 and diatomite 2.28, thus, diatomite has the lower specific gravity.
- The compressive strength values of the concrete samples depend on material type, substitution rate and concrete age; the speed of strength acquirance of the diatomite substituted concrete samples is slower than the one of reference concrete.
- The compressive strength predictions are very closer to the experimental data for all models. The statistical parameter values of R^2, RMS and MAPE, which compare experimental data and two ANN models, have confirmed the case. Similar processes were performed two models and it found statistically significant correlations.
- The compressive strength values of reference and concrete containing diatomite under the effect of sodium chloride can be predicted by using the ANN in a quite short period of time with tiny error rates.
- The developed ANN models are practicable methods for predicting compressive strength values of reference and concrete containing diatomite under the effect of sodium chloride.

ACKNOWLEDGEMENT

The authors would like to thank Duzce University Presidency of Scientific Research Projects that provided financial support with the project code number 2011.03.HD.009 and Duzce Yigitler Beton that enabled the tests to be carried out.

REFERENCES

[1] Erdoğan, T.Y., Concrete, METU Press Publishing Company, 2010, Ankara. (in Turkey)
[2] Neville, A.M., Properties of Concrete, Fourth Edition, Pearson Education Limited, ISBN-13: 978-0-582-23070-5, England, 2006.
[3] Koçak, Y., Dorum, A., Yılmaz, B., Uçar, A., Trasın Çimento Yüzey Özelliğine Hidratasyona ve Basınç Dayanımına Etkisi, E–Journal Of New World Sciences Academy Technological Applied Sciences, 5: 1, 1–14, 2010. (in Turkey)
[4] Kocak, Y., Tascı, E., Kaya, U., The effect of using natural zeolite on the properties and hydration characteristics of blended cements, Construction and Building Materials, 47: 720–727, 2013.
[5] Kocak, Y., Savaş, M., Effect of the PC, diatomite and zeolite on the performance of concrete composites, Computers and Concrete, 17: 6, 815–829, 2016.
[6] Gerengi, H., Kocak, Y., Jażdżewska, A., Kurtay, M., Durgun, H., Electrochemical investigations on the corrosion behaviour of reinforcing steel in diatomite– and zeolite–containing concrete exposed to sulphuric acid, Construction and Building Materials, 49: 471–477, 2013.
[7] Keleştemur, O., Demirel, B., Effect of metakaolin on the corrosion resistance of structural lightweight concrete, Construction and Building Materials, 81, 172–178, 2015.
[8] Subaşı, A., Emiroğlu, M., Effect of metakaolin substitution on physical, mechanical and hydration process of White Portland cement, Construction and Building Materials, 95, 257–268, 2015.
[9] Yıldız, K., Dorum, A., Koçak, Y., Pomza Zeolit Ve Cem I Çimentosunun Minerolojik Moleküler Elektrokinetik Ve Termal Uyumunun Yüksek Dayanımlı Betona Etkisinin Araştırılması, Journal of The Faculty of Engineering and Architecture of Gazi University, 25: 4, 867–879, 2010. (in Turkey)
[10] Kocak, Y., Nas, S., The effect of using fly ash on the strength and hydration characteristics of blended cements, Construction and Building Materials, 73, 25–32, 2014.
[11] Zhengqi, L., Drying shrinkage prediction of paste containing meta–kaolin and ultrafine fly ash for developing ultra–high performance concrete, Materials Today Communications, 6, 74–80, 2016.
[12] Zhao, H., Sun, W., Wu, X., Gao, B., The properties of the self–compacting concrete with fly ash and ground granulated blast furnace slag mineral admixtures, Journal of Cleaner Production, 95, 66–74, 2015.
[13] Okoye, F. N., Durgaprasad, J., Singh, N. B., Effect of silica fume on the mechanical properties of fly ash based–geopolymer concrete, Ceramics International, 42, 3000–3006, 2016.
[14] Kocak, Y., A Study on the Effect of Fly Ash and Silica Fume Substituted Cement Paste and Mortars, Scientific Research and Essays, 5 (9): 990–998, 2010.

[15] Aruntaş, H.Y., Tokyay, M., Katkılı çimento üretiminde diyatomitin puzolanik malzeme olarak kullanılabilirliği, Çimento ve Beton Dünyası, 1(4): 3–41, 1996. (in Turkey)
[16] Beycioglu, A., Emiroglu, M., Kocak, Y., Subasi, S., Analyzing the compressive strength of clinker mortars using approximate reasoning approaches – ANN vs MLR, Computers and Concrete, 15: 1, 89-101, 2015.
[17] Ashrafi, H. R., Jalal, M., Garmsiri, K., Prediction of load–displacement curve of concrete reinforced by composite fibers (steel and polymeric) using artificial neural network, Expert Systems with Applications, 37, 7663–7668, 2010.
[18] Atici, U., Prediction of the strength of mineral admixture concrete using multivariable regression analysis and an artificial neural network, Expert Systems with Applications, 38, 9609–9618, 2011.
[19] Yaprak, H., Karaci, A., Demir, I., Prediction of the effect of varying cure conditions and w/c ratio on the compressive strength of concrete using artificial neural networks, Neural Computing and Application, 22, 133–141, 2013.
[20] Subasi, S., Prediction of mechanical properties of cement containing class C fly ash by using artificial neural network and regression technique, Scientific Research and Essay, 4: 4, 289–297, 2009.
[21] TS 802, Design of concrete mixes, Turkish Standards, 2009, Ankara (in Turkey).
[22] TS EN 12350–2, Testing fresh concrete – Part 2: Slump test, Turkish Standards, 2010, Ankara (in Turkey).
[23] TS EN 12390–3, Testing hardened concrete – Part 3: Compressive strength of test specimens, Turkish Standards, 2003, Ankara (in Turkey).
[24] Goyal, S., Goyal, G. K., Radial Basis (Exact Fit) and Linear Layer (Design) ANN Models for Shelf Life Prediction of Processed Cheese, International Journal of u- and e- Service, Science and Technology, 5(1): 63-70, 2012.
[25] Ozcan, F., Atis, C. D., Karahan, O., Uncuoglu, E., Tanyildizi, H., Comparison of artificial neural network and fuzzy logic models for prediction of long–term compressive strength of silica fume concrete, Advances in Engineering Software, 40, 856–863, 2009.

HALİM DÜZGÜN HOUSE'S PROJECTS-RESTORATION STUDIES IN TARAKLI

A.C.Apay[1], Ö.Özkan Önür[2], and A. Bideci[1]

[1]*Department of Architecture, Faculty of Arts, Design and Architecture, Düzce University, Düzce, Turkey*
[2]*Department of* Interdisciplinary *Composite Material Technologies, Institute of Science and Technology, Düzce University, Düzce, Turkey*

E-mail: ozkanonurozlem@gmail.com

Abstract

It is an important settlement area where our cultural heritage is present with the examples of Ottoman architecture coming from past to day. For an effective restoration of the monumental and civil structures that Taraklı possesses, the physical structure is examined together with its historical, architectural values and surroundings.

In this study, the materials used in the construction of the works are provided and constructed during the historical development process, and the changing conditions are determined as the principle of their effect on these works. Architectural settlements, interior layouts, construction systems, features of the roofs, and number of floors of civil buildings are suitable for personal purposes. Monumental constructions are great works of social quality and there is a history story of the society in these structures. Restoration projects of the chosen Halim Düzgün House have been prepared and investigated in terms of necessary protection interventions without deteriorating the original texture.

The restoration works of Halim Düzgün House have been completed by carrying out the analysis studies supported by the projects and pictures and by performing the controls under the necessary supervision without deteriorating the originality of the techniques applied in the application.

Keywords: Taraklı, Restoration, Repair, Wood structure

1. INTRODUCTION

The geographical features of the region in terms of climatic and vegetation cover have been investigated in order to see the existence of the historical artifacts in Taraklı and the appropriate restoration contents of the structures found there. Population, demographic situation and historical development that determine social structure have been evaluated in terms of understanding the purpose of use of constructions. The architectural and structural features of civilizations designed according to most small families and foremost with their sofa plan for large families have been examined [1].

The architectural civil structures that make up Taraklı have been examined and the features of these structures have been presented supported by photographs. Architectural settlements, interior layouts, construction systems, features of roofs, number of floors and their qualities are specified for civil purposes. The properties of the materials used in the construction of the constructions and the locations of the constructions in the vicinity are discussed. In addition, information on the buildings to be preserved and repaired in Taraklı is given by focusing on the work of previous years (Figure 1).

The architectural and structural analysis of the Halim Düzgün House, one of the architectural examples chosen for the study, was carried out and drawings and restoration projects were drawn up. It is aimed to show how effective the repair techniques are in terms of the work done under light.

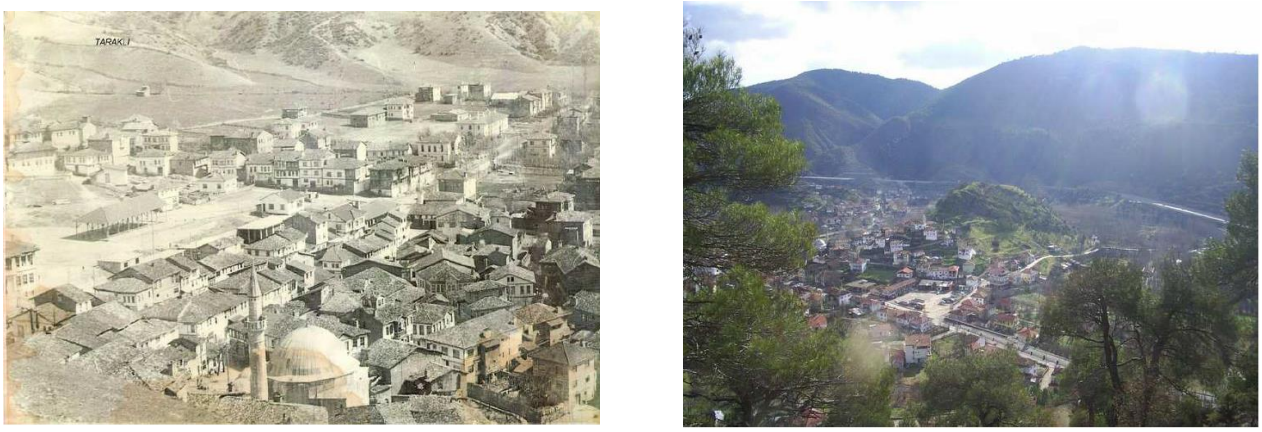

Figure 1. General view from Taraklı (1960-2007) [2]

2. PHYSICAL STRUCTURE AND HISTORICAL DEVELOPMENT OF THE TARAKLI

2.1. Physical Structure of the Taraklı

2.1.1. Geographical structure of the Taraklı

Taraklı is a district of Sakarya in the Marmara Region. The settlement, 65 km from Sakarya is located on the old Istanbul-Ankara highway between Göynük and Geyve districts [3]. The district 450 m high above the sea, Geyve, Sapanca, Pamukova districts from the west, Göynük from the east, surrounded by the lakes of the lake market from the north. Taraklı, which is located on 40.4 latitude and 30.5 longitudes, Tokar and Taşlık Hills, in the west is Tea Side Hill, Hıdırlık in the north and surrounded by the Kara Bayır Hills built into a valley [4].

2.1.2. Climate and flora of the Taraklı

Although the Taraklı is in the Marmara Region, its typical features of the terrestrial climate prevail since it has a mountainous terrain structure. So the climate is not like the climate of the province of Sakarya. Summers in Taraklı is hot and arid, winters are snowy and hard. Falling snow from December until the first months of spring. Autumn and spring are rainy. Average annual temperature is around 14 - 15 degrees. The annual precipitation is 630 mm. Taraklı is very rich in terms of natural vegetation. The mountains are completely covered with forests. There are pine, oak, hornbeam, beech, fir and boxwood varieties in these forests. Other areas include bushes and machines. Less plain are covered with agricultural and fruit products. Fruits are important among the people's livelihoods. But it is difficult to process the land in the district. “If you pain, you pain to Taraklı's ox” promise in district the land processor what is reflects that power is a business [4].

2.1.3. Economic structure of the Taraklı

Due to its location on the Istanbul-Ankara highway which is an important trade route during the Ottoman period the economic situation is pretty good district, during the Republican period the importance of this path is lost and the existing crafts depending on the disappearance of technological development declined. This situation, causing the people to turn to new sources of livelihood. Taraklı's current economic structure is based on fruit-making and the trades formed by a small group of tradesmen. Taraklı’s economic structure was based on fruit-making spoon-cutting and combing in the ottoman period. Until 1960 in Taraklı, the mountain villagers in the vicinity to silk looms in order to provide raw material silk bug making is being done, also, construction of wooden field tools, saddler, weaving, shoe making, spoon-cutting and carding crafts such as the economy it was a very important place. But nowadays, against the serial and cheap production of the crafts industry some of them have disappeared. For the revitalization of traditional

crafts various studies are being carried out. Until the 1950s, the fruit gardens of the Taraklı area, ties and olive groves, covered with hazelnuts and at that time It is known that Taraklı's apples and pears are famous. Today, there are quite a number of apple, plum and quince trees in the district. Most of the fruit trees are located in the north, east and west of Göynük Stream. However, with the decrease in income from fruit gardens some of the gardens have been turned into chords. In recent years, many fruit gardens and hills have begun to be used for artichoke planting due to the higher economic turnover [5].

2.1.4. Population and social structure of the Taraklı

According to the results of Taraklı's 2002 census, the total population is 9220. This population is settled at 4169 in the district center and 5051 in the villages. When you look at population structure; 46% of the population lives in the district center and 54% lives in the villages. Taraklı is one of the provinces with the lowest population density at province level. According to the census and the results of the determination, it is seen that the district of Taraklı is in the position of a migrant district. Approximately 28 people per km² in the district, which has an area of 334 km².According to the 2000 Population Census results, the general population growth rate of the province is 16.88%.The district was separated from Geyve district in 1988 as administrative structure, the first regular population census was conducted in 1990. According to the 1990 Population Census, the population of the district is 10.906 together with the villagers. The administrative units of the province are composed of 4 central districts and 22 villages. Within the scope of the County Population Directorate, there are 36 Population family logs which contain 4 neighborhoods and 22 village population records and events. Registers (Population family register books) are registered in approximately 37,500 people's registers. Directorate Population records were renewed in 1975 [5].

2.1.5. Transportation of the Taraklı

The main axis of district is Ankara Street, which forms part of the old Istanbul-Ankara highway. This axis, which passes through the settlement in northwest and northeast Byzantine and Ottoman periods It has been an important trade route between East and West. Until the Republican period, Istanbul-Ankara highway, which has quite significant and intensive vehicle traffic, During the Republican period Geyve and Taraklı section, especially its importance lost In the 1950s. This road which is not qualified to respond to the increased vehicle potential, despite being a state road at the 1st level, opening of İstanbul-Düzce-Bolu-Ankara highway and İstanbul-Ankara traffic with this route shifted, it has lost its significance and remained a local road. Today from this route only Istanbul-Göynük, Passing Adapazarı-Geyve-Taraklı traffic, from east of Beypazarı until Ankara.reached. The Geyve- Taraklı route is very disturbed due to the heavy traffic,

insufficient maintenance and landslides. Recently, road construction and maintenance work has been accelerated, geographical and topographical conditions on hand sections road expansion and asphalting work are done. However, some of the highways between Geyve and Taraklı still have difficult conditions due to geographical difficulties [6].

2.2. Historical Development of the Taraklı

The Taraklı region, which is referred to as 'Yenice Tarakçı' in the source, is a miniature Ottoman city and it is connected to the Bursa Tekfurluğu in the Byzantine period after the Hittites, Phrygians, Romans and Bitinans themselves [7]. Taraklı, a small settlement within a castle, from time to time, between the Byzantines and the Seljuks. One of the two most important names of Taraklı at the end of the 13th century in the Ottoman administration was Samsa Çavuş and the other was Köse Mihal. Harmankaya Tekfuru who accepted Islam and named Gazi Mikail and Samsa Sergeant have organized the raids on Sorkun, Kölpazarı (Gölpazarı), Tarakli Yenicesi, Köynek (Göynük) and Mudurnu sides at the beginning of the 1190's and have given the region to the Ottoman administration. Already, the region has hosted and hosted rulers such as Alexander the Great and Yavuz Sultan Selim, the greatest jihangirs of history. This route from Istanbul to the east; according to whom Silk Road, according to whom Baghdad Road, according to whom is the Road of Kings. XVI [8]. The second Kocaeli livas of the century belong to the province of Kastamonu Taraklı, in 1867; it was connected to the Hüdavendigar province of Kocaeli Sanjak. XIX. Towards the end of the century, the population of Taraklı, which has a population of around 5000, is busy with spoonbills, silk, honey and cheese. Taraklı, brought to the status of the district governed by Geyve in the structure of the Republic, in 1954, [9] it became a municipal administrative unit. On 27 June 1987 it became a district. According to Adapazarı, Taraklı, who had a very old and rich history, unfortunately could not show the expected development due to the passage of Istanbul-Ankara road from opposite direction. The rumors that the Istanbul-Ankara highway will pass through the Taraklı area have increased hopes for the region but the fact that it is not known that Taraklı was abandoned to fate with the construction of the motorway claimed to be on the fault line. Today tourism has become a new hope for the development of Taraklı and it is a tremendous natural phenomenon that arises from the fact that geography is co-crystallized with combed history [10].

3. HALİM DÜZGÜN HOUSE RESTORATION PROJECTS

3.1. Structure of Location and General Properties

Halim Düzgün House; It is located in Adapazarı province, Taraklı district, Hacı Murat Parish, Kozcağız Street, 3 section, 323 no parcel. The total building area is built on 195,39 m² and has a total of two floors. As a production system; stone on the base is wood-carcass adobe fill. The building consists of floor, first floor and cihannum. The original and current usage is the housing. The structure of crib roof is covered with alaturka tiles. The building was built in 1926 (Figure 2).

3.2. Halim Düzgün House of Rolove Studies

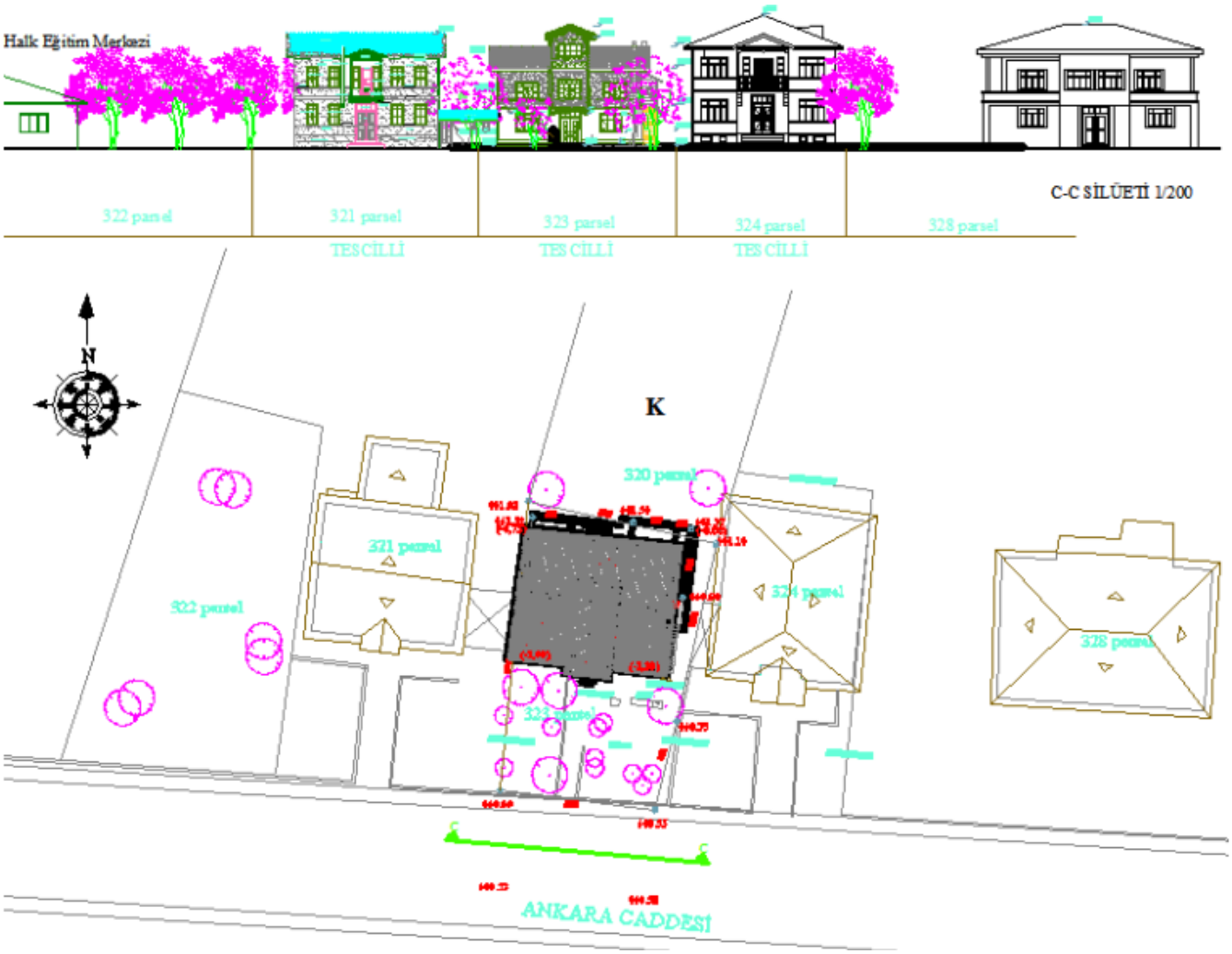

Figure 2. Halim Düzgün House's situation plan

3.2.1. Plan characteristics

The plan features of the building are made with wooden built-in ladder on the eastern side of the floor, with the floor blanket coming out losing its originality over time. The ladder in the interior is removed. There are two rooms on the ground floor, wc, kitchen, storage and hall. The ground floor is the basic upper level; above the floor level. Because the upper part of the foundation is high, the in the rooms was designed as a countertop with a slightly higher elevation in the kitchen. There is also a cooker in the kitchen. But the cooker is not used. Because this floor is used, it is well maintained according to the first floor. The ground floor walls are concrete plastered. The storage area on the floor is empty and is not used. There are no floors and ceilings in this section. On the first floor there are two rooms, wc and sofa. It has a central sofa plan feature and has the traditional Turkish house feature. There is a hall at the entrance to the first floor. This hall is formed by the division of the kitchen. Kitchen has shelves, stove and cupboard. The cupboard is used for the bath. The cupboard was expanded towards the back of the building. There is a shelf in the upper part of the bench next to the cooker. The ground floor plan and the first floor plan were not designed with similar features. There is cedar on the first floor. But there are no cedars in the rooms. From the first floor to cradle roof with a staircase. Cihannuma is used as storage. The first floor and cihannuma are not used because they are neglected. There are damage to the walls and surfaces. The structure of first floor windows, cihannuma windows and first floor doors are not maintenance. There are expressions on wooden floors and ceiling floors (Figure 3).

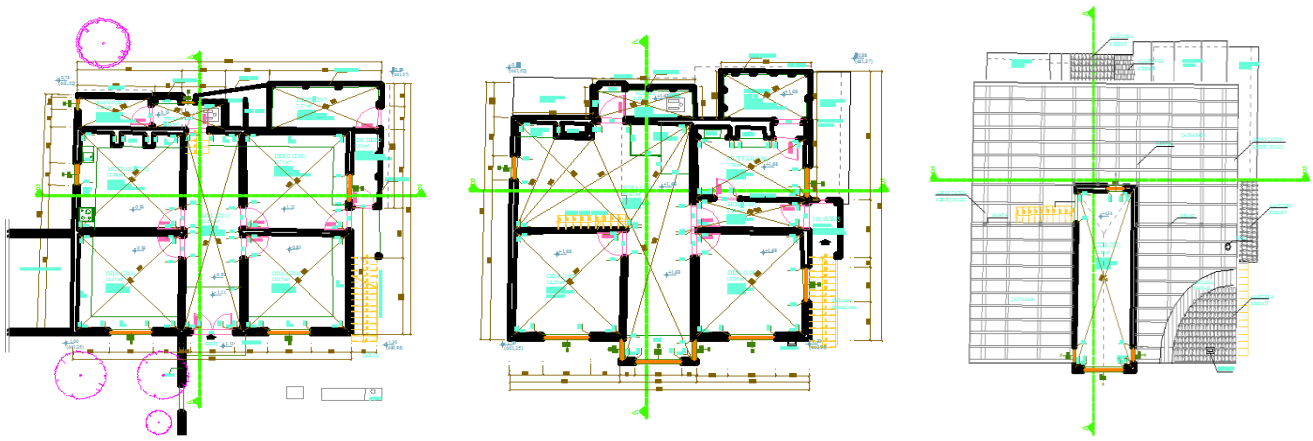

Figure 3. Halim Düzgün House's rolove ground floor plan, first floor plan and second floor plan

Because of the atmospheric conditions, the precipitation waters leading to the deterioration of the roof cover led to the decay both in the interior space and in the construction elements of the roof to enter the water. There are breaks in most of the roof tiles. There are also damages in the chimneys (Figure 4,5).

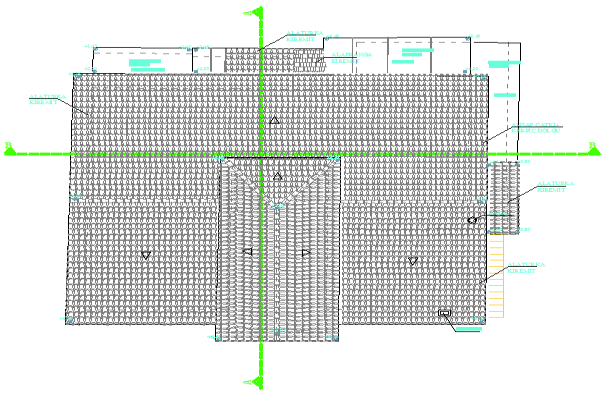

Figure 4. Halim Düzgün House's rolove roof plan

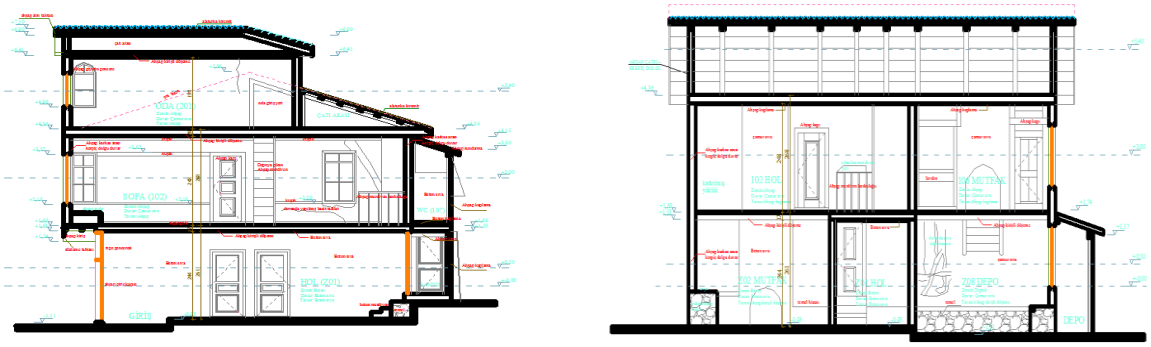

Figure 5. Halim Düzgün House's rolove a-a section and b-b section

3.2.2. Front characteristics

The entrance to the building is provided by double-wing wooden doors on the southern side of the building facing the Ankara Street. The most glamorous front of structure is the southern front. The Spanish-style windows on the ground floor and the windows on the front of the first floor are large rectangular. There is a Spanish-style window on the front of the cradle-roofed window, and some guillotine-type windows on the side of front. There is only one window on the western front and on the eastern front. There are adding on the northen front. This also disrupts the original texture of the structure. Ground floor between wooden carcass mud brick filler, on concrete plaster, first floor and cihannuma wood carcass mud brick filler and mud lining. There are damage to the walls and surfaces. There is a great deal of deformation in the plasters. (Figure 6-9).

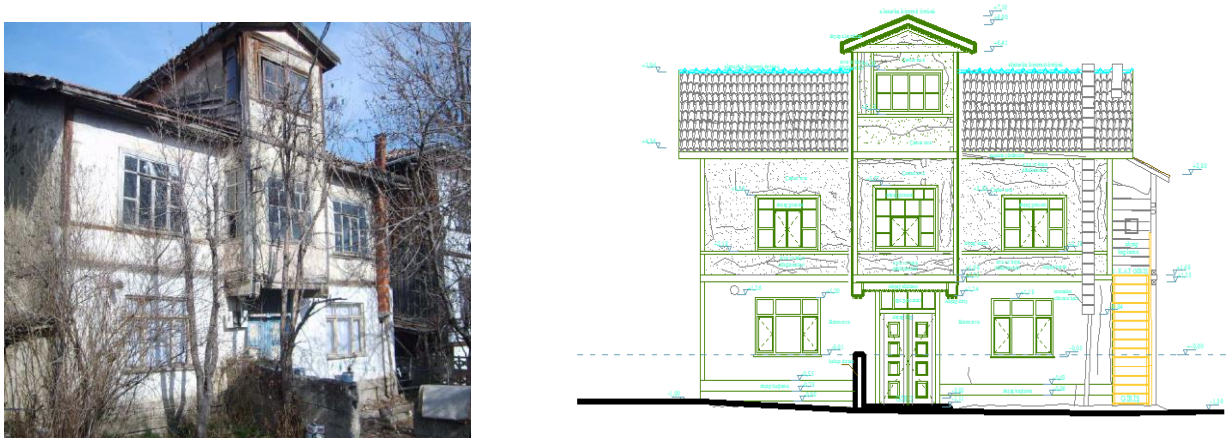

Figure 6. Halim Düzgün House's rolove southern front view and rolove southern view

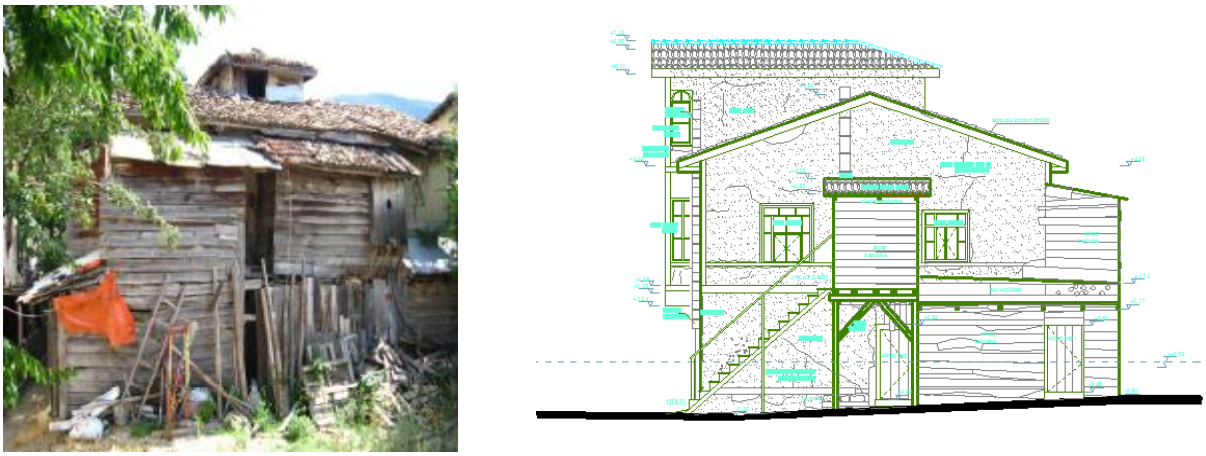

Figure 7. Halim Düzgün House's rolove northern front view and rolove northern view

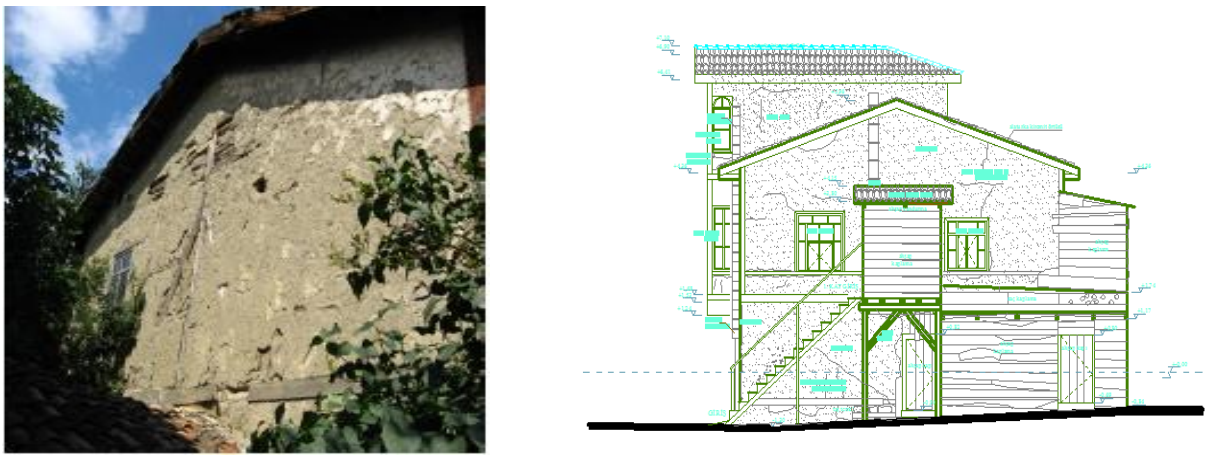

Figure 8. Halim Düzgün House's rolove eastern front view and rolove eastern view

Figure 9. Halim Düzgün House's rolove western front view and rolove western view

3. 3. Halim Düzgün House Restoration Study

4.3.1. Restoration of plan

First, roof tiles and deteriorated construction elements should be removed and replaced with new ones, it should be done with the original construction system and the insulation with the material. By scraping in the walls should be looked what the carrier system and it must be replaced with a suitable material. Elements in good condition should be cleaned, if it necessary, it should be onsite maintenance. Deteriorated parts should be replaced with material suitable for the original material. Wall fillings should be made with appropriate materials and techniques, the inner walls should be plastered with the plaster technique. Wooden windows must be repaired without spoiling the originality and it should be replaced with new windows that are in very bad condition. Wooden doors and upholstery should be repaired and damaged ceilings caused by water intake from the roof should be repaired. The stair steps and balustrades must be reconstructed without spooling from their originality. Cabinets in the room must be preserved and it must be re-used with on-site repairs. On facade covering, lime whitewash over mud brick, if upstairs it should be made in accordance with the original wooden coating (Figure 10,11).

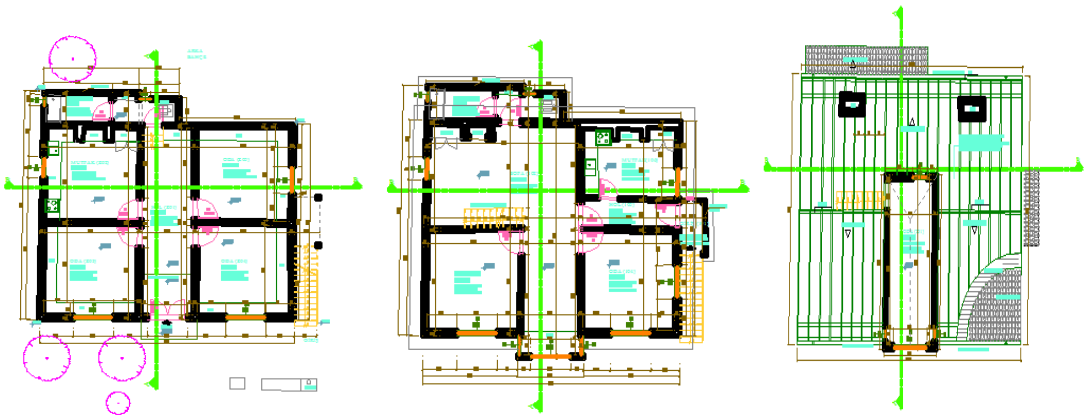

Figure 10. Halim Düzgün House's restoration ground floor plan, first floor plan and roof plan

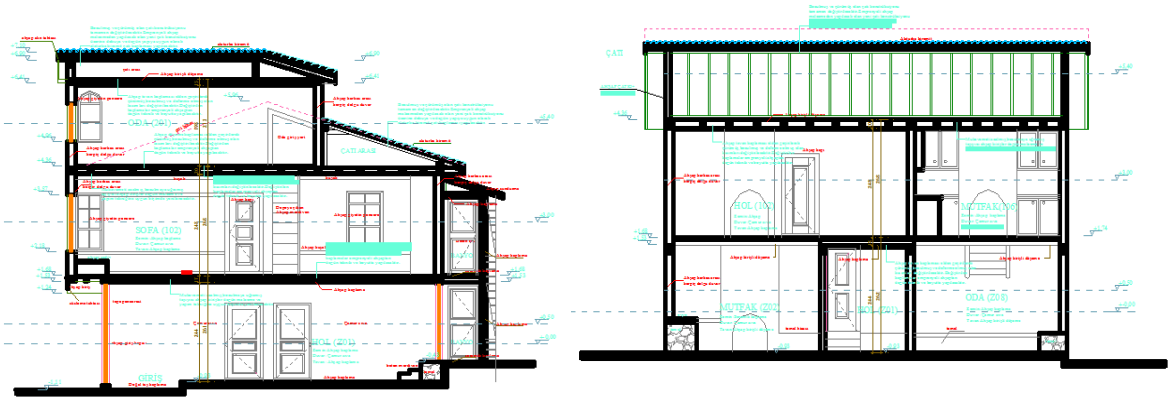

Figure 11. Halim Düzgün House's restoration a-a section and b-b section

3.3.2. Restoration of facades

On the northern front of structure deteriorated and rotten wooden floor windows will be replaced with new ones that will be made to match the original. Spoiled parts of the eastern and western facades will be repaired in a way that is appropriate to the construction technique. Deformed wooden beams on facades and broken and rotten wooden windows will be replaced by the originally impregnated wooden material. On the south facade, the parts that disrupt the originality of the structure and which are subsequently added will be removed to make it more suitable (Figure 12, 13).

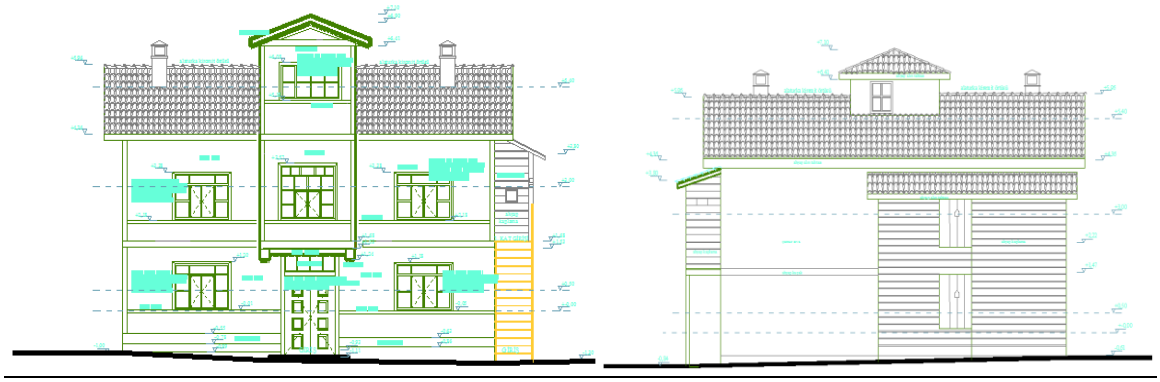

Figure 12. Halim Düzgün House's restoration southern view and northern view

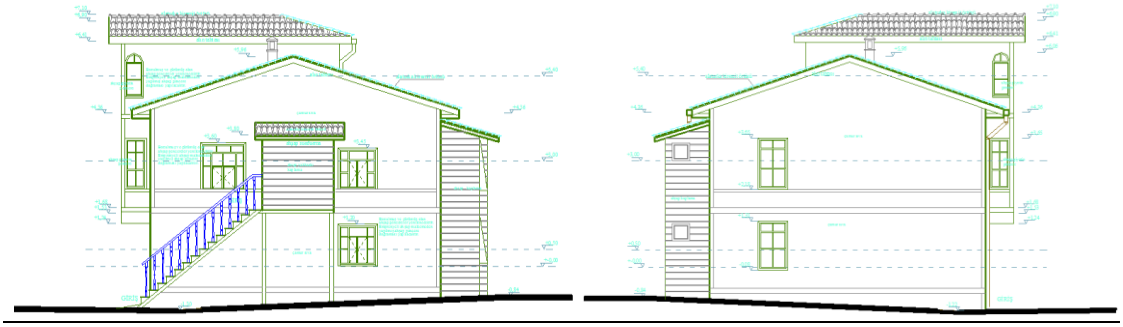

Figure 13. Halim Düzgün House's restoration eastern view and western view

3.3.3. Restoration of roof

The roof is subject to deterioration due to exposure to physical and chemical factors. These distortions will be repaired and the roof construction elements will be completely replaced. Instead of these factors resistant long-lasting impregnated wooden construction elements will be used. On this construction, alaturka tile covering will be done in accordance with the historical texture and the original structure (Figure 14).

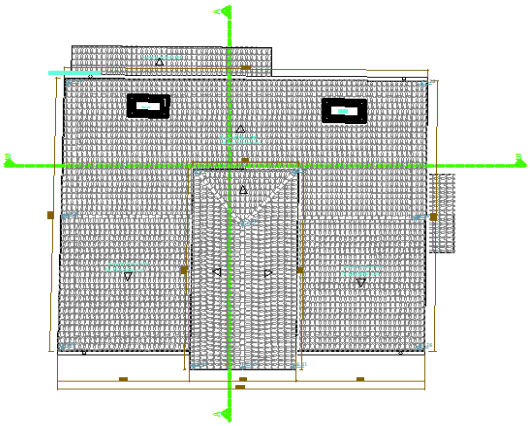

Figure 14. Halim Düzgün House's restoration roof plan

4. RESULTS

Due to Taraklı, geographical features and topography, it has a city texture where construction and transportation are difficult to solve. The freely arranged interiors we observed in civil architecture examples; reflecting our personal feelings and thoughts, is our most important cultural heritage to be moved to the future. Study topic selected Halim Düzgün House is a original structure of Turkish architecture. The biggest feature that differentiates the house from the others is its dimensions. In the house which is problematic in terms of architecture and structure, due to plaster plaster pouring, rotting wooden material serious damages has occurred. Taking into account these damages have been prepared rolove and restoration projects. Restoration works of Halim Düzgün House have been supported with projects and pictures, by making analysis studies with the techniques applied in practice, works have been completed with the necessary controls under control without deteriorating the originality of the structure. As a result; In order to wooden, masonry and mud brick structures to be long-lived without destroying the original texture of traditional Turkish houses, precautions should be taken and maintenance should be done with necessary protection proposals.

REFERENCES

[1] Altınoluk, Ü., Reuse of Buildings, 17, 1998.

[2] Taraklı Municipal Archive, 2009.

[3] Tuna, F., Akçakoyunluoğlu, S., Seven Color-Seven Climate Sakarya, 56, 2004.

[4] Demir, E., Historical environment values protection purposeful investigation in Taraklı, 3-4, 1988.

[5] Taraklı District Governor, The place where history meets nature Taraklı, 10-14, 2003.

[6] Sakarya River magazine, 42, 2004.

[7] Acun, H. Sakarya İli Taraklı İlçesi ve Yunus Paşa Camii, 19-34, 1996.

[8] Şentürk, M. H., Osmanlılar Döneminde Sakarya, Sakarya İli Tarihi, C.I, 181, 2005.

[9] Temelkuran, T., Çevik, M. Evliya Çelebi Seyahatnamesi, 580, 1984.

[10] Çetin, Y. Sakarya'da Türk Mimari Esreleri, 294-308, 2008,

[11] Özkan Ö., Civil architecture of examples is in Taraklı and Halim Düzgün House's protects and Ali Pektaş of House's restoration studies, 2009.

TWO NOVEL FLUORESCENT-BASED DOPAMINE SENSORS: STRUCTURAL CHARACTERIZATION AND SENSING ABILITIES

Hilal Kırpık[1]*, Ayşegül Köse[2], Muhammet Köse[1]

[1]*Department of Chemistry, Faculty of Science, Kahramanmanras Sutcu Imam University, Kahramanmaras, Turkey*

[2]*Department of Bioengineering and Sciences, Kahramanmanras Sutcu Imam University, Kahramanmaras, Turkey*

E-mail: hilalkrpk@hotmail.com

Abstract

In this study, two new imine compounds (**M1** and **M2**) derived from 4-formyl phenyboronic acid and 2-amino fluorene or 1,5-diaminonaphthalene were prepared. The molecular structure of **M1** was determined by a single crystal X-ray diffraction study. In the structure of **M1**, two molecules are linked by two concordant hydrogen bonds between the boric acid units resulting in a hydrogen bonded dimer. The absorption and excitation/emission properties of the compounds were studied in different solvents. The effect of the solvent on the absorption and emission properties were investigated. The compounds show a strong emission band at 370-425 nm range. The compounds were used as a fluorescent probe for the detection of dopamine. The compound **M2** exhibited the low LOD (3.8 μM) value and reasonable enhancement constant (K_{sv} = 7.40 × 10^3 M^{-1}) for fluorescent detection of dopamine.

Keywords: Imine compound, X-ray diffraction, Absorption, Photoluminescence, fluorescent dopamine detection.

1. INTRODUCTION

Neurotransmitters, also called as chemical transmitter or chemical messenger, transmit the electrical impulse from a neuron to the next across synapses [**1**]. Otto Loewi identified the first neurotransmitter, acetylcholine, in 1921 and after that about a hundred neurotransmitter was isolated [**2**]. The neurotransmitters were later classified according to their chemical structures such as biogenic amines, amino acids, peptides and gaseous neurotransmitters. The biogenic amines are dopamine, epinephrine, norepinephrine, serotonin, histamine and acetylcholine [**1**]. Dopamine (DA) is a catecholamine neurotransmitter and have a vital role in central nervous, hormonal, and cardiovascular systems of human body and brain [**3**]. In the biological systems, dopamine (chemical name known as 3, 4-dihydroxyphenyl ethylamine) is synthesised in a restricted set of cell types *via* the decarboxylation reaction of 3,4-dihydroxyphenyl alanine (L-DOPA) [**4**]. The Abnormal dopamine concentration in biological fluids (urine, blood or extracellular fluid) are thought to be indicator for many neurological disorders such as schizophrenia and Huntington's and Parkinson's diseases [**5**]. Due to its vital role in biological systems, sensitive and selective detection of dopamine concentration in biological fluids is crucial for clinical diagnosis of these neurological diseases. There are several instrumental methods employed for the determination on dopamine in biological fluids [**6**]. These are are electrochemical analysis, high-pressure liquid chromatography (HPLC), gas chromatography/mass spectrometry (GC/MS), UV-vis absorption, fluorescent and colorimetric methods [**7**]. However, these instrumental techniques have several drawbacks such as interference, time-consuming and demanding high cost. Recently, fluorescent-quenching based dopamine detection have taken increasing interest. Several fluorescent materials such as quantum dots, graphene-quantum dots and nanoclusters have been employed for the determination of dopamine levels [**8**].

Boronic acid have a high binding ability to the for the compounds with the diol groups. 2-Anthrylboronic acid was used as fluorescent probe which showed chelation based fluorescent quenching when interacts with polyols such as carbohydrates [**9**]. There are a few reports for fluorescence sensing of dopamine by the compounds having a boronic acid group [**10**]. In this work, two imine compounds (**M**^{1} and **M**^{2}) containing boric acid unit were synthesised and their structures were characterised by spectroscopic and analytical methods. Molecular structure of **M**^{1} was determined by X-ray diffraction study. The absorption and excitation/emission properties of the compounds were studied in different solvents. Finally, the sensing ability of the compounds for the detection of dopamine levels were investigated by fluorimetric method.

2. MATERIAL AND METHODS

Starting materials and solvents (4-formyl phenyl boronic acid, 2-amino fluorene and 1,5-diaminonaphthalene) were bought from commercial sources. FT-IR spectra of the compounds were measured on a Perkin Elmer Spectrum 100 FT-IR. The electronic spectra were taken on a Perkin Elmer Lambda 45 spectrophotometer. The fluorescence spectra were obtained on a Perkin Elmer LS55 luminescence spectrometer.

2.1 Synthesis of the probes

2-Formyl phenylboronic acid [0.3 g, 2 mmol for **M^1** and 0.6 g, 4 mmol for **M^2**] was dissolved in methanol (10 mL). To this solution, 2-amino fluorene (0.36, 2 mmol) or 1,5-diaminonaphthalene (0.32 g, 2 mmol) in methanol (20 mL) was added resulting in yellow colored clear solution. The reaction solution was refluxed for 4 h and cooled to the room temperature. The solvent was reduced to 5 mL and precipitations were collected by filtration and dried in air.

M^1: Color: Yellow, Yield: 87.24%. Mp: > 275 °C. **Elemental analysis**: Calc. For $C_{20}H_{16}BNO_2$ (M.W.: 313.16 g/mol): C, 76.71; H, 5.15; N, 4.47. Found: C, 76.51; H, 4.85; N, 4.32%. **FT-IR (ATR, cm^{-1}):** 3329, 3038, 2922, 1619, 1341, 1272, 1168, 1100, 1046, 934, 821, 763, 729, 662, 644, 493.

M^2: Color: Yellow, Yield: 66.16%. Mp: > 285 °C. **Elemental analysis**: Calc. For $C_{24}H_{20}B_2N_2O_4$ (M.W.:422.05 g/mol): C, 68.30; H, 4.78; N, 6.64. Found: C, 68.12; H, 4.53; N, 6.35%. **FT-IR (ATR, cm^{-1}):** 3456, 3305, 1613, 1554, 1343, 1271, 1155, 1107, 1000, 926, 778, 644, 625, 544, 500.

1.2 X-ray structure solution and refinement

X-ray diffraction data for compound **M^1** were collected at 293(2) K) on a Bruker D8 QUEST diffractometer using Mo-*Kα* radiation (λ= 0.71073 Å). Data reduction was performed using Bruker SAINT [**11**]. SHELXS97 was used to solve and SHELXL2014/6 to refine the structures [**12**]. The structure of the compound **M^1** were solved by direct methods and refined on F^2 using all the reflections. All the non-hydrogen atoms were refined using anisotropic atomic displacement parameters. The hydrogen atoms belong to carbon and oxygen atoms were located at calculated positions using a riding model. The crystallographic data for the compounds are listed in **Table 1** and hydrogen bond parameters are given in **Table 2**.

Table 1 X-ray data for **M1**

Empirical formula	$C_{23}H_{23}BN_2O_3$	Unit cell	a (Å)	8.8453(7)
Formula weight	386.24		b (Å)	5.9552(4)
Crystal color	Yellow		c (Å)	39.861(3)
Crystal system	*Monoclinic*		α (°)	90
Space group	*P2₁/c*		β (°)	96.257(3)
Volume (Å3)	2087.2(3)		γ (°)	90
Z	4	Ind. Refl. [R_{int}]		4277 [0.0814]

Table 2 Hydrogen bond parameters for **M1** [Å and °].

	D-H...A	d(D-H)	d(H...A)	<(DHA)
O(1)-H(1)...O(2)*	0.82	1.96	2.773(4)	171.9
O(2)-H(2)...O(3)	0.82	1.86	2.628(6)	155.4

Symmetry code:* -x,-y+1,-z+1

3. RESULTS AND DISCUSSION

In this work, two new imine compounds having boronic acid unit (**M1** and **M2**) were synthesized from the Schiff base condensation reaction between the 4-formyl phenyboronic acid and 2-amino fluorene or 1,5-diaminonaphthalene. The proposed structures of the compounds are shown in **Fig. 1a**. The yellow colored products are obtained in high yield and purity of the products were checked by t.l.c. The compounds are stable at room temperature in the solid state without decomposition. The compounds are soluble in methanol, chloroform, THF, DMF, and DMSO and partially soluble in water. FT-IR spectral data of the compounds are given in the experimental section. The azomethine $\upsilon_{(CH=N)}$ vibrations were observed at 1619 and 1613 cm^{-1} for **M1** and **M2**, respectively. In the spectrum of the compounds, the broad bands in the range of 3300-3400 cm^{-1} can be assigned to the O-H group vibrations. The single crystals of **M1** were obtained from slow evaporation of a DMF solution of the compound. Therefore, definite structure of the compound was determined by single crystal X-ray diffraction study. The molecular structure of **M1** is shown in **Fig. 1b**. The compound crystallizes in the monoclinic crystal system, *P2₁/c* space group. The bond lengths and angles of the compound are within the expected ranges. The N1–C7 bond length showed a double bond (C=N) character. Two molecules of **M1** are dimerized by a concordant B-OH···O-B hydrogen bond (**Fig. 2a**). In the structure of the compound, there is also a hydrogen bonded DMF solvate per molecule. Molecules are packed into 3D network by π-π and H-π interactions. Packing diagram of **M1** viewing down the *a* axis is given in **Fig. 2b**.

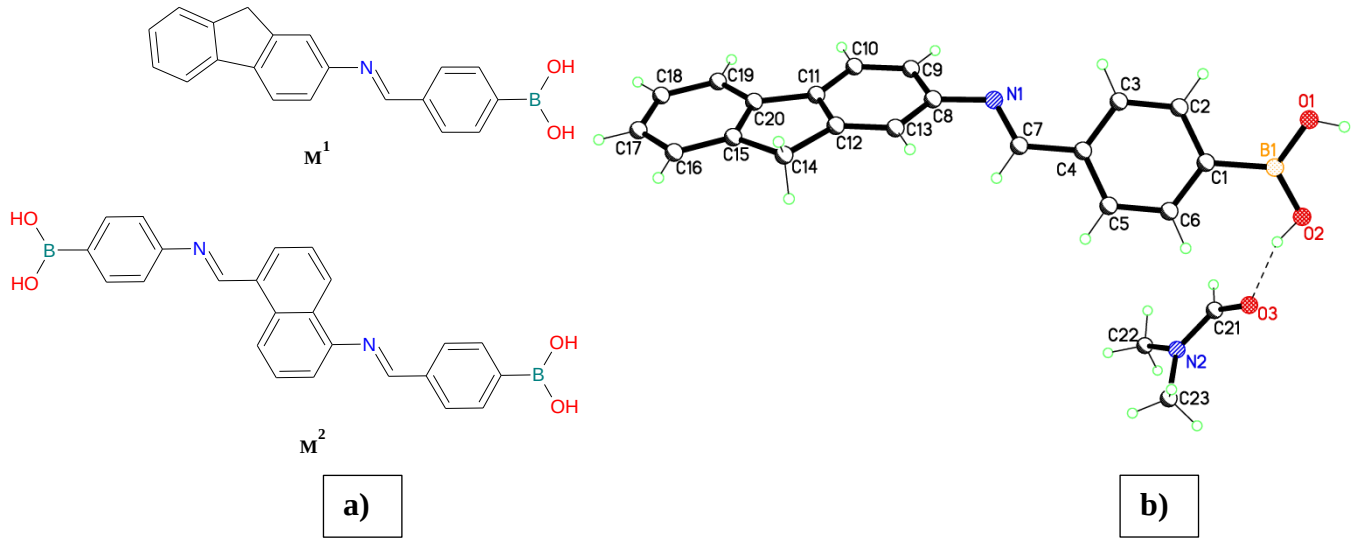

Fig. 1 a) Proposed structure of **M1** and **M2**. b) X-ray structure of **M1.**

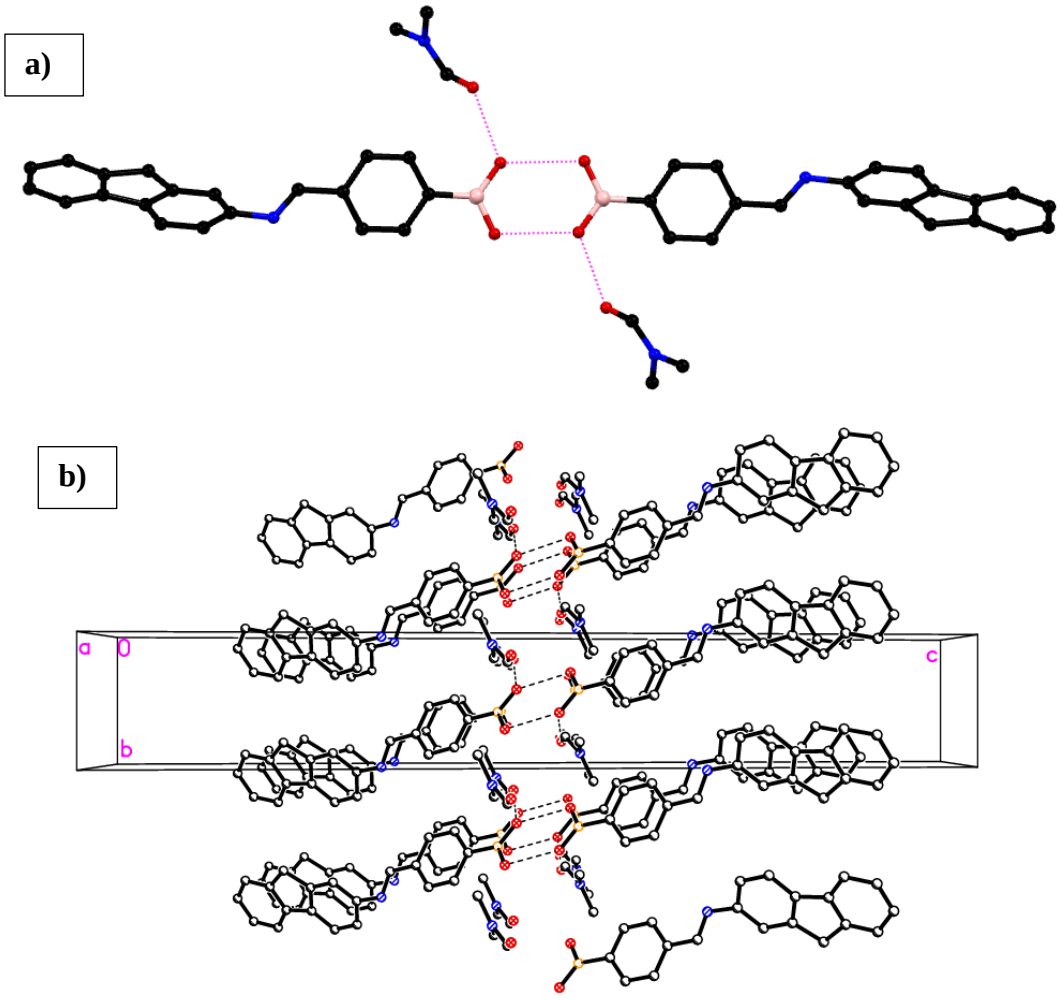

Fig. 2 a) Dimeric structure of **M1.** b) Packing diagram of **M1.**

3.1 Absorption and photoluminescence properties of the compounds

UV-Vis absorption spectra of the compounds were studied in chloroform ($CHCl_3$), methanol (MeOH), tetrahydrofuran (THF) and dimethylformamide (DMF) (10^{-4} M). Photophysical properties are given in **Table 3**. Compound **M1** showed a broad absorption band in the range of 300-400 nm in the solvents studied. the absorption band was assigned to the π-π* electronic transition. In $CHCl_3$, compound **M1** showed an emission maximum at 410 nm upon excitation at 310 nm with a Stokes shift of 95 nm. There are only slight shifts when MeOH, THF and DMF were used as solvents. In $CHCl_3$ solution (10^{-4} M), compound **M2** emits light at 373 nm (λ_{max}) when excited at 317 nm with a Stokes shift of 56 nm. In MeOH solution (polar protic solvent), while excitation band slightly shifted to lower value, the emission band considerably showed a red shift resulting in a higher Stokes shift (75 nm). In THF and DMF (polar aprotic solvents), the emission maximums were even more left shifted with higher Stokes shifts. The red shift in MeOH, THF and DMF is due to the strong hydrogen bond capability of these solvents with **M2** molecules. However, the emission intensity in THF and DMF is lower than in MEOH and $CHCl_3$ solution (quenching effect).

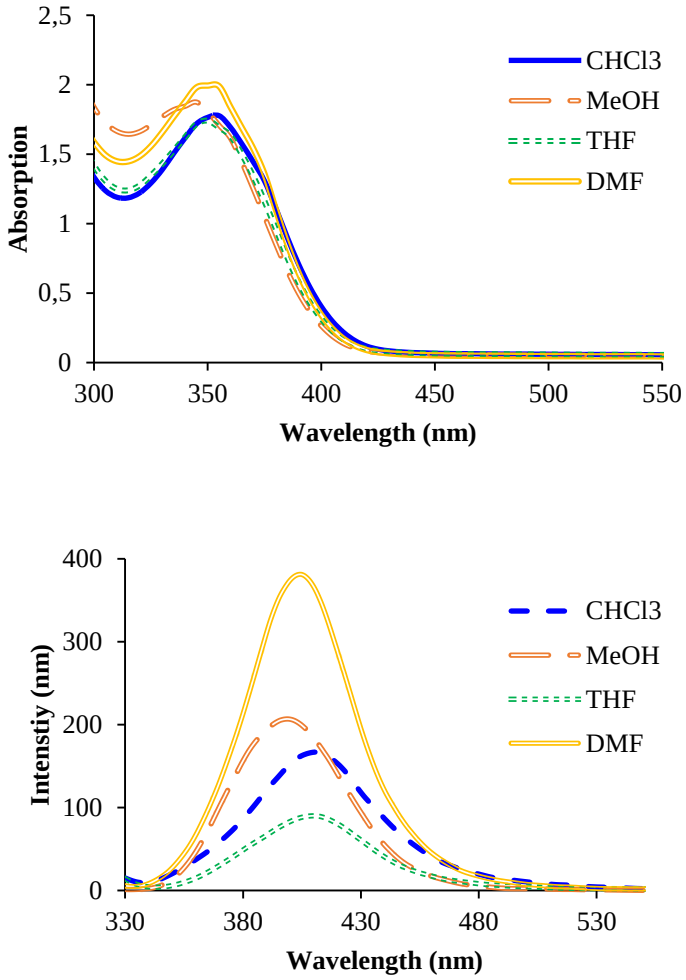

Fig. 3 Absorption and emission spectra of **M[1]** in different solvents.

Table 3 UV-vis and photoluminescence data for the compounds.

	M[1]				**M[2]**			
	Abs. ($\lambda_{max, nm}$)	Exc. (nm)	Em. (nm) [Int.]	Stokes shift (nm)	Abs. ($\lambda_{max, nm}$)	Exc. (nm)	Em. (nm) [Int.]	Stokes shift (nm)
$CHCl_3$	350	315	410[167]	95	375	317	373[490]	56
MeOH	345	306	397[206]	91	370	314	389[622]	75
THF	347	304	411[89]	107	365	317	435[26]	118
DMF	355	310	403[380]	93	375	321	425[91]	104

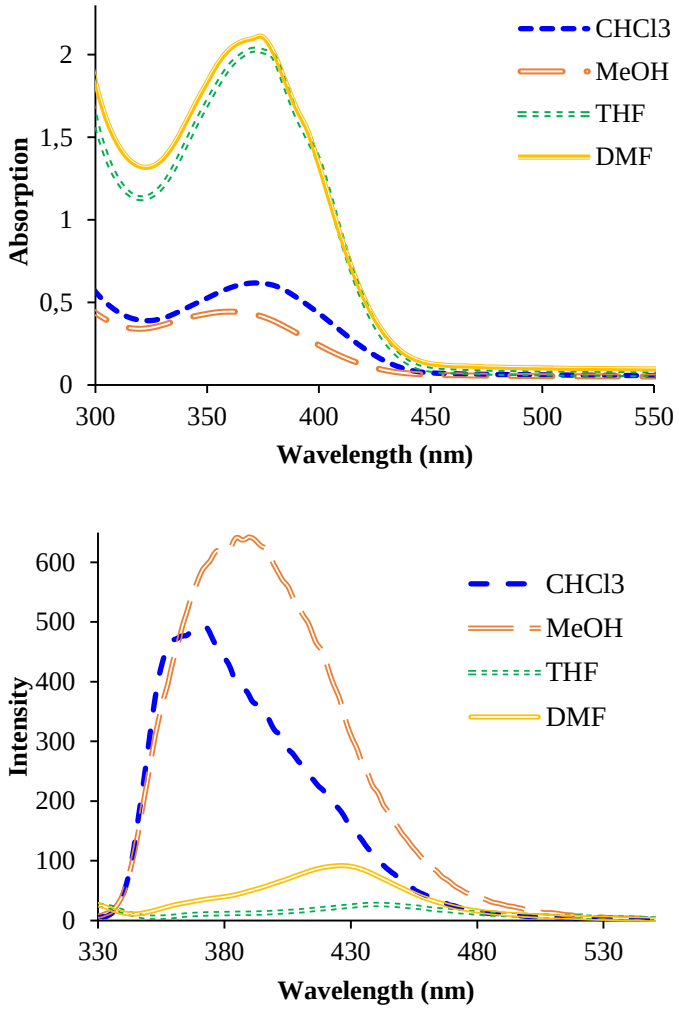

Fig. 4 Absorption and emission spectra of **M²** in different solvents.

3.2 Fluorimetric detection of dopamine

The emission band of the luminescent materials can be quenched or enhanced by dopamine *via* photoinduced electron transfer (PET) or fluorescence resonance energy transfer (FRET). This observation has led to prepare chemical probes for the fluorimetric detections of dopamine.

Compound **M¹** shows an emission band in the range of 360-480 nm in DMF (λ_{Exc} = 355 nm). Dopamine was gradually added to the DMF solution of **M¹** [concentration of **M¹** kept constant] and the emission bands of **M¹** were monitored by photoluminescence spectroscopy. Addition of dopamine to the DMF solution of **M¹** did not change the emission intensity (neither quenching nor enhancing effect). However, incremental addition of dopamine to a DMF solution of **M²** caused an enhancement in the emission intensity (**Fig. 5a**).

The efficiency of chemosensing properties of probe **M²** were compared using the enhancement efficiency which is obtained by using the Stern-Volmer (SV) equation [**13**],

$$I_0/I = 1 + K\text{sv}[A]$$

Where I_0: fluorescence intensity with no dopamine, I: fluorescence intensity after addition of dopamine, [A]: concentration of dopamine, and Ksv: Enhancement constant (M^{-1}).

The enhancement constant (Ksv) is a common tool to evaluate and compare the efficiency of a florescent probes. Ksv can be accurately obtained once linear graph is obtained the I_0/I vs [A] plot. Ksv graph for probe **M²** for dopamine is shown in **Fig. 5b**.

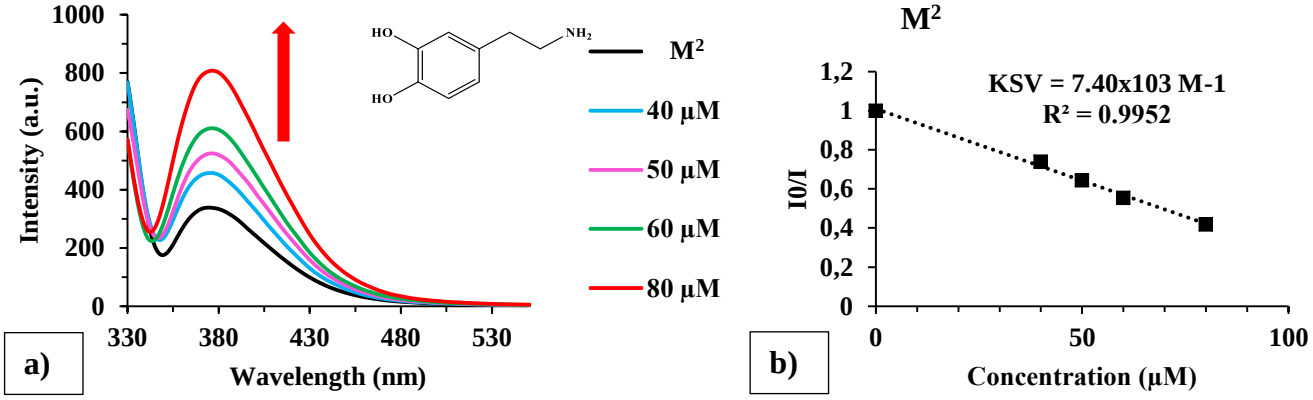

Fig. 5 a) The emission spectra of M^2 in DMF (10^{-5} M) different Dopamine concentrations in DMF under λ_{ex} = 321 nm (T: 298 K). b) Ksv graph for probe M^2 for dopamine.

The detection limit (LOD) for the flurorimetric detection of dopamine was obtained by using the following equation:

$$\text{LOD} = 3\sigma / k \ (\sigma\text{: standard, k: slope})$$

The compound **M²** exhibited the low LOD value for dopamine with 3.8 µM. The low LOD and high enhancement constant value for dopamine showed good sensitivity of the probe **M²** for the fluorescent sensing of dopamine in DMF solution.

Table 3 K_{sv} and LOD values for the probe **M²**

Compound	K_{SV} (M^{-1})	R^2	LOD (µM)
M²	7.40×10^3	0.9952	3.8

4. CONCLUSION

Two new imine compounds having phenylboronic acid moiety were prepared and their structures were determined by spectroscopic methods. The compounds were used as a fluorimetric probes for the sensing of dopamine in solution. The compounds showed good enhancement efficiency and low LOD value for dopamine and these compounds can used as fluorescent probes for detection of dopamine in biological fluids.

ACKNOWLEDGMENTS

Authors thank to Kahramanmaras Sutcu Imam University for providing technical facilities.

REFERENCES

[1] Pradhan, T., Jung, H. S., Jang, J. H., Kim, T. W., Kang, C., & Kim, J. S., Chemical sensing of neurotransmitters, Chemical Society Reviews, 43, (13), 4684-4713, 2014.

[2] Loewi, O., Über humorale übertragbarkeit der Herznervenwirkung, Pflüger's Archiv für die gesamte Physiologie des Menschen und der Tiere, 189, (1), 239-242, 1921.

[3] Wang, H. B., Zhang, H. D., Chen, Y., Huang, K. J., & Liu, Y. M., A label-free and ultrasensitive fluorescent sensor for dopamine detection based on double-stranded DNA templated copper nanoparticles, Sensors and Actuators B: Chemical, 220, 146-153, 2015.

[4] Eisenhofer, G., Kopin, I. J., & Goldstein, D. S., Catecholamine metabolism: a contemporary view with implications for physiology and medicine, Pharmacological reviews, 56, (3), 331-349, 2004.

[5] Ghasemi, F., Hormozi-Nezhad, M. R., & Mahmoudi, M., Identification of catecholamine neurotransmitters using fluorescence sensor array, Analytica chimica acta, 917, 85-92, 2016.

[6] Solich, P., Polydorou, C. K., Koupparis, M. A., & Efstathiou, C. E., Automated flow-injection spectrophotometric determination of catecholamines (epinephrine and isoproterenol) in pharmaceutical formulations based on ferrous complex formation, Journal of pharmaceutical and biomedical analysis, 22, (5), 781-789, 2000.

[7] Lin, Y., Chen, C., Wang, C., Pu, F., Ren, J., & Qu, X., Silver nanoprobe for sensitive and selective colorimetric detection of dopamine via robust Ag–catechol interaction, Chemical Communications, 47, (4), 1181-1183, 2011.

[8] Zhou, X., Ma, P., Wang, A., Yu, C., Qian, T., Wu, S., & Shen, J., Dopamine fluorescent sensors based on polypyrrole/graphene quantum dots core/shell hybrids, Biosensors and Bioelectronics, 64, 404-410, 2015.

[9] Sugihara, J. M., & Bowman, C. M., Cyclic benzeneboronate esters, Journal of the American Chemical Society, 80, (10), 2443-2446, 1958.

[10] Jang, Y. J., Jun, J. H., Swamy, K. M. K., Nakamura, K., Koh, H. S., Yoon, Y. J., & Yoon, J. Y., Fluorescence sensing of dopamine, Bulletin of the Korean Chemical Society, 26, (12), 2041-2043, 2005.

[11] a) Sheldrick, G. M., A short history of SHELX, Acta Crystallographica Section A: Foundations of Crystallography, 64, (1), 112-122, 2008.

b) Sheldrick, G. M., Crystal structure refinement with SHELXL, Acta Crystallographica Section C: Structural Chemistry, 71, (1), 3-8, 2015.

[12] Sheldrick, G. M., SHELXT–Integrated space-group and crystal-structure determination, Acta Crystallographica Section A: Foundations and Advances, 71, (1), 3-8, 2015.

[13] Campbell, K., Zappas, A., Bunz, U., Thio, Y. S., & Bucknall, D. G., Fluorescence quenching of a poly (para-phenylene ethynylenes) by C60 fullerenes, Journal of Photochemistry and Photobiology A: Chemistry, 249, 41-46, 2012.

USAGE POSSIBILITIES OF BIOSENSORS IN FOOD TECHNOLOGY

H. Uran[1] and H. Şanlıdere Aloğlu[1]

Kırklareli University, Faculty of Engineering, Dept. of Food Engineering, Kayali Campus, Kırklareli, Turkey

E-mail: haticealoglu@klu.edu.tr

Abstract

Biosensors are simply defined as the devices which can convert the biological response which is produced by a chemical compound to optic, thermal, and electrical signals. A biosensor contains primarily a biosensing material and a transducer and is used in the detection of biological and chemical agents. Combined with new technologies such as molecular biology, microfluidics and nanomaterials, they can be used for measure of pesticides, antibiotics, pathogens, toxins, proteins, nutrilites, odors, germs and more in agricultural production, food processing and environmental monitoring activities, plants, animals, foods, soil, air and water. The use of biosensor in the food industry is to detect the food component or to detect the presence of microorganisms. In this study, some information was given about the use of biosensors in food technology.

Keywords: Biosensor, Food technology, Food quality

1. INTRODUCTION

Biosensor is a progressing interdisciplinary research between analytical chemistry, biology and microelectronics [1]. Biosensors act as analytical devices employing a biological material or biomimic as a recognition molecules integrated within a physicochemical transducer or transducing microsysytems [2].

A biosensor (Figure 1) is defined by the International Union of Pure and Applied Chemistry (IUPAC) as a self-contained integrated device that is capable of providing specific quantitative or semi-quantitative analytical information using a biological recognition element (biochemical receptor), which is retained in contact direct spatial with a transduction element [3].

A biosensor can be defined as an integrated receptor transducer device, which is capable of providing selective quantitative or semiquantitative analytical information using a biological recognition element [1].

With the biosensors, the target analyses can be done with highly specific and highly sensitive. It is very easy, fast and economical to use compared to other measurement systems [4]. Biosensors research is booming around the world and the area of applications range from medical to agriculture. The types of instruments required for the agro-food diagnostics market can be divided into large multi-analysers, bench-top portable instruments and one-shot disposable sensors [2, 5].

2. BASIC COMPONENTS OF BIOSENSORS

2.1. Bioreceptor molecules

They are highly sensitive biological molecules that interact selectively with the substance to be analyzed. The most important features; high affinity and specificity against the target molecule to be detected. These molecules include enzymes, antibodies, aptamers and microorganisms.

Enzyme bioreceptors: Enzymes are popular biomolecules used as bioreceptors because they produce many measurable reaction products (such as protons, electrons, light and heat) when they participate in chemical reactions. Nowadays, enzymes such as β-galactosidase, β-lactamase, alkaline phosphatase, and protease are frequently used as bioreceptor enzymes.

***Antibody bioreceptors*:** The most important advantage of antibody-based biosensors is that there is no need to purify the target prior to detection. Many recombinant antibodies are used in the detection and identification of HIV, Hepatitis B, Hepatitis C, Ebola, *Salmonella typhimurium*, *Clostridium botulinum* toxins.

***Aptamer bioreceptors*:** Aptamers are oligonucleotides that can bind to a wide variety of molecules such as peptides, vitamins, drugs, microorganisms, bacterial spores with high affinity and specificity (DNA or

RNA). Detection of important microorganisms such as *Salmonella*, *Bacillus anthracis*, *Mycobacterium tuberculosis*, *Escherichia coli* can be done with these bioreceptors.

***Microorganism bioreceptors*:** Many biological molecules used as bioreceptors are microorganisms. Microorganisms themselves can also be used as bioresceptors. They are often used for the detection of inorganic or organic toxic chemicals and may identify a greater variety of chemical structures than other bioreceptor molecules [6].

2.2. Transducers

They are systems that convert biochemical signals into measurable electronic signals. This signal may be due to O_2 consumption, H_2O_2 formation, pH change and temperature/mass change [7]. A transducer can be electrochemical (including voltammetry, amperometric, potentiometric, conductive, capacitive, impedance), optical (absorption, surface plasmon resonance, chemical luminescence), biological luminescence, fluorescence, optical fiber, piezoelectric (quartz crystal microbalans, surface sound (acoustic) wave, calorimetric, magnetic form and others [4].

3. ADVANTAGES OF BIOSENSORS

The advantages of biosensors can be listed as follows;

- Quick (short response time),
- High selectivity and accuracy,
- Simple to use / lack of expertise,
- Real-time, suitable for automation and
- Portable / miniaturizable [7, 8].

4. DISADVANTAGES OF BIOSENSORS

The main disadvantage of biosensors is instability. Moreover, in some analyzes, the lower limit values of methods such as LC and / or LC-MS are not available. In addition, due to the complex structure and textural properties of the food matrix, a decrease in the analysis performance can be observed [8].

5. USE OF BIOSENSORS IN FOOD TECHNOLOGY

The food industry has a general need for methods which are simple; rapid; inexpensive; use readily available, stable reagents; require minimal labor input; and are, ideally, automated. Industry also has specific needs for the QC testing of both ingredients and finished products using rapid methods rather than the traditional, conventional techniques. Highly sensitive and specific methods are needed to detect (relatively) low levels of organisms while maintaining a low incidence of false-positive and false-negative results [9].

Apart from a few important analytes, such as sugars, alcohols, amino acids, flavours and sweeteners, food applications mainly focus on the determination of contaminants. Therefore, it is necessary to invest in the development of biosensors to the analysis of the quality of food, since they have proven to be an extremely viable alternative to traditional analytical techniques such as chromatography. However, very few biosensors play a prominent role in food processing or quality control. Considerable effort must be made to develop biosensors that are inexpensive, reliable, and robust enough to operate under realistic conditions. The potential uses of biosensors in agriculture and food transformation are numerous and each application has its own requirements in terms of the concentration of analyte to be measured, required output precision, the necessary volume of the sample, time required for the analysis, time required to prepare the biosensor or to reuse it and cleanliness requirements of the system. In the area of food the interest in the development of biosensors mainly focuses on analysis of food security (detection of compound contaminants, allergens, toxins, pathogens, and additives etc.) [3]. Table 1 shows the areas where biosensors are used in food technology.

Table 1. Main areas applying biosensors technologies in food industry [3].

FOOD SAFETY		
Xenobiotic Compounds	**Bacterial Toxins**	**Pathogenic Microorganisms**
Food additives	Mycotoxins	Viruses
Drugs	Marine toxins	Bacteria
Pesticides and fertilizers		Protozoans
Other contaminants: dioxins, PCB's, PAH's, heavy metals and biotoxins		
FOOD QUALITY		
Composition of Foods	**Shelf Life**	
Sugars	Polyphenols and fatty acids (Rancid)	
Amino acids	Sugars and organic acids (Maturation)	
Alcohols	Biogenic amines (Freshness)	
Organic acids	Aliina (Garlic and onions)	
Cholesterol		
PROSES CONTROL		
* Sugars (Fermentation and pasteurization); * Amino acids (Fermentation); * Lactic acid (Cheese production); * Alcohols (Fermentation)		
OTHER APPLICATIONS		
GMO's (Genetically Modified Organism)		

The concept of food safety involves ensuring the production and marketing of harmless food, and by that way ensure the health of the consumer. The quantity and types of food additives incorporated into food products are regulated by the legislation of each country, their detection and quantification are important to prevent fraud and malpractice by manufacturers, allergies and other adverse effects to determined groups of the population. Because of this, special attention has been given the way to detect the presence of contaminants, such as residues of heavy metals and components antinutritional. On the other hand, foods can naturally present anti-nutritional compounds that can generate disorders in the consumer, given that they hinder absorption and metabolize distinct nutrients causing them to have a deficiency. Antinutritional components (oxalate and glycoalkaloids) or allergen (gluten) can be contained naturally in foods. First mentioned are mostly detected by enzymatic amperometric biosensors, while for allergens are described immunosensors [3]. Biosensors used in anti-nutrients detection were shown in Table 2.

Table 2. Biosensors used in anti-nutrients detection [3].

Biological Component	Transducer	Analyte
Oxalate oxidase immobilized on chitosan	Potentiometric	Oxalate
Oxalate oxidase and peroxidase	Amperometry	Oxalate in urine
β-glucosidase	Potentiometric	Amygdalin
Peroxidase	Potentiometric	Amygdalin

6. COMMERCIALLY AVAILABLE BIOSENSORS FOR FOOD INDUSTRY

Despite the large number of publications on biosensors used in food analysis, only a few systems are commercially available (Table 3). Among some limitations that must be overcome are the limited lifespan of biological components, mass production, as well as convenience in handling. However, these problems can be managed in a near future, since the biosensors provide unique solutions for food analysis in terms of specificity and time saving [3].

Table 3. Commercial biosensors for food industry [3].

Biosensor	Country	Biosensor	Country
Fish deterioration tracking	China	Ethanol, methanol, glucose, sucrose, lactose, glutamine, ascorbic acid and oxalate	USA
Detection of *Escherichia coli* 0157:H7 in lettuce (Canary)	USA	Penaut allergens, antibiotics	USA
Detection of *Escherichia coli* O157:H7 and *Salmonella* in meat products	USA	*Staphylococcus aureus* and cholera toxin	UK
Detection of *Salmonella* and *ampylobacter* in pork industry	USA	Water soluble vitamins, chemical veterinary residues and mycotoxins	Sweden
Detection of *Staphylococcal* enterotoxin B and *Botulinum* toxin A in tomatoes, sweet corn, beans and mushrooms	USA	Glucose, fructose, malic acid and lactic acid (fermentation)	Italy
Detection of atrazine traces	Spain	Microorganisms	France
Escherichia coli 0157, *Salmonella*, *Listeria* and *Campylobacter*	USA	Microorganisms and toxic substances	USA
Proteins, toxins, virus, bacteria, spores, and fungi (simultaneous analysis)	USA	Microorganisms and GMO's	Japan
Ascorbic acid	Germany	Heavy metals	Rusia

7. CONCLUSION

Biosensors have a wide range of applications in many areas, including the food processing industry, due to their simple handling characteristics, high sensitivity, short analysis time, low analysis cost and potential to apply to real-time measurements. Most of the studies on biosensors are aimed at clinical diagnosis and identifications. However, it is thought that it will be possible to overcome these disadvantages by increasing the contribution of food science and technology experts to this field and the performance of biosensors in food analysis will increase.

REFERENCES

[1] Murali Naik, K., Srinivas, D., Sasi, B., Jakeer Basha, S.K., Biosensors in food processing-A review. International Journal of Pure & Applied Bioscience, 5(4): 1219-1227, 2017.

[2] Murugaboopathi, G., Parthasarathy, V., Chellaram, C., Prem Anand, T., Vinurajkumar, S., Applications of biosensors in food industry. Bioscience Biotechnology Research Asia, 10(2): 711-714, 2013.

[3] Da Costa Silva, L.M., Dos Santos, V.P.S., Salgado, A.M., Pereira, K.S., State of the Art in Biosensors - Environmental and Medical Applications. p: 151-168, 2013.

[4] Çoğal, S., Şen Gürsoy, S., Çelik Çoğal, G., Gürsoy, O., Sütte laktoz tayini için biyosensörlerin kullanımı. Akademik Gıda, 14(1): 33-42, 2016.

[5] Leonard, P., Hearty, S., Brennan, J., Dunne, L., Quinn, J., Chakraborty, T., O'Kennedy, R., Advances in biosensors for detection of pathogens in food and water. Enzyme and Microbial Technology, 32: 3-13, 2003.

[6] Otlu, B., Biyosensörler:Biyoreseptör moleküller. 6th International Advanced Technologies Symposium (IATS'11), Elazığ, Turkey, p: 5-7, 16-18 May 2011.

[7] Himmetağaoğlu, A.B., Erbay, Z., Baş, D., Biyosensörler ve süt teknolojisindeki uygulamaları. Türkiye 12. Gıda Kongresi, Edirne, p: 246-247, 5-7 Ekim 2016.

[8] Baş, D., Deniz, E., Gıda güvenliği ve kalite kontrolünde biyosensörler. Gıda, 40(4): 225-232, 2015.

[9] Schaertel, B.J., Firstenberg-Eden, R., Biosensors in the food industry: present and future. Journal of Food Protection, 51(10): 811-820, 1988.

INVESTIGATION OF ELECTRO OPTICAL PROPERTIES OF VARIOUS POLYMER-DOPED LIQUID CRYSTAL

[a]B. Coşkun, [b]A. Dere

[a]Department of Physics, Faculty of Arts and Sciences, Kırklareli University, Turkey

[b]Firat University, Nanoscience and Nanotechnology Laboratory, Elazig, 23200 TURKEY

E-mail: burhan.coskun@klu.edu.tr

Abstract

Liquid crystals find vast area of applications in technological devices due to their thermal and optical properties. In this study, the electro-optical of 4-cyano-4'-n-pentylbiphenyl (5 CB) liquid crystal doped by various polymers have been investigated. New liquid crystals were synthesized by doping 5CB liquid crystal with various dopants. Dielectric anisotropy properties of the liquid crystals were defined using Capacity-Voltage measurement method. It is seen that dielectric-anisotropy properties of the liquid crystals give different values for different dopant.

It was seen that the dielectric properties of the liquid crystals increased with temperature was observed. In addition, electro-optic of the liquid crystals alter with doping.

Key Words: Liquid Crystal, Dielectric Anisotropy, Electro-Optical Properties

1. INTRODUCTION

Liquid Crystals were discovered by Friedrich Reinitzer, an Australian botanist, in 1888 [1]. In his research Reinitzer synthesized Cholesteryl benzoate and he observed two different melting points in his experiment. Solid benzoate was melted at 145 °C and turned into a cloudy liquid and the cloudy liquid turned into a transparent liquid at 179 °C. The German Physicist Lemann investigated the liquid with polarisation microscope and concluded that the liquid was in anisotropic structure. Then, he named the liquid as "liquid crystal" [2, 3]. The liquid crystal state of matter is often considered as a special state where both liquid and solid properties of matter are observed. Liquid crystals show nonlinear optical properties since they are susceptible to even very low optical fields. The measurement methods such as refractive index, impedance, and dielectric spectroscopy can be used to determine the optical properties of liquid crystals [4].

Today, liquid crystals find vast area of applications in technological devices due to their thermal and optical properties. Liquid crystals can be used in display technologies in many devices calculators, watches, computers TV's etc. Structures and phases of liquid crystals show dramatic change with extrinsic factors. Electric and magnetic field, temperature and pressure change may affect the molecular anisotropy (orientation, placement, dispersion and double refraction) of liquid crystals cause optic and optoelectronic alterations. Therefore, liquid crystals can find many applications in devices like liquid crystal displays (LCD), holographic data recording, sensors [5-8].

One of the most important properties of liquid crystals is changing their optical properties when the electrical field is applied. Electro-optical and phase transition properties of nemetic liquid crystals which were doped with various polymers was investigated in this study.

2. MATERIALS AND METHODS

Spatulas, tubes and injectors used in the preparation and investigation of the liquid crystal systems are disinfected with alcohol and acetone and rinsed with pure water before each use. Organic compounds used in this research are 4- cyano-4'-n-pentilbifenil (5CB), poly [2-metoxy-5-(20-etilhekziloxi)-1,4-fenilenvynil] (MEH-PPV) and 3-tiyenilmetil metakrilat:6-(4 cynobifenil-4-oksi hexile acrylate (MTM-LC6). Chemical structures of the materials used in the experiment were presented in Figure 1.

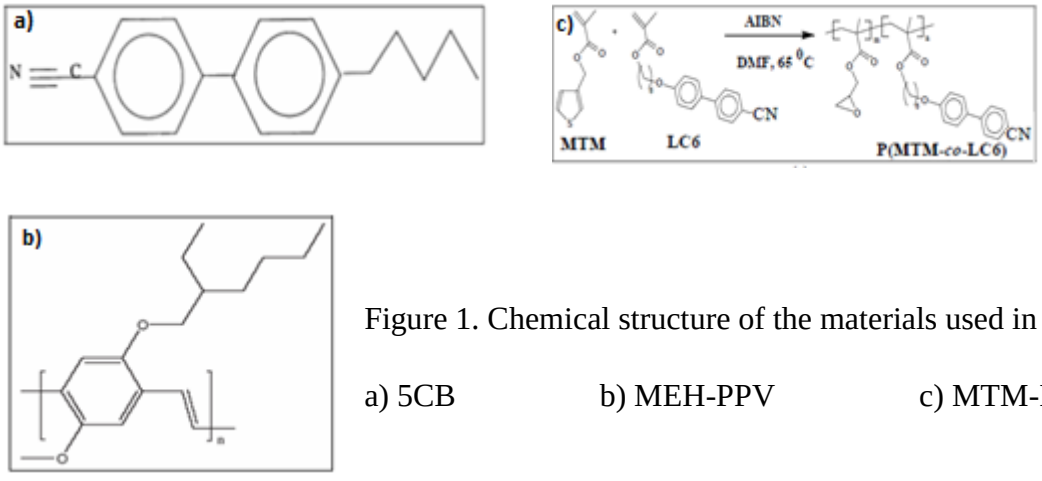

Figure 1. Chemical structure of the materials used in the experiment.

a) 5CB b) MEH-PPV c) MTM-LC6

4-cyano-4'-n-pentilbifenil, 4-cyano-4'-n-pentilbifenil: poli[2-metoxy-5-(20-etilhekziloksi)-1,4-fenilenvynil] (%1), 4-cyano-4'-n-pentilbifenil: poli[2-metoxy-5-(20-etilhekziloksi)-1, 4-fenilenvynil] (%2), 4-cyano-4'-n-pentilbifenil:3-tiyenilmetil metacrilate:6-(4-cynobifenil-4-oxy) hexilacrilate solutions were prepared and coded with the preparation order as follows 5CB, 5CBM, 5CBM2 and 5CBF. Thickness of liquid crystal cells are 5,5 µm for 5CB, 5,7 µm for 5 CBF, 5,3 µm for 5CBM and 5,4 µm for 5CBM2. After the preparation, the liquid crystal compositions were stirred with vortex and sonic shakers and filled into the Indium Thin Oxide (ITO) coated liquid crystal cells.

3. RESULTS AND DISCUSSION

3.1. Dielectric Anisotropy Properties

Dielectric anisotropy measurements of the liquid crystals were performed by using Capacity-Voltage (C-V) method. C-V curves obtained after measurements are presented in Figures 2, 3, 4 and 5. C-V results of the samples show that capacitance stay almost stable in low voltages. After a certain voltage value, capacitance increase dramatically and reach a value and reach a stable state. Minimum value of capacitance indicates the starting positions of molecules. Increase in the capacitance originates from the orientation change of molecules. The increase occurs due to the dielectric properties of liquid crystals. In this section, polymer effect in dielectric anisotropy of liquid crystals was investigated. It was concluded that Dielectric anisotropy properties of 5CB liquid crystal was changed with polymer doping.

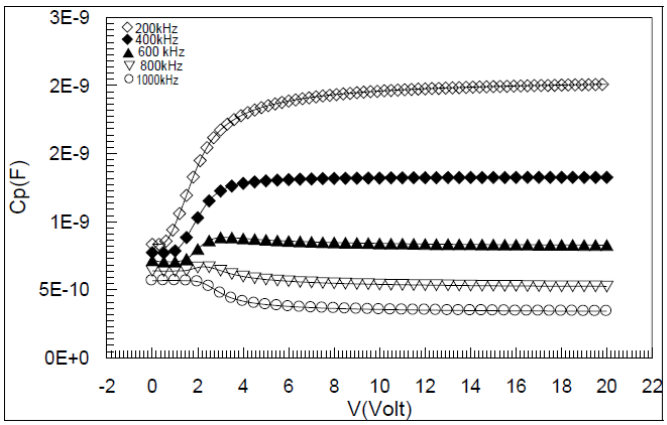

Figure 2. Capacitance-Voltage graph of 5CB liquid crystal in different frequencies.

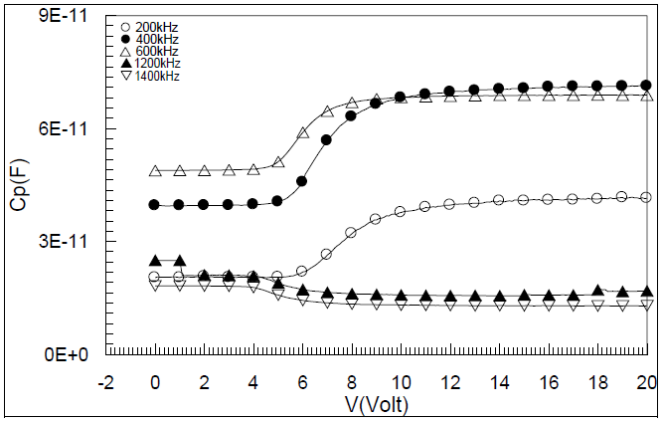

Figure 3. Capacitance-Voltage graph of 5CB liquid crystal in different frequencies.

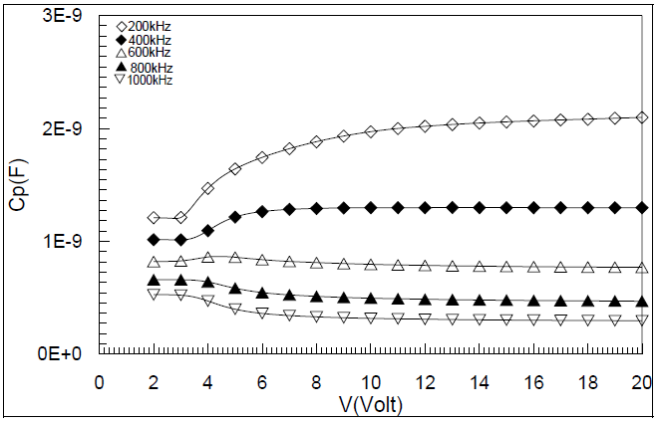

Figure 4. Capacitance-Voltage graph of 5CB liquid crystal in different frequencies.

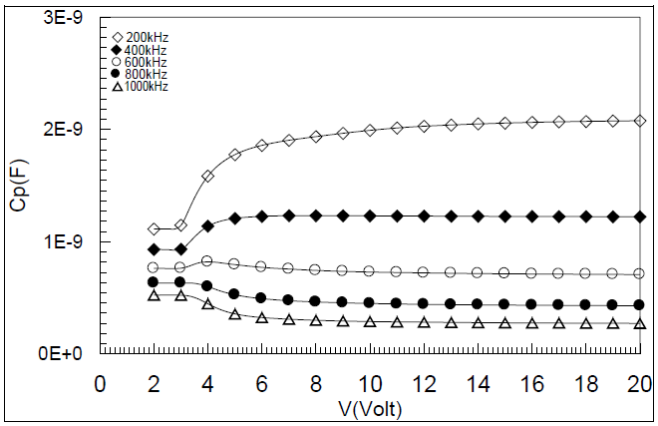

Figure 5. Capacitance-Voltage graph of 5CB liquid crystal in different frequencies.

In the case where the frequency of electric field was increased, C-V curves of samples were changed. This means the dielectric anisotropy properties of liquid crystals switch from negative dielectric anisotropy to positive. Dielectric anisotropy curves obtained from 5CBM and 5CBM2 were presented in the Figure 6 and Figure 7. Curves show that dielectric anisotropy values change with doping.

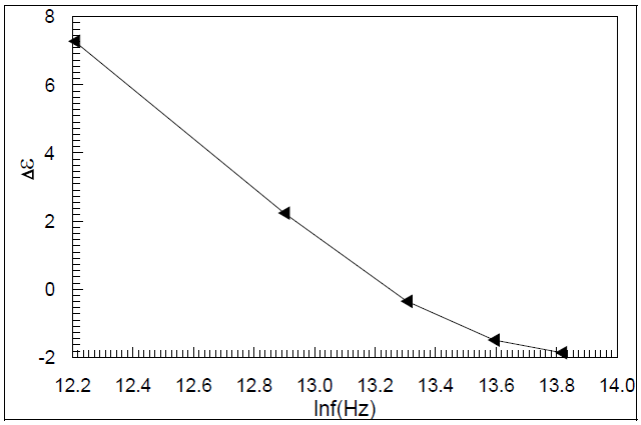

Figure 6. Δε - frequency graph for the sample 5CBM2.

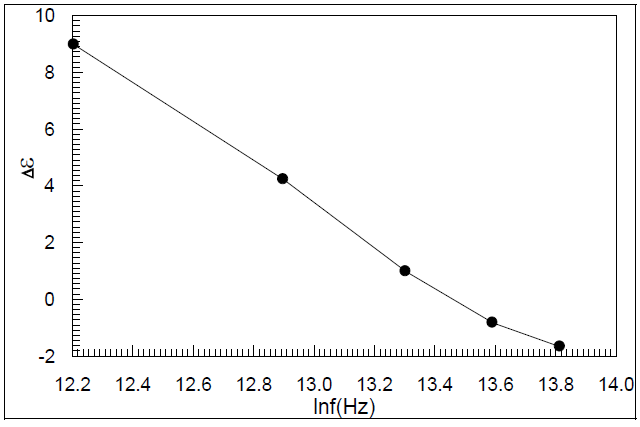

Figure 7. Δε - frequency graph for the sample 5CBM2.

3.2. Dielectric Properties of Liquid Crystals

Cole-Cole curves belong to the samples were presented in Figure 8 and Figure 9. Cole-Cole curves of liquid crystals often look like semi-circles. The curves obtained from the samples indicate that samples show Debye type dielectric relaxation. Radius of the circle increases with voltage that applied to liquid crystals. The increase in the radius indicates the orientation change of the molecules from being perpendicular to the electric field to being parallel to the electric field. Reaction mechanism of liquid crystals can be calculate as follows [9];

$$\varepsilon^*(\omega) = \varepsilon_\infty + \frac{\varepsilon_0 - \varepsilon_\infty}{1 + (i\omega\tau)^\alpha}$$

where ε^* complex dielectric constant, ε_0 dielectric constant in low frequency limit., ε_∞ dielectric coefficient in high frequency limit, τ relaxation time, ω angular frequency, α distribution parameter [10, 11]. α=1 indicates Dype type relaxation case.

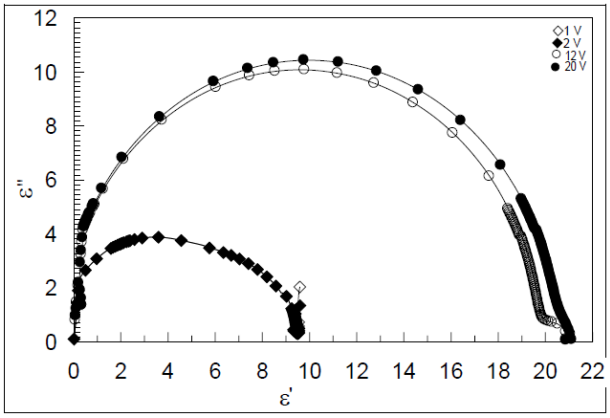

Figure 8. Exchange graph of imaginary and real dielectric coefficients (ε''-ε') for 5CBM.

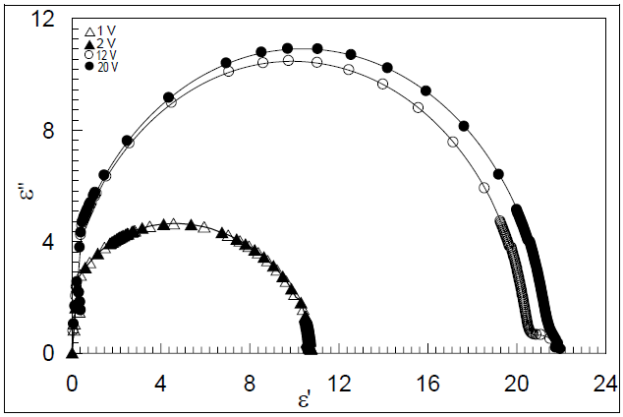

Figure 9. Exchange graph of imaginary and real dielectric coefficients (ε''-ε') for 5CBM2.

3.3. Electrical Conductivity Properties of Liquid Crystals

Figure 10, 11, 12 and 13 show parallel and perpendicular electrical conductivity dependence of liquid crystals. Conductivity of liquid crystals show two specific characteristics in low frequency and high frequency regions. In the first region conductivity does not change with frequency, on contrary in the second region conductivity increases with electrical frequency. Parallel and perpendicular conductivity of liquid crystals depend on frequency.

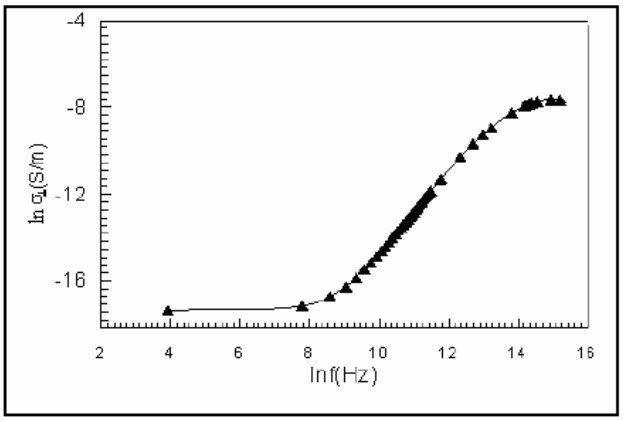

Figure 10. Frequency change $\sigma_{\perp}$ graph for 5CBM.

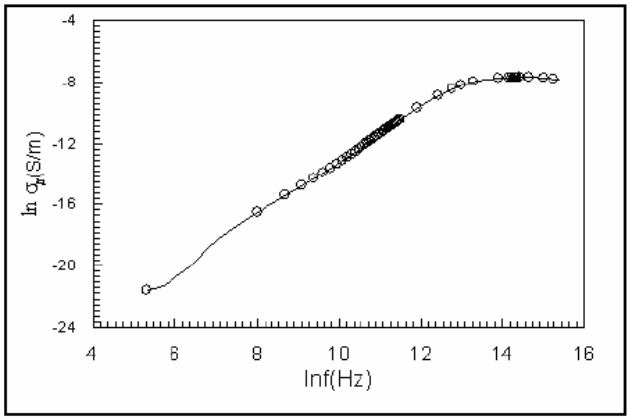

Figure 11. Frequency change $\sigma_{//}$ graph for 5CBM.

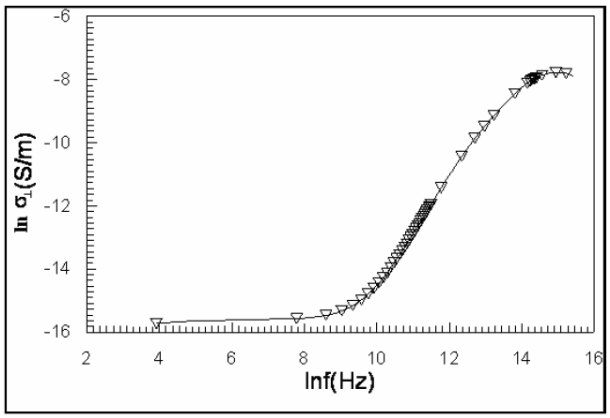

Figure 12. Frequency change $\sigma_{\perp}$ graph for 5CBM2.

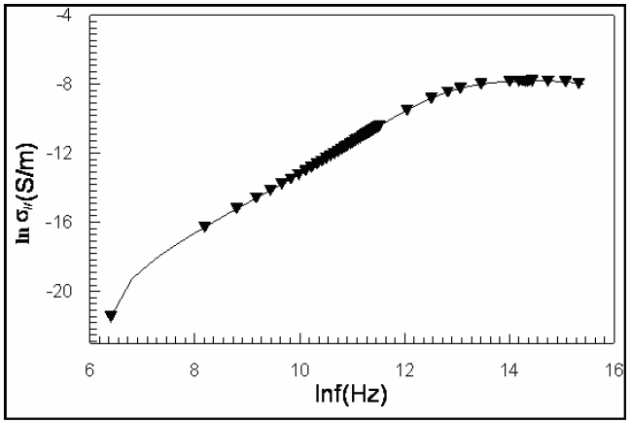

Figure 13. Frequency change $\sigma_{,,}$ graph for 5CBM2.

4. CONCLUSION

Electro optic properties of liquid crystals were investigated in this study. Liquid crystal 5CB was doped with various dopants new liquid crystal solutions were prepared. Capacity- Voltage measurements of liquid crystals were performed to determine dielectric anisotropy properties. It was seen that anisotropic structure of sample changed from positive dielectric anisotropy (p-type) characteristic to negative dielectric anisotropy (n-type). Dielectric anisotropy values of liquid crystals change with dopant. Dielectric reaction properties of liquid crystals determined with the change in imaginary and real dielectric constants. Dielectric reaction case analysed with using Cole-Cole curves. It was concluded that dielectric reaction mechanism shows Deby type relaxation characteristics.

Promising results were obtained from the study. The results indicate that liquid crystals can be modified with different dopants for optical applications. Refractive index spectra of liquid crystals reveal that refractive index change with dopant as well and refractive index curls shows regular dispersion characteristics. The results obtained from experiments clearly show that doping the liquid crystals with different polymers alters the electro-optic transition characteristics.

Acknowledgement

I present my very special thanks and gratitude to Prof. Dr. Fahrettin Yakuphanoglu, respectable academics of Department of Physics at Firat University.

References

[1] B Reinitzer F., Beitrage Zur C., 1888. Monatsh Chem, 9:421-41.

[2] Lehmann O., 1889. Uber Fliesende Krystalle, Zeitchriff für Physikalische Chemie 462.

[3] Coskun B., 2007. Sıvı kristallerin elektro-optik özelliklerinin incelenmesi. Fırat Üniversitesi, Fen Bilimleri Enstitüsü, Yüksek Lisans Tezi, 40s, Elazığ.

[4] Gennes P. G., Prost J., 1998. The Physics of Liquid Crystals, Oxford University Press.

[5] Yakuphanoglu F., Bilgin E. B., Ocak H., Oweimreen G. A., 2007. Phyica B 393, 270-274.

[6] Doane J. E., Vaz N. A., Wu B. G., Zumer S., 1986. Appl. Phys. Lett. 48, 269.

[7] Kato T., 2002. Science 295, 2414.

[8] Iannachione G. S., 2004. Fluid Phase Equilib. 222, 177.

[9] Johscher A. K., Dielectric Relaxation in Solids, 1983. Chelsea Dielectrics Press. London.

[10] Cole K. S., Cole R. H., 1969. J.Chem Phys; 9:341.

[11] Okutan M., San E. S., Koysal O., Yakuphanoglu F., 2005. Physica B:Condensed Matter, 362; 180-186

INVESTIGATION OF PHASE TRANSITION PROPERTIES OF VARIOUS POLYMER-DOPED LIQUID CRYSTAL

[a]B. Coşkun, [b]A. Dere

[a]Department of Physics, Faculty of Arts and Sciences, Kırklareli University, Turkey

[b]Firat University, Nanoscience and Nanotechnology Laboratory, Elazig, 23200 TURKEY

E-mail: burhan.coskun@klu.edu.tr

Abstract

Phase transitions in liquid crystals have been intensively studied during the last 40 years due to their numerous daily technological applications. The nematic liquid crystal the phase transition of 4-cyano-4'-n-pentylbiphenyl (5 CB) liquid crystal doped by various polymers have been investigated. New liquid crystals were synthesized by doping 5CB liquid crystal with various dopants. Phase transition properties of samples were calculated using dielectric constant- temperature method. Dielectric constant increases with temperature and shows phase transition peak.

It is seen that phase transitions properties of the liquid crystals give different values for different dopant. In addition, phase transitions of the liquid crystals alter with doping.

Key Words: Liquid Crystal, Dielectric Anisotropy, Phase Transitions

1. INTRODUCTION

Liquid crystals are highly nonlinear optical materials due to their susceptible property activating under even relatively low optical fields. Several nonlinear mechanisms investigated so far have revealed the promising characters of these materials [1, 2].

The investigation of the optical constants such as refractive index, extinction coefficient and dielectric constant of the liquid crystal materials are important for designing of new materials. Optical constants include the valuable information for technological applications. Furthermore, the changes in refractive index are important for controlling optical properties of liquid crystals. Optical properties of any liquid crystal are important for optical applications, because optical properties are directly related to their structural and electronic properties [3]

Liquid crystals show nonlinear optical properties since they are susceptible to even very low optical fields. The measurement methods such as refractive index, impedance, and dielectric spectroscopy can be used to determine the optical properties of liquid crystals [4].

Today, liquid crystals find vast area of applications in technological devices due to their thermal and optical properties. Liquid crystals can be used in display technologies in many devices calculators, watches, computers TV's etc. Structures and phases of liquid crystals show dramatic change with extrinsic factors. Electric and magnetic field, temperature and pressure change may affect the molecular anisotropy (orientation, placement, dispersion and double refraction) of liquid crystals cause optic and optoelectronic alterations. Therefore, liquid crystals can find many applications in devices like liquid crystal displays (LCD), holographic data recording, sensors [5-8].

One of the most important properties of liquid crystals is changing their optical properties when the electrical field is applied. Phase transition properties of nematic liquid crystals which were doped with various polymers was investigated in this study.

2. MATERIALS AND METHODS

Spatulas, tubes and injectors used in the preparation and investigation of the liquid crystal systems are disinfected with alcohol and acetone and rinsed with pure water before each use. Organic compounds used in this research are 4- cyano-4'-n-pentilbifenil (5CB), poly [2-metoxy-5-(20-etilhekziloxi)-1,4-fenilenvynil] (MEH-PPV) and 3-tiyenilmetil metakrilat:6-(4 cynobifenil-4-oksi hexile acrylate (MTM-LC6). Chemical structures of the materials used in the experiment were presented in Figure 1.

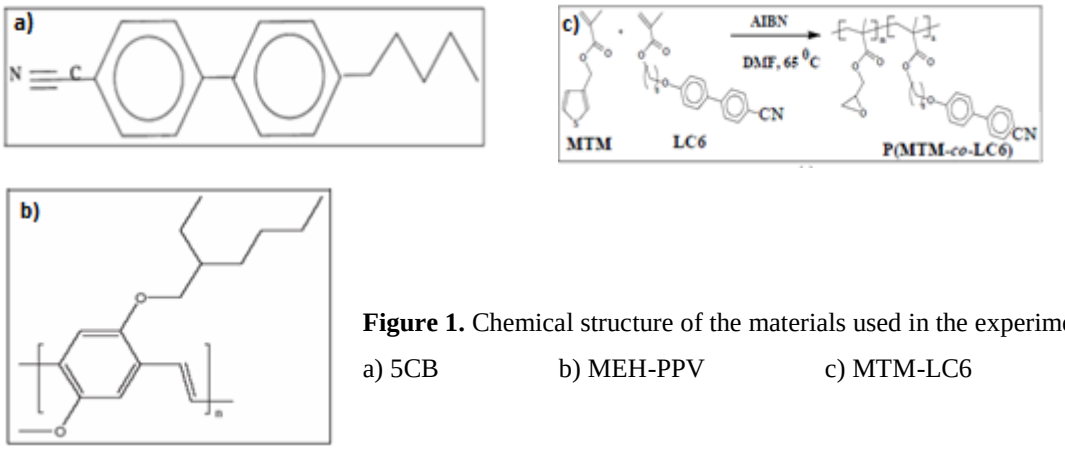

Figure 1. Chemical structure of the materials used in the experiment.
a) 5CB b) MEH-PPV c) MTM-LC6

4-cyano-4'-n-pentilbifenil, 4-cyano-4'-n-pentilbifenil: poli[2-metoxy-5-(20-etilhekziloksi)-1,4-fenilenvynil] (%1), 4-cyano-4'-n-pentilbifenil: poli[2-metoxy-5-(20-etilhekziloksi)-1, 4-fenilenvynil] (%2), 4-cyano-4'-n-pentilbifenil:3-tiyenilmetil metacrilate:6-(4-cynobifenil-4-oxy) hexilacrilate solutions were prepared and coded with the preparation order as follows 5CB, 5CBM, 5CBM2 and 5CBF. Thickness of liquid crystal cells are 5,5 µm for 5CB, 5,7 µm for 5 CBF, 5,3 µm for 5CBM and 5,4 µm for 5CBM2. After the preparation, the liquid crystal compositions were stirred with vortex and sonic shakers and filled into the Indium Thin Oxide (ITO) coated liquid crystal cells.

3. RESULTS AND DISCUSSION

3.1. Phase Transition and Optic Transition of Liquid Crystals

In order to determine the phase transition of the liquid crystals temperature-dielectric constants measurements were performed. Dielectric-temperature results obtained in the measurements are presented in Figure 2. The graph shows that dielectric constant increases with temperature and shows dramatic increase and a peak at a certain point. Peak temperature corresponds to the point where phase transition occurs. Peak temperatures for liquid crystals 5CB, 5CBF and 5CBM were determined as 55,3 °C, 45,12 °C and 43,01 °C. The phase of liquid crystals transfers from nematic phase to isotropic phase in these temperatures. For the liquid crystal 5CB, isotropic phase temperature is determined as 55,3 °C, the value shifts down with doping other materials.

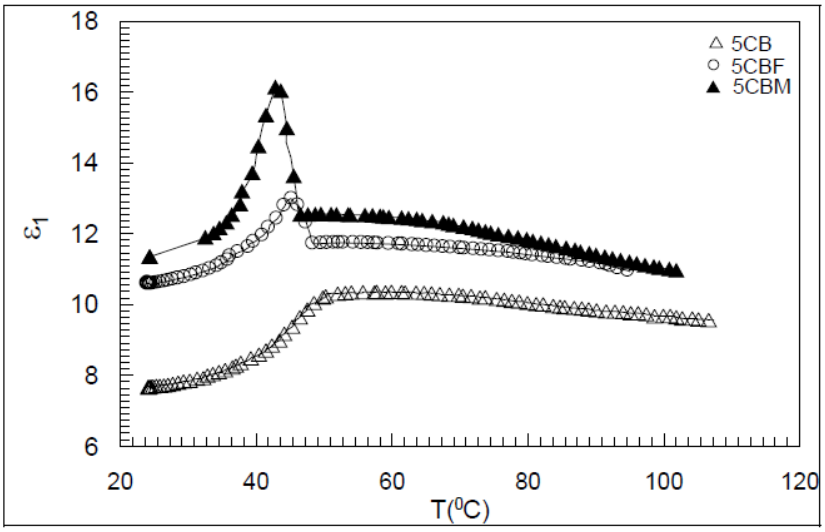

Figure 2. Dielectric constant- Temperature graph for 5CB, 5CBF and 5 CBM

Absorbance (A), Transitivity (T), Reflectance(R) properties of samples were investigated using their spectra. Optical spectra were obtained using Shimadzu UV-VIS-NIR 3600 spectrometer. Optic spectra of liquid crystals were presented in Figure 3.

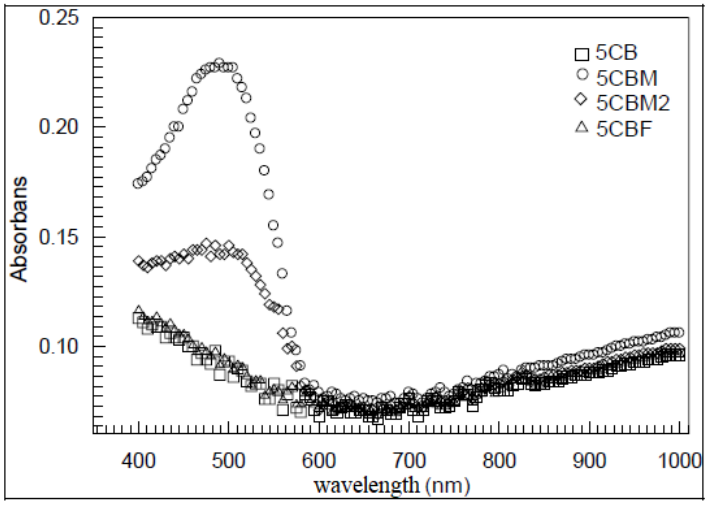

(a)

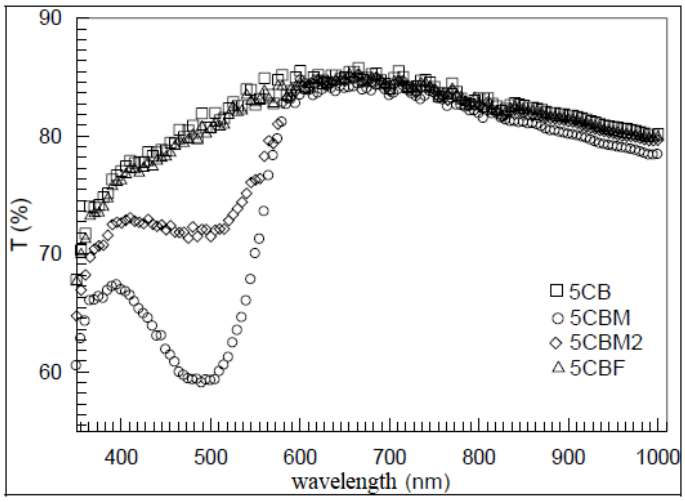

(b)

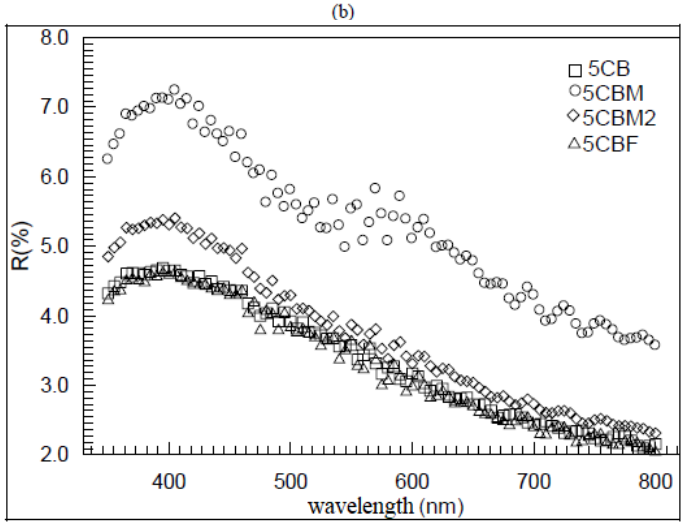

(c)

Figure 3. a) Absorbance b) Transitivity c) Reflectance spectra of liquid crystals.

Figure 3 shows A, R and T spectra of liquid crystals which are altered with doping made to 5CB. Especially, doping MEH-PPV polymer to 5CB liquid crystal cause sudden alteration in the transitivity spectra of sample. Regarding to these results liquid crystals can be modified for desired optical applications.

Refractive index is another important parameter for liquid crystals. Refractive indexes of liquid crystals were calculated by using refractive spectra of liquid crystals. In Figure 4 refractive index-wavelength graph was presented. As can be seen from graph, refractive indexes change with dopant. Doping MEH-PEV gives the highest refractive index value. Refractive indexes of liquid crystals show regular dispersion behaviour.

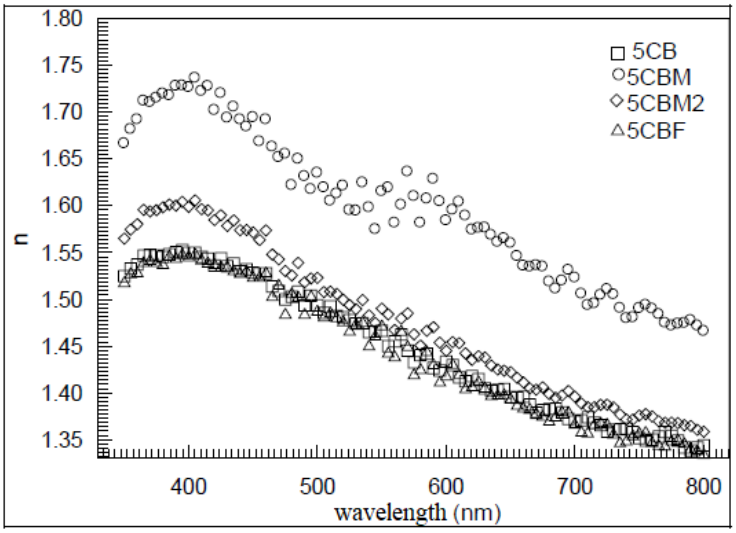

Figure 4. Wavelength-refractive index graph of liquid crystals

4. CONCLUSION

Phase transition properties of liquid crystals were investigated in this study. Liquid crystal 5CB was doped with various dopants new liquid crystal solutions were prepared. Phase transition properties of samples were calculated using dielectric constant- temperature method. Dielectric constant increases with temperature and shows phase transition peak. The position of phase transition peak differs from dopant type to another. This change indicates that the phase transition changes were caused by dopant. Regarding to the phase transition peak values obtained from experiment, it was concluded that the phase of liquid crystal samples switch from nematic phase to isotropic phase.

Absorbance, transitivity, reflectance spectra of liquid crystals change with doping the sample with organic dopant. Promising results were obtained from the study. The results indicate that liquid crystals can be modified with different dopants for optical applications. Refractive index spectra of liquid crystals reveal that refractive index change with dopant as well and refractive index curls shows regular dispersion characteristics. The results obtained from experiments clearly show that doping the liquid crystals with different polymers alters the phase transition characteristics.

Acknowledgement

I present my very special thanks and gratitude to Prof. Dr. Fahrettin Yakuphanoglu, respectable academics of Department of Physics at Firat University.

References

[12] I.C. Khoo, M. Shih, M.V. Wood, B.D. Guenther, P.H. Chen, F. Simoni, S.S. Slussarenko, O. Francescangeli, L. Lucchetti Proc. IEEE, 87 (11) (1999), p. 1897

[13] S. Bartkiewicz, A. Januszko, A. Miniewicz, J. Parka Pure Appl. Opt., 5 (1996), p. 799

[14] Y.J. Wang, G.O. Carlisle J. Mater. Sci., 13 (2002), p. 73

[15] Coskun B., 2007. Sıvı kristallerin elektro-optik özelliklerinin incelenmesi. Fırat Üniversitesi, Fen Bilimleri Enstitüsü, Yüksek Lisans Tezi, 40s, Elazığ.

[16] Gennes P. G., Prost J., 1998. The Physics of Liquid Crystals, Oxford University Press.

[17] Yakuphanoglu F., Bilgin E. B., Ocak H., Oweimreen G. A., 2007. Phyica B 393, 270-274.

[18] Doane J. E., Vaz N. A., Wu B. G., Zumer S., 1986. Appl. Phys. Lett. 48, 269.

[19] Kato T., 2002. Science 295, 2414.

ANALYTICAL SOLUTION OF SCHRODINGER EQUATION FOR A 2D CHARGED PARTICLE CONFINED BY EXTERNAL MAGNETIC AND AB FLUX FIELDS UNDER POWER INTERACTION POTENTIALS

H. Karayer

Department of Physics, Faculty of Arts and Sciences, Kirklareli University, Kirklareli, Turkey

E-mail: hale.karayer@klu.edu.tr

Exact eigenstate solutions of radial Schrödinger equation for a 2D charged particle interacting via a radially symmetrical potential under the external uniform magnetic field and Aharonov-Bohm (AB) flux fields are obtained by using extended Nikiforov-Uvarov (NU) method. The method is improved by changing the boundary conditions of the NU method in order to solve second order differential equations which have at most four singular points. Wave function is achieved in terms of biconfluent Heun polynomials without using any procedure for tranformation of radial Schrödinger equation to biconfluent Heun equation. Hereby various coordinate transformations or ansatzs in traditional solution methods are eliminated by extended NU method.

Keywords: Extended Nikiforov-Uvarov method, external magnetic field, biconfluent Heun equation

1. INTRODUCTION

Solution of radial Schrödinger equation (SE) has great importance in nonrelativistic quantum mechanics. If eigensatate solutions of the SE for a given potential are known, one can achieve all necessary information related to the physical system [1]. Eigenfunction of the SE $\psi(r,\theta,\phi) = R(r)Y(\theta,\phi)$ is given as product of radial part $R(r)$ with spherical harmonics $Y(\theta,\phi)$ when potential is central which means it only depends on distance r. Potentials for which the SE is exactly solvable are known as Morse potential, the Eckart potential, the Rosen-Morse potential, the trigonometric and hyperbolic Pöschl-Teller potentials, the Manning-Rosen potential, the Woods-Saxon potential, and the Scarf potential [2]. The power series method, the factorization method or the supersymmetric quantum mechanics approach and Nikiforov-Uvarov (NU) method are the most frequently used methods in order to obtain exact solution of the wave equation [1]. The NU method is based on reducing a second order differential equation to a hypergeometric type second order differential equation [3]. The reduced equation is called as basic equation of the method. Degrees of polynomial coefficients in the basic equation constitute boundary conditions of the method. In general the NU method is only succeed for second order differential equations which have at most three singular points. Therefore the number of differential equations which are solvable by NU method is restricted due to these boundary conditions.

We have extended the degrees of polynomial coefficients in the basic equation of the NU method and derived extended form of the NU method [4]. Any second order differential equations which have at most four singular points can be transformed to the derived basic equation in the extended method. It is also presented that Heun equation and its confluent forms can be solved analytically by the extended NU method [4,5]. Heun equation in which Gauss hypergeometric, confluent hypergeometric, Mathieu, Ince, Legendre, Laguerre, Bessel functions are involved, is a general second order linear differential equation [6]. Since the scientists encounter with Heun equation and its confluent forms in a wide range from quantum dots to black holes, extended NU method is an efficient method for many physical problems. Solutions of the Heun type equations have been obtained by traditional power series method in the literature.

Especially SE which is written for some physical problems namely the Coulomb problem on a 3-sphere, two Coulombically repelling electrons on a sphere, hyperbolic double-well potential, a two-electron quantum dot model is reduced to a Heun type equation using appropriate coordinate transformations or ansatzs. The wave equation can be solved directly by extended NU method. The equation which gives polynomial part of eigenfunction is obtained as a Heun type equation together with the eigenvalue equation which is equal to condition of existence of polynomial solution of the Heun type equation [7].

In this study analytical solutıon of SE for a 2D charged particle confined by external magnetic and AB flux fields under power interaction potentials is obtained by extended NU method.

2. EXTENDED NIKIFOROV UVAROV METHOD

If any second order differential equation is reduced to following equation, namely basic equation of the extended NU method;

$$\psi''(z)+\frac{\tilde{\tau}_e(z)}{\sigma_e(z)}\psi'(z)+\frac{\tilde{\sigma}_e(z)}{\sigma_e^2(z)}\psi(z)=0 \tag{1}$$

where $\tilde{\tau}_e(z)$, $\sigma_e(z)$ and $\tilde{\sigma}_e(z)$ are polynomials of at most second, third and fourth-degrees respectively, the differential equation can be solved analytically by the method. By taking $\psi(z)=\Phi_e(z)y(z)$ the basic equation is reduced to a more compherensible form;

$$\sigma_e(z)y''(z)+\tau_e(z)y'(z)+h(z)y(z)=0, \tag{2}$$

where $\tau_e(z)$, $h(z)$ and $\pi_e(z)$ are polynomials which are defined as;

$$\tau_e(z)=\tilde{\tau}_e(z)+2\pi_e(z),$$
$$h(z)-\pi_e'(z)=g(z),$$
$$\pi_e(z)=\frac{\sigma_e'(z)-\tilde{\tau}_e(z)}{2}\pm\sqrt{\left(\frac{\sigma_e'(z)-\tilde{\tau}_e(z)}{2}\right)^2-\tilde{\sigma}_e(z)+g(z)\sigma_e(z)}, \tag{3}$$

In order to specify the polynomial $\pi_e(z)$, the polynomial $g(z)$ under the square root sign must be known explicitly. The polynomial $\pi_e(z)$ must be a polynomial of at most second-degree due to the boundary conditions of the extended NU method. According to the restriction on the degree of the polynomial $\pi_e(z)$ requires that the expression under the square root sign must be square of a polynomial at most second-degree. Thus the polynomial $g(z)$ must be chosen appropriately. After determination of the polynomial $g(z)$, the polynomials $\tau_e(z)$, $h(z)$ and $\pi_e(z)$ can be obtained completely [4,5,6].

In order to generalize solution of Eq.(2), it is differentiated n times by using the representation $y^{(n)}(z)=v_n(z)$. If the coefficient of $v_n(z)$ is equal to zero, polynomial $h_n(z)$ can be defined;

$$h_n(z)=-\frac{n}{2}\tau_e'(z)-\frac{n(n-1)}{6}\sigma_e''(z)+C_n \tag{4}$$

where C_n is an integration constant. Equating the polynomials $h(z)$ and $h_n(z)$ one can get eigenvalue solution of the physical problem. Thus Eq.(2) has a particular solution of the form $y(z)=y_n(z)$ which is a polynomial of degree n. The function $\phi(z)$ in the initial transformation $\psi(z)=\phi(z)y(z)$ is defined as a logarithmic derivative;

$$\frac{\Phi_e'(z)}{\Phi_e(z)}=\frac{\pi_e(z)}{\sigma_e(z)} \tag{5}$$

3. ANALYTIC SOLUTION TO A GENERAL FORM UNDER EXTERNAL FIELDS

Consider a 2D charged particle with charge e and effective mass μ under the influence of external uniform magnetic field $\vec{B} = \hat{B}\{z\}$ and an AB flux field. SE with a vector potential $\vec{A}$ and an interaction potential $V(r,\phi)$ in polar coordinates (r,ϕ) could be written as;

$$\left[\frac{1}{2\mu}\left(\vec{p} + \frac{e}{c}\vec{A}\right)^2 + V(r)\right]\psi(r,\phi) = E\psi(r,\phi).$$

For the wave function $\psi(r,\phi) = \frac{1}{\sqrt{2\pi}}e^{im\phi}u(r)$, the radial potential $V(r) = ar^2 + br + d - \frac{g}{r} + \frac{k}{r^2}$ and the vector potential $\vec{A} = (\frac{Br}{2} + \frac{\phi_{AB}}{2\pi r})\hat{\phi}$ the radial SE can be obtained [8];

$$\frac{d^2u(z)}{dz^2} + \frac{1}{z}\frac{du(z)}{dz} + \left(\frac{\frac{-\epsilon^2}{\gamma}z^2 - \beta^2 - z^4 + \frac{g'}{\sqrt{\gamma}}z - \frac{b'}{\gamma^{3/2}}z^3}{z^2}\right)u(z) = 0, \quad (6)$$

where $-\epsilon^2 = E' - d' - \frac{\mu\,\omega_c}{\hbar}m'$, $\beta^2 = k' + m'^2$, $\gamma^2 = a' + \left(\frac{\mu\,\omega_c}{\hbar}\right)^2$, $g' = \frac{2\mu}{\hbar^2}g$, $b' = \frac{2\mu}{\hbar^2}b$, $E' = \frac{2\mu}{\hbar^2}E$, $d' = \frac{2\mu}{\hbar^2}d$, $k' = \frac{2\mu}{\hbar^2}k$,a$' = \frac{2\mu}{\hbar^2}a$, $\xi = \frac{\phi_{AB}}{\phi_0}$, $\phi_0 = \frac{hc}{e}$, $\omega_c = \frac{eB}{\mu c}$ and $m' = m + \xi$.

Comparing Eq.(6) with the basic equation of extended NU method, the polynomial coefficients are associated by physical parameters in radial the SE by taking $\sqrt{\gamma}r = z$;

$$\tilde{\tau}_e(z) = 1,$$

$$\sigma_e(z) = z,$$

$$\tilde{\sigma}_e(z) = \frac{-\epsilon^2}{\gamma}z^2 - \beta^2 - z^4 + \frac{g'}{\sqrt{\gamma}}z - \frac{b'}{\gamma^{3/2}}z^3.$$

Substituting these polynomials into Eq.(3) the polynomial $\pi_e(z)$ can be obtained as;

$$\pi_e(z) = \sqrt{z^4 + \frac{b'}{\gamma^{3/2}}z^3 + \left(\frac{\epsilon^2}{\gamma} + m\right)z^2 - \left(\frac{g'}{\sqrt{\gamma}} - n\right)z + \beta^2}\,. \quad (7)$$

According to the condition of the polynomial $\pi_e(z)$ being a second degree polynomial, the polynomial $g(z)$ must be chosen appropriately;

$$\pi_{e1}(z) = -z^2 - \frac{b'}{\gamma^{3/2}}z - \beta,$$

$$\pi_{e2}(z) = z^2 + \frac{b'}{\gamma^{3/2}}z + \beta$$

for $(z) = \left[\frac{b'^2}{4\gamma^3} - \frac{\epsilon^2}{\gamma} + 2\beta\right]z + \frac{b'}{\gamma^{3/2}} + \frac{g'}{\sqrt{\gamma}}$.

Each of polynomials $\pi_e(z)$ produce different solution of the radial SE. For the polynomial $\pi_{e1}(z)$, polynomials $\tau_e(z)$, $h(z)$ and $h_n(z)$ can be determined as;

$$h(z) = [\frac{b'^2}{4\gamma^3} - \frac{\epsilon^2}{\gamma} + 2\beta - 2]z + \frac{\beta b'}{\gamma^{3/2}} - \frac{b'}{2\gamma^{3/2}} + \frac{g'}{\sqrt{\gamma}}$$

$$\tau(z) = -2z^2 - \frac{b'}{\gamma^{3/2}}z - 2\beta + 1$$

$$h_n(z) = 2nz + \frac{nb'}{2\gamma^{372}} + C_{n1}$$

By equating the polynomials $h(z)$ and $h_n(z)$, the integration constant C_{n1} and eigenvalue solution can be achieved;

$$C_{n1} = \frac{b'}{2\gamma^{\frac{3}{2}}}(-2\beta + n + 1) + \frac{g'}{\sqrt{\gamma}}$$

$$\epsilon^2 = 2\gamma(-n + \beta - 1) + \frac{b'^2}{4\gamma^2}.$$

$$E_n = d + \frac{1}{2}\hbar m'\omega_c + \frac{\hbar^2}{2\mu}\sqrt{\frac{8\mu a}{\hbar^2} + \left(\frac{\mu\,\omega_c}{\hbar}\right)^2}\left(n + 1 - \sqrt{\frac{2\mu}{\hbar^2}k + m'^2}\right) - \frac{2\mu\frac{b^2}{\hbar^2}}{\frac{8\mu a}{\hbar^2} + \left(\frac{\mu\,\omega_c}{\hbar}\right)^2}. \quad (8)$$

For eigenfunction solution the function $\phi(z)$ is achieved from the logarithmic derivative given in Eq.(5);

$$\phi_e(z) = exp\left[-\frac{1}{2}\left(z^2 + \frac{b'}{\gamma^{3/2}}z\right)\right]z^{\beta}.$$

When $h(z) = h_n(z)$, Eq.(2) which gives polynomial part of eigenfunction solution is transformed to the following form;

$$zy''(z) + [1 - 2\beta - \frac{b'}{\gamma^{3/2}}z - 2z^2]y'(z) + \left[2nz + \frac{g'}{\sqrt{\gamma}} + \frac{\beta b'}{\gamma^{3/2}} - \frac{b'}{2\gamma^{3/2}}\right]y(z) = 0. \quad (9)$$

Eq.(9) is biconfluent Heun equation which is derived from Heun equation by coalescence of two finite regular singular points with infinity.

$$xy'' + (1 + a - b\,x - 2x^2)y' + \left\{(\eta - a - 2)x - \frac{1}{2}[\delta + (1 + a)b]\right\}y = 0$$

Biconfluent Heun equation has polynomial solution represented by $N(a, b, \eta, \delta, z)$ of degree n if and only if $\eta - a - 2 = 2n$ is provided. Since the condition which presents existence of polynomial solution of biconfluent Heun equation is achieved directly as eigenvalue solution of the radial SE, the polynomial part of eigenfunction solution can be given in terms of biconfluent Heun polynomials. Then the complete eigenfunction solution becomes for $\sqrt{\gamma}r = z$;

$$R_1(r) = \exp\left[\frac{1}{2}\left(\gamma r^2 + \frac{b'}{\gamma}r\right)\right](\sqrt{\gamma}r)^{\beta}N(-2\beta, \frac{b'}{\gamma^{3/2}}, \frac{b'^2}{4\gamma^3} - \frac{\epsilon^2}{\gamma}, -\frac{2g'}{\sqrt{\gamma}}, \sqrt{\gamma}r) \quad (10)$$

Using the above mentioned procedure the eigenstate solutions for the polynomial $\pi_{e2}(z)$ can be obtained;

$$E_n = d + \frac{1}{2}\hbar m'\omega_c + \frac{\hbar^2}{2\mu}\sqrt{\frac{8\mu a}{\hbar^2} + \left(\frac{\mu\,\omega_c}{\hbar}\right)^2}\left(n + 1 + \sqrt{\frac{2\mu}{\hbar^2}k + m'^2}\right) - \frac{2\mu\frac{b^2}{\hbar^2}}{\frac{8\mu a}{\hbar^2} + \left(\frac{\mu\,\omega_c}{\hbar}\right)^2} \quad (11)$$

$$R_2(r) = \exp\left[\frac{1}{2}\left(\gamma r^2 + \frac{b'}{\gamma}r\right)\right](\sqrt{\gamma}r)^{\beta}p_2(r) \quad (12)$$

4. CONCLUSION

In this study, a particular solution of the radial SE for a 2D charged particle with charge e and effective mass μ under the influence of external uniform magnetic field $\vec{B} = \hat{B}\{z\}$ and an AB flux field is obtained analytically by extended NU method. It is presented that the radial SE is reduced to biconfluent Heun equation directly. Moreover eigenvalue solution of the problem is obtained as equal to the condition for existing of polynomial solution of biconfluent Heun equation for the polynomial $\pi_{e1}(z)$. In this case the eigenfunction is achieved depending on the biconfluent Heun polynomials. Finally eigenvalue and eigenfunction solution can be obtained in an easy and efficient way by using extended NU method. This method eliminates the detailed procedure which is applied in the power series method or transformation of SE to a Heun type equation.

REFERENCES

[1] Pahlavani, M. R. 2012. “Theoretical Concepts of Quantum Mechanics”, Rijeka, Croatia.

[2] Iacob, F., Lute, M. 2015. "Exact solution to the Schr\"odinger’s equation with pseudo-Gaussian potential", J. Math. Phys. 56, 121501.

[3] Nikiforov, A. V., Uvarov, V. B. 1988. “Special Functions of Mathematical Physics”, Birkhauser, Boston.

[4] Karayer, H., Demirhan, D., Buyukkilic, F. 2015. “Extension of Nikiforov-Uvarov Method for the solution of Heun equation”, J. Math. Phys, 56, 063504.

[5] Karayer, H., Demirhan, D., Buyukkilic, F. 2015. “Some Special Solutions of Biconfluent and Triconfluent Heun Equations in elementary functions by Extended Nikiforov--Uvarov Method”, Rep. Math. Phys., 76(3), 271-281.

[6] Ronveaux, A. 1995. “Heun's Differential Equations”, Oxford University Press, New York.

[7] Karayer, H., Demirhan, D., Buyukkilic, F. 2018. “Solution of Schrödinger equation for two different potentials using extended Nikiforov-Uvarov method and polynomial solutions of biconfluent Heun equation”, J. Math. Phys, 59, 053501.

[8] Ikhdair, S. M., Falaye, B. J., Hamzavi, M. 2015. “Nonrelativistic molecular models under external magnetic and AB flux fields”, Ann. Phys., 353, 282-298.

ELECTROMAGNETIC INTERFERENCE PROPERTIES OF SN DOPED ZNO SEMICONDUCTORS

[a]A.Dere, [b]B. Coşkun

[a]*Firat University, Nanoscience and Nanotechnology Laboratory, Elazig, 23200 TURKEY*

[b]Department of Physics, Faculty of Arts and Sciences, Kırklareli University, Turkey

E-mail: ayse_fizik23@hotmail.com

Abstract

The microwave dielectric properties of Sn doped ZnO samples have been investigated as a function of microwave frequency in the range of 1 to 20 GHz. The applicability of Sn doped ZnO samples for electromagnetic wave shielding effectiveness at microwave frequency was studied. The real and imaginary parts of reflection of the Sn doped ZnO samples were changed with Sn doping. With Sn doping, the real part of the reflection is decreased with Sn doping. A maximum reflection for 0.5 Sn doped ZnO sample was observed at about 15 GHz. The obtained results indicate that zinc oxide can be used for various electromagnetic wave shielding applications at microwave frequency.

Keywords: Zinc oxide; Electromagnetic reflection

1. INTRODUCTION

Electromagnetic interference (EMI) is unwanted noise from electromagnetic waves.. EMI is divided to common mode (CM) and differential mode (DM). For this purpose, wireless electronic devices try to filter CM and DM in circuits. Therefore, with Sn doped ZnO semiconductors were studied in this study. EMI is generally do away with by difference techniques like grounding, filtering and shielding. From these techniques, the filtering has been proper for the our study. [1,2].

It is important that the materials produced in the EMI have thin, transparent and functional properties. In this way, they can be more easily applied to a complex structure by absorbing the electromagnetic waves better.In addition, EMI materials are expected to be flexible and refractory, resistant to corrosion and should be applicable at a wide frequency. [3-5].

Today, unwanted electromagnetic waves namely electromagnetic (EM) pollution have increased due to the widespread use of wearable and portable electronic devices. For this reason, several EMI materials have been developed for these long-term problems. [6-14].

Electromagnetic pollution can affect the performance of electronic devices, as well as nausea, vertigo and muscle stimulation, which can even affect the human body. [15,16].

Simple techniques with low cost and high shielding can be developed as electromagnetic interference (EMI) protection techniques [17]. EMI experiments have a permanent and continuous research field in our modern world [18,19]. Therefore, we only consider Sn and ZnO that are good at EMI shielding effect and price competitiveness.

2. MATERIALS AND METHODS

In present study, Zinc acetate dihydrate, Zn(CH3COO)2 2H2O and Tin (II) chloride dehydrate were used to prepare Sn doped ZnO samples. Firstly, Zinc acetate dehydrate was dissolved in an distilled water and then, the citric acid was added to this solution. After 30 stirring, Tin (II) chloride dehydrate (SnCl2.2H2O) was added to the soluiton. Ultrasonic stirring was applied to the solution for 10 min using a FYRONIX sonicator. The obtained solutions including various Sn contents were converted to ZnO:Sn powder samples at 350 C for 2h. The obtained powders of Sn doped ZnO samples were annealed at 500 C for 1h.

The electromagnetic shielding characteristics, the graph of the imaginary part of reflection and real part of reflection against the frequency and the graph of the dielectric constant (ε') against the frequency were analyzed by a network analyzer and the dielectric measurements was analyzed using FYTRONIX Dielectric Measurement System.

3. RESULTS AND DISCUSSION

Real part of dielectric constant, imaginary part of reflection and real part of reflection of Sn doped ZnO as a function of applied frequency in the range of 1-20 GHz and at room temperature is plotted in Fig. 1. As seen in from Fig. 1, it is depicted that the real dielectric constant at high frequencies is generally unchanged, while the change is shown at low frequencies. The cases that being high frequency of dielectric constant occurs at low frequencies. This situation same all tested samples. The real and imaginary parts of reflection of the Sn doped ZnO samples were changed with Sn doping. The real part of the reflection is decreased with Sn doping. A maximum reflection for 0.5 Sn doped ZnO sample was observed at about 15 GHz. The complex dielectric function is expressed by the flowing equation:

$$\varepsilon^* = \varepsilon' - j\varepsilon'' \quad \text{.....(1)}$$

where ε'' is the real part of the dielectric function and ε'' is the imaginary part of the dielectric function. The real pat of the dielectric constant is changed with Sn content.

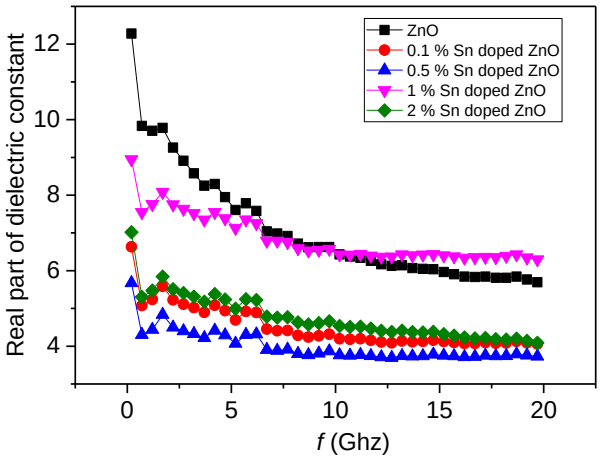

Fig. 1. Frequency dependence of real dielectric constant (ε')

The real and imaginary parts of reflection are shown in Fig. 2. The imaginary part of the reflection is decreased with the increasing frequency. By means of Sn content changed the imaginary part of the reflection. in this result, the dielectric polarization varies causing an variance in dielectric constant of Sn doped ZnO pellets.

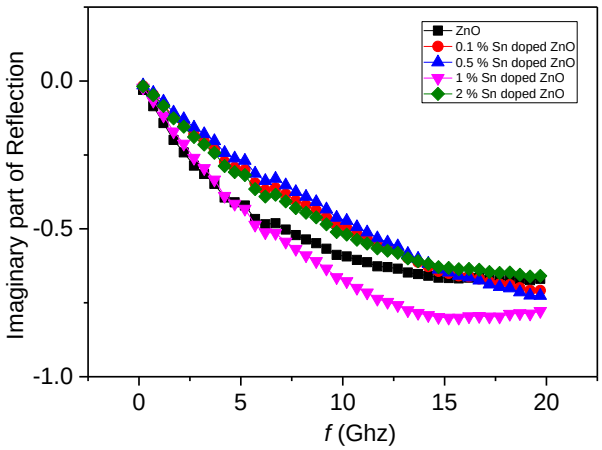

(a)

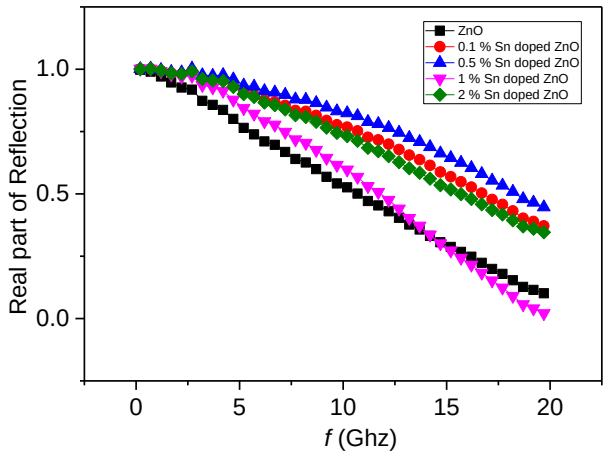

(b)

Fig. 2 a) Frequency dependence of imaginary part of reflection, b) Frequency dependence of real part of reflection.

In the real and imaginary curve of reflection, as seen in figure 2, reflections at low frequencies is higher in every 2 cases.

4. CONCLUSION

Sn doped ZnO samples were prepared for radar absorption applications. The radar absorbing properties of Sn doped ZnO samples were investigated by dielectric absorption method.

The obtained results indicate that the electromagnetic Interference properties of Sn doped ZnO samples are improved with Sn dopant.

References

[1] M. Satish Kumar a, A. Jhansi Rani, Reduction of conducted electromagnetic interference by using filters, Computers and Electrical Engineering 72 (2018) 169–178.
[2]. Fan Li , Xia F . The impedance mismatching on the EMI power filter design. In: Future wireless networks and information systems. Berlin, Heidelberg: Springer; 2012. p. 699–704 .
[3]. Fei-shuo Hung, Adding effects of Ni and Mn on electromagnetic interference (EMI) shield of Sn-based architectural materials, Trans. Nonferrous Met. Soc. China 23(2013) 2633−2637.
[4] Yin K M, Chen F R, Cang L, Kai J J, Chang C C, Ding P J, Chin B, Zhang H, Chen F S. The effect of oxygen in the annealing ambient on interfacial reactions of Cu/Ta/Si multilayers [J]. Thin Solid Films, 2001, 388(1−2): 15−21.
[5] Wolffenbuttel R F. Low-temperature intermediate Au−Si wafer bonding: Eutectic or silicide bond [J]. Sensors and Actuators A, 1997, 62(1−3): 680−686.
[6] Huixin Zhu, Yaqi Yang, An Sheng, Hongji Duan, Guizhe Zhao, Yaqing Liu, Layered structural design of flexible waterborne polyurethane conductive film for excellent electromagnetic interference shielding and low microwave reflectivity, Applied Surface Science 469 (2019) 1–9
[7] F. Shahzad, M. Alhabeb, C.B. Hatter, B. Anasori, S.M. Hong, C.M. Koo, Y. Gogotsi, Electromagnetic interference shielding with 2D transition metal carbides (MXenes),
Science 353 (2016) 1137–1140.
[8] C.H. Cui, D.X. Yan, H. Pang, L.C. Jia, X. Xu, S. Yang, Z.M. Li, A high heat-resistance bioplastic foam with efficient electromagnetic interference shielding, Chem. Eng. J. 323 (2017) 29–36.
[9] J. Lee, Y. Liu, Y. Liu, S.J. Park, M. Park, H.Y. Kim, Ultrahigh electromagnetic interference shielding performance of lightweight, flexible, and highly conductive copper-clad carbon fiber nonwoven fabrics, J. Mater. Chem. C 5 (2017) 7853–7861.
[10] Y. Chen, H.B. Zhang, Y. Yang, M. Wang, A. Cao, Z.Z. Yu, High-performance epoxy nanocomposites reinforced with three-dimensional carbon nanotube sponge for electromagnetic interference shielding, Adv. Funct. Mater. 26 (2016) 447–455.
[11] W. Zhai, S. Zhao, Y. Wang, G. Zheng, K. Dai, C. Liu, C. Shen, Segregated conductive polymer composite with synergistically electrical and mechanical properties, Compos. Part A Appl. Sci. Manuf. 105 (2018) 68–77.
[1] M. Satish Kumar a, A. Jhansi Rani, Reduction of conducted electromagnetic interference by using filters, Computers and Electrical Engineering 72 (2018) 169–178.
[2]. Fan Li , Xia F . The impedance mismatching on the EMI power filter design. In: Future wireless networks and information systems. Berlin, Heidelberg: Springer; 2012. p. 699–704 .
[3]. Fei-shuo Hung, Adding effects of Ni and Mn on electromagnetic interference (EMI) shield of Sn-based architectural materials, Trans. Nonferrous Met. Soc. China 23(2013) 2633−2637.
[4] Yin K M, Chen F R, Cang L, Kai J J, Chang C C, Ding P J, Chin B, Zhang H, Chen F S. The effect of oxygen in the annealing ambient on interfacial reactions of Cu/Ta/Si multilayers [J]. Thin Solid Films, 2001, 388(1−2): 15−21.
[5] Wolffenbuttel R F. Low-temperature intermediate Au−Si wafer bonding: Eutectic or silicide bond [J]. Sensors and Actuators A, 1997, 62(1−3): 680−686.

[6] Huixin Zhu, Yaqi Yang, An Sheng, Hongji Duan, Guizhe Zhao, Yaqing Liu, Layered structural design of flexible waterborne polyurethane conductive film for excellent electromagnetic interference shielding and low microwave reflectivity, Applied Surface Science 469 (2019) 1–9
[7] F. Shahzad, M. Alhabeb, C.B. Hatter, B. Anasori, S.M. Hong, C.M. Koo, Y. Gogotsi, Electromagnetic interference shielding with 2D transition metal carbides (MXenes),
Science 353 (2016) 1137–1140.
[8] C.H. Cui, D.X. Yan, H. Pang, L.C. Jia, X. Xu, S. Yang, Z.M. Li, A high heat-resistance bioplastic foam with efficient electromagnetic interference shielding, Chem. Eng. J. 323 (2017) 29–36.
[9] J. Lee, Y. Liu, Y. Liu, S.J. Park, M. Park, H.Y. Kim, Ultrahigh electromagnetic interference shielding performance of lightweight, flexible, and highly conductive copper-clad carbon fiber nonwoven fabrics, J. Mater. Chem. C 5 (2017) 7853–7861.
[10] Y. Chen, H.B. Zhang, Y. Yang, M. Wang, A. Cao, Z.Z. Yu, High-performance epoxy nanocomposites reinforced with three-dimensional carbon nanotube sponge for electromagnetic interference shielding, Adv. Funct. Mater. 26 (2016) 447–455.
[11] W. Zhai, S. Zhao, Y. Wang, G. Zheng, K. Dai, C. Liu, C. Shen, Segregated conductive polymer composite with synergistically electrical and mechanical properties, Compos. Part A Appl. Sci. Manuf. 105 (2018) 68–77.
[12] A. Chaudhary, R. Kumar, S. Teotia, S.K. Dhawan, S.R. Dhakate, S. Kumari, Integration of MCMBs/MWCNTs with Fe3O4 in a flexible and light weight
composite paper for promising EMI shielding applications, J. Mater. Chem. C (5) (2017) 322e332.
[13] Mondal S , Ganguly S , Das P , Bhawal P , Das TK , Nayak L , Khastgir D , Das NC . High-performance carbon nanofiber coated cellulose filter paper for electromagnetic interference shielding. Cellulose 2017;24(11):5117–31 .
[14] Kim CH , Lee Y . Fabrication and measurement of the performance of a printed EMI shielding mesh filter on PET film. Int J Precis Eng Manuf 2011;12(1):161–4 .
[15] Wang S , Maillet YY , Wang F , Lai R , Luo F , Boroyevich D . Parasitic effects of grounding paths on common-mode EMI filter's performance in power electronics systems. IEEE Trans Ind Electron 2010;57(9):3050–9 .
[16]. Duck Weon Lee, Jongwoo Park, Bum Joon Kim, Hyunsoo Kim , Changsoon Choi ,Ray H. Baughman , Seon Jeong Kim , *, Youn Tae Kim, Enhancement of electromagnetic interference shielding effectiveness
with alignment of spinnable multiwalled carbon nanotubes, Carbon 142 (2019) 528e534.
[17] F. Yakuphanoglu · Ahmed A. Al-Ghamdi ·
Farid El-Tantawy, Electromagnetic interference shielding properties of nanocomposites for commercial electronic devices, Microsyst Technol (2015) 21:2397–2405.
[18] Wertheimer N, Leeper E. Electrical wiring configurations and childhood cancer [J]. Am J Epidemiol, 1979, 109(3): 273−284.
[19] Ubeda A, Leaf J, Trillo M A, Delgado J M R. J Anat, 1982, 37: 513−536.

PHOSPHORUS DOPED GRAPHENE OXIDE BATTERY

[a]A. Dere, [b]B. Coşkun

[a]Firat University, Nanoscience and Nanotechnology Laboratory, Elazig, 23200 TURKEY

[b]Department of Physics, Faculty of Arts and Sciences, Kırklareli University, Turkey

E-mail: ayse_fizik23@hotmail.com

Abstract

Much effort has been made to produce high-efficiency, low-cost, small-sized and long-life batteries. In our research we have synthesized GO to make low-cost production of batteries attractive for this purpose Fİrstly, Firstly, graphene oxide was synthesized and then phosphorous was added to the synthesized graphene oxide at 1% atomic ratio. The electrical characteristics of the phosphorus doped graphene oxide battery were obtained at room temperature. The battery shows a high open circuit voltage (~0.13 V) and short circuit current (174 □A). The maximum power of the battery was found to be about 10 □W. The obtained results indicate that phosphorus doped graphene oxide battery can used for micropower applications.

Key Words: Organic Zinc oxide; Electromagnetic reflection

1. INTRODUCTION

The graphene consists of graphene monolayer graphite discovered by the method of mechanical exfoliation. the majority of researchers have investigate graphene oxide has many remarkable electronic features. The most important of these is the high carrier conductivity and thermal conductivity. [1]. Therefore, graphene oxide is an important material for many applications, especially batteries, sensors, diodes, capacitors, solar cells. [2-4].

The modified hummers method is one of the cheap and easy methods used for the synthesis of graphene oxide. synthesized graphene oxide can be deposited on many substrates. The oxygen within the GO provides more physical and chemical changes in the surface structure [5-9]. Graphene oxide was used in the production of batteries because it had photonic and electronic properties different from the conventional semiconductors.

Phosphorus has three allotropes, white, black and red. White phosphorus (P4) consists of 4 phosphorus atoms in the form of a plastic crystal at room temperature. The red phosphorus has many crystal types and 2 types of amorphous types. Black phosphorus can be synthesized in many different ways among allotropes of phosphorus. phosphorus is frequently used in energy storage systems due to its high performance and low cost. especially for red phosphorus lithium ion batteries, it is an anode material having high theoretical capacity and environmental friendly [10].

For new technologies, we requirement electronic energy storage devices with new functionality is very important for the future. For this reason, in present study,Phosphorus and GO based semiconductor battery was fabricated. The structural, optical and electrical properties of the prepared GO based composites were analyzed by various methods [11-15].

In the present work, we have utilized semiconducting nanocomposites of phosphor-graphene oxide to fabricate the batteries. The electrical characteristics of the battery were investigated by phosphorus content in particular.

2. MATERIALS AND METHODS

The graphene oxide (GO) was produced via the modified Hummers method. 2 grams of graphite as starting material.

2 g of graphite were mixed with a certain amount of NaNO3 in a certain volume of H2SO4. 6.0 g of KMNO4 was added slowly throughout 1 hour at 10 min intervals. this was done while the solution was in an ice bath. After 1 hour, the ice was removed from the mixture. Then adding 200 mL of deionized water solution was raised to 95 degrees. Then water (200ml) and H2O2 (30ml %35) were added and stirred for one hour then the reaction was terminated. The mixture was rinsed with water and HCl %5 (H2O:HCl,

2:20) until the pH was neutral and centrifuged. The resulting graphene powder was dried at 50 ° C for 2 days.

The synthesized GO was dispersed in deionized water (2 mg/mL) using stirring for 15 min. and then, it was ultrasonically sonicated for 1 h. GO doped Phosphours composites were prepared for %1 weight ratios of (x = GO : P). The solutions of the composite was coated on ultrasonic clean glass substrate by drop coating method. The diagram of the %1 phosphor doped GO battery is shown in figure 1. Also

3M copper chloride electrolyte CuCl2 was prepared in deionized water. The battery was prepared using two Al electrode battery . The surface morphology of the composites was analyzed using a EVO MA10 Carl Zeiss scanning electron microscope. The current-voltage characteristics of the batteries were measured using a FYRONIX electronic devices characterization system.

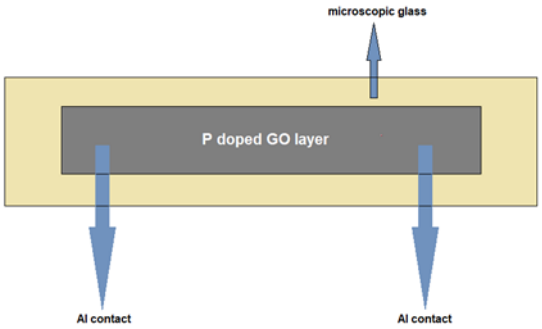

Fig 1. Diagram of %1P doped GO battery

3. RESULTS AND DISCUSSION

The structural properties of film %1 P doped graphene oxide was coated on the microscopy glass. was investigated using SEM. The scanning electron microscopy results of the composites are shown in Fig. 2(a–b) under various magnification. The P doped GO samples show the nano-sized particles and exfoliated graphene oxide. The current-voltage characteristics of the battery were analyzed at 30 oC. In Fig 3 shows power-voltage curve, as seen in Fig3, the battery exhibits a maximum power of 1.02 μW.

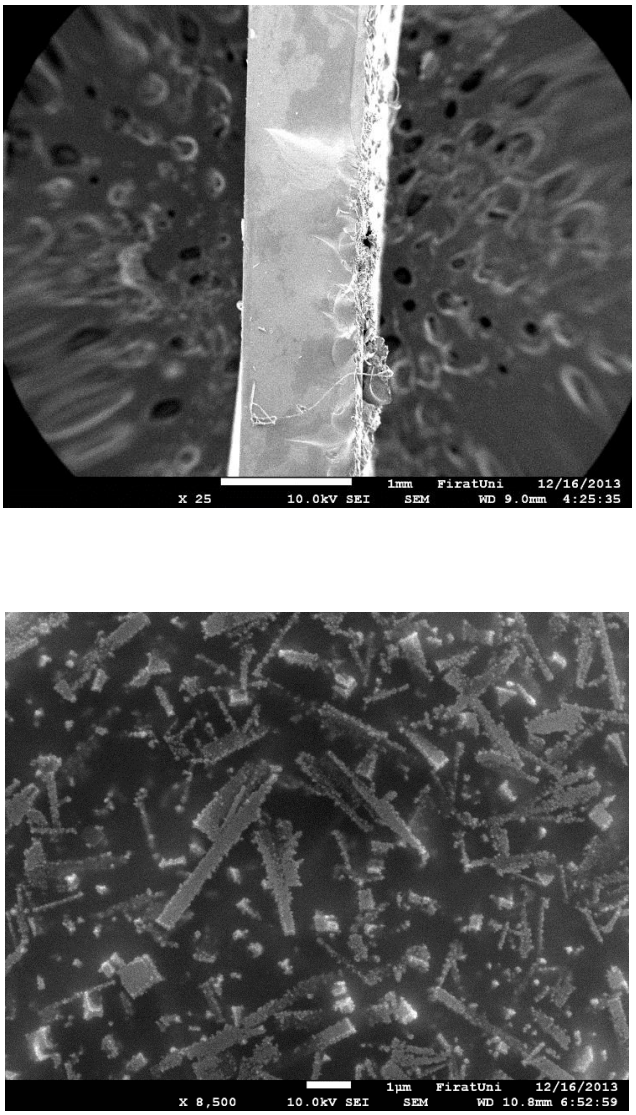

Fig.2. SEM images of the composites. a) %1 P doped GO electrode.

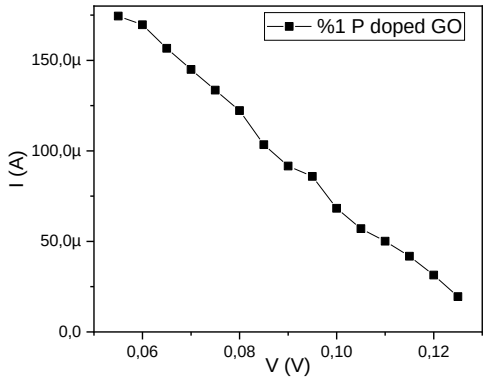

Fig3: I-V characteristics of %1 phosphorus doped graphene oxide battery.

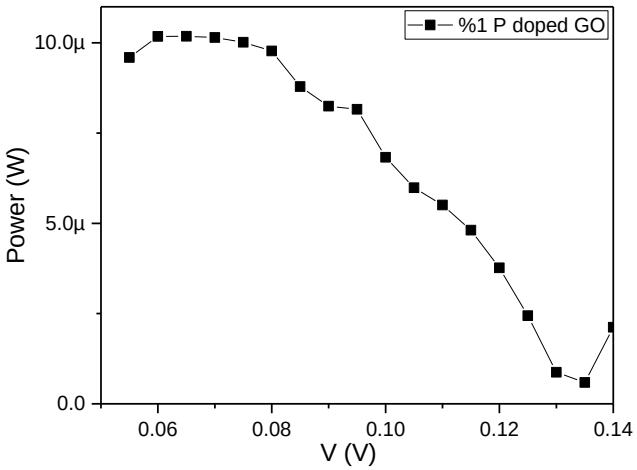

Fig4: P-V characteristics of %1 phosphorus doped graphene oxide battery.

1% P doped GO coated on glass substrate. 2 mm area is not coated on the sides of the glass base to prevent short circuit. One of the aluminum contacts is touched on the uncoated glass and the other on the coated surface. Then the CuCl2 electrode was dropped and the electrical properties of the battery were characterized.. The current-voltage (I-V) and power voltage (P-V) characteristics of the battery were measured using a FYRONIX battery system. I-V and P-V curves of the batteries are respectively, shown in Fig. 3 and Fig 4. The open circuit voltage Voc, short circuit current Isc, maximum power Pmax, maximum voltage Vmax and maximum current Isc values are given in Table 1. As seen in Table, the obtained electrical parameters of P doped GO based battery indicate that the studied battery can be used for micropower applications.

Table 1 Electrical parameters of the batteries.

Battery	I_{sc}(μA)	V_{oc} (V)	I_{max} (μA)	V_{max} (V)	P_{max} (μW)
%1 P: GO	174	0.13	14.57	0.07	10.2

As seen in Table 1,. The battery having P:GO=%1 composite exhibited the maximum voltage of 0.07 V.

4. CONCLUSION

P doped GO battery sample was synthesized using chemical method. The battery was prepared using FYRONIX two electrode battery holder. The battery gives open circuit voltage (130 mV) and short circuit current (174 μA) The results indicate that the electrical performance of the prepared battery can be improved with P contents.

References

[1] A.Mekki , A. Dere, Kwadwo Mensah-Darkwa, Ahmed Al-Ghamdi, R.K. Gupta, K. Harrabi , W.A. Farooq, Farid El-Tantawy, F. Yakuphanoglu, Graphene controlled organic photodetectors, Synthetic Metals, 217(2016)–56

[2]. R.K. Gupta, Z.A. Alahmed, F. Yakuphanoglu, Graphene oxide based low cost battery, MAterials Letters, Vol.112, 1 December 2013, Pag 75-77.

[3] K.S Novoselov, A.K. Geim, S.V. Mozorov, D.Jiang, M.I. Katsnelson, Grigorieva IV, et al., Two-dimensional gas of massless Dirac fermions in graphene, Nature, 438 (2005),pp. 197-200

[4] J. Hou, R. Wu, P. Zhao, A. Chang, G. Ji, B. Gao, et al., Graphene-TiO2 (B) nanowires composite material: synthesis, characterization and application in lithium-ion batteries., Materials Letters, 100 (2013), pp. 173-176.

[5] Feng H, Cheng R, Zhao X, Duan X, Li J. A low-temperature method to produce highly reduced graphene oxide. Nature Communications 2013;4:1539.

[6] Jin Y, Huang S, Zhang M, Jia M, Hu D. A green and efficient method to produce graphene for electrochemical capacitors from graphene oxide using sodium carbonate as a reducing agent. Applied Surface Science 2013;268:541–6.

[7] Marcano DC, Kosynkin DV, Berlin JM, Sinitskii A, Sun Z, Slesarev A, et al. Improved synthesis of graphene oxide. ACS Nano 2010;4:4806–14.

[8] He G, Li J, Chen H, Shi J, Sun X, Chen S, et al. Hydrothermal preparation of Co3O4@graphene nanocomposite for supercapacitor with enhanced capacitive performance. Materials Letters 2012;82:61–3.

[9], Dreyer DR, Park S, Bielawski CW, Ruoff RS. The chemistry of graphene oxide. Chemical Society Reviews 2010;39:228–40..

[10] Cheng Liu Xinpeng Han Yu Cao Shiyu Zhang Yiming Zhang Jie Sun, Topological construction of phosphorus and carbon composite and its application in energy storage, Available online 31 October 2018.

[11] A. Dere, Perylene-3,4,9,10-tetracarboxylic dianhydride (PTCDA) based composites organic battery, Physica B: Condensed Matter, 547, 2018 127-133.

[12] A. Jouili, S. Mansouri, Abdullah G. Al-Sehemi, Ahmed A. Al-Ghamdi, L. ElMira, F. Yakuphanoglu, Numerical studies of surface potential, mobility and Seebeck coefficient of organic thin film transistor based on 2,3 benzanthracene: light effect, Synth. Met. 233 (November 2017) 119–126

[13] Świst Agnieszka, Sołoducho Jadwiga, Organic semiconductors – materials of the future? CHEMIK 66 (4) (2012) 289–296.

[14] Simon Muench, Andreas Wild, Christian Friebe, Bernhard Häupler, Janoschka Tobias, Ulrich S. Schubert, Polymer-based organic batteries, Chem. Rev. 116 (16) (2016) 9438–9484

[15]. Haiyan Chen, Michel Armand, Gilles Demailly, Franck Dolhem, Philippe Poizot, Jean-Marie Tarascon, From biomass to a renewable LiXC6O6 organic electrode for sustainable Li-Ion batteries, ChemSusChem 1 (2008) 348–355.